APPLICATIONS OF THE INTERCEPT METHOD TO CORRECT STEADY-STATE RELATIVE PERMEABILITY FOR CAPILLARY END-EFFECTS

Robin Gupta and Daniel Maloney
ExxonMobil Upstream Research Company

This paper was prepared for presentation at the International Symposium of the Society of Core Analysts held in St. John's Newfoundland and Labrador, Canada, 16-21 August, 2015

ABSTRACT

During coreflood tests in the laboratory to determine relative permeability, capillary discontinuities at sample ends influence fluid flow and retention. When this influence or end-effect artifact is appreciable, the laboratory data incorrectly models the reservoir-condition scenario, which may result in serious errors in reservoir performance predictions. The end effect artifact is a well-known problem with unsteady-state test data. It is also an issue with steady-state data; it is typically handled by increasing sample length or experiment flow rates. Increasing sample length by arranging a series of core plugs to create a long composite is not a perfect fix to the end-effect issue, because end-effects can still exist between core plugs as well as at the end of the composite. Increasing flow rate may not be possible for gas-liquid or gas-condensate tests in which the experimentalist limits pressure drop because of mass transfer considerations.

The "Intercept Method" is a modified steady-state approach that corrects data for end-effect artifacts while conducting the test. Corrections are determined from simple calculations based on multiple rates versus pressure drop measurements at each test fractional flow condition. Application of the method does not depend upon a-priori characterization of capillary pressure versus saturation. This work focuses on the application of the Intercept Method and demonstrates lab examples of gas-liquid, gas-condensate and liquid-liquid systems in which end-effect errors induce the artifact of flow rate dependence in relative permeability measurements. However, after applying the Intercept Method on the same data, the rate-dependent family of curves collapse into a set of unique, flow rate independent, end-effect corrected curves. Along with end-effect correction, the method also simultaneously corrects errors from capillary discontinuities between core plug faces in a composite and pressure transducer zero-errors. The workflow of the method is explained and demonstrated through several lab test examples.

INTRODUCTION

The steady-state relative permeability method consists of co-injecting fluids in steps of increasing or decreasing fractional flow, allowing sufficient time at each step to establish equilibrium before recording data. Pressure and saturation data at steady-state conditions are used to generate relative permeability versus saturation curves for each fluid phase.

Capillary end-effects (CEE) yield pressure drop and saturation artifacts that cause errors in laboratory-measured steady-state relative permeability functions [1, 2]. Deviations of relative permeability with rate have been observed only where boundary effects are known to exist, and disappear as the boundary effect vanishes [2, 3]

The end-effect decreases as the length of the flooded system, rate of injection, or fluid viscosities are increased [4, 5]. However, the end effect can occur in the individual segments of a long composite core [1, 6] due to capillary discontinuities. Performing high injection rate or pressure drop tests might not be possible in many cases due to phase behavior (e.g., gas-condensate) or rock reactivity (e.g. clay-rich cores) considerations [1]. High pressure drop can yield problematic gas compressibility effects, phase behavior changes in gas-condensate tests, and fines migration issues in a clay-rich rock. For laboratory tests on tight rocks, pressure drops high enough to mask end-effects may be impractical to attain without causing other experimental artifacts.

Numerical approaches to correct relative permeability data for capillary end-effects are often complex and require additional information [7] (in-situ saturations, independent measures of capillary pressure versus saturation functions), and might not provide unique solutions. Another end-effect correction approach is to use internal pressure taps in combination with in-situ saturation monitoring [3], Using internal pressure taps is challenging for reservoir condition tests in which core is jacketed with metal foil to prevent gas permeation through the core sleeve. Also, additional pressure taps do not guarantee to eliminate end-effect errors between core plugs in stacked composites.

A plot of pressure drop (ΔP) versus flow rate (Q) is frequently used as a diagnostic in routine and special core analyses. If the data is linear but the intercept is not zero (Figure1a), the experimentalist may interpret that the offset is the result of a transducer zero shift or gravity head. When the data is subsequently "corrected" for the offset (Figure 1b), each measurement yields the same permeability. If an offset correction is not applied, a different permeability is calculated from each measurement (Figure 1c) and it will seem that permeability depends upon flow rate.

We have found in multiphase steady-state lab tests that when the length over which ΔP is measured is the entire length of the sample, capillary end-effects cause a positive or negative ΔP intercept shift similar to the illustration of Figure 1a. The effect is easy to identify when multiple rates are tested at each steady-state flow ratio or fractional flow condition. A simple saturation correction is also easily determined and applied. This work is a companion to a previous publication[1] that focused on descriptions of background, theory, and simulation followed by brief examples from two gas-condensate systems. The focus of this work is from an experimentalist perspective, with brief description of the method followed by examples of its use in gas-condensate, gas-water, and oil-water systems using published and in-house data.

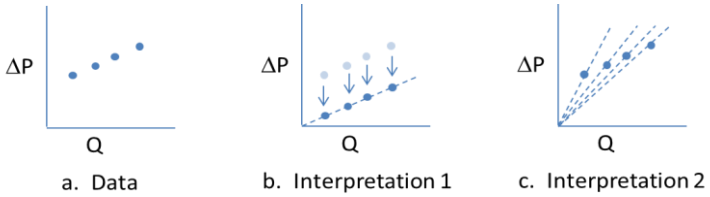

Figure 1: Conceptual relationships between pressure drop and rate for different flow scenarios.

CONCEPT

The capillary end-effect (CEE) results from a capillary discontinuity at the core outlet that causes accumulation of one phase relative to the other. Figure 2 is a schematic of water saturation in a water-oil steady-state coreflood test. In the figure, saturations are Sw_{CEE}, average water saturation in the CEE region; $Sw_{Measured}$, average measured water saturation; and Sw_{True}, water saturation in the non-CEE region. The CEE region, which develops because of the capillary discontinuity at the outlet end of the sample, influences both pressure drop and saturation measurements in a steady-state coreflood test. When a CEE artifact is appreciable, the laboratory data incorrectly models the reservoir scenario, which may result in erroneous reservoir performance predictions. Hence, it is important to estimate and correct CEE-related errors in lab tests.

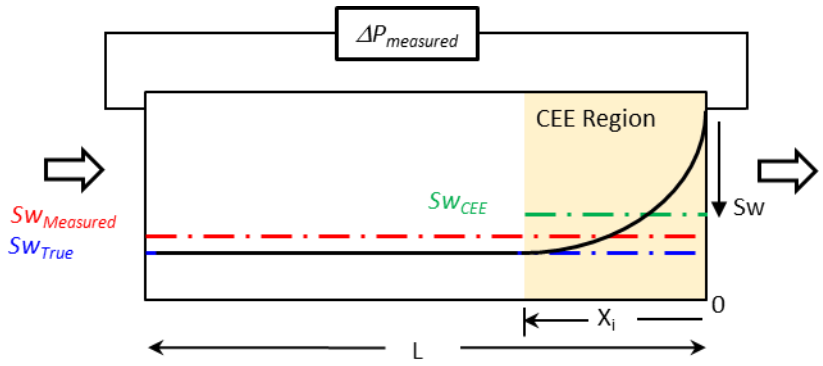

Figure 2: Schematic of water saturation in an oil-water steady-state coreflood[1], where $Sw_{Measured}$ = core average saturation, Sw_{CEE} = average saturation inside CEE region, and Sw_{True}= saturation outside CEE region.

The Intercept Method corrects CEE errors from both pressure and saturation measurements for each fractional flow condition during a steady-state coreflood test. Gupta and Maloney have described the theory in detail [1]. In a conventional steady-state relative permeability test, phases are co-injected with increasing or decreasing fractional flow, with a steady-state condition achieved at each fractional flow. For the Intercept Method, in addition to the conventional approach, the steady-state condition is achieved at multiple flow rates at each fractional flow. Trends in pressure drop and saturation versus rate are used to correct the data set for the capillary end effect at the current fractional flow. The corrected pressure and saturation data are subsequently used to calculate CEE-corrected relative permeability curves using Darcy's law.

Pressure Correction

The measured pressure drop across the core ($\Delta P_{measured}$) is the sum of the theoretical pressure drop ($\Delta P_{Corrected}$) which would occur if there were no CEE in the core plus the pressure drop resulting from the CEE (ΔP_{CEE}). Gupta and Maloney[1] demonstrated through analytical calculations that the ΔP_{CEE} is independent of the total flow rate (for Stokes flow or Darcy flow) for a given fractional flow (assuming CEE region is smaller than the core length) in a steady-state coreflood test. For the Intercept Method application, steady-state pressure drop versus total flow rate is plotted for a given fractional flow. The plot normally has a linear trend with a non-zero intercept (ΔP_I). This linear trend between $\Delta P_{measured}$ and total flow rate has been observed in lab tests discussed later in this paper and previous work [1]. Based on the above discussion, ΔP_I is equal to ΔP_{CEE}, assuming $\Delta P_{measured}$ are corrected for gauge zero offset. If a pressure gauge offset exists, then ΔP_I will equal ΔP_{CEE} plus the offset error. The offset error can be determined at the beginning or end of the test and can be discounted from ΔP_I to get the true ΔP_{CEE} value for each fractional flow. The CEE-corrected pressure drop is the difference of the measured pressure drop across the core ($\Delta P_{measured}$) and the intercept (Figure 3a).

$$\Delta P_{Corrected} = \Delta P_{measured} - \Delta P_I \quad (1)$$

Figure 4 is a schematic of phase pressures inside a composite at a steady state condition for a typical oil-water coreflood. CEE results in additional positive pressure drop resistance to one phase and a reduced resistance to the other. However, the CEE-corrected pressure drop of each phase is the same. The CEE-corrected phase pressures differ by a constant value equivalent to capillary pressure at CEE-corrected saturation (Sw_{True}). Hence, the Intercept Method can be applied using an apparatus in which pressure drop is measured for one phase instead of both phases.

Saturation Correction

Gupta and Maloney [1] demonstrated that the average saturation in the CEE region is independent of the total flow rate for a given fraction flow. They derived that the CEE-corrected saturation (Sw_{True}) for a given fractional flow is the intercept of the plot of $Sw_{avg}/(1-\beta)$ [y-axis] and $\beta/(1-\beta)$ [x-axis], where β is $\Delta P_I/\Delta P_{Corrected}$ and Sw_{avg} is the average saturation in the core (Figure 3b). The derivation assumes that drop measurements across the core are corrected for gauge zero offset. The Intercept Method corrects not only the capillary discontinuity at the core outlet end, but also the capillary discontinuities between the plug junctions in a composite when multiple core plugs are stacked in series (Figure 5). The additional pressure resistance from capillary discontinuities (inside and at the end) is reflected in the intercept (ΔP_I) of the pressure correction plot (Figure 3a). Subtracting the intercept (ΔP_I) from the lab measured pressure drop across the composite gives the CEE-corrected pressure drop.

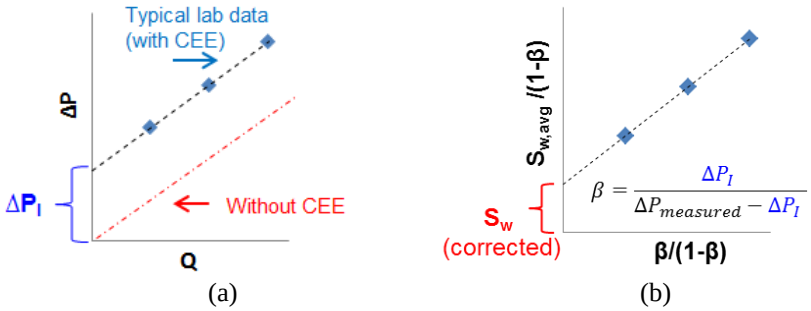

Figure 3: Schematic plots used during the Intercept Method application, (a) pressure drop versus total flow rate plot, where CEE-corrected pressure drop is the difference between the lab-measured pressure drop across the core and the intercept, and (b) saturation plot, where intercept is the CEE-corrected saturation.

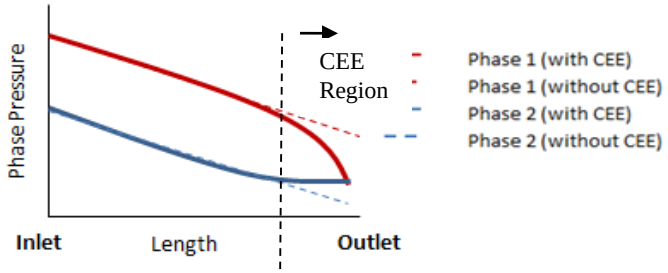

Figure 4: Schematic of phase pressures with and without CEE at steady-state condition inside a composite core.

For saturation correction, the capillary discontinuities between plugs only change the slope of the saturation correction plot (Figure 3b), but the intercept remains the same and equal to the CEE-corrected saturation. Similarly, the Intercept Method also corrects for the apparatus related errors, e.g., gauge zero errors, and from the pressure drop measurements. However, the apparatus-related pressure drop is subtracted from the intercept of pressure drop versus flowrate plot before performing saturation correction.

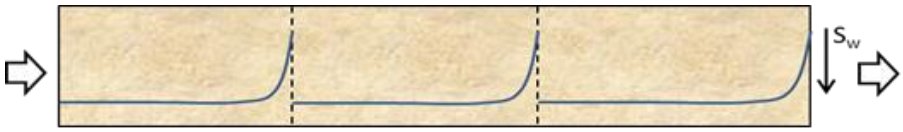

Figure 5: Schematic of water saturation in a composite core during an oil-water steady-state test with capillary discontinuities between the plugs.

METHOD APPLICATION AND DISCUSSION

The Intercept Method is applicable for liquid-liquid, gas-liquid, and gas-condensate steady-state relative permeability tests. The method provides CEE-correction for tests performed at low rates and pressure drops. Data are corrected as measured, without requiring in-situ saturation monitoring, internal pressure taps, or simulation. A common manifestation of CEE is the flowrate dependence artifact in "Stokes flow[8]" relative permeability measurements. Chen and Wood [3] demonstrated that steady-state relative permeability results were independent of test flow rates. The Intercept Method addresses the flow rate dependent artifact in measured relative permeability curves.

In a steady-state relative permeability test, application of the Intercept Method requires attaining steady-state at multiple rates for each fraction flow. A minimum of two total flow rates per fractional flow is required to apply the method; however, 3 to 4 total flow rates per fractional flow is recommended to generate high-confidence pressure and saturation correction plots (Figure 3). The time to attain additional steady-state points is very small compared to the first total flow rate for each fractional flow point. In theory, the additional steady-state total flow rates are instantaneous. Hence, the Intercept Method application adds relatively small incremental test time over that from a conventional steady-state test. Total flow rates are increased in steps to avoid hysteresis effects for the same fractional flow. The total flow rate can be reduced concurrently with stepping to the next fractional flow. Since the saturation change is significant between two consecutive fractional flows, reducing total flow rate between consequent fractional flows imposes minimal hysteresis. The Intercept method application requires CEE region to be shorter than the core length. Below a critical total flow rate, which is typically a low value, CEE region can encompass the entire core length. Below this critical rate, the pressure and saturation correction plots (Figure 3) are not linear [1]. While applying the method, it is recommended to discard the low total flow rate data that is off the linear trend [1].

Laboratory Application on Gas-Condensate System

Results of Henderson et al. [9] are evaluated by the methods of this paper. The rate, pressure drop, and saturation data are interpreted from figures in their paper. Fluid viscosities are assumed the same as those from Jamiolahmady et al. [10] The data sets are from steady-state gas-condensate relative permeability measurements with fluids of 0.14 mN/m and 0.9 mN/m interfacial tension (IFT).

Figure 6 shows pressure drop versus total flow rate for the two systems for three condensate-to-gas flow ratios (CGR). Trend lines through the data sets for each CGR are linear, but in each case, ΔP intercepts are non-zero. These non-zero intercepts (Figure 6) and shifts in saturation with increasing rate at constant CGR (Figure 7) are indicative of capillary end-effects. When intercept corrections are applied to the data sets, the net result is a set of relative permeability curves that are rate-insensitive rather than a family of curves that appear to be rate-sensitive. This is shown in Figure 7, which compares curves from the original work (white and grey data points) with those after correction for capillary end-effects ("final" data points). The corrected curve is close to that from the highest total flow rate test, which corroborates with the theory [4]. For a given IFT, the gas-condensate curve is unique (rate independent); however, change in IFT influences the curve. As expected, the relative permeability is higher at lower IFT (Figure 7).

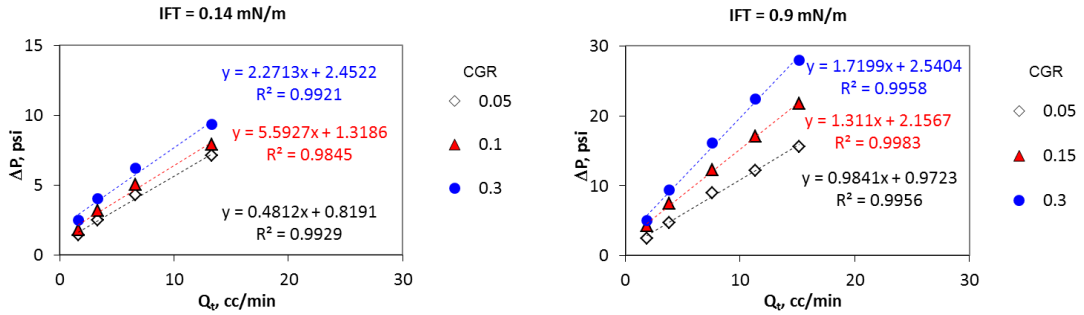

Figure 6: Pressure drop versus total flow rate for 0.14 and 0.9 dynes/cm interfacial tension systems.

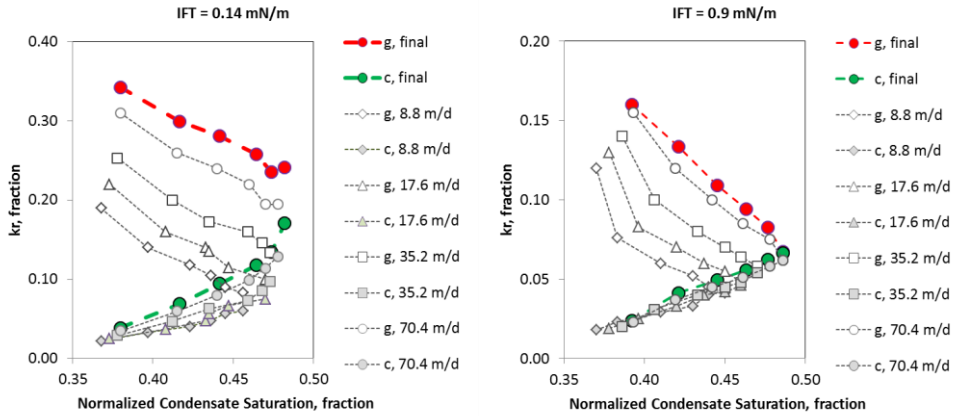

Figure 7: Gas and condensate relative permeability versus normalized condensate saturation.

Another condensate example that shows rate-independent relative permeability curves after the Intercept Method correction is provided by Gupta and Maloney [1]. Figure 6 of Ayyalasomayajula et al. [11], which is approximated as Figure 8a below, presents what is described as "typical rate versus pressure drop data" measured during gas condensate relative permeability measurements for samples from a deep marine sandstone reservoir. The data were used to show that condensate relative permeability curves are sensitive to rate and capillary number. In Figure 8b, stabilized pressure drops from Figure 8a are plotted against rate. The three data points are collinear (blue dashed line) with a ΔP intercept of almost 19 psi. Correcting for this non-zero intercept removes the rate-sensitivity that otherwise would be interpreted when the data points are considered independently (grey dashed lines on Figure 8b).

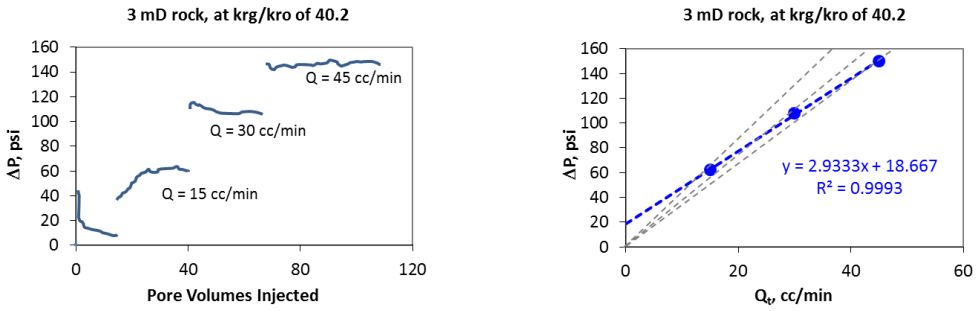

a) Pressure drop versus PV injected b) Pressure drop versus rate

Figure 8: (a) Pressure drop versus pore volumes injected[11], and (b) interpretation of results.

Laboratory Application on Gas-Water System

This example illustrates a laboratory application of the Intercept Method on a gas-brine drainage steady-state relative permeability test. The composite permeability was 8.7 mD. At the beginning of the test, the composite was completely saturated with synthetic formation brine. During the test, gas and synthetic formation brine were co-injected through the composite with increasing gas-to-brine flow ratios ranging from 0:1 to 1:0. At each steady-state condition, 3 to 4 sets of total flow rates were tested while maintaining the same gas-to-brine flow ratio. The Intercept Method was applied to correct capillary end-effect related errors in pressure drop and saturation data, which were later used to calculate corrected relative permeability curves.

Figure 9 shows steady-state relative permeability results with and without capillary end-effect corrections. Application of the Intercept Method resulted in up to 51 % pressure drop correction and brine saturation correction of up to 0.06 saturation fraction units. Because of the significant end-effect correction in this example, there is a substantial difference between uncorrected and corrected relative permeability curves (Figure 9). In this experiment, the coefficient of determination (R^2) was greater than 0.99 for all pressure and saturation correction plots except the last set (lowest S_w). Figure 10 shows the pressure and saturation correction plots for gas-to-brine flow ratio of 99:1. The experimental data follow linear trends for both the plots with about 50 % correction in pressure drop. The last point (lowest S_w) is off-trend potentially due to wrong phase pressure measurement or other experimental errors. Overall, this case study clearly demonstrates that capillary end-effects can be significant for a gas-water system, and that the Intercept Method can be applied to obtain capillary end-effect corrected relative permeability curves.

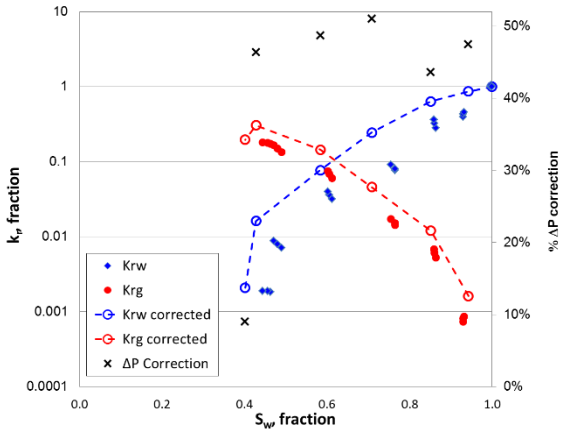

Figure 9: Gas-water drainage steady-state relative permeability test. Test data and Intercept Method corrected results are shown along with % pressure drop correction.

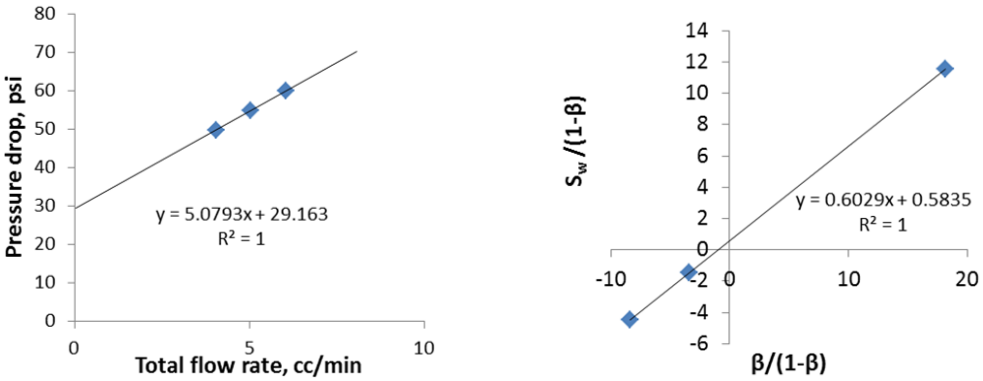

(a) (b)

Figure 10: Pressure drop (a) and saturation correction (b) plots using the Intercept Method at gas:brine flow ratio of 99:1.

Another example of ΔP intercept correction is shown by Grattoni et al. [12]. From transient pressure decay tests in rock partially saturated with water, they found that gas stopped flowing before pressure drop decayed to zero. They termed this non-zero ΔP the "water-blocking pressure." From multi-rate steady-state gas injection tests with constant water saturation, they also found that plots of pressure drop versus rate were linear but ΔP intercepts were positive. They suggested a saturation-dependent correction to the Darcy equation to correct for non-zero ΔP intercepts. Although there are several possible reasons for their non-zero intercepts, the data closely resembles that described in this paper.

Laboratory Application on Oil-Water System

This example illustrates a laboratory application of the Intercept Method on a data set from an oil-brine primary drainage steady-state relative permeability test. The data are from Virnovsky et al. [13] from a study in which steady-state drainage relative

permeabilities were measured during repeat tests with three distinct total flow rates (low, medium and high rates of 0.2, 0.5, and 5.0 mL/min). This data set was selected because it is descriptive and readily available from the literature. Relative permeability test results from low, medium, and high rate tests are shown in Figure 11 (grey data points). Without CEE correction, there appears to be flow rate dependence in the relative permeability curves of this test. The Intercept Method was applied. Corrected results are shown in Figure 11 (green and blue data points). The Intercept Method successfully collapsed the family of lab-generated curves into a unique, rate-independent set of relative permeability curves.

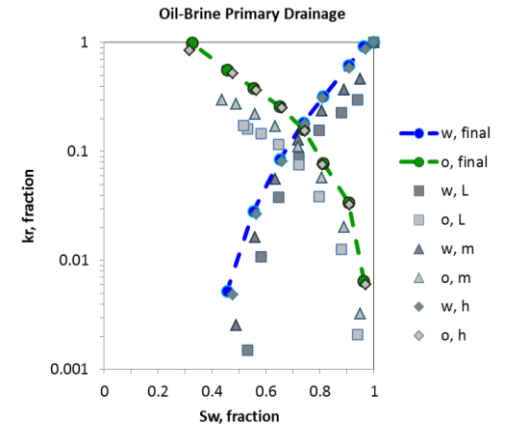

Figure 11: Lab generated, and the Intercept Method corrected primary drainage relative permeability curves.

Figure 12 shows the pressure correction plots for different water fractional flows for this test. The trends are linear with non-zero ΔP intercept. Similarly, saturation correction plots also were of good linearity (not shown). Pressure drops from measurements with the highest total flow rate (5 mL/min) were significantly higher than the non-zero ΔP intercepts in this test. For this reason, relative permeabilities from the highest total flow rate test (5 mL/min) are similar to the CCE-corrected curves.

The Intercept Method of this paper was developed after collectively reviewing data from a variety of multiphase steady-state laboratory flow tests in which several sets of rates and pressure drops were measured for each steady-state fractional flow. In each case, non-zero ΔP intercepts and saturation shifts were revealed, which led to the development of methods described in this paper.

We speculate that the need for an end-effect correction to steady-state relative permeability data has received little attention previously because most multiphase steady-state tests are not conducted with multiple rates at each fractional flow. In general, most studies that use multiple rates for each fractional flow look for rate effects, such as a velocity enhancement effect in gas-condensate systems or visco-inertial flow effects in high rate gas-liquid systems. Our impression is that when multi-rate data is available, the end-effect artifacts described herein will be evident.

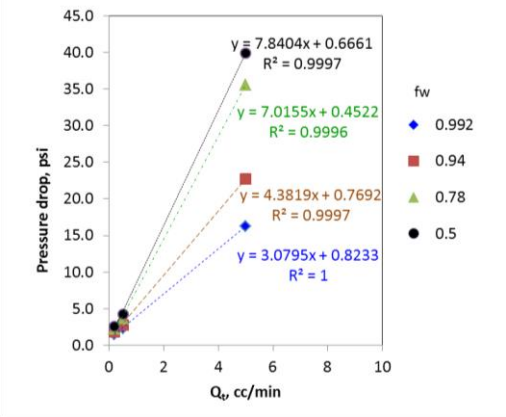

Figure 12: Pressure drop versus total flow rate at different water fractional flows for oil-water system.

Examples of this paper were drawn from the literature and in-house tests to demonstrate that end-effects influence multiphase flow laboratory data irrespective of fluids used and techniques applied in gaining the measurements. The methods of this paper are simple to apply in gaining steady-state data corrected for capillary end-effects.

CONCLUSIONS

This work demonstrates the Intercept Method that can correct capillary end-effect errors in steady-state relative permeability test data.

- The method enables attainment of CEE corrected steady-state relative permeability in systems where performing high pressure drop or high total flow rate tests would be challenging, such as in gas-liquid systems or when testing tight or clay-rich rocks.
- The Intercept Method can be applied during a test to correct for CEE errors as data is measured without necessitating the use of additional simulation, internal pressure taps, or in-situ saturation monitoring effort.
- The Intercept Method can be applied to liquid-liquid, gas-liquid and gas-condensate steady-state relative permeability data to correct for CEE artifacts. The CEE corrected plots are unique and independent of flow rates.
- The velocity enhancement effect that has been described in the literature from laboratory gas-condensate relative permeability measurements is likely the result of CEE artifacts. A gas-condensate curve is unique and flowrate independent; however, it is sensitive to IFT changes.

ACKNOWLEDGEMENTS

We thank Lisa Lun, Jim Kralik, Ted Braun (consultant), Bo Gao, David Laverick, Robert Longoria, Daniel Berry, Larry Poore, Brad Milligan, Loan Vo, Sergio Leonardi and Prateek Patel of ExxonMobil URC for their valuable contributions to this work. Appreciation is also expressed to ExxonMobil Upstream Research Company for the opportunity to present this work.

REFERENCES

1. Gupta, R., and Maloney, D. R.: "Intercept Method - A Novel Technique to Correct Steady-State Relative Permeability Data for Capillary End-Effects," Society of Petroleum Engineers, (November 10, 2014), doi:10.2118/171797-MS.
2. Osoba, J. S., Richardson, J. G., Kerver, J. K., Hafford, J. A., and Blair, P. M.: "Laboratory Measurements of Relative Permeability," Society of Petroleum Engineers, (February 1, 1951), doi:10.2118/951047-G.
3. Chen, A. L, and Wood, A. C.: "Rate Effects on Water-Oil Relative Permeability," Paper SCA2001-19 presented at the 2001 Symposium of the Society of Core Analysts, Edinburgh, Scotland, (September 19, 2001).
4. Rapoport, L. A., and Leas, W. J.: "Properties of Linear Waterfloods," Society of Petroleum Engineers, (May 1, 1953), doi:10.2118/213-G.
5. Richardson, J. G.: "The Calculation of Waterflood Recovery From Steady-State Relative Permeability Data," Society of Petroleum Engineers, (May 1, 1957), doi:10.2118/759-G.
6. Hinkley, R. E., and Davis, L. A.: "Capillary Pressure Discontinuities and End Effects in Homogeneous Composite Cores: Effect of Flow Rate and Wettability," Society of Petroleum Engineers, (January 1, 1986), doi:10.2118/15596-MS.
7. Qadeer, S., Dehghani, K., Ogbe, D. O., and Ostermann, R. D.: "Correcting Oil/Water Relative Permeability Data for Capillary End Effect in Displacement Experiments," Society of Petroleum Engineers, (January 1, 1988), doi:10.2118/17423-MS.
8. American Petroleum Institute (1998, February). *Recommended Practices for Core Analysis*, Recommended Practice 40, 2nd Edition, p. 107.
9. Henderson, G. D., Danesh, A., Tehrani, D. H., Al-Shaldi, S., and Peden, J. M.: "Measurement and Correlation of Gas Condensate Relative Permeability by the Steady-State Method," Society of Petroleum Engineers, (1996, June 1), doi:10.2118/31065-PA .
10. Jamiolahmady, M., Sohrabi, M., and Ireland, S.: "Gas Condensate Relative Permeability of Low permeability Rocks: Coupling Versus Inertia," Society of Petroleum Engineers, (January 1, 2009), doi:10.2118/120088-MS.
11. Ayyalasomayajula, P., Silpngarmlers, N., Berroteran, J., Sheffield, J., and Kamath, J.: "Measurement of Relevant Gas Condensate Relative Permeability Data for Well Deliverability Predictions for a Deep Marine Sandstone Reservoir," Paper SCA2003-33 presented at the International Symposium of the Society of Core Analysts, Pau, France, (September 21-24, 2003).
12. Grattoni, C., Al-Hinai, S., Guise, P., and Fisher, Q.: "The Role of Interstitial Water in Hydrocarbon Flow for Tight Rocks," Paper SCA2007-14 presented at the International Symposium of the Society of Core Analysts, Calgary, Canada, (September 10-12, 2007).
13. Virnovsky, G. A., Vatne, K. O., Skjaeveland, S. M., and Lohne, A.: "Implementation of Multirate Technique to Measure Relative Permeabilities Accounting for Capillary Effects," Society of Petroleum Engineers, (January 1, 1998), doi:10.2118/49321-MS.

NUMERICAL SIMULATION OF COMBINED CO-CURRENT/COUNTER-CURRENT SPONTANEOUS IMBIBITION

Douglas W. Ruth[1], Geoffrey Mason[2], Martin A. Fernø [3], Åsmund Haugen[4]
Norman R. Morrow[2], Rasoul Arabjamaloei[1]
[1]Centre for Engineering Professional Practice and Engineering Education, University of Manitoba, Canada
[2] Department of Chemical and Petroleum Engineering, University of Wyoming, USA
[3]Department of Physics and Technology, University of Bergen, Norway
[4]Statoil , Sandslihaugen, Bergen, Norway

This paper was prepared for presentation at the International Symposium of the Society of Core Analysts held in St.John's, Newfoundland and Labrador, Canada, 16-21 August, 2015

ABSTRACT

This paper describes a numerical study of combined co-/counter-current spontaneous imbibition of water into a core sample that is initially fully oil saturated with the two-ends-open-free (TEO-free) boundary geometry, as given by a sample with one end in contact with brine and the other in contact with oil. The present study uses an explicit simulator with an upstream differencing scheme which allows flows of the oil in both directions without blockage because of zero-saturation cells. The boundary conditions are modelled using zero-width boundary cells with fixed saturations. The saturation at the end face in contact with brine fixes the capillary bubble pressure (the pressure required to produce non-wetting fluid) at this face. All the simulations used a single set of relative permeability curves. The experimental results were matched using an automatic search technique with the capillary pressure curve as the fitting parameter. In all cases, tabular values of capillary pressure were used, with six points in the curves and linear interpolation between points. Fits were achieved using the oil productions at the two faces as the test data. It was found that all the data could be fitted using comparable capillary pressure curves. A comparison between the results obtained using the numerical simulator and a piston-like flow model published with the original experimental data provides support for the assumption of piston-like flow. The paper demonstrates both the power of numerical simulation and the urgent need for a method to either predict or accurately measure the imbibition face saturation during spontaneous imbibition.

INTRODUCTION

The problem of co-current and counter-current imbibition has attracted much recent interest in the petroleum community because these are the mechanisms whereby matrix

oil can be produced into fractures in a reservoir [1,2]. There is now a body of experimental data for short samples undergoing these processes as well as an approximate theory to explain the observed behaviour [3,4,5]. The present paper reports on a numerical-simulation study of a selection of these data. The numerical simulator is a further development of work reported previously [6,7,8,9].

The problem under consideration is shown schematically in Figure 1. A sample, originally saturated with oil, is confined radially by a sealed surface. It is then set up axially between two reservoirs, a reservoir that is filled with water and contacts the left face of the sample and a reservoir that is filled with oil and contacts the right face of the sample. The oil in the reservoir is identical to the oil that saturates the sample. It is assumed that the pressures of the fluids in the two reservoirs remain constant and equal throughout an experiment. It is assumed that the sample is strongly water-wet, and that the porosity and permeability are constant and uniformly distributed. In this configuration, it is possible for water to spontaneously imbibe into the sample, displacing oil in both a counter-current fashion (causing oil production at the left face of the sample) and a co-current fashion (causing oil production at the right face of the sample). A pressure tap is located toward the right face of the sample.

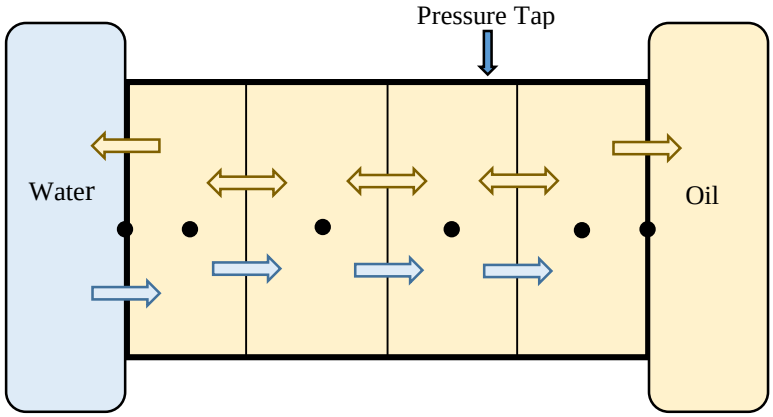

Figure 1. A schematic depiction of the problem under consideration during spontaneous imbibition with the TEO-free boundary condition.

Figure 1 shows the grid system that is used in the numerical simulation. At both ends of the sample, zero-width grid blocks are located to facilitate the definition of boundary conditions. The sample is then divided into a number of equal-width grid blocks. The simulation accounts for changes in saturation in a grid block by taking the difference between the flow rates across the boundaries. The flow rates at the boundaries are calculated using the modified-Darcy law equations. In the absence of gravity, these equations are:

$$\frac{Q_w\,\mu_w}{k\,A\,k_{rw}} = -\frac{dP_w}{dx} \tag{1}$$

$$\frac{Q_o\,\mu_o}{k\,A\,k_{ro}} = -\frac{dP_o}{dx} \tag{2}$$

$$Q_t = Q_w + Q_o \tag{3}$$

$$\frac{dP_c}{dx} = \frac{dP_o}{dx} - \frac{dP_w}{dx} \tag{4}$$

In these equations, Q is volumetric flow rate, μ is viscosity, k is permeability, A is cross-sectional area, k_r is relative permeability, P is pressure, and x is axial location. With regard to the subscripts, w denotes water, o denotes oil, t denotes total, and c denotes capillary. Equations 1 through 4 may be combined to obtain the following equation for the flow of oil:

$$Q_o = \frac{Q_t\,\mu_w\,k_{ro}}{k_{ro}\,\mu_w + k_{rw}\,\mu_o} - \frac{A\,k\,k_{ro}\,k_{rw}}{k_{ro}\,\mu_w + k_{rw}\,\mu_o}\,\frac{dP_c}{dx} \tag{5}$$

Because the simulation depends on calculating saturation changes, it follows that saturations will be known for each grid block at any time. However, this does not allow direct evaluation of Equation 5 because the total volumetric flow rate is not known *a priori* for spontaneous imbibition problems. This shortcoming can be overcome by combining Equations 2 and 5 to obtain

$$-\frac{dP_o}{dx} = \frac{Q_t}{k\,A}\frac{\mu_w\,\mu_o}{k_{ro}\,\mu_w + k_{rw}\,\mu_o} - \frac{k_{rw}\,\mu_o}{k_{ro}\,\mu_w + k_{rw}\,\mu_o}\,\frac{dP_c}{dx} \tag{6}$$

The pressures in the water reservoir at the left face of the sample and the oil reservoir at the right face of the sample are known (they have been assumed to have the same value and this value can arbitrarily be set to zero). Further, for the simulation model, if the saturation at the left face can be assumed or calculated, then the pressure in the oil at the two faces will be known. The right-hand-side of Equation 6 is a function only of saturation with Q_t being a constant value throughout the sample at any given time. Knowing the saturation profile at any time, integration of Equation 6 (in the simulator this integration is performed numerically) yields the following equation for the total volumetric flow rate:

$$Q_t = \frac{(P_{or} - P_{ol}) - \int_l^r \frac{k_{rw}\,\mu_o\,dP_c}{k_{ro}\,\mu_w + k_{rw}\,\mu_o}}{\frac{1}{k\,A}\int_l^r \frac{\mu_w\,\mu_o\,dx}{(k_{ro}\,\mu_w + k_{rw}\,\mu_o)}} \tag{7}$$

Here the subscripts r and l refer to the right and left faces of the sample.

A critical feature of the simulation is the assumption for the saturation used in calculating relative permeabilities for the flows across the grid-cell boundaries. In all cases, the saturation for a fluid is assumed to be the value for the upstream cell, the so-called

"upstream-differencing" assumption. That is, if the flow rate of fluid crossing a cell boundary is left-to-right, the saturation of the left-hand cell is used. It follows that, for the case of counter-current imbibition at a grid-block boundary, the relative permeability of the water is calculated using the saturation of water in the left-hand cell while the relative permeability of the oil is calculated using the saturation of oil in the right-hand cell. The fundamental importance of this assumption can be seen by considering the left-hand sample face condition. Upstream-differencing means that the flow into the sample is controlled by the saturation of the fluid saturating the zero-volume surface cell. As this cell has zero-volume, it can instantly take on any saturation. For the present study, the saturation of the left-face is assumed to be the final average saturation of the sample. This means that there is a finite relative permeability for water to enter the sample despite the fact that the sample is fully saturated with oil. (It is noted that a theoretical determination of the value of saturation and bubble pressure (the pressure required to produce non-wetting fluid) at the left-face in spontaneous imbibition problems is the most important unresolved issue for the problem of spontaneous imbibition.)

THE PROGRAM OF STUDY

For the present study, three previously published data sets [3,4] were considered. As can be seen in Table 1, these tests used samples with similar petrophysical properties, the same water, but oils with a wide range of viscosities.

Table 1 The petrophysical characteristics of the three samples under study.

Sample	ϕ	L (cm)	D (cm)	Tap (cm)	ρ_w (kg/m^3)	μ_w (cp)	ρ_o (kg/m^3)	μ_o (cp)	K (md)
CHP07	0.467	14.25	3.79	11.25	1005	1.09	740	1.47	5.50
CHP11	0.466	6.10	3.81	3.23	1005	1.09	870	137.0	4.40
CHP25	0.458	5.75	3.70	3.43	1005	1.09	840	83.3	4.08

The published results [3,4] report the range for the permeability to be 3 to 6 mD. For the purpose of simulation, more accurate values are needed. These values were determined by examining the early-time data (before a front could pass the pressure tap) for the pressure and right-face production rates. This calculation is illustrated in Figure 2 for Sample CHP07; the permeabilities calculated in this manner are shown in Table 1.

The history matches were achieved by using a single set of relative permeability curves and modifying the capillary pressure curve. Pressure behavior is more complex than production; the errors between the experimental and simulated results were based on the productions at the each face of the samples. Comparison of the predicted and the experimental pressures provides an independent test of the quality of the analysis.

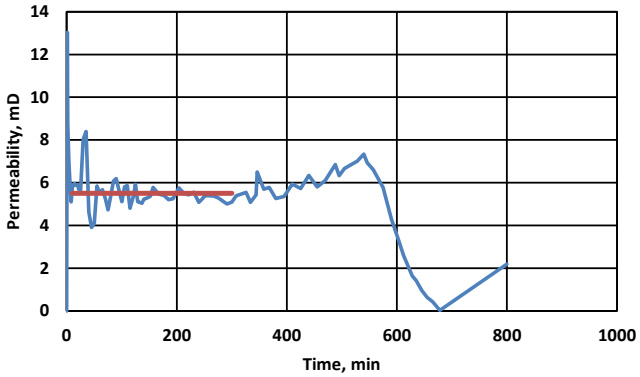

Figure 2. The calculated permeability for Sample CHP07 showing the range of times (the red line) used to determine the mean permeability.

The simulations used the relative permeabilities reported by [3]. These curves are shown in Figure 3. The history-matching process was straightforward. The capillary pressures were input as a 6-entry table. For the search, various stages of keeping the saturations constant and varying the capillary pressures, and *vice versa* were employed. For each assumed capillary pressure curve, a simulation was run and the errors between the simulated productions and the values calculated from experimental data were computed. By using an exhaustive search technique, the capillary pressure curve that led to the minimum error was determined.

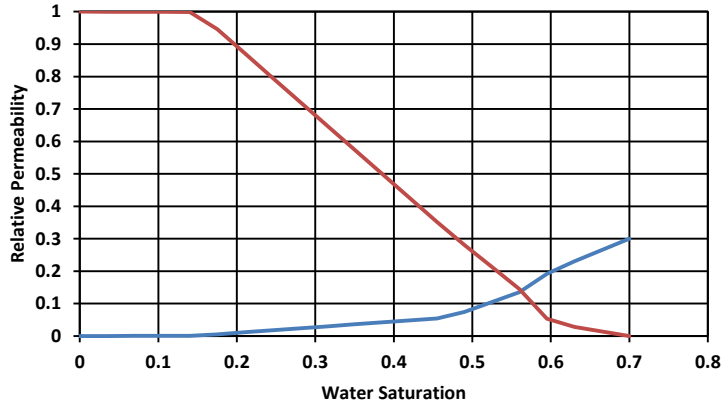

Figure 3. The relative permeability curves used in the simulations.

All simulations were run using a total of 50 grid blocks. Stability was controlled by limiting saturation changes in any one grid block to less than 0.0001. No stability problems were encountered and each test simulation ran in under 20 seconds.

RESULTS

Figure 4 shows the capillary pressure curves that lead to the best fits for the three samples. Also shown is the initial "guess" for the capillary curve which was based on the

data from [3]. All three simulation curves show similar shapes and magnitudes and do not greatly differ from the initial curve. It is noted that the small negative region at high water saturation are not physically reasonable for a strongly water-wet sample. They were included here because they were present in the original "initial" curve. In all cases, the simulations predicted capillary pressures in the positive region and water saturations never exceeded the zero-capillary pressure saturation. The shapes of these curves may appear to be unusual; however, it must be recalled that the region from $0 < S_w < 0.3$ does not actually occur in the tests and these values are really an artifact of the fitting technique.

The quality of the curve fits for the three samples can be seen in Figures 5 through 7. In all cases, agreement between the predicted and measured productions is very good. Of special interest is the remarkable agreement between the predicted and measured pressures. Recall that these data were not used in the history matches. In Figure 5, the spike in pressure after 600 minutes is clearly matched. For both Figures 6 and 7 the bi-modal nature of the pressure behavior is captured although agreement between the two data sets is not nearly as good as that demonstrated in Figure 5.

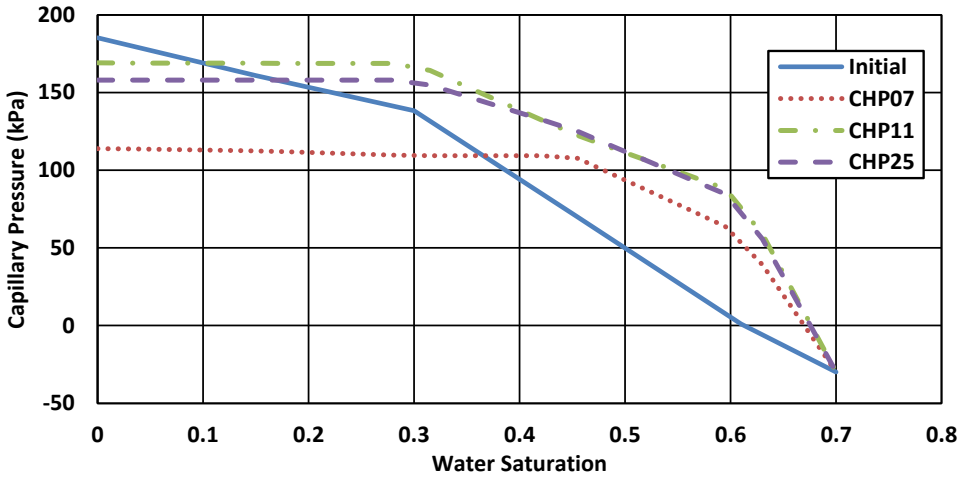

Figure 4. The capillary pressure curves that lead to the best fits of the experimental data. Also shown is the capillary curve from [3] (labelled "Initial").

In the case of Sample CHP07 (Figure 5), μ_o/μ_w equal to 1.35, production from the left hand face is minimal. The simulation was very successful in predicting both the small counter-current left-face production and the more substantial co-current right-face production. Production at the right-face became very slow near the end of the experiment; this feature was also captured by the simulator. This slowing of production corresponds to the arrival of water at the right-face. The pressure history of the experiment is quite complex with a sharp drop at early times, then a relatively gradual linear decline followed by a sharp peak just before the end of the imbibition process.. All of these features are predicted by the simulator. It must be emphasized that pressure was not used during the history-match. The agreement between experiment and simulation

provides confidence in the simulation. Note that for Sample CH07, production dropped off quickly after the water first arrived at the right face.

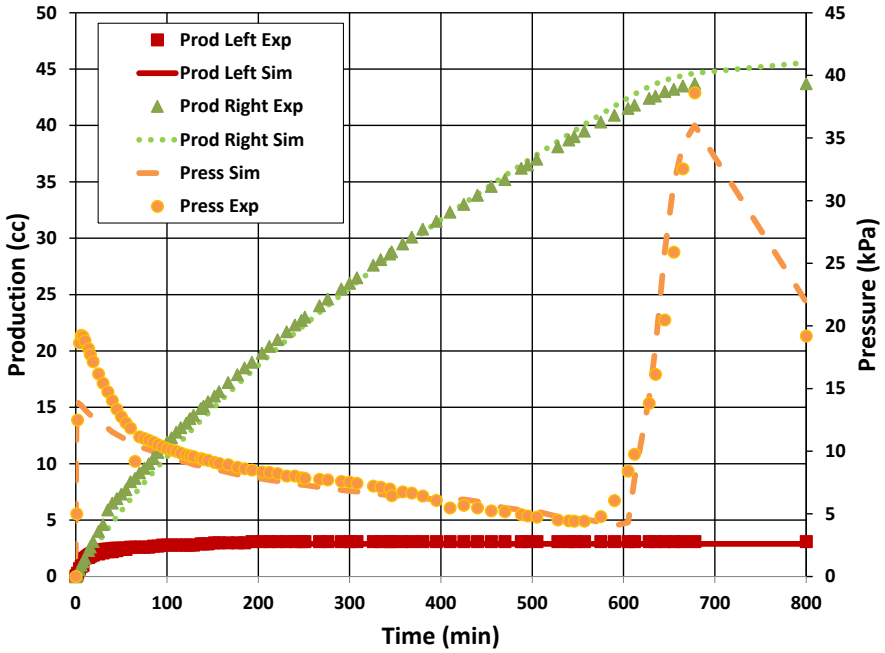

Figure 5. A comparison of experimental and simulated results for sample CHP07. Predominantly co-current oil production with a viscosity ratio (μ_o/μ_w) equal to 1.35.

In the case of Sample CHP11 (Figure 6), μ_o/μ_wequal to 125, production at the left-face is more substantial. Again the simulation captures the relative productions very well. Unlike the low viscosity ratio case (Sample CHP07) the production at the right end of the sample continues after about 600 minutes, although at a lower rate. This point roughly corresponds to a local minimum in the pressure – it also corresponds to the time the water first reaches the right-face of the sample. Although not a perfect match, the simulated pressure history shows all the features of the experimental curve: an initial rise, a drop to a local minimum, a second rise and an eventual tailing off. A significant difference between these results and the results for the low viscosity ratio case is that oil production at the right face continued, albeit at a reduced rate, after the arrival of water at this face.

In the case of Sample CHP25 (Figure 7), μ_o/μ_w equal to 76, all the main features of Sample CHP11 are demonstrated. The simulation does not match the experimental results as well as in the first two cases but the agreement is still very good.

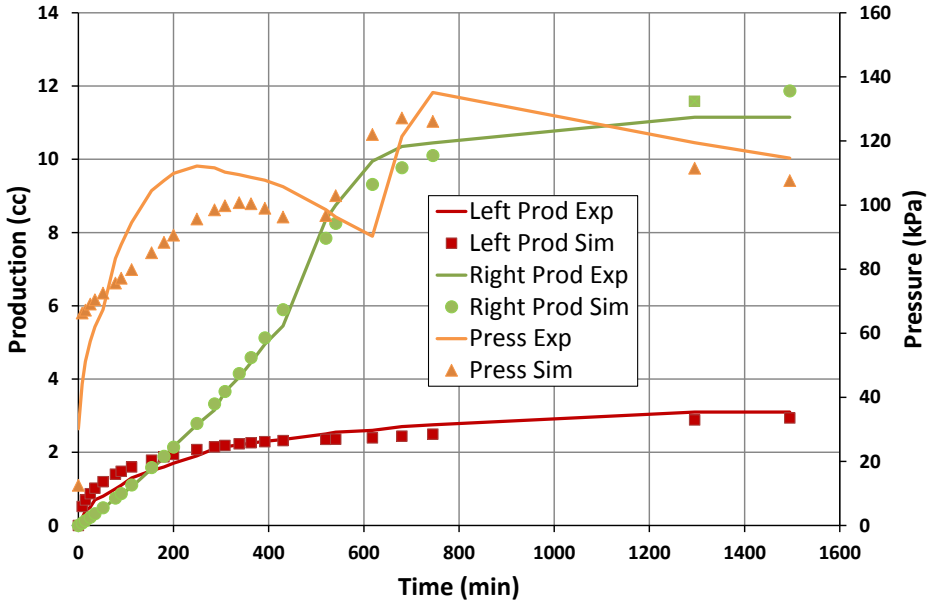

Figure 6. Results for sample CHP11. Sustained counter-current imbibition, but still predominantly co-current oil production with a viscosity ratio (μ_o/μ_w) equal to 125.

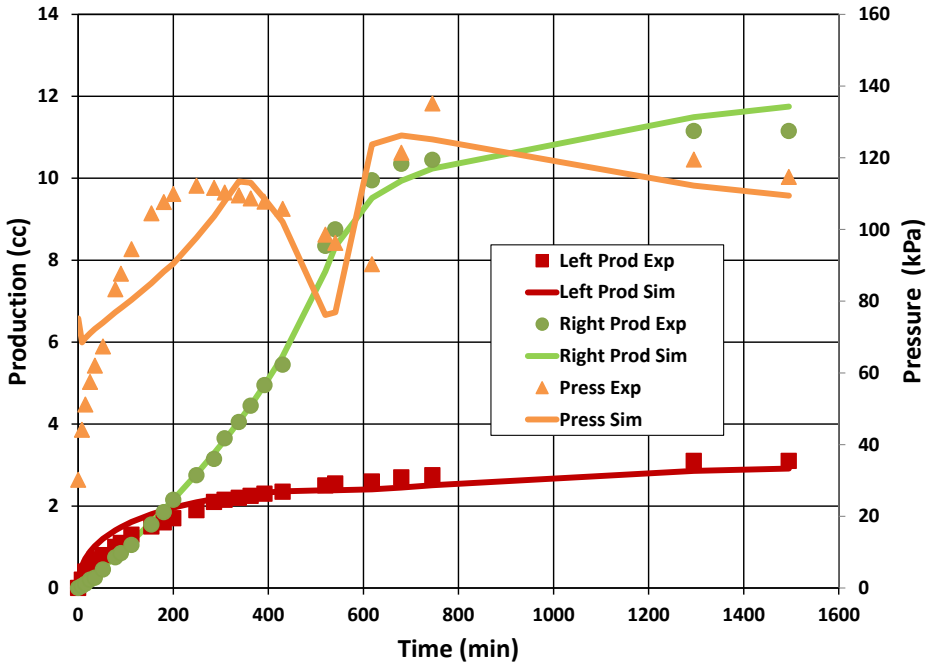

Figure 7. Results for sample CHP25. Sustained counter-current imbibition, but still predominantly co-current oil production with a viscosity ratio (μ_o/μ_w) equal to 76.

Comparison with Piston-Like Flow Theory

Figure 8 shows the calculated saturation profiles for Sample CHP25. A model which assumes piston-like flow has been published for both counter- and co-current imbibition [4]. This figure clearly shows that displacement takes place in an essentially frontal manner (tied to the low-to-zero permeability to brine for $S_w < 0.3$). However, with a wedge-shaped region extending from the imbibition face to the front, this is a clear departure from the piston model. However, the maintained similarity of the profiles is consistent with the close match to experimental results given by a piston-like flow model.

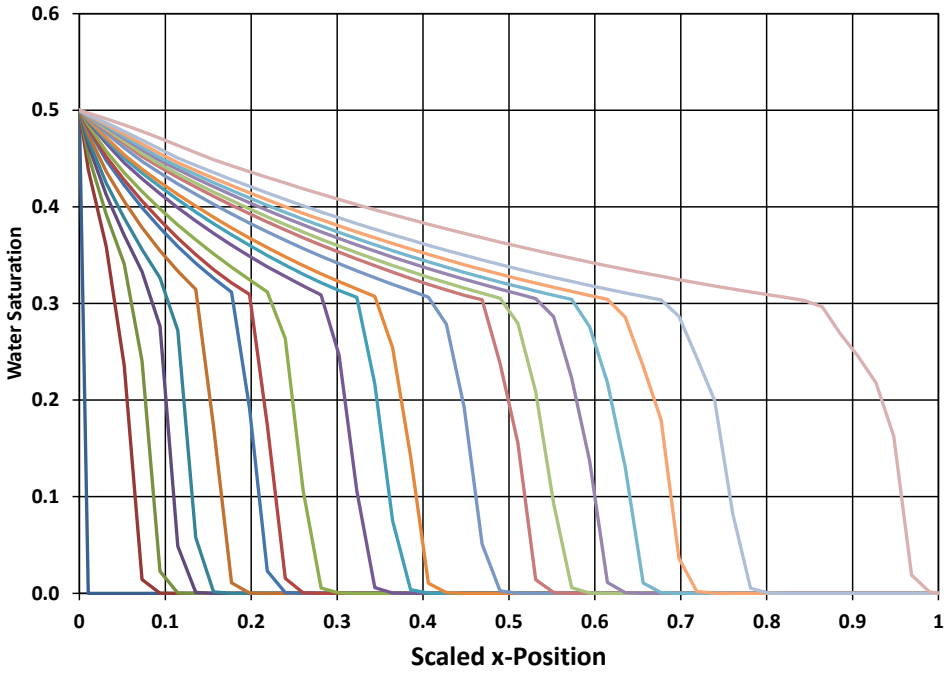

Figure 8. Water saturation profiles for CHP25.

Further comparisons between the results of the present study and the piston-like flow model are given in Table 2. These results show various levels of agreement. The permeability results differ because the present paper uses a different averaging procedure. However, these results are very similar. For the piston-like flow, the front is perfectly defined. However, in the simulations, fronts are generally smeared and a single saturation is hard to quantify. The capillary pressures at the front and at the inlet show reasonable agreement. The results for the relative permeabilities at the front do not show particularly good agreement. However, it must be noted that the simulation used a set of input curves based on independent experiments while the piston-like flow uses a single point calculation. In light of this, the agreement between the results for $k_{w,f}$ in Samples CHP11 and CHP25 is satisfactory.

Figure 9 gives a visual depiction of the agreement between the capillary pressure curves determined through simulation and the frontal saturation/capillary pressure points predicted by the piston-like flow theory. The piston-like flow theory is based on a single saturation point but the points for the two samples with published data agree very well with the points on the capillary pressure curves found by history matching with the simulator.

Table 2 A comparison between the results obtained by simulation and results obtained using piston-type flow theory.

Property	$k\ (md)$	$P_{c,o}$ (kPa)	$S_{w,f}$	$P_{c,f}$ (kPa)	$k_{w,f}$	$k_{nw,f}$
CHP07: Simulation	5.6	85	0.48	96	0.07	0.28
CHP07: Piston-like flow	5.0	34	NA	78	0.2	na
CHP11: Simulation	4.49	55	0.38	127	0.2	0.56
CHP11: Piston-like flow	4.58	80	0.45	128	na	0.77
CHP25: Simulation	4.08	117	0.31	166	0.023	0.64
CHP25: Piston-like flow	4.83	80	0.45	118	na	0.51

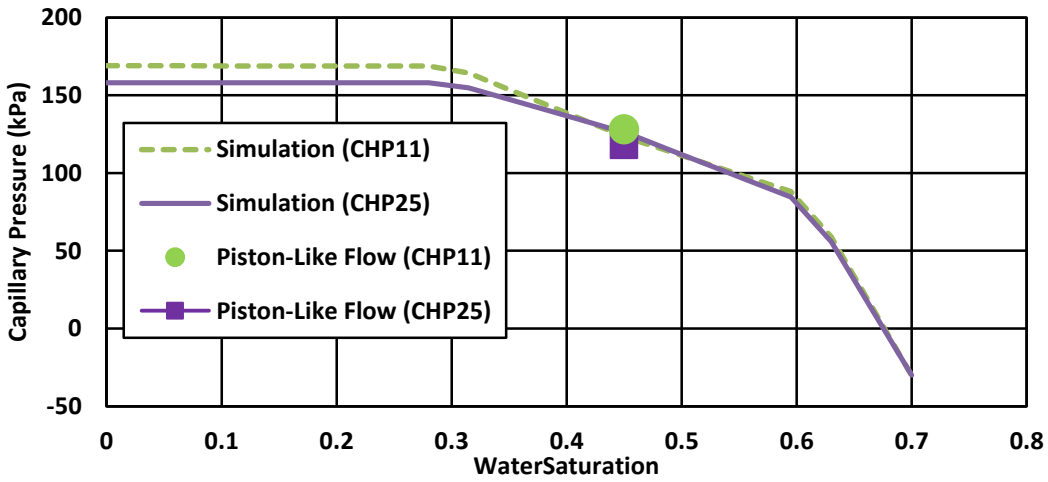

Figure 9. Comparison of Piston-like flow and Simulation Results.

Overall, the simulations support the conclusion that the piston-like flow gives a very good first estimate of the saturation functions.

DISCUSSION

Despite the very good history matches obtained in the present study, there are a number of issues that need further attention. The most important issue is that the present study uses relative permeability curves obtained in an independent experiment. The results therefore are founded on the assumption that the relative permeability curves are unique functions of the sample, not of the process. A related concern is that the relative

permeabilities obtained in the present study vary considerably from those obtained by the piston-like flow theory. Another important issue is that the saturation at the inlet face of the sample was simply set to the final average saturation of the sample. A method to theoretically predict this saturation, and its detailed physical significance, in a unique manner does not yet exist. A third issue is that experimental saturation profiles are not available for the comparisons in the present work. New, related imbibition results, with imaging of the advancing imbibing front, are now available [10] Close observation (not detailed above) of the various test values used in obtaining the best history matches shows that significantly different capillary pressure curves can lead to quite comparable levels of error. Until simulations that include production/pressure/saturation profile information are available, based on results such as those presented in [10], results from modeling this problem must be used with caution.

CONCLUSIONS

The following conclusions can be made based on the present study:

1. The results of three water-oil, combined counter- and co-current experiments, using a range of oil-viscosities, were successfully matched using a single set of relative permeability curves. The resulting, fitted capillary pressure curves were very comparable in both shape and magnitude.
2. The results of the simulations were largely consistent with the previously published results produced using a piston-like flow theory (see [4]).
3. Because of its complex behavior, the TEO-free boundary condition offers opportunities for evaluation several core/fluid properties from a single experiment. If a range of fluid viscosity is used then it is possible that more variables can be inferred [11].

ACKNOWLEGEMENTS

This work was supported in part by a grant from the Natural Sciences and Engineering Research Council of Canada.

REFERENCES

1. Mason, G. and N.R. Morrow, "Recovery of Oil by Spontaneous Imbibition", *Current Opinions in Colloid Interface Science*, (2001), Vol.6, pp.321-337.
2. Mason, G. and N.R. Morrow, "Developments in Spontaneous Imbibition and Possible Future Work", *Journal of Petroleum Science and Engineering*, (2013).
3. Haugen, Å., M.A. Fernø, G. Mason, N.R. Morrow, "The Effect of Viscosity on Relative Permeabilities Derived from Spontaneous Imbibition Tests", *Transport in Porous Media*,(2015), Vol.106, pp.383-404.
4. Haugen, Å., M.A. Fernø, G. Mason, N.R. Morrow, "Capillary Pressure and Relative Permeability Estimated from a Single Spontaneous Imbibition Test", *Journal of Petroleum Science and Engineering*, (2014), Vol.115, pp.66-77.
5. Fernø, M.A., Å, Haugen, G. Mason, N.R. Morrow, "Measurement of Core Properties Using a New Technique – Two Ends Open Spontaneous Imbibition", SCA2014-006, *International Symposium of the Society of Core Analysts*, (2014), Avignon, France, 8-11 September.
6. Ruth, D.W., G. Mason, N.R. Morrow, "A Numerical Study of the Influence of Sample Shape on Spontaneous Imbibition", SCA2003-016, *International Symposium of the Society of Core Analysts*, (2006), Pau, France, 21-24 September.
7. Ruth, D.W., N.R. Morrow, Y. Li, J.S. Buckley, "A Simulation Study of Spontaneous Imbibition", SCA2000-024, *International Symposium of the Society of Core Analysts*, (2000), Abu Dhabi, UAE, 18-22 October.
8. Ruth, D.W., G. Mason, N.R. Morrow, Y. Li, "The Effect of Fluid Viscosities on Counter-Current Spontaneous Imbibition", SCA2004-011, *International Symposium of the Society of Core Analysts*, (2004), Abu Dhabi, UAE, 5-9 October.
9. Li, Y., D.W. Ruth, G. Mason, N.R. Morrow, "Pressures Acting in Counter-Current Spontaneous Imbibition", Journal of Petroleum Science and Engineering, (2006), Vol.52, No.1-4, pp.87-99.
10. Fernø, M.A., Haugen Å., Brattekås, B., Mason, G. and Morrow, N.R. "Quick and Affordable SCAL: Spontaneous Core Analysis. SCA2015-A055, *International Symposium of the Society of Core Analysts*, (2015), St. John's, Canada, 16-21 August.
11. Meng, Q., H. Liu, and J.Wang, "Entrapment of the Non-wetting Phase during Co-current Spontaneous Imbibition" *Energy & Fuels*, 2015. 29(2): p. 686-694.

QUICK AND AFFORDABLE SCAL: SPONTANEOUS CORE ANALYSIS

M. A. Fernø[a], Å .Haugen[b], B. Brattekås[a,c], G. Mason[d] and N. Morrow[d]
[a] Dept. of Physics and Technology, University of Bergen, Norway
[b] Statoil, Bergen, Norway; [c] The National IOR centre, Dept. of Petroleum Technology, University of Stavanger; [d] Dept. of Chemical & Petroleum Engineering, University of Wyoming, USA

This paper was prepared for presentation at the International Symposium of the Society of Core Analysts held in St. John's Newfoundland and Labrador, Canada, 16-21 August, 2015

ABSTRACT

We present a quick and affordable special core analysis method that uses spontaneous imbibition to estimate absolute permeability, capillary pressure and relative permeability. The method uses the two-ends-open free (TEO-free) boundary condition where one end of the core is in brine and the other in oil. Counter-current and co-current flow are easily measured and quantified and from them we estimate end-point relative permeability and capillary pressure using, by most oil recovery standards, very simple analysis. The analysis is based on an assumption of a piston-like displacement and includes the capillary back pressure at the open face. Piston-like displacement was verified using *in-situ* imaging by positron-emission-tomography (PET) to visualize the imbibing water front during TEO-free imbibition.

INTRODUCTION

A widely used assumption is that the imbibition from a fracture to the rock matrix is counter-current. The most studied experimental approach is under counter-current flow [1] - a term we here use when oil and water flows through a cross-section in opposite directions. The core plugs used for analysis are small and gravity forces are negligible compared to capillary forces, in contrast to matrix blocks in oil producing fractured reservoirs, for which the height differences in the formation will promote significant co-current flow by gravity forces. The term co-current flow implies that oil and water both flow in the same direction through the rock cross-section. Water drive will generally involve both counter-current and co-current flow in various portions of the reservoir, depending on the magnitude of capillary to gravity forces [2]. Co-current imbibition prevails if the matrix blocks are partially exposed to water, for example in gravity segregated fractures, where oil will flow preferentially towards the boundary in contact with oil [3]. Co- and counter-current imbibition may coexist during imbibition in fractured reservoirs [4], but the flows are different: counter-current flow has lower fluid mobility, lower mobile saturations (lower relative permeabilities), and higher viscous interaction between the phases [5]. Consequently, counter-current laboratory

measurements on small cores may underestimate both production rate and ultimate recovery when scaled to field conditions.

Studied Boundary Geometries

In standard experiments, core plug sample boundaries are either sealed or fully submerged in brine at all times. Several boundary conditions have been studied extensively in the literature; the most frequent are All-Faces-Open (AFO) and One-End-Open (OEO). During AFO, an oil saturated core plug, normally with an initial water phase established by forced displacement with oil, is submerged in water and the water imbibes freely. The flows are a mix of counter-current and co-current. For OEO, the curved surface of the cylindrical core and one end face are sealed and only one end face is open for flow. A partially or fully oil saturated core plug is submerged in water and spontaneous imbibition starts. For OEO only counter-current flow will occur because water enters and oil escapes through the same open end. Other, less frequently studied, boundary conditions include Two-Ends-Open (TEO) and Two-Ends-Closed (TEC), see e.g. Mason *et al.* 2009 [6]. For the TEO boundary condition, oil production can be measured separately for each end and often features asymmetry [7]. Using the TEO boundary condition in horizontally positioned core plugs, the amount of oil produced from each open end face was often unpredictably asymmetrical, even though the amount of water imbibed from each end face was equal and symmetric with respect to the center of the core (sometimes referred to as the no-flow boundary). Hence, oil was produced by both co- and counter-current imbibition, even in a short system not influenced by gravity. The experimentally observed asymmetric oil production can be explained by the need to overcome the capillary back pressure at the outlet face of the matrix.

The Capillary Back Pressure

During imbibition, the capillary back pressure is defined as the pressure difference between the non-wetting phase ($P_{nw,o}$) and the wetting phase ($P_{w,o}$) at the brine face of the porous media. The wetting phase pressure at the open face is zero. For spontaneous imbibition to progress, the imbibition pressure has to exceed the capillary back pressure required for the production of the non-wetting phase from out of the largest pores at the open face. The capillary back pressure may also be referred to as the bubble pressure [8]. It exists because the production mechanism of the non-wetting phase at the open end face is similar to a drainage process. The capillary back pressure is determined by the largest pores at the surfaces where non-wetting phase is produced as droplets [9, 10].

The asymmetric oil flows from each open end face reported by Mason *et al.* 2010 [7] was shown to occur simultaneously with symmetric influx of brine from each end as quantified by nuclear tracer imaging [11]. Hence, pore-scale heterogeneities at the rock surface, related to production paths for oil, may have a disproportionately large effect on the recovery and flow of oil, whereas water influx was much less affected by small changes in the capillary back pressure This illustrates that the properties of the fracture/matrix boundary have significant impact on the exchange of fluids between

fracture and matrix. Measurement of the simultaneous production of oil and influx of water provides an account of water and oil flow across each open end face.

Relative Permeability and Capillary Pressure from Spontaneous Imbibition

The experimentally observed asymmetrical oil production is related to the values of the capillary back pressures acting at the outlet faces of the core. A small difference in capillary back pressure between the two open end faces may consume a substantial fraction of the capillary pressure driving the flow of oil. To study the capillary back pressure in a more controlled manner, the TEO-free boundary condition was implemented, whereby one of the core faces is in contact with oil rather than water Although this boundary condition has been studied previously [5, 12], an analysis of the governing parameters, including the capillary back pressure, has only been reported recently with the M^2HF model [13, 14].

Imbibition always starts out counter-currently for the TEO-free boundary condition. How long this mode continues depends on the mobilities of the two fluids. If the mobility of the oil is high (i.e. low viscosity oil) then counter-current imbibition soon ceases and imbibition becomes co-current with production varying approximately as the square root of time. However, if the resistance is mainly in the oil phase (high oil viscosity compared with water), the resistance to co-current flow decreases over time because the distance oil has to flow to reach the oil-filled end face decrease, i.e. imbibition rate increases with time.

Two-phase flow functions can be estimated during TEO spontaneous imbibition using three simple measurements that are individually standard, but are rarely, if ever, combined. First, the ratio between counter-current flow and co-current flow for the two-ends-open free boundary condition is quantified by measuring oil production separately from each end face. Second, the pressure development during the dynamic spontaneous displacement process is measured along the length of the core using pressure transducers. Thirdly, imaging of the advancing fluid fronts are obtained during the spontaneous imbibition tests to validate the assumption that displacement is piston-like.

PROCEDURES

Positron Emission Tomography

Techniques for *in situ* visualization are vital tools for studying details of flow within opaque systems such as porous rock samples. Non-invasive, non-perturbing methods include X-ray, X-ray computed tomography (CT), nuclear tracer imaging (NTI), nuclear magnetic resonance (NMR), nuclear tracer imaging (NTI) and magnetic resonance imaging (MRI). Positron emission tomography (PET) is a frequently used explicit method for clinical oncology and clinical diagnosis, where detectors register gamma ray pairs emitted indirectly by a positron-emitting radionuclide in a tracer fluid injected into the patient. Although primarily used as a clinical diagnostic tool, PET has also more

recently been used to visualize, and partly quantify, fluid transport in geomaterials [15, 16].

In positron decay, a positron is emitted from the nucleus accompanied by an electron to balance atomic charge. After emission, the positron loses kinetic energy by interactions with the surroundings, and at near-zero momentum, the positron combines with an electron and annihilates at a finite distance outside the radioactive nucleus. The electromagnetic radiation, in the form of two 511 keV photons emitted in opposite directions to conserve momentum, is registered only if the photon pair is within the coincidence window and the line-of-response (LOR) acceptance angle [17]. PET scanners are well suited for flow studies because 511 keV photons penetrate the aluminum confinement vessel holding the rock sample at elevated pressures. For practical purposes, the beta decay is insensitive to temperature and pressure [18], making PET suitable for visualization of flow in porous rocks held under pressurized in confinement vessels.

Preparing core plugs with the TEO-FREE boundary geometry

With the TEO-free condition one end is in contact with brine and the other end in contact with oil at the same pressure. Under these circumstances brine can only enter one end of the core, but the oil can leave from either one or both ends. Ratios of oil/brine flow can be readily measured for each end. The experimental procedure using the TEO-free boundary geometry was as follows:

1. Cylindrical chalk core plugs of different lengths were cut on a lathe. Sandstone cores were drilled from quarried slabs. The core plugs surfaces were gently washed using water to remove loose particles
2. Cores were dried at room temperature for at least 24 hours before drying them in a heated oven until stable weight
3. Diameters and lengths were measured to obtain bulk volume
4. The circumference of a core was sealed by coating with a thin layer (less than 5 mm) of epoxy resin
5. An end-piece with a void was attached at one the end face (later filled with oil and serving as the oil-filled end face). The end piece was machined from polyoxymethylene (POM)

5*. With PET (or other) imaging: Attach an end piece at the inlet with void for accumulation and transport of liquids

6. Attach a short stainless steel tube at the end piece for oil production

6*. With pressure measurements: Drill a 10 mm hole into the curved surface of the epoxy-coated surface of the cylindrical core to allow insertion of a steel tube (1/8in OD). Cement the outside of the steel to the rock with epoxy.

7. Record the dry weight of the core and end piece. Saturate the core and end pieces with oil under vacuum. Check that the rock is fully saturated with oil by calculating the average porosity of the rock from the increase in weight. (The volume of the end piece and the pressure and production tubes are excluded). Core permeabilities were not measured: however, values of 3-8mD (chalk) and 1200mD (sandstone) have previously been measured.

8. To reduce "induction time" effects, start the imbibition experiments as soon as possible after filling with oil, preferably on the same day. Submerge the oil-saturated assembly in brine and record the oil produced in inverted graded funnels set at each end of the core.

Spontaneous imbibition in PET/CT

The epoxy-coated oil-filled (decane μ_o=0.74) core was placed within a rectangular Plexiglas box on the standard patient table on the combined PET/CT scanner. Pre-installed software and lasers were utilized for accurate placement of the rock system with respect to the CT gantry and the PET detector array. The rock sample was placed in the center of the bore (diameter 700 mm) to optimize CT and PET images. The rock system was stationary within PET detector array, with an axial field of view of 169 mm. Temporal resolution was determined in post processing for optimal visualization of the displacement process. Changes in pressure and volume were monitored and recorded. Radioactive 1wt% NaCl brine with water-soluble ^{18}F-FDG (μ_w=1.09 cP) was circulated through the inlet end piece using a constant rate injection pump to start the imbibition process, see Figure 1. External pressure transducers measured pressure changes during imbibition, and volumetric oil measurements were registered manually over time. Fluid saturations were found from the linear relationship between the number of disintegrations and the saturation of the labelled fluid.

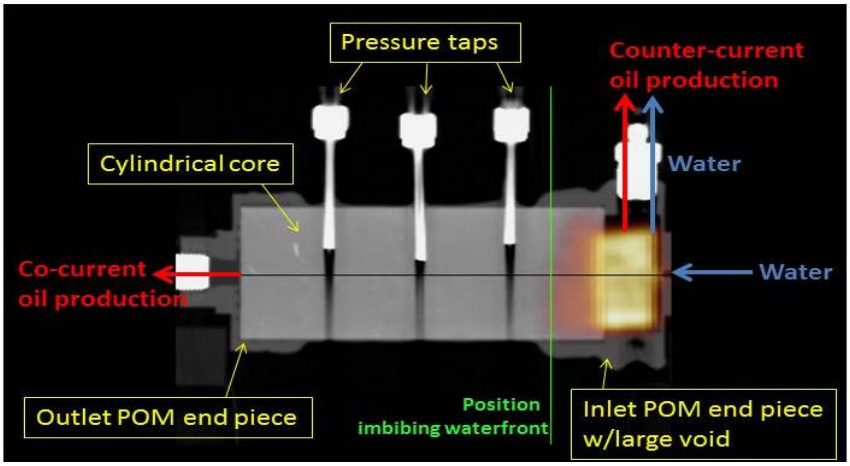

Figure 1. Experimental setup for spontaneous imbibition with PET imaging using the TEO-free boundary condition. The CT image shows a horizontal chalk plug with three pressure tappings and POM end pieces for water inflow and counter-current and co-current oil production. Volumetric measurements were performed outside the PET ring, and a cylinder pump ensured continuous cycling of water into the end piece for the duration of the test [19].

Calculating Relative Permeability and Capillary Pressure

The M^{2}HF model based on piston-like displacement was previously developed for pure 1D counter-current or co-current spontaneous imbibition [13, 14]. During co-current imbibition, the expected position of the imbibition front at time *t* can be found from

$$\frac{X_f}{L} = -D + \sqrt{D^2 + Et} \quad D > 0 \tag{1}$$

where X_f is the distance of the imbibition front (cm), L is the sample length (cm) and t is the imbibition time (min).

The constant D is defined as

$$D = \frac{1}{\left(\mu_w/k_{rw}\right)\left(k_{rnw}/\mu_{nw}\right)-1} \tag{2}$$

where μ_w is the wetting phase viscosity (mPa s), μ_{nw} is the non-wetting phase viscosity (mPa s), k_{rw} is wetting phase relative permeability *behind* the imbibition front and $k_{rnw}$is the non-wetting relative permeability *ahead* of the imbibition front.

The constant E is defined as

$$E = \frac{2KP_{c,f}}{100\varphi L^2 S_{wf}} \frac{1}{\mu_w/k_{rw} - \mu_{nw}/k_{rnw}} \tag{3}$$

where φ is the porosity, K is the absolute permeability, S_{wf} is the average wetting phase saturation behind the imbibition front, and $P_{c,f}$ is the capillary pressure at the imbibition front (kPa). Equations 1−3 can be used to calculate the distance of advance of the imbibition front if imaging is not available. In this work, local saturation measurements are measured directly with PET. The samples do not contain an initial water saturation as is usual in practice. The (k_{rnw}) ahead of the imbibition front is unity (1). The average water saturation (S_{wf}) behind the imbibition front can be obtained from the amount of oil production divided by the pore volume behind the imbibition front. Hence, there are only two unknown parameters in Eq. 2 and 3; the relative permeability to brine behind the imbibition front (k_{rw}) and the capillary pressure at the imbibition front ($P_{c,f}$).

The capillary back pressure at the open face was obtained from the oil production curve by recording the pressure at which counter-current production stops. This occurs when the non-wetting phase pressure at the front equals the capillary backpressure at the open face and there is no differential pressure to drive the non-wetting phase towards the inlet. The pressure measured with a transducer can be scaled to the pressure at the front and thus to the capillary back pressure by using simple geometry, assuming linear pressure drops,

$$P_{nw,f} = P_{c,o} = P_{nw,t} \frac{L - x_f}{L - x_t} \tag{4}$$

where $P_{nw,f}$ is the non-wetting pressure at the imbibition front, $P_{c,o}$ is the capillary back pressure at the open face, $P_{nw,f}$ is measured (oil) pressure in the transducer, and X_t the position of the transducer.

RESULTS

Figure 2 shows results using the TEO-free boundary conditions for two chalk plugs CHP26 and CHP27. The low viscosity mineral oil used (n-decane) promotes co-current

imbibition with this boundary geometry because the dominant resistance is in the aqueous phase.

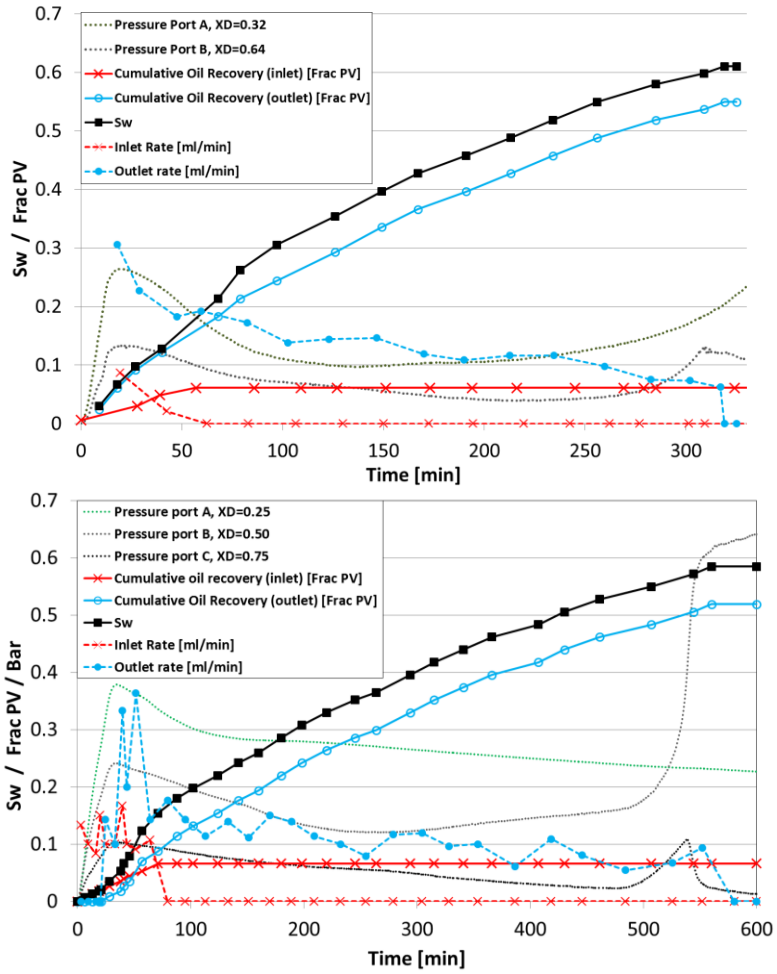

Figure 2. Spontaneous imbibition using the TEO-free boundary condition in core plugs CHP26 (top) and CHP27 (bottom). The counter-current inlet (end face in contact with brine) oil production (solid red line with crosses) was less compared to the co-current outlet (end face in contact with oil) oil production (solid blue line with open circles). Counter-current oil production was 10% for CHP26 and 11.2% for CHP27. Imbibition time increases with core length. Total production (CHP26: R_F=61 %OOIP; CHP27: R_F=58 %OOIP), with a uniform distribution. The locations of pressure ports are included for both tests. The recorded pressures are used to calculate the capillary back pressure.

Access to local water saturation during the imbibition process using PET/CT imaging allowed us to test the assumption of piston-like displacement that forms the basis for calculating relative permeability and capillary pressure from these tests. The front position can be found (without imaging) from the amount of brine imbibed (equal to the total oil produced) divided by the brine imbibed when the front reaches the end of the core. Figure 3 (left) shows these calculations for CHP26 and CHP27 versus square root of time compared to the tracked imbibition front using PET. These two independent measurements fell into alignment by the time counter-current imbibition ceases at the

inlet end. These results verify that the imbibition front is piston-like and co-current. Figure 3 (right) shows the calculated front position X_f given by Eq. 1 plotted against the experimentally measured X_f using PET. A value of D can be found that gives a straight line. From D, a value of E can be determined that gives a gradient of unity. Once the values D and E are determined, values of krw and $P_{c,f}$ are found using Eq. 2 and Eq. 3. The $P_{c,o}$ is calculated using Eq. 4. Table 1 lists relative permeabilities and capillary pressures.

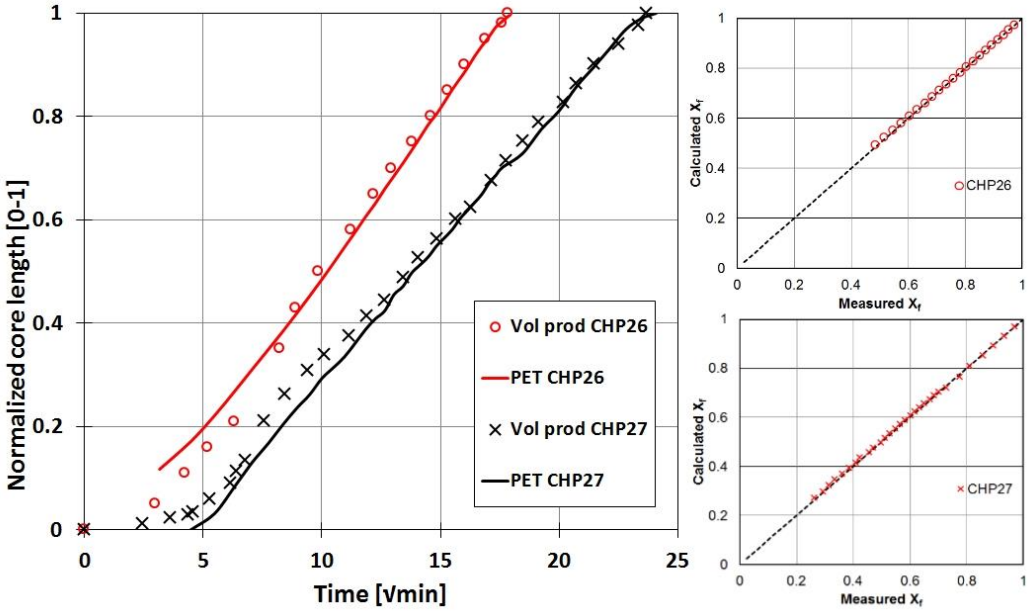

Figure 3. Left: Front position based on piston-like displacement (red open circles: CHP26; black crosses: CHP27) and visualized front position (solid red line: CHP26; solid black line: CHP27) vs. time. Right: Calculated front position (X_f) using Eq. 1 vs. measured front position using PET for core plugs CHP26 (top) and CHP27 (bottom).

Table 1. Core properties, calculated relative permeability and capillary pressures

	L [cm]	D [cm]	Por [frac]	k_{rw}	$P_{c,f}$ [kPa]	$P_{c,o}$ [kPa]	$P_{c,o}/P_{c,f}$
CHP26	8.88	5.08	0.455	0.33	64.2	21.8, 22.2	0.34
CHP27	11.8	5.08	0.468	0.31	78.2	33.7, 32.7, 28.1	0.40

Figure 4 shows the development of imbibing water (the labelled phase) during spontaneous imbibition with the TEO-free boundary geometry using PET/CT. The core is positioned horizontally during the experiment. The PET signal only measures the water and is overlaying a CT image to align with system geometries. The locations of the three pressure ports can be seen on the CT images, and appear brighter than surrounding rock due to higher density. Shadows on the CT image below the pressure ports are artefacts and does not represent areas of low CT numbers. The porosity was uniformly distributed along the length of the core. Water was injected into the void of the inlet end piece and

appears bright yellow (high intensity) on the images. Each image is an accumulation of PET signal during 10 min of imbibition and the advancing imbibition front may look slightly dispersed on the images. Figure 4 shows the position of the front at 4 selected times, and the advancing front progress as a piston.

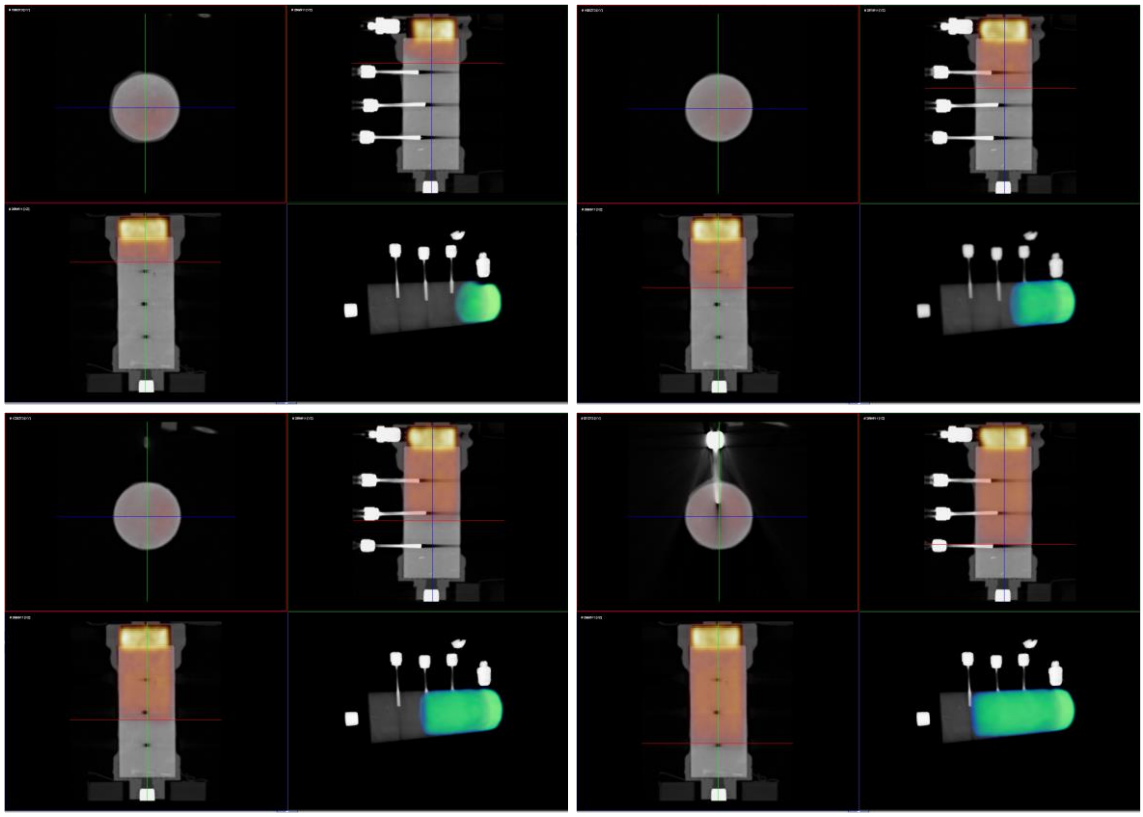

Figure 4. Qualitative PET visualization (color) overlaying CT (gray scale) of spontaneous imbibition with the TEO-free boundary condition for core plug CHP27.The location of the front is shown at four times (TOP: 40 min (left), 110min (right); BOTTOM: 200min (left), 300min (right)). Each image shows four orientations: cross-section (XY) at imbibition from (upper right); 2D slice (YZ) with pressure ports (upper left); bird eye 2D slice (XZ); and 3D image (XYZ). Colors on 2D images: high intensity (yellow) area is brine-filled void in inlet end piece; red is advancing water in core. Colors on 3D image: darker green is brine in void spacer and light green is the advancing water in the core. The water advances as a near-perfect piston from the inlet towards the outlet.

Figure 5 shows quantitative one dimensional saturation profiles for selected times during the imbibition process for core plug CHP27. The calculations are based on the PET signal and have been reduced from 3D to 1D by averaging. No additional smoothing has been applied. An assumption of uniform water distribution at the end of the test (S_w=0.58) is used to scale the normalized PET signal. We observe that this assumption was valid as the last signal intensity at the end was (within experimental uncertainty) a straight line. The front was not a perfect piston-like displacement, but the imbibition front was self-similar and maintained its shape throughout the test. The profiles slightly dispersed

because they are based on 10 min time-averaged PET images rather than snapshots of the water-distribution.

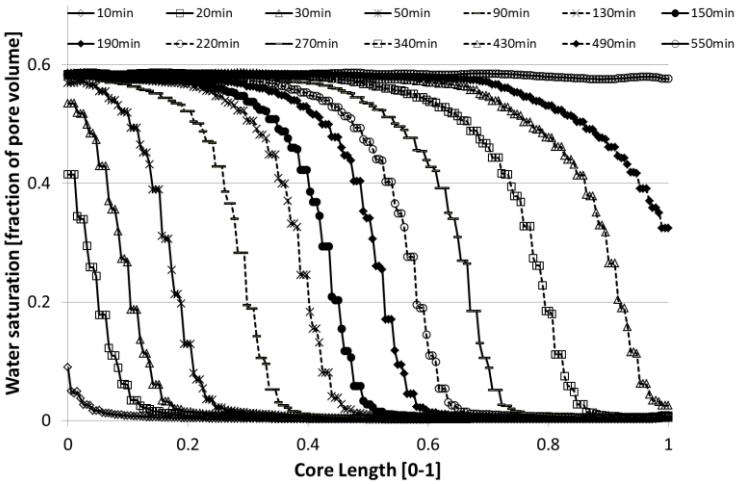

Figure 5. One dimensional water saturation profiles during TEO-free spontaneous imbibition in core plug CHP27. A sharp front advances through the core during imbibition; its shape is maintained during the displacement process.

The results in Figure 5 demonstrate the use of PET as an imaging tool for oil-water displacement in porous media with quantified local fluid saturations. Because PET relies on direct measurement of the labelled phase (water in this work) PET is superior compared to CT for determining front progression during flow injection tests and for determining spatial fluid saturation. We also learned that PET imaging has a great potential for study of low porosity samples because of the explicit fluid measurements provide high image quality and high signal to noise ratio (SNR) independent of low pore volume.

DISCUSSION

Imbibition is usually modelled by numerical solution of a set of differential equations. The solution requires functions of capillary pressure, and the relative permeabilities to both flowing phases, which are not usually known. If they are known, the values are commonly determined from separate experiments which may not be representative of flow during spontaneous imbibition [5].

A relatively straightforward mathematical analysis of co-current imbibition predicts that the volume of oil produced will depend on the square root of time. This is useful for correlation purposes. However, this behavior only allows determination of a single parameter which involves a group of core and liquid properties. The experimentally observed oil flows with the TEO-free boundary geometry, in this work and elsewhere, can only be explained by the influence of the capillary back pressure at the brine end of the core. The observation that counter-current oil production stops entirely after just 10% of total production implies that the driving pressure (the capillary pressure at the front) is

lower than some threshold. We describe this threshold as the capillary back pressure. The back pressure resists oil production because oil is produced as bubbles on the open end face during imbibition. This pressure was estimated using pressure measurements in combination with the position of the imbibing front when the counter-current production stopped. Although small in absolute value, the capillary back pressure was approximately 1/3 of the driving pressure.

Recently, the M^2HF-model [13, 14], initially developed in high-capillary chalk, was demonstrated in unconsolidated sand packs by Meng *et al.* [20]. By varying the liquid viscosity ratios, the water saturation behind the front was varied to establish a wider range of saturation on the relative permeability curve. They installed a disc with smaller pore sizes at the inlet end face in contact with water to force pure co-current imbibition. This demonstrates that the method is applicable in media for which acting capillary pressures are low. We expect the methodology to work equally well, as indicated by initial tests, in low-permeability/porosity rocks such as tight gas sands where standard core analysis is tedious and often inaccurate.

CONCLUSIONS

Using the M^2HF-model, the oil production measured separately from each end face during spontaneous imbibition using the TEO free boundary geometry can be used to estimate the relative permeability to brine behind the front and the effective capillary driving pressure at the front.

The capillary back pressure at the open face is not zero, as is commonly assumed. The capillary pressure is an essential factor in analysis of imbibition data.

The assumption of piston-like displacement during spontaneous imbibition (without initial water) was confirmed with PET imaging. We demonstrate the use of PET as a novel methodology to study flow in geomaterials, for explicit flow visualization.

REFERENCES

1. Morrow, N.R. and G. Mason, *Recovery of oil by spontaneous imbibition.* Current Opinion in Colloid & Interface Science, 2001. **6**(4): p. 321-337.
2. Bourbiaux, B.J., *Understanding the Oil Recovery Challenge of Water Drive Fractured Reservoirs*, in *International Petroleum Technology Conference*, 2009. International Petroleum Technology Conference: Doha, Qatar.
3. Pooladi-Darvish, M. and A. Firoozabadi, *Cocurrent and Countercurrent Imbibition in a Water-Wet Matrix Block.* SPE Journal, 2000. **5**(1): p. 3-11.
4. Karpyn, Z.T., P.M. Halleck, and A.S. Grader, *An experimental study of spontaneous imbibition in fractured sandstone with contrasting sedimentary layers.* Journal of Petroleum Science and Engineering, 2009. **67**: p. 48-65.
5. Bourbiaux, B.J. and F.J. Kalaydjian, *Experimental study of cocurrent and countercurrent flows in natural porous media.* SPE Reservoir Eval. & Eng., 1990. **5**: p. 361– 368.

6. Mason, G., H. Fischer, N.R. Morrow, D.W. Ruth, and S. Wo, *Effect of sample shape on counter-current spontaneous imbibition production vs time curves.* Journal of Petroleum Science and Engineering, 2009. **66**(3-4): p. 83-97.
7. Mason, G., H. Fischer, N.R. Morrow, E. Johannesen, A. Haugen, A. Graue, and M.A. Fernø, *Oil Production by Spontaneous Imbibition from Sandstone and Chalk Cylindrical Cores with Two Ends Open.* Energy & Fuels, 2010. **24**: p. 1164-1169.
8. Mason, G. and N.R. Morrow, *Developments in spontaneous imbibition and possibilities for future work.* Journal of Petroleum Science and Engineering, 2013. **110**(0): p. 268-293.
9. Li, Y., D. Ruth, G. Mason, and N.R. Morrow, *Pressures acting in counter-current spontaneous imbibition.* Journal of Petroleum Science and Engineering, 2006. **52**(1-4): p. 87-99.
10. Unsal, E., G. Mason, N.R. Morrow, and D.W. Ruth, *Bubble Snap-off and Capillary-Back Pressure during Counter-Current Spontaneous Imbibition into Model Pores.* Langmuir, 2009. **25**(6): p. 3387-3395.
11. Graue, A. and M.A. Fernø, *Water mixing during spontaneous imbibition at different boundary and wettability conditions.* Journal of Petroleum Science and Engineering, 2011. **78**(3-4): p. 586-595.
12. Dong, M., F.a.L. Dullien, and J. Zhou, *Characterization of Waterflood Saturation Profile Histories by the 'Complete' Capillary Number.* Transport in Porous Media, 1998. **31**(2): p. 213-237.
13. Haugen, A., M.A. Fernø, G. Mason, and N.R. Morrow, *The Effect of Viscosity on Relative Permeabilities Derived from Spontaneous Imbibition Tests.* Transport in Porous Media, 2015. **106**(2): p. 383-404.
14. Haugen, Å., M.A. Fernø, G. Mason, and N.R. Morrow, *Capillary pressure and relative permeability estimated from a single spontaneous imbibition test.* Journal of Petroleum Science and Engineering, 2014. **115**(0): p. 66-77.
15. Dechsiri, C., A. Ghione, F. van de Wiel, H.G. Dehling, A.M.J. Paans, and A.C. Hoffmann, *Positron emission tomography applied to fluidization engineering.* Canadian Journal of Chemical Engineering, 2005. **83**(1): p. 88-96.
16. Kulenkampff', J., M. Gruundig, M. Richter, and F. Enzmann, *Evaluation of positron-emission-tomography for visualisation of migration processes in geomaterials.* Physics and Chemistry of the Earth, 2008. **33**(14-16): p. 937-942.
17. Bailey, D.L., D.W. Townsend, P.E. Valk, and M.N. Maisey, eds. *Positron Emission Tomography*. Basic Sciences. 2005, Springer.
18. Emery, G.T., *Perturbation of Nuclear Decay Rates.* Annual Review of Nuclear Science, 1972. **22**(1): p. 165-202.
19. Fernø, M.A., Å. Haugen, G. Mason, and N.R. Morrow. *Spontaneous Imbibition Revisited: A New Method to Determine Kr and Pc by Inclusion of the Capillary Backpressure* at *IOR 2015 – 18thEuropean Symposium on Improved Oil Recovery*, Dresden, Germany, 14-16 April, 2015.
20. Meng, Q., H. Liu, and J. Wang, *Entrapment of the Non-wetting Phase during Co-current Spontaneous Imbibition.* Energy & Fuels, 2015. **29**(2): p. 686-694.

ION TUNING WATERFLOODING IN LOW PERMEABILITY SANDSTONE: COREFLOODING EXPERIMENTS AND INTERPRETATION BY THERMODYNAMICS AND SIMULATION

Quan Xie; Desheng Ma; Qingjie Liu; Weifeng Lv
Research Institute of Petroleum Exploration and Development of CNPC

This paper was prepared for presentation at the International Symposium of the Society of Core Analysts held in St. John's Newfoundland and Labrador, Canada, 16-21 August, 2015

ABSTRACT

In recent years, ions tuning water flooding (ITWF) has been a promising technique to recover oil in sandstone reservoirs. In view of research results for the last decade, it is acknowledged that substantial oil recovery beyond conventional waterflooding from sandstone is wettability alteration. However, the major contributor to wettability alteration is still uncertain. Therefore, this paper investigates this major mechanism and shows how it is due to involved in the process of IOR. Rock and oil surface chemistry were tested to explain the influence of zeta potential on the disjoining pressure. Coreflood experiments with permeability less than 1mD were performed with two different brines. Moreover, the impact of different wettabilities ranging from strong water- to slight water -wet on ITWF recovery was investigated with combination of thermodynamic theory and corefloods experiments. Relative permeability curves were obtained by history matching the corefloods experiments for both oil-wet and water-wet cores with consideration of salinity effect. Thermodynamics of wettability by ion tuning waterflooding was analyzed to characterize the surface forces between the surfaces of oil/water and water/rock.

Zeta potential results showed that decreasing divalent cations and salinity makes the electrical charges at both oil/brine and brine/rock interfaces become strongly negative, which results in elevation of the repulsive forces between oil and rock, and as a result the rock turns more water-wet, which was confirmed by thermodynamics characterization. Coreflooding experiments showed that a high potential in oil-wet reservoirs can be achieved by ion tuning waterflooding due to the double layer expansion. The relative permeability curves obtained by history matching showed that ITW improves oil recovery by accelerating oil production (relative perm changes) and reducing residual oil saturation in oil-wet rock but not in water-wet rock. Thermodynamics of wettability analysis indicated that the mechanism of ion tuning waterflooding can be interpreted by disjoining pressure calculation. These findings can help in composition design of ion tuning water to maintain higher potential to recover oil in oil field.

INTRODUCTION

Waterflooding technology has been the most successful approach to improve oil recovery. The key point to reach this success of waterflooding is that the differential pressure can be formed by the water injection which is necessary to displace oil out of formation. And also, waterflooding involves much lower cost investment and convenient operation. However, it was found that water chemistry and salinity level have a significant influence on oil recovery from the experiment in the laboratory and field trials [1, 2]. In recent years, several mechanisms were proposed to account how the ions tuning waterflood to recover additional oil. (1) Fines migration and clays swelling caused by ions tuning waterflood are the main mechanism of improved oil recovery [3, 4]. (2)Multi-component ionic exchange between the rock minerals and the injected brine was proposed to be as the major mechanism to enhance oil recovery [5, 6] . (3) Expansion of the double layer to be as the dominant mechanism of oil recovery improvement[7]. The general agreement among researchers is that low salinity waterflooding cause reservoirs become more water-wet [1]. The general agreement among researchers is that low salinity waterflooding cause reservoirs become more water-wet. The main objectives of this work are (1) to examine the performance of LSW in sandstone rocks with different wettability, and investigate the role of salinity and brine composition on the performance of LSW on the secondary and tertiary recovery modes. (2) To derive the relative permeability curves from corefloods experiments to better understand the LSW performance in different wettability reservoirs. (3)Moreover, in order to have deeper understanding the mechanism of the low salinity EOR-effect, the thermodynamics of wettability was analyzed with investigation of surface chemistry of interfaces of oil/water and water/rock.

EXPERIMENTAL

Fluids

In order to investigate the impact of the rock wettability on the low salinity EOR-effect, the crude oil from the Changqing Oil Field was used in zeta potential test and corefloods experiments. The ingredients of the experimental oil from Changqing Oilfield were shown in Table 1. The experimental oil was rich in aromatic hydrocarbon and asphaltic bitumen, the main source of the carboxy and amino groups. The density of oil sample was 0.81 g/cm^3 with viscosity at 9.0 cp at temperature of 65℃.

Two different brines were used in the corefloods and zeta potential tests; the one was synthetic brine according to the formation brine formula. Another is the low salinity brine, which was diluted 10 times by adding deionized water. The composition of the formation brine and LSW were given in Table 2. The total salinity of the brine water was 57114mg/L with the concentration of Ca^{2+} and Mg^{2+} at 2460mg/L and 317mg/L, respectively.

Mineralogy of Reservoir Cores

The core plugs for coreflood experiments were extracted from the Chang Qing oilfield and outcrop in Chang Qing. The content of clays was analyzed by X-ray test to unveil the importance of the clays on the low salinity EOR-effect in low permeability reservoirs, as shown in Table 3. The reservoir cores were rich in clays, which was more than 23% in total. 92.8% quartz and 4.2% clay content were observed from the outcrop core plugs. The composition of the outcrop indicated that it could be water-wet because of high content of quartz in the rock.

Table 1 Ingredients of the oil sample from Changqing Oilfield

Ingredients	Saturated hydrocarbon	Aromatic hydrocarbon	Non-hydrocarbon	Asphaltic bitumen
wt%	65.05	23.30	6.68	4.97

Table 2 Composition of the formation brine and low salinity water (LSW)

Brines	Ingredients（mg/l）					TDS (mg/l)
	K^++Na^+	Ca^{2+}	Mg^{2+}	HCO^{3-}	Cl^-	
Formation brine/HSW	19249	2460	317	308	34780	57114
Ion tuning water/ITW	1924.9	246	31.7	30.8	3478	5711.4

Table 3 Mineralogy of the experimental core plugs

Sample	Relative content of clay minerals（%）				Mineral types and content（%）				Total clay minerals（%）
	Mix	I	K	C	quartz	potassium feldspar	plagioclase	calcite	
Outcrop	25	25	5	45	92.8	/	1.4	1.6	4.2
Reservoir core	32	12	28	28	43.2	11.9	20.9	0.4	23.6

Note: I-illite, K-Kaolinite, C-Chlorite, Mix-Illite/Smectite

Zeta Potential

Zeta potential technique was applied to understand the relation between electric double layer and wettability regarding the charges at interfaces of oil/brine and solids/brine. Rock wettability is closely related to the thickness of water film between rock surface and crude oil, which depends on the electrical double layer repulsion and Van der Waals force. Wettability of the rock will be determined by the stability of the water film which is bounded by the interfaces of oil/brine and solid/brine [8, 9]. An unstable water film, or thin water film, may cause the wettability preferential to be oil-wet. Therefore, injection water with different ions types and concentration will trigger the alternation of the surface charges at both interfaces – oil/brine and solids/brine. Then, oil film may detach from the pore wall by increase of electrical double layer repulsion and the oil recovery will be improved.

In this study, the protocol of zeta potential tests was shown in a published paper [10]. Results of zeta potential of oil/brine and solid/brine interfaces were given to investigate the influence of the double layer expansion on low salinity EOR-effect in oil-wet and water-wet core plugs, as shown in Figure 1. The pHs of the two different brines with adding powders of rocks and crude oil were measured after equilibrium, as shown in Figure 2, due to the zeta potential magnitude varying with pH value.

Figure 1 shows that LSW resulted in stronger negative charges at the surface of reservoir rock/brine, outcrop rock/brine and crude oil/brine. This is consistent with most of the zeta potential test for low salinity waterflooding. However, LSW increased the negative surface charges at interface of outcrop rock/brine, compared to HSW, This result shows that the mineral and clay content of the rock is closely related to the zeta potential for certain brine. Basically, the larger the clay content, the more sensitive the zeta potential to the brine salinity, regarding to the variation of the brine salinity. Zeta potential of reservoir rock with LSW and HSW also proves that salinity strongly impact on the electric surface charge at the oil/brine and rock/brine interfaces [7].

Figure 2 shows that pH of outcrop rock/HSW and outcrop rock/LSW was about 7.0 and 7.5, respectively. However, the pH of reservoir rock/HSW and reservoir rock/LSW was about 6.2 and 8.0, respectively. The pH increase in the LSW compared with HSW was interpreted by the chemical equilibrium given as below moving to the right because of the low salinity water invasion [11].

$$NaAlSi_3O_8 + H_2O \longleftrightarrow HAlSi_3O_8 + Na^+ + OH^- \quad (1)$$

$$Clay\text{-}Ca^{2+} + H_2O \longleftrightarrow Clay\text{-}H^+ + Ca^{2+} + OH^- \quad (2)$$

$$R\text{-}COOH \longleftrightarrow R\text{-}COO^- + H^+ \quad (3)$$

Chemical Equation (1) and (2) also indicate that the higher pH increase could be observed if the rock is rich in clays and $NaAlSi_3O_8$, which is consistent with the rock mineralogy, as shown in Table 3.

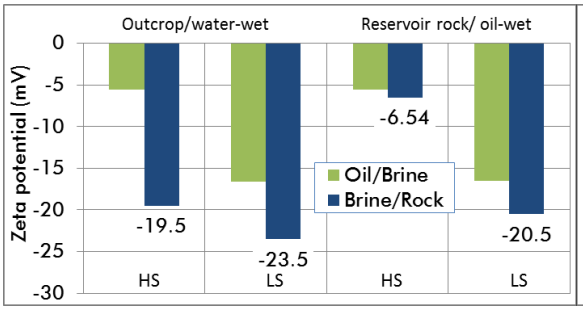

Figure 1 zeta potential results of oil/brine and solid/brine interfaces

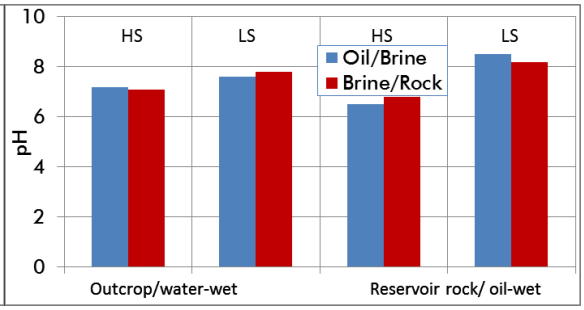

Figure 2 pHs of the two different brines with adding powers of rocks and crude oil

Wettability Measurement

The Amott test is one of the most widely used empirical wettability measurements for reservoir cores in petroleum engineering. Wettabilities of preserved core plugs were measured with the improved Amott water index method which is slightly different from the conventional procedure. This Amott water index approach combines spontaneous imbibition and forced imbibition processes. The experimental procedures adopted in this paper were introduced in a literature [12]. Crude oil from Changqing oil field was used to desaturate the core plugs, then they were put into an oven at 65^{o}C for aging four weeks to restore the wettability.

The magnitude of I_w is from 0 to 1. The higher I_w , the more water-wet. The results of wettability test were given in Table 4, which shows that the outcrop core plug OC-1# was strongly water-wet and reservoir rock RC-1# was slightly water-wet. The two types of the core plugs with different wettability were used to conduct corefloods experiments for investigation of LSW performance, which was discussed later in this study.

Table 4 Physical properties of cores and the Amott test results

Core sample	Core properties					Amott test		
	Diameter (cm)	Length (cm)	Pore volume (mL)	Porosity (%)	Swi (%)	Sws (%)	Sor (%)	Iw
OC-1#	2.5	7.15	4.60	13.1	26.8	60.2	64.9	0.88
RC-1#	2.5	7.2	4.45	12.6	31.1	41.2	54.8	0.43

S_{wi}, initial water saturation; S_{ws}, water saturation after spontaneous imbibition of water; S_{or}, residual oil saturation after forced displacement.

COREFLOODING EXPERIMENTS AND SIMULATIONS

Coreflooding Experiments Protocols

In order to investigate the influence of wettability on low salinity water EOR effect, corefloods experiments were executed by using two reservoir cores and two cores from the outcrop. For each type of wettability, low salinity water was used under secondary and tertiary mode with the core plugs, which were initially saturated by formation brine. Due to the small changes in saturation followed by low salinity waterflooding under tertiary mode, unsteady state (USS) under tertiary and secondary by using low salinity water flooding were history matched to derive the low salinity water relative permeability curves [13]. All of the coreflood experiments were conducted at 65^{o}C. The brine permeability of the experimental cores was lower than 1 mD, as shown in Table 5 and Table 6. The injection rate was 0.025ml/min. The procedures of corefloods experiments and set-up were selected from literature [10].

Methodology of History Matching in Core Scale

A one-dimensional homogeneous permeability core model was established to simulate the characteristics of oil recovery by forced imbibition with the finite difference simulator ECLIPSE 100. There were 22 equal-sized grid blocks in the core model. The first grid

which was located at the upstream of the core was saturated with 100% formation brine with 100% porosity, but 1000 D permeability was assigned to simulate the experimental injection. The last grid at the outlet of the core was saturated 100% oil with 0.001% porosity and 1000 D permeability since at beginning of the forced imbibition the outlet of the core was filled with 100% experimental oil. Porosity and permeability of each of the cells except of inlet and outlet cells was assumed to be equal. Porosity was obtained by Helium Porsimeter (PHI-220) under room temperature and permeability was measured through coreflooding experiment by injection of formation brine with saturated core plugs. The summary of composite core model for experiments and simulation model were given in Table 5.

According to the waterflooding simulation through ECLIPSE 100, the significant parameters dominating oil recovery and differential pressure by forced imbibition are the capillary pressure and relative permeability curves. The functional forms in Eqs. (4)-(6) are

$$k_{rw} = k_{rw}^{*}\left(\frac{S_w - S_{wi}}{1 - S_{or} - S_{wi}}\right)^{n_{rw}} \tag{4}$$

$$k_{ro} = k_{ro}^{*}\left(1 - \frac{S_w - S_{wi}}{1 - S_{or} - S_{wi}}\right)^{n_{r0}} \tag{5}$$

$$P^c = \sqrt{\frac{\phi}{k}}\sigma J^{*}\left(1 - \frac{S_w - S_{wi}}{S_{w0} - S_{wi}}\right)^{n_{pc}} \tag{6}$$

Where k_{rw} is the water relative permeability and k_{ro} is the oil relative permeability. P_c is the capillary pressure, and S is the phase saturation. The subscripts w, w_i and w_o represent water, initial water, residual oil at water saturation where the capillary pressure is equal to zero, respectively. The superscript $*$ denotes the end-point.

Table 5 Summary of composite core model for four experiments

Properties	Outcrop		Reservoir cores	
Samples	OC-2#	OC-3#	RC-2#	RC-3#
Flooding sequences	HS + LS	LS	HS + LS	LS
Porosity	0.136	0.140	0.129	0.123
Kw (mD)	0.331	0.340	0.92	0.82
Pore volume (cm^3)	4.770	4.810	4.3665	4.2029
Length (cm)	7.115	6.990	6.867	6.927
Diameter (cm)	2.504	2.504	2.5059	2.5068
Bulk volume (cm^3)	35.03	34.37	33.849	34.170
Cross sectional area (cm^2)	4.924	4.917	4.9292	4.9328
Grid block dimensions	20 × 1 × 1	20 × 1 × 1	20 × 1 × 1	20 × 1 × 1
Width (cm)	0.35575	0.34955	0.34335	0.34635
Height (cm)	2.219009	2.217431	2.2202	2.2210

Table 6 Summary of composite core model for four experiments

Properties	Outcrop		Reservoir cores	
Samples	OC-2#	OC-3#	RC-2#	RC-3#
Flooding sequences	HS + LS	LS	HS + LS	LS
no	2.2	2.1	5.2	3.2
nw	6.2	6.3	3.1	4.8
Krw(Sorw)	0.09	0.09	0.35	0.2
Kro(Swc)	1.0	1.0	1.0	1.0
Sorw	0.363(HS)/0.331 (LS)	0.339	0.412	0.382
Swc	0.268	0.291	0.322	0.315

Effect of Low Salinity Waterflooding on Reservoir Cores

Low salinity EOR-effect has been closely related to the change of wettability of reservoirs according to studies during the past more than a decade. However, the influence of the wettability in low permeability reservoirs on the low salinity waterflooding is rarely reported with combination of corefloods experiments, core-scale history matching. Therefore, this paper unveils the deeper understanding of low salinity EOR-effect through corefloods experiments on various wettability cores, core-scale history matching and thermodynamics analysis, which will be discussed at the last part of this study. Two reservoir cores, either flooded by low salinity water under secondary or tertiary mode, were implemented to conduct coreflooding. Both oil recovery and differential pressure by high and low salinity waterflooding were successfully history matched to derive the relative permeability curves, as shown in Figure 3, Figure 4 and Figure 5.

Figure 3 and Figure 4 show that low salinity waterflooding can improve oil recovery about 10% of OOIP under both secondary and tertiary mode, compared with high salinity waterflooding. Both of the Figures also indicate that the low salinity water can accelerate the oil production rate and reduce the residual oil saturation, with comparison of the high salinity waterflooding. This coreflood phenomenon proves that the great potential of low salinity waterflood effect may be observed as the reservoir is slightly water wet. This difference between LSWF and HSWF might be interpreted as a change in reservoir's wettability with invasion of low salinity brine. This can be proved by relative permeability curves derived by core-scale history matching, which was discussed below. In conclusion, low salinity water can accelerate the oil production rate and decelerate the water production rate by reduction of the residual oil saturation in reservoirs.

Low salinity EOR-effect on reservoir cores were also observed by the relative permeability curves (Figure 5), which were derived from the core-scale history matching by ECLIPSE 100 with low salinity model. Figure 5 shows that relative permeability curves for low salinity waterfood moves toward to the right, which might be interpreted as the transition of the wettability towards more water-wet. The capillary pressure curves were not shown here, due to the insensitivity to the core-scale history matching in the low permeability corefloods. As the corefloods experiments shown, the differential pressure was 1 to 2 MPa, which was much higher than the capillary pressure.

The incremental oil recovery by LSW compared to HSW could be attributed to the expansion of the electric double layer, which is caused by LSW as a result of increasing the magnitude of the negative electric charge at the interfaces of oil/brine and rock/brine. HSW caused weak surface charges at both oil/brine and rock/brine interfaces. However, more negative charges at oil/brine and brine/rock were generated by LSW. According to the theoretical calculation of thermodynamics, which will be discussed at the last part of this study, more negative charges at the interfaces of oil/LSW and LSW/rock and corresponding increase of the repulsive forces might detach the oil film from the rock surface.

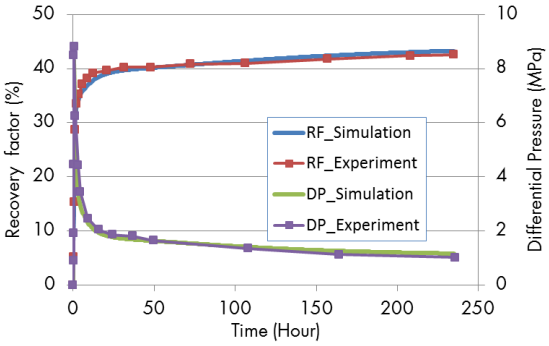

Figure 3 Low salinity waterflooding under secondary mode with the core from the reservoir (slightly water-wet)

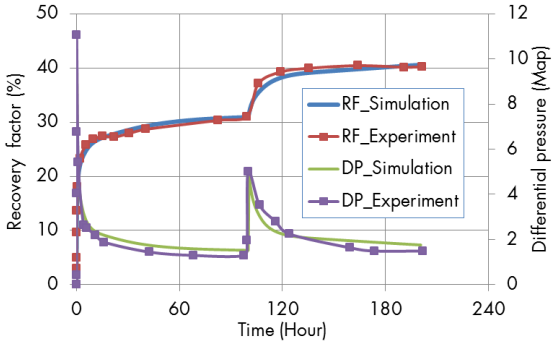

Figure 4 Low salinity waterflooding under tertiary mode with the core from the reservoir (slightly water-wet)

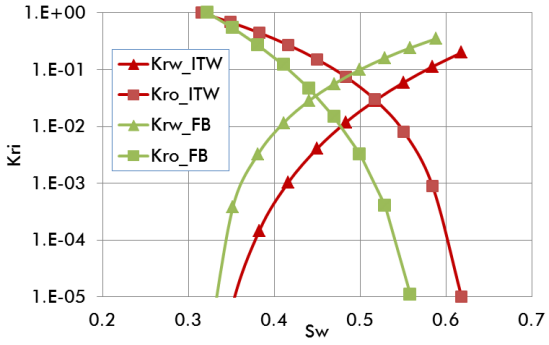

Figure 5 Relative permeability curves of low salinity and high salinity waterflooding (reservoir cores)

Effect of Low salinity Waterflooding on Water-wet Reservoir

According the the literature, the low salinity EOR-effect was rarely observed in the water-wet reservoirs. In order to further confirm and reveal the mechanism behind his phenomenon, two core plugs extracted from the outcrop were used to perform coreflooding with low salinity water, either in secondary mode or tertiary mode (Figure 6 and Figure 7). The experimental oil was from the Changqing Oil Field and the core plugs were put into the oven with 65°C for four weeks after the cores desaturated with experimental oil to restore the wettability. Additionally, the corefloods experiments were

successfully history matched to acquire the relative permeability curves, as shown in Figure 8.

Figure 6 and Figure 7 show that slight low salinity EOR-Effect was observed from low salinity waterflooding under secondary and tertiary mode. Figure 6 presents that 50.5% oil recovery of OOIP was accumulated by low salinity waterflooding. Figure 7 also shows that 50.0% oil recovery of OOIP was obtained by the high salinity waterflooding under secondary mode. Additional 3.4% oil recovery of OOIP was observed by low salinity waterflooding under tertiary mode. Relative permeability curves illustrates that the wettability of the outcrop was preferential to water-wet and minor wettability change during the low salinity waterflood was observed (Figure 8). Coreflooding experiments, by using water-wet outcrop core plugs, verified that low salinity effect may not work in the water-wet reservoirs. Moreover, with comparison of Figure 4 and Figure 7, piston-like displacement was found for high salinity water flooding as the core was water-wet, while the oil was produced over much longer periods for high salinity water flooding as the core was slightly water wet. This could be due to the more favorable mobility ratio formed by the low salinity water flooding in the reservoir [14].

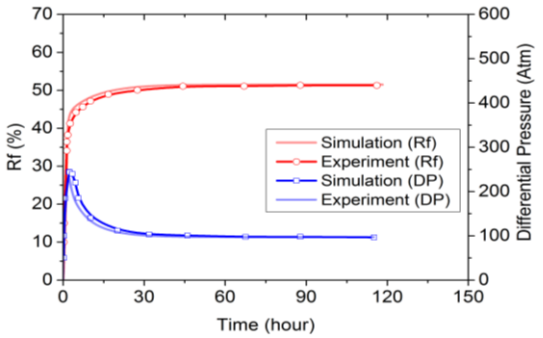

Figure 6 Low salinity waterflooding under secondary mode with the core from outcrop (water-wet)

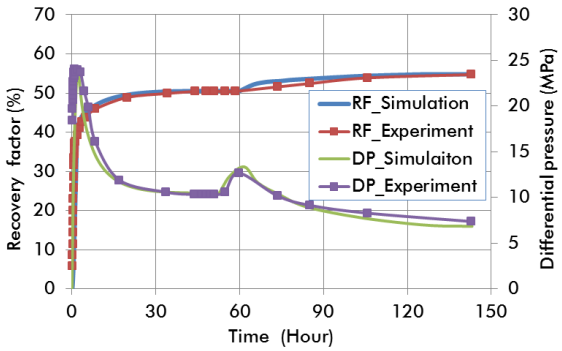

Figure 7 Low salinity waterflooding under tertiary mode with the core from outcrop (water-wet)

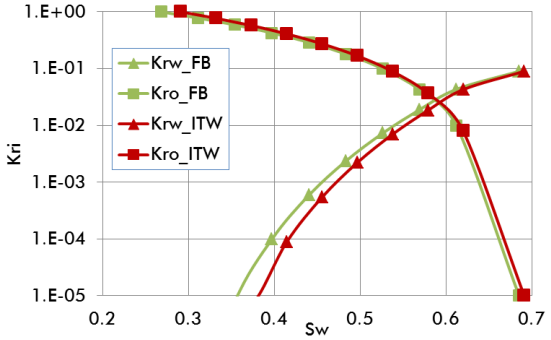

Figure 8 Relative permeability curves of low salinity and high salinity waterflooding (outcrop, water-wet)

THERMODYNAMICS ANALYSIS

Thermodynamics Background

Hirasaki has investigated the thermodynamics of the thin films to determine the interdependence of spreading, contact angle and capillary pressure using the DLVO theory and Laplace-Young Equation [8]. The intermolecular forces comprise of the van der Waals, electrical and structural forces.

$$\Pi_{Total} = \Pi_{Van-der-Waals} + \Pi_{electrical} + \Pi_{structural} \quad (7)$$

Where, Π_{Total} is the disjoining pressure of the specific intermolecular interactions which reflects the interactive forces between the interface of water/oil and water/rock. In this study, dielectric constants for each of medium were tested through N5224A microwave network analyzer, 2.84×10^{-21}J was used as the Hamaker constant for outcrop/brine/oil system, 3.70×10^{-21}J was used for reservoir rock/brine/oil system, A brief introduction of the forces and calculation procedures are presented in literatures [15].

Thermodynamic Calculation on Reservoir Cores and Outcrop

According to the theoretical model, structural forces were assumed to be as same with respect to the variation of molarity and zeta potential. Therefore, the variations of disjoining pressure could be explained by only considering the electrostatic interactions and Van der Waals forces, calculated with consideration of mineralogy difference. With combination of zeta potential measurement and composition of the brines, the disjoining pressure versus water film thickness was calculated (Figure 9) to unveil the deeper mechanism behind the low salinity waterflooding.

Figure 9 shows that the formation brine resulted in attractive force between the interface of oil/brine and interface of brine/rock in the slightly water wet rock. However, the repulsive force between the interfaces of oil/brine/rock was formed by low salinity water due to the low salinity and highly negative zeta potential for both interfaces of oil/water and water/rock. Figure 9 also shows that the water film was thicker in high salinity brine, compared with the low salinity brine due to the double layer expansion. Thicker water film indicates that the rock surface is preferential to water-wet with lower surface energy with presence of low salinity brine. Moreover, the thermodynamic isothermal calculation is consistent with the results of wettability test and corefloods experiments for the reservoir rocks.

Figure 10 illustrates that both formation brine and low salinity water causes the repulsive force between the interfaces of oil/water and water/rock in the water-wet rock. This also fits the results of wettability test and corefloods experiments for the water-wet outcrop rocks. Even though the thicker water film and repulsive force were formed as result of double layer expansion in low salinity brine, repulsive force still remained in the formation brine with thinner water film. The thermodynamic analysis for water-wet rock discloses that low salinity EOR-effect would not be observed in the water-wet reservoirs. Therefore, the conclusions can be drawn are: firstly, the thermodynamic isothermal can be applied to unveil the mechanism behind the low salinity EOR-effect. Secondly, it can

be used to screen the candidate reservoirs for low salinity waterflooding. Thirdly, composition of injection brine can be manipulated by the calculation of thermodynamics.

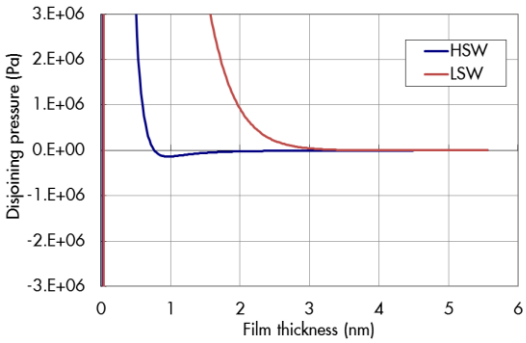

Figure 9 Disjoining pressure versus film thickness with formation brine and LSW in oil-wet rock

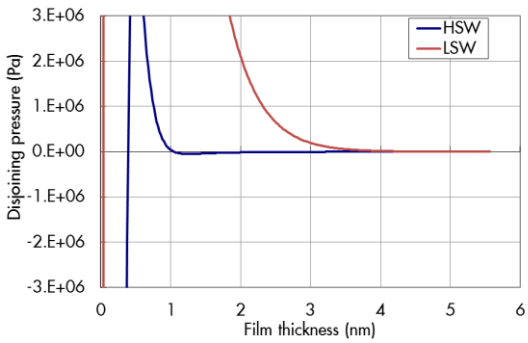

Figure 10 Disjoining pressure versus film thickness with formation brine and LSW in water-wet rock

CONCLUSION

In this study, the influence of rock wettability on the low salinity EOR-Effect was investigated by coreflood and history matching through ECLIPSE 100. Several observations were made in this study.

- Low salinity EOR-effect was observed during the low salinity waterflooding at both secondary and tertiary mode in the slightly water wet reservoir rock.
- Low salinity water can accelerate the oil production rate and decelerate the water production rate by reduction of the residual oil saturation in slightly water wet reservoirs.
- Slight wettability change and additional oil recovery were observed during the low salinity waterflood in the water-wet outcrop rock.
- Low salinity EOR-effect might be interpreted by thermodynamics of wettability. Thermodynamic calculation could help design the composition of the injection brine to enhance oil recovery.

ACKNOWLEDGEMENTS

The authors would like to thank Research Institute of Petroleum Exploration and Development of PetroChina for permission to publish this paper.

REFERENCES

1. Myint, P.C. and A. Firoozabadi, Thin liquid films in improved oil recovery from low-salinity brine. Current Opinion in Colloid & Interface Science, 2015. 20(2): p. 105-114.
2. Sheng, J.J., Critical review of low-salinity waterflooding. Journal of Petroleum Science and Engineering, 2014. 120(0): p. 216-224.

3. Sohrabi, M. and A. Emadi, Visual Investigation of Oil Recovery by Low Salinity Water Injection: Formation of Water Micro-Dispersions and Wettability Alteration, in SPE Annual Technical Conference and Exhibtion. 2013, 2013, Society of Petroleum Engineers: New Orleans, Louisiana, USA.
4. Morrow, N. and J. Buckley, Improved Oil Recovery by Low-Salinity Waterflooding. Journal of Petroleum Technology, 2011. 63(5): p. 106-112.
5. Lager, A., et al., Low Salinity Oil Recovery-An Experimental Investigation1. Petrophysics, 2008. 49(1).
6. A.Lager, K.J.W., C.J.J.Black, M.Singleton, K.S.Sorbie, Low salinity oil recovery-an experimental investigation. SCA2006-36, 2006.
7. Nasralla, R.A. and H.A. Nasr-El-Din, Double-Layer Expansion: Is It A Primary Mechanism of Improved Oil Recovery by Low-Salinity Waterflooding?, in SPE Improved Oil Recovery Symposium. 2012, Society of Petroleum Engineers: Tulsa, Oklahoma, USA.
8. Hirasaki, G.J., Wettability:fundamentals and surface forces. SPE Formation Evaluation, 1991. 6(2): p. 217-226.
9. Tang, G.-Q. and N.R. Morrow, Influence of brine composition and fines migration on crude oil/brine/rock interactions and oil recovery. Journal of Petroleum Science and Engineering, 1999. 24(2-4): p. 99-111.
10. Xie, Q., et al., Ions tuning water flooding experiments and interpretation by thermodynamics of wettability. Journal of Petroleum Science and Engineering, 2014. 124(0): p. 350-358.
11. Austad, T., A. Rezaeidoust, and T. Puntervold, Chemical Mechanism of Low Salinity Water Flooding in Sandstone Reservoirs, in SPE Improved Oil Recovery Symposium. 2010: Tulsa, Oklahoma, USA.
12. Xie Quan, H.S., Pu Wanfen, The Effects of Temperature and Acide Number of Crude Oil on the Wettability of Acid Volcanic Reservoir Rock From the Hailar Oilfield. Petroleum Science, 2010. 7: p. 93-99.
13. Masalmeh, S.K., et al., Low Salinity Flooding: Experimental Evaluation and Numerical Interpretation. 2014, International Petroleum Technology Conference.
14. Jerauld, G., et al., Modeling low-salinity waterflooding. SPE Reservoir Evaluation & Engineering, 2008. 11(6): p. 1000-1012.
15. Hirasaki, G.J., Wettability:fundamentals and surface forces. SPE Formation Evaluation, 1991c. 6(2): p. 217-226.

CONTRADICTORY TRENDS FOR SMART WATER INJECTION METHOD: ROLE OF PH AND SALINITY FROM SAND/OIL/BRINE ADHESION MAPS

Mathilde Didier, Annabelle Chaumont, Thibaut Joubert, Igor Bondino, and Gérald Hamon
TOTAL SA, CSTJF, Avenue Larribau, Pau, France

This paper was prepared for presentation at the International Symposium of the Society of Core Analysts held in St. John's Newfoundland and Labrador, Canada, 16-21 August, 2015

ABSTRACT

Smart Water Injection Methods (SWIM) requires a good understanding of the evolution of wettability not only as a function of salinity but also of pH. In order to have a better understanding of this parameter, adhesion tests were performed on crude oil/sand/brine systems. These tests were developed according to an in-house experimental protocol which guarantees full control of pH during its various stages and when crude oil/brine/rock are in equilibrium. Fontainebleau and Ottawa sands were used to understand the effect of pH and salinity on wettability. The brine was composed of a mixture of NaCl and $CaCl_2$ (ratio 9/1). The salinity varies from 7.9 to 785 mM and pH from 2 to 12.

Firstly, our adhesion tests are in good agreement with previous adhesion maps from the literature, although the experimental techniques are very different. Moreover our tests incorporate the effect of divalent ions and long term interactions between oil/water and the solid, which were not accounted for in previous studies. Our results confirm that at low salinity and acidic pH (pH < 7), oil adhesion increases for both sands, although quite more importantly for Fontainebleau. In that respect, our adhesion maps highlight contradictory results compared to the recent literature regarding the effect of salinity on wettability.

Secondly we find three distinct oil adhesion areas (for salinity from 0.5 to 50 g/L) which vary with equilibrium pH: from pH = 2.5 to 6 and pH = 8.5 to 12 showing oil wettability, pH = 6 to 8.5 showing water wettability. Interestingly it is found that critical pH thresholds exist in the range pH = 6 to 8.5 at which large variations in the adhesion between oil and sand are seen. This critical pH might be rock dependent: these three areas are specifically pronounced for Fontainebleau sand compared to Ottawa sand where the water wet area is more important (pH = 5.5 to 10). Considering the fact that both sands are mainly composed of quartz, it would imply that the predominant mineral species is not an impacting factor on wettability and therefore on SWIM.

INTRODUCTION

SWIM (Smart Water Injection Methods) have been widely investigated in the last 15 years. This is an emerging EOR (Enhanced Oil Recovery) technique highlighted by Tang and Morrow [1] in Berea sandstone, which is more and more studied due to its

economical aspect and feasibility. There are in the literature, numerous papers on this topic in order to understand the mechanism, but at this time, the real mechanism or combination of mechanisms which lead to the increase of the oil recovery have not been clearly defined. Several authors have various approaches to explain this effect as fine migration [2] controlled by clay particles, alkaline-flooding behavior which relies on interfacial tension reduction caused by pH increase [3], Multiple-Ion-Exchange (MIE) process [4], pH elevation [5] and formation of water micro-dispersions in the oil phase [6]. None of these mechanisms on its own can be retained to explain the increase in oil recovery: rather it is nowadays accepted that a combination of several factors and a mix of all these mechanisms is behind the SWIM effect [7]. A general consensus is that low salinity water may induce a change in the wettability towards a more water wet condition, which would somehow help in releasing additional oil from the pore space. But this mechanism has not yet been visualized or demonstrated in a convincing manner.

Since wettability is an important parameter which determines the fluids distribution and has an effect on oil recovery, several authors performed adhesion experiments in order to understand the interaction between crude oil, brine and rock [8-12]. Usually the reservoir sandstone rock is represented by crystalline quartz or various glass surfaces and classically two kinds of experiments are performed: contact angle [9, 10, 12] measurement and adhesion of a drop of crude oil on the surface [8, 10, 12]. In both cases, crude oil is surrounded with a brine composed of sodium chloride at various salinities and with a pH which varies from 2 to 10 and several parameters are normally tested as pH, Temperature, I (ionic strength), nature of oil, amongst others. From these results, adhesion maps are built which give a rapid and semi-quantitative means for characterizing crude oil interactions with a brine/solid system. Most researches have highlighted three areas in the adhesion map as a function of pH, brine salinity [9, 10] whose extension depends on crude oil's nature, brine's ionic composition, temperature and nature of solid:

- Adhesion at low pH (pH < 6) and low salinity (TDS < 5.8 g/L)
- Non-adhesion for pH comprised between 6 and 9 at moderate salinity (TDS ≈ 50 g/L)
- Adhesion at high pH (pH > 9) and high salinity (TDS > 50 g/L)

Lebedeva and Fogden [13] have shown similar results for kaolinite. It is seen that pH has a non negligible effect on adhesion. These results also highlight that there is more adhesion at lower salinity, which is difficult to reconcile with the claim that at low salinity, the system become more water wet. Nevertheless all these previous experiments were performed in a very short time for the contact between oil and glass (less than 10 min) which means that the system equilibrium may not have been reached. Moreover, no divalent ions were present in surrounding brine and for some authors [14, 16, 24-26], their presence in the brine is essential to observe a low salinity effect.

In this paper, we developed adhesion tests with a home-made protocol which allow the equilibrium of the system for various pH and salinities. Simple solids were used as pure

sands. This study allows us to evaluate the combined effect of salinity and pH on oil adhesion to the rock grains.

EXPERIMENTAL PROCEDURES

Materials

Minerals

For this study, two pure sands were used, Fontainebleau (from VWR) and Ottawa sands (from Fischer Chemical) in order to mimic sandstone reservoirs. These samples have been chosen for their purity in terms of mineralogy. Both sands are comparable in terms of mineralogy and are mainly composed of quartz (SiO_2) (Table 1).

Table 1: Mineralogy of sands from XRF measurements

Sands	SiO_2	CaO	K_2O	P_2O_5	Fe_2O_3	TiO_2	Ba
Fontainebleau	99.914	0.070	0.006	0.014	0.017	0.017	0.045
Ottawa	99.896	0.071	0.013	0.019	0.021	0.007	0.000

These samples were also characterized with a binocular magnifier to evaluate their external structure (Figure 1). We can remark that the sands have completely different structure. These sands were also characterized by laser granulometry. Ottawa sand has bigger particles with a size of 880 µm compared to Fontainebleau which has a particle size of 260 µm.

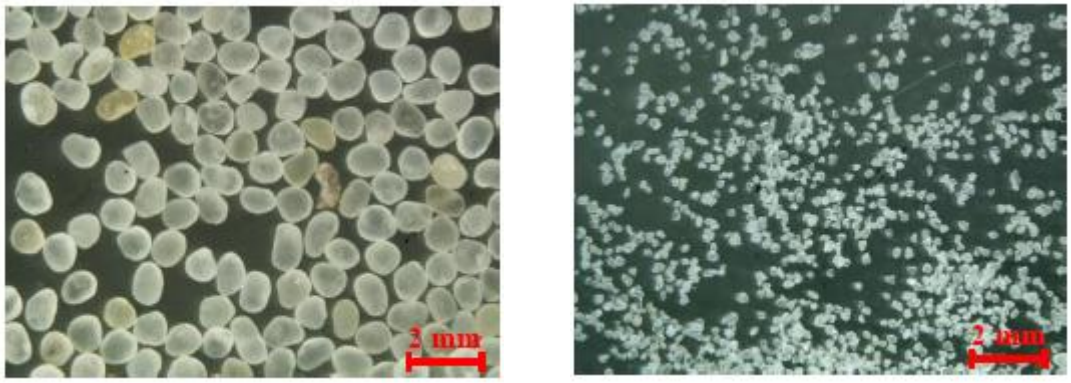

Figure 1: Sand observations with the binocular magnifier, Ottawa sand (left) and Fontainebleau sand (right)

Crude Oil

The same crude oil was used for all the adhesion tests. The oil has been filtered at 40 µm before use. Table 2 highlights its properties.

Table 2: Analysis of crude oil

Property	Units	Crude oil
TAN	mg/g KOH	0.2
TBN	mg/g KOH	1.77
Density @ 40 °C	kg/m^3	834
Density @ 60 °C	kg/m^3	820
Viscosity @ 40 °C	cSt	6.26
Viscosity @ 60 °C	cSt	3.94
% Asphaltenes	weight %	2.9
TCC*	°C	35

*TCC: Critical Temperature of Crystallization

Brines

Synthetic brine solutions were prepared at various salinities with 90 wt% of NaCl and 10 wt% of $CaCl_2$. NaCl(s) and $CaCl_2$(s) were manufactured by Sigma Aldrich® with a purity higher than 99.9%. Demineralized water was used. Brine solution pH was adjusted with HCl(aq) or NaOH(aq) solutions at 0.1 or 1 M. After stirring, all the solutions were filtered at 0.45 µm, pH varies from 2 to 12 and it was controlled during manipulation. Tested TDS (Total Dissolved Salts) were 0.5, 1, 3, 7, 11, 15, 25 and 50 g/L. The properties of the brine used in this study are summarized in the Table 3.

Table 3: Salinity, molar concentration and ionic strength of used brines

TDS(g/L)	0.5	1	3	7	11	15	25	50
C (mM)	7.85	15.7	47.1	11	17.3	23.6	39.3	78.5
I*	0.019	0.036	0.11	0.25	0.40	0.55	0.91	1.82

*: Ionic Strength

Experimental Protocol

Sand Cleaning

In order to eliminate all contaminations, mainly by iron, the sand was washed beforehand with an acid solution (HCl(aq), 1M), then neutralized with sodium bicarbonate ($NaHCO_3$(aq), 1M), rinsed thoroughly with demineralized water and finally oven dried at 60°C for 24 h.

Protocol of Adhesion Tests

The test tube experiment is a fast screening of sand/oil/brine interactions permitting to focus on the effect of one parameter at the time. These batch experiments use a static procedure which is described below.

1. Prepare brine at the chosen salinity.
2. Place a known mass of cleaned sand in contact with a known volume of brine. The brine has to be in excess compared to the sand.
3. Add HCl(aq) at C = 0.1 M or 1 M or NaOH(aq) at C = 0.1 M to adjust the pH to the chosen value.
4. Leave the solution at 60°C during 24h for equilibration; regularly shake manually to homogenize the sand/brine system.
5. Measure the pH.
   If the target pH is not reached, repeat the steps 3 and 4 to eliminate the buffering effect of sand.
6. When the target pH is reached and is seen to be stable, mark this pH as *initial pH* (pH_i). Now add a known volume of oil to the system.
7. Shake manually the glass vial to free the oil that is trapped under the weight of the sand and not actually adhering to it.
8. Leave the system at 60°C during 48 h under continuous stirring.
9. Observe wetting state at equilibrium at T = 60°C. The wetting state is the evaluation of the oil quantity which is in adhesion on and in the sand compared to the oil which stays above the brine phase (Figure 4 for example). Three states were defined; adhesion, transition and non-adhesion. When the oil quantity in the sand is higher than in the brine, then there is adhesion. If there is

quite the same quantity of oil in the sand and in the brine phase, then it is transition state. Finally when no oil adheres in the sand, then it is non-adhesion state.

10. Shake manually, wait for equilibrium and observe the wetting state. As previously, manual shake makes the system more homogeneous and helps to estimate visually the actual sand and oil adhesion by freeing the oil that is trapped under the weight of the sand.
11. Measure the *final pH* (pH_f) after filtration at 0.45 µm of the brine in the system.
12. Report the observed wetting state at fixed pH in an adhesion map
13. Perform this protocol for another initial pH until the adhesion map is complete with all the tested salinity and initial pH

Remark: Equilibrium was estimated with tests at various experiment durations. It was estimated that after 48h of stirring, the interaction between oil, sand and brine stays the same even after more hours of stirring at temperature.

This protocol allows removal of the buffering effect of the sand (which can be quite important) and to control the initial and final pH of the system. The key parameter in this study is the control of pH. The final pH could be estimated with the pHi-pHf diagram of the used crude oil (Figure 2). We can remark in this graph that the evolution of pH is the same at low salinity (1 g/L) as at high salinity (50 g/L). For this studied oil, when initial pH is comprised between 4 and 10, the final pH is between 6 and 8. This oil is mainly a basic one.

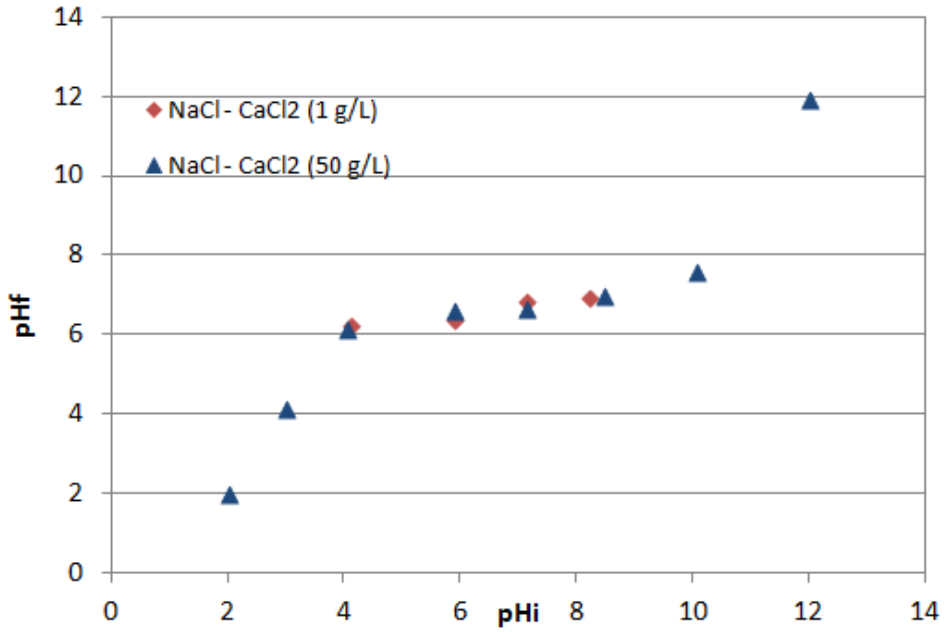

Figure 2 : pHi-pHf diagram of the tested crude oil at 45°C in NaCl/$CaCl_2$ brine at low and high salinity (TDS = 1 and 50 g/L)

RESULTS AND DISCUSSIONS

The adhesion map of Fontainebleau sand is displayed in Figures 3a and 3b.

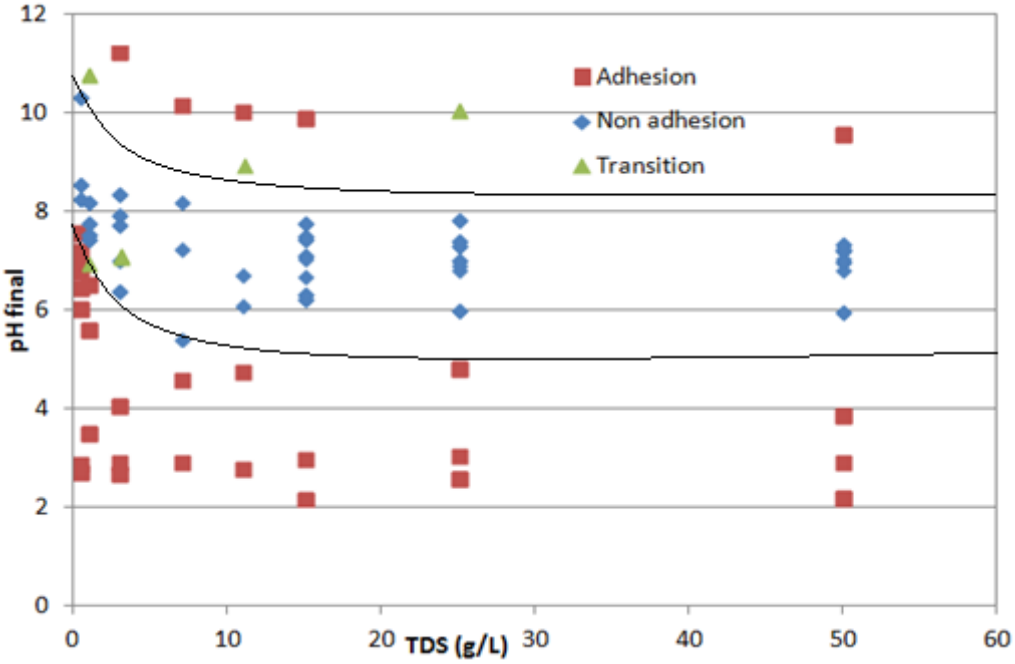

Figure 3a: Adhesion map of Fontainebleau sand

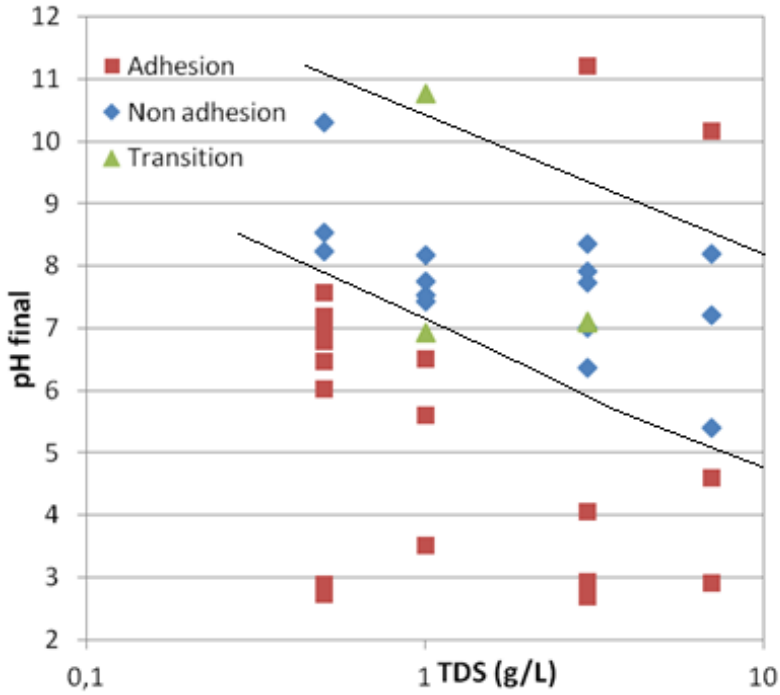

Figure 3b: Adhesion map of Fontainebleau sand (zoom on low salinity (TDS<10 g/L))

The information in this map can be approximated by three main adhesion areas roughly situated at:

- 2 < pH < 6 : oil adheres to grains
- 6 < pH < 8 : oil does not adhere to grains
- 8 < pH < 12 : oil adheres to grains

An example of test tube experiments is displayed in Figure 4 to illustrate this adhesion map at 7 $g.L^{-1}$. In this example, adhesion occurs at final pH equal to 5.42 and at higher pH_f (10.17), whilst non-adhesion is seen for pH_f = 7.23.

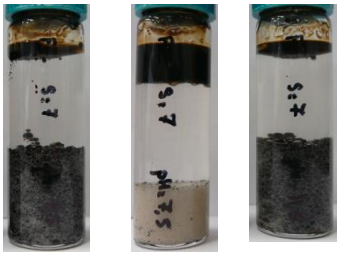

5.42 7.23 10.17

Figure 4: Glass vial adhesion map results at fixed salinity (7 $g.L^{-1}$) and for three pH (pHf) values. From left to the right: adhesion, non-adhesion, adhesion.

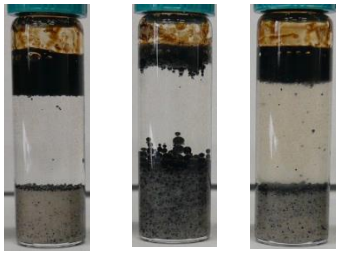

6.38 7.11 7.74

Figure 5: Glass vial adhesion map results at fixed salinity (3 $g.L^{-1}$) and for three pH (pHf) values. From left to the right: non-adhesion, transition, non-adhesion.

By decreasing the pH, whatever the salinity, a greater adhesion of oil on the Fontainebleau sand is visible, a result in agreement with the work of Yang et al. [10] and Drummond et al. [9]. Oil adhesion is systematic for pH below 5 as well as for pH higher than 10. In addition, at low salinity (TDS < 3 g/L), the zone of oil adhesion extends towards higher pH. In this area (6 < pH < 8) small variations of salinity for a given pHf can create very different adhesion results (Figure 5).
This observation is very important since pH values expected at reservoir conditions would cover the interval 5 < pH < 7 [22]: wettability being so sensitive in these pH-salinity ranges, could create an important variability of outcomes and would render SWIM performance not trivial to assess.

In conclusion, the result obtained for Fontainebleau shows that the rock becomes more oil wet when salinity decreases, in contradiction to comments in literature on smart water techniques ([14-17]) where when decreasing the salinity, the water wetness of the solid increases, leading to the increase of oil recovery.

In Figure 6 the adhesion map for Ottawa sand is displayed. There are three main areas of adhesion, mainly controlled by pH, as for Fontainebleau, but here there is much less influence of salinity. The oil adheres when pH decreases (pH < 5) and for low salinity (TDS < 10 g/L) as well as for basic pH (> 11) for all salinities. The last area in this adhesion map shows water wet condition.

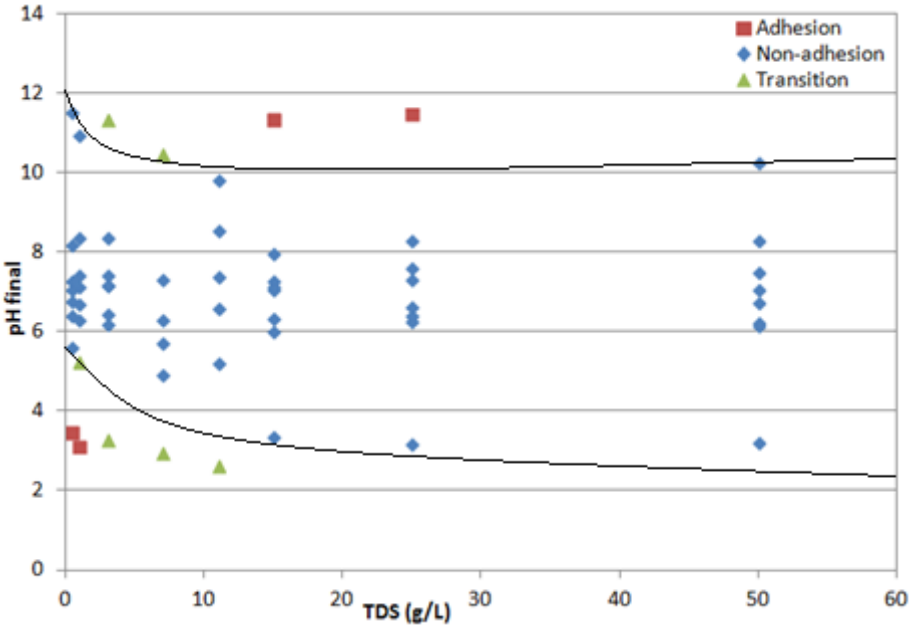

Figure 6: Adhesion map of Ottawa sand

Since both sands share a very similar mineralogy, then we would conclude that for this case sample mineralogy does not have an important effect on wettability.
The three areas in the adhesion maps of Fontainebleau and Ottawa sands could be partially explained by adsorption of oil components on sand and electrostatic repulsion, at least at low pH (Figure 7).

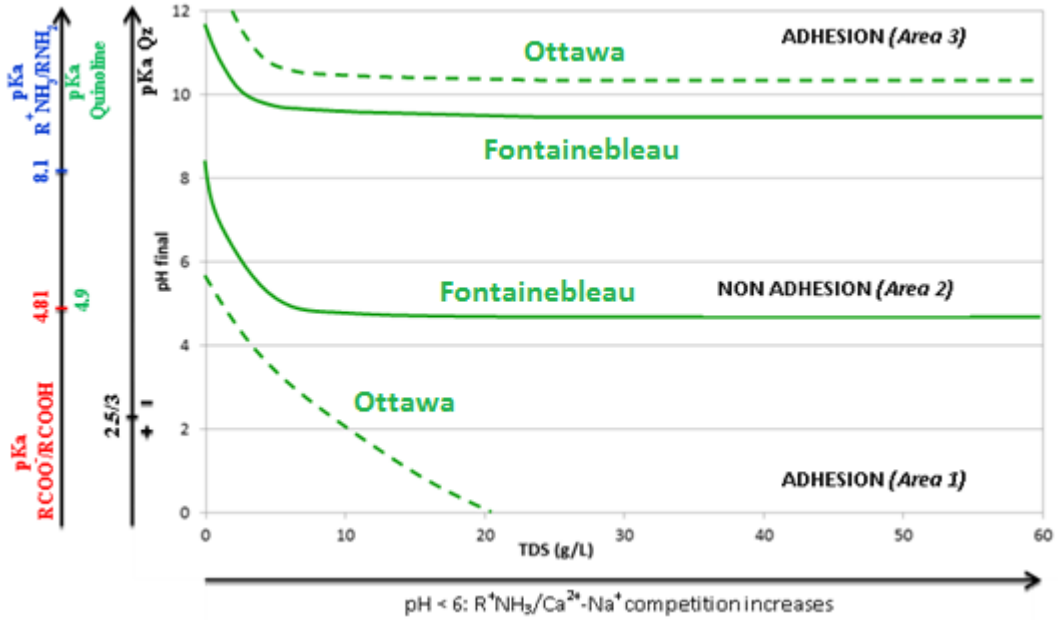

Figure 7: Interpretation of adhesion maps. Continuous and dotted green curves show the transition from water-wet to oil-wet for Fontainebleau and Ottawa sand respectively

The results of this study could be compared with those from Bondino et al. [18], where the authors used similar experimental setup to evaluate oil adhesion on sand. They highlighted also oil adhesion at high and low salinity conditions (TDS = 1 and 50 g/L)

and for acidic pH (pHi < 5). Water wetness is observed at basic pH (pH > 7) and for low salinity. Nevertheless the main difference between the two studies is that in [18], the pH was not controlled and measured at the end of the experiment (therefore the pH discussed in the paper happens to be the initial one). Regarding our results, we demonstrate pH is a key parameter in wettability variation and has to be controlled and measured all along the experiment.

These results are comparable with those from the literature [8-12] where adhesion maps highlight also three areas which depend on pH and salinity range. Oil adhesion occurs also for low pH (< 6) and high pH (> 9) and non-adhesion for intermediate pH (6< pH < 10) and salinity (≈ 50 g/L). Transition zone for low salinity (TDS < 5.8 g/L) is located for pH close to 6 and 8, as observed in this paper. This pH area is therefore critical and pH seems to be a key parameter in oil adhesion. This study confirms these previous contradictory results where oil adhesion increases for low salinity range. Nevertheless the test tube experiments presented in this paper seem to be more representative of SWIM compared to the previous adhesion tests. Indeed, compared to the results of [8-12], duration of experiments is longer and led to equilibrium within the system oil/brine/sand. Moreover brines were composed of mono and divalent ions as Ca^{2+} which is favourable for low salinity effect [4, 16] compared to brines with only monovalent ions in the cited literature.

Adhesion maps (Figures 3 and 6) could be explained by electrostatic interaction between oil and sand. The isoelectric point of quartz is estimated to be close to 2.5 ([19, 20]) which means that quartz (Qz) is negatively charged for pH higher than 2.5 (Figure 8). Usually, acid and base components of oil are simplified by RNH_2, RCOOH and Quinoline. pKa of these redox couples are illustrated in Figure 8. At low pH (< 4.9), oil components are essentially positive and inversely at basic pH (> 8.1).

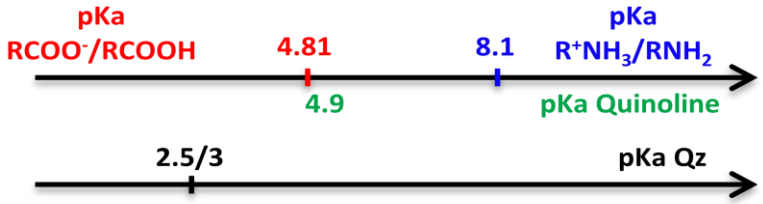

Figure 8: pKa of oil components (RNH2, RCOOH, Quinoline) and isoelectric point of Quartz (Qz)

Figure 7 summarizes adhesion maps with adhesion areas for Fontainebleau and Ottawa sands. In ***Area 1***, adhesion occurs at low pH (2.5 < pH <5) due to reduction of electrostatic interaction between sands negatively charged and oil components positively charged (R^+NH_3, Quinoline positively charged). In ***Area 2***, non adhesion occurs at higher pH (pH > 4.9) due to repulsion between sands still negatively charged and neutral (RNH_2, Quinoline) and negative (CH_3COO^-) oil components. However, when salinity increases in ***Area 1***, oil adhesion occurs at lower pH for Fontainebleau sand but not for Ottawa sand. One hypothesis is the influence of roughness and granulometry which could increase specific surface area of sand grains and therefore increase the probability of adhesion. The roughness of Fontainebleau sand seems higher than Ottawa's, therefore its specific surface area could be higher and this will increase the probability of oil adhesion. Similar observations were already highlighted

in the literature [21]. In the ***Area 3***, oil adhesion at very basic pH (pH > 10) is more difficult and complex to explain: further investigations are ongoing.

This variation of adhesion with pH suggests also that not only the final pH is necessary to know, but also the initial pH of the system. If there is a pH evolution during the waterflooding experiment in the system rock/brine/oil, we could have a change of wettability which could have an impact on the recovery.

This study could be useful for understanding spontaneous imbibitions tests, as adhesion maps were elaborated with test tube experiments without dynamic aspect. In the literature, some authors highlight high response variability for spontaneous imbibitions tests with various carbonates rocks [22] or various type of oil on Berea sample [23] for example. Romanuka et al. [22] show various wettability modification in function of rock samples or ionic composition of injected water. Suijkerbuijk et al. [23] found very different oil recovery during spontaneous imbibitions with ten different oils on Berea sandstones. Adhesion tests as described in this study could be useful screening tests for understanding the variability in response of SWIM spontaneous imbibitions experiments.

CONCLUSIONS

In this paper, test tubes experiments were performed in order to implement adhesion map for crude oil/sand/brine system. A home-made protocol allows the system to reach equilibrium at temperature with full control of the pH. Indeed, pH appears to be an essential parameter in wettability, more than the salinity. Adhesion map of Fontainebleau sand highlights oil adhesion at low salinity (TDS < 3 g/L) in reservoir pH area (6 < pH < 8) and non adhesion for a salinity higher than 3 g/L in this pH area. Moreover, this domain is very sensitive to pH variation. A little variation in pH will change drastically the wettability. This highlight that pH has to be well monitored during waterflooding experiments.

The fact that low salinity increases the oil wettability is contradictory to what is expected in the literature for SWIM, where low salinity waterflooding is seen to increase water wetness and then the oil recovery. In light of these results, we think that it would be more appropriate to state that oil recovery depends from the transition from some initial to some final state, and not simply from a system becoming more water wet.

It was rather interesting to note that Ottawa and Fontainebleau highlight different adhesion maps despite the fact that their mineralogy is quite similar. Therefore the mineralogy may not always be a determinant parameter in low salinity effect. Moreover both sands have various roughness, which could be an important parameter for adhesion behavior. The effect of surface roughness and granulometry is currently under investigation. Finally electrostatic interactions between acid and base components of the oil seem to control the adhesion on the solid.

ACKNOWLEDGEMENTS

The authors would like to gratefully acknowledge TOTAL SA for funding this project and for the technical support.

NOMENCLATURE

SWIM	Smart Water Injection Methods	I	Ionic Strength
EOR	Enhanced Oil Recovery	wt%	Weight %
TCC	Critical Temperature of Crystallization	C	Molar Concentration
TDS	Total Dissolved Salts	M	mol/L

REFERENCES

[1] G.Q. Tang, N.R. Morrow, Salinity, Temperature, Oil Composition, and Oil Recovery by Waterflooding, in: SPE Reservoir Engineering, Society of Petroleum Engineers, Denver, Colorado, 6-9 October, 1997, SPE-36680-PA.

[2] G.-Q. Tang, N.R. Morrow, Influence of brine composition and fines migration on crude oil/brine/rock interactions and oil recovery, *Journal of Petroleum Science and Engineering*, **24** (1999) 99-111.

[3] P.L. McGuire, J.R. Chatham, F.K. Paskvan, D.M. Sommer, F.H. Carini, Low Salinity Oil Recovery: An Exciting New EOR Opportunity for Alaska's North Slope, in: Society of Petroleum Engineers, Society of Petroleum Engineers, Irvine, California, 30 March - 1 April, 2005, SPE 93903.

[4] A. Lager, K.J. Webb, C.J.J. Black, M. Singleton, K.S. Sorbie, Low Salinity Oil Recovery - An Experimental Investigation1, in: SCA2006-36, Society of Petrophysicists and Well-Log Analysts, Trondheim, Norway, 12-16 September, 2006.

[5] T. Austad, A. Rezaeidoust, T. Puntervold, Chemical Mechanism of Low Salinity Water Flooding in Sandstone Reservoirs, in: S. 129767 (Ed.), Society of Petroleum Engineers, 2010.

[6] A. Emadi, M. Sohrabi, Visual Investigation of Oil Recovery by LowSalinity Water Injection: Formation of Water Micro-Dispersions and WettabilityAlteration, in: S. 166435 (Ed.) Society of Petroleum Engineers, Society of Petroleum Engineers, New Orleans, Louisiana, USA, 2013.

[7] B. Soraya, C. Malick, C. Philippe, H.J. Bertin, G. Hamon, Oil Recovery by Low-Salinity Brine Injection: Laboratory Results on Outcrop and Reservoir Cores, in, Society of Petroleum Engineers.

[8] J.S. Buckley, N.R. Morrow, Characterization of Crude Oil Wetting Behavior by Adhesion Tests, in: S. 20263 (Ed.) Society of Petroleum Engineers, Society of Petroleum Engineers, Tulsa, Oklahoma, 22-25 April, 1990.

[9] C. Drummond, J. Israelachvili, Fundamental studies of crude oil–surface water interactions and its relationship to reservoir wettability, *Journal of Petroleum Science and Engineering*, **45** (2004) 61-81.

[10] S.Y. Yang, G.J. Hirasaki, S. Basu, R. Vaidya, Mechanisms for contact angle hysteresis and advancing contact angles, *Journal of Petroleum Science and Engineering*, **24** (1999) 63-73.

[11] S.Y. Yang, G.J. Hirasaki, S. Basu, R. Vaidya, Statistical analysis on parameters that affect wetting for the crude oil/brine/mica system, *Journal of Petroleum Science and Engineering*, **33** (2002) 203-215.

[12] L. Liu, J.S. Buckley, Alteration of wetting of mica surfaces, *Journal of Petroleum Science and Engineering*, **24** (1999) 75-83.
[13] E.V. Lebedeva, A. Fogden, Wettability alteration of kaolinite exposed to crude oil in salt solutions, *Colloids and Surfaces A: Physicochemical and Engineering Aspects*, **377** (2011) 115-122.
[14] M. Rotondi, C. Callegaro, F. Masserano, M. Bartosek, Low Salinity Water Injection: eni's Experience, in, Society of Petroleum Engineers (2014).
[15] R. Julija, H. Jan, L. Dick Jacob, S. Bart, M. Fons, O. Sjaam, B. Niels, L. Hilbert van der, A. Hakan, A. Tor, Low Salinity EOR in Carbonates, in: SPE Improved Oil Recovery Symposium, Society of Petroleum Engineers, Tulsa, Oklahoma, USA (2012).
[16] S. Strand, E.J. Hognesen, T. Austad, Wettability alteration of carbonates - Effects of potential determining ions (Ca^{2+} and SO_4^{2-}) and temperature, *Colloids and Surfaces A: Physicochemical and Engineering Aspects*, **275** (2006) 1-10.
[17] A.A. Yousef, S.H. Al-Saleh, A. Al-Kaabi, M.S. Al-Jawfi, Laboratory Investigation of the Impact of Injection-Water Salinity and Ionic Content on Oil Recovery From Carbonate Reservoirs, in.
[18] I. Bondino, S. Doorwar, R. Ellouz, G. Hamon, Visual microscopic investigations about the role of pH, salinity and clay on oil adhesion and recovery, in: SCA, NAPA Valley, California, 2013.
[19] F.C. Schoemaker, D.M.J. Smeulders, E.C. Slob, Electrokinetic Effect: Theory And Measurement, in, Society of Exploration Geophysicists.
[20] P.L. Churcher, P.R. French, J.C. Shaw, L.L. Schramm, Rock Properties of Berea Sandstone, Baker Dolomite, and Indiana Limestone, in, Society of Petroleum Engineers.
[21] M.C. Michalski, S. Desobry, J. Hardy, Adhesion of Edible Oils and Food Emulsions to Rough Surfaces, *LWT - Food Science and Technology*, **31** (1998) 495-502.
[22] J. Romanuka, J. Hofman, D.J. Ligthelm, B. Suijkerbuijk, F. Marcelis, S. Oedai, N. Brussee, H. van der Linde, H. Aksulu, T. Austad, Low Salinity EOR in Carbonates, in, Society of Petroleum Engineers, 2012.
[23] B. Suijkerbuijk, J. Hofman, D.J. Ligthelm, J. Romanuka, N. Brussee, H. van der Linde, F. Marcelis, Fundamental Investigations into Wettability and Low Salinity Flooding by Parameter Isolation, in, Society of Petroleum Engineers, 2012.
[24] P. Zhang, M.T. Tweheyo and T. Austad, Wettability Alteration and Improved Oil Recovery in Chalk: the Effect of Calcium in the Presence of Sulfate, *Energy & Fuels*, **20** (2006) 2056-2062
[25] R. Gupta et al., Enhanced Waterflood for Middle East Carbonate Cores – Impact of Injection Water Composition, Manama, SPE 142668 (2011).
[26] S.J. Fathi, T. Austad and S. Strand, Smart Water as wettability Modifier in Chalk: The effect of salinity and ionic composition, *Energy Fuels*, **24** (2010) 2514-2419.

LOW SALINITY WATER FLOODING: FACTS, INCONSISTENCIES AND WAY FORWARD

G. Hamon
TOTAL

This paper was prepared for presentation at the International Symposium of the Society of Core Analysts held in St. John's Newfoundland and Labrador, Canada, 16-21 August, 2015

ABSTRACT

15 years after the first experimental evidence of increased oil recovery by low salinity water injection (LSWI), clear understanding of the mechanisms has not emerged yet out of more than 500 published laboratory experiments.

Firstly, it is shown that there is increasing experimental evidence that published tertiary LSWI core floods do not often succeed in increasing significantly the recovery within the 2-3 first PVs of tertiary injection, despite strong claims of positive results.
Then, this paper focuses on sandstones and mostly on studies where secondary LSWI performs better than secondary high salinity water injection (HSWI). Even in such cases, some examples show that the efficiency of tertiary LSWI may range from poor to nil. These cases satisfy all "required conditions", such as presence of clay, of connate water, and mixed wettability.

Conditions of existence of a double saturation shock, effects of dispersion in water phase at $Sorw_{HS,}$ and the direction of wettability modification are the hypotheses discussed in this paper to understand poor performance of tertiary LSWI. Some key experimental observations are then compared to these possible explanations. They may explain the vast majority of published studies, but counter examples can also be produced for any single proposed mechanism.

This paper also puts in evidence that some types of experimental measurements have been neglected and would deserve more attention, comments on the effect of interfacial tension and suggests a new approach for investigating the efficiency of tertiary low salinity water flooding.

INTRODUCTION

There is a clear evidence that:

- Spontaneous imbibition by LSWI is able to increase oil recovery compared to high salinity [21, 44, 46, 59]. In such cases, LSWI can be used to increase oil recovery of very heterogeneous matrix reservoirs or highly fractured reservoirs.
- Secondary LSWI is able to increase oil recovery compared to HSWI in a large number of studies [11, 17, 18, 22, 23, 28, 29, 40, 45, 48, 51, 52, 55]. Significant additional oil is often observed at water breakthrough or immediately after. In such cases, LSWI can

be used to increase recovery of undeveloped fields. The comparison of secondary recoveries between LSWI and HSWI also showed cases with either very weak benefit of LSWI [55] or no difference [34] or even negative result [19, 37, 52]. Some authors [20, 51] suggested that LSWI was always successful but they also showed a wide variation in positive results. Other authors [5, 55] highlighted that the main challenge would be to explain the very large scatter in incremental recoveries by LSWI: from nil to $\Delta Sorw = -13$ saturation units. Morrow [27] concluded that "*Identification of the sufficient conditions for LSE and understanding the circumstances under which there is little or no LSE remain as outstanding challenges*".

A large number of laboratory studies consist of tertiary LSWI after secondary HSWI. The motivations behind tertiary floods are:

1. Reproduce the saturation history of mature, waterflooded reservoirs and check whether LSWI can be an efficient EOR process,
2. Cope with scarce availability of reservoir cores. Comparison of secondary waterfloods requires at least twin samples or more if different recipes of injected water are tested

Almost all laboratory tertiary LSWI tests start at $Sorw_{HS}$ and consist of continuous injection of low salinity afterwards. A lot of authors conclude that tertiary LSWI has positive effects, based upon final incremental recovery after very long injection periods. In fact this conclusion is much more debatable than for secondary LSWI. If we decide that a realistic, positive effect means 1) The arrival of the oil bank at approximately 0,5-0,6 PV injected or 2) Additional recovery of at least +5%ooip after 1 PV injected, the scene looks quite different:

- Studies showing production of significant incremental oil after a short tertiary injection period of low salinity water are very scarce [20, 22, 38, 45, 51].
- When significant incremental oil is produced during tertiary LSWI, oil is very often delayed or oil is produced at a low pace over several PVs of injection [3, 10, 11, 21, 22, 23, 31, 32, 33, 45, 49, 55, 56]
- Nil or very poor additional recovery by tertiary LSWI has now been largely reported. It has been suggested that such failures were related to use of outcrop cores, rather than reservoir cores [52]. In fact, very poor additional recoveries are shown for both:
    - Outcrop: [16, 19, 28, 34, 35, 40, 41, 43, 52, 53, 55]
    - And reservoir cores [5, 15, 17, 33, 37, 42, 52].
    - Taking into account the overrepresentation of outcrop cores in published laboratory work about LWSI, the conclusion about outcrop versus reservoir cores remains questionable.

It is worth noting that the three necessary conditions, as defined in [27] for positive effect of LSWI, were almost always satisfied in these studies.

In the following, the possible reasons of the poor performance of tertiary LSWI are investigated. Unfortunately, the vast majority of these experiments are not accompanied by any other type of tests: neither secondary LSWI nor wettability, etc. It prevents detailed analysis. Therefore, this paper focuses mainly on the scarce laboratory studies which: 1)

Report both secondary and tertiary LSWI 2) Show larger oil recovery by LSWI than by HSWI on secondary floods. These studies represent crude oil/brine/rock systems where LSWI effect does exist in secondary mode and we can eliminate debates about causes which trigger positive low salinity effect.

FACTS, HYPOTHESES AND INCONSISTENCIES

Existence of a Double Saturation Shock

Firstly, we might hypothesize that the evolution of oil production during tertiary LSWI, starting at $Sorw_{HS,}$ strongly depends on conditions which control the existence of a double saturation shock [30], particularly on fractional flows for secondary high and low salinity water floods. When reviewing literature LSWI results, viscosity ratio and secondary water/oil relative permeabilities (Krs) for both LSWI and HSWI would be necessary to evaluate these conditions for each study. In fact, they are almost never reported. However, coarse estimation can be done when the viscosity ratio and the evolution of differential pressure during secondary floods are reported.

Simulations in figure *1a* have been performed using a set of Krs for secondary water floods where ΔSorw = -0,1 between high and low salinity waters:

- With favorable fractional flows, here μ_o/μ_w =2, an oil bank is created in tertiary mode by LSWI and breaks through rather early, at about 0,5-0,6 PV injected, as suggested also by other simulations [26] or analytical calculations.
- At unfavorable conditions, here for μ_o/μ_w=7, the oil bank vanishes. Incremental oil is delayed and is produced very slowly. It represents the slow arrival at the outlet of the spreading wave related to the LSWI. For μo/μw=18, tertiary oil production is postponed to very late times.

Experimental observations of a clear oil bank during tertiary LSWI are very scarce in the literature. When this behavior is reported [20, 22, 45, 51], lack of information often prevents the comparison of experimental conditions with theoretical estimations about the existence and stability of the second saturation shock. Oil banking during tertiary LSWI is consistent with low viscosity oils and with the type of Kr curves for secondary floods shown by Webb in [51] on three reservoirs: very small difference in Krw(Sorw) between HS and LS despite significant reduction in residual oil saturation: ΔSorw~ -0,05 to -0,07.

In fact, most of published tertiary LSWI have been carried out at large [16, 31, 32, 33, 35] to very large (μo/μw~18 [40], ~23 [49], ~32 [55], ~40 [52, 53], ~54 [56]) viscosity ratios. They might explain the absence of oil bank, the delayed oil bump if any, as well as very slow oil production. Shehata [40] performed tertiary LSW on Bandera sandstone. Significant benefits were clear in secondary mode by LSWI: ΔRec~+9% oip. The delayed arrival of the oil bump, after 1,5 PV injected in figure *1b*, is consistent with the unfavorable viscosity ratio. In the same study, he obtained even better results in secondary mode on Buff Berea: ΔRec~+16% OIP, but no tertiary incremental oil by LSWI. Again, this is consistent with large viscosity ratio.

More surprising are some rare core floods where a fast and strong oil bank is reported in conditions where it should disappear. Loahardjo's [22] cores 2065/1 R1/C1 and 2060/1 R1/C1 did produce a strong oil bank at 0,42 PV tertiary LSWI despite very unfavorable viscosity ratio (μo/μw~30). However a 5-10 fold increase in differential pressure is reported immediately after starting LSWI, which may be related to dispersion of kaolinite with salinity shock. Although endpoints are not explicitly reported, it shows that $Kw(Sorw_{LS}) << Kw(Sorw_{HS})$, despite $\Delta Sorw \sim -0,05$. This reduction in total mobility might contribute to the stabilization of tertiary saturation front.

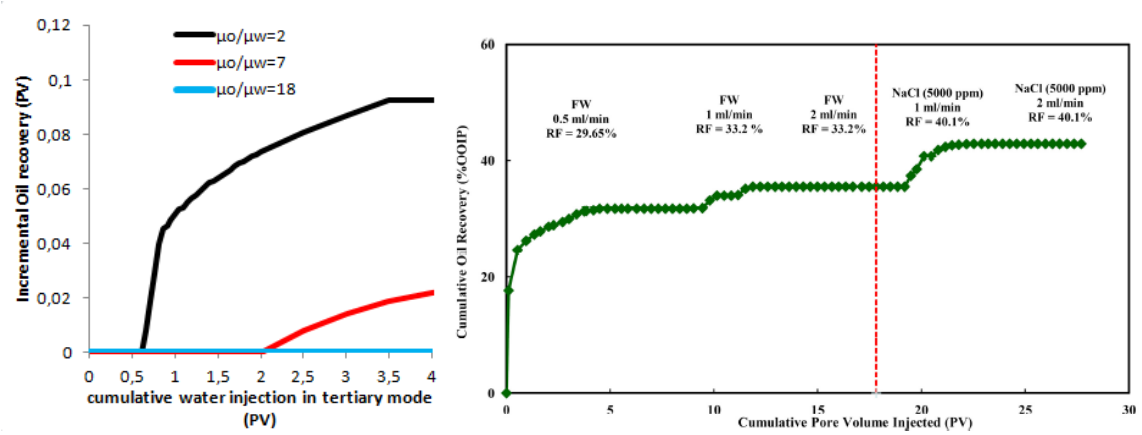

Figure 1: a) simulations of tertiary LSWI as a function of viscosity ratio b) delayed oil recovery during tertiary LSWI from Shehata, 2014

Can we assume that the evolution of oil production during tertiary LSWI is only controlled by the fractional flows at high and low salinities?

Cissokho [11] presented positive results of secondary LSWI compared to HSWI, and a wide range of results in tertiary LSWI on companion sandstone samples with the same reservoir oil. Unreleased results and analysis are offered in the following. Two tertiary LSWI at different temperatures, (DU3-D-9, μo/μw=5,4; DU3-0-5, μo/μw=7,5) showed large differences in the amount and timing of incremental oil by LSWI, as illustrated in figure *2a*. It can hardly be explained by conditions related to the existence of a double saturation shock, as the most significant bump in tertiary oil production is observed for:

- The coreflood with the largest viscosity ratio,
- For DU3-0-5, where evolutions of differential pressure show that $Kw(Sorw_{HS})=Kw(Sorw_{LS})$, whereas the smallest oil bump is observed for DU3-D-9, where $Kw(Sorw_{HS})>Kw(Sorw_{LS})$

It shows that other parameters than the fractional flows at high and low salinities also control the tertiary behavior during LSWI.

Effect of Dispersion in Water Phase at $Sorw_{HS}$

We might also hypothesize that the evolution of oil production during tertiary LSWI depends on dispersion in the water phase.

During tertiary LSWI (1g/l) by Cissokho on samples DU3-0-5 (fig. *2b*), salinity shock arrives at the outlet almost simultaneously as the oil bump, after approximately 1 PV injected. The evolution of chloride concentration shows that 2 PV of LSWI are required before the produced brine has decreased below 2g/l. The threshold salinity which triggers tertiary incremental oil is 2,5 g/l in this set of experiments [11]. This observation shows that dispersion at $Sorw_{HS}$ is significant and might delay the effect of LSWI.

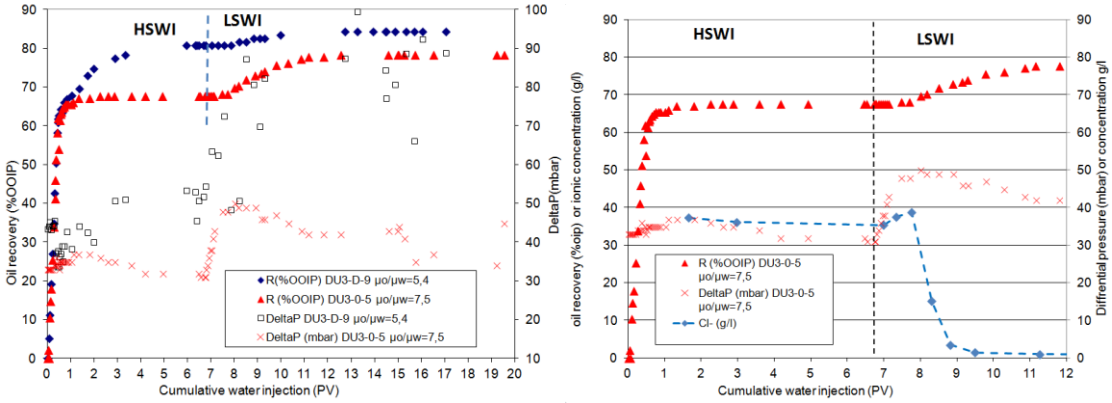

Figure 2: a) Evolution of tertiary recovery during LSWI at slightly different viscosity ratios b) Evolution of recovery, differential pressure and salinity during secondary HSWI and tertiary LSWI

Figure *3a* shows the comparison of results of tertiary LSWI carried out by Cissokho on samples DU3-0-5 and DU3-A-4. Although there is indirect evidence of the salinity shock through the increase in differential pressure as soon as the low salinity water contacts the sample in both experiments, there is no incremental oil in tertiary LSWI on DU3-A-4. Figure *3b* shows the comparison between the normalized concentrations during brine tracer tests which have been performed on sample DU3-A-4 at Sw=1 and at Sorw [11]. At Sw=1, the effluent curve is symmetrical and injected concentration was produced after 1,7 PV of injection. It confirms that the core is rather homogeneous. At Sorw, the effluent curve is largely skewed, and injected concentration was not produced before more than 3,5 PV of injection. It shows again that dispersion at Sorw might be quite significant, even in homogeneous rock samples. This observation is in agreement with previous studies, such as tests PF8A and PF8C in [24]. It shows that residual oil distribution is responsible for increased dispersion. Significant incremental oil on DU3-0-5 by tertiary LSWI may be correlated to limited dispersion in water phase at $Sorw_{HS}$ whereas much larger dispersion on DU3-A-4 correlates with no tertiary recovery.

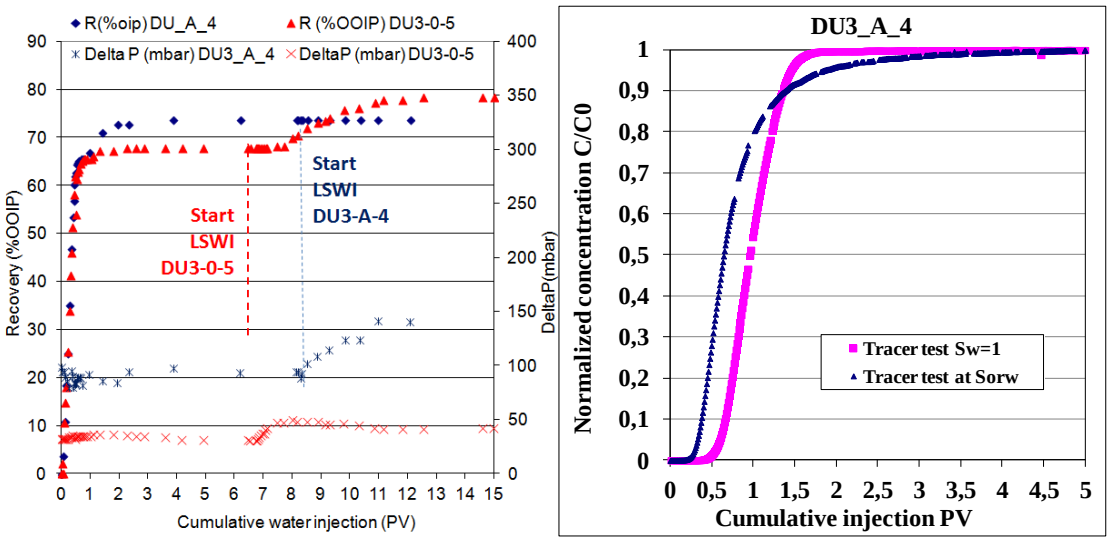

Figure 3: a) recovery during secondary and tertiary LSWI; b), tracer tests at Sw= 1 and at Sorw (from Cissokho)

Nasralla [28] shows water floods on four companion Berea sandstone samples, with different brine salinities: 174, 55, 5,5 Kppm as well as distilled water. Distilled water injection recovered +19% oip in secondary mode than the injection of 174Kppm brine, as shown in figure *4a*. At the end of each secondary flood, tertiary injection of distilled water was performed over several PVs, but never exhibited any incremental oil. Although the viscosity of crude A is measured at ambient temperature only: 7,2 cP, the usual extrapolation at core test temperature: 100°C suggest that the viscosity ratio may partially explain the very poor performance of tertiary LSWI. Moreover, the evolution of ionic composition during tertiary LSWI shows (fig *4b*) that the composition of injected water (deionized water) is not reached at the outlet after more than 5 PV injected, on these 15 cm long cores. Reported information does not allow to separate core heterogeneity from added dispersion by residual oil, but clearly shows strong dispersion at $Sorw_{HS}$. Strong dispersion in brine phase at $Sorw_{HS}$ delays the decrease towards very low salinity all over the core. It suggests that the combined effect of unfavorable viscosity ratio and strong dispersion at Sorw might totally suppress positive effect of tertiary LSWI, even when secondary floods put in evidence very significant benefits.

Which factors may have large effects on brine/brine displacement at Sorw?
Single phase dispersion might already be large. Sample heterogeneity along flow axis would be a major cause. Rock characteristics may also have strong effects: 15 fold differences in single phase dispersion coefficient between various outcrop sandstones at the same velocity have been reported [13]. Berea sandstone (300 mD) exhibited the sharpest displacement front and the least amount of tailing. Wide pore-size distributions in sandstones lead to higher dispersion coefficients [6].

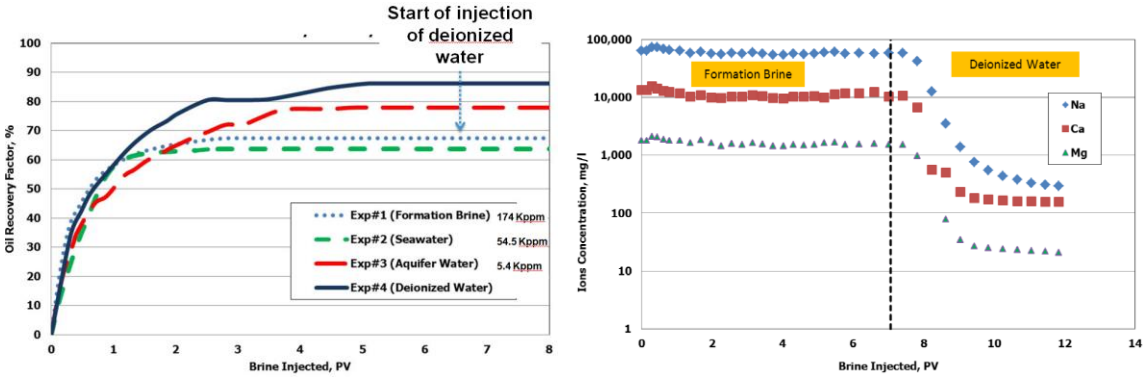

Figure 4: a) Comparison between HS, LSWI in secondary and tertiary modes; b) evolution of ionic concentration during tertiary LWSI ; from Nasralla, 2011

However, single phase tracer tests are almost never reported in experimental studies devoted to tertiary LSWI. This is surprising, particularly when authors specify that samples are taken parallel to bedding.

Core lengths might also have a significant impact, as dispersive flows depend on the ratio between the dispersion length and the length of the system. In that respect, short cores (5, 7,5 cm) are most at risk. Assuming a dispersion length of 6-7mm at $Sorw_{HS}$, consistently with observations made in [50] on mildly wet sandstone, this ratio would approach or exceed 0,1 for 5 and 7,5 cm long cores. It might be even worse when HSWI is carried out at unfavorable viscosity ratios which trigger water fingers. This is a significant concern for a large number [10, 16, 19, 31, 32, 35, 41, 49, 52, 53, 55, 56] of tertiary LSWI studies. On the other hand, too short core lengths cannot be systematically called to explain the absence of any tertiary response during LSWI. Shehata [40] performed tertiary LSWI, observed significant benefits in secondary mode, but no incremental oil during tertiary LSWI on 50 cm long cores.

Others parameters may also have an effect on the evolution of salinity during laboratory tertiary LSWI. Difference in viscosity between secondary HSW and tertiary LSW may reach unfavorable values of viscosity ratios up to 1,5-1,6. This range of viscosity ratio may trigger fingering in the water phase during tertiary LSWI and the salinity profile might be smeared. Flow velocity might also be important, as dispersion coefficient may increase as interstitial velocity increases, both at Sw=1 [4] and at Sorw [36].

Effect of Wettability Modifications Between HSWI and LSWI

Published tertiary LSWI results are very rarely accompanied by secondary HSWI or wettability tests. None is reporting a full Amott Harvey or USBM test. In the absence of wettability tests, it is often assumed that LSWI shifts systematically wettability towards more water wet, based on observations of increased recovery during LSW spontaneous imbibition compared to HSW. Evolution of Krs between LSW and HSW is then guessed according to this assumption. In fact, this spontaneous recovery might be sometimes misinterpreted as demonstrated below using Zhou's results [57]. Zhou changed the

wettability of Berea sandstone by changing the length of aging time at 88°C with Prudhoe Bay crude oil. Three data sets are reported, showing the same behavior as shown in figures *5a, b*. Water imbibition rate decreases, but final oil recovery by imbibition increases as the ageing time increases from 0 to 24 hours. In the same way, waterflood oil recovery increases as the ageing time increases from 0 to 24 hours. It is obvious that outcrop samples cannot become more water wet by increasing ageing time with reservoir oil... It clearly means that increase in recovery by spontaneous water imbibition does not always mean more water-wet. Zhou's experimental results were successfully simulated using distribution of contact angles [0-89°] in [14]. Consequently the very similar results of LSWI by Tang [46, 48, 49], within the water-wet domain, might have been misinterpreted, and might not represent a systematic shift towards water wet. Moreover, other sources of information, such as adhesion maps [7] or flotation tests clearly show increased oil adhesion, when salinity decreases. This topic is addressed in a companion paper [12].

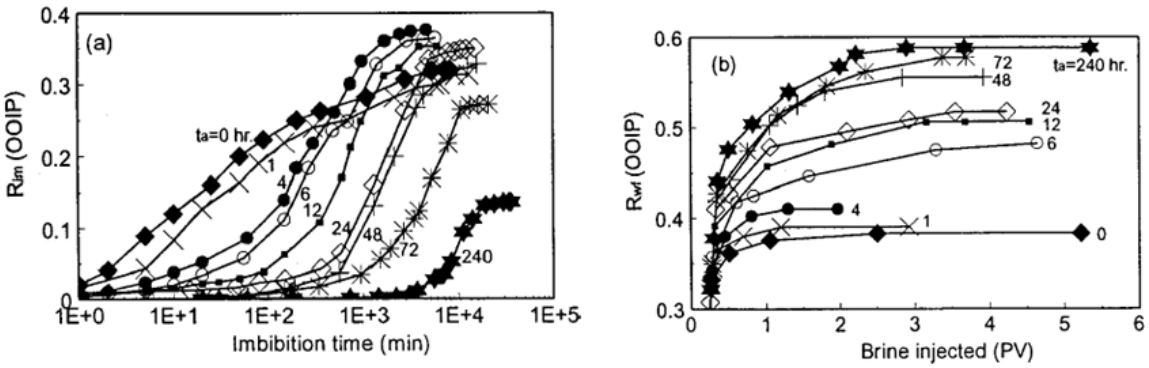

Figure 5: evolution of spontaneous (left) and forced (right) oil recoveries as a function of ageing time (from Zhou, 2000)

Then, in the absence of full wettability test or of any comparison between secondary LSWI and HSWI, there is a doubt about the direction of change of wettability when the rock is contacted by LSWI. Figure 6 shows simulations results of incremental recovery during tertiary LSWI when the viscosity ratio equals 2. Two cases are compared: LSWI might change wettability towards either more water wet ($Sorw_{HS}$=0,3; $Sorw_{LS}$=0,2; $Krw(Sorw_{HS})$ = $Krw(Sorw_{LS})$ =0,3), as often assumed in the absence of both secondary LSWI Krs and wettability tests, or less water-wet, ($Sorw_{HS}$=0,3; $Sorw_{LS}$=0,2; $Krw(Sorw_{HS})$=0.3 $Krw(Sorw_{LS})$ =0,6) as suggested by the general trend of adhesion maps. In such a case $Krw(Sorw)_{LS}$ can be much larger than $Krw(Sorw)_{HS}$. Capillary pressure is not taken into account.

The reduction in Sorw during secondary floods is 10 saturation units in both cases. Even with a very favorable viscosity ratio, tertiary incremental is delayed and poor if LSWI shifts wettability towards less water wet. Note that situation is totally consistent with experimental results on secondary waterfloods [59]: when the initial wettability is within the water-wet domain, a shift towards less water wet increases secondary recovery, but

may lead to poor recovery in tertiary LSWI. Moreover, shifting towards less water wet may increase dispersion within the water phase, as observed in [36, 50].

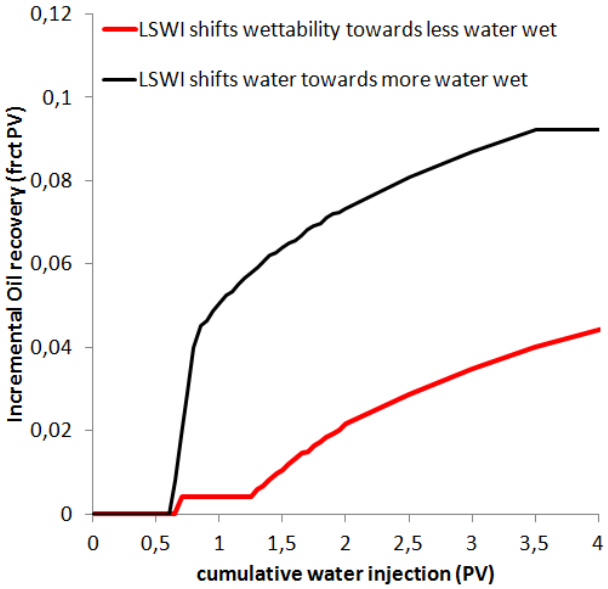

Figure 6: simulations of tertiary LSWI as a function of direction of wettability change

CONCLUSIONS AND WAY FORWARD

Conditions of existence of a double saturation shock, effects of dispersion in water phase at $Sorw_{HS,}$ and uncertainty in the direction of wettability change may explain a lot of experimental studies, where tertiary LSWI performs poorly. Counter examples can also be produced for any single proposed mechanism, but their combination deserves further attention. The absence of relevant experimental data in published studies is the main difficulty when trying to decipher the causes of poor tertiary LSWI results. An ideal set of experiments should incorporate:

- A brine/brine tracer test at Sw=1 on each rock sample used for corefloods
- Secondary HS and LS water floods, including evolution of recovery, differential pressure, in situ saturations, as well as salinities after breakthrough
- Full Amott Harvey wettability tests for both HS and LS brines. The negative part of the forced imbibition capillary pressure curves can be derived from the forced displacements if carried out by centrifugation.
- Tertiary LS water flood including evolution of recovery, differential pressure, as well as salinities and ionic compositions
- Fluid characteristics at test temperature and pressure, including the evolution of water-oil interfacial tension (IFT) as a function of salinity. This last item has received very little attention. However, several studies [9, 47, 54, 25, 2] reported decrease in IFT as salinity decreases. Based on conventional understanding of oil mobilization, water-oil IFT must be reduced by several orders of magnitude to mobilize oil and the reductions

of IFT with salinity are often deemed too small to have any significant effect. On the other hand, when successful, tertiary LSWI illustrates that oil can be mobilized at very low capillary numbers. In that respect, small variations of IFT should deserve attention.

ACKNOWLEDGEMENTS

The author would like to thank TOTAL for permission to publish this paper.

REFERENCES

1. Alotaibi M, Azmy R, Nasr El Din H: "Wettability studies using low salinity water in sandstone reservoirs" OTC20718, 2010
2. AlShaikh M, Mahadevan J: "Impact of brine composition on carbonate wettability: a sensitivity study" SPE 172187-MS, April 2014
3. Austad T, Rezaeidoust A, Puntervold T: "Chemical mechanism of low salinity water flooding in sandstone reservoirs" SPE129767 2010
4. Bear J: "Dynamics of Fluids in Porous Media"1972 American Elsevier. NY.
5. Boussour S, Cissokho M, Cordier P, Bertin,H, Hamon G: " Oil recovery by low salinity brine injection: Laboratory results on outcrop and reservoir cores" SPE 124277, 2009
6. Bretz R, Specter R, Orr F: "Effect of pore structure on miscible displacement in laboratory cores" SPERE, August 1988 p 857-866
7. Buckley J, Morrow N: "Characterization of crude oil wetting behavior by adhesion tests" SPE 20263, 1990
8. Buckley J, Fan T: "Crude oil/brine interfacial tensions" SCA 2005-01, International symposium of the Society of Core Analysts 2005
9. Cai B, Yang J, Guo T: "interfacial tension of hydrocarbon +water/brine systems under high pressure" Journal of chemical and engineering data 41 (3) p 493-496
10. Callegaro, C, Bartosek M, Masserano F, Nobili M, et al: "Opportunity of enhanced oil recovery by low salinity water injection: from experimental work to simulation study up to field proposal" SPE 164827, 2013
11. Cissokho, M, Boussour S, Cordier P, Bertin H, Hamon G: " Low salinity oil recovery on Clayey sandstone: Experimental study" PETROPHYSICS, VOL. 51, N°. 5 (Oct 2010); p 305-313
12. Didier M: "Contradictory trends for Smart Water Injection Method: role of pH and salinity from sand/oil/brine adhesion maps" SCA 2015 A14
13. Donaldson E, Kendall R, Manning F: "Dispersion and tortuosity in sandstones" SPE 6190, 1976
14. Dixit A, McDougall S, Sorbie K: " Pore scale modeling of wettability effects and their influence on oil recovery" SPE/DOE 35451, 1996
15. Fjelde I, Asen S, Omekeh A: " Low salinity water flooding experiments and interpretation by simulations" SPE 154142 2012
16. Gamage P, Thyne G: " Comparison of oil recovery by low salinity waterflooding in secondary and tertiary modes" SPE147375, 2011
17. Hadia N, Lehne H, Kumar K, Selboe K, Stensen J, Torsaeter O: "Laboratory investigation of low salinity waterflooding on reservoir rock samples from the Froy field" SPE 141114, 2011
18. Hadia N, Ashraf A, : "Laboratory investigations on effects of initial wettabilities on performance of low salinity waterflooding" JPSE 105 (2013) 18-25

19. Hamouda, A, Valderhaug O, Munaev, R, Stangeland H: "Possible mechanisms for oil recovery from chalk and sandstone rock by low salinity water " SPE 169885, 2014
20. Lager, A., Webb, K.J., Black C.J: "Impact of brine chemistry on oil recovery" 14th symposium on Improved oil recovery Cairo, Egypt, 22-24 April 2007
21. Ligthelm D, Gronsveld J, Hofman, J, Brussee N, et al: "Novel waterflooding strategy by manipulation of injection brine composition" SPE 119835, 2009
22. Loahardjo N, Xie X, Yin P, Morrow N: " Low salinity waterflooding of a reservoir rock" SCA 2007-29, 2007
23. McGuire, PL, Chatham, JR,: " Low Salinity Oil recovery: An Exciting New Opportunity for Alaska's North Slope" SPE 93903, 2005 Western Regional Meeting, Irvine, April 2005
24. Meyers, K.; Salter, S: "Concepts pertaining to reservoir Pretreatment for chemical flooding" SPE/DOE 12696, April 1984
25. Moeini F, Hemmati-Sarapardeh A., Ghazanfari M, et al : "Toward mechanistic understanding of heavy crude oil/brine interfacial tension: The roles of salinity, temperature and pressure" Fluid Phase Equilibria 375 (2014) 191–200
26. Mohammadi H, Jerauld G: "Mechanistic modeling of the benefit of combining polymer with low salinity water for enhanced oil recovery" SPE 153161, 2012
27. Morrow N, Buckley J: " Improved oil recovery by low salinity water flooding" JPT, May 2011 p 106-112
28. Nasralla R, Alotaibi M, Nasr el din H: " Efficiency of oil recovery by low salinity water flooding in sandstone reservoirs" SPE 144602, 2011
29. Nasralla R, Nasr el Din H: "Double layer expansión: is it a primary mechanism of improved oil recovery by low salinity wáter flooding?" SPE 154334, 2012
30. Pope G: "The application of fractional flow theory to enhanced oil recovery" SPEJ June 1980, p191-205
31. Pu H, Xie X, Yin P, Morrow N: "Application of coalbed methane water to oil recovery by low salinity waterflooding" SPE 113410, 2008
32. Pu H, Xie X, Yin P, Morrow N: "Low salinity waterflooding and mineral dissolution" SPE 134042, 2010
33. RezaeiDoust A, Puntervold T, Austad T: "A discussion of the low salinity EOR potential for a North Sea sandstone field" SPE 134459, 2010
34. Rivet S, Lake L, Pope G: " A coreflood investigation of low salinity enhanced oil recovery" SPE 134297, 2010
35. Romero M, Gamage P, Jiang H, Chopping C, Thyne G: "Study of low salinity waterflooding for single and two phase experiments in Berea sandstone cores" JPSE 110 (2013) p 149-154
36. Salter, S.; Mohanty, K: "Multiphase flow in porous media: 1: Macrocopic observations and modelling" SPE 11017, 1982
37. Sandengen K, Tweheyo M, Raphaug M, et al: "Experimental evidence of low salinity waterflooding yielding a more oil-wet behavior" SCA2011-16
38. Sohrabi M, Mahzari P, Farzaneh S, Mills J, Tsolis P, et al: "Novel insights into mechanisms of oil recovery by low salinity water injection" SPE 172778, 2015
39. Sandengen K, Tweheyo M, Raphaug M, et al: " Experimental evidence of low salinity water flooding yielding a more oil wet behavior" SCA 2011-16
40. Shehata A, Nasr el Din H: "Role of sandstone mineral compositions and rock quality on the performance of low salinity waterflooding" IPTC 18176, 2014
41. Shiran B., Skauge A.: " Wettability and oil recovery by low salinity injection" SPE 155651, 2012

42. Skrettingland K, Holt T, Tweheyo M: “Snorre low salinity water injection core flooding experiments and single well field pilot” SPE 129877, 2010
43. Spildo K, Johannessen A, Skauge A: “Low salinity waterflood at reduced capillarity” SPE154236, 2012
44. Suijkerbuijk B, Hofman J, Ligthelm D, Romanuka J et al: “Fundamental investigations into wettability and low salinity flooding by parameter isolation” SPE 154204, 2012
45. Suijkerbuijk B, Sorop T, Parker A et al.: “Low salinity waterflooding at West Salym : Laboratory experiments and field forecasts” SPE 169102, 2014
46. Tang G, Morrow N: “ Salinity, temperature, oil composition, and oil recovery by waterflooding” SPERE, November 1997, p269-276
47. Tang, G : “Brine Composition and waterflood recovery for selected crude Oil/Brine/Rock systems” Ph.D Dpt of Chemical and Petroleum Engineering UW, May 1998
48. Tang G, Morrow N: “Influence of brine composition and fines migration on crude oil/brine/rock interactions and oil recovery” 1999, JPSE 24 (2-4) p99-111
49. Tang, G, Morrow N: “Oil recovery by waterflooding and imbibitions invading brine cation valency and salinity” SCA 9911, 1999
50. Wang F: “Effect of wettability alteration on water/oil relative permeability, dispersion, and flowable saturation in Porous Media” SPERE, May 1988,
51. Webb K, Lager A , Black C: “Comparison of high/low salinity water/oil relative permeability” SCA 2008-39, 2008
52. Winoto W, Loahardjo N, Xie X, Morrow N: “ Secondary and tertiary recovery of crude oil from outcrop and reservoir rocks by low salinity waterflooding” SPE 154209, 2012
53. Winoto, Loahardjo N, Morrow N: “Assessment of oil recovery by low salinity waterflooding from laboratory tests” SPE 169886, 2014
54. Yousef A, Al Kaabi A, Al Jawfi M: “Laboratory investigation of the impact of injection water salinity and ionic content on oil recovery from carbonate reservoirs” SPE Reservoir Evaluation & Engineering October 2011 578-593
55. Zhang Y Morrow N: “Comparison of secondary and tertiary recovery with change in injection brine composition for crude oil/sandstone combinations” SPE 99757, 2006
56. Zhang Y Xie X Morrow N: “waterflood performance by injection of brine with different salinity for reservoir cores” SPE 109849, 2007
57. Zhou W, Morrow N, Ma S: “Interrelationship of wettability, initial water saturation, aging time, and oil recovery by spontaneous imbibition and waterflooding” SPEJ 5 (2) June 2000, p199-207
58. Wickramathilaka, S, Morrow N, Howard J : “ Effect of salinity on oil recovery by spontaneous imbibition” SCA 2010-12, 2010
59. Jadhunandan P, Morrow N : “Effect of wettability on waterflood recovery for crude oil brine rock systems” SPERE, February 1995, pp40-46

THE FATE OF OIL CLUSTERS DURING FRACTIONAL FLOW: TRAJECTORIES IN THE SATURATION-CAPILLARY NUMBER SPACE

M. Rücker[2,1], S.Berg[1], R. Armstrong[3,1], A. Georgiadis[1,5], H. Ott[1,6], L. Simon[2], F. Enzmann[2], M. Kersten[2], S. de With[4,1]

[1]Shell Global Solutions International, Kesslerpark 1, 2288 GS Rijswijk, Netherlands
[2]Geosciences Institute, Johannes-Gutenberg University, 55099 Mainz, Germany
[3]School of Petroleum Engineering, University of New South Wales, New South Wales, Sydney, Australia
[4]Technical University Delft, Stevinweg 1, 2628 CN Delft, Netherlands
[5]also at: Department of Chemical Engineering, Imperial College London, SW7 2AZ UK
[6]also at: Department of Earth Science and Engineering, Imperial College London, SW7 2AZ UK

This paper was prepared for presentation at the International Symposium of the Society of Core Analysts held in St. John's Newfoundland and Labrador, Canada, 16-21 August, 2015

ABSTRACT

Fractional flow has been studied at the pore scale under dynamic flow conditions by using fast synchrotron-based X-ray computed micro-tomography. The pore-scale flow regimes have been mapped in a "phase diagram" where the regimes of connected pathway flow and ganglion dynamics are characterized by fractional flow and capillary number. The regimes are identified from the respective pore scale dynamics that can be conveniently characterized by using a saturation-(cluster-based) capillary number diagram. Therein connected pathway flow is represented by a fixed point (because all parameters are constant over time) and in ganglion dynamic regime the oil clusters follow trajectories because saturation and cluster length are changing over time. Ganglion dynamics is composed of breakup and coalescence processes. During coalescence processes, both cluster volume and length increases, i.e. clusters move "up" the trajectory. During break-up processes, on the other hand, both properties decrease and clusters move "down" the trajectory.

Ganglion dynamics occurred even though the (cluster-based) capillary number of the average flow field was at least two orders of magnitude smaller than unity, i.e. the average flow field indicates capillary-dominated regime. However viscous mobilization can also be triggered by more complex break-up and coalescence processes that have much higher local flow velocities than the average flow field suggests. Most situations encountered are a combination of connected pathway flow and ganglion dynamics, where a combination of viscous and capillary-driven processes accounts for the net transport of oil. Static simulation approaches are not capable of capturing such regimes, as they require connected pathway flow.

INTRODUCTION

During the recovery of oil from an underground reservoir by water flooding, the non-wetting oil phase is displaced by the wetting water phase. Corresponding to the Buckley–Leverett equation [1], the two fluids flow simultaneously through narrow pore space once the saturation front has passed. In order to determine the relative permeability of this simultaneous flow, commonly steady-state core flooding experiments (e.g., experiments on 5cm-long rock samples) are conducted [2]. However, core flood experiments often show fluctuations of parameters such as saturation, pressure and resistivity depending on the fractional flow (Figure 1). The reason for these fluctuations is not fully clear yet, but may be related to different flow regimes [3, 4, 5].

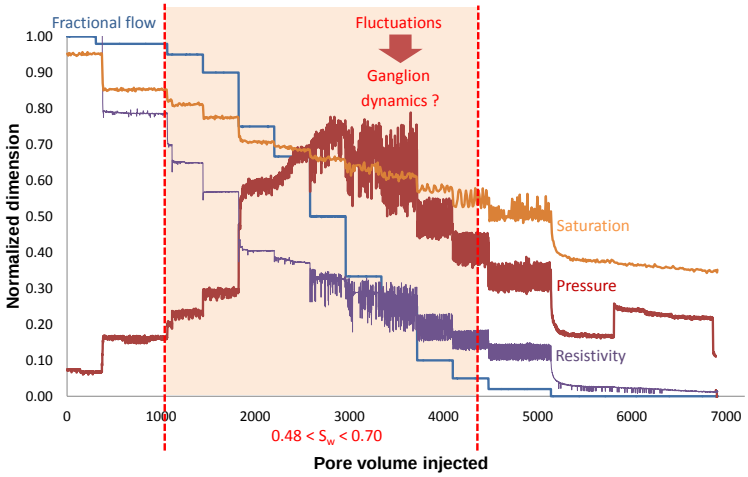

Figure 1 Results of a core flood experiment measured on a 5 cm rock sample (right) show a variation of fluctuations in different parameters such as saturation, pressure, and resistivity depending on the fractional flow (left).

On the pore scale, Avraam and Payatakes [3] observed three types of flow regime, which are (i) connected pathway flow, (ii) drop traffic flow, and (iii) ganglion dynamics. During connected pathway flow, the non-wetting and the wetting phases move mainly through their respective connected networks [3]. The drop traffic regime describes the flow of oil through disconnected droplets smaller than the diameter of the pore throats [3]. These are formed by vigorous break-up of the oil ganglia and are stabilized by the flow of the surrounding water, which prevents the growing of ganglia via coalescence [3]. The most complex flow regime is the ganglion dynamics, whereby oil is disconnected into ganglia with sizes larger than a pore. These ganglia move or get immobilized in narrow passages, they break into smaller ganglia and get trapped even more easily, or they collide with other ganglia, grow and get remobilized [3]. The thus prevailing flow regime depends on different parameters such as viscosity, wettability, surface tension, flow rate ratio, capillary number, etc. [4]. For specific fluids in a specific porous medium most parameters are constant and the relative permeability appears to be a function of capillary number and flow rate ratio [8].

While most previous studies performed on dynamic two-phase flow are either based on 2D models [3,9] or on 3D but indirectly measured [4, 5] or on simulations [6, 7], in this study we image directly the 3D development of clusters in real time by fast synchrotron based X-ray μCT. Recent studies using this technique allowed the first insights into pore-scale processes during drainage and imbibition [10, 11, 12, 13] such as Haines jumps [14, 15, 16], coalescence [17,18] and snap-off [18, 19]. In this study we analysed ganglion dynamics by co-injection of two fluids at different ratios and velocities in porous media in order to determine the prevailing flow regime.

MATERIALS AND METHODS

For this experiment, n-decane was used as nonwetting phase and brine as wetting phase. A strongly water-wet sintered glass sample (4 mm diameter, 20 mm length, embedded into a polycarbonate tube by heat-shrinking) with a porosity of 35% and permeability of 22±2 D was mounted at the top of a flow cell. The flow cell was specially designed for fractional flow experiments and contained two remotely controlled micro piston pumps, which enables continuous rotation of the sample and constant data acquisition in the field of view during the experiment. A full 3D image with a voxel size of 2.2 μm was obtained in 1 min. The measurements were performed at a fast synchrotron-based X-ray computed microtomography facility (TOMCAT beamline, Swiss Light Source, Paul Scherrer Institute). Details on the flow cell and the experimental settings were described previously [20]. The reconstructed μCT images were filtered, segmented and processed with the software package AVIZO 8 (Visualization Science group).

Subsequently, the resulting binarized images containing the porous medium and the oil and water phases were used for further analyses, e.g., for estimation of the relative permeability. The single-phase flow simulation by the software package GeoDICT (Math2Market) was used in the Navier-Stokes mode to calculate the permeability through the connected portion of the oil- and water-phase for each time step.

Furthermore, all flow events occurring during the experiment were determined and separated into oil-filling and water-filling events. While the former event type describes a situation in which pores drained from water are filled by oil, the latter type corresponds to oil being replaced by water. The events are determined by generating a differential image of two consecutive 3D binary images containing only the oil phase. The differential image gives the positon and size of both water- or oil-filling events. A single event is defined as a spatially separated fluid change at a specific position. The event size is defined as the volume of the spatially separated change. To reduce effects due to noise, small events ($< (21\ \mu m)^3$ corresponding to 10 voxels in each direction) are ignored.
In addition, the development of clusters was observed. To follow a chosen cluster through the different time steps, the space occupied by this cluster in the first time step is compared to the same space in the next time step. All clusters inside this space or connected to this space are then used as a mask for the next time step. This procedure is

iterated over all measured time steps, enabling clusters to be tracked over time and statistics to be obtained.

RESULTS AND DISCUSSION

The flow regime depends on the fractional flow and the capillary number. The fractional flow is given by the injection rate ratio of each fluid to the total fluid, while the capillary number in this study is determined by the macroscopic cluster-based definition [9, 24]:

$$Ca^{macro} = \frac{l^{cl}}{r_p} \varphi \frac{\mu_w v_w}{\gamma_{w,nw}}, \quad (1)$$

With the cluster length (l^{cl}), radius of a pore throat (r_p), porosity (φ), viscosity of the wetting phase (μ_w), interstitial velocity of the wetting phase (v_w), and interfacial tension ($\gamma_{w,nw}$). The radius of the peak pore size of the pore size distribution calculated by the software code GeoDICT was used as pore throat radius. The velocity is derived from the injection rate and represents the average flow field, which is often used to characterize a flow regime. An overall $\overline{Ca}^{macro}$ was calculated by averaging l^{cl} of all clusters as described in [24]. The fractional flow-capillary number diagram (Figure 2) shows how the experiments were conducted, starting at a high water fraction and low total injection rate of 4x10^{-6} m/s corresponding to a low $\overline{Ca}^{macro}$. The total injection rate increased stepwise up to 4x10^{-4} m/s before changing to a lower oil fraction. For all experiments $\overline{Ca}^{macro} < 1$ indicating capillary dominated flow regime. However, since local velocities may deviate from the overall velocity, the transition from capillary dominated to viscous dominated regimes is rather smooth.

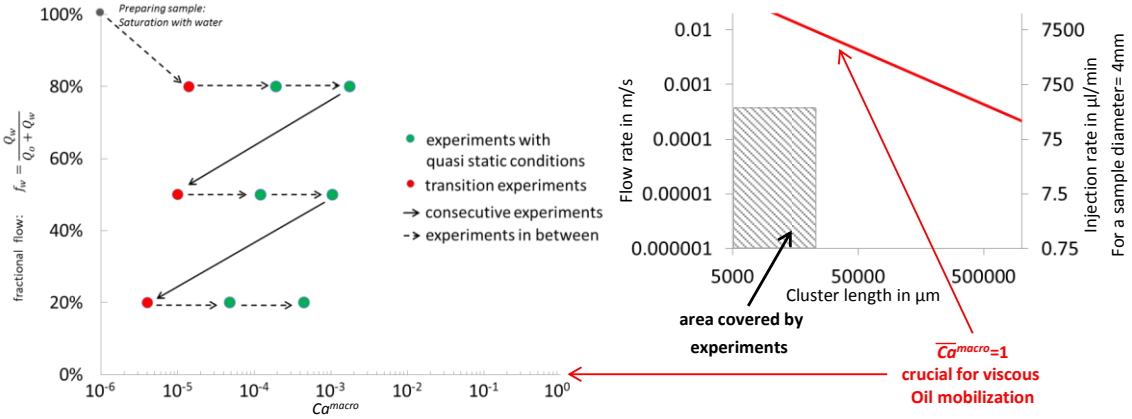

Figure 2 The experiments started with a high water fraction (80% water) and a low flow rate (4x10^{-6} m/s). The total injection rate was increased stepwise up to 4x10^{-4} m/s before repeating the experiments at a lower oil fraction (left). In all experiments, a $\overline{Ca}^{macro} < 1$ corresponding to a capillary-dominated system (right).

In our experiments, we captured the transient regime when changing flow rates followed by the quasi steady-state regime. This transition could be recognized by the initial change in saturation. At low flow rates, the transition took longer and, therefore, was ideal for

observing growing and decreasing clusters. An increase in oil-saturation with a high frequency of oil-filling events appeared as Haines jumps and coalescence, while a decrease in saturation was dominated by snap-offs and led to disconnected clusters. For this reason, initial drainage led to a high connectivity, while in general a low saturation corresponded to low connectivity.

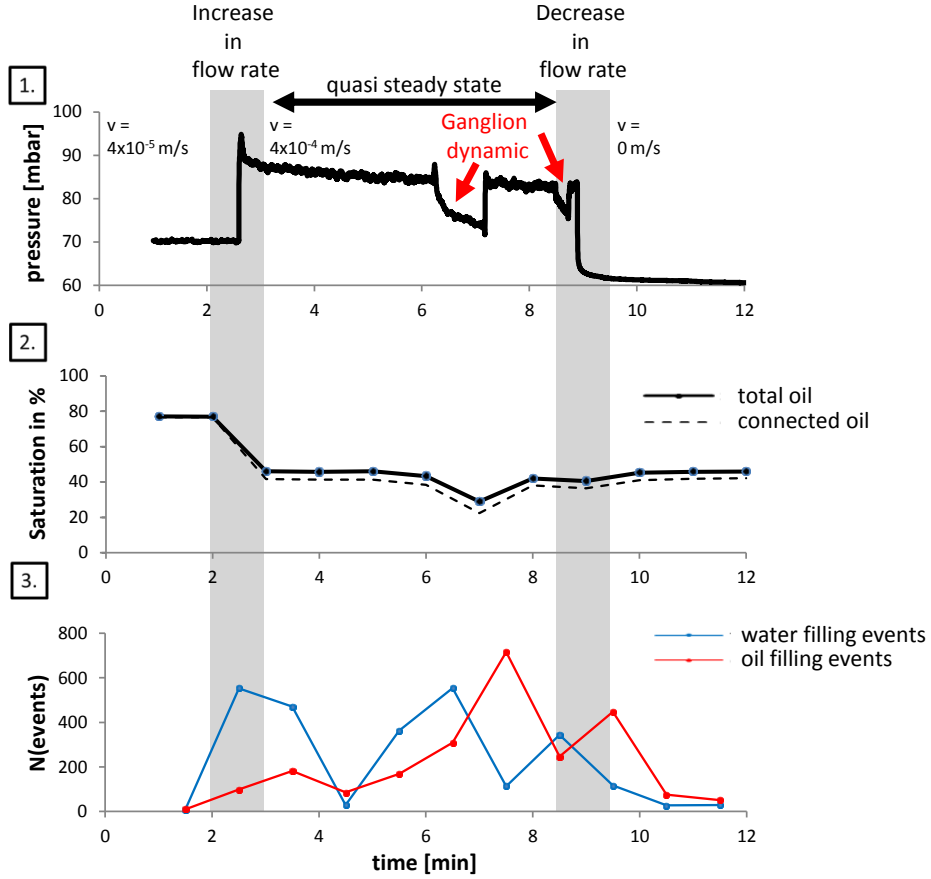

Figure 3 Pressure (1), saturation (2), and event statistics (3) for an experiment at $f_w = 0.5$ and a total flow rate of $4x10^{-4}$ m/s. Transitions between different fractional flows / flow rates where the target conditions had not been fully reached are marked by the grey bars. In these transition regimes, we observed natural changes in pressure, saturation, and pore-filling events, because flow conditions have been changed externally. However, in the quasi steady-state regime there are also pressure data and saturation fluctuations, which coincide with pore-scale water- and oil-filling events as signature of ganglion dynamics behavior.

The term "quasi" steady-state is chosen to indicate that fluctuations and events may still occur even though the average saturation has adjusted to the new injection rate. These fluctuations may be indicative of ganglion dynamics. At quasi steady-state conditions the saturation remained mostly stable and the number of events was smaller. Nevertheless, some fluctuations could be observed at water fraction $f_w = 0.5$ and high total flow rates ($4x10^{-4}$ m/s, Figure 3). A sudden pressure drop followed by an increase occurred between the sixth and eighth minute (Figure 3.1). In the same time period, the oil volume dropped (Figure 3.2) and the number of water- and oil-filling events increased (Figure 3.3).

This observation is very similar in terms of saturation and pressure fluctuation to the results of core flood experiments at $f_w = 0.5$ and 5 cm long rock samples.

Growing and Shrinking Clusters

We tracked individual clusters to gain further insights into ganglion dynamics. In Figure 4, the development of a cluster that grows over time is shown.

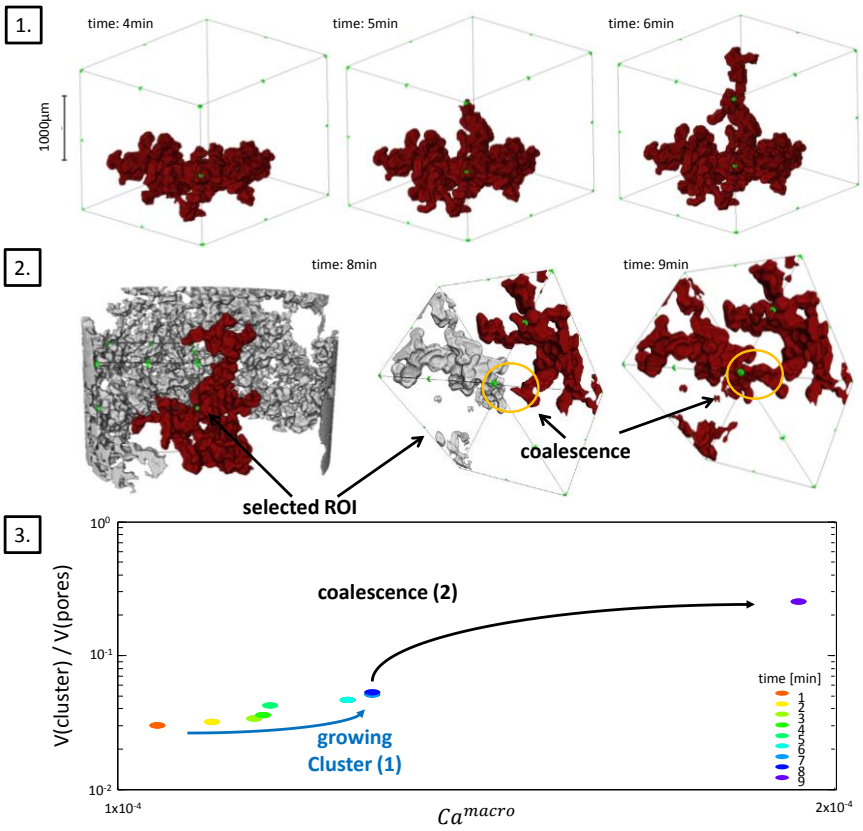

Figure 4 Tracking a growing cluster at $f_w = 0.8$ and v=4x10^6 m/s: In the first phase (1), the cluster continuously increases in volume. For this reason, the corresponding cluster-trajectory in the cluster volume-capillary number (*V-Ca*) space moves slowly towards high volume and capillary number, before it suddenly jumps (3) due to a coalescence with another cluster (2).

The cluster grows first through pathways outside the field of view by invading adjacent pores (Figure 4.1) before it coalesces with another cluster (Figure 4.2). In the volume-Ca^{macro} space, this development is visible in a trajectory moving from low *V*-Ca^{macro} to high *V*-Ca^{macro} regime.

A "shrinking" cluster behaves differently, because in addition to a decrease in volume due to water film swelling [11] (and oil moving out the field of view), we also observe fragmentation. As shown in Figure 5, the cluster first decreases until snap-off events lead to fragmentation. The evolution of the saturation distribution of a shrinking cluster is

shown in Figure 5.1. The initial cluster A snaps off apart into two smaller clusters A and B. After redistribution of oil the volume apparently further decreases which is an imaging artifact from moving oil due to snap-off (few milliseconds [22]) during the acquisition time of a tomogram (60 s). Then cluster B snaps off into B and C. The corresponding trajectory in the *V-Ca*^{macro} space is in this case moving, vice versa, towards low volume and *Ca*^{macro}.

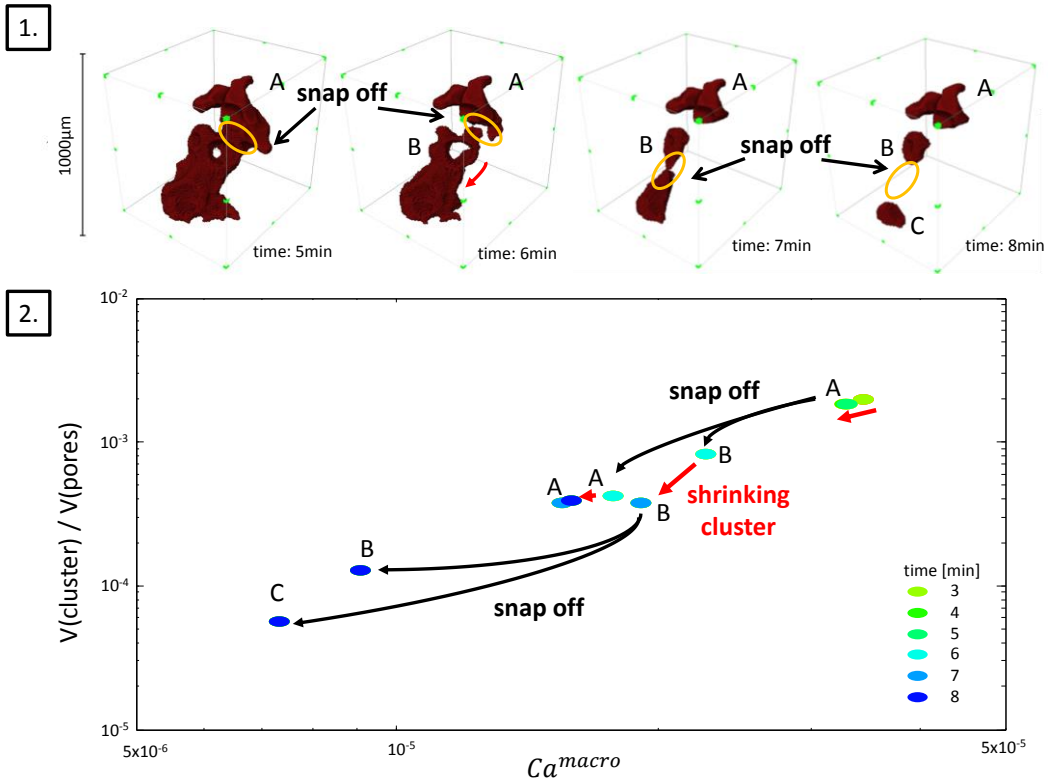

Figure 5 Tracking a decreasing cluster at f_w = 0.5 and high Ca. First, the cluster slowly decreases due to film swelling, before snap-off events fragment it into smaller ones, which further decrease in size and break apart. The clusters shown in (1.) correspond to the clusters shown in the trajectory (2.), where the single new appearing fragments are named A-C to indicate which fragment in later time steps is represented by which point in the diagram.

The cluster trajectories in the *V-Ca*^{macro} space move upwards when they are growing by coalescence or Haines jumps, and downwards while they snap off during shrinkage. However, all clusters have to be taken into account in order to determine the flow regime.

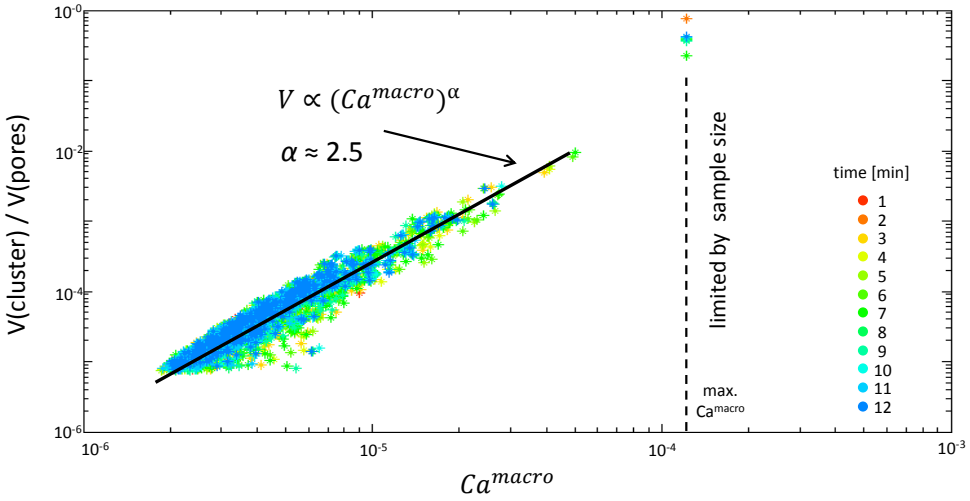

Figure 6 All clusters for each time step at f_w = 0.5 and v = 4x10^{-4} m/s follow a power-law distribution with an exponent α ≈ 2.5, which gives information about the shape of the clusters. The capillary number of the largest clusters is limited by the sample size leading to a bias.

Figure 6 shows the distribution of all clusters for all time steps at f_w = 0.5 and v = 4x10^{-4} m/s. The distribution of the clusters appears to follow a power-law like behavior, $V(cluster) \propto (Ca^{macro})^{\alpha}$, with an average exponent $\alpha \approx 2.5$. Since $Ca^{macro} \propto l^{cl}$, the exponent gives information regarding the shape of the cluster. The exponent of $\alpha = 2.5$ indicates a cluster shape between an area-filling shape, where volume scales as (length)^2, and a volume-filling shape (such as spheres) where volume scales as (length)^3 Furthermore, the exponent corresponds to the fractal dimension of invasion percolation and indicates that the volume of clusters during fractional flow scales within percolation universality class. The length of the largest cluster is restricted by the length of the sample and/or field of view and, therefore, the largest clusters do not follow the general distribution. Once a cluster percolates from bottom to the top of our field of view, we can observe volume increase but cannot observe increase in length. This finite size effect is displayed as the maximum Ca^{macro} in all following figures.

Pathway flow and Ganglion dynamics in the *S*-*Ca*-diagram

So far only individual clusters have been analyzed, while in the following we aim to characterize the complete flow regime involving all clusters. Therefore we consider average properties like saturation but also the averaged capillary number $\overline{Ca}^{macro}$, taking into account that each cluster has a different length and volume.

Trajectories based on the average $\overline{Ca}^{macro}$ are shown in Figure 7. When ganglion dynamics occurs where the connected oil (grey) gets disconnected (yellow) and reconnected (Figure 7.1), the trajectory moves up and down in saturation and $\overline{Ca}^{macro}$ (Figure 7.2). The reason for this is that when more clusters are disconnected, the saturation decreases, since the narrow pore throats connecting the oil phase are filled by water instead of oil. Moreover, the volume of the disconnected clusters and their

corresponding length becomes also smaller, which leads to a decrease in $\overline{Ca}^{macro}$. When the oil clusters become reconnected, the saturation and $\overline{Ca}^{macro}$ increases again. Since $\overline{Ca}^{macro}$ is limited due to the sample size, the trajectory is deflected at high saturations. On the other hand, the trajectory in connected pathway flow does not show any changes (Figure 7.4). Since the oil and water are moving through independent pathways, the cluster shape is not changing as shown in Figure 7.3.

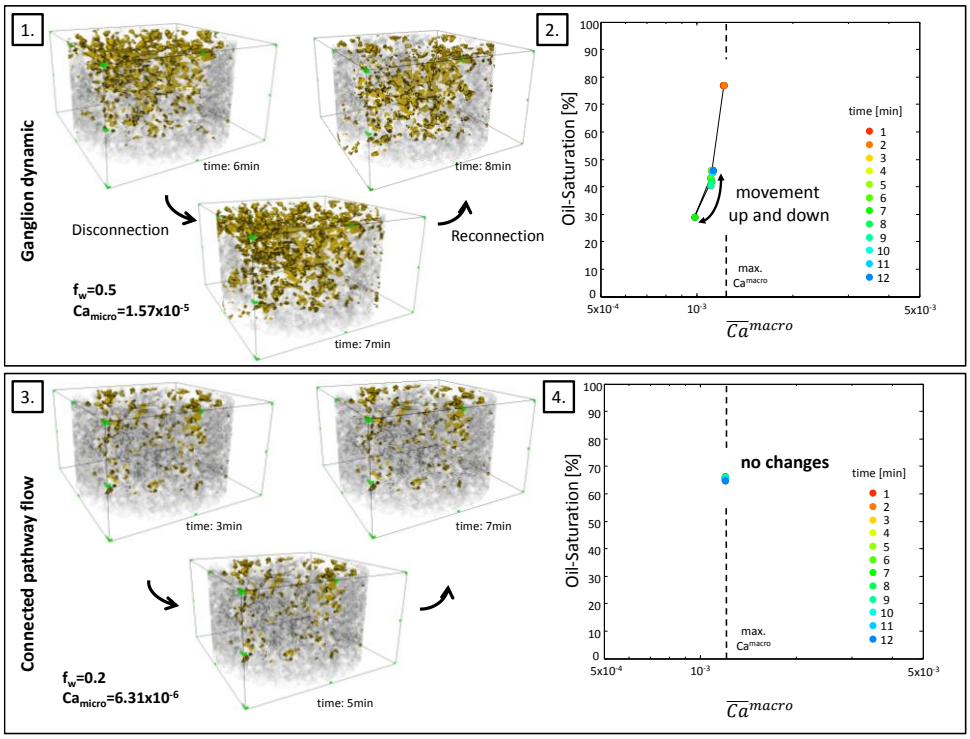

Figure 7 It depends on f_w whether ganglion dynamics (f_w = 0.5) or pathway flow (f_w = 0.2) occurs. While at f_w = 0.5 the oil gets disconnected (yellow) and reconnected (grey) during quasi steady-state conditions (1), the oil distribution remains constant at f_w = 0.2. The S-Ca_o^{macro} diagram shows that the clusters at f_w = 0.5 move up and down the trajectory (2), while the clusters at f_w = 0.2 remain at one point (4). However, in both cases $\overline{Ca}^{macro}$ is close to the maximal possible Ca^{macro}, which is limited by the sample size.

Contribution to the relative permeability

Since the ganglion dynamics observed on the S-$\overline{Ca}^{macro}$ diagram correlates with the pressure and saturation fluctuations, all observations in core flood experiments appearing at the same water fraction (f_w = 0.5) may be also associated with ganglion dynamics. However, at least at the pore scale, the impact on relative permeability is not as clear so far. In Figure 8, the development of the relative permeability through the continuous oil and water phase with time is shown, excluding the contribution of disconnected clusters via ganglion dynamics. Since the injection rate and water fraction f_w was constant over time, the deflection in relative permeability between the sixth and eighth minutes represents the contribution of ganglion dynamics.

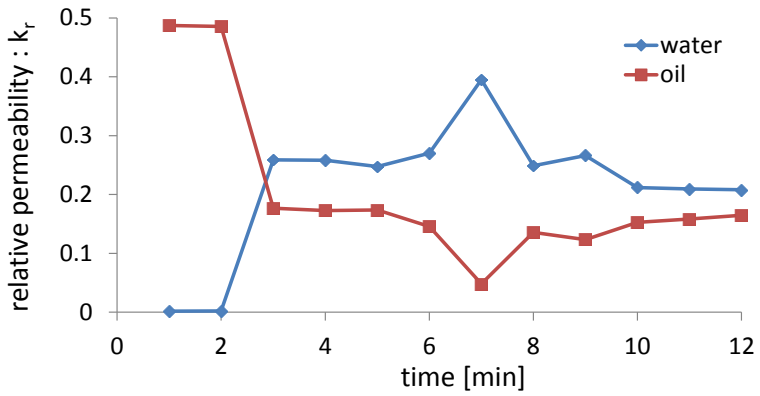

Figure 8 Relative permeability at $f_w = 0.5$ and high *Ca* during time. At this high flow rate, the quasi steady-state conditions are reached already after one minute. As the saturation (Figure 2) and the relative permeability of the oil and the water remains stable, a disconnection and reconnection (Figure 7) corresponding to a moving ganglion can be observed, whereby a disconnection causes an increase of the relative permeability of the water and a decrease for oil.

CONCLUSIONS

Flow regimes during fractional flow have been characterized by imaging the pore-scale fluid distribution using synchrotron-based fast X-ray computed microtomography. We observed regimes of connected pathway flow but also ganglion dynamics regime. These flow regimes can be categorized in the fractional flow vs. capillary number (f_w-*Ca*) space. In order to construct a phase diagram indicating which flow regime prevails at which conditions, we sampled this space by conducting steady-state μCT flow experiments, which in addition to pressure and saturation data allows us to identify the respective flow regimes from the pore-scale displacements and oil cluster (ganglion) movement.

Oil clusters follow distinct trajectories in the saturation-*Ca* space, which is caused by pore-scale displacement events. Pore-scale processes such as cluster coalescence and growing cause an increase in cluster volume and length so that the clusters move up a trajectory in a saturation and capillary number diagram. In break-up processes, both volume and length decreases and clusters move down the trajectory. Averaging over all clusters of a measurement for each time step allows us to characterize the flow regime involving all clusters in our field of view. Since almost no events occur at connected pathway flow, no changes can be observed at the saturation-*Ca* diagram. On the other hand, ganglion dynamics cause a movement both up and down the trajectory.

These pore-scale processes clearly affect two-phase flow at larger scales. Fluctuations in saturation and pressure, as observed in Darcy-scale steady-state relative permeability experiments, have very similar characteristics to those observed in our μCT flow experiments. That clearly indicates that the pressure and saturation fluctuations observed on a 5 cm-long rock sample at intermediate fractional flow and saturation ranges are likely to be related to ganglion dynamics. The different flow regimes contribute differently to the total flow. Due to break-up and coalescence in a ganglion dynamics

flow regime, the connectivity is changing what affects the flow and causes change in relative permeability. This has to be considered for describing two-phase flow by numerical models.

ACKNOWLEDGEMENTS

We would like to acknowledge Kevin Mader and Marco Stampanoni (Tomcat beamline at the Swiss Light Source of Paul Scherrer Institute, Villigen, Switzerland). We thank Alex Schwing and Rob Neiteler for the design of the flow set-up and instrumentation, Ab Coorn, Fons Marcelis and Niels Brussee for sample preparation, Hilbert van der Linde, Niels Brussee and Sebastiaan Pieterse for the steady-state relative permeability measurements, and Axel Makurat for helpful discussions and leadership support. We gratefully acknowledge Shell Global Solutions International B.V. for permission to publish this work.

REFERENCES

1. Buckley, S. and Leverett, M., "Mechanism of fluid displacement in sands", *Transactions of the AIME* (1942) 146.01, 107–116.
2. Berg, S., Cense, A. W., Hofman, J. P., Smits, R. M. M., "Two-Phase Flow in Porous Media with Slip Boundary Condition", *Transp Porous Med,* (2007) 74:275–292.
3. Avraam, D. G. and Payatakes, A. C., "Flow regimes and relative permeabilities during steady-state two-phase flow in porous media", *Journal of Fluid Mechanics* (1995) 293, 207–236.
4. Tsakiroglou, C. D., Aggelopoulos, C. A., Terzi, K., Avraam, D. G., Valavanides, M., "Explicit correlation of the steady-state-two phase relative permeability functions of porous media with the local flow rate", SCA2014-041.
5. Datta, S. S., Dupin, J. B. and Weitz, D. A., "Fluid breakup during simultaneous two-phase flow through a three-dimensional porous medium". *Physics of Fluids* (2014) 26(6), 062004.
6. Raeini, A. Q., Blunt, M. J., Bijeljic, B, "Direct simulations of two-phase flow on micro-CT images of porous media and upscaling of pore-scale forces", *Advances in Water Resources* (2014) 74, 116-126.
7. Lopez, O., Mock, A., Skretting, J., Petersen, E.B.Jr, Øren, P.E., Rustad, A.B., "Investigation into the reliability of predictive pore-scale modeling for siliciclastic reservoir rocks", SCA2010-41.
8. Valavanides, M. S. (2014), "Operational efficiency map and flow characterization for steady state two-phase flow in porous media", SCA2014-047.
9. Armstrong, R. T. and Berg, S., "Interfacial velocities and capillary pressure gradients during Haines jumps", *Physical Review E* (2013) 88(4).
10. Youssef, S., Bauer, D., Bekri, S., Rosenberg, E., Vizika, O. "3D In-Situ Fluid Distribution Imaging at the Pore Scale as a New Tool for Multiphase Flow Studies", SPE (2010) 135194.

11. Georgiadis, A., Berg, S., Makurat, A., Maitland, G., Ott, H., "Pore-scale micro-computed-tomography imaging: Nonwetting-phase cluster-size distribution during drainage and imbibition", *Physical Review E* (2013), 88, 033002.
12. Youssef, S., Bauer, D., Peysson, Y., Vizika, O., "Investigation of Pore Structure Impact on the Mobilization of Trapped Oil by Surfactant Injection", SCA2014-064.
13. X. Pak, T., Butler, I.B., Geiger, S., Van Dijke, M.I.J. and Sorbie, K.S., "Droplet fragmentation: 3D imaging of a previously unidentified pore-scale process during multiphase flow in porous media." (2015), *Proceedings of the National Academy of Sciences*, 112(7), 1947-1952.
14. Haines, W. B., "Studies in the physical properties of soil. V. The hysteresis effect in capillary properties, and the modes of moisture distribution associated therewith", *The Journal of Agricultural Science*, (1930) 20(97), 97–116.
15. Berg, S., Ott, H., Klapp, S. A., Schwing, A., Neiteler, R., Brussee, N., Makurat, A., Leu, L, Enzmann, F., Schwarz, J.-O., Wolf, M., Kersten, M., Irvine, S., Stampanoni, M., "Real-time 3D imaging of Haines jumps in porous media flow", *Proceedings of the National Academy of Sciences*, (2013) 110(10), 3755–3759.
16. Berg, S., Armstrong, R. T., Georgiadis, A., Klapp, S. A., Schwing, A. Neiteler, R., Brussee, N., Makurat, A., Leu, L, Enzmann, F., Schwarz, J.-O., Wolf, M., Khan, F., Kersten, M., Irvine, S., Stampanoni, M., "Multiphase flow in porous rock imaged under dynamic flow conditions with fast x-ray computed microtomography", SCA2013-011.
17. Youssef, S., Rosenberg, E., Deschamps, H., Oughanem, R., Maire, E., Mokso, R., "Oil ganglia dynamics in natural porous media during surfactant flooding captured by ultra-fast x-ray microtomography", SCA2014-023.
18. Berg, S., Armstrong, R. T., Georgiadis, A., Ott, H., Schwing, A. Neiteler, R., Brussee, N., Makurat, A., Rücker, M., Leu, Wolf, M., Khan, F., Enzmann, F., Kersten, M., "Onset of oil mobilization and non-wetting phase cluster size distribution", SCA2014-026.
19. Roof, J. G., "Snap-off of oil droplets in water-wet pores", SPEJ (1970) 10(1), 85–90.
20. Armstrong, R. T., Ott, H., Georgiadis, A., Rücker, M., Schwing, A., Berg, S., "Subsecond pore-scale displacement processes and relaxation dynamics in multiphase flow", *Water Resources Research* (2014) 50, 9162–9176.
21. Tuller, M. and Or, D., "Hydraulic conductivity of variably saturated porous media: Film and corner flow in angular pore space", *Water Resources Research*, (2001) *37*(5), 1257–1276.
22. Morrow, N., "Physics and thermodynamics of capillary action in porous media", *Ind. Eng. Chem*. (1970) 62(6), 32–56.
23. Wildenschild, D.; Culligan, K. A.; Christensen, B. S. B., "Application of x-ray microtomography to environmental fluid flow problems", In U. Bonse (Ed.), *Developments in X-Ray Tomography IV Proceedings of SPIE* (2004) *5535*, pp. 432–441.
24. Armstrong R. T., Georgiadis, A., Ott, H., Klemin, D., Berg, S., "Desaturation studied with fast X-ray computed microtomography", *Geophysical Research Letters* (2014), 41, 55–60.

CAPILLARY DESATURATION CURVE PREDICTION USING 3D MICROTOMOGRAPHY IMAGES

Souhail Youssef, Yannick Peysson, Daniela Bauer , Olga Vizika
IFP Energie nouvelles, 1, avenue de Bois-Préau, 92852 Rueil-Malmaison, France

This paper was prepared for presentation at the International Symposium of the Society of Core Analysts held in St. John's Newfoundland and Labrador, Canada, 16-21 August, 2015

ABSTRACT

In this work, we investigated experimentally the relationship between the *Capillary Desaturation Curve* (CDC) and microscopic properties at the pore scale: the oil cluster size distribution and the porous structure. Experiments were performed on a set of water-wet sandstones with different petrophysical properties. Synchrotron based fast X-ray microtomography was used to capture the dynamics of oil cluster displacements and to get insight into the mechanisms that govern trapped oil mobilization by surfactant injection. Oil cluster size distribution as well as pore geometrical properties were also quantified using lab based microtomography (µ-CT) images at the pore scale. Results showed how the CDC depends on the pore structure and on the oil cluster size distribution at residual oil saturation. We show that rescaling CDC at the macroscopic scale using the relative permeability allows the curves to collapse into one curve. Finally, we propose a new method to predict CDC based on structural properties determined experimentally by µ-CT. We demonstrate, that based on these microscopic properties, the CDC measured on macro plugs can be directly predicted from 3D images.

INTRODUCTION

Enhanced Oil Recovery (EOR) with surfactant can improve significantly the total volume of oil produced from a reservoir. In water-wet reservoirs, at the end of the water flooding, the capillary trapping of the oil phase within the rock micro-structure can lead to a high residual oil saturation. At the pore scale, the oil is trapped at the center of the pores in the form of disconnected droplets or clusters. This remaining oil can be produced if the capillary barrier is suppressed by surfactant injection. In this case, the viscous stresses developed by the water flooding are high enough to mobilize the disconnected oil phase. The evolution of the residual oil saturation as a function of the trapping number N_t (capillary number plus Bond number), is known as the Capillary Desaturation Curve (CDC) and it constitutes an important input parameter in chemical EOR flooding. In this work, we investigate experimentally the relationship between CDC and microscopic properties at the pore scale: the oil cluster size distribution and the porous structure.

In the Oil & Gas area, first attempts to predict CDC from structural parameters have been proposed by Stegemeier [1] or Chatzis *et al.* [2] in the late seventies. They proposed correlations based on the pore throat radii distribution to evaluate the capillary desaturation curve. They obtained, in the domain of application of their correlation, a

quite good estimation of measured CDC. However, these approaches using correlations are difficult to extrapolate to other rock types. Yet, these pioneer works show the dependency of CDCs on two main structural parameters: the throat size distribution and the trapped cluster size, which impacts the accessibility path of the flooding fluid. Nowadays, with the renewal of the interest of Chemical EOR methods, new experimental techniques have been developed aiming at the visualization of the oil clusters and the determination of CDC in the case of model porous structures (glass beads or microfluidic network) [3-4]. In the present work we used X-ray tomography [5-7] at two scales (micron and centimeter scale) to provide information on the dependency of capillary desaturation curve with the local microstructure.

MATERIAL AND METHODS

Fluid and Rock Properties

Displacement experiments were conducted using potassium iodide brine KI (4 wt. %) and n-Decane. These two fluids have a significant X-ray absorption contrast, allowing a satisfactory estimation of the two-phase saturations using CT-scan or µ-CT. The interfacial tension between the brine and n-Decane was 40 mN/m. Lower interfacial tension was obtained by adding 0.025 wt. % of Sodium Dodecyl Benzene Sulfonate (SDBS). The interfacial tension between n-Decane and surfactant-brine solution, measured by Spinning Drop method, was 0.3 mN/m. Highly consolidated, water-wet, clean Berea, Bentheimer, Fontainebleau and Clashach sandstones were investigated. Their main petrophysical properties namely permeability (K_0) and porosity (ϕ) as well as the residual oil saturation (S_{or_macro}) are reported in Table 1. $S_{or\_macro,}$ are obtained after spontaneous imbibition for at least 72 h. The core is then scanned and then water flooded at very low Nc ($7.6\ 10^{-8}$) et re-scanned again to check for the stability.

Table 1. Petrophysical properties of the cores used in coreflood experiments

Core type	K_0 (mD)	Porosity ϕ (%)	S_{or_macro} (%)
Berea	208	19.4	48.2
Bentheimer	2676	22.1	37.2
Fontainebleau	304	11.9	25.0
Clashach	426	14.1	38.4

Core Flood Experiments

Coreflood experiments on macro-plug (33 mm in diameter) were combined with CT-scan imaging to accurately measure the mean residual oil saturation. Samples were first saturated with brine and drained by n-Decane injection using a centrifuge at a Bond number around 10^{-6} . Then, we displaced the oil by injecting brine (or a surfactant added brine) at different capillary numbers and the pressure between the inlet and outlet was continuously measured. More details on experimental procedure and sample properties can be found in [6]. We have also conducted dynamic experiments (drainage, imbibition and surfactant injection) at the TOMCAT synchrotron beam line of the Swiss Light Source (SLS) on a Bentheimer sandstone mini-plug (5.8 mm in diameter and 8 mm in

length). 3D images of oil clusters mobilization during the surfactant injection sequence have been captured at different capillary numbers. 3D images were taken with a voxel size of 5 µm and a time interval of 3s. This experiment is described with more details in [8]. Finally mini-plugs (5.6 mm in diameter) of each rock type, were also submitted to drainage under n-Decane by centrifugation followed by a free spontaneous imbibition. Samples were then imaged by a lab µ-CT at residual oil saturation conditions with 3 µm resolution. Porous structure statistics data were determined using the pore extraction methodology developed by Youssef *et al*. [5]. Different structural parameters were computed: pore radii, pore throat radii, pore to throat aspect ratio. 3D volume reconstruction at residual oil saturation conditions permitted then the determination of the oil cluster size distribution for each sample.

EXPERIMENTAL RESULTS

Capillary Desaturation Curves at The Core Scale

Figure 1.a shows the normalized residual oil saturation measured on the four sandstones as a function of the trapping number. Normalized residual oil (S^*_{or}) is expressed by:

$$S^*_{or} = \frac{S_{or}}{S_{ori}} \tag{1}$$

where S_{ori} is the residual oil saturation after the first waterflood (at very low trapping number ~10^{-7}). The trapping number (N_t) is introduced to combine capillary and Bond effect; it is expressed by the following equation :

$$N_t = N_c + N_b \tag{2}$$

where N_c and N_b are respectively capillary number and Bond number given by:

$$N_c = \frac{V\,\mu_w}{\sigma\cos\theta} \;\; ; \;\; N_b = \frac{\Delta\rho\, g\, K_0 K_{rw}}{\sigma\,\cos\theta} \tag{3}$$

where V is the Darcy velocity, μ_w the viscosity of the brine, σ the oil/brine interfacial tension, θ the contact angle, K_0 the absolute permeability, K_{rw} the brine relative permeability and $\Delta\rho$ the oil/brine density difference.

Residual oil saturation mobilization occurs at trapping number values higher than 10^{-6}. CDC shapes are quite close for all cores. The Fontainebleau sample exhibits a more pronounced slope due to its low S_{ori} plateau. We also observe a significant shift (one decade in N_t) between the decreasing part of all CDC. This shift is attributed to pore structure differences between the samples, since experimental conditions and fluids composition were identical.

Brine Relative Permeabilities at Residual Oil Saturation

Brine relative permeabilities at S_{or} were computed from each imposed flow rate Q and the corresponding measured stabilized pressure difference ΔP by:

$$K_{rw} = \frac{\mu_w}{K_0} \frac{Q}{A} \frac{L}{\Delta P} \quad (4)$$

where A is the section of the plug, L its length, Q the flow rate.

Figure 1.b shows K_{rw} as a function of the trapping number N_t for the different samples. In order to better visualize the curve shape, experimental data were fitted by a polynomial fit. Relative permeability curves are distinct for each sample, their characteristic shape depends on the specific microstructure of the samples. As can be seen, for the low range of trapping numbers, K_{rw} curves remain constant at a low value and independent of N_t. These low values are due to large clusters situated in the center of the pores, that have not yet been mobilized. Then, for higher values of N_t, a strong increase in K_{rw} is observed, that corresponds to the increase of the number of paths accessible to the wetting phase as oil clusters have been evacuated. Once a major part of the oil clusters has been mobilized and evacuated (high N_t values), increase of relative permeability becomes slower and K_{rw} tends to 1. The dependence of K_{rw} on N_t in the intermediate trapping number range stands for the existence of a regime in which the pressure difference does not scale linearly with the flow rate as it is the case for the classical Darcy law. These observations are confirmed by Sinha et al. [9], Tallakstad et al. [10] and Yiotis et al. [11] that investigate steady state immiscible two-phase flow. They observed the existence of three regimes, when expressing the normalized pressure gradient as a function of the capillary number.

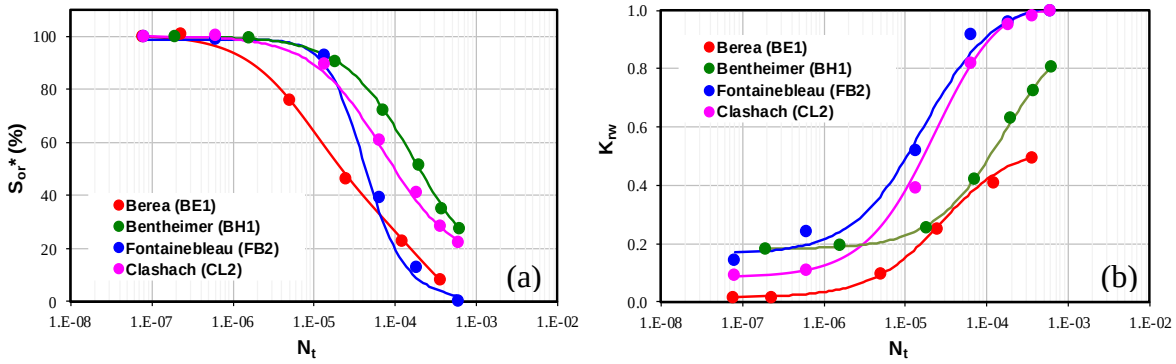

Figure 1: Capillary desaturation curves (a) normalized S_{or} vs. N_t (S_{or} is normalized by S_{ori} which is the residual oil saturation at the end of the waterflood) (b) Brine relative permeabilities as a function of the trapping number N_t for the four sandstones investigated.

Pore Scale Dynamic Observations

To study the behavior of oil clusters during surfactant injection, we have analyzed the size of disconnected oil clusters. These data are extracted from 3D images of the surfactant injection time-series captured during the dynamic experiment described in [8]. In Figure 2.a we report the mean cluster size as well as the size of the largest cluster as a function of the time. The surfactant injection rate was increased each 30 s allowing an increase in the trapping number. This graphic shows that at the beginning of the second and the third stage of surfactant injection at respectively 30 s and 60 s, as soon as the

injection rate is increased the size of the largest cluster increases immediately then it decreases to reach almost a constant plateau. This behavior can be explained as follows: once the capillary number has reached a sufficiently high value (critical capillary number) oil cluster menisci begin to move. As the interfacial tension is relatively low, menisci can merge as soon as they get in contact, leading to cluster coalescence and increasing in this way the size of the largest cluster. Afterwards this largest cluster is partially evacuated from the sample and then breaks up in smaller clusters. This is evidenced by Figure 2.b where we can see the evolution of the largest cluster in the time interval from 33 s to 42 s.

In parallel to that, we can see that the mean cluster size decreases rapidly once the capillary number is increased and then converges to a constant value. One important observation is that the level of this plateau decreases for the mean cluster size as well as for the largest cluster size when the capillary number is increased. These observations suggest that statistically the capillary number imposes an upper threshold to the cluster size distribution. This confirms a first order dependency of the cluster size to the capillary number. This point will be developed theoretically in the last part of this paper.

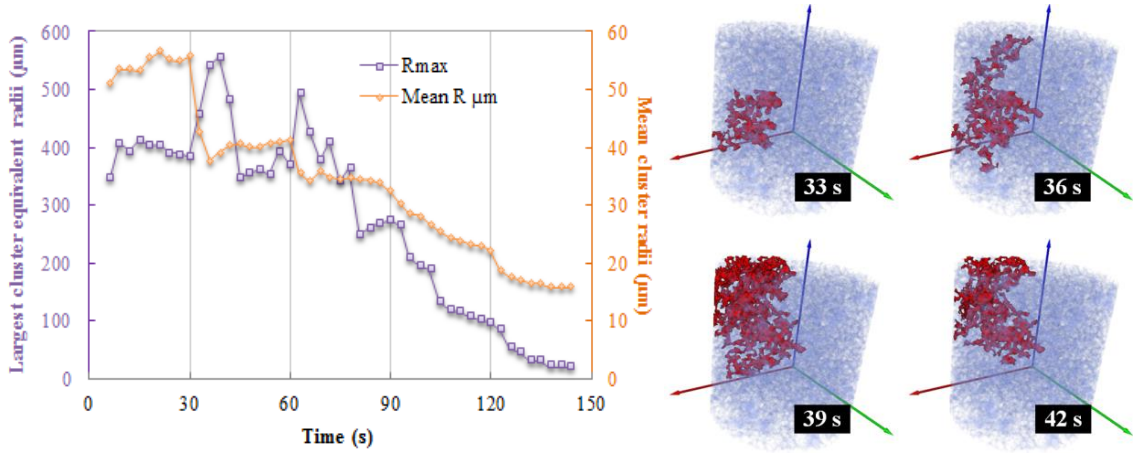

(a) (b)

Figure 2 (a) Evolution of the largest cluster size (R_{max}) and the mean cluster size (R) as a function of the time. (b) Formation and progression of the largest cluster in the time interval from 33s to 42s.

Pore scale statistics

Figure 3 shows 3D images of the four rock types at Sor. Minerals and brine are respectively represented in light gray and dark gray. Oil clusters are represented in color. The color code corresponds to a size classification beginning with the largest clusters in yellow followed by red, green, orange, dark blue and finally the smallest clusters are represented in light blue. The different mean properties computed from these images are reported in Table 2. Image-based porosities are comparable with the macroscopic porosity measurements except for the Clashach sample, certainly due to a local heterogeneity of the sample. The residual oil saturations estimated from the mini-plugs of

the samples are systematically higher than those obtained from the macro-plugs (with the exception of the Berea sample where we obtained a similar value). This can be explained by the following fact: spontaneous imbibition of mini-plugs were realized with both faces open, which can create a side effect and increase Sor above the macroscopic value. Finally we also observe that the mean cluster sizes are very close to the mean pore sizes for the four samples.

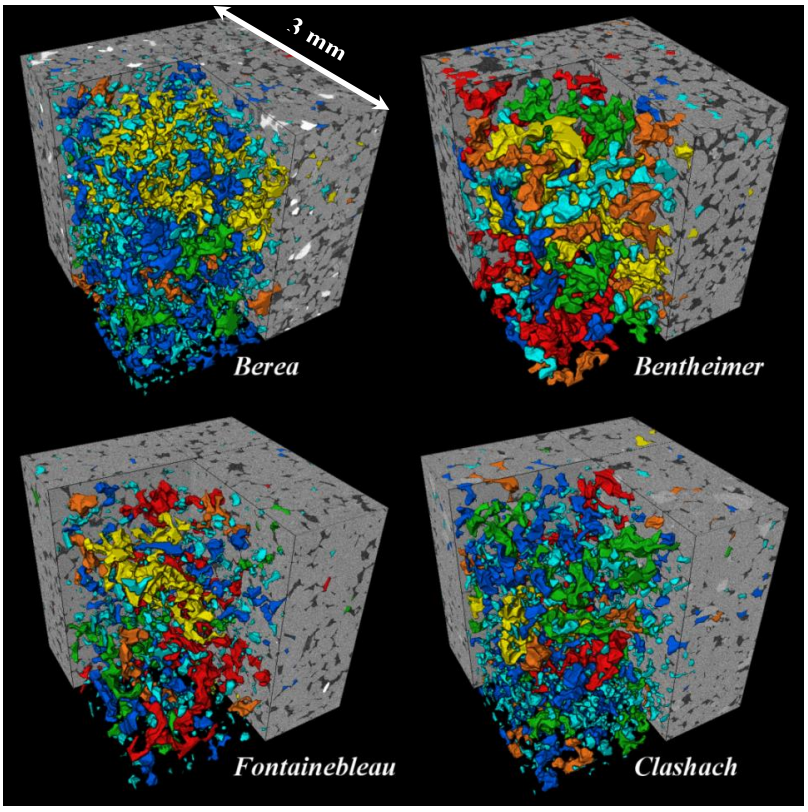

Figure 3: 3D µ-CT images of the four sandstones at residual oil saturation state. Minerals are represented in light gray, brine in dark gray and oil clusters in color. Color code corresponds to a size classification from the largest to the smallest: yellow, red, green, orange, dark blue and light blue.

Table 2. Statistic data of samples used in µ-CT experiments.

Core type	**ϕ_{img} (%)**	**Sor_{img} (%)**	**R (µm)**	**r (µm)**	**R_b (µm)**
Berea	17.6	45.2	28.6	10.5	31.5
Bentheimer	23.1	45.2	36.9	14.8	40.1
Fontainebleau	12.0	37.2	41.4	13.0	38.6
Clashach	10.5	58.2	38.7	12.7	37.2

Figure 4 shows the radius distributions of the oil cluster R_b, pore bodies R, pore bodies containing water and oil and pore bodies containing only water. It can be seen for the four rock types, that mainly small pores contain only water (pink curves). On one hand this is

due to the fact that during drainage oil does not invade the smallest pores. On the other hand, water invades pores during spontaneous imbibition in the case of a water wet system in increasing order. The equivalent radius R_b of each oil cluster was computed assuming that the cluster shape is spherical. Mean values of R_b are comparable to mean pore body radii (cf. Table 2) but the largest clusters can extend over hundreds of pores.

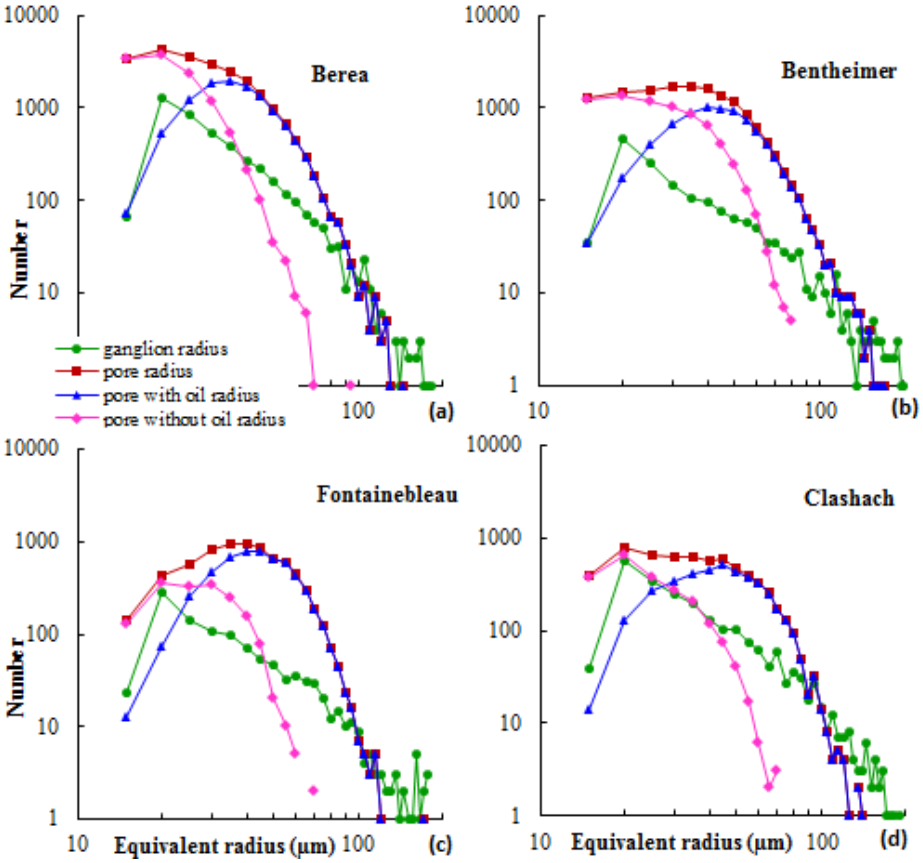

Figure 4: Radius distributions of the oil clusters (R_b), pore bodies (R), pore bodies containing water and oil and pore bodies containing only water (Results are obtained at the mini-plug scale).

Trapping of the oil phase due to spontaneous imbibition might be described by a percolation process [12], as the wetting phase invades first the small pores, leaving disconnected oil clusters in larger pores. Percolation theory suggests that the number of oil clusters of volume V follows a power law given by $N(v) \sim v^{-\tau}$ with $\tau = 2.189$. This has been confirmed by Datta *et al.* [13] and Tallakstad *et al.* [10] for glass beads and Iglauer *et al.* [12] for sandstones. They all observed a power law behavior for the range of lower clusters volume followed by an exponential cutoff for larger clusters. We have fitted our data by a power law using a Levenberg-Marquardt algorithm, that is generally used for non-linear fitting problems (cf. Figure 5). We made a cutoff at 100 μm^3 as it is the minimum volume we can measure and found the following exponents: Bentheimer

τ=2.37, Berea τ=2.31, Clashach τ=2.05, Fontainebleau τ=2.07. Also, our data seem to show an exponential cutoff, however the number of data points for large clusters is not sufficient to validate this behavior.

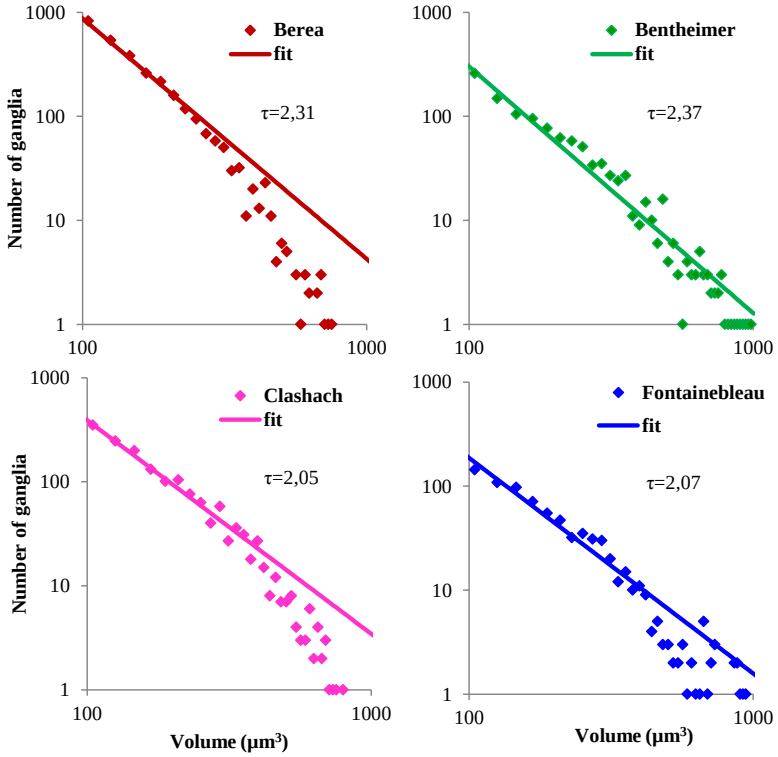

Figure 5: Number of oil ganglia as a function of the ganglia volume and corresponding power law fit. (Results are obtained at the mini-plug scale).

Capillary Desaturation Curve and The Clusters Size Distribution at S_{or}

We have investigated the relation between the clusters size distribution measured at S_{or} and the measured capillary desaturation curve. Figure 6 shows a schematic depiction of an oil ganglion of length $\mathbf{2R_b}$ trapped in a single pore of radius **R**. The pore is oriented in vertical direction. In the pore, pressure and gravity forces act in the same direction in favor of the mobilization of the oil ganglion through the pore throat (blocking pore throat) of radius $\mathbf{r_p}$, while capillary forces hinder the mobilization.

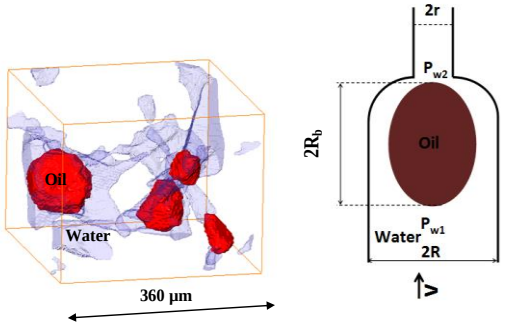

Figure 6: 3D view of trapped oil blobs from Clashach sample and the equivalent pore model scheme.

At the pore scale, we can write a force balance to evaluate the threshold of clusters mobilization [14]. The minimum pressure drop (ΔP_{min}) required to mobilize the oil blob is equal to the Laplace pressure given by:

$$\Delta P_{\min} = P_{w1} - P_{w2} - \rho_o g(2R_b) = 2\sigma\cos\theta\left(\frac{1}{r_p} - \frac{1}{R}\right) \quad (8)$$

where ρ_o represents the oil density, g the gravity acceleration, R the pore radius and r_p the blocking pore throat radius. Darcy's law is expressed by:

$$V = -\frac{K_0 K_{rw}}{\mu L}\left(P_{w2} - P_{w1} + \rho_w g\,(2R_b)\right) \quad (9)$$

where V is the Darcy velocity.

Substituting (P_{w1} - P_{w2}) deduced from equation (9) in equation (8) leads to:

$$\frac{V\mu}{\sigma\cos\theta} + \frac{(\rho_w - \rho_o)gK_0K_{rw}}{\sigma\cos\theta} = \frac{K_0K_{rw}}{R_b}\left(\frac{1}{r_p} - \frac{1}{R}\right) \quad (10)$$

Using the definition of the trapping number equation (10) becomes:

$$N_t = \frac{K_0K_{rw}}{R_b}\left(\frac{1}{r_p} - \frac{1}{R}\right) \quad (11)$$

As a consequence, and considering $1/r_p >> 1/R$, an oil blob can be mobilized if the following inequality is respected:

$$N_t \geq \frac{K_0K_{rw}}{r_pR_b} \quad (12)$$

This equation shows that the trapping number at the threshold of clusters mobilization is linked to three main parameters: the effective brine permeability (K_0K_{rw}), the throat radius of the trapping pores and the clusters size. However, these three parameters are not independent. Indeed, the effective permeability depends on the available path that is controlled at the pore scale by the pore throat radius and the size of the blocking oil cluster. It is also obvious, that during a capillary desaturation process the mean size of the trapped oil cluster changes. Indeed, experimental observations in [7,8,10,14] show that the mean size of the trapped clusters decreases when the capillary number increases during the capillary desaturation process. Equation (5) can be written as:

$$\frac{N_t}{K_0K_{rw}} \geq \frac{1}{r_pR_b} \quad (13)$$

Parameters of the left hand side of the latter equation are defined at the macro plug scale whereas parameters of the right hand side are defined at the pore scale (mini plug). We now assume that the aspect ratio (α) between the oil cluster radius and the corresponding trapping radius is constant ($r_p = R_b/\alpha$) and multiply the two sides of equation (6) by the square of the mean pore throat radius $< r >^2$. We can then define two equivalent scaling groups :

$$N_t^* = \frac{N_t < r >^2}{K_0 K_{rw}} \geq \frac{\alpha < r >^2}{R_b^2} \qquad (14)$$

Figure 7 shows the CDC obtained on macro plugs and plotted as a function of the reduced trapping number. Using this new scaling group the four CDC quasi superimposed with a critical capillary number around $N_t^*=10^{-2}$ and a total desaturation at $N_t^*=1$.

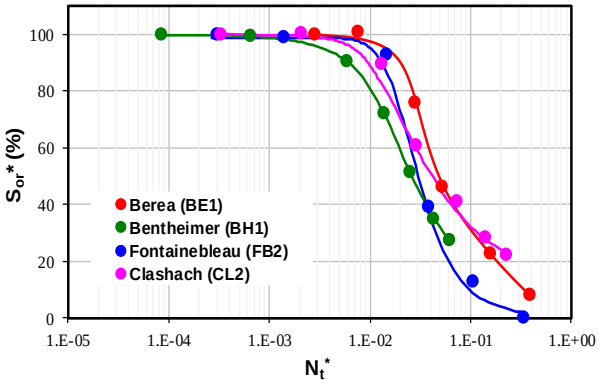

Figure 7 Comparison of capillary desaturation curves plotted using S_{or}^* vs N_t^*. Data are collected on the macro plug experiments for the four sandstones (S_{or}^* is the residual oil saturation normalized by the residual oil saturation after the first waterflood, see [6] for the experimental details).

According to equation (13) we can consider that after flooding at a given reduced trapping number N_t* all the clusters with a size greater than R_b are removed. At this trapping number the normalized residual oil saturation $S^*_{or}(N_t^*)$ in the mini plug can be expressed as:

$$S_{or}^*(N_t^*) = \frac{4\pi}{3V_{ori}} \sum_{R_{bi} \leq R_b} R_{bi}^3 f(R_b = R_{bi}) \qquad (15)$$

where R_{bi} is the ith class size of ganglion radius distribution function f(R_b) and V_{ori} is the total volume of oil in the mini plug after spontaneous imbibition. One can notice that the function S^*_{or} (N_t*) is the volume weighted cumulative function of the ganglion size distribution. In Figure 8 we plot S^*_{or} obtained on macro plugs as a function of $\frac{N_t < r >^2}{K_0 K_{rw}}$ and S^*_{or} obtained by equation (15) as a function of $\frac{\alpha < r >^2}{R_b^2}$ which correspond respectively to the CDC at the macro and mini plug scale.

For this study we consider that α is constant. The aspect ratio α is computed from the ratio between $<R_b>$ and $< r >$, supposing that $< r > \sim < r_p >$ as $< r_p >$ cannot be obtained easily from the μ-CT images since the flow direction is not known.From these curves we can see that the CDCs defined at the two different scales match very well for all samples. These results show that CDCs can be estimated using structural parameters and that ganglion size distribution is a first order parameter.

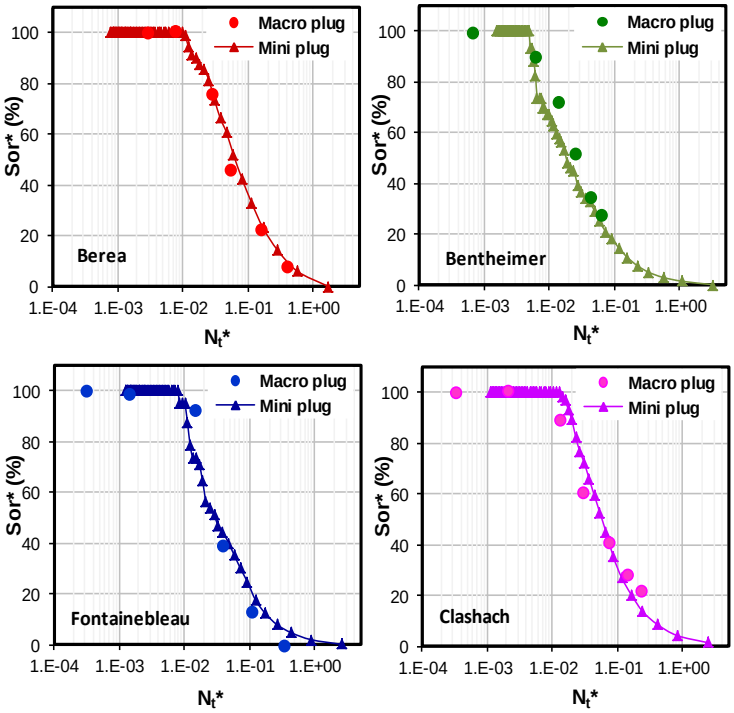

Figure 8: Capillary desaturation curves as a function of the modified trapping number (from macro plug experiments (points) and from mini plug image properties computed at Sor (triangles).

CONCLUSION

In the present work, we performed brine and surfactant flooding experiments in Berea, Bentheimer, Fontainebleau and Clashach sandstone in order to investigate the influence of the pore structure on the mobilization of oil clusters. X-ray Computed Tomography at two scales was used to provide information on the rock local microstructure and to measure the mean residual oil saturation at different trapping number values. A modified trapping number was introduced, that takes into account effective brine permeability, or, in other words, the size of the effective pathways through which fluid flow occurs. Use of the modified trapping number permits rescaling CDC on quasi unique curves. Experimental results showed that by using pore scale geometrical properties extracted from 3D X-ray images we were able to predict satisfactorily the capillary desaturation curve for the different samples from the size distribution of the trapped oil at initial residual saturation. Our observation highlights the importance of the initial distribution of disconnected oil clusters to understand the properties of capillary desaturation curves. From the observation of the relative permeability variation with the trapping number for all rock types, we deduced also a specific scaling for the trapping number. All these results give new insights in recovery mechanisms and interpretation of capillary desaturation of a discontinuous non-wetting trapped phase in a porous media. Introducing this new experimental approach in a chemical EOR process design allows to save time compared with conventional core flood methods and gives valuable information on the rock properties at the early beginning of the workflow.

REFERENCES

1. Stegemeier, G.L., Mechanisms of Entrapment and Mobilization of Oil in Porous Media, D.O. Shah and R.S. Schechter, Editors, *Improved Oil Recovery by Surfactant and Polymer Flooding*, Academic Press, Inc., New York, 55-91, (1977)
2. Chatzis I., Morrow N.R., Lim H.T., Magnitude and detailed structure of residual oil saturation SPEJ, 23 (2), 311-326, SPE-10681-PA, (1983)
3. Krummel A.T., Datta S.S., Munster S., Weitz D.A. Visualizing Multiphase Flow and Trapped Fluid Configurations in a Model Three-Dimensional Porous Medium. *AIChE Journal*, 59: 1022-1029, (2013)
4. Romano M., Chabert M., Cuenca A., and Bodiguel H., Strong influence of geometrical heterogeneity on drainage in porous media, *Phys. Rev. E*, 84: 065302, (2011)
5. Youssef S., Rosenberg E., Glan N., Bekri S., Vizika O., Quantitative 3D characterization of the pore space of real rocks : improved µ-CT resolution and pore extraction methodology, SCA2007-17, *Int. Sym. of the Society of Core Analysts*, Calgary, Canada (2007)
6. Oughanem, R., Youssef S., Peysson Y., Bazin B., Maire E., and Vizika O., Pore-scale to core-scale study of capillary desaturation curves using multi-scale 3D imaging, SCA2013-27, *Int. Sym. of the Society of Core Analysts*, Napa Valley, *California (2013)*
7. Berg S., Armstrong R., Ott H., Georgiadis A., S. Klapp A., Schwing A., Neiteler R., Brussee N., Makurat A., Leu L, Enzmann F., Schwarz J.-O., Wolf M., Khan F., Kersten M., Irvine S., Stampanoni M., Multiphase flow in porous rock imaged under dynamic flow conditions with fast x-ray computed microtomography, *SCA2013-11, Int. Sym. of the Society of Core Analysts*, Napa Valley, *California (2013)*
8. Youssef S., Rosenberg E., Deschamps E., Oughanem R., Maire E., Mokso R., Oil clusters dynamics in natural porous media during surfactant flooding captured by ultra-fast x-ray microtomography, SCA2014-23 *Int. Sym. of the Society of Core Analysts, Avignon, France (2014)*
9. Sinha, S. and A. Hansen: "Effective rheology of immiscible two-phase flow in porous media," *Europhysics Letters* (2012), 1-5
10. Tallakstad K.T., Knudsen H.A., Ramstad T., Løvoll G., Maløy K.J., Toussaint R., and Flekkøy G.E., Steady-state, simultaneous two-phase flow in porous media: An experimental study, *Phys. Rev. E*, 80: 036308, (2009)
11. Yiotis, A.G., Talon, L., Salin, D.: Blob population dynamics during immiscible two-phase flows in reconstructed porous media. *Phys. Rev. E*, 87, (2013)
12. Iglauer S., Favretto S., Spinelli G., Schena G., and Blunt M.J., X-ray tomography measurements of power-law cluster size distributions for the non-wetting phase in sandstones, *Phys. Rev. E*, 82: 056315 (2010)
13. Datta S.S, Ramakrishnan T.S., David A. and Weitz D.A. Mobilization of a trapped non-wetting fluid from a three-dimensional porous medium. *Phys. Fluids* 26: 022002, (2014)
14. Lenormand, R. and Zacone C., Physics of Blob Displacement in a Two-Dimensional Porous Medium, *SPE Formation Evaluation*, 3 (1): 271-275, (1988)

DYNAMIC DRAINAGE AND IMBIBITION IMAGED USING FAST X-RAY MICROTOMOGRAPHY

M. Andrew, H. Menke, M. J. Blunt & B. Bijeljic
Imperial College London, Department of Earth Sciences & Engineering, London SW7 2AZ, UK

This paper was prepared for presentation at the International Symposium of the Society of Core Analysts held in St. John's, Newfoundland, 16-21 August, 2015

ABSTRACT

Recent developments in X-ray microtomography have allowed for multiple fluids to be imaged directly in the pore space of natural rock with temporal resolutions of tens of seconds, allowing for the direct observation of pore-scale displacements . This technique was used to image, with a spatial resolution of 3.64 µm and a temporal resolution of 45 seconds, the injection of supercritical CO_2 (drainage) and brine (imbibition) into a carbonate sample at conditions of pressure, temperature and salinity representative of subsurface flow (10 MPa, 50^{o}C, 1.5 M) using a novel technique for flow control at extremely low flow rates. Capillary pressure was measured from the images by finding the curvature of terminal menisci of both connected and disconnected CO_2 clusters, identified using local curvature anisotropy.

Snap-off in this system was examined by analysing a single snap-off event during drainage and imbibition. Capillary equilibrium concepts do not explain the low capillary pressures seen in the snapped off regions of the pore-space during drainage. The disconnected region created during drainage instead preserves the extremely low dynamic capillary pressures generated during a drainage event (Haines jump). Imbibition appeared isotropic with no clear macroscopic gradients in saturation developed. Snap-off in this system appears to be an equilibrium process, with no observable difference in interface curvature between the connected and disconnected non-wetting phase regions generated after snap-off.

INTRODUCTION

Recent developments in rapid synchrotron-based microtomography have, for the first time, allowed researchers to examine systems with a temporal resolution sufficient for the imaging of dynamic displacement processes, with pioneering papers by Berg *et al.*[1] and Armstrong *et al.* [2] examining Haines jumps and capillary desaturation respectively. At the same time recent developments have shown that, as microtomography is non-invasive, it is possible to conduct experiments at representative subsurface conditions, investigating capillary trapping [3, 4, 5, 6] and measuring contact angle [7, 8]. Synchrotron imaging at representative subsurface conditions has been used to examine multiple points of changing capillary pressure during drainage [9], however temporally resolved studies have still remained a challenge.

Multiphase flow is controlled by a complex set of variables, such as pore structure, interfacial tension and wettability. These are in turn a function of system conditions such as pressure, temperature, and salinity, e.g. Espinoza & Santamarina [10]. In such a complex system the experiments of flow processes at representative subsurface conditions becomes highly attractive. We present results from experiments examining drainage and imbibition conducted on the CO_2-brine-carbonate system at 10 MPa and 50^{o}C, conditions representative of subsurface flow in reservoirs and aquifers.

Drainage, or the injection of non-wetting phase (CO_2) into a porous medium saturated with wetting phase (brine), is extremely complicated in reservoir rocks. A qualitative understanding of the process at the pore-scale can be found using a network-based approximation of the pore-space, where the arbitrarily complicated pore-space is simplified into geometric and well-defined pores, connected by equally well-defined throats. Using this description drainage can be described using invasion percolation theory where the non-wetting phase (CO_2) displaces the wetting phase (brine) from each pore in a sequence of pore-scale events called Haines jumps [11]. These jumps represent the change between two states at capillary equilibrium, however as the jumps tend to proceed on the millisecond time-scale [12, 13], the dynamics of the transition between these two equilibrium states may display disequilibrium features [14]. Although these features (such as low dynamic capillary pressure) are transient, disappearing in connected regions of non-wetting phase as the system re-equilibrates after the transition (and so inaccessible to dynamic tomography with a temporal resolution of 45s), they may be preserved if regions of the pore-space filled with CO_2 are disconnected from the rest of the connected non-wetting phase prior to interface re-equilibration [15]. We present an example of such a phenomenon, showing that snap-off during drainage is due to a disequilibrium process.

In contrast, during imbibition (brine injection) regions of the pore-space full of wetting phase appear to swell uniformly over the length scale of the sample, with no clear fluid front developing. In this case snap-off occurs when the capillary pressure in a throat falls below the threshold snap-off capillary pressure of that throat, causing the throat to rapidly fill with brine, disconnecting a region of non-wetting phase from the rest of the (connected) non-wetting phase. We show that in this case there is no dis-equilibrium between the connected and disconnected non-wetting phase regions, at the point of snap-off, shown by the fact that there is no difference in their interface curvatures after snap-off is complete.

EXPERIMENTAL METHODS

The core assembly is shown in figure 1 and experimental apparatus shown in figure 2. The principal challenges when imaging the dynamic displacement of fluids at representative subsurface flow conditions are associated with system dead volume. The equipment used to control flow at high pressure includes large syringe pumps, connected to the core using long lengths of flexible tubing. Imaging the CO_2-brine system increases

these problems, as system dead volume is further increased by the incorporation of large batch reactors used to control fluid-fluid and fluid-solid reactions. This means that the dead volume of the system (defined as all the volume of fluid outside the rock core, estimated at around 1L) is many orders of magnitude greater than the internal pore-volume of the core (<0.5ml). Small changes in ambient temperature (or errors in the temperature control of heated elements of the system) cause changes in volume of the fluids in the system, potentially causing flow through the core. At high flow rates, such as those used in traditional core-flooding experiments, and in experiments imaging fluid distributions at the end of displacement processes, this is typically not an issue, as any induced flow by these changes in temperature is typically small compared to the flow rate applied across the core [4].

At the very low flow rates required for the examination of dynamic flow, however, flow induced by these changes in system dead-volume becomes important. In order to better constrain the flow boundary conditions for the core we propose a new micro-flow arrangement. A constant pressure drop is applied across a low permeability porous plate on the outlet face of the core (Figure 1). As this plate has a much lower permeability than the rock (with a rock to disk permeability ratio of around 1:200,000) essentially the entire of the applied pressure drop occurs across the plate. As the plate has a high capillary entry pressure, it remains saturated, resulting in a steady wetting phase (brine) flow through it. In this method a constant and extremely low flow rate boundary condition is applied directly at the outlet face of the core. In this way, changes in system volume are accommodated by changes in pump volume (pumps 1 and 3), rather than across the core. For this a hydrophilic modified semi-permeable disk (aluminium silicate, Weatherford Laboratories, Stavanger, Norway) of dimensions 4mm in diameter and 4mm in length and a permeability of 14×10^{-17} m^2 (14×10^{-6} D) was used. In this experiment flow rates of 1.75×10^{-15} m^3/s, equating to a capillary number of 1.10×10^{-11}**.**

Experiments were conducted on a single carbonate sample, Ketton Limestone, an Oolitic Grainstone from the Upper Lincolnshire Limestone Member (deposited 169-176 million years ago). Small cores around 4mm in diameter and 10-20mm in length were drilled from a large core plug around 38mm in diameter. The low permeability porous plate was mounted at the outlet face of the core and both were wrapped in aluminium to prevent diffusive CO_2 exchange across the confining sleeve. An X-ray transparent 4mm outer diameter polymeric tube was placed at the inlet face of the core so that the CO_2-brine interface could be easily monitored during pressurization prior to drainage. The core was then placed in a flouro-polymer elastomer (Viton) sleeve, which was attached to metal fittings connecting the core to the pore-fluid flow lines. A thermocouple was mounted near the base of the core outside the viton sleeve, which was then wrapped twice more with aluminium foil and placed within a high-temperature high-pressure Hassler type flow cell. The thermocouple was connected to a custom PID temperature controller, which heated the cell using an external Kapton insulated flexible heater. The position of the thermocouple is crucial for accurate temperature control, and by siting it in the

confining annulus by the base of the core it is possible to have a constant temperature xin the cell throughout the experiment.
The brine used was Potassium Iodide (KI) with a salinity of 1.5M. In order to prevent reaction between the carbonate rock and carbonic acid formed when $scCO_2$ is mixed with brine the three phases were mixed together prior to injection in a heated reactor. High-pressure syringe pumps were used to maintain system pressure and control the flow of fluids with an incremental displacement resolution of 25.4nL.

The experimental protocol is as follows:

- Raise the pressure and temperature in the reactor to that desired for the pore fluid during the experiment (50^oC and 10MPa).
- Load the core into the coreholder without the flowlines connected to the pumps, and establish a confining pressure of 1 MPa in the cell. This is to establish the same conditions of differential pressure (with the confining pressure 1 MPa above the pore pressure) as during the experiment.
- Centre the core in the field of view.
- Image the core along its entire length using a large number of projections (3600 per 180^o rotation). This creates a high quality unsaturated image from which the pore-space could be analysed in detail and to which saturated images could be compared.
- Bring the temperature of the coreholder up to the desired reservoir temperature.
- Bring the core up to reservoir pressures.
- At reservoir conditions there may be some constant offset between the readings in pumps 1 and 3, even if they were correctly calibrated at ambient conditions. In order to find this difference stop pump 3 while running pump 1 in constant pressure mode.
- Close valves 6, 7 and 8 then open valve 9. The difference between the pressure readings in pumps 1 and 3 will then be the pressure offset between the two pumps.
- Close valve 9 and open valves 6, 7 and 8. Reduce the pressure in pump 3, considering the transducer offset between pump 1 and 3, until there is a pressure drop of 5 kPa across the porous plate. This begins drainage.
- Begin taking scans. Exposure time and the number of projections per tomographic scan will depend specifically on the detector and synchrotron light source used. The results presented in this study were acquired using 800 projections with an exposure of 0.04s. from each image.
- The qualitative progress of the drainage process can be monitored without stopping the tomographic sequence by monitoring changes in the first radiograph.
- After drainage is complete, increase the pressure in pump 3 until it reaches 5 kPa pressure drop across the porous plate, in the opposite direction to that applied during drainage.
- Begin taking scans. Exposure time and the number of projections per tomographic scan will depend specifically on the detector and synchrotron light source use.

IMAGE ACQUISITION AND PROCESSING

Imaging was performed at Diamond Imaging Beamline I13 (Diamond Light Source, UK). Imaging was conducted under pink-beam conditions, with each scan taking around 45 seconds to acquire, with 32 seconds projections and around 13 seconds returning to the initial state and preparing for the next scan. To reduce the impact of beam heating on fluid distributions the pink-beam was then filtered by 2 mm of in-line graphite, 2 mm of in-line aluminium and 10 μm of in-line gold.

All image processing was conducted using Avizo Fire 8.0 and imageJ programs. Each image in the time-series was reconstructed using a filtered back projection algorithm[16], binned then cropped such that each image consisted of around 1100×1100×1100 voxels with a voxel size of 3.64 μm. The images were filtered using a non-local means denoising filter and registered to the first image in the dynamic sequence. The difference between each image and the first in the sequence (prior to non-wetting phase invading the pore-space during drainage) was computed for both drainage and imbibition, giving a high contrast map of non-wetting phase distributions. The time sequence of these maps of the non-wetting phase was then rendered in 3D to identify individual events of interest. Once these events had been identified subvolumes were extracted from the 4D data temporally located around each event. These subvolumes were then segmented using a seeded watershed algorithm [17]. Surfaces were generated across the non-wetting phase using a smoothed marching cubes algorithm [18], and interface curvature were calculated by approximating the surface locally as a quadratic form [15]. Terminal menisci from the wetting-non-wetting phase interface were identified using the anisotropy of the curvature vector (only taking measurements where the smallest principal radius of curvature of the interface was very close in magnitude to the largest principal radius of curvature). The radii of curvature of these regions of the wetting-non-wetting phase interface were maximised relative to the voxel size, making the estimation of mean curvature more reliable and were furthest away from the three phase contact line, minimising the impact of smoothing on resulting curvature distributions. Details about this technique will be included in an upcoming paper.

DRAINAGE

During drainage non-wetting phase invasion does not occur uniformly, but instead as a discrete set of events where regions of the pore-space which were previously occupied by wetting phase (brine) become occupied by non-wetting phase (CO_2) (Haines jumps [19]). The progress of these events is not resolved with the temporal resolution provided by synchrotron based dynamic tomography. Micromodels have been used to show that pores drain on the millisecond timescale, and that the time taken for the jump to occur is independent of the macroscopic capillary number [12, 13]. This behavior can be understood by describing these events and changes between two states at capillary equilibrium; before and after each of the non-wetting phase jumps. Dynamic tomography therefore allows us to see the sequence of these jumps during drainage, and by looking in detail at the fluid distributions before and after each of the jumps, we can examine and test some of the assumptions in descriptions of multi-phase flow. Specifically it allows us to examine the relative processes by which regions of non-wetting phase can become

isolated from the rest of the pore-space occupied by connected non-wetting phase in the process of snap-off. This is particularly interesting as the disconnected non-wetting phase region preserves the conditions present at the point of snap-off, even as flow continues around it.

Snap-off occurs during drainage by the following mechanism. As the wetting-non-wetting interface emerges from a pore throat during a drainage event, the curvature across that interface will decrease. This causes curvature disequilibrium between the leading region and other regions of the wetting-non-wetting phase interface. As the interface attempts to re-equilibrate, the curvature in the pore-throat connecting the leading portion on the non-wetting phase from the rest of the connected non-wetting phase starts to decrease. If the curvature in this throat decreases below the threshold snap-off capillary pressure for that throat, the leading portion of non-wetting phase will snap-off, disconnecting it from the rest of the connected CO_2.

This process can be seen in the experiments examined in this study in two successive tomographic scans in the 4D dataset, separated by 45 seconds (figure 3, A-B). Surface curvature is measured, using curvature anisotropy (the relative magnitude of the larger and smaller principal curvature vectors), for both the connected and disconnected CO_2 phase before and after the jump (figure 3C).

The interface curvatures measured on the disconnected ganglion are much lower than those of the connected CO_2 region either before or after the invasion – snap-off sequence has occurred. We propose that this is due to significant dynamic capillary pressure gradients generated in the leading region of the non-wetting phase during the drainage event, out of capillary equilibrium. These cause the low capillary pressures required for throat snap-off, which are then preserved in the disconnected ganglion. The capillary pressure of the ganglion is defined by the threshold snap-off capillary pressure of the disconnecting throat, defined by the local pore geometry, consistent with the findings of Andrew *et al.* [6], where the capillary pressures of a population of disconnected ganglia were observed to be controlled by local pore geometry (and so threshold snap-off capillary pressures). After the invasion/snap-off event has completed the rest of the connected non-wetting phase interface will re-equilibrate to some new stable interface curvature, however the disconnected region will not, thereby retaining and preserving the low dynamic curvatures generated during the invasion event on the time scale resolvable with synchrotron based microtomography.

IMBIBITION

During imbibition the wetting phase invades the pore-space in a uniform fashion, with no clear front developing over the length scale observable in the experiment. No macroscopic gradients in saturation (“front”) develop on the length-scale of the image as the connected wetting-non-wetting interface remains at capillary equilibrium (displaying no gradients in the interface curvature of the connected non-wetting-wetting phase interface). As capillary pressure decreases, corresponding to an increase in wetting phase

saturation, wetting phase regions appear to swell uniformly throughout the imaged volume.
If we look at snap-off in this system (during imbibition) the connected non-wetting phase curvature is not distinctly different before or after the snap-off event, and the disconnected non-wetting phase region curvature is not distinctly different to the connected non-wetting phase region either before or after the event (figure 4). These results can be understood by thinking of imbibition (and resulting snap-off) as an equilibrium process. As wetting layers swell during wetting phase invasion, capillary pressure slowly decreases across the entire wetting-non-wetting phase interface. When it gets below the threshold snap-off capillary pressure for a particular throat, that throat snaps off rapidly, but because prior to snap-off the entire wetting-non-wetting interface was at equilibrium, there is no gradient in capillary pressure between the connected and disconnected non-wetting phase regions. The connected non-wetting phase will then continue to be displaced out of the system by the invading wetting phase, reducing connected surface capillary pressure. The disconnected ganglion, however, will retain the capillary pressure present at snap-off.

This is in contrast to snap-off occurring during drainage, where dynamic forces generated by a Haines jump decrease curvature in a throat to below its threshold snap-off curvature. Because these changes in capillary pressure are due to dynamic forces (occurring on the millisecond time-scale), they are not represented in the curvature of the connected phase in the next image in the time sequence (with an image time resolution of around 45 seconds). As the capillary pressure of the disconnected phase is primarily controlled by the threshold snap-off capillary pressure, as defined by the local pore geometry, dynamic curvatures are preserved in the disconnected ganglion, creating a difference in interface curvature between connected and disconnected non-wetting phase regions.

CONCLUSIONS

We have used synchrotron based dynamic tomography to image the drainage (non-wetting phase invasion) and imbibition (wetting phase invasion) process in a carbonate sample at representative subsurface conditions with a time resolution of around 45 seconds. Snap-off has been observed in both processes, disconnecting non-wetting phase regions. Curvature distributions show a difference in interface curvature between the disconnected and connected non-wetting phase region after snap-off, whereas during imbibition there is no clear difference between the interface curvature distributions. We propose that this difference in interface curvature is due to a difference in the physics causing the snap-off in each system.

Snap-off in the drainage process is due to dynamic forces, arising due to low interface curvatures generated as a non-wetting phase (CO_2) region invades a region of the pore-space occupied by wetting phase (brine) in a Haines jump. This reduces interface curvatures in the invaded pore throat to below its threshold snap-off capillary pressure. Snap-off during imbibition, however, is due to the equilibrium swelling of wetting phase regions during brine invasion, until the threshold snap-off capillary pressure of a throat is

reached. At this point the throat rapidly fills with wetting phase, however prior to snap-off the interface was at equilibrium, meaning that the resulting connected and disconnected non-wetting phase regions have no difference in interface curvature.

Future work could focus on examining the relative statistical importance of snap-off processes during drainage, or the correlation of modelled snap-off capillary pressures to experimentally observed interface curvatures. Another interesting area for future research is how the results of these experiments at extremely low flow rates correspond to more rapid displacements seen in realistic subsurface conditions, and how the interaction between viscous pressure gradients, causing flow, and capillary forces can cause changes in pore-scale displacement processes on the individual pore and ganglion scales.

ACKNOWLEDGEMENTS

We thank Diamond Light Source for access to beamline I13 and especially the assistance of Dr. Christoph Rau and Dr. Joan Vila-Comamala who contributed to the results presented here. We acknowledge funding from the Imperial College Consortium on Pore-Scale modelling. We also gratefully acknowledge funding from the Qatar Carbonates and Carbon Storage Research Centre (QCCSRC), provided jointly by Qatar Petroleum, Shell, and Qatar Science & Technology Park.

REFERENCES

1. Berg, S. *et al.* Real-time 3D imaging of Haines jumps in porous media flow. *Proc. Natl. Acad. Sci. U. S. A.* **110,** 3755–9 (2013).
2. Armstrong, R. T., Georgiadis, A., Ott, H., Klemin, D. & Berg, S. Critical capillary number: Desaturation studied with fast X-ray computed microtomography. *Geophys. Res. Lett.* **41,** 55–60 (2014).
3. Andrew, M., Bijeljic, B. & Blunt, M. J. Pore-scale imaging of geological carbon dioxide storage under in situ conditions. *Geophys. Res. Lett.* **40,** 3915–3918 (2013).
4. Andrew, M., Bijeljic, B. & Blunt, M. J. Pore-scale imaging of trapped supercritical carbon dioxide in sandstones and carbonates. *Int. J. Greenh. Gas Control* **22,** 1–14 (2014).
5. Chaudhary, K. *et al.* Pore-scale trapping of supercritical CO2 and the role of grain wettability and shape. *Geophys. Res. Lett.* **40,** 3878–3882 (2013).
6. Andrew, M., Bijeljic, B. & Blunt, M. J. Pore-by-pore capillary pressure measurements using X-ray microtomography at reservoir conditions: Curvature, snap-off, and remobilization of residual CO2. *Water Resour. Res.* **50,** 8760–8774 (2014).
7. Aghaei, A. & Piri, M. Direct pore-to-core up-scaling of displacement processes: Dynamic pore network modeling and experimentation. *J. Hydrol.* **522,** 488–509 (2015).
8. Andrew, M., Bijeljic, B. & Blunt, M. J. Pore-scale contact angle measurements at reservoir conditions using X-ray microtomography. *Adv. Water Resour.* **68,** 24–31 (2014).

9. Herring, A. L., Andersson, L., Newell, D. L., Carey, J. W. & Wildenschild, D. Pore-scale observations of supercritical CO2 drainage in Bentheimer sandstone by synchrotron x-ray imaging. *Int. J. Greenh. Gas Control* **25,** 93–101 (2014).
10. Espinoza, D. N. & Santamarina, J. C. Water-CO2-mineral systems: Interfacial tension, contact angle, and diffusionImplications to CO2 geological storage. *Water Resour. Res.* **46,** 1–10 (2010).
11. Wilkinson, D. & Willemsen, J. F. Invasion percolation: a new form of percolation theory. *J. Phys. A. Math. Gen.* **16,** 3365–3376 (1999).
12. Mohanty, K. K., Davis, H. T. & Scriven, L. E. Physics of Oil Entrapment in Water-Wet Rock. *SPE Reservoir Engineering* **2,** (1987).
13. Armstrong, R. T. & Berg, S. Interfacial velocities and capillary pressure gradients during Haines jumps. *Phys. Rev. E - Stat. Nonlinear, Soft Matter Phys.* **88,** 1–9 (2013).
14. Moebius, F. & Or, D. Pore scale dynamics underlying the motion of drainage fronts in porous media. *Water Resour. Res.* **50,** 8441–8457 (2014).
15. Armstrong, R. T., Porter, M. L. & Wildenschild, D. Linking pore-scale interfacial curvature to column-scale capillary pressure. *Adv. Water Resour.* **46,** 55–62 (2012).
16. Titarenko, V., Titarenko, S., Withers, P. J., De Carlo, F. & Xiao, X. Improved tomographic reconstructions using adaptive time-dependent intensity normalization. *J. Synchrotron Radiat.* **17,** 689–699 (2010).
17. Jones, A. C. *et al.* Assessment of bone ingrowth into porous biomaterials using MICRO-CT. *Biomaterials* **28,** 2491–2504 (2007).
18. Hege, H., Seebass, M., Stalling, D. & Zockler, M. A Generalized Marching Cubes Algorithm Based On Non-Binary Classifications. *ZIB Prepr.* **sc-97-05,** (1997).
19. Haines, W. B. Studies in the physical properties of soil. V. The hysteresis effect in capillary properties, and the modes of moisture distribution associated therewith. *The Journal of Agricultural Science* **20,** 97 (1930).

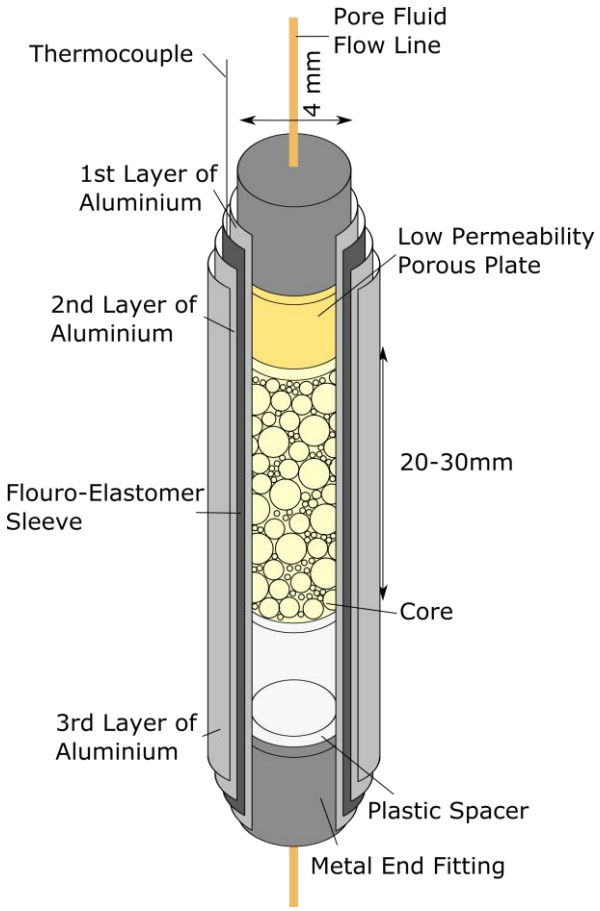

Figure 1: Core Assembly, showing the relative positioning of the low permeability porous plate, the core and the plastic space (allowing for the wetting-non-wetting interface to be seen prior to invasion in the core.

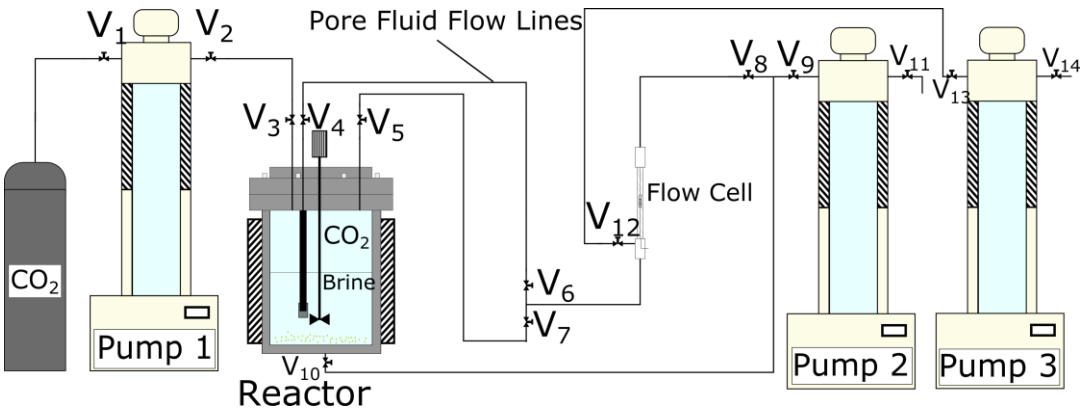

Figure 2: Experimental flow apparatus, showing how high-pressure syringe pumps were connected to the flow cell.

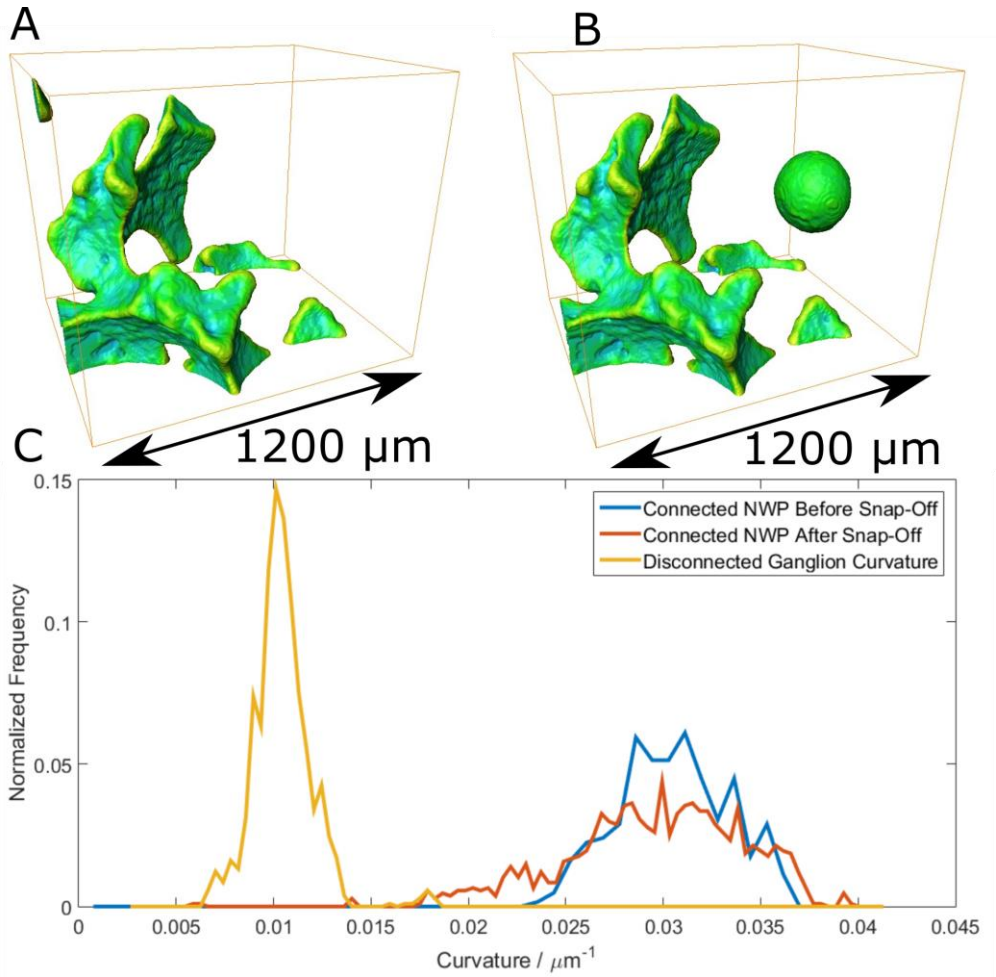

Figure 3: A-B: Connected and disconnected non-wetting phase (CO_2) after invasion & snap-off during drainage, taken from two subsequent tomographies. In this rendering the wetting phase (brine) and the rock grains are see-through. The surfaces are coloured according to the magnitude of the mean interface curvature. C: The distribution of curvatures, as measured on terminal menisci identified using curvature anisotropy. The disconnected non-wetting phase region formed by snap-off has a lower interface curvature than the connected non-wetting phase region either before or after the snap-off event.

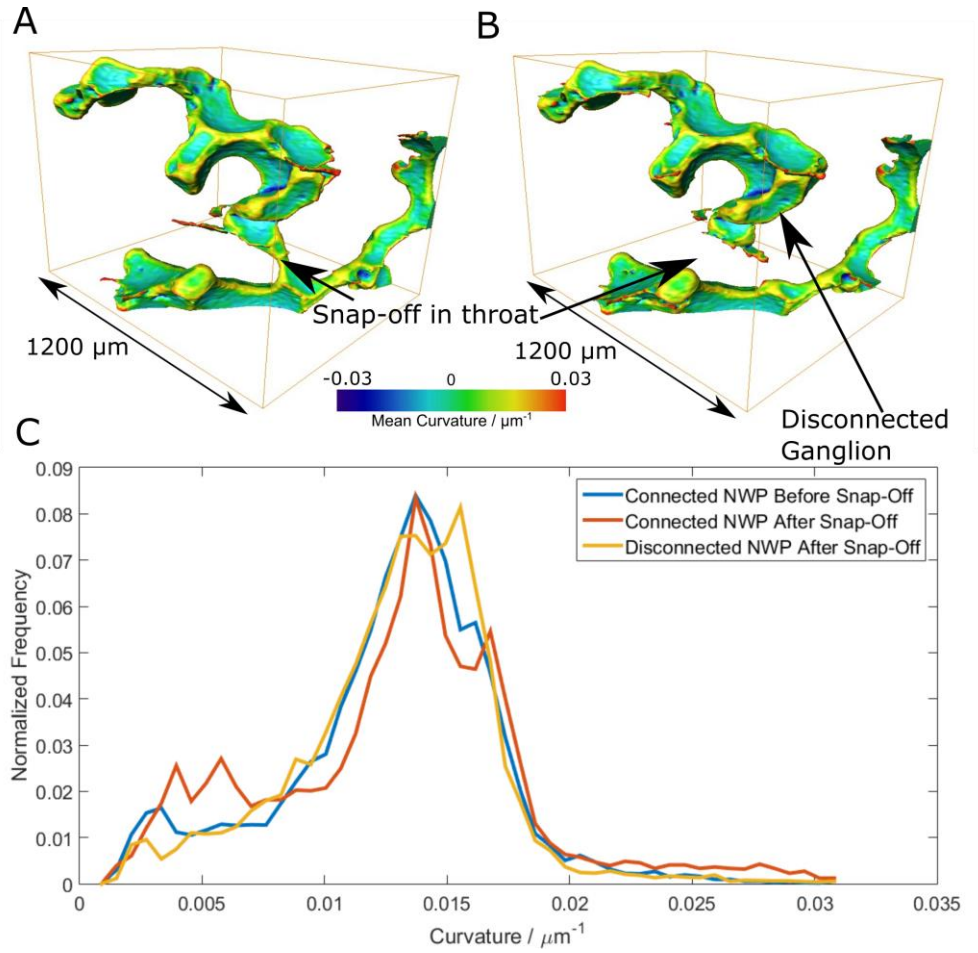

Figure 4: A-B: Connected and disconnected non-wetting phase (CO_2) after invasion & snap-off during imbibition, taken from two subsequent tomographies. In this rendering the wetting phase (brine) and the rock grains are transparent. The surfaces are coloured according to the magnitude of the mean interface curvature. C: The distribution of curvatures, as measured on terminal menisci from the wetting-non-wetting fluid-fluid interface, identified using curvature anisotropy. The disconnected non-wetting phase region formed by snap-off has an indistinguishable interface curvature to the connected non-wetting phase region either before or after the snap-off event.

WETTABILITY ANALYSIS USING MICRO-CT, FESEM AND QEMSCAN, AND ITS APPLICATIONS TO DIGITAL ROCK PHYSICS

Nasiru Idowu[1], Haili Long[1], Pål-Eric Øren[1], Anna M. Carnerup[2], Andrew Fogden[3], Igor Bondino[4] and Lars Sundal[5]
[1] FEI Trondheim AS, Trondheim, Norway; [2] FEI Australia Pty Ltd, Canberra, Australia;
[3] Australian National University, Canberra, Australia; [4] Total E&P, Pau, France;
[5] DEA Norge AS, Oslo, Norway

This paper was prepared for presentation at the International Symposium of the Society of Core Analysts held in St. John's Newfoundland and Labrador, Canada 16-21 August, 2015

ABSTRACT

This study presents an integrated methodology for determining the pore-scale distribution of wettability of rock samples to guide pore network modeling. Wettability was characterized by spatial registration of rock images from X-ray micro-computed tomography (MCT), Field Emission Scanning Electron Microscopy (FESEM), and Quantitative Evaluation of Minerals by SEM (QEMSCAN). The approach was applied to miniplugs of an outcrop and a reservoir sandstone, which were drained and aged in oil and underwent spontaneous and forced imbibition of brine. Tomogram acquisition after each preparation step showed that, from similarly low initial water saturation, oil recovery by spontaneous imbibition was high in the outcrop and virtually zero in the reservoir sample, while the additional recovery by forced imbibition was the opposite. These results and the pore-scale distributions of remaining oil suggest different wettabilities for each sample though their petrophysical properties (porosity and permeability) are similar.

The cleaned miniplugs were then subjected to FESEM mapping of raw cut faces to visualize local wettability alteration, and to QEMSCAN of polished faces to relate this to surface mineralogy. The established wettability information was then used to assign plausible wettability parameters to pores and throats of topologically equivalent networks. The simulated oil/water displacement results for the reservoir sandstone showed good agreement with available SCAL data.

INTRODUCTION

Optimal recovery from hydrocarbon reservoirs during waterflooding and enhanced oil recovery techniques depends largely on a good understanding of crude oil/brine/rock interactions – wettability [1]. To classify reservoir wettability either as water- or oil-wet is a gross oversimplification that can lead to unexpectedly low oil recovery and inefficient reservoir management [2, 3]. A mixed-wet state is often inferred, but without sufficient information to determine its detailed distribution. The three standard

measurement methods for quantitatively characterizing wettability of rock samples are contact angle goniometry [4], and the Amott [5] and USBM [6] tests based on spontaneous and forced imbibition/drainage. Goniometry is restricted to a prepared rock section, which often limits measurement precision. Amott and USBM tests only yield an averaged wettability measure of a core sample, and the former is relatively insensitive near neutral wettability. Complementary wettability information can be obtained from, e.g. spontaneous imbibition rates, relative permeability, calorimetry, flotation of crushed rock or microscopy of model substrates, although the results are often less quantitative or less directly relevant. Nuclear magnetic resonance (NMR) methods have also been used to provide quantitative wettability indices [7, 8].

Advanced, high-resolution imaging techniques such as MCT and FESEM have recently been used to determine the pore-scale distribution of oil in rock plugs before, during or after waterflooding and to visualize the asphaltene films remaining on cleaned rock surfaces due to local wettability alteration [9-13]. To date, establishment of quantitative links between these imaging studies and connections to prediction of residuals are limited. Andrew *et al*. [14] recently presented a method for contact angle measurement from MCT of a supercritical CO_2-brine system in a Ketton limestone. However, this rock has simple mineralogy, comprising 99.1% calcite and 0.9% quartz [14].

In this study, we establish the wettability of reservoir and outcrop sandstone samples by integrating imaging results from MCT, FESEM and QEMSCAN. Secondly, we use this information to assign plausible wettability parameters to pores and throats of topologically equivalent pore networks extracted from the segmented pore space. Finally, we simulate oil/water displacements with a quasi-static pore network model and compare the results with available experimental data.

MATERIALS AND METHODS

Two sandstone samples were used in this study. MCT (by HeliScan) of the received core plugs (25 mm) showed that the outcrop Sample 1 was fairly homogenous while the reservoir Sample 2 was highly heterogeneous with several laminations. Locations within these low resolution tomograms were chosen for subsampling of two miniplugs of 6 mm × 15 mm and 9 mm × 10 mm from each, using a manually-fed drill press. The miniplugs were cleaned by hot Soxhlet extraction in toluene, methanol and chloroform/methanol azeotrope, and then dried. Mercury injection capillary pressure (MICP) measurements were performed on the 9 mm diameter miniplugs while the 6 mm diameter miniplugs were used in the remainder of the study. The measured petrophysical properties are summarized in Table 1.

Tomograms of the pair of 6 mm miniplugs were acquired (at 3.7 or 3.9 μm/voxel resolution for Samples 1 and 2, respectively) in a series of five prepared states, starting with their cleaned, dry state. Each miniplug was then infiltrated, under vacuum followed by high isostatic pressure, with brine comprising 5 g/l $CaCl_2$, doped with 1.5 M NaI, after which this brine-saturated state was scanned. Primary drainage was then carried out by

centrifugation in the supplied crude oils to a maximum capillary pressure of 500 kPa for a minimum of 12 h, followed by 14 days of ageing at 60°C or 83°C for Samples 1 and 2, respectively. The third tomogram was acquired in this state of established initial water saturation and wettability alteration. The miniplug was then immersed in the same brine and temperature as mentioned above for 7 days of spontaneous imbibition, followed by re-scanning. Forced imbibition was then performed by centrifugation in this brine to a maximum pressure of 17.5 or 14.0 kPa for Samples 1 and 2, respectively, for at least 18 h, after which this fifth state was imaged.

Table 1. Measured petrophysical properties of the two sandstone samples.

Sample No.	Porosity (%)	Kabs (mD)
1 (outcrop)	22.5	524
2 (reservoir)	22.7	853

Each miniplug was then cleaned of its remaining oil using decalin and heptane, followed by centrifugation in the undoped brine, prior to being cut in half crosswise using a Struers saw with water-based coolant. After removal of salt by soaking in methanol, the bottom half was re-scanned and then imaged by FESEM (Helios 600 NanoLab, FEI) using a secondary electron detector. Its raw cut face was first mapped at 0.59 µm/pixel, followed by acquisition of higher magnification micrographs at selected locations to resolve the asphaltene footprint (or lack of) on pore walls. The top half of the miniplug was resin embedded for preparation of a polished face for analysis by SEM (Quanta 650 FEG, FEI) using a backscattered electron detector for imaging and Energy-dispersive X-ray spectroscopy for mineral identification, automated by MAPS software and QEMSCAN.

RESULTS

MCT Imaging and Analysis

For each of the two 6 mm miniplugs, their series of five tomograms were post-processed by Mango software for 1) spatial registration to within one voxel, 2) correction of beam hardening artifacts, 3) cylindrical masking of the damaged periphery, and 4) rescaling of attenuation. The processed tomograms and their differences were then segmented using converging active contours algorithms to identify solid grains, pores and sub-resolution microporosity. The oil and brine occupancy of each voxel of these latter two categories at the end of primary drainage and ageing (PD), and spontaneous (SI) and forced imbibition (FI) was identified. For the segmented porosity and water saturation of Samples 1 and 2, Table 2 lists their tomogram averages, Figure 1 plots their (radially-averaged) longitudinal profiles, and Figure 2 shows a representative cross-sectional slice, in which rock, oil and water correspond to grayscales, red and blue, respectively. The top (≈ 5 mm) and more porous part of the Sample 2 miniplug broke after PD and the remaining piece was used for aging, SI and FI. The lower segmented porosity in Table 2 compared to Table 1 and the shorter profile length in Figure 1 are due to this breakage.

Table 2. Average segmented porosity and water saturation from MCT of 6 mm diameter miniplugs.

Sample No.	Porosity (%)	Swi_PD (%PV)	Sw_SI (%PV)	Sw_FI (%PV)
1	20.7	3.0	59.3	62.9
2	17.4	3.2	4.5	34.1

The two miniplugs have similar measured petrophysical properties (Table 1) and comparable S_{wi} after primary drainage and aging (Table 2, which may be underestimated due to limitations in resolving brine thin films). However, the corresponding profiles in Figure 1 show that the outcrop Sample 1 is homogeneous while the reservoir Sample 2 is heterogeneous with tighter and more open laminations. The two miniplugs also exhibit very different imbibition response. Sample 1 shows very strong spontaneous imbibition, while Sample 2 has almost none, aside from the rise near the ends which is common to both. Additional recovery by forced imbibition is limited for Sample 1, but substantial for Sample 2, and with heterogeneities partly mirroring those of its porosity profile. The computed Amott water indices (I_w) from segmentation of the oil and water phases in Samples 1 and 2 are in the ranges 0.60-0.94 and 0.01-0.04, respectively.

Figure 2a shows that the irreducible water of the 6 mm Sample 1 miniplug resides as expected in the tightest locations and in the relatively rare clay-aggregate particles. Given the predominance of grain-lining clays, much of the water may remain connected, in spite of its overall low saturation. By contrast, the irreducible water of the 6 mm Sample 2 miniplug in Figure 2d appears less connected, due to its smoother grains with less clay lining and the occlusion of tighter pores by a slightly lower-attenuating (darker) mineral cement. However, it should be borne in mind that S_{wi} of this slice is only 1.5 %, as it comes from the lowest-saturation dip of the blue curve (Swi_PD profile) in Figure 1b.

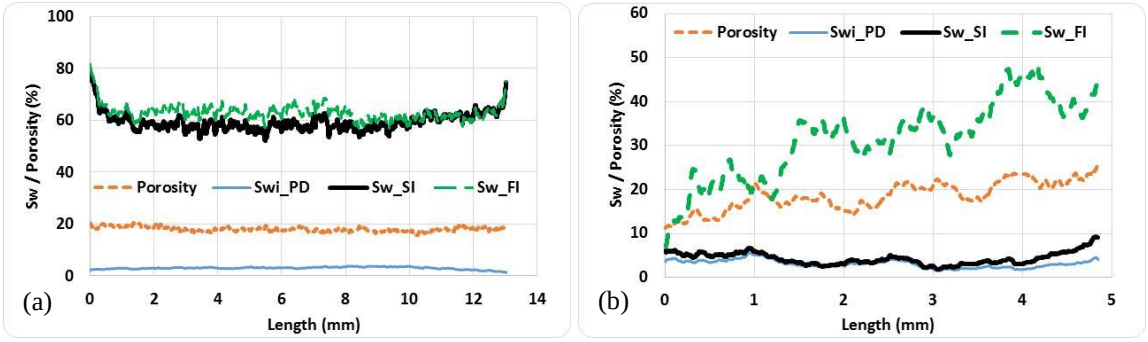

Figure 1. Longitudinal profiles of porosity (% bulk volume) and S_w (% PV) after primary drainage, spontaneous and forced imbibition, for the miniplugs of (a) Sample 1 and (b) Sample 2.

The substantial spontaneous imbibition into Sample 1 in Figure 2b recovers virtually all oil from smaller pores and near grain surfaces to leave large blobs in pore bodies (e.g. highlighted with green boxes), presumably due to snap-off in throats. Virtually no further change is seen on forced imbibition in Figure 2c. Conversely, the change in Sample 2 from Figure 2d to 2e due to spontaneous imbibition is almost imperceptible, while subsequent forced imbibition in Figure 2f results in complete recovery of oil from many

of the larger pores (e.g. highlighted with yellow circles). The remaining oil generally occupies narrower pores closest to grain surfaces, and retains higher connectivity than for Sample 1. Larger uninvaded clusters, e.g. at upper left in Figure 2f, may be due to the miniplug heterogeneity. The computed I_w and the pore-scale remaining oil distributions suggest that Sample 1 is water-wet while Sample 2 is oil-wet.

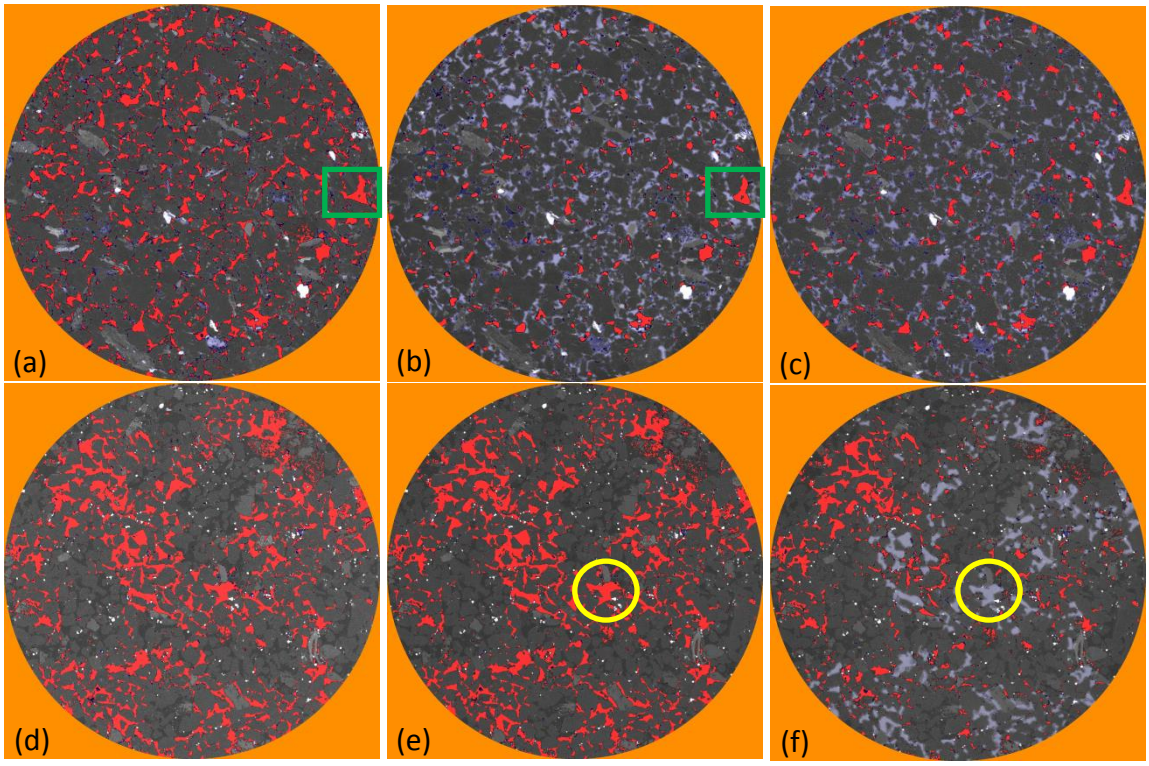

Figure 2. Registered tomogram slices of (a-c) Sample 1 and (d-f) Sample 2, showing oil (red) and brine (blue) distribution after (a, d) primary drainage, (b, e) spontaneous and (c, f) forced imbibition.

QEMSCAN

Figure 3 shows registered automated maps from backscattered electron SEM imaging and QEMSCAN mineral identification on a polished embedded section within the upper half of the miniplugs of Samples 1 and 2, which do not coincide with the tomogram slices in Figure 2. From Figure 3b, almost 40% of all grains in Sample 1 comprise Na plagioclase, although these are indistinguishable from the quartz grains in Figures 2a-c and 3a owing to their similar X-ray attenuation and electron density, respectively. Feldspar corresponds to the slightly brighter grains in MCT, which are relatively rare. The prevalent flaky particles are mainly muscovite with occasional biotite, and particles and seams of detrital chlorite are fairly common. These clays are the brighter mineral features in Figures 2a-c and 3a, while the brightest grains correspond to the densest trace minerals. Illite and biotite in the form of grain-lining plates are under-represented due to resolution limitations of both QEMSCAN (2.4 µm/pixel) and MCT. Figure 3d shows that Sample 2 is also dominated by quartz and Na plagioclase. The latter is the cement-like phase in

Figures 2c-f and 3c of slightly lower X-ray attenuation and electron density, respectively, than the surrounding quartz grains. Feldspar is more prevalent than in Sample 1, while clays are less common, although their presence as grain linings may again be underestimated. Figure 3c shows quite substantial damage to Sample 2 during resin stub preparation, while Sample 1 in Figure 3a remained intact.

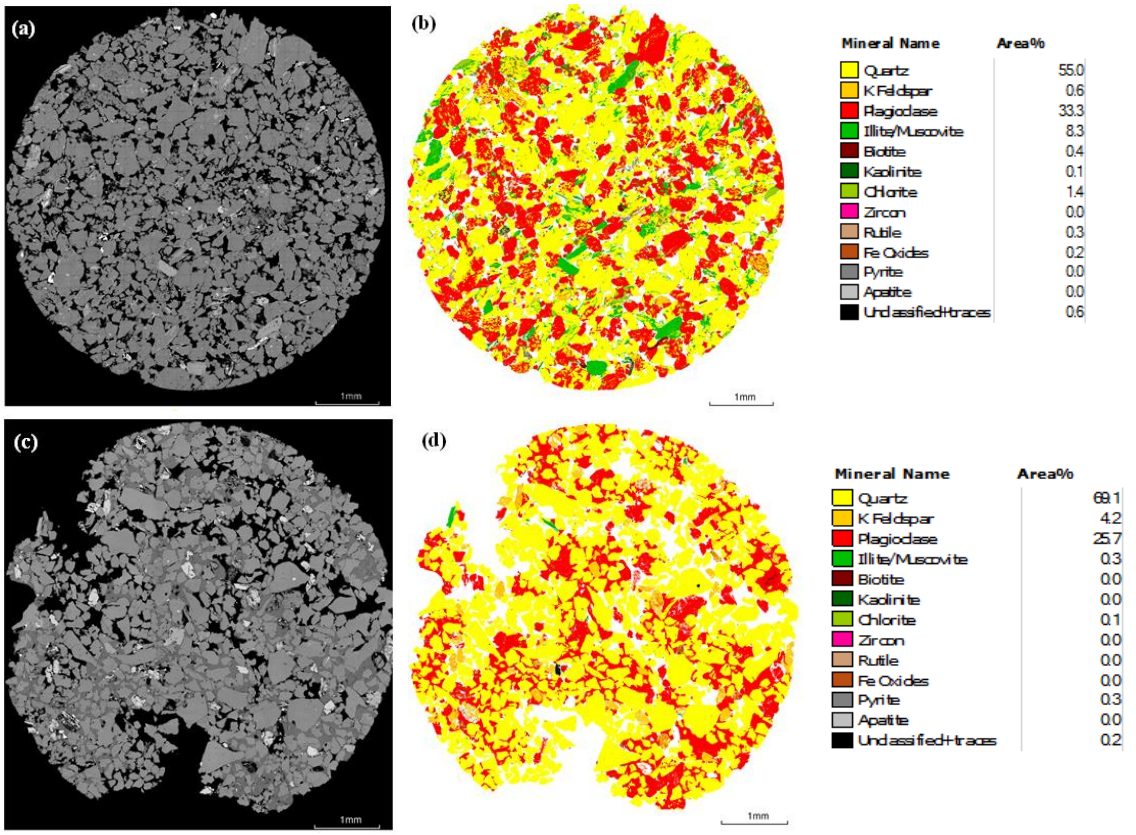

Figure 3. Registered maps of a polished cross-section of the 6 mm miniplugs of (a-b) Sample 1 and (c-d) Sample 2, by (a, c) backscattered electron SEM mapping and (b, d) QEMSCAN mineral mapping.

FESEM Imaging

The FESEM map of a rectangular subarea of the raw cut face of the cleaned, dry miniplug of Samples 1 and 2 is shown in Figures 4a and 4c, respectively. This 2D map was registered into the 3D tomogram series via the intermediate step of registering the tomogram of the cut (half-) miniplug to its uncut counterpart [12]. The uppermost voxel at each position on the cut face was identified by segmentation to yield its height map. The FESEM map was then 2D-2D registered to the vertical projection of these uppermost voxels onto a flat plane. The voxels corresponding to this same height map in the original miniplug tomogram, and all others in the series, were then similarly projected. Smoothing of the grain-hugging height map was also performed so that it spans the pore bodies. Figures 4b and 4d show the resulting registered projection of the tomograms after spontaneous and forced imbibition of Samples 1 and 2, respectively. This procedure served to identify subregions in the FESEM map which were free from debris and

plucking damage and where the oil's pore occupancy and grain contact displayed interesting imbibition history, for inspection by higher-resolution FESEM imaging.

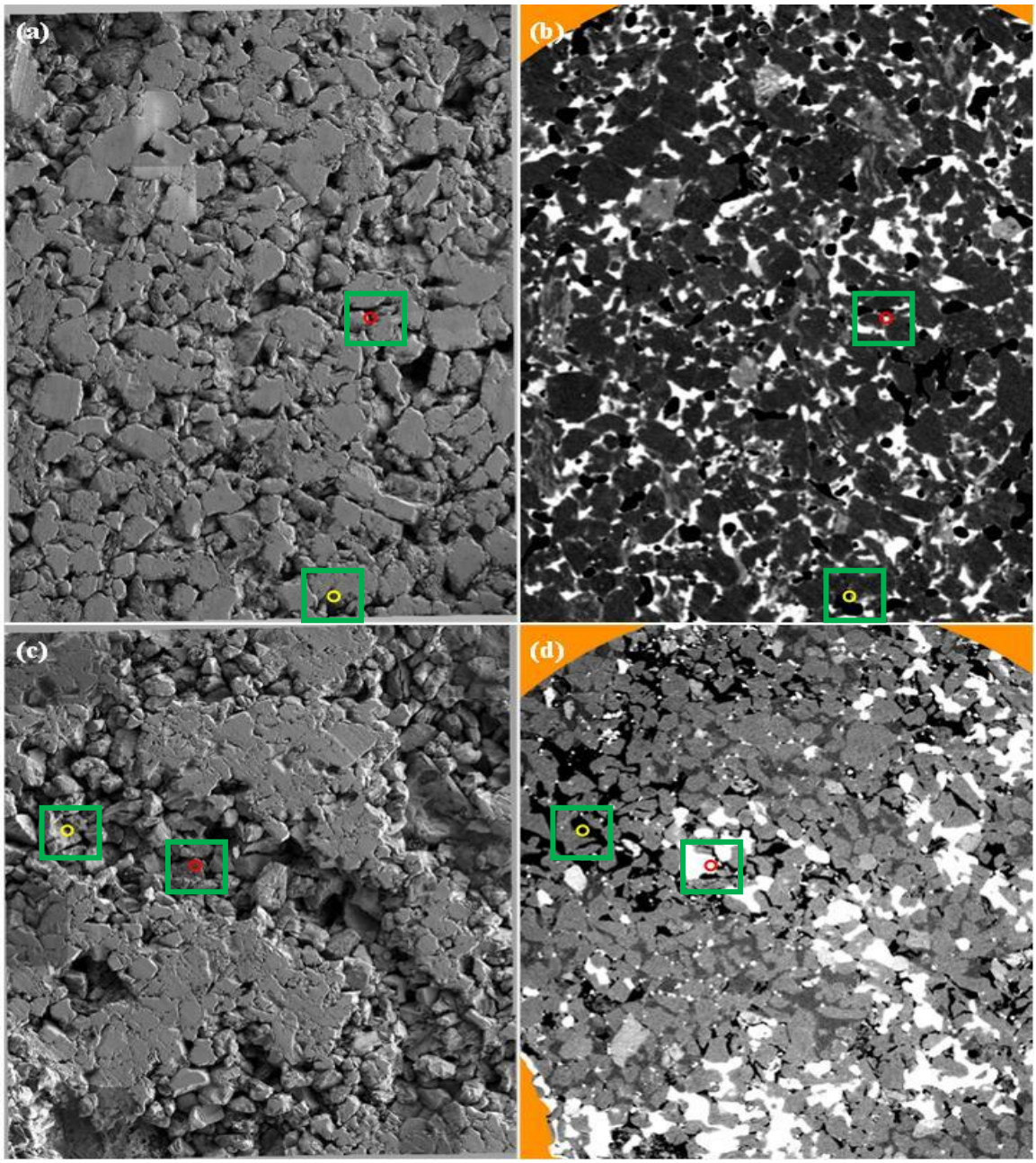

Figure 4. Low resolution FESEM mosaic of cut face of (a) Sample 1 (3.3 mm x 4.5 mm) and (c) Sample 2 (3.8 mm x 4.5 mm), and registered smoothed tomogram projection of (b) Sample 1 after spontaneous imbibition and (d) Sample 2 after forced imbibition, with brine in white and oil in black.

The micrographs in Figure 5 are from the center of the circles marked in Figure 4, all of which were oil-filled after primary drainage. Within the yellow circle in Figure 4b of

Sample 1, the oil blob trapped in this pore body after spontaneous imbibition is locally anchored to a grain. The corresponding close-up of a quartz overgrowth of this grain in Figure 5a shows a light scattering of asphaltene nanoparticles, suggestive of a weakly water-wet surface and possibly accounting for the blob attachment there. Moreover, none of the multitude of high resolution FESEM images acquired of Sample 1 showed substantially greater asphaltene coverage than this, implying that the majority of its surfaces are weakly to strongly water-wet. Figure 5a also exhibits another common feature of Sample 1, namely debris in the form of very fine clay platelets on oil-exposed regions. Within the red circle in Figure 4b, spontaneous imbibition detached the oil from an illite-coated grain. The corresponding close-up in Figure 5b, and others in this neighborhood, displays no asphaltene deposit, in line with the expectation that grain-lining clays aid retention of water and water-wetness to cause oil snap-off.

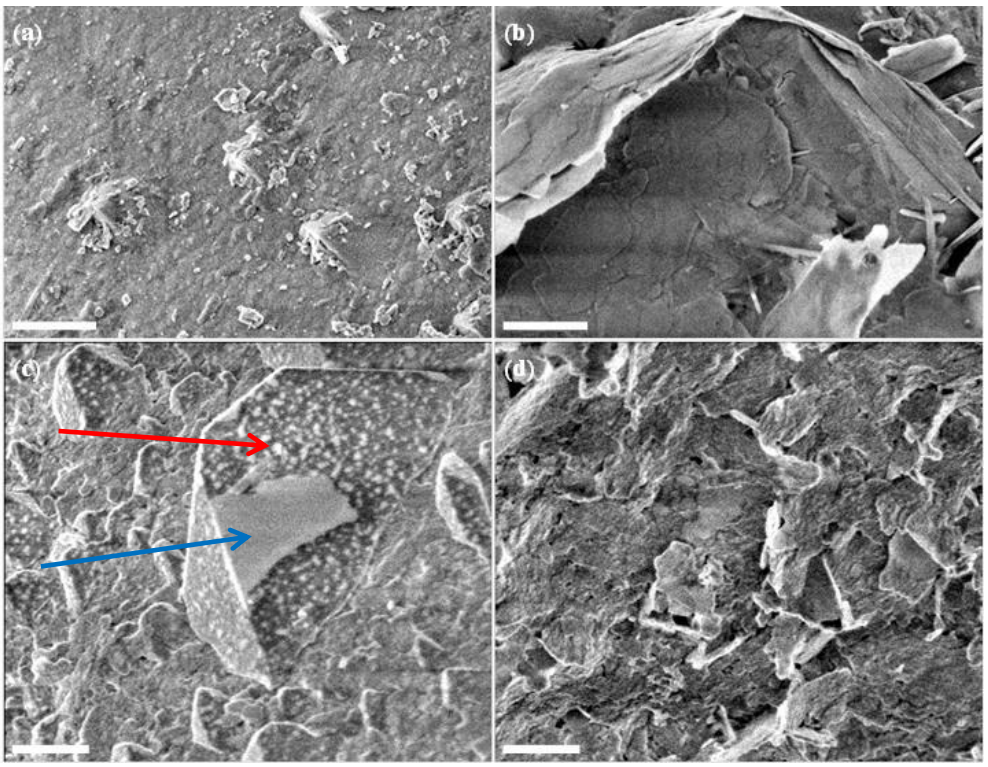

Figure 5. High resolution FESEM images, all with 0.5 µm scale bars, of raw cut face of Sample 1 at the location of the (a) yellow and (b) red circle in Figure 4a-b, or of Sample 2 at the location of the (c) yellow and (d) red circle in Figure 4c-d.

Within the yellow circle in Figure 4d of Sample 2, the pore remains oil-filled after forced imbibition. The close-up in Figure 5c of a grain with quartz overgrowths bounding this pore is representative of the much heavier deposits of asphaltene than on Sample 1. Film coverage is almost complete, aside from the so-called dalmation pattern of bright perforations from brine nano-droplets trapped under the film during primary drainage and aging (arrowed). Other occasional bare patches (also arrowed) may be caused by fines detachment by moving contact lines during cleaning.

Within the red circle in Figure 4d, forced imbibition removes oil from a grain that is partly smooth and partly lined by clay, a close-up from the latter of which is given in Figure 5d. In contrast to Sample 1, the clay linings of Sample 2, in this and all other inspected regions, appear completely covered by asphaltene. This is again consistent with the oil-wetness inferred from MCT, and suggests that local retention of oil, such as in the vicinity of Figure 5c, is due to reasons other than mineralogy. QEMSCAN in Figures 3b and 3d showed that Samples 1 and 2 are both dominated by quartz and plagioclase, lined by illite to varying extents. Further, the same brines were used for both samples and were drained to similar Swi values. Thus the strong wettability differences observed in MCT and FESEM are most likely due to the different crude oils, with density of 835 and 900 kg/m^3, used for Samples 1 and 2, respectively.

COMPARISON OF SIMULATED RESULTS WITH EXPERIMENTAL DATA FOR SAMPLE 2

Topologically equivalent pore networks [15] were extracted from the segmented pore space of the miniplug dry tomogram. To establish whether or not the pore networks are representative, oil/water primary drainage displacement was simulated using a quasi-static pore network model [16]. The resulting oil/water $P_c - S_w$ curves were scaled into mercury/air $P_c - S_w$ curves using interfacial tensions and contact angles [17]. Figure 6a compares the measured MICP data on the 9 mm diameter miniplug with the simulated data on the 6 mm miniplug, and Figure 6b shows the oil/water primary drainage relative permeability curves. The measured and simulated MICP are in good agreement within the limits of image resolution, suggesting that the pore networks are representative.

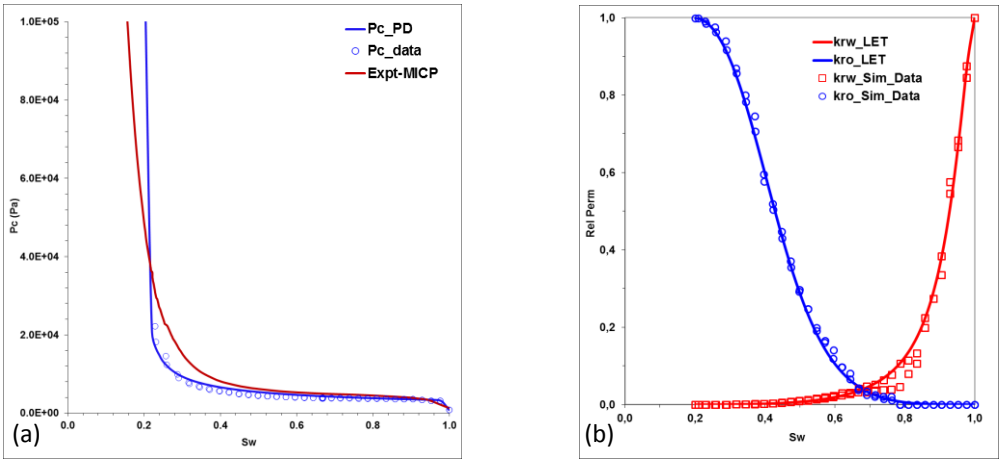

Figure 6. (a) Comparisons of simulated (Sim) and experimental (Expt) MICP data, and (b) primary drainage oil/water relative permeability curves for Sample 2. The blue circles and red squares are the simulated data points fitted to the corresponding lines.

Based on the wettability results presented above, we then assigned plausible wettability input parameters to pore network elements of Sample 2 for simulation of imbibition processes. In particular, the fraction of pores contacted by oil that changed wettability

from water- to oil-wet was 1.0, and the minimum and maximum advancing contact angle for oil-wet pores was 100° and 150°, respectively. Simulations of oil/water displacements were then performed for comparison with available data from special core analysis.

The experiments used a composite core of four plugs, from the same formation as Sample 2, with a porosity of 24% and effective oil permeability of 854 mD at S_{wi} of 0.251. The simulation was on pore networks extracted from the Sample 2 miniplug with a porosity of 17.4%, computed grid permeability of 699 mD and simulated S_{wi} of 0.20. Figure 7a compares the porous plate primary drainage (PD) and spontaneous imbibition (SI) capillary pressure data, using dead crude oil on the four plugs, with simulated data. Forced imbibition (FI) measurement carried out on one of the four plugs gave one additional data point at -60 kPa as shown in Figure 7b. The volume of water spontaneously imbibed and the calculated I_w from the porous plate experiments, MCT imaging and simulations are summarized in Table 3, with good quantitative agreement between the data.

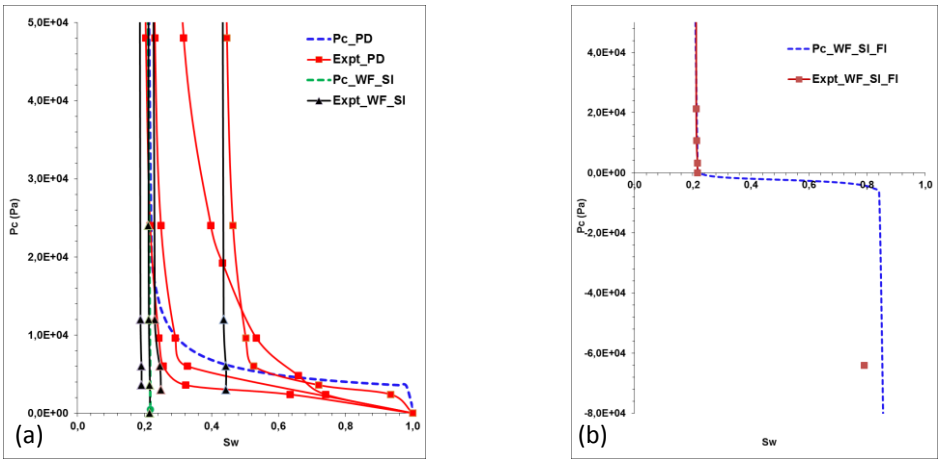

Figure 7. Comparisons of simulated (dashed line) with porous plate experimental capillary pressure data (solid line) for Sample 2. (a) Primary drainage (PD) and spontaneous imbibition (SI), and (b) SI and forced imbibition (FI).

Table 3. Volume of brine spontaneously imbibed and calculated Amott water indices.

	Volume of brine spontaneously imbibed (% PV)	**Calculated I_w**
Porous plate experiment	1.0-5.0	0.014
MCT imaging	1.3	0.010-0.040
Simulation	1.2	0.018

To eliminate the influence of the different S_{wi} values, the imbibition relative permeability data were normalized. The composite core measured data were history-matched with a Sendra core flooding simulator to produce the experimental LET [18] curve fit. Figure 8 compares the normalized simulated relative permeability results to those from experiment. Considering the heterogeneity of Sample 2 and the difference in scale

between the core experiment and the miniplug simulation, the measured relative permeability compares qualitatively well with the simulation.

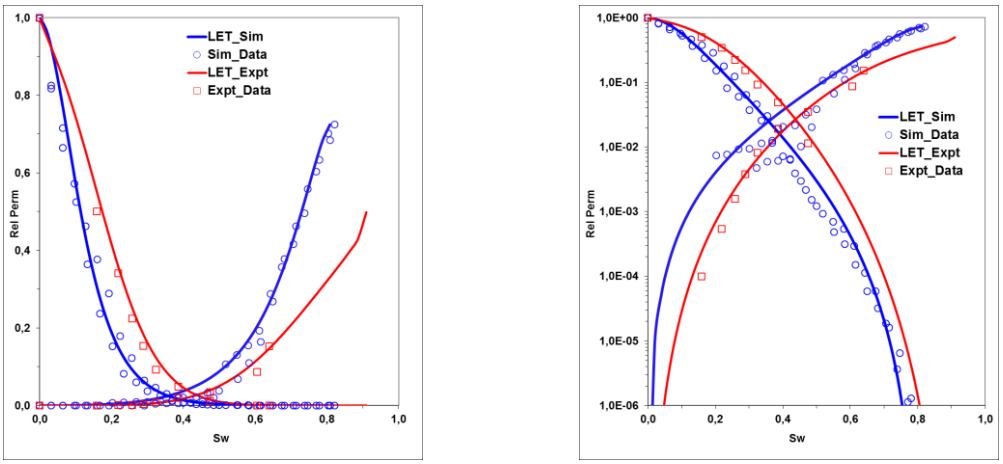

Figure 8. Comparisons of simulated (Sim) and experimental (Expt) oil/water relative permeability curves for Sample 2. The blue circles and the red squares are the simulated data points fitted to the corresponding lines.

CONCLUSIONS

The pore-scale distribution of water in the initial state, and spontaneously and forcibly imbibed, from MCT imaging and registration can provide useful information on the pore-scale distribution of wettability. Integration of FESEM images at raw surfaces provides complementary insight at higher resolution, and combination with QEMSCAN of embedded sections can shed light on mineral-specific wettability. Although the two samples studied proved to be fairly uniformly water-wet and oil-wet, this imaging framework can greatly benefit the interpretation of more complex mixed-wet samples. Network modelling of multiphase transport properties incorporating this wettability identification showed good quantitative/qualitative agreement with experimental data, despite the difference in scale.

ACKNOWLEDGMENTS

The authors acknowledge FEI Trondheim AS for granting permission to publish this paper, which is partly funded by DEA Norge AS and Norwegian Research Council through PETROMAKS Project Number: 208772/E30, titled: “Physically based three-phase relative permeability relations”. We also thank STATOIL, TOTAL and DEA for sharing their samples and data with us. Jill Middleton (ANU) is thanked for assistance with FESEM-MCT registration.

REFERENCES

1. Anderson, W.G., “Wettability Literature Survey – Part 1: Rock/Oil/Brine Interactions and the Effects of Core Handling on Wettability”, *J. Pet. Tech.* (1986), **38**: 1125-1144.

2. Morrow, N.R., "Wettability and its Effects on Oil Recovery", *J. Pet. Tech.* (1990), **42**: 1476-1484.
3. Abdallah, W., Buckley, J.S., Carnegie, A., *et al*., "Fundamentals of Wettability", *Oilfield Review*. Summer 2007: 44-61.
4. Anderson, W.G., "Wettability Literature Survey – Part 2: Wettability Measurement", *J. Pet. Tech.* (1986), **38**: 1246-1262.
5. Amott, E., "Observations Relating to the Wettability of Porous Rock", *Trans. AIME*, (1959), **216**: 156-162.
6. Donaldson, E.C., Thomas, R.D. and Lorenz, P.B., "Wettability Determination and its Effect on Recovery Efficiency", *SPE Journal*, (1969) **9**: 13-20.
7. Freedman, R., Heaton, N., Flaum, M., *et al*., "Wettability, Saturation, and Viscosity From NMR Measurements" *SPE Journal*, (2003) **8**: 317-327.
8. Looyestijn, W. J., and Hofman, J., "Wettability Index Determination from NMR Logs", SPE-93624-MS (2005). doi:10.2118/93624-MS.
9. Kumar, M., Fogden, A. and Senden, T., "Investigation of Pore-Scale Mixed Wettability", *SPE Journal*, (2012) **17**: 20-30.
10. Fogden, A., Kumar, M., Morrow, N.R., *et al*., "Mobilization of fine particles during flooding of sandstones and possible relations to enhanced oil recovery", *Energy Fuels*, (2011) **25**: 1605-1616.
11. Marathe, R., Turner, M.L., and Fogden, A., "Pore scale distribution of crude oil wettability in carbonate rocks", *Energy Fuels* (2012), **26**: 6268-6281.
12. Dodd, N., Marathe, R., Middleton, J., *et al*., "Pore-Scale Imaging of Oil and Wettability in Native-State, Mixed-Wet Reservoir Carbonates", Paper IPTC 17696, (2014).
13. Lebedeva, E.V. and Fogden, A., "Micro-CT and wettability analysis of oil recovery from sandpacks and the effect of waterflood salinity and kaolinite", *Energy Fuels*, (2011), **25**: 5683-5694.
14. Andrew, M., Bijeljic, B., and Blunt, M.J., "Pore-scale Contact Angle Measurements at Reservoir Conditions Using X-ray Microtomography", *Advances in Water Resources*. (2014), **68**: 24-31.
15. Bakke, S., and P.E. Øren, "3-D pore-scale modelling of sandstones and flow simulations in the pore networks," *SPE Journal*, (1997), **2**, 136-149.
16. Øren, P.E., S. Bakke, and O.J. Arntzen, "Extending Predictive Capabilities to Network Models", SPE Journal, (1998), **3**, 324-336.
17. Idowu, N., Nardi, C., Long, H., *et al*., "Improving Digital Rock Physics Predictive Potential for Relative Permeabilities From Equivalent Pore Networks", Paper SCA2013-17, Proceedings of the 2013 SCA Symposium, Napa Valley, California, USA, 16 -19 September , 2013.
18. Lomeland, F., Ebeltoft, E., and Thomas, W. H., "A new versatile relative permeability correlation", Paper SCA2005-32. Proceedings of the 2005 SCA Symposium, Toronto, Canada, 21-25 August, 2005.

IMPACT OF DISPLACEMENT RATE ON WATERFLOOD OIL RECOVERY UNDER MIXED-WET CONDITIONS

Yukie Tanino[1], Blessing Akamairo[2], Magali Christensen[1], Stephen A. Bowden[2]
[1]School of Engineering, University of Aberdeen, UK, [2]School of Geosciences, University of Aberdeen, UK

This paper was prepared for presentation at the International Symposium of the Society of Core Analysts held in St. John's Newfoundland and Labrador, Canada, 16-21 August, 2015

ABSTRACT

Under uniformly water-wetting conditions, it is well established that waterflood oil recovery remains independent of flood rate while the flow is capillary-dominated and, furthermore, that the rate dependence emerges when the microscopic capillary number exceeds $O(10^{-5})$. In contrast, there is no equivalent framework for interpreting the flood rate-dependence of oil recovery under mixed-wet conditions representative of oil reservoirs. Indeed, not even the appropriate definition of capillary number under mixed-wet conditions is established. In this paper, we focus specifically on oil recovery from mixed-wet porous media at high initial oil saturation and its dependence on water injection rate. We present laboratory measurements of oil distribution and its evolution during secondary waterflood at 2.5, 5.0, and 500 ft day^{-1}. Oil distribution was directly imaged at the pore scale using a high-speed camera coupled to an optical microscope in a bed of calcite grains packed into a microfluidic chip. These measurements are benchmarked against bulk measurements of remaining oil saturation in limestone cores.

Data to date suggest that remaining oil saturation, S_o, after the same volume of water injection, displays a dependence on injection rate qualitatively similar to the classic capillary desaturation curve for uniformly water-wet media, with the rate dependence emerging at a higher injection rate under mixed-wet conditions than under water-wet conditions. However, unlike in uniformly water-wet media, the long-time (residual) S_o does not display a dependence on the rate. These findings may have important implications not only for oil recovery, but for a wide range of engineering applications involving mixed-wet porous media, e.g., geological CO_2 storage, remediation of non-aqueous phase liquid (NAPL)-contaminated soils and aquifers, and irrigation.

INTRODUCTION

Even in the absence of heterogeneities that may give rise to poor sweep, only 40 to 70% of oil can be recovered by waterflooding. This incomplete recovery is attributed to capillary trapping, the naturally-occurring phenomenon whereby the non-wetting phase in the larger pores of a porous medium is immobilized against advection in the form of pore-scale ganglia by capillary forces.

Capillary trapping is controlled by the pore structure, wettability, properties of the fluids, the initial oil saturation S_{oi}, and the flow rate. This paper focuses on the impact of flow rate on capillary trapping during secondary waterflood of rock with high S_{oi}. The dependence of oil recovery on flow rate is traditionally characterized by the capillary number, most commonly defined as

$$\mathrm{Ca} = \frac{\mu_w U_w}{\sigma}, \quad (1)$$

where μ_w is the dynamic viscosity of the flood water, U_w is its Darcy velocity, and σ is its interfacial tension with the oil phase. While more relevant definitions of capillary number have been derived (see Ref. [1] for a detailed discussion), Eq. (1) has the advantage of being a function only of fluid properties. For convenience, the microscopic capillary number as defined in Eq. (1) will be used in the present paper.

While many studies report measurements of remaining oil saturation at different Ca, literature that focus on the Ca dependence controlled by variations in flow rate are limited (e.g., Ref. [2] and references therein). If we further restrict our consideration to laboratory experiments in which (a) the wetting state of the model reservoir is unambiguous, (b) S_{oi} at the onset of waterflood was established by displacement of the oil into a porous medium – the scenario relevant to oil recovery, geological carbon storage, and NAPL contamination of groundwater aquifers – and (c) σ is representative of field conditions, available data are limited (Table 1). This paper presents new laboratory measurements of oil recovery to complement the existing data set. We consider recovery from two limestones and a packed bed of calcite grains at injection rates corresponding to U_w = 0.0015 to 12 mm s^{-1}. In particular, we focus on mixed-wet conditions established by wettability-altering constituents in the oil phase. The results are compared to the behaviour of uniformly water-wet media.

METHODS

Two techniques were used to measure the remaining oil saturation, S_o, as a function of time during waterfloods: lab-on-a-chip methods and conventional corefloods. For both, each experiment comprised three stages: complete saturation of the porous medium with the model connate water, primary drainage, and secondary waterflood at constant injection rate. To remove ambiguity in the wettability of the system, a new porous medium was used in each experiment.

Fluids

The oil phase was a degassed sample of a stock oil held at University of Aberdeen in the lab-on-a-chip experiments and a 6.62 × 10^{-2} M solution of either cyclohexanepentanoic acid (Sigma-Aldrich, 98%) or cyclohexanepropionic acid (99%) in *n*-decane (≥ 99%) in the corefloods. The crude sample was topped (light components removed) prior to use by heating at 40ºC under a nitrogen stream to yield an oil with an API of 28º to 30º. The aqueous phase was seawater with a salinity equivalent of 34 ppt in the lab-on-a-chip experiments and an aqueous solution of 5wt.% NaCl and 1wt.% KCl in the corefloods.

The latter was further saturated with the rock to prevent dissolution of the core during the coreflood. Basic properties of the fluids are summarized in Table 2.

The interfacial tension of the two oil/water pairs considered in the corefloods are approximately the same at $\sigma \approx 30$ mN m^{-1} [7, 8]; the measurement of σ of the crude oil with the seawater is pending. The organic acids naturally found in the crude oil sample and added artificially to the synthetic oils have been shown to alter the wettability of carbonates (e.g., [9]). Preliminary measurements of contact angle on a calcite substrate using the sessile drop method confirm the wettability alteration capacity of the oil phases used presently, with the crude oil, 6.62×10^{-2} M cyclohexanepentanoic acid in *n*-decane, and 6.62×10^{-2} M cyclohexanepropionic acid in *n*-decane yielding a static contact angle of $\theta \approx 60°$, 140° and 110°, respectively.

Table 1 Studies that report oil recovery by waterflood at constant injection rate for multiple injection rates. Only experiments in which (a) the wetting state of the test samples are well defined, (b) initial oil saturations were larger than $S_{oi} > 0.6$ and (c) were established by displacement of oil into a water-saturated core, (d) remaining oil saturation at the limit of low Ca ($\leq 10^{-5}$) was measured, and (f) $\sigma > 30$ mN m^{-1} are listed.

reference	aqueous phase	non-aqueous phase	σ [mN m^{-1}]	porous media	ϕ	k [$\times 10^{-15}$ m^2]	marker in Fig. 5
Tanino & Blunt [3]	5wt.% NaCl, 1wt.% KCl	*n*-decane	52.3 ± 0.4 [7]	Ketton limestone	0.226	2880	blue ●
Tie & Morrow [4]	5% $CaCl_2$; seawater	Cottonwood crude	29.7	Whitestone limestone	0.26	7.4; 13.5	red □
				Edwards limestone	0.21	11.3; 13.5	red ○
Abrams [5]	various synthetic	various synthetic	32.8; 50.0	Berea sandstone	0.209	306	blue +
			50.0	Bandera sandstone	0.226	31.6	blue -
			50.0; 33.7; 35.5	Paluxy sandstone	0.268	1840	blue dot
			32.8; 50.0	Dalton sandstone	0.276	484	blue ×
			50.0; 33.7; 32.0; 36.3	Gallup sandstone	0.267	1130	blue *
Chatzis & Morrow [6] Fig. 6	2% $CaCl_2$	Soltrol 130 or 170 oil	34.8	Berea sandstone	0.214	501	blue ▲
			35.9		0.204	419	blue Δ
			35.9		0.211	479	blue ◊
			34.8		0.187	115	blue ■
			34.8		0.177	75.0	blue ○

Table 2 Properties of the fluids used in the waterfloods. All values were measured at ambient temperature (22°C).

fluid	density [kg m^{-3}]	viscosity [mPa s]
topped crude oil	874.3	80
6.62×10^{-2} M cyclohexanepentanoic acid in *n*-decane	731.6	0.950
6.62×10^{-2} M cyclohexanepropionic acid in *n*-decane	731.3	0.910
seawater	1023.4	0.950
synthetic brine used in the corefloods	1041.5	1.0315

Lab-on-a-chip Experiments

The porous medium was a quasi-two-dimensional bed of granulated calcite, with an average diameter of 35 ± 3 μm, packed in a 1200 μm-wide and 50 μm-deep channel etched in soda lime. The fabrication of the microfluidic chip (Dolomite Centre Ltd.) is described by Bowden et al. [10]. The porosity of the packed bed was ϕ = 0.45 and the pore volume was 0.05 μL in all experiments.

Waterflood procedure

The packed bed was first saturated with the seawater to establish connate water saturation (Fig. 1a). Next, oil was injected (Fig. 1b) until a uniform oil saturation of $S_{oi} \approx 1$ was established (Fig. 1c). To establish mixed wettability, the packed bed was aged at elevated temperature for 30 minutes. Once the system cooled to ambient temperature, seawater was injected at constant flow rate using a high precision syringe pump (Fig. 1d). At the end of a waterflood, the bead pack was dissolved with 10% hydrochloric acid (Fig. 1e). The channel was further cleaned by flushing dichloromethane and methanol through it before a new bed was packed with fresh calcite grains.

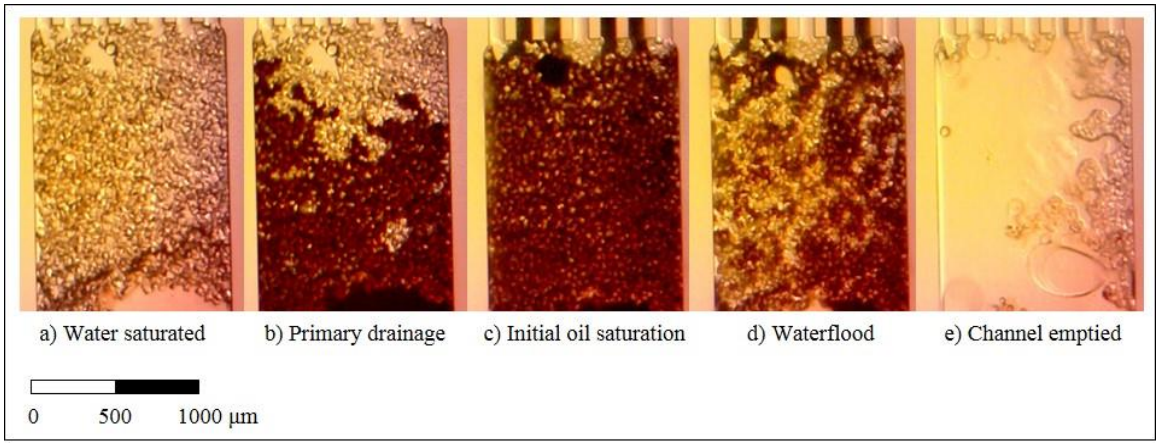

Figure 1 The packed bed at different stages of a lab-on-a-chip experiment: connate water injection (a); oil injection (b) to establish initial oil saturation (c); waterflood (d), and acid injection in preparation for the next experiment (e). Flow direction is bottom to top.

The evolution of the depth-integrated oil distribution inside the packed bed during the waterflood stage was captured using a high-speed camera coupled to a microscope at a resolution of 3.3 to 3.4 μm pix^{-1} (Fig. 2); the chip was lit from below. The acquired still images were first converted to grey scale. Next, the still image corresponding to the instance immediately prior to the onset of waterflood was subtracted from all subsequent images. The remaining oil saturation at a given instance is then given by $S_o(t) = 1 - n_w / (N \phi)$, where N is the total number of pixels in the region of interest (the packed bed) and n_w is the number of pixels in the same region with a greyscale level larger than a threshold value.

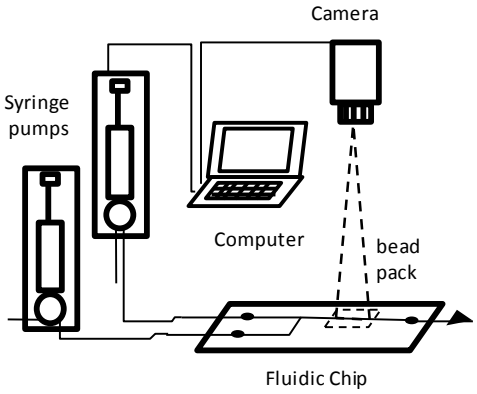

Figure 2 Setup for the lab-on-a-chip experiments.

The primary source of error in the lab-on-a-chip experiments is the non-uniform propagation of the flood water in the microfluidic channel as it approaches the packed bed. Specifically, the flood water tends to enter the packed bed from one part of its cross-section at early times in the waterflood. The errors arising from this deviation were quantified by evaluating $S_o(n)$ for the left and the right half of the packed bed separately for each waterflood.

Corefloods

Experiments were performed on cores from two naturally water-wet rocks: Ketton limestone (ϕ = 0.23; permeability to brine $k = 3 \times 10^{-12}$ m^2) and Indiana limestone [ϕ = 0.15; k = (1.9 to 14) $\times 10^{-15}$ m^2]. The pore structure of the two rocks differ considerably: Ketton limestone has a distinct bimodal pore (entry) size distribution as measured by mercury injection porosimetry, while Indiana limestone displays a more complex structure (Fig. 3). All cores were 37.6 – 37.7 mm in diameter and L = 76 mm (Ketton) or L = 89 mm (Indiana) in length.

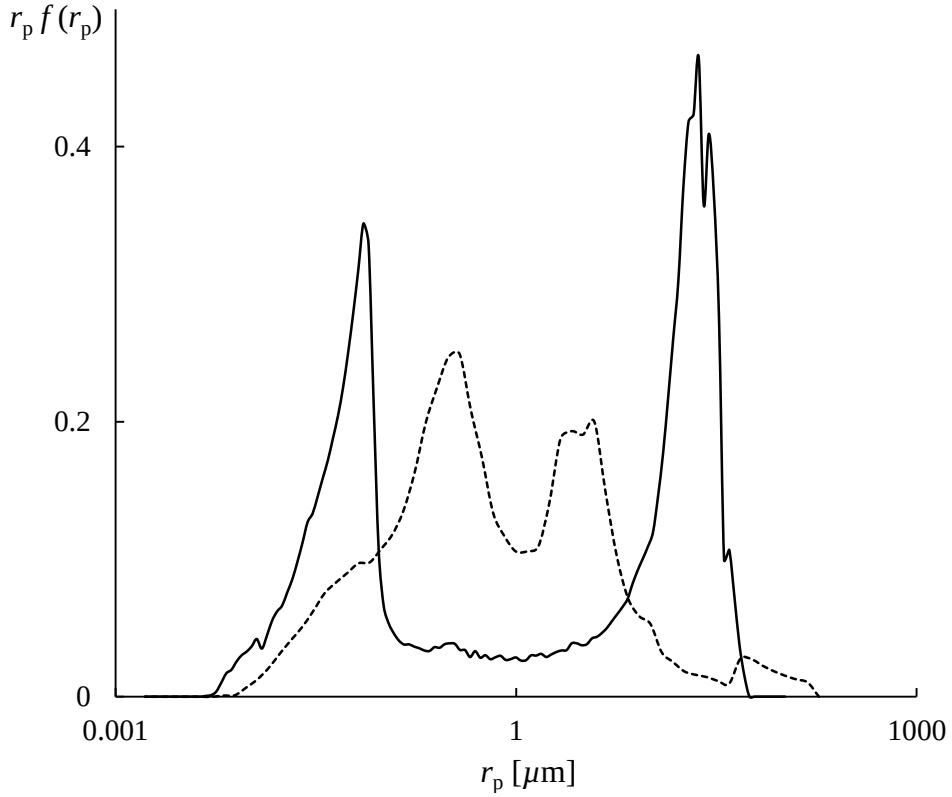

Figure 3 Pore entry size distribution for Ketton limestone (solid line) and Indiana limestone (dashed) as determined from mercury injection capillary pressure measurements. r_p is the equivalent pore throat radii to the applied capillary pressure, $P_{c,\,Hg}$, and is given by $r_p = 2\,\sigma_{Hg}\,|\cos\,\theta_{Hg}\,| / P_{c,Hg}$, where the interfacial tension and contact angle of mercury with its vapour are taken to be σ_{Hg} = 485 mN m^{-1} and θ_{Hg} = 135°, respectively [11]; f (= dS_w /dr_p) is the probability distribution function for pores with a capillary entry pressure corresponding to r_p.

Waterflood procedure

Corefloods were performed under radial confining pressure in custom-made horizontal Hassler-type cells. Initial oil saturations of S_{oi} = 0.83 to 0.93 were established using the porous plate method, whereby oil is injected into a brine-saturated core at constant pressure against a hydrophilic permeable disk that retains the oil in the core while allowing the brine through. This technique ensures that a uniform oil saturation is established across the core. Subsequently, brine was injected into the core at a constant volumetric flow rate of Q_w = 0.750, 100, and 800 ml min.$^{-1}$ for Ketton limestone and Q_w = 0.100, 0.200, and 2.000 ml min^{-1} for Indiana limestone. These flow rates correspond to Ca ranging from Ca = 6×10^{-8} to 8×10^{-4}. After a selected volume of water, n [pv], was injected the core was removed from the cell and weighed to determine $S_o(n)$. The relative permeability of a core to the flood water during waterflood was estimated as

$$k_{rw}(n) = \frac{\mu_w}{k}\frac{U_w L}{\overline{\Delta p(n)}}, \qquad (2)$$

where $\overline{\Delta p(n)}$ is the pressure drop across the length of the core temporally averaged over a window of 1 pv. Additional details of the coreflood procedure are provided in Ref. [3].

RESULTS

Remaining oil saturations normalized by their initial saturation are presented in Figs. 4 and 5 for the unconsolidated bed of calcite chips and the two limestones, respectively. Note that, in Fig. 5, the ordinate has been further normalized by S_o / S_{oi} at the lowest Ca considered for that rock to facilitate comparison between rocks of different pore size distributions.

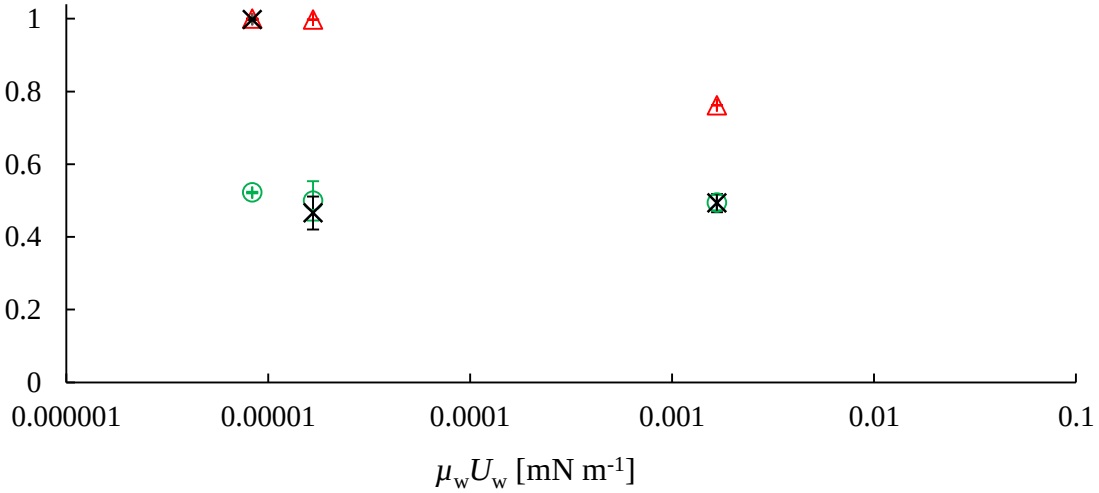

Figure 4 Normalized remaining oil saturation, S_o / S_{oi}, at different $\mu_w U_w$ [mN m^{-1}] in a mixed-wet bed of calcite chips after n = 1 (triangle), 5 (×), and 10 (circle) of water injection. $S_{oi} \approx 1$.

During any waterflood, S_o decreases with time until it asymptotes to its residual state. After n = 1 pv of water injection, S_o in the packed bed was constant at $S_o/S_{oi} \approx 1$ between $\mu_w U_w = 8\times10^{-6}$ to 2×10^{-5} mN m^{-1}, then decreased to $S_o/S_{oi} = 0.76$ at $\mu_w U_w = 2\times10^{-3}$ mN m^{-1} (Fig. 4, triangle). This dependence is qualitatively similar to the capillary desaturation curve for uniformly water-wet media. However, unlike in water-wet media, S_o/S_{oi} approached the same value ($S_o/S_{oi} \approx 0.5$) at all U_w, with this limit being achieved earlier (i.e., at lower n) at higher U_w, such that the dependence on U_w can no longer be discerned after n = 10 pv (circle).

We now consider recovery from consolidated rock. In the two limestones considered presently S_o/S_{oi} remained constant within experimental uncertainty from Ca = 6×10^{-8} to Ca = 10^{-4}, then decreased between Ca = 10^{-4} and 8×10^{-4} (Fig. 5). Thus the transition to Ca dependence occurs at a Ca two orders of magnitude larger than in uniformly water-wet rock (Fig. 5, blue markers), for which the threshold generally falls between Ca = 10^{-6} and 10^{-5}.

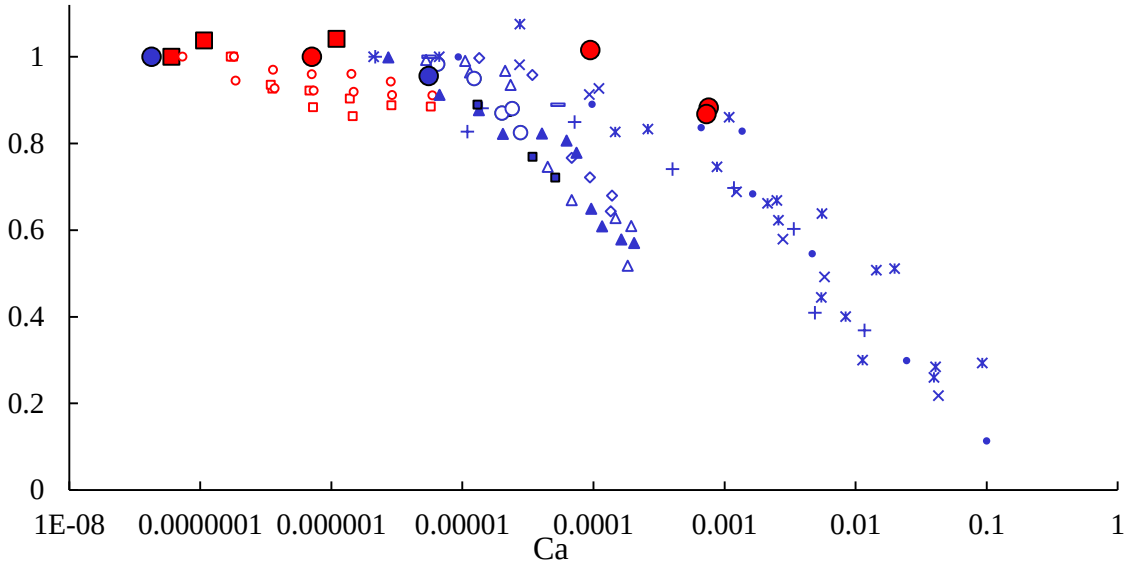

Figure 5 Normalized remaining oil saturation, S_o/S_{oi}, at different Ca under mixed-wet conditions (red) and uniformly water-wet conditions (blue) measured in Ketton (solid circle, n = 105 - 122) and Indiana (solid square, n = 17 - 19) limestones from the present study, in Whitestone and Edwards limestones by Tie and Morrow [4], in Berea sandstone by Chatzis & Morrow [6], and in five sandstones by Abrams [5]. The ordinate is normalized by S_o/S_{oi} at the lowest Ca considered for that rock in a particular study. For marker definition of data from literature, see Table 1.

Interestingly, the two mixed-wet limestones considered by Tie & Morrow [4] do not display a Ca-independent regime even at Ca as low as Ca = 10^{-7} (red open circle, open square). The discrepancy with the present experiments may be attributed to the degree of wettability alteration by the constituents in the oil phase: oil-contacted grain surfaces are rendered oil-wet (i.e., $\theta > 90°$) in the present corefloods, while wettability alteration is inferred to have been relatively minor ($\theta < 90°$) in Tie & Morrow [4]'s corefloods.

Table 3 Summary of experimental conditions for the corefloods and the measured remaining oil saturation (S_o) and k_{rw}.

rock	ϕ	**oil (concentration of acid in *n*-decane)**	**Ca**	$S_o(n)$	$k_{rw}(n)$	**marker in Fig. 5**
Ketton limestone	0.233	6.62×10^{-2} M cyclohexane-pentanoic acid	7.1×10^{-7}	0.38 (106)		red ●
	0.230		9.4×10^{-5}	0.39 (114)	0.55 (77-107)	
	0.235		7.6×10^{-4}	0.31 (105)		
	0.218		7.3×10^{-4}	0.35 (122)		
Indiana limestone	0.143	6.62×10^{-2} M cyclohexane-propionic acid	6.0×10^{-8}	0.28 (18)	0.56 (17)	red ■
	0.154		1.1×10^{-7}	0.28 (19)	0.61 (18)	
	0.153		1.1×10^{-6}	0.29 (17)		

The relative permeability to the flood water, at n corresponding to the S_o measurements, was approximately $k_{rw} \approx 0.6$ in all three corefloods for which it could be measured (Table 3). This value corresponds to saturation-normalized relative permeabilities of $k_{rw}/(1-S_o) \approx 0.8$ (Indiana limestone) and 0.9 (Ketton), which are significantly larger than $k_{rw}/(1-S_o) \approx 0.2$ measured previously in the same rocks under uniformly water-wet conditions [3, 7]. The elevated k_{rw} indicate that the flood water was not restricted to the smallest pores, presumably because a significant fraction of the surface of the grains that constitute the cores has been rendered oil wet [7].

CONCLUSIONS

Laboratory measurements of remaining oil saturation established under mixed-wet conditions in two limestones and in a bed of unconsolidated calcite chips were presented. As Ca increased from Ca $\approx 10^{-8}$ to 10^{-3}, remaining oil saturation in the limestones remained constant up to Ca = 10^{-4}, and then decreased from Ca = 10^{-4} to 10^{-3}. Analogous measurements in packed beds suggest that – in contrast to uniformly water-wet conditions – this Ca dependence is a transient phenomenon, and that the residual (long-time) saturation depends only weakly on Ca. Future laboratory work will focus on larger Ca (> 10^{-3}) and a wider range of θ.

ACKNOWLEDGEMENTS

This material is based on work supported by the University of Aberdeen Chevron Fund, a Society of Petrophysics and Well Log Analysts grant, and an Aberdeen Formation Evaluation Society scholarship. M.C. was supported by the University of Aberdeen College of Physical Sciences scholarship. The authors thank undergraduate student Matthew P. Wilkie for the measurements of density and viscosity of the synthetic brine and Colin Taylor for the mercury injection porosimetry measurements on Indiana limestone.

REFERENCES

1. Hilfer, R. & Oren, P.-E. (1996) Dimensional analysis of pore scale and field scale immiscible displacement. *Transp. Porous Media* 22(1), 53–72.
2. Lake, L.W. (1989) *Enhanced Oil Recovery*. Old Tappan, NJ: Prentice Hall.
3. Tanino, Y. & Blunt, M.J. (2012) Capillary trapping in sandstones and carbonates: Dependence on pore structure. *Water Resour. Res*. 48(8), W08525. doi: 10.1029/2011WR011712.
4. Tie, H. & Morrow, N.R. (2005) Low-flood-rate residual saturations in carbonate rocks. *Proc*., International Petroleum Technology Conference, 21-23 Nov., Doha, Qatar.
5. Abrams, A. (1975) The influence of fluid viscosity, interfacial tension, and flow velocity on residual oil saturation left by waterflood. *SPE J*. 15(5), 437-447. doi:10.2118/5050-PA.
6. Chatzis, I. & Morrow, N.R. (1984) Correlation of capillary number relationships for sandstone. *SPE J*. 24(5), 555-562. doi:10.2118/10114-PA.

7. Tanino, Y. & Blunt, M.J. (2013) Laboratory investigation of capillary trapping under mixed-wet conditions. *Water Resour. Res.* 49(7), 4311-4319.
8. Christensen, M., Dufour, R. & Tanino, Y. Non-aqueous phase recovery from mixed-wet media: dependence on pore-scale wettability contrast. *Water Resour. Res.*, in prep.
9. Wu, Y., Shuler, P.J., Blanco, M., Tang, Y. & Goddard, W.A. (2008) An experimental study of wetting behavior and surfactant EOR in carbonates with model compounds. *SPE J.* 13(1), 26-34. doi:10.2118/99612-PA.
10. Bowden S.A., Cooper, J.M., Greub, F., Tambo, D. & Hurst, A. (2010) Benchmarking methods of enhanced heavy oil recovery using a microscaled bead-pack. *Lab Chip* 10(7), 819-823.
11. Good, R.J. & Mikhail, R.S. (1981) The contact angle in mercury intrusion porosimetry. *Powder Technol*. 29(1), 53 – 62. doi = 10.1016/0032-5910(81)85004-8.
12. Moore, T.F. & Slobod, R.L. (1955) Displacement of oil by water: effect of wettability, rate, and viscosity on recovery. *Proc*., Fall Meeting of the Petroleum Branch of AIME, 2 - 5 Oct., New Orleans, Louisiana.

COMBINED CT AND MAGNETIC SCANNING TECHNIQUES FOR MULTIMODAL IMAGING OF FLUID FLOW IN POROUS MEDIA: APPLICATION TO HEAVY OIL WATERFLOODING

Petar Petrov[1], David K. Potter[1], Shauna Cameron[2], Mike London[2],
James Donald[2] and *Wade Waterman[2]
[1]Department of Physics, University of Alberta, Edmonton, Alberta, Canada
[2]Alberta Innovates - Technology Futures, Edmonton, Alberta, Canada

This paper was prepared for presentation at the International Symposium of the Society of Core Analysts held in St. John's, Newfoundland and Labrador, Canada, 16-21 August, 2015

ABSTRACT

Waterflooding is one oil recovery process used in heavy oil reservoirs. However, little has been published in terms of imaging heavy oil waterfloods, mainly due to the similar densities of water and heavy oil, which makes it difficult to track the advancement of the water/heavy oil front. The present study used computer tomography (CT) and magnetic susceptibility techniques to attempt to quantitatively image waterflooding of a heavy oil saturated sandpack, and monitor the progress of the water/heavy oil front in real time. A low concentration of superparamagnetic nanoparticles (20 nm diameter maghemite) was added to water during the flooding. These particles act as dual response contrast agents, having an extremely high magnetic susceptibility that can be monitored magnetically via a surrounding sensor, and an increased X-ray attenuation over water alone for CT scanning. Jar tests were first undertaken to establish the optimum conditions for both CT and magnetic susceptibility scanning.

Waterflooding, with the dilute nanoparticle suspension, of a heavy oil saturated sandpack revealed the formation, growth and movement of a significant positive magnetic susceptibility peak. This formed at the injection end of the flow cell and migrated towards the production end as the waterflooding progressed. The peak was likely due to a higher concentration of nanoparticles collecting at the main water/heavy oil front. This appears to provide a means of quantitatively tracking the position of the front in real time. The increased accumulation of nanoparticles at the main front was further supported by material collected in the production jars. Whilst the CT attenuation profiles in part of the sandpack showed some correspondence with the magnetic results, the CT profiles did not show a recognizable front. This may be due to the low contrast between the water + nanoparticles and the heavy oil, to the presence of trapped gas, and to the shallow and diffuse nature of the front in a waterflood with heavy oil. Once the main water/heavy oil front had passed through the sandpack the magnetic profiles had a constant shape similar to the porosity profile (confirmed by the CT derived porosity variation). The magnetic technique has potential for monitoring larger scale commercial waterflooding operations.

INTRODUCTION

There is little in the literature regarding quantitatively imaging waterflooding of a heavy oil saturated sandpack (simulating one of the oil recovery processes employed in the oilsands of Northern Alberta and elsewhere), although there are related studies on viscous fingering [1] and using CT scanning of waterflooding in low permeability chalk [2]. The main aim of this project was to provide a means of quantitatively imaging the waterflooding of a heavy oil saturated sandpack, and tracking the water / heavy oil front in real time. Monitoring such waterflooding using CT scanning, without the addition of a contrast agent, is very difficult due to the similar densities of water (1.00 g/cc) and heavy oil (0.99 g/cc). Therefore it was proposed that the addition of superparamagnetic nanoparticles to the water (or brine) phase might improve the CT contrast between the water (or brine) phase and the heavy oil. Moreover, these nanoparticles would act as dual contrast agents, and their progress can be also be independently monitored by a magnetic susceptibility sensor [3]. The advantage of the nanoparticles is that they have an enormously higher magnetic susceptibility compared to the sandpack, the water or the heavy oil. The sandpack (quartz) and fluids are dominantly diamagnetic, which means they have very low negative values (quartz theoretically has a mass magnetic susceptibility of -0.62×10^{-8} m^3 kg^{-1} and the magnetic susceptibility of typical reservoir fluids is given in [4]). The superparamagnetic maghemite nanoparticles, on the other hand, have a value around $55{,}000 \times 10^{-8}$ m^3 kg^{-1} (which varies a bit depending upon how they are dispersed). A series of jar tests (without porous media) were initially conducted in order to identify the most appropriate nanoparticles for both CT and magnetic use, and to determine the optimum conditions for their dispersion and stability over prolonged time periods in water and various brines. A waterflooding experiment was then undertaken on a heavy oil saturated sandpack to evaluate the effectiveness of the nanoparticle injection for the CT and magnetic scanning techniques.

METHODS

Jar Tests Prior to Waterflood Experiment

A series of superparamagnetic nanoparticle dispersions (testing maghemite, magnetite and nickel ferrite nanoparticles) were first prepared for magnetic susceptibility scanning and CT scanning jar tests without porous media. We prepared brine samples where the nanoparticles were dispersed in sodium chloride or in sodium iodide. In each case a small amount of dispersant, sodium dodecylbenzeno sulfonate (DDBS), was added to each sample. This was followed by sonication for several minutes. Tests had shown that this anionic dispersant (rather than a cationic dispersant such as cetyltrimethyl ammonium bromide), followed by sonication, was the most effective way of dispersing the nanoparticles. The maghemite nanoparticles remained in suspension longer than the other types, and were thus chosen for the subsequent waterflood experiment. Nevertheless, these maghemite nanoparticles still tended to settle out in a timescale of around 1 hour. CT contrast tests indicated that there could potentially be enough X-ray contrast to observe a waterflood with any of the nanoparticles, but that the variability of measured values, combined with the expected porosity and saturation contrast, made such a

conclusion uncertain. Substituting iodine for chlorine in the brine enhanced the oil-brine contrast.

A second set of jar tests were carried out to determine the optimum conditions required for creating long term stable maghemite nanoparticle suspensions. The stability with time of different solution compositions (nanoparticle, DDBS dispersant, sodium iodide and sodium chloride concentrations), as well as different mixing processes (mechanical and sonication), was determined using a Bartington MS2C sensor. The jar tests revealed that the addition of sodium iodide or sodium chloride, either before or after the formation of the suspension, caused the nanoparticles to agglomerate and settle out relatively fast. The jar tests composed of only nanoparticles and DDBS dispersant mixed in deionised water displayed remarkable stability over long periods of time, consistent with our previous stability and flow experiments [3]. Therefore we decided to use deionised water rather than brine in the waterflood experiment, and the CT contrast would be provided by the nanoparticles themselves.

Experimental Set-up for Waterflood Experiment

A PEEK flow cell was assembled and leak tested in preparation for the waterflood experiment. We used a Hassler-type vessel with a confining pressure (radial) of 600 kPa during the waterflooding. A Viton sleeve was packed with around 78 g of sand and then inserted into the flow cell. The sandpack was 114.3 mm long and approximately 22.2 mm in diameter. The core material is water wet Ottawa sand, F110 from the U.S. Silica Company. F110 is a pure quartz sand (99.8% SiO_2) with minor amounts of Fe_2O_3, Al_2O_3 (<0.1% each), and other oxides. Grain diameter is 50–150 μm. Particles are subangular, and the size distribution is as follows: 8% 53–75 μm, 25% 75–106 μm, 44% 106–150 μm, 18% 150–212 μm, and 4% 150–212 μm, with <1% beyond the upper and lower limits. The median particle diameter is 85 μm, the median pore diameter 46 μm, and the median throat diameter 18 μm. The absolute permeability was estimated to be 5 Darcy. Dry CT scans were performed as a baseline measure at 135 kVp and 100 mA with an Aquilion One CT scanner. All CT scans for the remainder of the experiment, were collected at these settings. The experimental setup of the flow cell, magnetic susceptibility sensor and CT scanner for the waterflood experiment is shown in **Figures 1 and 2**. A Bartington MS2C coil magnetic susceptibility sensor, connected to an MS2 meter, surrounded the flow cell. The coil sensor could be moved so as to make measurements at any desired point along the flow cell. The majority of the magnetic susceptibility signal is contained within a thin disc-shaped slice approximately 16 mm wide, 8 mm either side of the measure point (the centre of the plane of the sensor coil). New non-metallic (PEEK) end fittings were manufactured for the flow cell, which reduced the background noise signal during the magnetic susceptibility measurements. The flow cell assembly was modified so that the magnetic sensor could be removed after each CT scan, allowing the re-zeroing of the magnetic sensor prior to each magnetic scanning sequence.

Table 1 summarises the main conditions of the waterflood experiment. Two pore volumes (PV) of deionised water were first injected into the sandpack at approximately 60 mL/hour. Each pore volume was approximately 15 cc. CT scans were again performed at this stage for baseline values. The MS2C magnetic sensor was also employed to gather baseline readings at this stage. Measurements were taken every 0.5 cm along the 15 cm length of the sandpack within the vessel. An oil flood, using Lloydminster heavy oil of 20,000 cP viscosity, was then undertaken at an average flow rate of approximately 0.5 mL/hour for 1.2 pore volumes, followed by a set of baseline oil CT scans and a set of MS2C magnetic sensor measurements. The oil flood is a kind of Swi setting.

Table 1. Summary of the main conditions of the waterflood experiment.

Conditions for Waterflood Experiment	
Heavy oil saturation:	
Injection rate	0.5 mL/hr
Total injected	1.2 PV
Waterfloods:	
Maghemite nanoparticle concentration	0.6 wt %
DDBS concentration	0.81 wt %
Sonication	20 min
Sodium iodide	none
FLOPAAM	none
Shaker for accumulator	no
Injection rate	1 mL/hr
Breakthrough (produced) volume	0.04 PV
Total deionised water injected	1.75 PV
Total oil produced	0.2 PV

For the waterflood, maghemite nanoparticles were added to deionised water at 0.6 wt% (**Table 1**) and mechanically agitated. The dispersing surfactant sodium dodecylbenzenesulfonate (DDBS) was then added at a concentration of 0.81 wt%. The solution was mechanically agitated and sonicated for 20 minutes in an ice bath prior to injection into the sandpack. The target injection rate was 1 mL/hour for the duration of the experiment. A total of 1.75 pore volumes of solution were injected into the sandpack and 13 sets of CT scans and magnetic sensor measurements were collected at regular intervals during injection. The nanoparticle tracer is not expected to go into the oil. One Dean Stark test was performed post experiment to determine oil, water, and solids.

RESULTS AND DISCUSSION

Figure 3 shows the produced oil versus the injected water during the waterflood. **Figure 4** shows a few smoothed CT attenuation profiles of differences from the oil saturated scan for the first 60mm of the sandpack, and **Figure 5** shows the final change from the oil

saturated state for the entire length of the sandpack. The vertical scale on **Figure 4** has been expanded to show the differences. Based on the calibrated nanoparticle-oil contrast of 24 Hounsfield units (HU) and a porosity of about 1/3, the peak value of 4 HU corresponds to an increase in saturation of 50%. The CT profiles clearly showed an increase in the attenuation between profiles 1 and 7 consistent with an increased magnetic susceptibility (due to injection of nanoparticles) as shown in **Figure 6**. Moreover, the CT attenuation dropped once the main front (identified from the magnetic susceptibility results and the material collected in the production jars) passed through the sandpack, consistent with the magnetic susceptibility profiles of **Figure 7**. However, the CT profiles did not exhibit a clearly recognisable front to the waterflood (neither did an earlier waterflood experiment using a sodium iodide solution). The CT profiles also showed a region of high attenuation (a "hump" at 70-80 mm from the inlet) followed by low attenuation in the downstream part of the sandpack (**Error! Reference source not found.**). The latter prevented any meaningful calculation of saturation profiles downstream of the hump. The low attenuation may have been caused by gas that was trapped in the pack during the initial water saturation and not fully swept out by the oil saturation. The CT attenuation responds to the nanoparticles and the fluids, including any trapped gas. The origin of the hump feature is unclear at present. It remained in the same position in each CT profile and did not appear to correlate with the magnetic susceptibility peak (**Figure 6**) which evolved and moved during the waterflooding as detailed below.

Eight volume magnetic susceptibility profiles were measured during the first day of nano-fluid injection (Error! Reference source not found.**6** shows profiles 3-8). The points on the profiles directly represent the content of maghemite nanoparticles at each point in the sandpack along the flow cell. The profiles revealed the progressive formation, growth and movement of a significant positive magnetic susceptibility peak, which initially formed on the left injection side of the flow cell (Error! Reference source not found.**6**, profiles 3 and 5) and migrated towards the right production (outlet) side as the injected volume of nanoparticle suspension increased (Error! Reference source not found.**6**, profiles 6-8). The peak is likely the result of a higher concentration of nanoparticles collecting at the site of the main water-heavy oil front during the flooding process. The peak may not necessarily reflect a higher water saturation at the peak (compared to portions of the sandpack closer to the inlet), since it appears that the nanoparticles agglomerate at the front (from material collected in the production jars as discussed later). First breakthrough (nano-fluid recovered at the production end) was observed after an injection of approximately 8.46 ml (0.2 PV injected or 0.04 PV produced) halfway between profiles 5 and 6. This is consistent with the observed magnetic susceptibility profiles. Profile 5 shows negative magnetic susceptibility at the production end (right side of the graph) indicative of the absence of nanoparticles, while profile 6 has a clear positive magnetic susceptibility signal on the production end, which can only occur if nanoparticles are flowing through that section. Therefore it appears that breakthrough of the nanoparticle suspension occurred before the main front, whose progress was tracked by the magnetic susceptibility peak, reached the production end. This may happen if, for

instance, viscous fingering is occurring. The results of Error! Reference source not found.**6** show how magnetic sensing of a nanoparticle suspension can track the progress of the main front during water flooding of a heavy oil saturated sandpack. This would appear to be a significant result. The shape of the front is likely to be complex, but the overall position of the main front appears to be tracked by the peak in magnetic susceptibility in each of the curves of **Figure 6**. The physical mechanism as to why the nanoparticles agglomerate at the front is not completely understood at present. A review of processes affecting nanoparticles at fluid interfaces is given by Bresme and Oettel [5]. In our case we think it may be due to a weakening of the repulsive electrical double layer around the nanoparticles, making them more likely to agglomerate. One possible cause of the weakening of the electrical double layer could be due to adsorption of hydroxyl ions at oil-water interfaces as described by Marinova et al. [6].

After the main front had passed through the production end of the flow cell the magnetic profiles of Error! Reference source not found.**7**, taken on the second day, show that the maximum magnetic susceptibility was lower than the peak observed in Error! Reference source not found.**6**. This would be expected if nanoparticles are no longer collecting at a major front. The magnetic profiles shown in Error! Reference source not found.**7** also had a relatively constant shape, which was expected to reflect the porosity profile. Higher porosity areas should give larger magnetic signals due to the higher volume of nanoparticles. CT scanning (Error! Reference source not found.**8**) confirmed that the porosity profile was very similar to the magnetic profiles. In particular, the decrease in magnetic susceptibility (Error! Reference source not found.**7**) just before 60 mm from the inlet end seems to correspond with a similar decrease in the CT porosity profile (Error! Reference source not found.**8**). There is also a correspondence because the Sor value is quite homogeneous within the sandpack because the brine volume measured is locally a function of phi*(1-Sorw) and not phi only. Note that the magnetic and CT values are the result of different “thickness slices” at each point (16 mm for the magnetics versus 0.35 mm for the CT), and this might explain differences between the two types of profile. Note also that the magnetic susceptibility values decrease slightly at both the inlet and outlet ends of the flow cell because the sensor is sensing outside the region of the sandpack at these points. **Figure 7** also indicates that there were slight increases in magnetic susceptibility with time. This is likely due to an increase in the volume of magnetic nanoparticles within the pore spaces, as nano-fluid was continuously displacing the oil.

The growth and migration of the magnetic susceptibility peak shown in Error! Reference source not found.**6** strongly suggests that the nanoparticles accumulated at the main front. This was further supported by observations of the material in the production jars (Error! Reference source not found.**9**). The production jar relating to the main front (JAR #5) contained nanoparticle agglomerates that had settled out of suspension. Such agglomerates were not subsequently seen in the later production jars after the main front had passed through the production end. These later jars (JARS #6 and #7) had nanoparticles still in suspension.

CONCLUSIONS

1. The formation, growth and movement of a magnetic susceptibility peak during the waterflood is consistent with a higher concentration of nanoparticles collecting at the site of the main front during the flooding process. This appears to provide a means of quantitatively tracking the progression of the front in real time. The aggregation of the nanoparticles at the front, however, may mean that the magnetic susceptibility values might not quantitatively relate to the water saturation as the front is passing through the sandpack.
2. Further independent evidence for a higher concentration of nanoparticles accumulating at the main front was provided by the material collected in the production jars.
3. Once the main water/heavy oil front had passed through the production end of the flow cell the magnetic profiles had a relatively constant shape, which reflected the porosity profile of the sandpack as confirmed by the CT results. After the main front has passed through the sandpack the magnetic results should potentially provide a quantitative measure of water saturation, since the nanoparticles were dispersed and in suspension at this stage (as seen from the material collected in the production jars) similar to the originally injected nano-fluid.
4. The CT attenuation profiles do not presently show a recognizable front. Part of the reason for this could be the relatively low contrast between the water + nanoparticles and the heavy oil, whereas for the magnetic results there is a substantially larger contrast between the magnetic susceptibility of the nanoparticles and that of the sandpack or fluids. It may also be due to the smallness of the change in saturation that the front represents. In addition, the CT attenuation results appear to have been corrupted by trapped gas in the downstream part of the sandpack.

ACKNOWLEDGEMENTS

We thank Alberta Innovates - Technology Futures (AITF) for funding for this project, in particular Marlene Huerta of AITF for all her support.

REFERENCES

1. Da Costa e Silva, A. (1995). Analysis of viscous fingering reproducibility in consolidated natural porous media. *Society of Core Analysts conference*, Paper Number 9504, pp. 1–10.
2. Mogensen, K., Stenby, E. H., & Zhou, D. (2001). Studies of waterflooding in low-permeable chalk by use of X-ray CT scanning. *Journal of Petroleum Science and Engineering*, **32**, 1–10.

3. Khan, S., Potter, D. K. & Kuru, E. (2015). Quantifying the transport of superparamagnetic nanoparticles in porous media using an acrylic flow cell and integrated magnetic susceptibility sensor technique. *Transport in Porous Media*, **106** (issue 3), 691-705.
4. Ivakhnenko, O. P. and Potter, D. K. (2004). Magnetic susceptibility of petroleum reservoir fluids. *Physics and Chemistry of the Earth*, **29**, 899-907.
5. Bresme, F. and Oettel, M. (2007). Nanoparticles at fluid interfaces. *Journal of Physics: Condensed Matter*, 19 (issue 41), Article Number 413101 (33pp). DOI: 10.1088/0953-8984/19/41/413101.
6. Marinova, K. G., Alargova, R. G., Dencov, N. D., Velev, O. D., Petsev, D. N., Ivanov, I. B. & Borwankar, R. P. (1996). Charging of oil-water interfaces due to spontaneous adsorption of hydroxyl ions. *Langmiur*, **12**, 2045-2051.

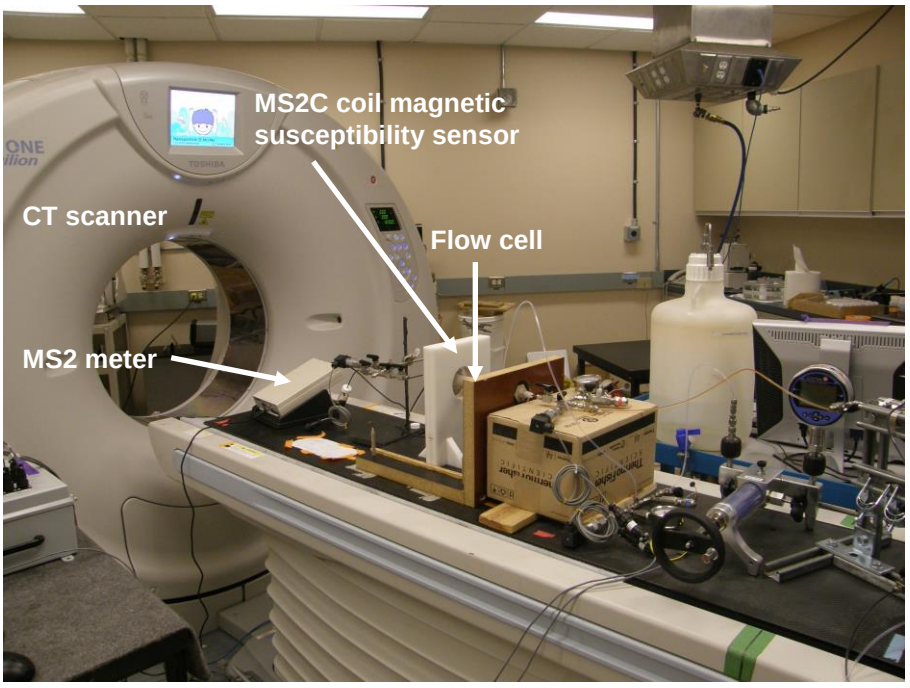

Figure 1. The experimental setup on the CT couch for the waterflood experiment, with the flow cell and magnetic sensor in place.

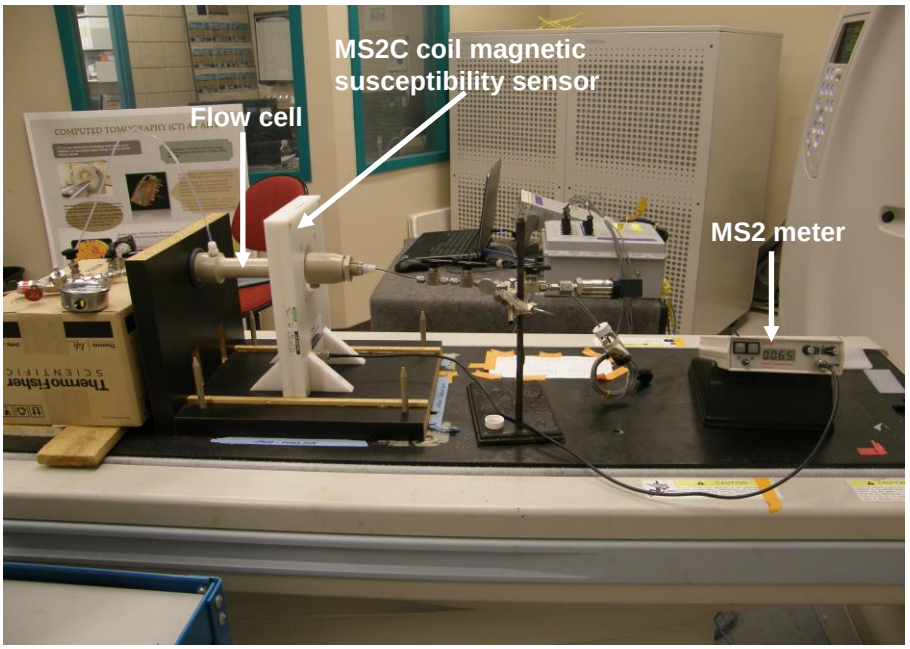

Figure 2. Close up of the flow cell and magnetic sensor on the CT couch for the waterflood experiment. Water injection is from left to right.

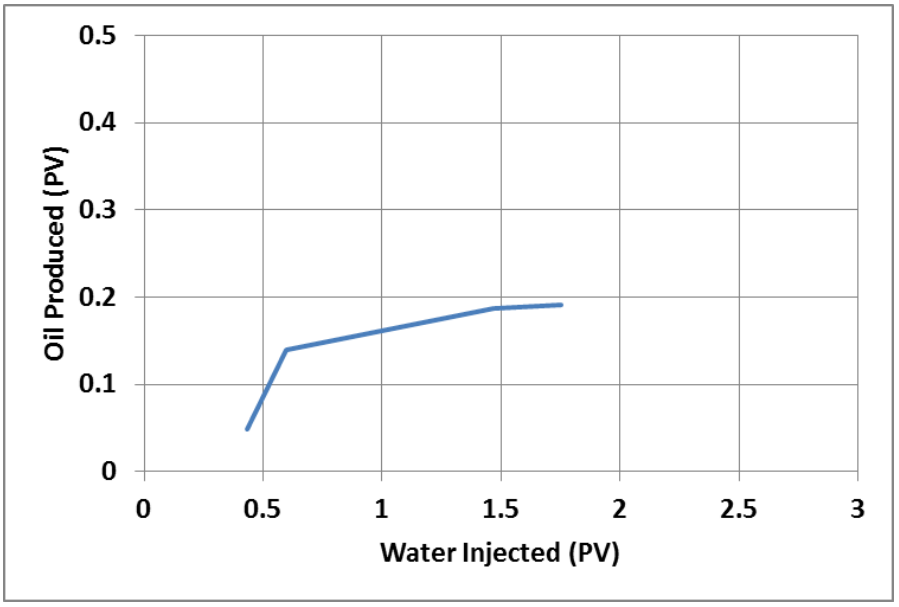

Figure 3. Produced oil versus injected water during the waterflood. Breakthrough occurred at about 0.04 PV produced or 0.2 PV injected. This was observed before the first production jar was removed, therefore before the first point on the production curve in **Figure 3**. Before and after breakthrough, production behaved as if there were compressible fluid present. Our analysis of the pressure drop across the pack suggests between 0 and 1 ml of gas (depending on where it may have been lodged) trapped in the pack. The rest (accounting for the discrepancy between injected and produced volumes) could have been in either the production or the injection plumbing (or both).

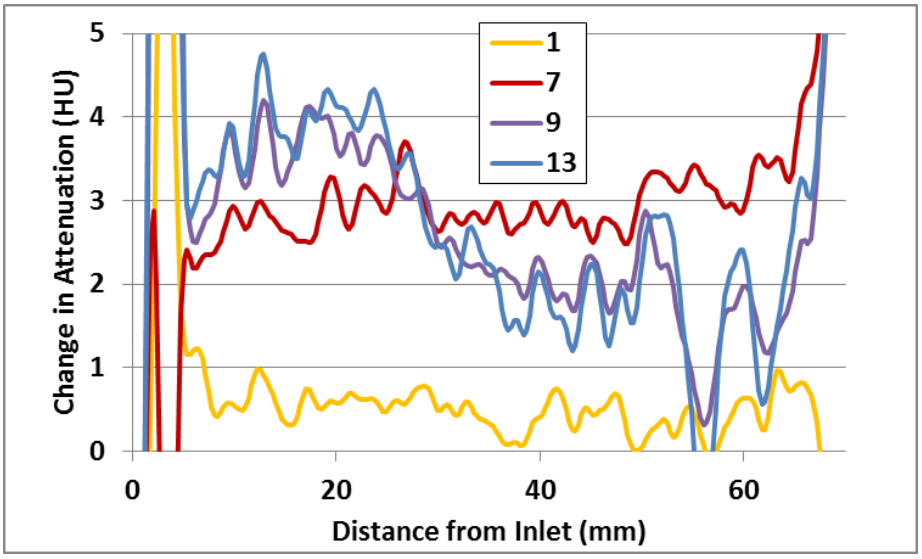

Figure 4. CT attenuation profiles for the upstream portion of the sandpack. Attenuation values are given in Hounsfield units (HU). Profile 13 was taken about a day after profile 1. Injection is from left to right.

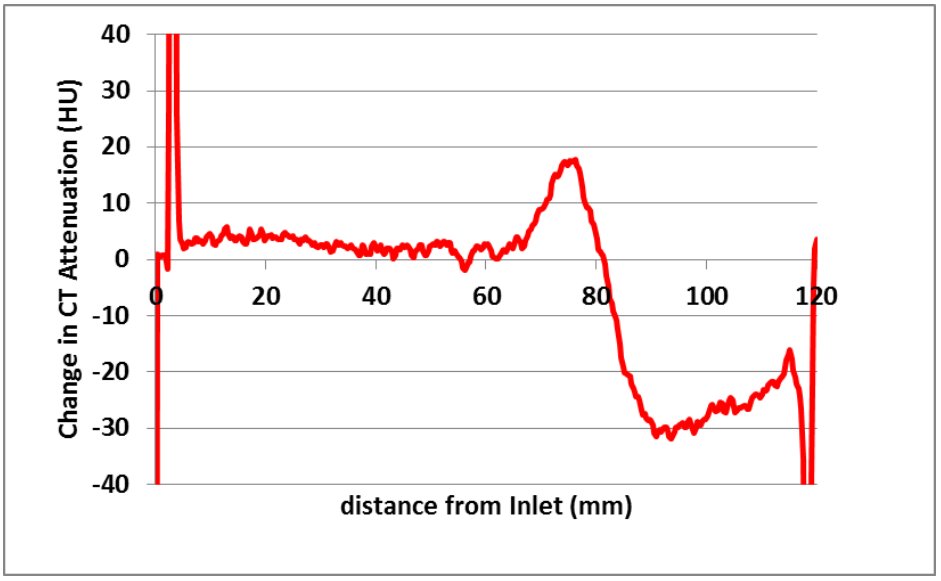

Figure 5. Final change in attenuation from the oil saturated scans observed in the medical CT scanner after 1.75 pore volumes of water + dispersed nanoparticles were injected into the heavy oil saturated sandpack. The figure shows a small increase in attenuation in the first 60 mm, due mainly to the nanoparticles. The

features beyond 60 mm appear to be artefacts. The hump feature at 70-80 mm is presently unexplained, but does not correlate with the magnetics. The low attenuation beyond 80 mm appears to be due to trapped gas.

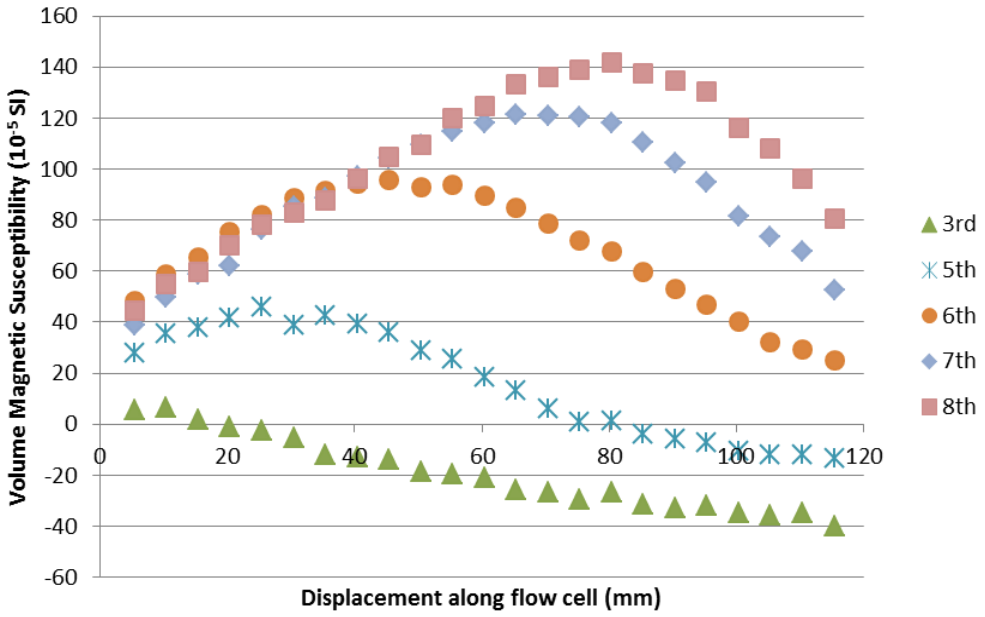

Figure 6. Volume magnetic susceptibility profiles taken during day one of the nano-fluid flooding of a heavy oil saturated sandpack.

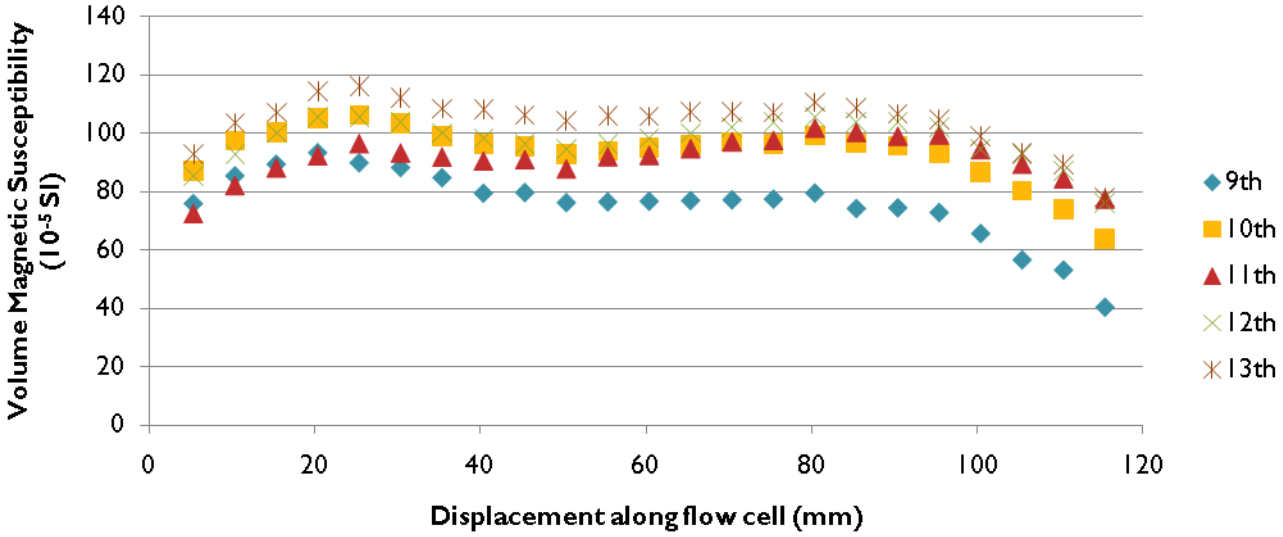

Figure 7. Volume magnetic susceptibility profiles taken during day two of the nano-fluid flooding.

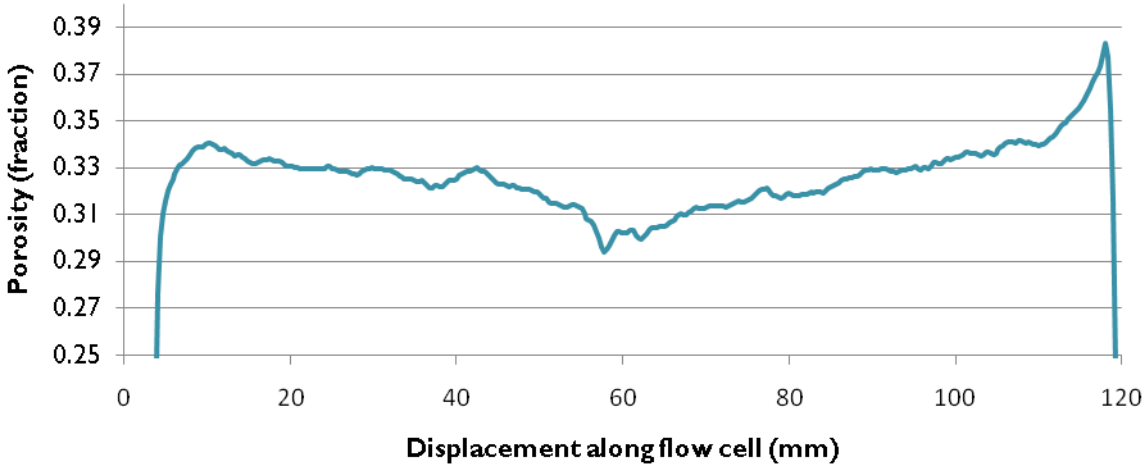

Figure 8. CT scanning porosity profile of the sandpacked flow cell. Note the overall similar shape to the magnetic susceptibility profiles in **Figure 7**.

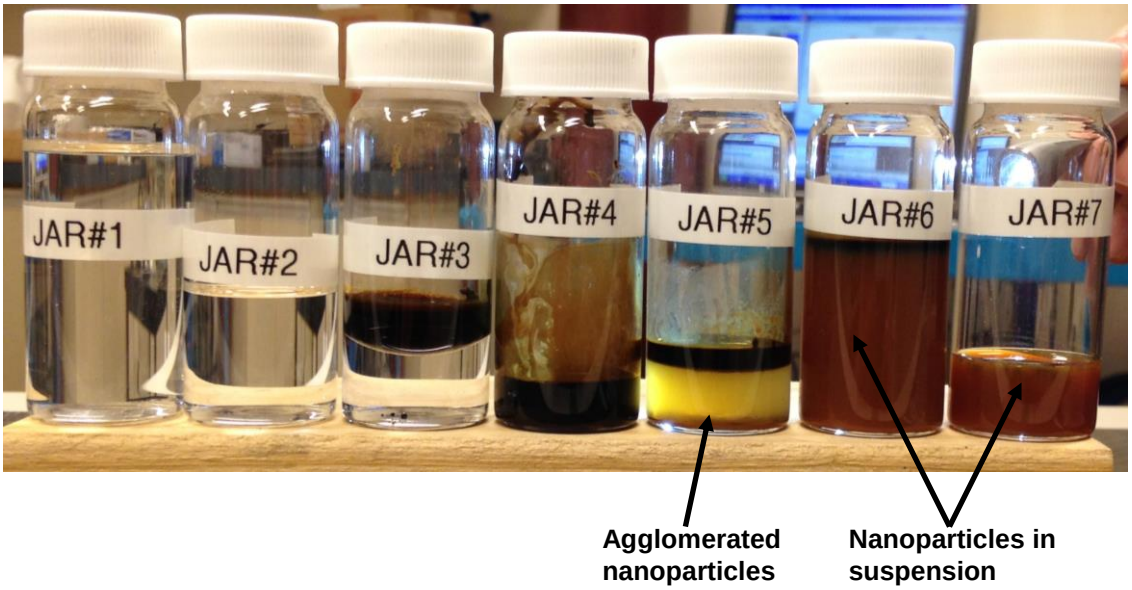

Figure 9. Production jars from the waterflood experiment: initial waterflood JAR #1, oil flood JARS #2 and #3, nanoparticle suspension flood JARS #4 to #7. Production JAR #5 clearly shows that nanoparticles have agglomerated and come out of suspension (lower thin brown layer). Above this is a yellow layer which comprises water plus some nanoparticles, and this is overlain by a heavy oil layer (black layer). The later production JARS #6 and #7 clearly show nanoparticles in suspension and not separated out.

CHARACTERIZING FLUID PRESENCE AND TRANSPORT IN ROCK CORES AT RESERVOIR-LIKE CONDITIONS VIA SPATIALLY RESOLVED NMR RELAXATION/DIFFUSION MAPS

Huabing Liu[1], Mark Hunter[1,2], Sergei Obruchkov[1], Evan McCarney[2], Mitch Robison[3], Robin Dykstra[1,2], Petrik Galvosas[1]
[1] Victoria University of Wellington, SCPS, MacDiarmid Institute for Advanced Materials and Nanotechnology, Wellington, New Zealand,
[2] Magritek Ltd., Wellington, New Zealand
[3] University of Auckland, Auckland, New Zealand

This paper was prepared for presentation at the International Symposium of the Society of Core Analysts held in St. John's Newfoundland and Labrador, Canada, 16-21 August, 2015

ABSTRACT
The properties of fluids saturating rocks depend strongly on temperature and pressure. Therefore, ambient laboratory conditions may not be desirable for the investigation of fluids in reservoir rocks. To mimic the reservoir, a pressurized and temperature controlled (overburden) cell, compatible with Nuclear Magnetic Resonance (NMR), was assembled within a 2 MHz NMR Rock Core Analyzer. 1D NMR relaxation and 2D diffusion-relaxation correlation distributions of fluid-saturated rock cores were measured in conjunction with 1D NMR imaging. By performing these spatially resolved NMR relaxometry and diffusometry experiments within the environment of the overburden cell, it is possible to obtain porosity, fluid saturation and residual fluid content profiles under reservoir-like conditions. Here we show for the first time that these spatially resolved NMR relaxometry and diffusometry experiments could be performed under elevated pressures and temperatures for fluids flooding rock cores in the laboratory. Experiments performed with this NMR setup may allow one to study the oil properties under reservoir conditions, which may inform oil recovery enhancement strategies.

INTRODUCTION
NMR is one of the non-invasive techniques to deliver substantial petrophysical parameters, such as pore volume, permeability and fluid saturation in rock plugs [1]. In particular, low-field ^{1}H NMR has become an important tool to study rock core plugs from oil reservoirs, and is established as an industry standard to calibrate NMR well-logging data [2]. In this context, the relaxation time/diffusion coefficient distributions, as well as their multi-dimensional correlation maps, are routinely utilized to characterize pore size, wetting state, fluids types, and quantify individual fluid phase saturations [3-5]. Meanwhile, magnetic resonance imaging (MRI) was introduced in rock core analysis to monitor "real-time" fluid invasion profiles during core flooding experiments [6]. To reveal the spatial fluid properties with saturating/flooding multi-phase fluids, it is desirable to combine NMR imaging techniques with 1D relaxation time/diffusion coefficients or 2D diffusion-relaxation correlation measurements. Subsequently, it allows one to extract the local profiles of

pore structure, saturation of individual fluid phases as well as wettability information [7-9].

Most reservoir rocks are buried in the formation approximately thousands meter deep, where the *in-situ* temperatures and pressures are much higher as compared to conditions on the surface [10, 11]. In this case, fluid properties (*e.g.* viscosity) in porous rocks behave differently according to local pressure and temperature, leading to a complex mechanism of oil recovery in oilfields [12]. Therefore, in order to characterize and model fluid properties and transport, it is necessary to confine and flush rock cores at reservoir-like temperatures and pressures whilst NMR experiments are performed in laboratory measurements.

In this work, an overburden system was assembled to pressurize rock cores at required temperatures and pressures. Furthermore, spatially resolved NMR techniques were combined with relaxation time (T_1 and T_2) and relaxation-diffusion correlation (D-T_2) experiments and implemented on a low-field NMR rock core analyzer. Since NMR signal intensity is inversely proportional to temperature, imaging was restricted to one dimension (1D) only, to ensure sufficient Signal-to-Noise Ratio (SNR). The property and distribution of oil saturating rock core were studied at different temperatures before flooding experiment. Subsequently, the conditions of secondary oil recovery were investigated by flooding water through an oil-bearing rock plug.

HARDWARE CONFIGURATION

A commercial 2 MHz NMR analyzer equipped with a shielded 1D gradient coil (Magritek, Ltd.) is used to acquire NMR data in this work [13]. The RF probe has a dimension of 10 cm length and 5.4 cm diameter. This setup is complemented with a Daedalus Innovations overburden rock holder (Figure 1 a), which maintains required temperatures and pressures for the rock plug under study [14]. It is worth noting that the materials of the rock holder, especially the section close to the detection volume of the NMR system, are chosen to be non-magnetic to avoid disturbing NMR signals.

Before the experiments, the rock core is placed between two PEAK mounts first, wrapped by heat shrink sleeve, and then loaded in the chamber of overburden holder (Figure 1 a). Two parts are screwed in each end of the holder housing to seal the overburden cell. Subsequently, the overburden cell within rock plug is inserted in the bore of NMR system, and is connected to two external circuits. These two circuits will provide pressurized fluid flooding through rock samples (left plumbing in Figure 1 b), and the confining pressure and temperature for rock plug (right loop in Figure 1 b), respectively. To achieve the desired confining temperature and pressure for the rock plug, two ISCO syringe pumps are used to drive confining fluid flow (right part in Figure 1 b). Perfluro polyether (PFPE, non-hydrogen signal) is chosen as the confining fluid to circulate in the plumbing and rock holder chamber. A heating bath after the syringe pump ensures the required temperature of PFPE before entering the pressure cell. Another bath after the cell will cool down the confining fluids before entering a back pressure regulator (BPR 1) which controls the pressure surrounding the rock core. On-site pressures and temperatures are logged to monitor the real-time confining conditions of the loaded rock core. Furthermore, a high-pressure crank

pump is connected to the inlet end of the flooding channel of the overburden rock holder to provide flooding conditions. Water can be imbibed and then pressurized through the rock core in this work.

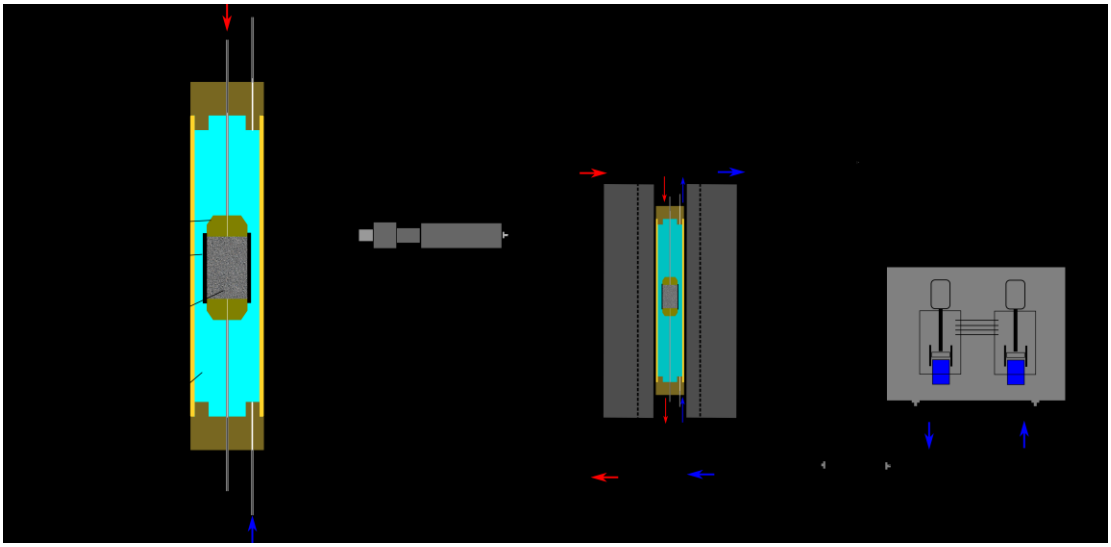

(a) (b)

Figure 1. Schematic of overburden rock holder (**a**) and its combination with low-field NMR system for high pressure and temperature experiments (**b**). Red and blue arrows indicate the flow direction of flooding fluid and confining fluid, respectively. The bold line in the confining part represents the tubing insulation. P in the circuit stands for pressure gauge and T for thermocouple.

Thermal conditions arising from the core holder within the NMR system have been modeled and simulated for different temperatures with SolidWorks. Results obtained by these simulations confirm the compatibility between operational NMR system and the overburden system.

NMR METHODOLOGIES

MRI methods are generally based on either frequency or phase encoded imaging [15]. A magnetic field gradient is applied during signal acquisition for frequency encoded imaging, ensuring spatially distributed resonance frequencies which return the image of the sample upon Fourier transform of the acquired MRI signal. The field of view (FOV) for this imaging method is determined to be: $2\pi/\gamma g\Delta t$, where g is the gradient strength and Δt is the time interval between neighboring acquired points (aka dwell time). In order to obtain an image using the phase encoded MRI method, a set of gradients within variable amplitudes is applied during a fixed time period δ before acquisition. This returns a set of experiments with varying phases in the acquired MRI signal, which again provides an image after Fourier transform. In this case, the FOV is determined as $m\pi/\gamma g_{max}\delta$ with g_{max} being the maximum intensity of the phase gradient. The imaging resolution ΔZ is FOV/m, where m is the number of acquired points in frequency-encoded imaging and the number of gradient steps in phase encoded imaging, respectively.

Since the spatial information can be encoded in a one-shot signal acquisition under fixed amplitude of the imaging gradient, frequency-encoded methods are generally faster as compared to phase-encoded. However, T_2 effects will irreversibly impact the

obtained imaging profile during the acquisition time, leading to the absence of signal with short T_2 relaxation time. The phase-encoded method on the other hand uses short signal acquisition time on the cost of experimental time, and can therefore offer more accurate imaging profiles. Both methods were employed in this work, depending on required time efficiency and accuracy.

In the context of petrophysical analysis using low-field NMR measurements, the longitudinal relaxation T_1 and transverse relaxation T_2 are mostly studied for fluid-saturated rock cores. This may provide information on the pore volume and pore size distributions. The 1D phase encoded imaging technique combined with T_2 relaxation measurements, as shown in Figure 2, can yield spatially resolved T_2 profiles [16]. The first period covered by T_{E1} is the phase encoded imaging part of the experiment, providing the 1D image (profile). The following section, consisting of the 180° pulse train acquires the NMR echo decay, which is determined by the transverse relaxation T_2. Similarly, spatially resolved T_1 profiles can be obtained by measuring T_1 using inversion/saturation recovery or rapid acquisition schemes as suggested in [17, 18], again in conjunction with the 1D imaging method.

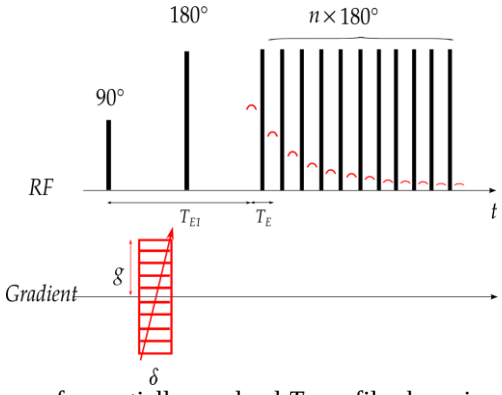

Figure 2. NMR pulse sequence for spatially resolved T_2 profiles by using phase encoded methods [16]. g is the imaging gradient which has variable intensities with a duration of δ. T_E is the echo spacing during the acquisition of the T_2 measurement.

The acquired data for spatially resolved T_2 experiments can be expressed as

$$M\left(k, nT_E\right) = \iint F\left(z, T_2\right) \times e^{i2\pi kz} \times e^{-\frac{nT_E}{T_2}} dz dT_2, \tag{1}$$

while the data obtained by spatially resolved T_1 techniques (using rapid acquisition) is

$$M\left(k, nT_{ACQ}\right) = \iint F\left(z, T_1\right) \times e^{i2\pi kz} \times \left(e^{-\frac{nT_{ACQ}}{T_1}} \sin\alpha \times \cos^{n-1}\alpha\right) dz dT_1 \tag{2}$$

with $k=\gamma g\delta/2\pi$. z is the gradient direction which coincides with the cylindrical axis of the rock cores in this work. α represents the small tip angle and T_{ACQ} is the signal evolution time in rapid encoding T_1 method.

Both spatially resolved T_1 and T_2 imaging methods yield two-dimensional datasets and a two-step data process is needed to extract the spatial relaxation distribution

function $F(z, T_1)$ or $F(z, T_2)$. Firstly, Fourier transform is employed to transform the encoded phase information into positions, returning the fluid content in each resolved slice (pixel). The Inversion Laplace transform algorithm is then consecutively applied slice by slice, yielding the spatial resolved relaxation distribution function. It is worth noting that $F(z, T_1)$ and $F(z, T_2)$ are akin to the curves from NMR well logging operated in the oilfield, where the sensor is pulled from the down-hole up to the surface and provide relaxation distributions from each vertical layer in the formation.
Besides relaxation measurements, diffusion coefficients of fluids can be uniquely measured by NMR techniques [15, 19]. This allows one to identify different fluid types and quantify fluid saturation in rock samples. In this case, 2D D-T_2 NMR correlation technique provides substantial information in rock core analysis, such as fluid typing and wettability identification in multi-phase experiments. Furthermore, spatially resolved D-T_2 distribution provides the aforementioned information along a certain core axis and potentially indicates progress of oil recovery or monitors the saturation level of rock cores [8]. While incorporating 2D relaxation-diffusion correlation experiment with 1D imaging technique, the entire experimental time should be taken into account for practical reasons. Therefore, the frequency encoding method is preferred because of the equivalent experimental time as compared to 2D correlation experiment without spatial resolution.

The pulse sequence for spatially resolved D-T_2 distribution is shown in **Figure 3** and the signal decay is expressed as

$$M\left(k,G,nT_E\right)=\iiint F\left(z,D,T_2\right)\cdot e^{i2\pi kz}\cdot e^{-\gamma^2\delta^2G^2D\left(\Delta-\frac{\delta}{3}\right)}\cdot e^{-\frac{nT_E}{T_2}}\,dz\,dD\,dT_2 \qquad (3)$$

where $k=\gamma g t_p/2\pi$. Δ is diffusion observation time and δ is gradient duration. The result is a 3D data matrix acquired during the spatially resolved D-T_2 experiment. To obtain the final map, Fourier transform is performed on each acquired echo to obtain the spatial imaging profile. Then 2D ILT algorithm is applied subsequently for the 2D exponential decay data in each slice, in order to extract the local D-T_2 distribution function $F(z,D,T_2)$ [20].

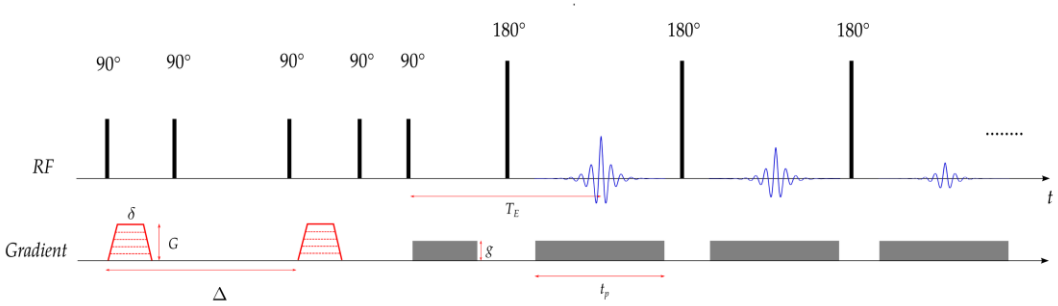

Figure 3. NMR pulse sequence for spatially resolved D-T_2 map, details are shown in [8]. Δ is the diffusion observation time and δ is the gradient duration. G and g are the gradients for encoding diffusion coefficient and position, respectively. T_E is the echo spacing and t_p is the echo acquisition time.

MATERIALS AND EXPERIMENTAL STRATEGIES

Sample. A Edwards Brown limestone core was used in this work to study fluid presence and multi-phase fluid flooding at different temperatures. The core porosity is

36.5% and the permeability is 90 mD. The rock core has a dimension of 6.3 cm length and 3.84 cm diameter. Before the experiment, the core plug was dried in an oven at 60°C for 48 h, until no hydrogen signal was detected in NMR measurements. Afterwards it was saturated with diesel (Hydrogen index HI=1.023).

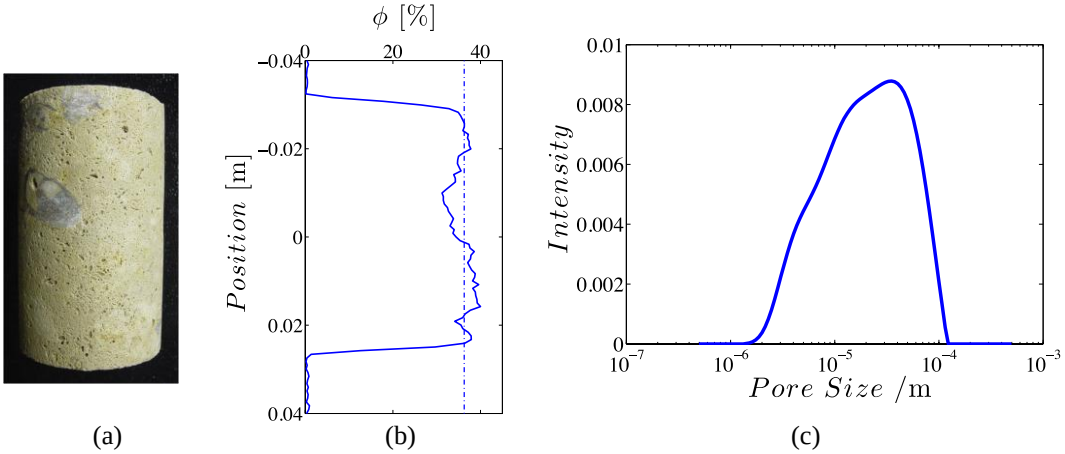

(a) (b) (c)

Figure 4. Edwards Brown plug used in this work (**a**), its porosity profile (**b**) determined by 1D imaging, and its pore length scales (**c**) determined by DDIF technique [21]. The heterogeneity of the rock sample can be recognized from the comparison of the acquired porosity profile and weighing porosity indicated by a dashed line. Large grains existing close to the plug middle might lead to the section with reduced porosity. This rock plug has a wide range of pore length from approximately 1 µm to 100 µm, indicating a highly heterogeneous pore system.

Basic parameters in NMR experiments. The duration of 90 and 180° pulses in the NMR experiments were kept to be 25 µs (to ensure the same RF-pulse frequency bandwidth) while the amplitudes were adjusted accordingly. T_1, T_2 and D-T_2 experiments were performed as routine measurements for determining the global properties of the fluid in the rock core. Relaxation time T_2 distributions were determined using the CPMG [22] pulse sequence with an echo spacing of 150 µs and 12000 echoes. A dataset with SNR=450 was acquired within a 4-scan measurement lasting 45 s. In the fast encoding T_1 measurement, the small tip angle α was set to be 5.3° and the number of small tip angle pulse is 250. The acquisition time T_{ACQ} was optimized to be 25.6 ms. The entire experiment time was 6 min within 32 scan acquisition. D-T_2 correlation distributions were obtained with a gradient duration δ = 5 ms and diffusion observation time Δ = 40 ms. The gradient G for encoding diffusion varied up to 0.4 T/m in 40 steps linearly. The echo spacing was 150 µs and the number of echoes was 12000.

Before flooding*: *static measurement. Because of the smaller impact of T_2 relaxation during the imaging encoding period, the phase-encoded T_2 method was used to extract spatially resolved T_2 profiles in the case of static fluid measurement. The spatial resolution was 1.5 mm and the number of imaging gradients m was 64. The echo spacing in the first stage T_{E1} was set to be 500 µs and the duration of phase gradient was 100 µs. The echo spacing in the second stage was set to be 150 µs and the number of echoes was 12000. With an 8-scan measurement for each imaging gradient step, phase-encoded T_2 profile datasets have been acquired within 1.5 h. For phase encoded T_1 measurement, the spatial resolution was 3 mm and the number of imaging

gradients *m* was 32. The data can be acquired within 3.5 h with a 32-scan measurement for each imaging gradient step.

Before flooding, the confining pressure was set to be 1000 psi by adjusting BPR 1 in the confining circuit. To study the temperature-dependence of oil properties and distribution in rock plug, the temperatures of rock sample were set to be 25°C, 55°C and 80°C with a constant flow rate of 150 mL/min for the confining fluid PFPE heated in the heating bath. During this measurement, the inlet and outlet of flooding channel were both switched off to avoid the saturated oil being driven out during providing confining pressure.

Flooding measurements. In the flooding experiment, to obtain spatially resolved *D*-T_2 distribution efficiently, frequency encoded imaging method was used. Parameters have been optimized to ensure comparable results obtained from frequency encoded T_2 profiles as compared to phase encoded T_2 method. The intensity of the frequency gradient *g* was chosen to be 12 mT/m. The number of acquired data points for each echo was 256 and the dwell time was 2 μs. This ensured the acquisition of the full echo (as determined by T_2^*, which is close to T_2 at low-field NMR measurement). The echo spacing with T_E = 800 μs was chosen accordingly to suit the acquisition of the full echo. The number of echoes was 3000. For the acquisition in the diffusion dimension, the gradient duration δ was 5 ms and the diffusion observation time Δ was 40 ms. The gradient *G* for diffusion encoding varied up to 0.4 T/m in 12 steps linearly. The experimental time was 20 min with a 16-scan acquisition.

To investigate the oil recovery procedure, water was injected into the oil-saturated rock core confined in the overburden cell. During the flooding experiment, to avoid water bypassing the core and travel between the core sample and confining fluid, the overburden pressure in this work was set to be at least 300 psi higher than the inlet pressure of crank pump. Therefore, the pressure before BPR 1 was kept to be 1000 psi and the initial pressure for crank pump was 700 psi. The pressure before BPR 2 was set to be 500 psi in this work. The entire flooding procedure is carried out in small individual steps as visualized on the horizontal axis in **Figure 8**. The crank pump needs to be suspended after each flooding step. Spatially resolved *D*-T_2 NMR measurements are carried out after there are no reading changes from these two pressure gauges between the confined rock core. The above procedure is repeated till there is no noticeable decrease of the oil signal detected as estimated from spatially resolved *D*-T_2 maps. Subsequently, the confining temperature of the prepared rock plug is increased and a further set of flooding and NMR measurement is performed, in order to investigate the temperature dependence of water-flooding-oil process of rock core. Three experimental temperatures, 25°C, 55°C and 80°C, will be adopted in this work.

POROSITY PROFILE AND FLUID DISTRIBUTION

Before spatially resolved measurements were performed, T_2, T_1 and *D*-T_2 distributions at three temperatures under 1000 psi were acquired (**Figure 5**). T_2 distributions at the three temperatures indicate two components of oil in the pore space (light component corresponds to larger T_2 value while heavy components has a smaller T_2 value). With

increasing temperature, T_2 distribution gradually shifts towards longer relaxation time, which implies decrease of oil viscosity [23, 24]. When the sample confining temperature was increased from 55°C to 80°C, the heavy component was less shifted as compared to the light counter-part, which might be caused by weaker temperature dependence as compared to light one. Compared to T_2 distributions, T_1 results obtained from rapid encoding method have only the distribution from light component. This is caused by long signal evolution time T_{ACQ} used in the signal acquisition. Likewise, T_1 values progressively increase with heating up the rock core, which suggest the decrease of oil viscosity.

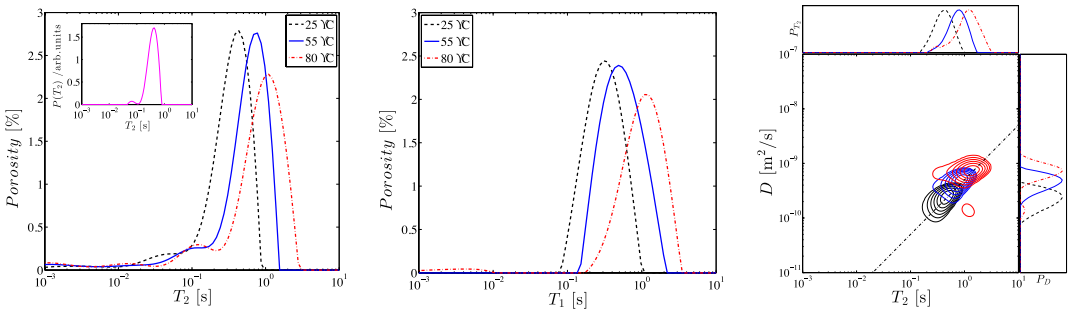

Figure 5. (**a**) Transverse relaxation T_2 and (**b**) longitudinal relaxation T_1 distributions of oil saturating rock under 1000 psi. The dash, solid and dot dash lines represent the distributions at 25°C, 55°C and 80°C respectively. The regularization factor during the inversion is 1 in T_2 and 33 in T_1 data process. (**c**) Diffusion-relaxation time correlation D-T_2 distribution under 1000 psi. The slope dash line represents hydrocarbon correlation line of D=5×10^{-10} T_2. The T_2 distribution of bulk diesel at 25°C is given in the inset of (**a**).

The diffusion-relaxation time correlation distribution were obtained and presented in Figure 5 c. Because of relaxation effect during the diffusion observation time, the heavy component with short T_2 relaxation time in the correlation experiments were missing compared to 1D relaxation results. Nevertheless, a reasonable prediction of oil properties is still accessible since the light component predominates this oil as shown in 1D T_2 spectra. Meanwhile, these 2D distributions exhibit a strong correlation between diffusion coefficient D and relaxation time T_2, a feature that is similar to that in bulk oil. It indicates non oil-wet status for this rock plug. This is probably ascribed to the thin water film absorbed at the pore walls that have not entirely dried out during the sample preparation. This amount of water, although was hardly to be detected during the experiment, results in the wettability of this rock plug. The distributions shift along the hydrocarbon line even at temperatures of up to 80°C, which proves a decrease of oil viscosity. While the shape of D and T_2 distributions remain almost the same, indicating a nearly stable composition of oil in pore space within our temperature range [24].

Spatially resolved T_1 and T_2 profiles at 25°C are presented in Figure 6 a and b, respectively. Similar features, such as the heterogeneity of porosity profile, can be observed along the cylindrical axis in both maps. Because of the long T_{ACQ} time adopted here, heavy component of oil is absent in all resolved T_1 profiles, while is still visible in T_2 profiles. Both projected T_1 and T_2 distributions are comparable with the bulk results shown in Figure 5 a and b. Furthermore, spatially resolved T_2 experiments

were performed at confining temperatures of 55°C and 80°C in order to investigate the oil temperature-dependent behaviour. The varying T_2 and spatial features as seen at 55°C and 80°C are not understood yet and remain subject to further research. However, projections onto the spatial and T_2 domains remain reasonable and confirm a shift of T_2 towards higher temperatures as expected.

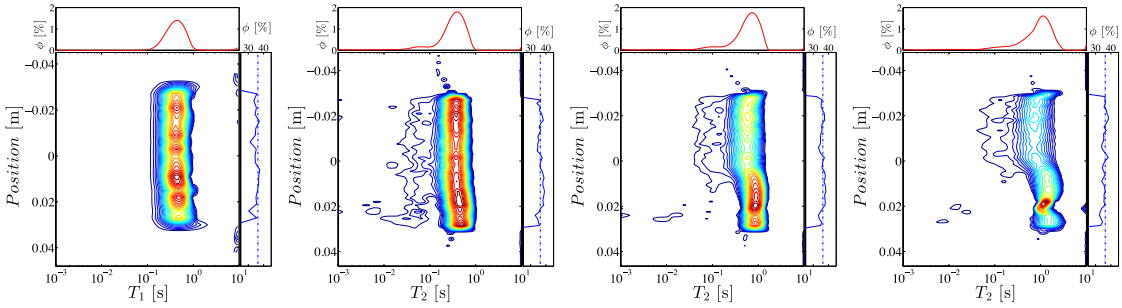

Figure 6. (**a**) Spatially resolved T_1 profile at 25°C and T_2 profiles at (**b**) 25°C, (**c**) 55°C and (**d**) 80°C under 1000 psi. The top panel presents the projected T_2 relaxation distribution and right panel gives the porosity profile. The blue dashed line in the right panel corresponds to the weighing porosity value.

In summary, the oil situated in the rock core becomes less viscous with increasing the confining temperature, which is revealed from T_1, and T_2 distributions as well as from the D-T_2 correlation distributions. The spatial T_2 profile resolves the T_2 distributions along cylindrical core dimension, also exhibiting distinct oil properties and distributions at different confining temperatures.

IN-SITU WATER-FLOODING MEASUREMENTS

In this section, multi-phase fluid transport processes at different temperatures are observed by using the spatially resolved D-T_2 technique. The oil-saturated rock plug was firstly flooded by water at 25°C and 1000 psi. Subsequently, two further flooding steps at 55°C and 80°C were performed to investigate the temperature dependence during the flooding process. The spatially resolved D-T_2 profiles before, during and after water flooding at 25°C are compared and presented in Figure 7. In order to visualize the existence of two different fluid phases, two reference planes indicating oil (left) and water (right) were added in to the figures as grey planes.

The distribution function $F(z,D,T_2)$ before water flooding (shown in Figure 7 a) mainly extends along the hydrocarbon plane indicating oil saturating from top to bottom in the rock plug. After flooding an amount of water corresponding to 0.1 pore volume through the rock (0.1 PV water flooding), there appears a distinct distribution neighbouring the oil signal and laying along water reference plane (Figure 7 b). This signal extends along the water plane after 1 PV water flooding (shown in Figure 7 c). From the reference planes, it can be distinguished that the left column represents residual oil while the right one is the injected water. Therefore, it is feasible to extract the spatially resolved residual oil and water saturation from this distribution, and estimate oil recovery efficiency. The volume of flooding water was incremented up to 2.2 PV and two subsequent flooding experiments at 55°C and 80°C were performed with equal amount of water flooding.

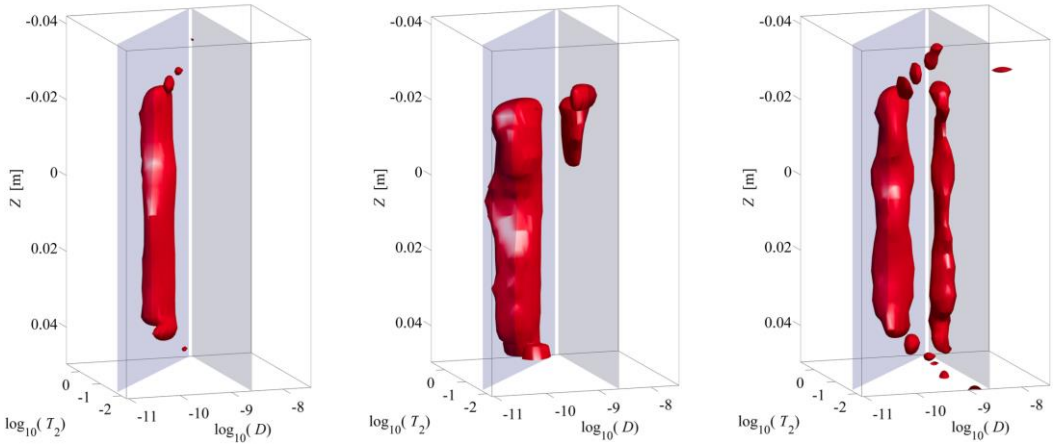

(a) (b) (c)

Figure 7. Spatially resolved D-T_2 profile before water flooding (**a**), and after 0.1 PV (**b**) and 1 PV (**c**) water flooding at 25°C. Two reference planes indicating hydrocarbon and water were plotted in order to identify the spatial distributions of oil and water signals.

The intensities of oil and water signals in the spatially resolved D-T_2 maps of each water flooding step can be readily summed up and plotted as relative water and oil saturation (shown in Figure 8).

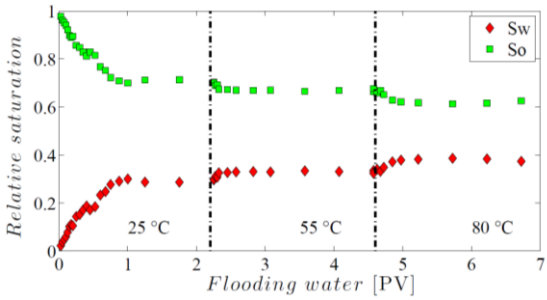

Figure 8. Relative water (red diamond) and oil (green square) saturation estimated from the spatially resolved D-T_2 maps. The entire flooding procedure is performed under three confining temperatures (25°C, 55°C and 80°C). The amount of flooding water is normalized with the pore volume (PV) of the rock plug here. During the flooding in each temperature, the water volume is incremented to 2.2 PV.

For the water-flooding procedure at 25°C, the relative oil saturation drops rapidly with increasing the flooding water volume, and reaches to a plateau level after 1 PV water injection. The further flooding shows no obvious oil yield in this rock plug. By increasing the rock temperature, the relative oil saturation continues to decrease because of the higher oil mobility, and quickly converges to a constant level afterwards. The residual oil saturation is still above 50% even at rock temperatures up to 80°C, which is a higher value as compared to common water-flooding-oil experiments (lower than 40% of residual oil saturation). This may due to the relatively high flow rate of the flooding water (approximately 0.25 mL/s) provided by the crank pump in this case. In order to investigate the multi-phase fluid interaction, all distributions under three temperatures were projected into the D-T_2 dimension and shown in Figure 9.

Regardless of longitudinal relaxation during the diffusion observation time, the ratio of water and oil varies gradually with increasing the rock temperature, which can be observed from the projected diffusion coefficients in the right panel of each distribution. These results exhibit the same features as shown in the relative saturation data in Figure 8, and imply a process of enhanced oil recovery by flooding the rock

plug at higher temperatures. Further oil recovery strategy, such as gas, thermal or chemical polymer injection may be justified.

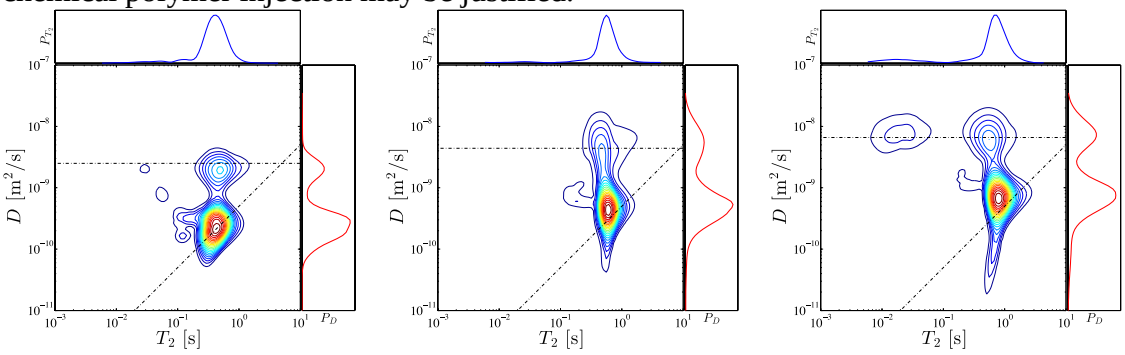

(a) (b) (c)

Figure 9. Projected diffusion-relaxation correlation distribution at (**a**) 25°C, (**b**) 55°C and (**c**) 80°C. The horizontal lines represent water diffusion coefficient at 25°C (=2.3×10^{-9} m^2/s), at 55°C (=4.4×10^{-9} m^2/s), and at 80°C (=6.6×10^{-9} m^2/s) [25]. The slope dash line represents hydrocarbon correlation line of D=5×10^{-10} T_2. The top panel presents the projected relaxation distribution and right panel shows the projected diffusion coefficient distribution.

CONCLUSION

Based on the constructed high pressure/temperature NMR measuring system, spatially resolved T_1 and T_2 relaxation techniques provides direct insight into local properties of fluid situated in the pores of rock core at reservoir-like conditions. Furthermore, a spatially resolved D-T_2 method yields substantial information regarding flooding experiments, such as wetting status, residual oil/water saturation profiles, and their dependence on temperature. The current hardware set-up and the implemented NMR methods provide the base for further investigations of the residual oil saturation and displacements in the context of enhancement oil recovery.

ACKNOWLEDGEMENTS

The project was supported by the New Zealand Ministry of Business, Innovation, and Employment via the Grant "New NMR Technologies". Magritek Ltd. is acknowledged for providing the overburden cell. R. Peterson (Daedalus Innovations LLC), S. Buchanan (Magritek Ltd.) and T. Brox (VUW) are acknowledged for the technical suggestions. H-B. Liu thanks the financial supports from Chinese Scholarship Council (CSC).

REFERENCES

1. Dunn, K.-J., D.J. Bergman, G.A. Latorraca, *Nuclear magnetic resonance: Petrophysical and logging applications*, Pergamon, (2002).
2. Mitchell J., L.F. Gladden, T.C. Chandraseker, E.J. Fordham, "Low-field permanent magnets for industrial process and quality control," *Progress in Nuclear Magnetic Resonance Spectroscopy*, (2014) 76, 1–60
3. Hürlimann M.D, "The diffusion–spin relaxation time distribution function as an experimental probe to characterize fluid mixtures in porous media," *The Journal of chemical physics*, (2002) 117, 22, 10223–10232.
4. Sun, B.Q., M. Olson, J. Baranowski, S. Chen, W. Li, D. Georgi, "Direct fluid typing and quantification of Orinoco Belt heavy oil reservoirs using 2D NMR logs", *SPWLA 47th Annual Logging Symposium*, Veracruz, Mexico, June 4-7, (2006).

5. Hürlimann, M.D., M. Flaum, L. Venkataramanan, C. Flaum, R. Freedman, G.J. Hirasaki, "Diffusion-relaxation distribution functions of sedimentary rocks in different saturation states," *Magnetic Resonance Imaging*, (2003) 21,3-4, 305–310.
6. Kim, K., S.-H. Chen, F.-F. Qin, A.T. Watson, "Use of NMR Imaging for determining fluid saturation distributions during multiphase displacement in porous media." *International Symposium of the Society of Core Analysis*, (1992) 9219.
7. Sun B.-Q., K.-J. Dunn, G.A. LaTorraca, D.M. Wilson, "NMR imaging with diffusion and relaxation," *International Symposium of the Society of Core Analysts*, Pau, France, September 21-24, (2003), SCA2003-24.
8. Rauschhuber, M., G. Hirasaki, "Determination of saturation profiles via low-field NMR imaging," *International Symposium of the Society of Core Analysts*, Noordwijk, Netherlands, September 27–30, (2009), SCA2009-09.
9. Mitchell, J., "Magnetic resonance core analysis at 0.3 T," *International Symposium of the Society of Core Analysts*, Avignon, France, September 8–11, (2014), SCA2014-10.
10. Utracki, L.A., "Temperature and pressure dependence of liquid viscosity," *The Canadian Journal of Chemical Engineering*, (1983) 61, 5, 753-758.
11. Dandekar A.Y., *Petroleum reservoir rock and fluid properties*, CRC press, (2013).
12. Tiab D., E.C. Donaldson, *Petrophysics: theory and practice of measuring reservoir rock and fluid transport properties*, Gulf professional publishing, (2011).
13. http://www.magritek.com.
14. http://www.daedalusinnovations.com/apparatus/rockcore.html.
15. Callaghan, P.T., *Principles of nuclear magnetic resonance microscopy*, Oxford University Press, Inc., New York, (1991).
16. Perlo J., F. Casanova, and B. Blümich, "3D imaging with a single-sided sensor: an open tomograph", *Journal of Magnetic Resonance*, (2004) 166, 228–235.
17. Hsu, J.-J., I. J. Lowe, "Spin-lattice relaxation and a fast T_1-map acquisition method in MRI with transient-state magnetization", *Journal of Magnetic Resonance*, (2004) 169, 270-278.
18. Chandrasekera T.C., J. Mitchell, "Rapid encoding of T_1 with spectral resolution in n-dimensional relaxation correlations", *Journal of Magnetic Resonance*, (2008) 194, 1, 156-161.
19. Tanner, J.E., "Use of the stimulated echo in NMR diffusion studies," *The Journal of Chemical Physics*, (1970) 52, 5, 2523-2526.
20. Venkataramanan, L., M.D. Hürlimann, Y-Q. Song, "Solving Fredholm integrals of the first kind with tensor product structure in 2 and 2.5 dimensions," *IEEE Transactions on Signal Processing*, (2002) 50, 5, 1017–1026.
21. Song, Y.-Q., S. Ryu, P. N. Sen, "Determining multiple length scales in rocks", *Nature*, (2000) 407, 178-181.
22. Meiboom, S., D. Gill, "Modified spin-echo method for measuring nuclear relaxation times," *Review of Scientific Instruments*, (1958) 29, 8, 688-691.
23. Freed, D.E., M.D. Hürlimann, "One-and two-dimensional spin correlation of complex fluids and the relation to fluid composition," *Comptes Rendus Physique*, (2010) 11, 2, 181–191.
24. Freed, D.E., "Temperature and pressure dependence of the diffusion coefficients and NMR relaxation times of mixtures of alkanes", *The Journal of Physical Chemistry B*, (2009) 113, 13, 4293-4302.
25. Holz, M., S. R. Heil, A. Sacco, "Temperature-dependent self-diffusion coefficients of water and six selected molecular liquids for calibration in accurate ^{1}H NMR PFG measurements", *Physical Chemistry Chemical Physics*, (2000) 2, 4749-4742.

TRACER DISPLACEMENTS FOR EOR EXPERIMENTS: THEORY, MODELING, AND EXPERIMENTS.

Roland Lenormand, Guillaume Lenormand and Fabrice Bauget
Cydarex

This paper was prepared for presentation at the International Symposium of the Society of Core Analysts held in St. John's Newfoundland and Labrador, Canada, 16-21 August 2015

ABSTRACT

During Enhanced Oil Recovery (EOR) experiments, front spreading is due to various mechanisms: pore-scale mixing, channeling due to permeability heterogeneity, viscous fingering, capillary effects, etc. This paper gives a review of existing models for the simplest case of tracer spreading and a discussion of their validity based on comparison with laboratory experiments.

We first recall the definitions and the physical mechanisms describing pore-scale mixing and spreading, and their modeling at the scale of a Representative Elementary Volume (REV, local or Darcy-scale approach) called "microdispersion". When used as local input in 3-Dimensional (3-D) simulations, the Darcy-scale approach can describe the plug-scale spreading related to permeability heterogeneity. In a 3-D heterogeneous medium, even a displacement started as a piston-type at the Darcy-scale leads to a dispersion behavior.
However, laboratory experiments are rarely simulated with 3-D models, but only with 1-D models. A local microdispersion displacement in a 1-D simulation cannot model the large spreading observed at the plug-scale. Consequently, additional parameters must be introduced in 1-D local laws to compensate for the missing information on heterogeneities, and we recall here the existing up-scaled (or homogenized) models (microdispersion, macrodispersion and convective channeling).

These models are compared to our tracer experiments. Displaced and injected fluids have different salinities, and local saturation profiles were measured using ten electrodes along the sample. Our results confirm previously published results that channeling convective models are more suitable than standard dispersion models. The best result is obtained by calculating a permeability distribution function in a stratified model. This model accounts for the long tail in the effluent production and the in-situ concentration profiles.

INTRODUCTION

During Enhanced Oil Recovery (EOR) experiments, front spreading is due to various mechanisms: pore-scale mixing, channeling due to permeability heterogeneity, viscous fingering, capillary effects, etc.
The main objective of this paper is to clarify the mechanisms linked to the spreading of a tracer in a porous medium and to present the equations used to model the concentration as a function of time and space (transport equation) at the scale of a plug of real rock. We

will show that a transport equation written at the scale of a REV needs to be modified when applied to a plug, due to the presence of heterogeneities. This effect, called homogenization (up-scaling), will be discussed, and existing models will be compared to our experiments. We first give some definitions, then present existing models used at the REV scale, and finally we describe homogenized transport equations.

Definitions

A "tracer" is a soluble substance, like dye or salt, which at low concentration does not change the fluid properties. "Dispersion" is used as a general term equivalent of spreading, independently of fluids characteristics: miscible or not, with or without viscosity contrasts. Originally "diffusive" spreading was referring to the physical mechanism of molecular diffusion leading to a transport equation with a second order derivative with respect to space. By extension, this term is now generally used when spreading is described by a term of transport equation with a second order spatial derivative, leading to the width of the front being proportional to the square root of the travelled distance, even if the physical mechanism is not molecular diffusion. We will see that an uncorrelated velocity field also leads to a front spreading with square root of travelled distance. When molecular diffusion is negligible, spreading is due to spatial differences in velocities, either at pore level or at larger scale (permeability heterogeneities) and dispersion is called "hydrodynamic" (or advective).

In general, a transport equation in concentration as function of time and distance contains three terms: the transient term with a derivative with respect to time, a term with a first order derivative in space, called the "convective" term, and a term with a second order in space, called the dispersive term.

Flux and concentration

All the equations are written at the Darcy scale, meaning that a REV of porous medium contains a large number of pores (such as the micromodel in Figure 1).

The tracer "concentration" C is the mass of tracer per unit volume. The "flux" F is the mass of tracer crossing a given surface per unit of time. The "flux density" f is the flux per unit surface.

In an elementary volume (length dx in the direction of flow, cross-section area dA, porosity ϕ, and volume $dV = dA\phi dx$), the mass balance equation implies that the accumulation of solute during dt, $dA\phi dx\, \partial C/\partial t\, dt$, is equal to the quantity of tracer entering in x, $dAf(x)dt$, minus the quantity of tracer leaving the volume, $dAf(x + dx)dt$. This leads to the 1-D mass balance equation, valid with no tracer adsorption:

$$\frac{\partial C}{\partial t} + \frac{1}{\phi}\frac{\partial f}{\partial x} = 0. \qquad (1)$$

In order to derive the concentration as function of time and distance, the dispersion equation, relating the flux density f to the concentration C is required. In addition to the mass balance and the dispersion equation, Darcy's equation is used to calculate the local velocity as function of fluid properties and pressure gradient.

In the following sections, we will study the local dispersion equation for tracer flow. Then we will describe the integration of this local equation for a 2 or 3-D flow, leading finally to the 1-D homogenization, average in a 1-D flow as commonly used to represent laboratory experiments.

Tracer local equation (Microdispersion)

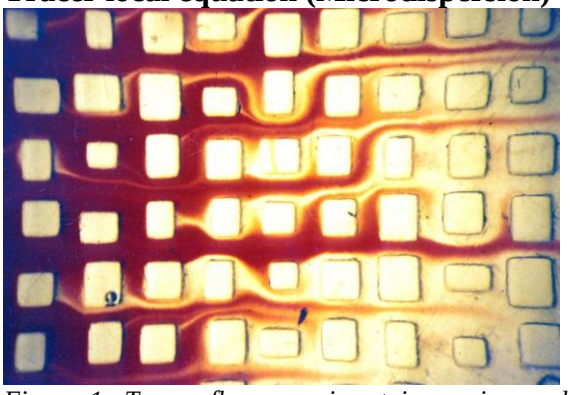

Figure 1- Tracer flow experiment in a micromodel. The tracer in red is injected at a constant flux on the left

Spreading in the direction of the mean flow is due to the combined effect of the variation of velocities inside the pores (the tracer follows the streamlines) and molecular diffusion between streamlines that smears the color near the entrance (Figure 1). The molecular diffusion allows the invasion of the tracer in "dead-end" pores and zones with very low velocities.

We can derive the dispersion equations (relationships between flux and concentration) in some limiting cases:

Piston-type flow: A theoretical case of transport without any dispersion (not possible in porous media). All the particles are transported at the same Darcy velocity *U*. The flux density is therefore: $f = UC$.

Pure molecular diffusion: With no velocity, spreading is due to molecular diffusion and Fick's law gives the flux density proportional to the concentration gradient. In a liquid, the coefficient of proportionality is the molecular diffusion D_m. In a porous media, this coefficient is an apparent diffusion coefficient D_A. Its ratio with D_m reflects the presence of solid and pore space tortuosity: $D_A/D_m = 1/f_f$ where f_f is formation factor: $f = -\phi D_A \frac{\partial C}{\partial x}$.

Hydrodynamic dispersion: With no molecular diffusion, the spreading due to pore scale variations in the velocity field can be described using a stochastic approach. If the distribution of pore size is random with no spatial correlation, the invasion of the tracer follows the statistic law of large numbers of uncorrelated events, and the spreading is proportional to the square root of distance (similar to the macrodispersion described below). This mechanism can be represented by a transport equation, sum of a convective term (plug flow without spreading) and a diffusive term leading to the spreading in square root of travelled distance with a dispersion term D_c:

$$f = UC - \phi D_c \frac{\partial C}{\partial x}. \quad (2)$$

When both molecular diffusion and pore scale velocity field act together, the mechanism is called "microdispersion" and the flux density is assumed to have the same form as Eq.

2 but with a dispersion coefficient D that includes molecular diffusion and hydrodynamic dispersion.

Effect of molecular diffusion on microdispersion

Microdispersion involves both molecular diffusion and hydrodynamic dispersion (Pfannkuch in 1963 [1]; Fried and Combarnous [2]). The balance between molecular diffusion and hydrodynamic dispersion is quantified using the molecular Péclet number, defined as the ratio of the molecular diffusion characteristic time l^2/D_m to the advective characteristic time l/v: $Pe_m = vl/D_m$, where v is a characteristic velocity (i.e. Darcy velocity U or front velocity $V = U/\phi$). l is a characteristic length, i.e. mean grain diameter for unconsolidated porous media or of the order of $\sqrt{K}$ for a consolidated media. Pfannkuch presented a graph with dispersion coefficient normalized by molecular diffusion as function of Péclet number (Figure 2).

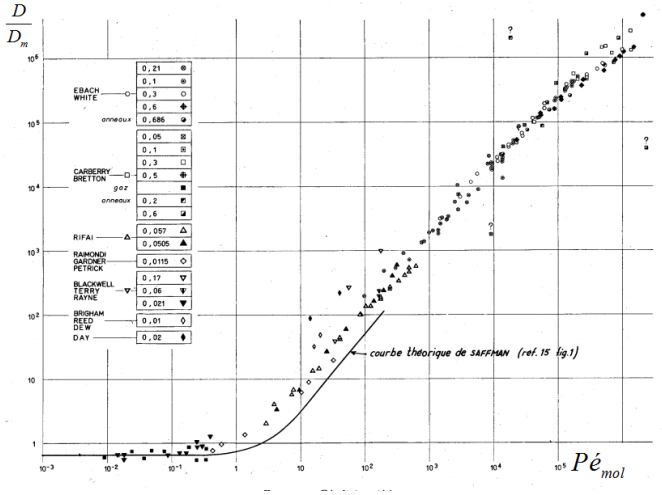

Figure 2 – Dispersion coefficient as function of Péclet number (after Pfannkuch [1]).

At very low flow rate (Pé < 1) The dimensionless dispersion coefficient is constant and equal to the apparent molecular diffusion coefficient, a regime of pure diffusion controlled by the apparent diffusion coefficient D_A described above. For Pé > 1000: the dispersion coefficient is roughly proportional to the Péclet number. In this regime the dispersion coefficient is independent of molecular diffusion and proportional to the front velocity:

$$D = \alpha V \tag{3}$$

α is called the dispersivity and is around 1.8 times grain diameter for granular material. V is the front velocity $V = U/\phi$, with U the Darcy velocity. In laboratory, the determination of the dispersion coefficient is performed in this regime.

DISPERSION THROUGH A PLUG

In laboratory, the dispersion coefficient is derived from tracer injection through a cylindrical plug with uniform injection and production on the inlet and outlet faces. The concentration is measured in the effluent and sometimes locally using in-situ

measurements (X-rays, resistivity, etc.). A constant concentration C_0 starting at time t=0 is injected continuously. Several models have been proposed for the boundary conditions:

Inlet boundary condition

In laboratory, even if the tracer is injected at constant concentration, it is the flux that is imposed at the entrance and not the concentration. This is well illustrated in a micromodel (Figure 1): A tracer is injected at a constant concentration on the left-hand side of the picture. Considering this picture as a REV, the concentration is constant at the pore scale, in the first rows of pores, but not at the REV scale. Consequently, the boundary condition at the REV scale should be a constant flux density $f = QAC_0$. However, experimental data are often interpreted with a constant concentration boundary condition. We will compare these two assumptions when presenting the experimental results, but the difference is insignificant.

Outlet boundary conditions

In pure molecular diffusion (without flow), the outlet boundary condition should be the concentration imposed at the outlet face. In hydrodynamic regime, the tracer follows the streamlines from inlet to outlet with no backflow. Velocity and dispersion inside the plug are not influenced by the value of concentration at the outlet or the length of the plug. The equation is the same as for an infinite medium, with the condition of zero flux at infinite distance (non infinite mass).

Dispersion through a homogeneous plug

In a homogeneous plug, permeability is uniform and flow lines are parallel to the axe of the plug. The velocity is uniform and a 1-D mass balance equation can be written (equation 1). Using the microdispersion relationship between flux and concentration leads to the standard 1-D dispersion equation.

$$\partial C/\partial t + U/\phi \ \partial C/\partial x = \phi D \ (\partial^2 C)/\partial x^2 \qquad (4)$$

Analytical solutions are obtained using Laplace's transforms. With the "classical" assumption of constant concentration at entrance, the solution is the following (Fried & Combarnous [2]):

$$C = \frac{C_0}{2}\,\mathrm{erfc}\left(\frac{x-Vt}{2(Dt)^{1/2}}\right) + \frac{C_0}{2}\exp\left(\frac{Vx}{D}\right)\ \mathrm{erfc}\left(\frac{x+Vt}{2(Dt)^{1/2}}\right) \qquad (5)$$

With the condition of constant flux at the entrance, the solution is:

$$f = \frac{f_0}{2}\,\mathrm{erfc}\left(\frac{x-Vt}{2(Dt)^{1/2}}\right) + \frac{f_0}{2}\exp\left(\frac{Vx}{D}\right)\ \mathrm{erfc}\left(\frac{x+Vt}{2(Dt)^{1/2}}\right) \qquad (6)$$

Then the concentration is calculated using the mass balance equation with the boundary condition:

$$C = \frac{C_0}{2}\left(\mathrm{erfc}(z_1) - \left(1 + \frac{V}{D}(x+Vt)\right)\exp\left(\frac{Vx}{D}\right)\mathrm{erfc}(z_2) + \left(\frac{V^2 t}{\pi D}\right)^{\frac{1}{2}}\exp(-{z_1}^2)\right), \qquad (7)$$

with $z_1 = \frac{x-Vt}{2(Dt)^{1/2}}$ and $z_2 = \frac{x+Vt}{2(Dt)^{1/2}}$

At the outlet face, the flux density is derived from the measurement of the effluent concentration C. The calculation is similar to the inlet flux: $f(L,t) = QC/A$. The concentration of the effluent is not equal to the concentration at the outlet inside the plug (difference between flux and concentration), such as immiscible flow where fractional flow (flux) is not equal to saturation.

Dispersion through a heterogeneous plug

In heterogeneous media, the permeability is non-uniform and spreading is mainly controlled by the variation of velocity due to permeability heterogeneity. This type of dispersion is called macrodispersion because mechanisms are at a higher scale than the pore scale. Except in artificial media such as filters or chromatographic columns, spreading due to microdispersion is generally negligible compared to macrodispersion.

The 2 or 3 -D approach

Figure 3(a) shows two examples of heterogeneous permeability fields with the calculation of flow lines (b) solving Darcy's equation for an uncompressible fluid and the simulation of injection of a tracer in black (c) [3]. The tracer is displaced along the flow lines and is transported according to the local velocities. In these simulations, microdispersion is assumed to be negligible and the tracer is a piston-type displacement along the flow line (either black and white, no grey).

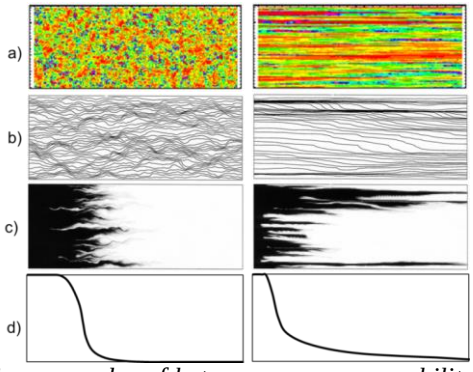

Figure 3- Two examples of heterogeneous permeability fields with the corresponding flow lines and tracer injection assuming piston-type displacement along the flow lines.

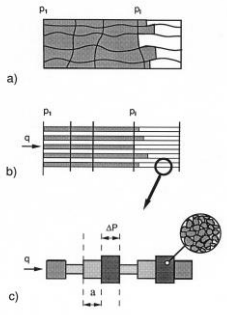

Figure 4 – Principle of stochastic calculation for spreading in a heterogeneous plug

Homogenization for 1-D flow

Macrodispersion can be described by hydrodynamic dispersion model (Eq. 2) that accounts for 2 or 3 -D local heterogeneities. However, in laboratory studies, plugs are rarely described using 2 or 3 -D permeability fields. Instead 1-D models with variables averaged over a cross-section are used, and the 1-D permeability becomes uniform, this is called "homogenization". (Figure 3 d). With the "local" plug-flow rule $f = UC$ in a 1-D

model, there will be no spreading. The information on heterogeneity is lost, and the local dispersion equation must be changed. We study below three cases of homogenization: random, stratified, and intermediate medium.

Random permeability field in the flow direction

Gelhar and Axness [4] assumed a diffusive process with proportionality between the flux and the concentration gradient (as in Fick's law) with a lognormal permeability distribution. They derived an expression for the dispersion coefficient $D = V\alpha$, where the dispersivity α is related to the variance of the logarithm of permeability K and the correlation length λ: $\alpha \propto \lambda\sigma^2_{LogK}$. However, mechanism at the origin of dispersion is not the concentration gradient but the spatial variations of the velocity field.

A model only based on hydrodynamic spreading can leave to the same result The principle is represented in Figure 4 [5]: the complex stream tubes geometry (a) is modeled by a bundle of parallel tubes (b) with variable cross-section area of elementary volumes (c). The tracer front is irregular due to randomness in the elements volumes. The spreading of the front is calculated as a function volumes linked to the permeability distribution. The result is similar to Gelhar if randomness is assumed (correlation length small compared to travelled distance) and transport equation is similar to the microdispersion case equation (4), but with a dispersion coefficient linked to the size of heterogeneity (correlation length) instead of pore size. The spreading is “diffusive” and the width of the front grows with the square root of travelled distance. This model will be noted "D" for the simulations, with the two possibilities for the inlet boundary condition: constant flux or constant concentration. The corresponding flux and concentrations are given by Eq. 5 to 7.

Homogenization: stratified medium

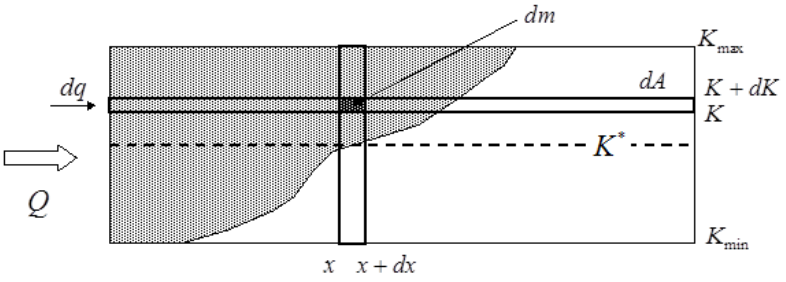

Figure 5 - Perfectly layered medium: principle of the calculation of tracer transport

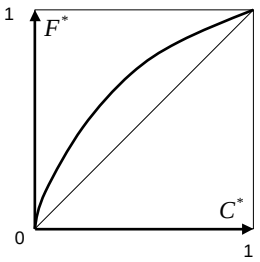

Figure 6 - relationship between flux and concentration for a stratified medium

Stratified media have been extensively used as model of heterogeneous media either for immiscible or miscible flows (for instance Fourar [6], and with a simplified model of 2 layers by Dauba et al. for carbonate studies [7]).

The heterogeneous porous medium is represented by a perfectly layered medium with a permeability distribution function $G(K)$. Microscopic dispersion is assumed to be negligible and the tracer follows the streamlines. To simplify the calculation, the layers

are re-arranged with increasing permeability (Figure 5). At a given time, the front of tracer is calculated using the flow rate in each layer and the concentration, by averaging over the cross-section:

$$C(x,t) = C_0 \int_{K^*}^{K_{max}} G(K)dK, \quad (8)$$

where $K^* = \frac{K_{eq}}{V}\frac{x}{t}$ is the lower limit of the invaded layers and K_{eq} is the effective permeability. The flux at the same position is calculated by summing the flow rates in all invaded layers:

$$F(x,t) = \int_{K^*}^{K_{max}} C_0 \; dq = C_0 Q \frac{1}{K_{eq}} \int_{K^*}^{K_{max}} K \; G(K)dK. \quad (9)$$

In the general case, there is no analytical relationship between flux and concentration, but the curve can be determined numerically by elimination of the parameter K^*. The shape is similar to the fractional flux curve for immiscible flow, but without the front discontinuity (Figure 6). The transport equation is "convective" with no second order derivative and the width of the front is proportional to travelled distance.
Fourar [6] used a lognormal permeability distribution and defined a heterogeneity factor as the ratio of the standard deviation to the effective permeability. Here we will keep the general form of the permeability distribution.

Homogenization: general case
For real rock samples, the spreading is a combination of "convective" flow in the channels of various permeabilities (preferential paths) and "diffusive" spreading inside these channels due to random heterogeneities.
One approach is to use the stochastic tube model with long-range correlations to represent the transition between diffusive and layered. Results are close to the Continuous Time Random Walk model introduced by Berkowitz [8]. Models with non-integer derivative order (between 1 for convective and 2 for diffusive) have also been proposed [9].
In this study, we tested a simpler empirical model called H-D [10], built as the sum of a convective term and a diffusive term:

$$f = \frac{f_H}{C}\left(U\,C - D\frac{\partial C}{\partial x}\right), \text{ with } f_H = \frac{C}{C+(1-C)/H}. \quad (10)$$

This approach is justified by assuming that convective effects take place at a larger scale than dispersive effects. The calculation is similar to the microdispersion case, but instead of the front velocity in the flux equation, an apparent front velocity is used since the injected fluid is moving faster.

EXPERIMENTAL RESULTS

Tracer are injected at constant concentration, using 35 and 20 g/l NaCl solutions. Several plugs have been leading to similar results. Experiment 8 described here is performed on a 5 cm long Claschasch sandstone plug, 1 inch in diameter, with porosity 0.14 and permeability 300 mD. In-situ concentration profiles are measured along the plug with 10 electrodes. The effluent concentration is measured with a conductimeter placed 5 cm from

the outlet face. Injection is performed through a spiral groove, flushed before the beginning of the experiment. Injection rate is 10 cc/h with a Pharmacia pump. Temperature is controlled at 0.2 °C accuracy (ion conductivity is strongly dependent on temperature).

Effluents

The measured effluent flux normalized between 0 and 1 is plotted in Figure 7 as function of dimensionless time (unity corresponds to the time needed to displace the pore volume).

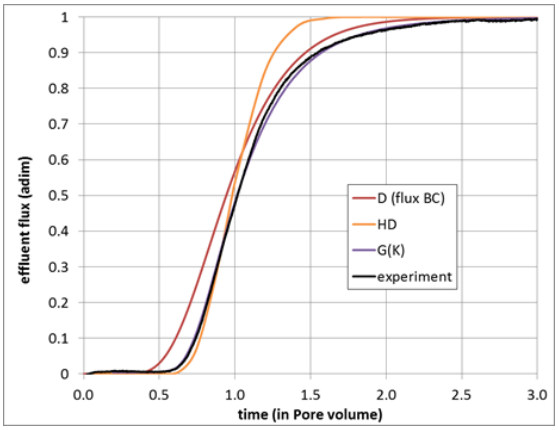

Figure 7 - Effluent flux profiles: experiment and models.

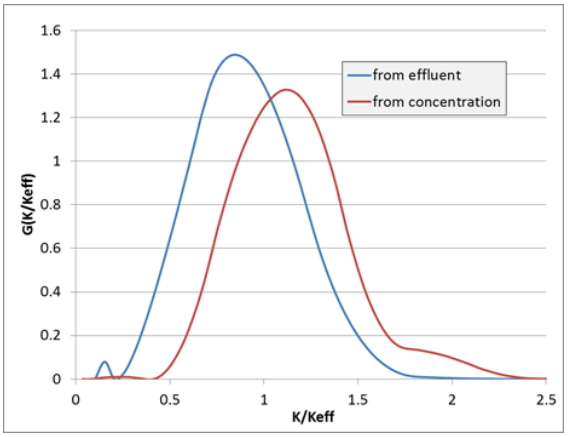

Figure 8 – Permeability distribution G(K) calculated from effluent flux and in-situ concentrations.

For the stratified model, the permeability distribution "from effluent" is derived by plotting the experimental flux (figure 7) as a function of x/t and calculating $G(K)$ after fitting by spline functions, following Eq. 9. The G(K) "from concentration" is calculated from the measured concentration using Eq. 8. The results are plotted in Figure 8 in dimensionless form. Curves noted D, HD, G(K) are best fits with the corresponding models (models defined below).

Concentration profiles

Only 5 profiles over the 10 measured are represented in Figure 9 for better readability of the figures. Symbols represent experiments and the solid lines are the results of the 4 models using CYDAR™:

- D model with the two boundary conditions at entrance: constant concentration (conc. BC, Eq. 5) or constant flux (flux BC, Eq. 7)
- HD model with convective and dispersive terms (Eq. 10), manually adjusted for the best fit.
- Stratified model with G(K) calculated using Eq. 10. In this equation, the variable is K^* proportional to x/t. Therefore, all concentration profiles are plotted as function of the scaling variable x/t and data are fitted using splines functions (Figure 10). The permeability distribution $G(K)$ derived from concentration profiles is plotted in Figure 8 for comparison to the value derived from the effluent flux.

In Figure 10, we have also plotted the concentration profiles for the model D with the scaling variable $(x - Vt)/\sqrt{t}$. If the experiment follows the model D, all points should collapse on the same curve.

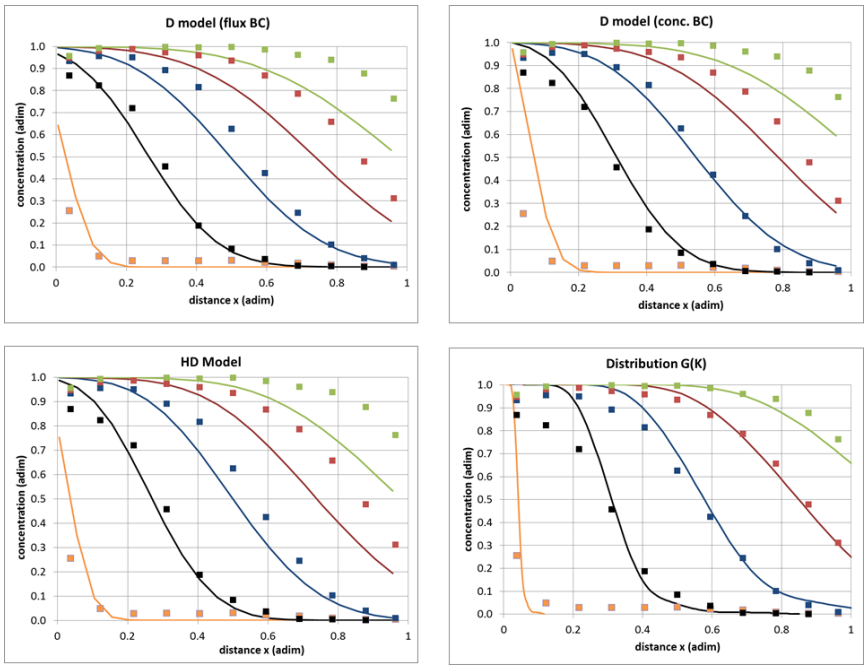

Figure 9 – In situ concentration profiles measured along the plug at different times. Symbols represent the experiment and the solid lines are the results of the various models at the same times. For the flux and concentration D model, D= 0.05 (dimensionless). For the HD model, D=0.025 and H=1.1.

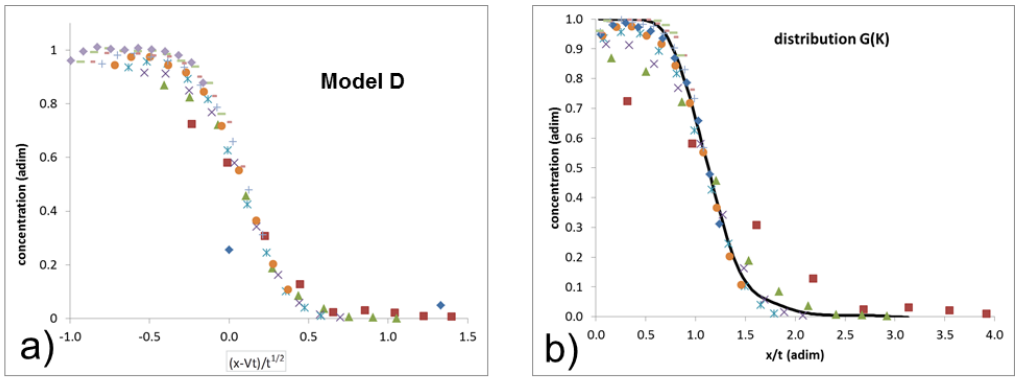

Figure 10 – a) Scaling laws for the measured in-situ concentration profiles for the D model (scaling in $x - Vt/\sqrt{t}$) - b) the stratified G(K) model (scaling in x/t).

DISCUSSION

Effluent profiles

Models D and HD cannot reproduce the dissymmetry and the long tail of the effluent flux production accurately (Figure 7). 2-D numerical simulations performed on heterogeneous

permeability field with intermediate correlation lengths permeability field show that the injected fluid starts to flow in permeable zones of the medium (channeling), leading to a fast displacement. At the end of the displacement, the injected fluid flows in much lower permeability zones and the production is slower, explaining the dissymetry of the curve. Recently Zik et al. [11] used a model involving exchange by molecular diffusion between flowing and stagnant zones (model generally called Coats and Smith). This model allows the representation of long tails by diffusion, but the representation of the concentration profiles have not been experimentally verified. From the estimate of the diffusion time scale, this effect might be valid in chromatographic columns, but comes into play at a different scale for displacement in heterogeneous plugs. The agreement between experiments and results of G(K) model is good since this distribution is calculated from the effluent. The small differences are introduced by the fit with splines functions.

Concentration profiles

1) From Figure 9, we see that the best fit is obtained with the stratified model, using the G(K) permeability distribution. However, the first profiles are not well represented; the model gives the maximum concentration in contradiction with the experiment. This discrepancy is also visible in Figure 10, where the brown squares represent the first profile. This discrepancy could be an experimental artifact during flushing of the inlet end-piece spiral, with displacing fluid entering partially into the plug.

2) D model with the flux boundary condition is the only model that represents the increase of concentration at the entrance. However, after a small distance, both boundary conditions give similar results.

3) Scaling laws for the D and G(K) models (Figure 10) lead to similar results. Therefore this test cannot efficiently discriminate between models.

4) The G(K) distributions determined from the flux and the one determined from the concentration (Figure 8) are different, although G(K) should theoretically be unique. The observed difference may arise from a delay in effluent production in the outlet spiral. The volume of the outlet spiral is not negligible (0.3 cc compared to 5 cc of pore volume). This dead-volume introduces a delay that would lead to a lower observed permeability.

CONCLUSION

When used as local input in 3-D simulations, the Darcy-scale approach can accurately describe the plug-scale spreading related to permeability heterogeneity. In a 3-D heterogeneous medium, even a displacement started as piston-type at the Darcy-scale leads to a dispersion behavior due to the spatial differences in velocities.

- We have presented several up-scaled (or homogenized) models:microdispersion, macrodispersion, convective channeling).
- Our results confirm previously published results that channeling convective models are more suitable than the standard dispersion models.
- The best result is obtained by calculating a permeability distribution function $G(K)$ in a stratified model. This model captures both the long tail in the effluent production and the in-situ concentration profiles.

REFERENCES

[1] H.-O. Pfannkuch, «Contribution à l'étude des déplacements de fluides miscibles dans un milieu poreux», Revue de l'Institut Français du Pétrole et annales des combustibles liquides, vol. 28, pp. 1-54, 1963.

[2] J. J. a. C. M. A. Fried, «Dispersion in Porous Media», Advances in Hydroscience, vol. 7, pp. 169-282, 1971.

[3] R. Lenormand and M. Thiele, «Homogeneization of Flow equations with viscous Instabilities: Numerical Validation of the MHD model», European Conference on the Mathematics of Oil recovery (ECMOR V), 1996.

[4] L. W. Gelhar and C. L. Axness, «Three-dimensional stochastic analysis of macrodispersion in aquifers», Wat. Resour. Res., vol. 19, pp. 161-180, 1983.

[5] R. Lenormand, «A stream tube model for miscible flow. Part 1: Macrodispersion in homogeneous porous media», IEA Collaborative Project on Enhanced oil Recovery, Salzburg, Austria, 1993.

[6] M. Fourar, «Characterization of heterogeneities at the core-scale using the equivalent stratified porous medium approach», SCA2006-49, Trondheim, Norway, 2006.

[7] C. Dauba, G. Hamon, M. Quintard and F. and Cherblanc, «Identification of parallel heterogeneities with miscible displacements» SCA paper 9933,, Golden, USA, 1999.

[8] B. a. S. H. Berkowitz, «The role of probabilistic approaches to transport theory in heterogeneous media», Transport in Porous Media, vol. 42, pp. 241-263, 2001.

[9] R. Lenormand, «Use of Fractional Derivatives for Fluid Flow in Heterogeneous Media», 3rd European Conference on the Mathematics of Oil Recovery, 1992.

[10] R. Lenormand, «Determining Flow Equations from Stochastic Properties of a Permeability Field», SPE Journal, vol. 1, 1996.

[11] B. Vik, K. Djurhuus, D. Doublet, K. Spildo and A. Skauge, «Characterization of vuggy carbonates by miscible process», SCA2008-28, Abu Dhabi UAE, 2008.

[12] F. A. L. Dullien, «Porous Media: Fluid Transport and Pore Structure», Academic Press ed., San Diego, California, 1992, p. 574.

[13] K. Sorbie, H. Zhang and N. Tsibuklis, «Linear viscous fingering: new experimental results, direct simulation and the evaluation of averaged models», Chemical engineering science, vol. 50, n° %14, pp. 601-616, 1995.

[14] A. Koval, «A Method for Predicting the Performance of Unstable Miscible Displacement in Heterogeneous Media», SPE Journal, pp. 145-154, June 1963.

[15] M. Sahimi, M. R. Rasaei and M. Haghighi, «Gas injection and fingering in porous media», Gas Transport in Porous Media, C. Ho and S. Webb, Eds., Springer, 2006, pp. 133-168.

[16] M. Fourar, G. Konan, C. Fichen, E. Rosenberg, P. Egermann and R. Lenormand, «Tracer tests for various carbonate cores using X-Ray CT», SCA 2005-56, Society of Core Analysts, Toronto, Canada, 2005.

[17] A. Fick, «Ueber Diffusion», Annalen der Physik, vol. 170, pp. 59-86, 1855.

[18] K. H. Coats and B. D. Smith, «Dead-end pore volume and dispersion in porous media», Society of Petroleum Journal, pp. 73-84, 1964.

[19] G. Taylor, «Dispersion of soluble matter in solvent flowing slowly through a tube», Proceedings of the Royal Society of London, Series A, Mathematical and Physical Sciences, vol. 219, pp. 186-203, August 1953.

[20] G. Taylor, «The Dispersion of Matter in Turbulent Flow through a Pipe», Proceedings of the Royal Society of London A: Mathematical, Physical and Engineering Sciences, The Royal Society, vol. 223, pp. 446-468, 1954.

[21] R. Aris, «On the Dispersion of a Solute in a Fluid Flowing through a Tube», Proceedings of the Royal Society of London A: Mathematical, Physical and Engineering Sciences, The Royal Society, vol. 235, pp. 67-77, 1956.

EFFECT OF THE PRESENCE OF INTERSTITIAL BRINE ON GAS-OIL CAPILLARY PRESSURE

F. Pairoys, D. Simons, K. Bohn, M. Alexander, V. Odu, R. DeLeon, J. Ramos
Schlumberger Reservoir Laboratories, Houston, Texas, 77041, United States

This paper was prepared for presentation at the International Symposium of the Society of Core Analysts held in Newfoundland and Labrador, Canada, 16-20 August, 2015

ABSTRACT

Gas-oil centrifuge capillary pressure experiments were performed on two outcrop samples in the presence and absence of a third immobile phase in order to highlight effects on final recovery.

Two core plugs with different porosity and permeability properties were respectively drilled from an Indiana limestone block and Berea sandstone block. They were solvent cleaned and measured for routine core analysis before starting the SCAL program. Two centrifuge capillary pressure experiments were run on the samples at different saturation conditions. Both samples were first saturated with brine and displaced by oil up to irreducible brine saturation using centrifuge (primary drainage). Gas-oil gravity drainage was then performed using multistep centrifuge method for capillary pressure measurement. The samples were then cleaned, measured again for basic properties, and saturated with oil. The second experiment was a new gas-oil multistep centrifuge drainage using same capillary pressure steps than in the first test, but directly performed on the samples initially saturated with oil.

The objective was to highlight the effect of the interstitial brine on the capillary pressure curves and on the oil recovery. It is finally shown that the use of only two phase capillary pressure may result in an invalid capillary pressure relationship between the two mobile fluids in the presence of a third. The Hassler-Brunner method for the determination of the local capillary pressure curves in presence and absence of a third phase is discussed. The study also confirms the necessity of using the Forbes method to avoid inaccurate data results.

INTRODUCTION

Almost all reservoirs contain three fluid phases within their pore network, respectively water, oil and gas. Water and oil are immiscible together, whereas gas can be miscible with oil or/and can be dissolved in the aqueous phase according to the reservoir conditions and fluid properties. Assuming that miscibility and dissolution are not involved, the three phases may be mobile or static according to their saturations; in a three phase system, there is at least one mobile phase. The capillary pressure P_c is an important parameter for the reservoir engineers who are using this petrophysical input in their numerical simulations, in addition to the relative permeability K_r, to anticipate the

reservoir behavior. Capillary pressure P_c is a two-phase phenomenon resulting from a discontinuity in pressure across the interface between two immiscible fluids. Capillary pressure is affected by a multitude of parameters; fluid properties, saturation, saturation history [1], pore size, pore shape, pore distribution, tortuosity, wettability [4]. It is evident that oil recovery in a reservoir is affected by the capillary pressure P_c since trapping mechanisms depends on the listed parameters.

Gravity drainage is the drainage process of gas displacing oil in a reservoir or sample. In certain cases, it is an efficient recovery mechanism which can result in very low residual oil saturation compared to waterflooding displacements [2]. Three phase capillary pressure test as described by Kantzas *et al.* [3] with three mobile phases is not considered in this study; two phase -gas/oil- capillary pressure experiments in presence or absence of a third immobile phase -brine- are investigated. Hassler *et al.* [4] and other others such as Kyte *et al.* [5] or Hagoort [6] concluded that the gravity drainage could be considered as two phase flow displacement at low water irreducible saturation. There is a lack in experimental investigation of the effect of connate water on the final oil recovery during gravity drainage. Dumore [7] showed that the presence of connate water during gravity drainage test in permeable medium leads to very low residual saturations due to film flow [8]. Hagoort [6] observed a decrease in residual oil saturation with an increase of water saturation due to more streamlined flow channels. One study from Carlson [9] showed that the presence of irreducible water had no effect on the residual oil saturation. Earlier, a same observation was made by Tiffin and Yellig [10].

The purpose of this paper is to compare gas-oil capillary pressure in presence or absence of connate water during a multistep centrifuge experiments. The centrifuge tests were performed at ambient conditions and immiscible conditions. Because capillary pressure is, *inter alia*, affected by pore size, two different rock types were tested to compare the effect of irreducible water on the final oil recovery during drainage cycle. The Hassler-Brunner method [4] to calculate the local capillary pressure at the inlet of the core samples is also discussed in this paper. The core analysis software CYDAR was used for data processing.

BACKGROUND

In centrifuge gravity drainage experiments, the fluid flow is controlled by the density difference between fluids. The local velocity u for each fluid is given by the generalized Darcy's law:

$$u = -\frac{KK_r}{\mu}\left(\frac{\partial P}{\partial x} - \rho\omega^2 r\right) \quad (1)$$

With K the absolute permeability in m^2, K_r the relative permeability, μ the fluid viscosity in Pa.s, P the fluid pressure in Pa, ρ the fluid density in Kg/m^3, ω the rotational speed in rad/s and r the distance between the position on the rock sample and the centrifuge axis in m.

The capillary pressure P_{ce} at the inlet of a sample during a centrifuge experiment can be expressed as follows:

$$P_{ce} = \frac{1}{2}\Delta\rho\omega^2\left(r_2^2 - r_1^2\right) \quad (2)$$

With P_{ce} the inlet capillary pressure in Pa, $\Delta\rho$ the density contrast between the two fluids in Kg/m^3, r_2 the distance between the outlet of the sample and the centrifuge axis in m, and r_1 the distance between the inlet of the sample and the centrifuge axis in m.
A sketch of rock sample loaded in centrifuge core holder is shown below:

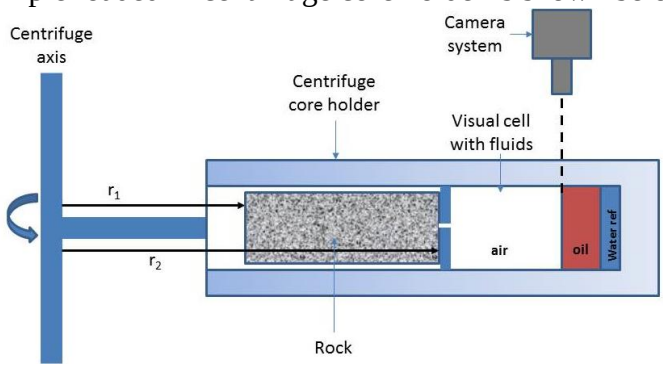

Figure 1: Sketch of core plug loaded in centrifuge core holder

During a multi-speed experiment, when the production of the displaced phase ceases at the end of each rotational speed, the average saturation <*S*> can be calculated from the effluent production. <*S*> is linked to the local inlet capillary pressure P_{ce} at equilibrium by the following Hassler and Brunner equation:

$$\langle S(P_{ce})\rangle = \frac{1}{r_2 - r_1}\int_{r_1}^{r_2} S(P_{ce})dr \quad (3)$$

The Hassler-Brunner method [4] is commonly used in the industry to approximate the local saturation at the capillary pressure P_{ce} using the following equation:

$$S(P_{ce}) = \frac{d}{dP_{ce}}\left[P_{ce} < S(P_{ce})>\right] \quad (4)$$

The differentiation of this equation was performed by differentiating a modified hyperbolic function which best fits the product P_{ce}<$S(P_{ce})$>. The Forbes method [11] after smoothing the data [13] was used when the Hassler-Brunner method did not give satisfying local capillary pressure curve.

The Hassler-Brunner method is valid for short cores spinning far enough from the centrifuge axis to assume that the variation of the centrifugal field is negligible; in this study, the ratio r_1/r_2 in Figure 1 was found to be equal to 0.6. The maximum Bond number N_b obtained at the highest speed was less than 10^{-4}.

ROCKS, FLUIDS AND EXPERIMENTAL SETUP

Two rock types were tested respectively Berea sandstone and Indiana limestone. Berea sandstone is unimodal in pore and pore throat sizes whereas Indiana limestone is bimodal. It is confirmed by mercury injection capillary pressure (MICP) and NMR T_2 distributions obtained respectively from two rock chips and two 100% brine saturated core samples cut from each block (Figure 2):

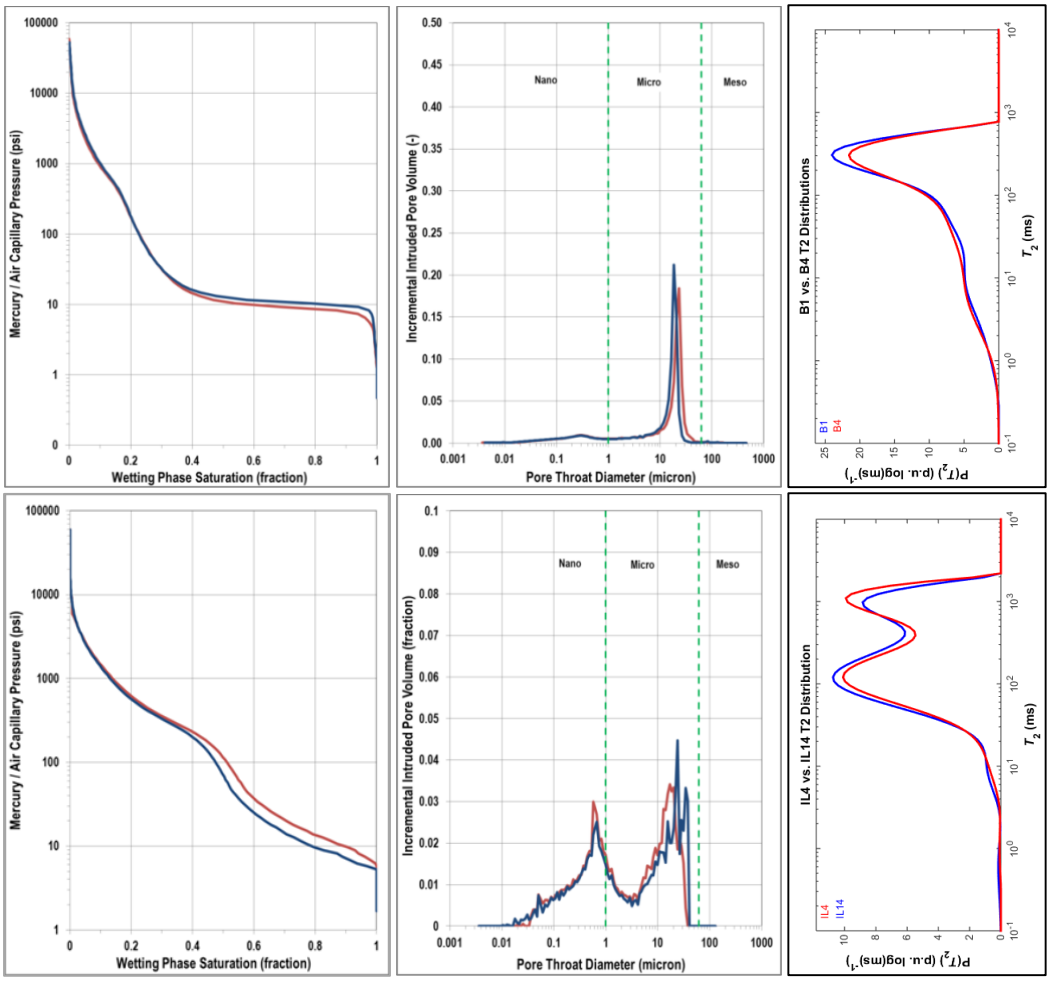

Figure 2: Capillary pressure (left), pore throat size distribution (middle) and NMR T_2 distribution (right)

Figure 2 shows that the two rock types have different signatures as expected and also shows that measurements on twin plugs obtained from the same block are almost identical. The two samples tested in this study came from the same blocks as the samples tested for MICP and T_2 NMR from Figure 2. There is a clear correlation between the NMR pore size distribution and the MICP pore throat distribution for each rock type. Both MICP and NMR highlight respectively the unimodal pore structure of the Berea sandstone and bimodal pore structure of the Indiana limestone. Additional rock information obtained from the same Berea sandstone and Indiana limestone blocks can be

found in Pairoys *et al.* [14].

Several core plugs were obtained from the Berea sandstone Indiana limestone blocks, but only data results of sample B2 (Berea sandstone) and sample IL20 (Indiana limestone) are reported. After having Soxhlet cleaned the samples, routine core analysis was performed on the samples. Data results are listed in Table 1:

Table 1: Dry core plug properties

Sample Id	Type	ρ_g (g/cc)	ϕ (%)	PV (cc)	K_g (mD)	K_{kl} (mD)
B2	Berea sandstone	2.65	25.23	10.473	735.7	727.8
IL20	Indiana limestone	2.69	15.43	6.772	31.8	30.4

Fluid properties (brine, oil and air) at ambient temperature and atmospheric pressure are reported in Table 2:

Table 2: Fluid properties

Fluid	Salinity (Kppm NaCl)	Density ρ (g/cc)	Viscosity μ (cp)
Brine	200	1.130	1.345
Isopar-L	-	0.762	2.049
Air	-	0.001	0.018

The capillary pressure experiments were run with an Ultra Rock Centrifuge from Beckman allowing monitoring fluid production using a camera system. The two samples were first saturated with Isopar-L before being loaded in drainage centrifuge cells and tested for multistep capillary pressure P_c. Ten P_c steps were applied, from 0 to 84 psi.
At the end of the drainage cycle, the samples were Soxhlet cleaned using Toluene and Methanol, dried, and re-measured for gas permeability and porosity. Because the rock properties did not change after the first P_c test and cleaning, they were used again for the second P_c test in presence of connate water. The two cleaned samples were then saturated with brine, loaded in drainage cells for brine-oil primary drainage up to irreducible water saturation S_{wi} using one single maximum step (8000 rpm – around 100 psi for all samples). Then, they were tested in the same drainage core holders for gas-oil displacement. They were spun at the exact same capillary pressure steps than those applied during the first test with samples initially saturated with oil.

EXPERIMENTAL RESULTS

Centrifuge gas-oil capillary pressure experiments were run on the two samples, IL20 and B2, initially 100% saturated with oil and later saturated with oil at irreducible water saturation S_{wi}. The main objective is to see if the capillary pressures curves and productions are affected by the presence of irreducible water saturation.

Gas-Oil Drainage at Initial Oil Saturation S_o=100%:
The samples B2 and IL20 were directly tested for gas-oil multistep capillary pressure. Ten capillary pressure steps were applied; they were chosen according to a preliminary designing test on sample IL20 100% oil saturated only (using CYDAR software). The average saturations were fitted with a bi-exponential curve to obtain the average saturation at equilibrium. Figure 3 represents the oil production curves during the centrifuge P_c experiment.

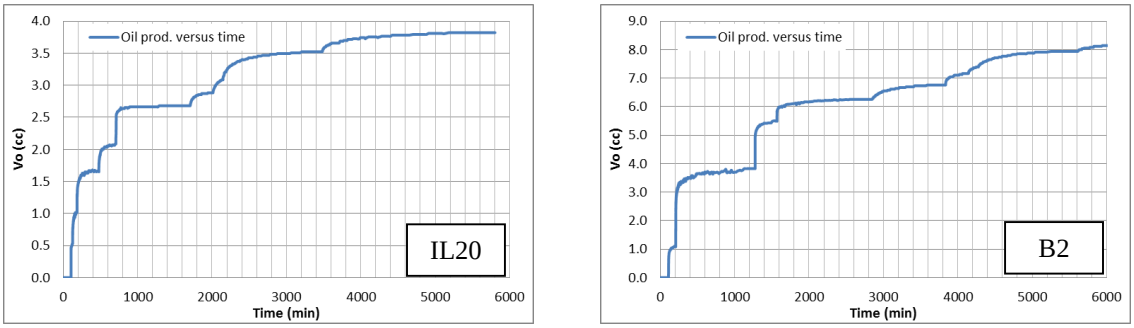

Figure 3: Drainage oil productions (raw data) for samples IL20 (left) and B2 (right)

Sample IL20: A total of 3.82 cc of oil was produced, leading to residual oil saturation S_{or} close to 43.6%. S_{or} was found to be high due to the presence of the oil-filled nanopore population highlighted in Figure 2; at the applied pressure steps, it is not possible to displace the oil in these tiny pores. The production curve also shows that equilibrium was not completely reached at all P_c steps. The oil production was fitted with multistep bi-exponential function to obtain the saturation at equilibrium.

Sample B2: A total of 8.40 cc of oil was produced from sample B2. The residual oil saturation was found to be equal to 19.8%, significantly lower than for the Indiana limestone IL20; these two rocks have different pore size and throat signatures, partially responsible for this difference.

In Figure 4, the capillary pressures P_c versus average oil saturations S_o at equilibrium are plotted for both samples (in blue). Modified hyperbolic functions were used to fit the capillary pressure curves before calculating the local saturations (in red). Local capillary pressure curve is obtained from Hassler and Brunner method in green). As QC technique, the average saturations $<S_o>$ were recalculated (in purple) and compared to the analytical P_c curves (in red) in order to assess the Hassler-Brunner method.

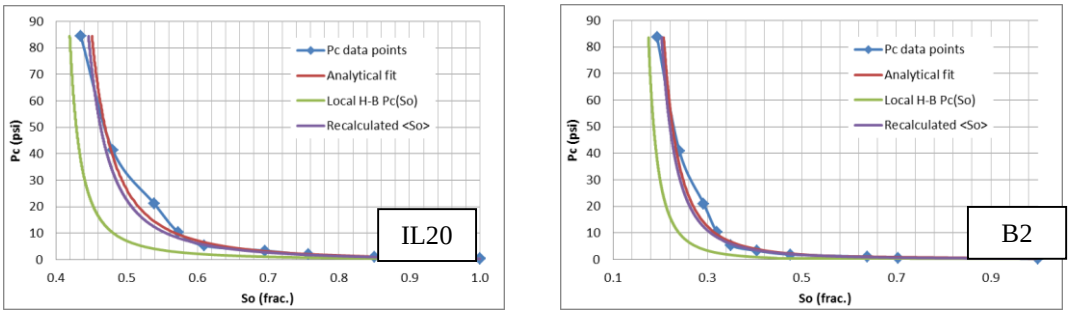

Figure 4: Measured, analytical fit, local Hassler-Brunner and recalculated capillary pressure curves

Figure 4 shows that the Hassler and Brunner method provides more acceptable result for sample B2 than for sample IL20; the recalculated average saturation matches well the analytical fitted curve. The exact same experimental protocol was performed on the same cores but at irreducible saturation S_{wi} as initial condition.

Gas-Oil Drainage at Initial Irreducible Water Saturation S_{wi}:

For the sake of more clarity, an asterisk * was added to the plug number containing irreducible water at initial conditions. At the end of the previous test, samples were Soxhlet cleaned, dried and measured for routine core analysis; porosity and permeability were found were close to the ones reported in Table 1. After brine saturation of sample B2* and IL20*, a primary drainage, oil displacing brine, was performed. They were spun in centrifuge at a single speed of 8,000 rpm, so approximatively 100 psi of oil-brine capillary pressure P_c up to irreducible water saturation S_{wi}. Cores were also flipped to get a more uniform fluid distribution along the samples [15]. The irreducible water saturation S_{wi} for sample IL20* was found to be equal to 36.1% whereas S_{wi} for sample B2* was found to be equal to 16.6%. The presence of nanopores (Figure 2) explains the high S_{wi} value for sample IL20*. The samples were then loaded in the drainage centrifuge cells for air-oil multistep capillary pressure experiment. Tests were run with the same capillary pressure steps than those applied on the samples initially saturated with oil. No brine production was observed during the gas-oil centrifuge P_c experiments.

IL20*

The same increasing capillary pressure steps were applied during the gas-oil drainage displacement of sample IL20*.

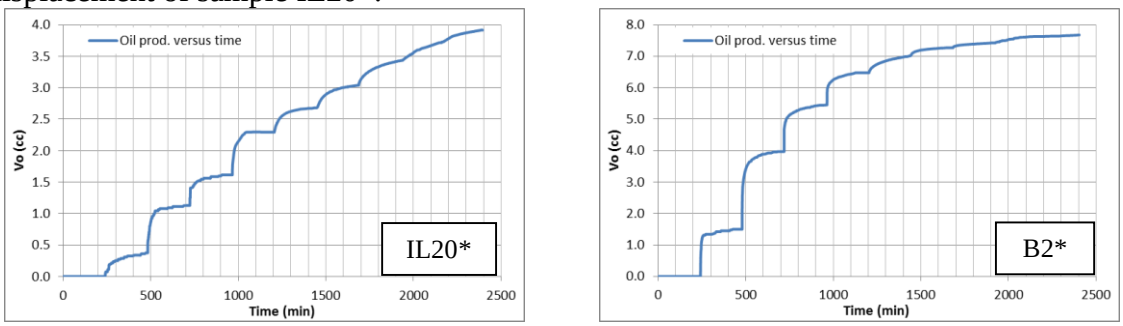

Figure 5: Drainage oil productions (raw data) for sample IL20* (left) and B2* (right)

Figure 5 represents the oil production versus time during the multistep centrifuge experiment with samples initially at S_{wi}. The production curves show that equilibrium was not completely reached at all P_c steps, leading to an overestimation of the residual oil saturation S_{or}. The same fitting process than the one described on the experiment with samples initially saturated with oil was used to obtain the saturation at equilibrium.

Sample IL20*: A total of 3.92 cc of oil was produced, leading to residual oil saturation S_{or} close to 6.1%. The produced volume was found to be almost the same than the one obtained on the same sample initially saturated with oil. It is explained by the bimodal porosity system of this limestone rock. Only oil occupying the micro-pore population highlighted in Figure 2 can be mobilized and produced. The main difference is the final recovery of the original oil in place (OOIP), which is obviously much higher when the water occupied the small pores (nano-pores population for this Indiana limestone rock).

Sample B2*: A total of 7.68 cc of oil was produced from sample B2, leading to 10.1% of residual oil saturation. The oil production was found to be less than the one obtained for the same sample at 100% oil initial condition. The capillary pressure P_c versus average oil saturation S_o at equilibrium is then plotted for both samples (blue curve in Figure 4):

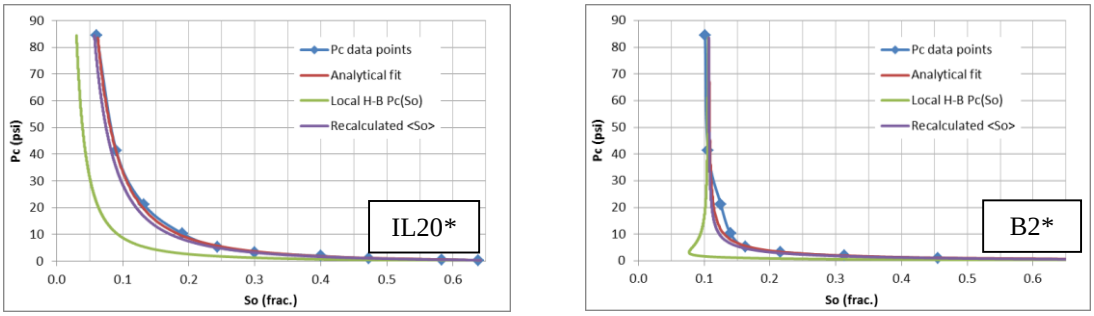

Figure 6: Measured, analytical fit, local H-B and recalculated capillary pressure curves

As observed in Figure 4 for samples initially saturated with oil, the back calculation of average oil saturation $<S_o>$ for sample IL20* does not perfectly fit the analytical curve used for fitting the P_c data points. The non-monotonic local P_c of sample B2* obtained with the Hassler-Brunner method may be explained by the choice of the modified hyperbolic fitting function and the imperfect equilibrium of the P_c data points. Despite of this observation, an acceptable match between analytical data fit P_c (red) and recalculated P_c at average saturation (purple) is obtained for sample B2*.

For the local P_c calculation, whatever the initial conditions (with or without presence of irreducible water saturation), the Hassler and Brunner method seems more appropriate for the sandstone sample B2/B2*; the match between the analytical function used to fit the P_c data points and the recalculated $<S_o>$ function for the Indiana limestone is less good than the match of the same curves for the Berea sandstone. The reason could be the bimodal character of the limestone rock. Because of the non-monotonic Hassler-Brunner local P_c curve of sample B2* shown in Figure 6, the Forbes method with initial splines fit was

tested (Figure 7):

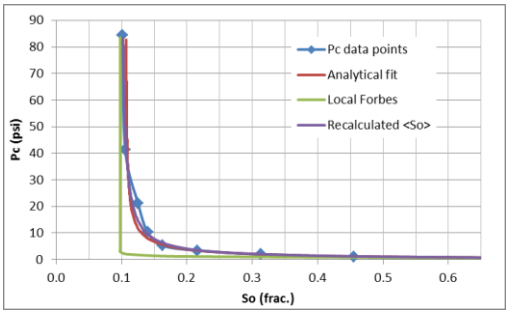

Figure 7: Measured, analytical fit, Forbes-splines and recalculated <.S_o> P_c curves for sample B2*

In addition to the observed monotonic local P_c curve, the match between the analytical and recalculated P_c was improved using Forbes method with splines. All capillary pressure curves P_c were then normalized for saturation (reduced oil saturation S_o* on X axis), plotted on a same graph, and compared (Figure 8).

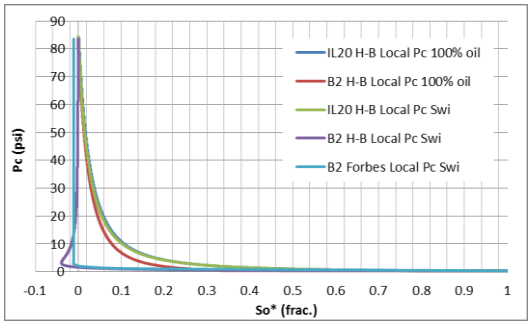

Figure 8: Comparison of local P_c curves for sample IL 20 and B2, S_o=100% versus initial Swi

Figure 8 shows that, whatever presence or absence of irreducible water, the local capillary pressure curves of IL20/IL20* are overlapping. Using two phase capillary pressure centrifuge test without connate water may be representative of the two phase capillary pressure with connate water for this sample. However, for sample B2/B2*, the capillary pressure curves are different. In that case, the use of two phase capillary pressure without connate water may not be representative of the two phase capillary pressure with connate water. One of the reasons may be the change of gas-oil interface curvature in presence of irreducible water.

Additional tests need to be performed to confirm that the Hassler-Brunner outflow condition was not violated due to high Bond number N_b, invalid constant centrifugal field condition (geometry), or presence of irreducible water at the outlet of the samples. NMR or X-ray measurements before and after the gas-oil drainage displacement could help in ensuring that the outlet saturation does not change. The failure of Hassler-Brunner method for obtaining reliable local P_c curve for B2* may also be due to one or combination of the enounced factors, showing the complexity of such experiments.

Recovery Analysis:
Table 3 compares the productions at different initial conditions, with and without irreducible water saturation. For the sake of more clarity, an asterisk * was added to the plug number containing irreducible water at initial conditions.

Table 3: Summary of production according to the initial conditions

Sample Id	*PV* (cc)	S_{wi} (frac.)	S_o (frac.)	V_o prod. (cc)	ORF (%)	S_{or} (frac.)	S_g (frac.)	$K_g(S_{or})$ (mD)
IL20	6.77	0.000	1.000	3.82	56.4	0.436	0.564	32.9
IL20*	6.77	0.361	0.639	3.92	90.5	0.061	0.579	31.8
B2	10.47	0.000	1.000	8.40	80.2	0.198	0.802	747.8
B2*	10.47	0.166	0.834	7.68	87.9	0.101	0.734	727.0

Sample IL20/IL20*:
The presence of irreducible water S_{wi} in IL20* results in very low residual oil saturation S_{or} close to 6.1%. It can be explained by the rock water wettability. First, the small pores are initially saturated with brine; no oil could displace the water in the nanopore zone. Then, water spreads on the pore wall, making easy the oil displacement by gas in the large pores. It also explains the large oil recovery factor ORF of IL20* with almost 90.5% of the original oil in place produced by gas. The gravity drainage in IL20 (no S_{wi}) is much less efficient. The main reason is that oil initially trapped in nanopores (see Figure 2) cannot be mobilized by gas at the applied capillary pressure steps, in addition to the oil wettability of the rock in presence of oil and gas only (no lubrication effect like IL20*). Around 56.4% of oil in place was recovered; this value can be considered low compared to the generally high recovery (>60% from case histories) observed during gravity drainage at secondary conditions (no waterflooding before gas injection in oil reservoirs).

Sample B2/B2*:
The residual oil saturation and recovery factor of sample B2/B2* are less affected by the presence or absence of irreducible water saturation S_{wi} compared to IL20/IL20*. One of the reasons is the unimodal signature of the pore space. The oil recovery factor is higher in presence of connate water. It is also observed that the values at S_{or} of B2 and IL20 are in the same range but slightly higher than the values of S_{wi} of B2* and IL20*; same range because the capillary trapping mechanism is similar for both tests (B2 being oil-wet in presence of gas only and B2* being water-wet in presence of gas and oil) and slightly higher gas/oil S_{or} than brine/oil S_{wi} because of the difference in maximum applied P_c (100 psi for oil displacing brine up to S_{wi} and 85 psi for gas displacing oil up to S_{or}).
Steady-state gas permeability measurements were performed on the samples at the end of the gas-oil drainage to obtain the relative permeability k_g at S_{or}. Results are reported in Table 3 as well. It shows that for sample IL20/IL20*, the presence of a third immobile phase does not change the effective permeability to gas; both values at S_{or} and at S_{or} and S_{wi} are similar. One of the reasons is that, in presence or absence of irreducible water, the

couple IL20/IL20* and the couple B2/B2* have close final gas saturation S_g; whatever liquids (oil or water + oil) are inside the rock, they do not affect the flow of the strongly non-wetting phase such as gas. The effective gas permeabilities are also very close to the absolute gas permeabilities (Table 1). The residual oil and irreducible water do not hamper gas flow because gas is strongly non-wetting the rock compared to liquids. Effective permeability values are even slightly higher than the absolute one; this phenomenon is known as lubrication effect [16].

At the end of the experiment, the samples initially saturated with brine were Dean Stark extracted to validate the irreducible water saturation S_{wi} obtained by material balance during the primary drainage. Irreducible water saturation S_{wi} obtained by material balance during the centrifuge tests and irreducible water saturation obtained by Dean-Stark were found to be very close, ensuring that no connate water was dried or produced during the gas injection. Moreover, to ensure that the samples were not damaged during the centrifuge tests, porosity and absolute gas permeability were measured; no significant rock property changes were observed (Table 4).

Table 4: Dean Stark results and dry rock properties before and after the tests

Sample Id	Material balance S_{wi} (frac.)	Dean Stark S_{wi} (frac.)	Initial ϕ (%)	Final ϕ (%)	Initial K_g (mD)	Final K_g(mD)
B2*	0.166	0.159	25.23	25.40	735.7	728.6
IL20*	0.361	0.355	15.43	15.24	31.8	31.0

CONCLUSION

Two-phase, gas-oil, centrifuge capillary pressure measurements were performed on different rock types in presence or absence of interstitial water. Two different rock types were tested to assess the effect of pore size distribution on final oil recovery. Results of the investigation show that a third brine phase saturation can significantly change the residual oil saturation S_{or} and the oil recovery factor ORF, the shape of the capillary pressure curve and saturation distribution in the cores. It is also shown that the Hassler and Brunner method, used for determining the inlet saturation in centrifuge experiments, can be improved using Forbes method with splines. It is finally concluded that the presence of a third phase can have a significant effect in determining the capillary pressure-saturation relationships between two fluids in a three phase system. Additional work is required for validating the Hassler-Brunner outlet boundary condition using NMR or X-ray spectroscopy.

For oil recovery, the rock saturation history is an important parameter: more oil volume is obtained from samples initially saturated with oil, but higher oil recovery factor ORF is observed in presence of irreducible water. It is also very important to know the pore size/pore throat distributions to get a better understanding of the oil production scenario. The gas floods leads to low residual saturation in swept zones but poor volumetric rock sweep in the bimodal Indiana limestone sample initially saturated with oil.

REFERENCES

1. Brown, R.J.S., Fatt, I., "Capillary Pressure Investigations", *Trans. AIME*, **192**, pp. 67-74, 1951
2. Leverett, M.C., "Capillary Behavior in Porous Solids", *Trans. AIME*, **142**, pp. 152-169, 1941
3. Kantzas, A., Chatzis, I., Dullien, F.A.L., "Enhanced Oil Recovery by Inert Gas Injection", SPE/DOE Paper 17379, 1988
4. Hassler, G.L., Brunner, E., "Measurement of Capillary Pressure in Small Core Samples", *Trans. AIME* 160:114-123, 1945
5. Kyte, J.R., Stanclift, R.J. Jr., Stephan, S.C., Rapoport, L.A., "Mechanism of Water Flooding in the Presence of Free Gas", *Trans. AIME*, **207**, pp. 215-221, 1956
6. Hagoort, J., "Oil Recovery by Gravity Drainage", *SPE Journal*, pp. 139-150, June 1980
7. Dumore JM, Schools RS, "Drainage Capillary Pressure Functions and the Influence of Connate Water", SPE 4096, *SPE Journal*, pp. 437-444, October 1974
8. Nenniger, E. Jr., Storrow, J.A., "Drainage of Packed beds in Gravitational and Centrifugal-Force Fields", *AIChE*, Vol. 4, Issue 3, pp. 305-316, September 1958
9. Carlson, L.O., "Performance of Hawkins Field Unit Under Gas Drive – Pressure Maintenance Operations and Development of EOR Project", SPE/DOE paper 17324, 1988 SPE/DOE Symposium on EOR, Tulsa, Oklahoma, US, 17-20 April 1988
10. Tiffin, D.L., Yellig, W.F., "Effects of Mobile Water on Multiple-Contact Miscible Gas Displacement", *SPE Journal*, pp. 447-455, June 1983
11. Forbes, P., "Simple and Accurate Methods for Converting Centrifuge Data into Drainage and Imbibition Capillary Pressure Curves", Society of Core Analysts, SCA1991-07, 1991
12. Nordtved, J.E., Kolitvelt, K., "Capillary Presure Curves from Centrifuge Data by Use of Spline Functions", *SPERE*, pp. 497-501, November 1991
13. Bauget, F., Gautier, S., Lenormand, R., Samouillet, A., "Gas-Liquid Relative Permeability from One-Step and Multi-Step Centrifuge Experiments", Society of Core Analysts, SCA2012-13, Aberdeen, Scotland, 27-30 August, 2012
14. Pairoys, F., Nadeev, A., Kirkman, K., Poole, G., Bohn, K., Alexander, M., Radwan, N., Abdallah, W., Akbar, M., "Assessment of Sidewall Cores for Routine and Special Core Analyses", Society of Core Analysts, SCA2015-A003, Newfoundland and Labrador, Canada, 16-20 August 2015, Scotland, 27-30 August, 2012
15. Pairoys, F., Al-Zoukani, A., Nicot, B., Valori, A., Ali, F., Zhang, T., Ligneul, P., "Multi-Physics Approach for Aging Assessment of Carbonate Rocks", SPE 149080, Society of Petroleum Engineer, ATSE, Al-Khobar, Saudi Arabia, 15-18 May 2011
16. Berg, S., Cense, A.W., Hofman, J.P., Smits, R.M.N., "Flow in Porous Media with Slip Boundary Condition", Society of Core Analysts, SCA2007-13, Calgary, Canada, 10-12 September 2007

REMOVAL OF MUD COMPONENTS FROM RESERVOIR SANDSTONE ROCKS

Ingebret Fjelde, Aruoture Voke Omekeh and Mona Wetrhus Minde
International Research Institute of Stavanger (IRIS)

This paper was prepared for presentation at the International Symposium of the Society of Core Analysts held in St. John's Newfoundland and Labrador, Canada, 16-21 August, 2015

ABSTRACT

Laboratory experiments using reservoir rock/oil are used extensively to estimate reservoir oil recovery processes. Mud contamination of the reservoir rock can change the flow conditions by changing the rock surface chemistry and permeability. Representative data can then only be generated if mud contamination is removed. The objective for study was to investigate the removal of these mud components during cleaning of sandstone reservoir core plugs. Effluent samples were analysed, and wettability of cleaned core plugs was characterized. Samples of core plugs after cleaning and after water flooding were analysed by scanning electron microscopy (SEM) and the oil residue in cleaned reservoir rock was analysed by gas chromatography.

When formation water (FW) was injected to uncleaned or solvent cleaned reservoir core plugs with potential contamination by water-based mud, ions from the mud were produced for relatively long periods. SEM analyses showed that polymers, clay and barite from the mud were present in the pores of cleaned high permeability reservoir core plugs. Even after water flooding, mud components were found in this rock. Polymers and particles can reduce the permeability of the rock. Invasion of clay from the mud will increase the surface area and ion-exchange capacity of the rock. Clay invasion and/or wrong FW composition can affect the established wettability and thereby the estimated potential for water flooding and EOR methods.

Contamination of sandstone rocks with oil-based mud was shown to alter the wettability. Emulsifiers from the mud were slowly removed during cleaning by crude oil injection. The cleaning procedure for reservoir rock with potential oil-based mud contamination, was shown to affect the measured capillary desaturation curve.

Mud components should be removed during cleaning of the reservoir core plugs, otherwise the core plugs should not be used. Analyses of effluent samples for these components during core plug preparation should be included in the standard preparation procedures. For some mud components, chemical analysis can be challenging. The cleaning procedure should also be evaluated for the actual reservoir rock by analysing cleaned core plugs for wettability, oil residue and mud components. Important minerals should not be removed from the original reservoir rock during cleaning.

INTRODUCTION

Both pressure and temperature are reduced during retrieval of reservoir rock samples [1]. This can change the solubility of minerals and organic and inorganic components in the residual reservoir fluids. A gas phase will also be formed when the pressure is reduced below bubble point. Invasion of mud components can alter the rock properties [2]. Wettability can be changed by adsorption of mud components. Invasion of particles, polymer and resins from the mud can also reduce the permeability of the rock. The ionic composition of the brine in the mud system is different from the formation water (FW) composition. The surface properties of the minerals can therefore be changed due to mud filtrate invasion. In the preparation of reservoir rock in the laboratory it is important to establish wettability conditions representative of the oil reservoir [2]. Mud contamination and precipitates from the reservoir fluids should be removed, prior to testing. It is important that the selected composition of the FW is as similar as possible to the real reservoir FW. Preparation of the reservoir rock with incorrect compositions of the FW can give unrepresentative surface properties of the minerals and thereby wettability conditions which are not representative of the reservoir.

The first aim of the presented study was to evaluate the cleaning procedure of high permeability reservoir sandstone core plugs with potential contamination by water-based mud. The second aim was to explore cleaning of sandstone rock (medium permeability) with oil-based mud contamination. Another reservoir sandstone rock with the potential contamination with oil-based mud was cleaned by different procedures before determination of the capillary desaturation curve.

METHODS

Water-Based Mud: Evaluation Cleaning Procedure

The procedure for cleaning of high permeability reservoir sandstone rock with potential contamination by water-based KCl mud was evaluated using core plugs drilled from the same seal peel parallel to bedding.

Cleaning

The core plugs were first flooded with synthetic formation water (SFW, Table 1) in tri-axial core-holders at 60^{o}C using injection rate of 0.5ml/min. The core plugs were then cleaned by methanol/toluene cycles at 60^{o}C with an injection rate of 0.5ml/min until the effluent was colourless, 4 cycles with 5 pore volumes (PV) of each solvent in each cycles. The total period with cleaning was approximately 6 weeks, including injection and storage. The cleaning was finished with a 17 PV injection of methanol. The methanol was then replaced with SFW at room temperature at an injection rate of 0.5 ml/min, before absolute permeability was determined. Effluent brine samples were analysed for elements by Inductively Coupled Plasma (ICP) in both SFW injection steps.

Analyses Of Cleaned Reservoir Cores

Spontaneous imbibition and forced imbibition experiments were performed to characterize the wettability of cleaned core plugs. After drainage to S_{wi} by Isopar H

(synthetic oil) using the confined porous plate method the spontaneous imbibition of SFW was studied in Amott cells at room temperature. Water flooding with SFW was then carried out in tri-axial core-holder at room temperature. Samples from inlet, mid and outlet of one cleaned core plug were extracted with dichloromethane, and the extracts were analysed by gas chromatography to characterize the oil residue. Distribution of mud components from inlet to outlet of cleaned reservoir core plug was studied by a ZEISS Supra 35 VP field emission SEM. An EDAX Energy-dispersive X-ray spectroscopy (EDS)-detector was used for analyses of the elemental composition.

Oil-Based Mud: Evaluation Cleaning Procedures

Cleaning By Stock Tank Oil Injection

Sandstone core plugs (100-200mD) drained to S_{wi} were aged with STO at 90˚C for 14 days. Oil-based mud filtrates were prepared by stepwise filtration from 120μm down to 5μm. The mud filtrate was injected to core plugs through an inlet filter of 0.45μm using an injection rate of 0.5ml/min. The rock was then aged again for 14 days at 90°C before cleaning by STO injection. Emulsifier production was studied by determination of the interfacial tension (IFT) between the effluent oil phase and SFW using the spinning drop technique [3]. Wettability after this cleaning was then characterized by spontaneous imbibition of SFW.

Capillary Desaturation Curve With Different Solvent Cleaning

To evaluate the potential for surfactant flooding in a sandstone reservoir, capillary desaturation curve (CDC) was determined. Two different cleaning procedures were used for the reservoir rock with potential contamination by oil-based mud: 1. Injection of methanol until colourless effluent, and 2. Injection of methanol/toluene (33pore volume (PV)), acetic acid (33PV) and ethanol (33PV). After cleaning, the composite reservoir core was saturated with isopropanol. Fluid systems of different IFT were prepared using solvent systems of 2w%$CaCl_2$/iso-octane/isopropanol [4, 5]. It was assumed that the solvent system has similar flooding behaviour at reduced IFT as surfactant systems.

RESULTS

Water-Based Mud: Evaluation Cleaning Procedure

Analysis of effluent samples and cleaned reservoir rock were carried out in the evaluation of the cleaning procedure for high permeable reservoir rock with potential contamination with water-based mud.

Element Composition Of Effluent During SFW Injections

SFW was first injected before cleaning with solvents to remove water-soluble mud components. In the beginning the effluent potassium (K) concentration was much higher than in injected SFW (Figure 1a) The K concentration gradually reduced, but was still higher than in SFW at the end of this injection step. In the beginning of the second SFW injection after solvent cleaning, the K concentration was also higher than injected before it became similar in the levels in SFW. These results show that the core plugs were contaminated by KCl-mud, and that all the contamination was not removed during the

solvent cleaning. Before solvent cleaning the effluent sulphur (S) concentration was also much higher than in SFW at the start of injection, and was still higher than in SFW at the end of this step (Figure 1b). When SFW was injected the second time, the S-concentration was still higher than in SFW at the start of injection but became similar at the end of the injection. The development in effluent concentrations of K and S were rather similar in the first SFW injection (Figure 1), and the sulphur source is therefore probably the mud.

During the first SFW injection the effluent calcium (Ca) concentration was lower than in SFW, but at the end of this injection step was similar to the concentration in SFW (Figure 1c). This also confirmed the mud invasion, because the concentration of Ca in the mud filtrate is lower than in SFW. In the second SFW injection after solvent cleaning, the Ca concentration was largely stable. In the first SFW injection the effluent magnesium (Mg) concentration was also lower than injected and was still approaching the SFW level at the end of this step (Figure 1d). This again confirmed the mud contamination. At the end of the second SFW injection, the Mg concentration was similar as in SFW. The mud contamination was also confirmed by low effluent sodium (Na) concentration in the beginning of the first SFW injection and was still approaching SFW level at the end of this step (Figure 1e). At the end of the second SFW injection, the effluent Na concentration was as in SFW.

It is the water soluble mud components that should be easiest to remove during injection of SFW, especially the ions. The ICP-analysis of effluent samples during the two steps with SFW injection, clearly show that it is necessary to inject several pore volumes to remove the mud contaminations. It would have been more difficult to remove these mud contaminations from more heterogeneous core plugs. The results in the first SFW injection also indicated that cleaning of core plugs with only injection of SFW and crude oil, will require many pore volumes of SFW to remove the mud contaminations.

SEM-Analysis

After cleaning with solvents, inlet, mid and outlet samples of reservoir core were analysed by SEM. Examples of SEM-images are shown in Figure 2. Clusters of barite, clay and polymers were found in some samples. Bentonite clay in the mud has similar elemental composition as other clay minerals, and is difficult to identify by the used SEM-method. Since clay was found together with barite particles, it is likely that the samples also contained bentonite. In the images, polymers similar as in the reference samples were found. The SEM-images showed that the reservoir core plugs contained mud components even after cleaning with solvents. The elemental compositions based on EDS-spectra of the cleaned reservoir rock samples are given in Table 2. Since all samples contained barite, Ba and S were present in the samples. No systematic variation of elemental concentrations from the inlet to outlet was found. The reservoir core plugs were also drilled from the seal peel in the longitudinal direction. In another study reservoir cores were also cleaned by toluene/methanol cycles before they were drained to S_{wi}, aged with STO and used in water flooding experiments. After new toluene/methanol

cleaning after water flooding, the core plugs were also found to contain mud contaminations. See examples of SEM-images in Figure 3.

Oil Extract

Chromatogram of crude oil showed typical crude oil pattern of n-alkanes at least up to C_{41} (Figure 4a). The GC-analysis of extracts showed that crude oil components were still present in the core plug even after cleaning with toluene/methanol cycles (Figure 4b, c and d). Since mainly high molecular weight components were present in the cleaned reservoir rock, it indicated precipitates of these components which were difficult to remove during cleaning with toluene/methanol cycles. Since the amount of extractable material was increasing from inlet to outlet in the core plug (Table 3), it appears that the solubility with these oil components has been low.

Spontaneous Imbibition And Forced Imbibition

To confirm that toluene/methanol cleaning resulted in water-wet rock, spontaneous and forced imbibition were studied by preparing two cleaned reservoir core plugs using Isopar H (synthetic oil) as oil. Established S_{wi} was similar for the two core plugs, 0.18 and 0.19 respectively. The spontaneous imbibition was rather high and fast for both core plugs (Figure 5). When viscous flooding was carried out with SFW after the spontaneous imbibition experiments, no additional oil was produced. Increase in the injection rate from 3 to 7ml/min gave no oil production and the differential pressure across the core plugs was rather stable at the different rates. No capillary end effects were therefore observed. These results showed that the core plugs were water-wet.

Even though the cleaned core plugs were found to be water-wet, the wettability after aging with crude oil may be affected by invasion of mud particles. Barite has rather small area/weight ratio, and will be water-wet. Clay has high area/weight ratio and invasion of bentonite clay will increase the surface area. Aging with crude oil may therefore give less water-wet conditions than without invasion. In addition, invasion of mud particles may have altered the permeability.

Oil-Based Mud: Evaluation Cleaning Procedures

Cleaning With STO Injection

Sandstone core plugs were first aged with STO at S_{wi}. When STO was displaced by the mud filtrates, the oil permeability was only slightly changed (Table 4). After new aging for 14 days, the mud filtrate was replaced by STO. The oil permeability then became only slightly higher than before the exposure to the mud filtrates. Minor changes in oil permeability was observed when STO was injected instead of mud filtrate in the reference core plug. For the core plug exposed to the mud filtrate with mineral base oil (MFM), the STO injection was stopped after approx. 4PV, because the differential pressure across the core plug was stable. IFT between the oil-phase effluent and SFW was at this point in the same range as between MFM and SFW (Figure 6a). This means that at least one emulsifier was still released from the rock, and equilibrium conditions were not established inside the core plug. For the core plug exposed to the mud filtrate

with synthetic base oil (MFS), IFT was found to increase from approx. 3PV to approx. 7.3PV (Figure 6a). IFT was then still lower than between STO and SFW. This also showed that at least one emulsifier was produced during a rather long period with back-production. The release of emulsifier(s) was therefore slow in both plugs exposed to mud filtrate. After cleaning with STO injection, the wettability of the core plugs was characterized by spontaneous imbibition of SFW. The spontaneous imbibition of SFW was in the beginning slower for the core plugs exposed to mud filtrates than for the reference core plug not exposed to mud filtrate (Figure 6b). This means that the mud exposed core plugs were less water-wet than the reference core plug.

Capillary Desaturation After Mild And Strong Cleaning

An atypical CDC was determined after methanol cleaning of the composite reservoir core (Figure 7). The same reservoir core was then prepared by cleaning with methanol/toluene, acetic acid and ethanol. The CDC profile was then as expected for water-wet rock where the residual oil at low capillary number is distributed as isolated droplets (Figure 7). This showed the importance of the type of cleaning procedure. When these measurements were carried out, the understanding was that sandstone rock should be water-wet. Since atypical CDC was measured after methanol cleaning, it was based on results presented by Garnes et al. [6] assumed that the reservoir core was contaminated by oil-based mud. During injection of acetic acid the mineral composition of the reservoir rock was probably altered, e.g. dissolution of carbonate minerals. Today many of the sandstone oil reservoirs are characterized as mixed-wet. In recent years it has been shown that atypical CDC can be determined for the wetting phase [5] and also for mixed-wet rocks [7].

DISCUSSION

All mud components should ideally be removed during preparation of reservoir core plugs. The main challenge is that the muds and mud filtrates contain many components. It has been shown in the present study that analysis of effluent samples during cleaning of core plugs can confirm that the mud components that are easiest to remove are removed, e.g. ions in water-based mud and emulsifiers in oil-based mud. If these components are still present in the rock, the rock is probably not representative. It has also earlier been reported that emulsifiers can adsorb onto the rock and thereby alter the wettability [8]. Emulsifiers will not give any colour to the effluent, but the effluent can be analysed for these components or IFT can be measured. If the reservoir rock has been invaded by water-based mud, it is important that the composition of brine in the rock is changed to FW composition. It has been shown in other studies that potassium can reduce the concentration of divalent cations onto clay surfaces and thereby alter the wettability to more water-wet [9, 10]. Differential pressure across the core plugs can't be used to confirm that mud contaminations have been removed, because low concentrations of such contamination will have minor effects on viscosity.

After cleaning, the rock can be crushed and analysed for mud components (e.g. by SEM) and oil residue (e.g. by analysing oil extracts on GC). These methods are destructive.

Often extra core plugs are cleaned and prepared in experimental programs, and the additional plugs can be analysed to confirm the quality of the cleaning. An alternative is to analyse cores/plugs after the SCAL- or EOR-experiments in the same way. It was not possible to identify bentonite clay by the used SEM method, but invasion of clay from water-based muds will increase the surface area. This can affect the established wettability conditions during aging with stock tank oil. The organoclay in oil-based muds are oil-wet, and invasion of this clay will also alter the wettability of the reservoir rock.

It is challenging to analyse for all the mud components, because the muds their filtrates contain many components of technical grade (i.e. standard set for quality is not established). If mud components are present, the question is to what extent do they affect the results. If several SCAL- or EOR-experiments have been carried out, it can be investigated whether the results depend on the amount of mud invasion in the different cores/plugs. The best chance will be to get as low mud invasion as possible during coring. Invasion will depend on the sampling conditions, mud design, and over balance used in the coring process, but will in general decrease with decreasing permeability.

The cleaning procedure for reservoir core plug can be improved by including chemical analyses. Details in the preparation procedure will depend on the composition of the rock, reservoir fluids and mud system. In the evaluation of the cleaning procedure for water-based muds, oil components with high molecular weight were found in the oil residue. The solvent cleaning was carried out at 60°C. It will probably be possible to remove these components more efficiently by cleaning the core plugs at higher temperatures. Cleaning at higher temperature will increase the diffusion rate and the solubility of the high molecular oil components. This is an example of how chemical analysis can be used to improve the core preparation procedure.

CONCLUSIONS

In evaluation of the cleaning procedure for high permeability sandstone reservoir core plugs with potential contamination by water-based mud, injection of several PV with SFW were required to change the brine composition in the core plugs back to SFW composition. Mud components were found by SEM-analysis to be present in cleaned reservoir rock, also after water flooding. The cleaned reservoir rock was water-wet, but mud components present in the rock affect the wettability conditions prepared by aging with crude oil. Cleaned reservoir rock was also found to contain oil components of high molecular weight.Slow release of emulsifiers from mud filtrate of oil-based muds was observed during cleaning of sandstone with STO injection. After this cleaning the core plugs exposed to mud filtrate were found to be less water-wet than reference core plug without exposure.

The measured CDC for sandstone reservoir rock with potential contamination with oil-based mud, was found to depend on the cleaning procedure. Atypical CDC was measured after methanol cleaning, and typical CDC was measured for water-wet rock after strong cleaning (methanol/toluene, acetic acid and ethanol). The strong cleaning probably altered the rock composition.

Mud components with the potential to affect the flow conditions should be removed during cleaning of reservoir core plugs, otherwise, ideally, these core plugs should not be used. In preparation of core plugs it is recommended to analyse effluent samples for mud components to confirm that they are removed, at least the easiest removable components. The cleaning procedure should be evaluated for the actual reservoir rock by analysing cleaned plugs for wettability and mud components. For some mud components, chemical analysis can be challenging because they are of technical grade, have similar structures as other mud components and are in complex mixtures. Important minerals should not be removed from the original reservoir rock during cleaning. It is recommended to analyse core plugs in experimental programs to investigate whether the presence of mud components may have affected the results.

ACKNOWLEDGEMENTS

The authors acknowledge Lundin Norway for financing and supporting the work on water-based mud presented in this paper. They also acknowledge the Research Council of Norway and the industry partners; ConocoPhillips Skandinavia AS, BP Norge AS, Det Norske Oljeselskap AS, Eni Norge AS, Maersk Oil Norway AS, DONG Energy A/S, Denmark, Statoil Petroleum AS, GDF SUEZ E&P NORGE AS, Lundin Norway AS, Halliburton AS, Schlumberger Norge AS, Wintershall Norge AS of The National IOR Centre of Norway for support.

REFERENCES

1 Skopec, R. A. 1994. Proper Coring and Wellsite Core Handling Procedures: The First Step Toward Reliable Core Analysis. SPE-28153. *JPT*. **46** (04).

2 Anderson, W. G. 1986. Wettability Literature Survey- Part 1: Rock/Oil/Brine Interactions and the Effects of Core Handling on Wettability. SPE-13932. *JPT*: 38 (10).

3 Adamson, A.W., *Physical Chemistry of Surfaces*. 5th ed. New York: John Wiley and Sons, Inc., ISBN 0-471-61019-4, 1990, p.777.

4 Morrow, N.R., Chatzis, I., & Taber, J.J. 1988. Entrapment and Mobilization of Residual Oil in Bead Packs. SPE-14423 *SPE Res Eng* **3** (3): 927-934.

5 Chukwudeme, E.A., Fjelde, I., Abeysinghe, K.P., & Lohne, A. 2014. Effect of Interfacial Tension on Water/Oil Relative Permeability on the Basis of History Matching to Coreflood Data. SPE-143028. *SPE Res Eval & Eng* **17** (01): 37-48.

6 Garnes, J.M., Mathisen, A.M., Scheie, A., & Skauge, A. 1990. Capillary Number Relations for Some North Sea Reservoir Sandstones. SPE-20264, IOR Symp., Tulsa, 22-25 April.

7 Fjelde, I., Lohne, A. & Abeysinghe, K. P. 2015. Critical Aspects in Surfactant Flooding Procedure at Mixed-wet Conditions. SPE-174393. Europec 2015, Madrid, 1-4 June.

8 Yan, J. N., Monezes, J. L. & Sharma, M. M. 1993. Wettability Alteration Caused by Oil-Based Muds and Mud Components. SPE-18162. *SPE Drill&Compl*. **8** (01): 35–44.

9 Fjelde, I., Polanska, A., Asen, S. M. & Taghiyev, F. 2013. Low Salinity Water Flooding: Retention of Polar Oil Components in Sandstone Reservoirs. A24. 17th European Symp. IOR. St Petersburg, Russia. 16-18 April.

10 Omekeh, A., Friis, H. A., Fjelde, I. & Evje, S. 2012. Modeling of Ion-Exchange and Solubility in Low Salinity Water Flooding. SPE-154144. IOR Symp., Tulsa, 14-18 April.

Table 1. Composition of SFW.

Ion	Concentration (mg/l)
Na^+	16105.6
K^+	278.0
Mg^{2+}	581.0
Ca^{2+}	2920.0
Sr^{2+}	103.5
Ba^{2+}	5.6
Cl^-	31744.4
NO_3^-	146.5
SO_4^{2-}	281.1

Table 2. Elemental compositions (w%) of inlet, mid and outlet samples of cleaned reservoir core plug based on EDS-spectra.

Element	**Inlet**	**Mid**	**Outlet**
O	36.3	37.7	38.5
Na	1.2	0.6	0.4
Mg	0.1	0.1	0.2
Al	6.9	6.6	5.4
Si	45.5	43.6	45.2
S	1.0	0.9	1.0
K	3.8	5.3	4.0
Ba	3.7	3.5	3.5
Fe	1.5	1.8	1.8

Table 3. Amount of oil extracted from cleaned reservoir core plug.

Sample id	Extracted material (mg/kg Rock)
Inlet	62
Mid	132
Outlet	604

Table 4. Less water-wet core plugs (by aging with STO) and exposed to mud filtrates with mineral and synthetic base oils (MFM and MFS).

Step	Ref. core plug $ke_o(S_{wi})$ [mD]	MFM core plug $ke_o(S_{wi})$ [mD]	MFS core plug $ke_o(S_{wi})$ [mD]
After first aging with STO	96	112	130
After aging with mud filtrate (reference aged with STO)	----------	96	136
After second aging STO	99	119	144

Element	First FW injection	Second FW injection
a. K	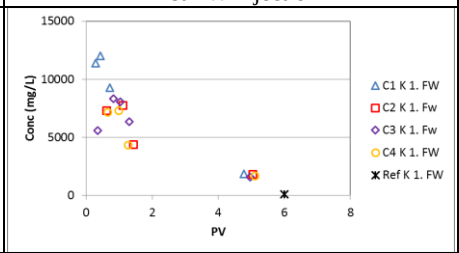	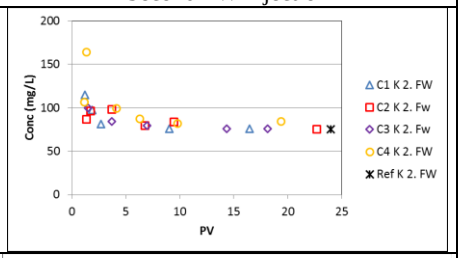
b. S	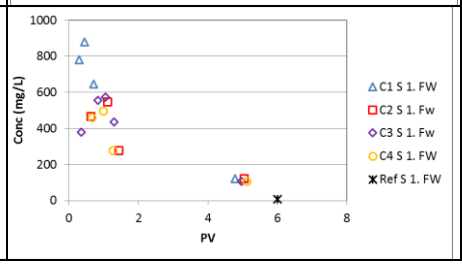	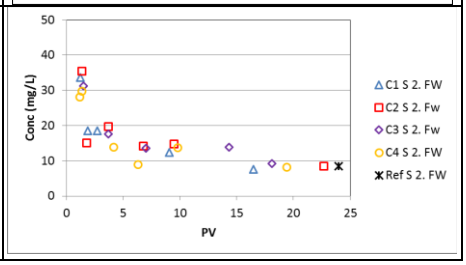

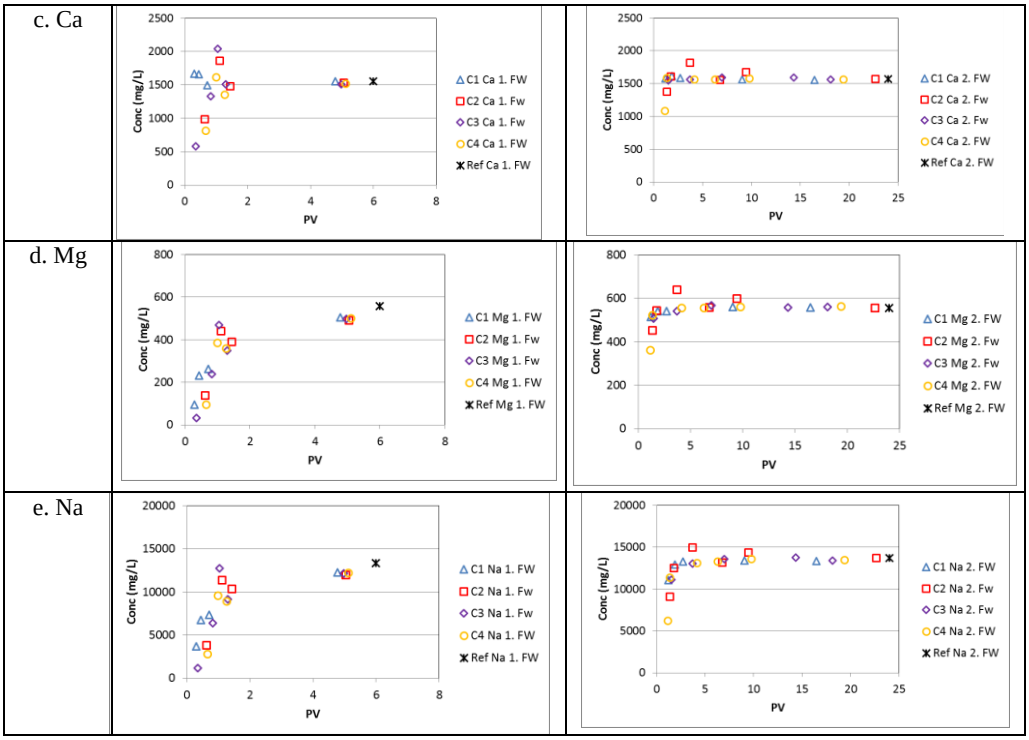

Figure 1. Effluent element concentrations during SFW injection before and after solvent cleaning of four core plugs.

	Quartz grain with clusters of clay, polymers and barite	Barite and clay
Inlet	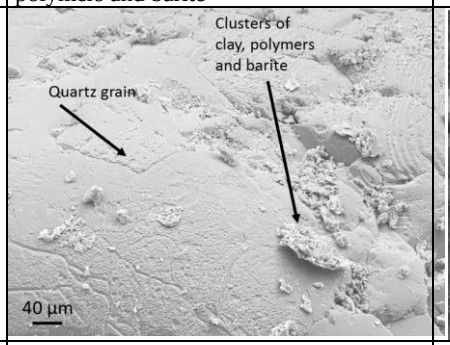	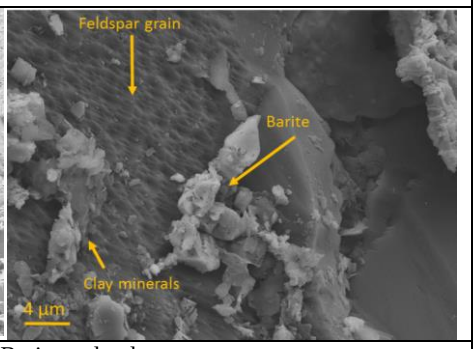
Mid	Quartz grain with clay and polymer	Barite and polymer
	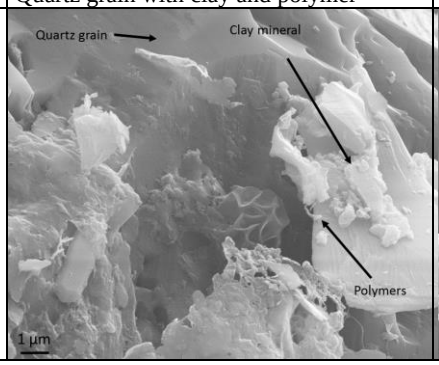	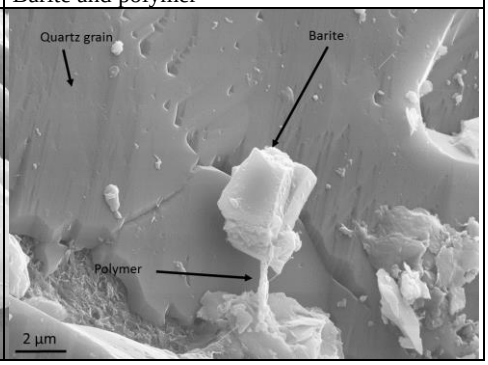

Outlet	Quartz with coating of clay and barite	Feldspar with coating of clay, polymers & barite

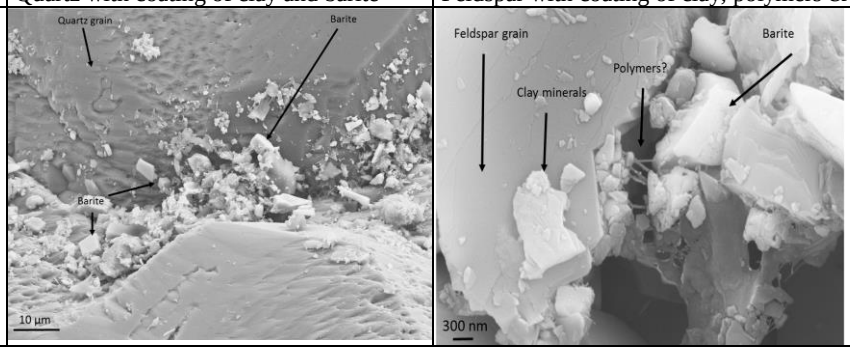

Figure 2. Examples of SEM-images of samples from cleaned reservoir core.

Barite and clay	Barite and clay

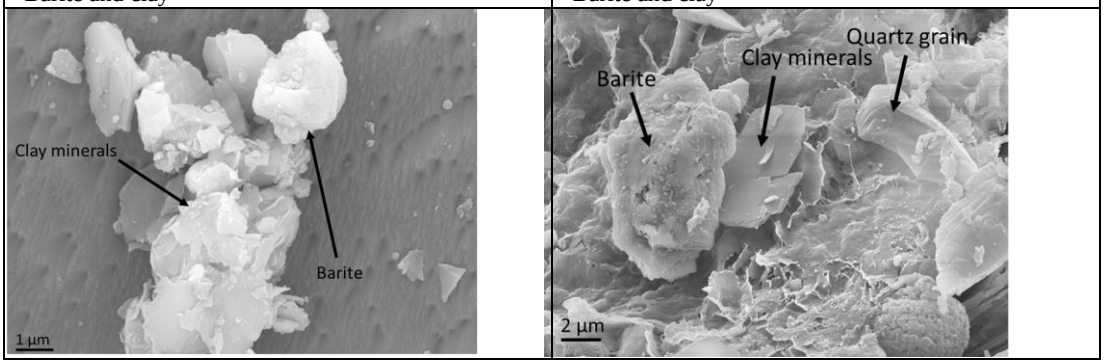

Figure 3. Examples of SEM-images of samples from water flooded reservoir core plugs.

a. Crude oil	b. Inlet sample
c. Mid sample	d. Outlet sample

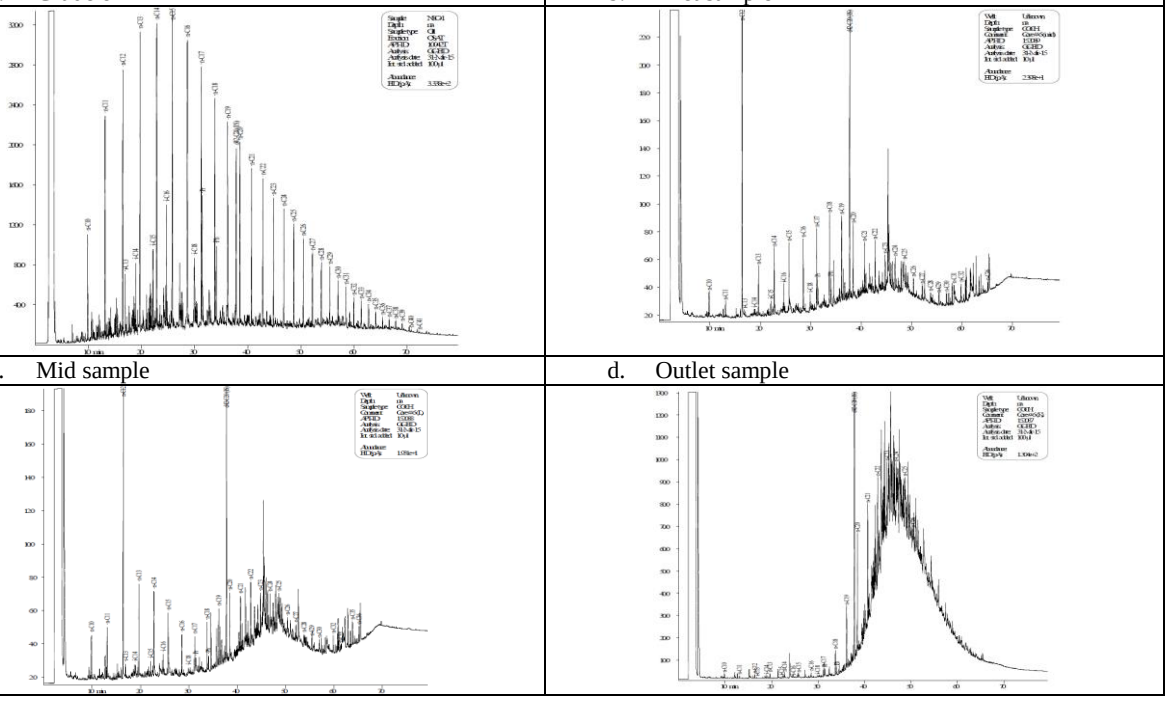

Figure 4. Gas chromatogram of crude oil and oil extracts from inlet, mid and outlet of cleaned reservoir core plug.

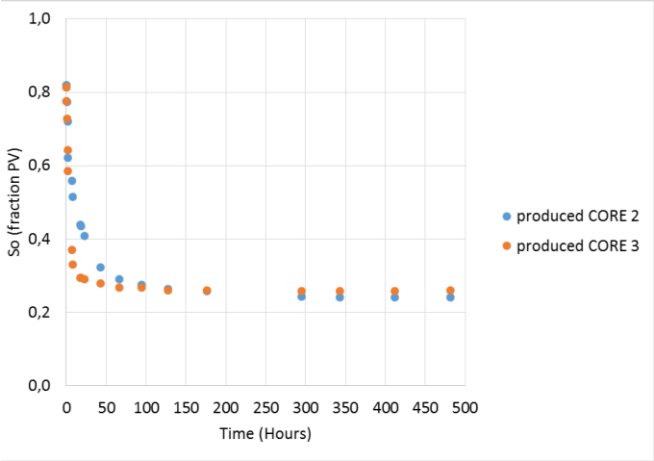

Figure 5. Oil saturation (S_o) as function of time during spontaneous imbibition of SFW into reservoir core plugs.

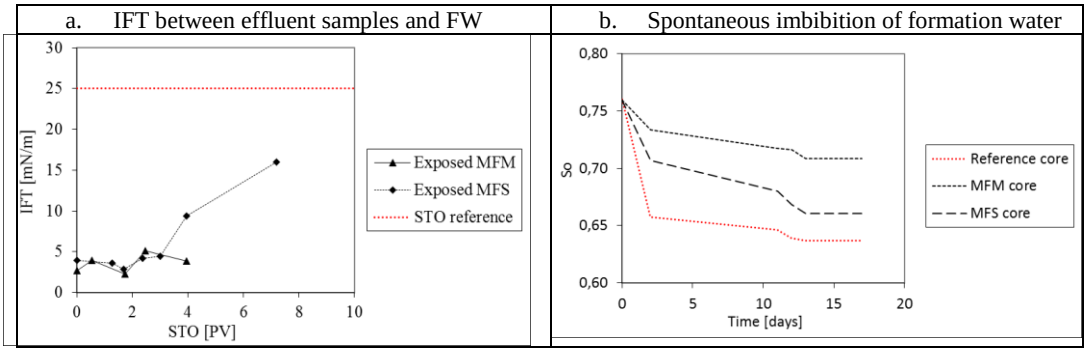

Figure 6. IFT between effluent samples and FW during soft cleaning by STO and the following spontaneous imbibition experiments with SFW. (MFM and MFS: Mud filtrates with mineral and synthetic base oils.

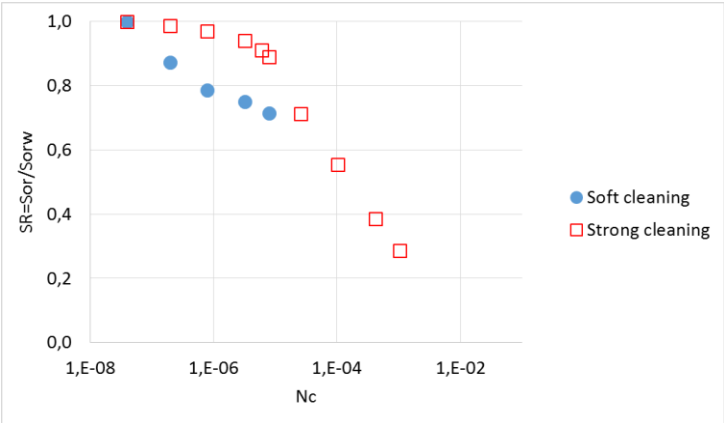

Figure 7. CDC, normalized residual saturation vs capillary number (S_{or}/S_{orw} vs N_c) after methanol cleaning (soft) and after cleaning with methanol/toluene, acetic acid and ethanol cleaning (strong) of reservoir core.

PRESERVING INITIAL CORE WETTABILITY DURING CORE RESTORATION OF CARBONATE CORES

Paul Hopkins, Tina Puntervold and Skule Strand
University of Stavanger, Norway

This paper was prepared for presentation at the International Symposium of the Society of Core Analysts held in St. John's Newfoundland and Labrador, Canada, 16-21 August, 2015

ABSTRACT

A correct restoration of carbonate cores is very important because the wettability will influence the results of relative permeability, capillary pressure and oil recovery tests. The acidic polar components in the crude oil are the main wetting parameter for carbonates, and will dictate the wettability of the rock surface. This work aims to determine the suitability of using mild core cleaning with kerosene and heptane during core restoration to preserve the initial reservoir wettability in the reservoir cores during core restoration. Initially a water-wet outcrop chalk core with S_{wi} was flooded with crude oil. Effluent samples of produced oil were collected and the acid number (AN) was measured as a function of pore volume injected. The results showed that the Acidic polar components in the crude oil were adsorbed onto the rock surface, and gradually an equilibrium between the AN in the injected oil and AN in the effluent oil was achieved. A wettability test confirmed that the water-wetness of the core was drastically reduced. The chalk core was then put for restoration. First, the core was mildly cleaned by flooding with kerosene to displace the crude oil, followed by heptane for removal of kerosene. During the second crude oil saturation and flooding, the adsorption of acidic organic polar components onto the rock surface was drastically reduced, confirming that the rock surface had maintained approximately 3/4ths of the initially adsorbed acidic polar components during the mild core cleaning process.

INTRODUCTION

In carbonate reservoirs, the success of an oil recovery is primarily linked to the initial wetting conditions of the rock. In an oil reservoir, the initial wettability is established by a chemical equilibrium between oil, brine and rock over millions of years of interaction. The properties of the initial wetting state will decide physical parameters such as the capillary pressure, the relative permeabilities and fluid distribution. The AN, acid number, is a measure of the content of surface-active components, and is regarded as one of the most important parameters dictating the initial wetting of a carbonate rock. The AN is related to the amount of carboxylic groups that are present in the oil. It may be measured and quantified by titration and has the unit mg KOH/g oil. When analysing reservoir core material it is essential that the initial wetting is preserved, so that the wettability of the core may be investigated in the most representable state. Therefore, in a laboratory, it is crucial that steps are taken during preparation to preserve the initial core

wettability. Core material is often cleaned to a completely water-wet state and the core is aged with the formation water and reservoir oil to build up the initial conditions [1]. In practice, it is common to clean core material with Toluene followed by methanol. Toluene should remove hydrocarbons including asphaltenes and adsorbed polar components. Methanol displaces both water and toluene. The questions asked in this paper are: Will a more representative wettability be achieved by using mild cleaning, and can we perform wettability tests to validate that polar components have been preserved on the surface?

The wettability will be determined by a chromatographic wettability test at S_{or} (residual oil saturation) [2]. In this chromatographic wettability test, a separation of ions will only take place on the water-wet areas of the pore surface. The area between a non-adsorbing tracer and sulphate is proportional to the water-wet area. The ratio of this area against the area of a completely water-wet core will determine a wettability index in chalk, ranging from 0-1.

EXPERIMENTAL

Materials

Outcrop chalk from Stvens Klint, Copenhagen, Denmark, was used as model rock. The chalk has high porosity (45-50%) and low permeability (2-3 mD) and is relatively homogeneous. The outcrop chalk core consists of 98% pure biogenic $CaCO_3$ and is considered similar to North Sea chalk reservoirs. The properties of the core are given in Table 1.

Brine Composition

Synthetic formation water, VB0S, modelled on the Valhall field, was the brine used as the formation water in the experiments. SW0T and SW½T are brines used for the chromatographic wettability test. Brine compositions are reported in Table 2.

Oil Properties

A crude oil was diluted with heptane in the ratio of 60/40 respectively. The oil was centrifuged and filtered through a 5μm Millipore filter. An acid number (AN) of 1.7 mgKOH/g oil was measured. A part of this oil was treated with silica gel to remove surface active polar components and thereafter filtered, giving an AN of ~0.0 mgKOH/g oil.

A mixture of treated and untreated oil was prepared at a specific ratio and analysed. The designed oil, RES40-0.35, had an AN of 0.35 mg KOH/g and a base number (BN) of 0.25mg KOH/g. The oil properties are given in Table 3.

Analyses Of Acid And Base Numbers In Crude Oil Samples

The acid and base numbers, AN and BN, of the crude oil samples were analysed by potentiometric titration. The methods used are modified versions of ASTM 665 and

ASTM 2898 [3]. The reproducibility of the acid number titration tests is presented in Table 4.

Preparation Of Chalk Core

The cores were prepared following a procedure set by Puntervold et al.[4]. All cores used were initially flooded with 5 pore volumes (PV) of de-ionized water (DI) for a removal of easily dissolvable salts and sulphate. The cores were dried to a constant weight at 90 °C.

Establishing Initial Water Saturation

The initial water saturation, S_{wi}, was established using the desiccator technique [5]. After the core had achieved a S_{wi} of 10%, the core was equilibrated in a sealed container for 4 days to allow the even distribution of salts within the core.

Oil Saturation And Establishing Core Wetting

The chalk core with S_{wi} =0.1 was mounted in a Hassler core holder with an overburden pressure of 20 bar and with a back pressure of 6 bar. The core was oil flooded at 50 °C at a rate of 0.1 ml/min. Effluent samples of produced oil were collected in sealed vials using a fraction-collector.

The core was flooded with oil until the AN in the effluent samples reached the same concentration as initially present in the oil, AN = 0.35 mg KOH/g. A total of 15 PV of oil was flooded through the core. By plotting the AN against PV of oil injected, the adsorption of acidic oil components onto the rock surface can be expressed.

Core Aging

Once the core had been flooded with 15 PV of crude oil, it was wrapped in Teflon tape. The wrapped core was placed in an aging cell surrounded by oil, and aged at 50 °C for two weeks to achieve a homogeneous core wetting.

Core Wettability By Chromatographic Wettability Test

The chromatographic wettability test was designed by Strand et al.[2] and is based on the chromatographic separation between sulphate and a non-adsorbing tracer. The test is performed at S_{or} at ambient temperature. The chromatographic separation of the sulphate and the tracer is proportional to the water-wet area of the chalk core surface.

The core is flooded with the brine SW0T. SW0T is depleted in sulphate and is used to displace the remaining fluid in the core to bring the sample to S_{or}, as well as to establish a stable flow. Then the SW½T brine, containing SCN^- and SO_4^{2-}, is injected and effluent samples are collected into sealed vials. SO_4^{2-} ions have an affinity towards the water-wet chalk surface, and the chromatographic separation area, A_{wet}, between SCN^- and SO_4^{2-} eluent curves gives a relative measure of the water-wet rock surface. Compared with the area determined from a completely water-wet chalk core, A_{WW}, the wettability index I_{CW} describing the water-wet fraction of the chalk surface can be calculated according to equation 1 below.

$$I_{CW} = \frac{A_{wet}}{A_{WW}} \quad (1)$$

Ionic Concentration Analyses

The ionic concentrations of the effluent samples from the chromatographic wettability test were analysed using an ion chromatograph, ICS 3000, delivered by Dionex Corporation, USA. The samples were diluted 1:200 times prior to the analysis. The anionic concentrations in the effluent were calculated using an external standard method.

Core Restoration

After the first polar component adsorption test, the core was restored. A mild core cleaning procedure with low aromatic kerosene and heptane was performed to remove the residual oil. The first step of the procedure is a miscible fluid displacement using kerosene. When the core is clean and the effluent is clear or consistent in colour, the second step of the procedure is to displace the kerosene with n-heptane. As the final step, the core was flooded with DI water to remove heptane and easily dissolvable salts. The water and heptane was afterwards removed by evaporation in a standard heating chamber, at 90°C, until constant weight. The procedure was then repeated, establishment of initial water saturation and core saturation with oil, ageing, water flooding to S_{or}, and wettability determination.

EXPERIMENTAL RESULTS

A correct initial wetting condition is crucial for achieving reliable experimental results from core analyses. The initial wetting conditions in the core dictates capillary pressure measurements and are very important for relative permeability calculations which is an important parameter in most reservoir modelling and simulations. Oil recovery tests and "Smart Water" effects are also dictated by the initial wetting properties of the restored cores. An optimized core restoration laboratory procedure that preserves the initial reservoir wetting during core cleaning is of great interest for the industry.

In this work, a water-wet outcrop chalk core was used. The effect of core cleaning and core restorations on rock wettability is discussed.

Initial Wetting of the Outcrop Chalk Core

The outcrop chalk cores used in these experiments are initially completely water-wet. Cores saturated with oils without polar components, like mineral oils, will not change the initial wettability. Restored cores imbibe water very rapidly giving oil recoveries above 70 % OOIP. The chromatographic wettability test was performed at ambient temperature on an outcrop core at 100% initial water saturation, Figure 1. The core details are presented under reference core on Table 1. The results show a large separation between the non-adsorbing tracer thiocyanate and sulphate which adsorbs to water-wet chalk surfaces. The calculated area between the tracer and sulphate eluent curves is A_{ww} = 0.254, represents a very water-wet rock surface area.

Initial Adsorption of Carboxylic Material Onto Water-Wet Chalk Surface
The chalk core used was initially very water-wet. After establishing S_{wi} = 0.1, the core was mounted in a core holder with a confining pressure of 20 bar and with a back pressure of 6 bar. The core was flooded at 50 °C with the oil containing polar components with an AN=0.35 mg KOH/g oil. Effluent samples of the produced oil were collected and analysed for the content of acidic polar components, AN. Figure 2 shows the AN in the effluent with increasing PV injected.

The results confirm adsorption of polar acidic components towards the pore surface in the chalk core. The initial measurements, the first 2 PV, show that the effluent oil has a very low AN, Figure 2. This shows that the acidic polar material in the oil adsorbs onto the surface of the chalk core, which results in an effluent oil with minimal acidic components. As more oil is flooded into the chalk core the surface becomes more saturated with acidic polar material. There is less ability for the acidic polar groups to adsorb on to the surface, due to the lack of available surface sites. As a consequence, the AN in the oil effluent increases. After 13PV of injected oil, the system establishes an equilibrium, where the AN in the effluent samples is equal to the AN of the injected oil, 0.35 KOH/g oil.

Core Wetting Of The Outcrop Chalk Core After Oil Flooding
A new chromatographic wettability test was performed on the oil flooded core. The core was successively flooded with SW0T to S_{or}, 0.25, at ambient temperature, and the chromatographic test was performed by switching to SW½T at ambient temperature. The results from the chromatographic wettability test is presented in Figure 3.

The chromatographic separation between SCN^- and SO_4^{2-} is given in Figure 3. The calculated area between the tracer curve and sulphate curve is now dramatically lower compared to the initially water-wet core, in Figure 1. The calculated area is now A_{wet} = *0.055*, confirming a dramatic reduction in water-wet sites on the pore surface after flooding 15 PV with an acidic oil.

Adsorption Of Acidic Organic Compounds In A Second Oil Flood
The Core#1 was then prepared for a second oil flooding test. The core, at S_{or}, was first mildly cleaned by kerosene, heptane and then flooded with DI water and dried. Initial Swi=0.1 was established and the core#1 was mounted in a core holder. The core was once again flooded at 50 °C with a RES40-0.35 oil containing polar components. Effluent samples of produced oil were collected and then analysed for the content of acidic polar components. The results of the adsorption of acidic components on a chalk surface that has previously seen oil are shown in Figure 4. Unlike the first adsorption test, the AN in the effluent samples starts relatively high, 0.13 mg KOH/g. This indicates that there is something preventing a full adsorption of the carboxylic material onto the chalk surface as seen in the first adsorption test on a water-wet sample. This further implies that the pore surface already has acidic organic components adsorbed to the pore surface, and

reduces the adsorption of more acidic organic material. The slope of the AN curve is relatively sharp, and is brought to a new equilibrium within 6 PV of oil flooded.

Core Wetting of the Outcrop Chalk Core after Oil Flooding

The core wetting after the secondary Oil Flooding was tested by using the chromatographic wettability test. The core was flooded with SW0T to S_{or}, 0.2 at ambient temperature, and the chromatographic test was performed flooding SW½T at ambient temperature. The results from the chromatographic wettability test are presented in Figure 5. This result shows a very low separation between the tracer and sulphate curve. The calculated area, *Awet = 0,008*, is dramatically reduced compared with the previous wettability tests for water wet core, the core that has been injected 15 PV of crude oil. The test shows that the wettability of the core has become even less water-wet.

DISCUSSION

In this experimental work, we started with an initially water-wet core sample. This could simulate the initial situation in a reservoir before crude oil accumulates into the water filled reservoir trap. The first oil flooding we performed on a water-wet core sample could represent the process when the crude oil migrates from source rock into a water saturated reservoir trap. This oil-flooded core could represent the initial situation inside the reservoir regarding adsorption of acidic polar components and the initial reservoir wetting properties that could be established. Initial content of acidic polar components in the crude oil that migrates into the reservoir, and number of crude oil reservoir refilling during geological time will definitely contribute with large uncertainties to a correct wettability description.

Results show that the initial adsorption of acidic organic compounds increases with increasing PV of acidic oil injected, Figure 2, and that the adsorption at the end reaches an equilibrium. The adsorption of polar components onto the rock surface, reduced the water-wet surface area of the core dramatically, which is clearly seen when we compare Figure 1 and 3. The area between these curves in the water-wet core is $A_{ww} = 0.254$ and for the core flooded with crude oil, the area is $A_{wet}=0.055$ which corresponds to a fraction of water-wet surface area:

$$I_{CW} = \frac{A_{wet}}{A_{ww}} = \frac{0.055}{0.254} = 0.22 \quad (2)$$

The mild core cleaning that was performed on the oil flooded core, preserved large amount of polar components that were adsorbed to the pore surface. This is clearly shown when we compare Figure 2 and 4, Figure 7.

During the second oil flooding far less acidic polar components was adsorbed compared to the first oil flooding. The area above the adsorption curves represent the total amount of acidic organic material adsorbed onto the surface, AA_T. The Acid Adsorption (AA) was determined for both adsorption tests, before and after mild cleaning.

$$AA = \frac{AN_{plateau} - AN_x}{AN_{plateau}} \quad (3)$$

AN plateau is the average highest acid number when the oil reaches equilibrium with the surface. ANx is the acid number value of a given sample number. Giving the total acid adsorption, AA_T:

$$AA_T = \sum \Delta PV \cdot AA \quad (4)$$

The calculated area above the curve shown in Figure 2 was $AA_T = 1.47$. The corresponding area in Figure 4 was $AA_T = 0.37$. This partly represents the amount of acidic organic components removed from the pore surface during the mild core cleaning, and partly the amount of acidic components that could be re-adsorbed during the second core restoration. Approximately 75% of the initial adsorbed material was still present on the pore surface. An increased number of PV injected with oil, will reduce the water-wet surface area inside the core. This could have dramatic effects on initial wetting and on the capillary pressure.

There is not a direct link between the AA_T and the water-wet surface area measured by the chromatographic wettability test when we compare wettability tests from 1st restoration, Figure 3, and the 2nd restoration, Figure 5, shown in Figure 8.

The separation area between these curves are now Awet= 0.055, 1st restoration, and Awet= 0.008, 2nd restoration, which corresponds to the water-wet fraction of Icw= 0.22 and Icw=0.03 respectively.

Even though the total acidic adsorption capacity, AA_T, was reached in both experiments, the wettability test showed a reduction in available water-wet surface area, I_{CW} , from 22% to 3 % after the second oil flood. This could be explained by the presence of acidic organic components in the crude oil with different surface reactivity. The more PV of oil flooded through the core, the more higher reactive acidic components will be concentrated at the rock surface, compared to what is initially present in the crude oil [6, 7]. Injection of 15 PV of crude oil in the second restoration was too large to reproduce the initial wetting achieved in the first restoration.

CONCLUSIONS

In this work, a water-wet outcrop chalk core was used. The effect of core cleaning and core restorations on rock wettability is discussed.

- The results showed that the adsorption of acidic organic compounds onto the pore surface increases with increasing PV of acidic oil injected.
- The adsorption of acidic organic compounds reached an equilibrium after 13 PVs of crude oil flooded in the first restoration.

- The adsorption of polar components to the pore surface reduced the water-wet core surface.
- Mild core cleaning preserved approximately 3/4 of the polar components that were adsorbed to the pore surface.
- In the second restoration acidic the adsorption equilibrium was reached after only 8 PVs of crude oil.
- After 15 PV crude oil injected in the second restoration, the water surface area had been reduced from 22% to 3%, giving a less water wet core compared to the first restoration.

The mild core cleaning procedure preserved most of the adsorbed acidic components. Lower crude oil volume was needed to restore the initial core wetting.

NOMENCLATURE

AN	Acid number
BN	Base number
ASTM	American Society for Testing and Materials
D	Core diameter
L	Core length
Φ	Core porosity
PV	Pore volume
S_{wi}	Initial water saturation
K_{ro}	Relative permeability of oil
K_{rw}	Relative permeability of water
A_{wet}	The area between the thiocyanate and sulphate curve of a sample
A_{WW}	The area between the thiocyanate and sulphate curve of a water-wet sample
VB0S	Valhall brine with no sulphate
TDS	Total dissolved salt
SW0T	Seawater without thiocyanate tracer
SW½T	Seawater that contains thiocyanate tracer
C/Co	Relative concentration of ion in effluent fractions
I_{CW}	Chromatographic wettability index

AKNOWLEDGEMENTS

BP is acknowledged by the authors of this work for financial support and for the permission to publish this work.

REFERENCES

1. Shariatpanahi, S.F., et al., *Wettability restoration of limestone cores using core material from the aqueous zone.* Petroleum Science and Technology, 2012. **30**(1-9).

2. Strand, S., D.C. Standnes, and T. Austad, *New wettability test for chalk based on chromatographic separation of SCN- and SO42-*. Journal of Petroleum Science and Engineering, 2006. **52**(1-4): p. 187-197.
3. Fan, T. and J.S. Buckley, *Acid Number Measurements Revisitied* Society of Petroleum Engineers, 2007.
4. Puntervold, T., S. Strand, and T. Austad, *New method to prepare outcrop chalk cores for Wettability and oil recovery studies at low initial water saturation.* Energy & Fuels, 2007. **21**(6): p. 3425-3430.
5. Springer, N., U. Korsbeck, and K. Aage. H, *Resistivity index measurement without the porous plate: A desaturation technique based on evaporation produces uniform water saturation profiles and more reliable results for tight North Sea chalk.* Prepared for presentation at the International Symposium of the Society of Core Analyst, 2003.
6. Fathi, S.J., T. Austad, and S. Strand, *Wettability alteration in Carbonates: The Effect of Water-Extractable Acids in Crude Oil.* Energy & Fuels, 2010. **24**(5): p. 2974-2979.
7. Fathi, S.J., T. Austad, and S. Strand, *Effect of Water-Extractable Carboxylic Acids on Wettability in Carbonates.* Energy & Fuels, 2011. **25**(6): p. 2587-2592.

Table 1. Core data for chalk cores used.

Core material			
Stvens Klint Chalk	A1	A1b	Reference core
Dry weight, g	96,78	92,28	84,27
Length, cm	6,21	6,21	5,43
Diameter, cm	3,74	3,74	3,70
Bulk Volume, cm3	68,22	68,22	58,33
Sat. Weight, g	128,56	119,79	112,01
Density of FW 10xD g/cm^3	1,00	1,00	1,02
Pore Volume, ml	31,69	27,43	27,14
Porosity %	46 %	40 %	47 %

Table 2. Compositions of the brines used.

Brine Reference	VB0S	SW0T	SW1/2T
Salt	mole/l	mole/l	mole/l
HCO_3^-	0,009	0,002	0,002
Cl^-	1,066	0,583	0,583
SO_4^{2-}	0	0	0,012
SCN	0	0	0,012
Mg^{2+}	0,008	0,045	0,045
Ca^{2+}	0,029	0,013	0,013
Na^+	0,997	0,460	0,427
K^+	0,005	0,01	0,022
Li^+	0	0	0,012
Density g/cm^3	-	1,022	1,022

Table 3. Properties of the oil used.

Crude oil	
AN mgKOH/g	0,33-0,35
BN mgKOH/g	0,24
Viscosity cP 25°C	3,25
Density g/cm3 25°C	0,808

Table 4. The reproducibility of Acid Number titration tests.

AN range	Trial 1	Trial 2	Trial 3	Stdev.
Sample of low AN	0,06	0,06	0,06	0,00
Sample of medium AN	0,27	0,27	0,26	0,01
Sample of high AN	0,34	0,34	0,34	0,00

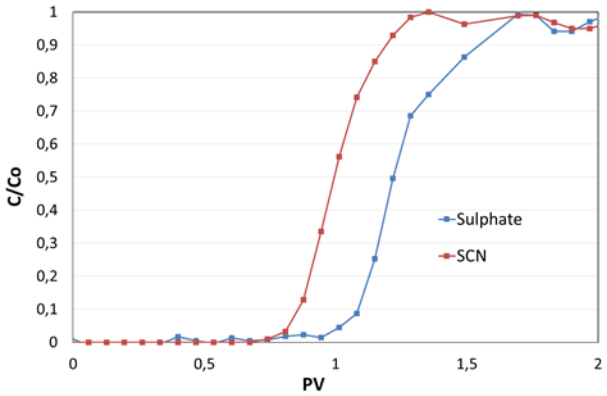

Figure 1. Chromatographic wettability test on a 100% water saturated core, Core#1. The relative effluent concentrations of SCN^- and SO_4^{2-} are plotted vs. PV injected.

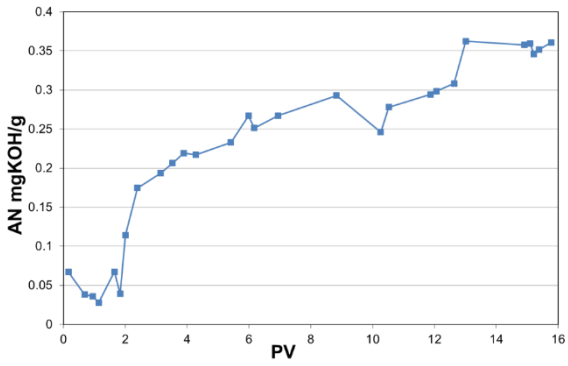

Figure 2. The adsorption of carboxylic material during flooding of an oil with AN=0.35 mgKOH/g into chalk Core#1 at 50°C, with a flow rate of 0.1 ml/min (4 PV per day). The AN in the effluent samples is presented vs. PV injected.

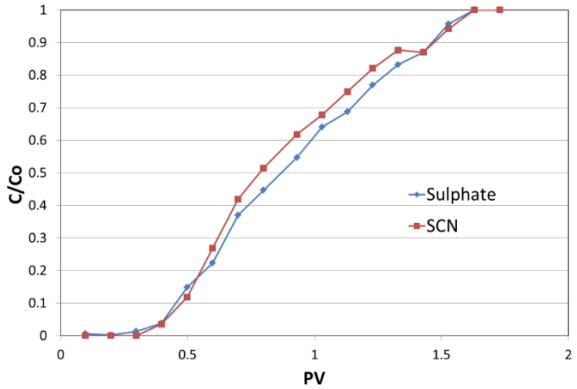

Figure 3. Chromatographic wettability test of Core#1 after the first oil flooding of 15 PV with an oil having AN = 0.35 mgKOH/g oil. The test on Core#1 was performed at S_{or}. The relative effluent concentrations of SCN^- and SO_4^{2-} are plotted vs. PV injected.

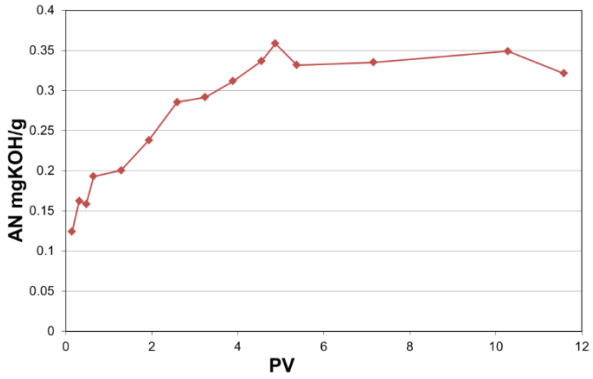

Figure 4. The adsorption of Acidic organic material during the second Oil flooding of Chalk Core#1 at 50°C with RES40-0.35 oil, with a flow rate of 0.1 ml/min (4 PV per day). The AN in effluent samples is presented vs. PV injected.

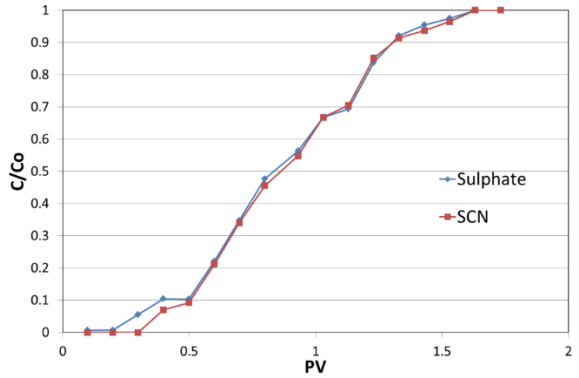

Figure 5. Chromatographic wettability test of Core#1 after the second oil flooding of 15 PV with RES40-0.35 oil. The test on Core#1 was performed at S_{or}. The relative effluent concentrations of SCN^- and SO_4^{2-} are plotted vs. PV injected.

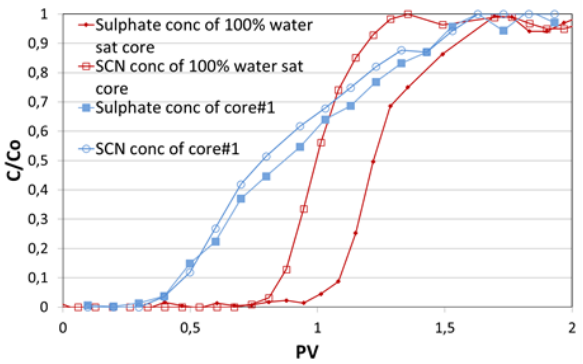

Figure 6. Chromatographic wettability test of a reference core and Core#1 after the first oil flooding of 15 PV with RES40-0.35 oil. The reference core was 100% saturated. The test on Core#1 was performed at S_{or}. The relative effluent concentrations of SCN^- and SO_4^{2-} are plotted vs. PV injected.

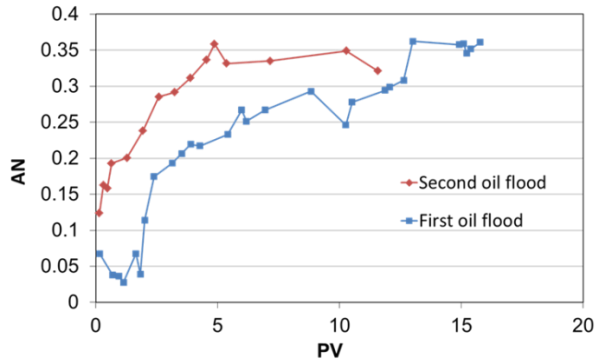

Figure 7. A comparison for the adsorption of Acidic organic material for both first and second Oil flooding of Chalk Core#1. The tests were performed at 50°C with RES40-0.35 oil, with a flow rate of 0.1 ml/min (4 PV per day). The AN in effluent samples is presented vs. PV injected.

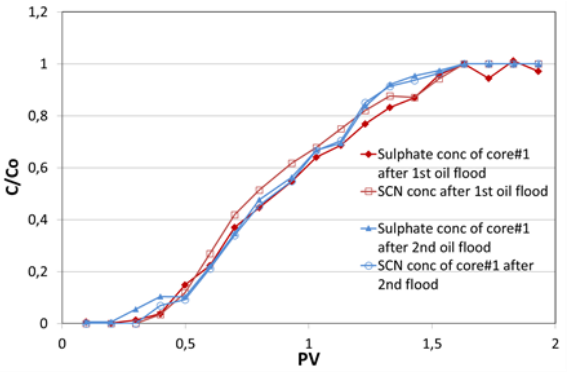

Figure 8. Chromatographic wettability test of Core#1 for both the first oil flood and second oil flood. 15 PV was flooded with RES40-0.35 oil. Both tests on Core#1 was performed at S_{or}. The relative effluent concentrations of SCN^- and SO_4^{2-} are plotted vs. PV injected.

THE IMPACT OF RESERVOIR CONDITIONS ON WETTING AND MULTIPHASE FLOW PROPERTIES MEASUREMENTS FOR CO_2-BRINE-ROCK SYSTEM DURING PRIMARY DRAINAGE

Ali Al-Menhali[1,3], Ben Niu[2,3], Samuel Krevor[1,3]
[1]Department of Earth Science & Engineering, Imperial College London
[2]Department of Chemical Engineering, Imperial College London
[3]Qatar Carbonates and Carbon Storage Research Center, Imperial College London

This paper was prepared for presentation at the International Symposium of the Society of Core Analysts held in Newfoundland and Labrador, Canada, 16-20 August 2015

ABSTRACT

The wettability of CO_2-brine-rock systems will have a major impact on the management of safe carbon sequestration in subsurface geological formations. The wetting properties of a system controls the mobility and trapping efficiency of CO_2 during injection processes for carbon storage as well as for enhanced oil recovery operations. Recent contact angle measurement studies have reported significantly different wetting behaviour with regard to pressure, temperature and water salinity. We report the results of an experimental investigation into the wetting properties of CO_2 and brine solutions in a single Berea sandstone utilising measurements of the multiphase flow properties under a wide range of reservoir conditions with pressures (5 to 20 MPa), temperatures (25 to 50 °C) and ionic strengths (0 to 5 M kg-1 NaCl). Primary drainage capillary pressure curves were measured in a horizontal core flooding apparatus using the semi-dynamic method to investigate the wetting properties during CO_2 injection process. The observations were made using a reservoir condition core-flooding laboratory that included high precision pumps, temperature control, the ability to recirculate fluids for weeks at a time and in situ saturation monitoring with x-ray CT scanner. The wetted parts of the flow-loop are made of anti-corrosive material that can handle co-circulation of CO_2 and brine at reservoir conditions. Measurements in the Berea sample were made using CO_2-brine and N_2-water. The capillarity of the system, scaled by the interfacial tension, were equivalent to the N_2-water system. Thus reservoir conditions did not have a significant impact on the capillary strength of the CO_2-brine system through a variation in wetting. The capillarity is consistent with general characteristics of drainage in strongly water-wet rocks. The fluid distributions were observed using x-ray computed tomography and the spatial saturations were investigated and were found to be invariant with different reservoir conditions in homogeneous samples.

INTRODUCTION

While recent contact angle measurements have shown CO_2 to generally act as a non-wetting phase in siliciclastic rocks, some observations report significantly different

wetting behaviour, if not entirely contradictory results, with regard to pressure, temperature and water salinity of CO_2-brine-rock systems. Additionally, there is a wide range of reported contact angles for this system, from strongly to weakly water-wet. In the case of some minerals, intermediate wet contact angles have been observed. Using contact angle measurements on smooth crystal surfaces, [1] found that the CO_2-brine system was strongly water-wet on quartz and calcite with no impact on pressure and a small shift with salinity up to 3.5M NaCl. [2] have also observed the system to be water-wet on quartz with little impact of both pressure and salinity from atmospheric to 10 MPa and 0.01-1M NaCl solutions. In the case of mica, however, the system shifted from water wet to intermediate wet with increasing CO_2 pressure (> 10 MPa). Water wettability was reduced by 25^o with salinity change from 0.1 to 1 M NaCl. However, the results at 0.01 M NaCl didn't obey the trend. [3] have found that contact angles on silica increased up to 17.6° ± 2.0° as a result of reactions with supercritical CO_2. The observed increase occurred primarily within the pressure range 7−10 MPa, but remain nearly constant at pressure greater than 10 MPa. They also observed that the contact angle increased with ionic strength nearly linearly with a net increase of 19.6° ± 2.1° at 5.0 M NaCl. Pressure had only a minor influence on the ionic strength effect. [4] have observed the system to be water-wet on quartz with contact angle $<30^o$ for both low and high temperature and pressure ($T=30^o$ P=7 MPa vs. $T=50^o$ P=20 MPa). However, they observed that the contact angle decrease with ionic strength for both conditions. In microfluidic experiments with silica micromodels, [5] observed contact angles ranging from water-wet to mixed wet for the supercritical CO_2-brine system as the salinity is increased from 0.01-5M NaCl.

In this study, we make several primary drainage (CO_2 displacing brine) capillary pressure measurements of at different reservoir conditions to investigate the effective wettability during CO_2 injection process that can last for decades in CCS projects. This process is a very important if not the most critical stage in CCS projects for safe CO_2 injection. A solid and clear understanding of the wettability of the system is essential for proper reservoir management and simulation of multiphase flow (CO_2 plume) during CO_2 injection. Figure 1 show that capillarity and multiphase flow effects may or may not be important depending on the rock properties of the storage target and thus it can be important to understand these properties in some detail. All of those graphs, however, were scaled from the mercury-air system assuming that the CO_2-brine system is strongly water wet. This assumption presumes maximum capillarity in the system. If the system is in fact less strongly water wet this manifests as a weakening of capillarity. As the system becomes less wet with respect to a given phase, it matters less and less what the particular pore structure looks like, the multiphase flow effects will be largely nullified.

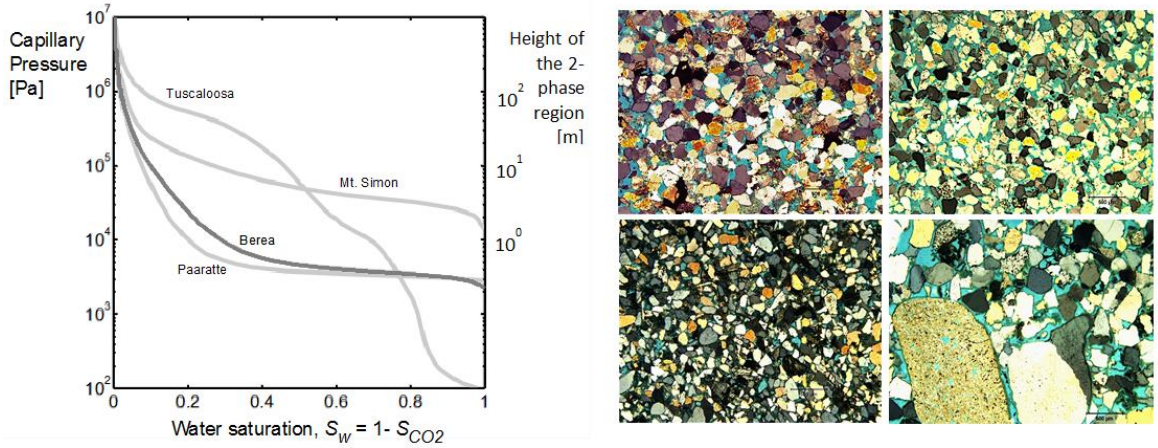

Figure 1. Reproduced from [6] showing the impact of capillarity on the height of 2-phase region. On the left, capillary pressure functions reproduced from plotted from observations with mercury-air displacement (MICP) scaled to interfacial tension values relevant to the CO_2-brine system. The Pc was converted to height to demonstrate the height of the 2-phase region in a CO_2 plume for different rock types. On the right, thin sections under cross-polarized light to compare grain size and distribution of the four sandstone rock types showing in the Pc curves graph. Blue die is used to visualize the pores. Clockwise from upper left: Berea, Paaratte, Tuscaloosa, Mt. Simon.

Figure 2 shows two end member examples reproduced from the model developed in [7, 8] of a buoyant CO_2 plume migrating upwards and along an impermeable boundary. Weak capillarity results in a very narrow range in the plume over which the saturation varies, corresponding to a relatively compact and fast moving plume. On the other hand, strong capillarity results in a much larger range over which the saturation varies, and an overall larger plume volume for the same mass of fluid and thus a more slowly migrating system. Once the injection phase is completed, imbibition plays a major role in CO_2 residual trapping. The impact of different reservoir conditions on residual trapping and hysteresis is investigated on the same Berea sample and conditions and discussed in details in earlier work [9].

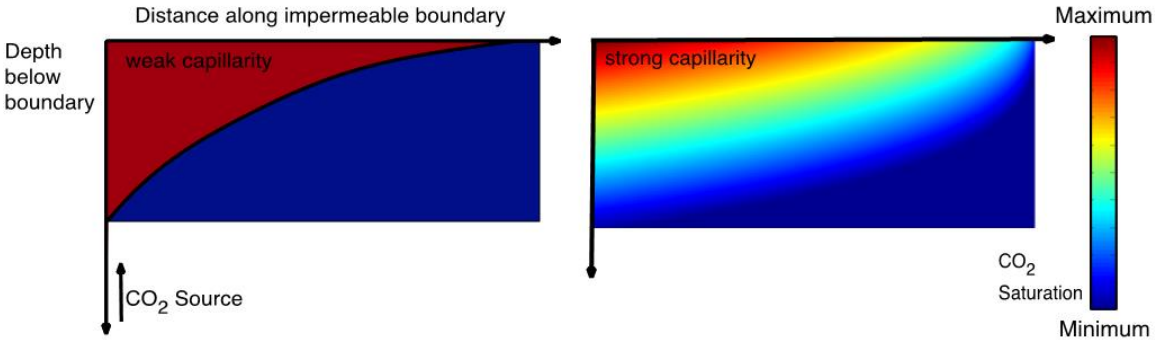

Figure 2. Two end member examples reproduced from the model developed in [7, 8] of a buoyant CO_2 plume migrating upwards and along an impermeable boundary.

The measurements of this work uses X-ray CT imaging in a state of the art core flooding laboratory designed to operate at high temperature, pressure, and concentrated brines.

This is the first study looking systematically at the impacts of reservoir conditions on the effective wettability in the CO_2-brine-sandstone system in a single rock sample. We also make measurements using N_2 and water to assess the ability to use analogue fluids to represent CO_2 and brine systems and developed a method to quantify shifts in effective wetting properties with changing reservoir conditions. We find no significant impact on wetting during primary drainage within the range of reservoir and flow conditions relevant to CO_2 storage, consistent with traditional multiphase flow theory but despite observations by others suggesting that wetting properties and multiphase flow in this system are sensitive to pressure, temperature and brine salinity [10]. In this paper, we report some of the results showing the impact of pressure on effective wettability and on spatial saturations distributions.

MATERIALS AND EXPERIMENTAL CONDITIONS AND SETUP

The Rock Sample and Fluids

A single homogeneous 20.32 cm long, 3.81 cm diameter Berea sandstone core sample was used for the entire tests performed in this study. Berea sandstone is an outcrop rock from the United States which is widely used in studies as a benchmark and for its utility in making comparisons with other studies. The sample was fired at 700 ^oC for 4 hours to prevent fines migration by stabilizing swelling clays that otherwise would cause permeability changes during core flooding tests. The faces of the core were machined flat to ensure good contact with the end-caps. The sample was vacuum dried in air at 70 ^oC overnight before each test. The absolute permeability of the sample to water was 212 mD with an average porosity of 21% as measured by x-ray CT scanning by following a protocol described in [11]. The skeletal density of the sample is 2.601 g/cm^3 measured with Helium pycnometer (AccuPyc 1330, Micromeritics) at 24 ^oC and 20 psi on a sub-sample (~ 0.8 cm^3) that was cut from a section adjacent to the inlet face of the core sample. Carbon dioxide and Nitrogen were used as the non-wetting phases in the core-flooding experiments both with 99.9% purity (BOC Industrial Gases, UK). The wetting phase fluids used were deionized water or brine. The brine solutions were made of deionized water and NaCl with total salt molality ranging from 0 to 5 mol kg^{-1}. In this paper, we report the capillary pressure experimental results investigating the impact of pore pressure on wetting properties and CT x-ray images. The fluids interfacial tension values as well as density and viscosity ratios for the experimental conditions are summarized in Table 1. Experiment N. 4, as described in the table was the only experiment where the wetting phase solution was deionized water doped with 5 wt% Sodium Iodide. This was necessary to compare and quantify the saturation distribution for the high density CO_2 experiments as will be discussed in a later section.

Table 1. Experimental conditions and fluids properties of experimental results investigating the impact of pore pressure on wetting properties and CT x-ray images

Experiment number	Non-wetting fluid	Wetting fluid	*Pressure* [Mpa]	*Temperature* [C]	σ^{ab} [mN/m]	$\mu_w/\mu_{nw}{}^{cd}$	$\rho_w/\rho_{nw}{}^{cd}$
1	gCO_2	H_2O	5	50	47	32	9.5
2	*scCO2*	H_2O	10	50	36	19	2.6
3	$scCO_2$	H_2O	20	50	30	8	1.3
4	$scCO_2$	H_2O with 5wt% NaI	20	50	-	8	1.3
5	N_2	H_2O	10	25	67	45	9

[a] CO_2 IFT from correlation developed in [12], [b] N_2 IFT from [13], [c] CO_2 densities and viscosities from NIST chemistry web book [14], [d] Water and brine densities and viscosities from [15]

Core-flooding Experimental Setup

The experimental work was conducted using a state of the art multi-scale imaging laboratory (core and pore scale) recently developed at Imperial College London designed to characterise reactive transport and multiphase flow, with and without chemical reaction for CO_2-brine systems in both sandstone and carbonate rocks at reservoir conditions [16]. The experimental setup is designed to replicate in-situ conditions of up to 120 ^oC and 30 MPa. Details of the experimental apparatus are reported in [11].

METHODOLOGY

Core-flooding was performed for capillary pressure measurements. Total injection flow rates varied from 0.5 up to 50 mL min^{-1}. The dimensionless capillary number, $N_c = V\mu/\sigma$, was used to ensure that local capillary equilibrium conditions applied during all of the experimental flow rates. Where V [m/s] and μ [Pa s] are the CO_2 superficial velocity and dynamic viscosity, respectively, σ [N/m] is the interfacial tension between CO_2 and brine. Capillary numbers around 10^{-4}-10^{-5} indicate that viscous and capillary forces are equivalent for the reservoir rock [17]. In this study, the capillary numbers for the highest flow rates applied ranged between 10^{-7} to 10^{-6} and the pore-scale fluid distribution was thus controlled by capillary forces.

We used the semi-dynamic capillary pressure method to measure the capillary pressure in the whole core. The technique was developed by [18] based on a model proposed by [19] and has been recently applied to measurements in CO_2-brine systems by [20, 21]. The technique applied here is described in [11] but we do not fit MICP to measurements for effective contact angle estimation. We use a more practical reference know to be strongly water-wet to evaluate wetting strength. We do this by measuring the semi-dynamic Pc of N_2-water on the same core sample and use it as a benchmark. The technique was developed further in this work and the main modifications were (1) the use of a spacer at the downstream end of the core to control the outlet boundary condition and (2) the use of a numerical simulator to design the parameters for the test, e.g., the injection flow rate. Brooks-Corey curves were fit to the core-flooding capillary pressure measurements [22].

$$P_c = P_e \left(\frac{S_w - S_{w,irr}}{1 - S_{w,irr}} \right)^{-1/\lambda} \quad (1)$$

Where Pe [Pa] is the entry pressure (i.e. the minimum pressure required for the entry of CO_2 into the pores of the rock), S_w represent the water saturation, while $S_{w,irr}$ represent the irreducible water saturation, λ is a fitting parameter known as the pore size distribution index.

Experimental Procedures

The first step was to expel air from the flow loop by flowing CO_2 through all parts of the experimental setup at an elevated pressure and exhausting to the atmosphere. This was done at different stages by isolating different sections of the flow loop to insure that air is expelled entirely. Then the system was pressurized with CO_2 and heated to the experimental pressure and temperature. This step was required to obtain the CO_2 saturated core background scan. Next, water or brine, depending on the experimental fluid, was injected into the loop to displace and dissolve all of the CO_2 out of the core at experimental pressure and temperature. A scan of the brine saturated core was obtained for porosity measurements. Porosity and saturations calculations with full experimental procedures for absolute permeability, fluids equilibration and semi-dynamic capillary pressure are described in details in earlier work [11].

RESULTS

A stable pressure drop was achieved for each CO_2 injection flow rate applied for semi-dynamic Pc before taking x-ray scans to measure saturations. The horizontal and vertical error bars of the Pc measurements represent uncertainty caused by pressure fluctuations during X-ray imaging time and saturation uncertainty based on the range of saturations seen from 10 repeated scans, respectively. The measured Pc curves were fitted with Brooks-Corey model, Eq. (1), objectively using a MatLab code. A single value was assigned for λ as a single rock sample was used for the entire study.

The Impact of Reservoir Pressure on Wettability

To evaluate the effect of pressure on wettability three experiments were carried out at pressures of 5, 10 and 20 MPa pore pressure at 50^{o}C and 0 Mol kg^{-1}. The pressures range such that CO_2 phase is transitioning from gas to low density $scCO_2$ and finally to high density $scCO_2$. With increasing pressure, the interfacial tension between the fluids decreased from 47 to 30 mN/m, Table 1. This was reflected in the capillary pressure and observable in the measurements with a lower entry pressure as the interfacial tension decreases, Figure 3a. Each Pc curve was scaled by its respective interfacial tension to allow for seeing if there is a weakening of the capillarity of the system through a change in wettability, Figure 3b. The scaled data set collapse nicely suggesting no change in the wettability with regard to pressure.

Analogue Fluids

A core-flood was performed using N_2 and deionized water at lab temperature, 25°C, and 10 MPa pore pressure for the purpose of comparison with a different fluids pair. The N_2-water system experiment is quicker and much easier than CO_2-brine experiments. Carbon dioxide-brine system is corrosive fluids pair and requires the entire wetted parts in the experimental apparatus to be anti-corrosion such as Hasteloy and Titanium. The solubility of CO_2 and N_2 at 25°C and 10MPa are 31.75cm^3/g (cm^3 of gas at standard conditions per gram of water) [23] and 1.264cm^3/g [24] respectively, i.e., the solubility of N_2 is more than 25 times less than CO_2. Therefore, N_2 equilibrates with water much faster compared to CO_2. The thermophysical properties of N_2 at 25°C and 10MPa were similar to CO_2 at 5MPa and 50°C, as shown in Table 1. Nitrogen and CO_2 capillary pressure curves scaled by their respective IFT are similar with slight shifts with regard to wettability as discussed in previous sections. Therefore, it is possible that the capillary pressure for CO_2-brine in sandstone to be estimated using N_2-water fluids pair particularly where the experimental apparatus for handling CO_2-brine systems is not readily available.

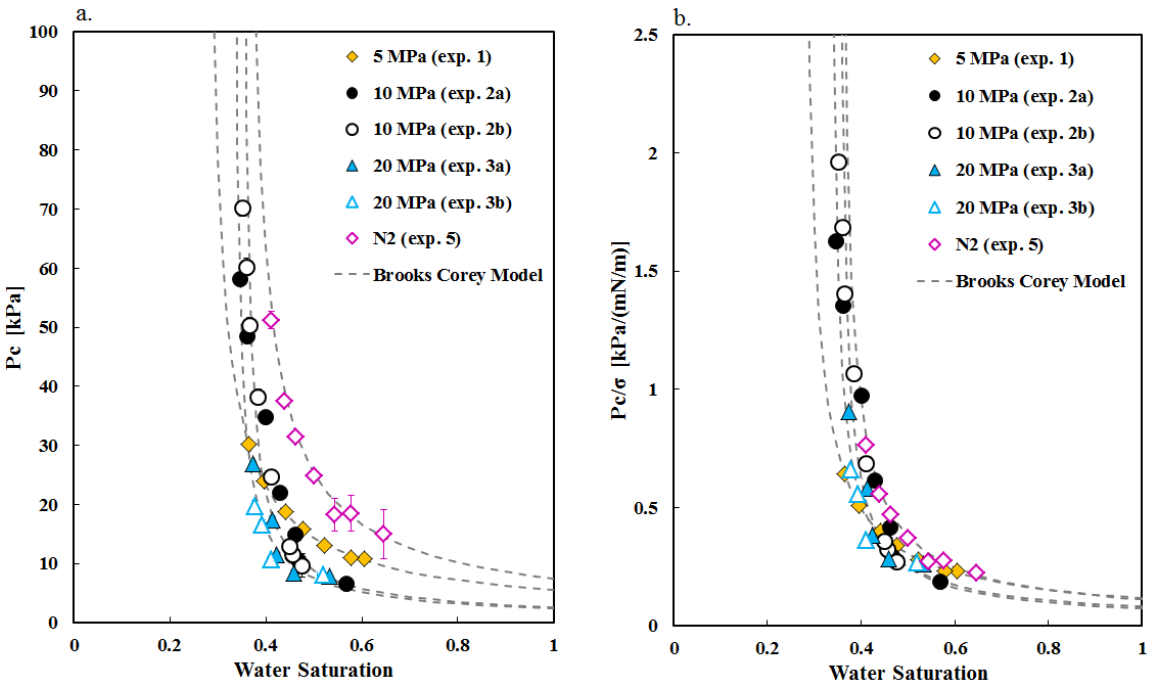

Figure 3. [10] a. Core-flood capillary pressure measurements of CO_2-water system at 50 °C, 0 mol/kg and pressures ranging from the gas phase (5 MPa) to low density scCO^2 (10 MPa) to high density scCO$_2$ (20 MPa). Nitrogen-water capillary pressure was included for comparison and to show the effect of IFT on Pc as measured by semi-dynamic technique. The repeats demonstrate the reproducibility of the semi-dynamic Pc measurements performed in this study. b. The Pc curves were scaled by IFT values representative of the experimental conditions, Table 1, and show no significant change in wettability with regard to pressure.

CT Images Accuracy as a Function of Fluids Density Ratio

Fluids saturations were measured in-situ by CT scanner using a combination of experimental and background scans as described in a previous section. This method depends on the contrast in density between the imaged phases (rock, wetting and non-wetting fluids). The density ratio between the wetting and non-wetting fluids varies depending on the experimental conditions as shown in Table 1. Thus, CT image quality is dependent on the density ratio of the experimental fluids and the noise associated with CT images can affect the corresponding reconstruction of 3-D saturation map. Depending on the significance of noise, a false fluids saturation distribution can be measured without proper coarsening. Figure 4 shows the saturation distribution of experiments 1 to 4 where CO_2 phase transfers from the gas phase to $scCO_2$ and finally to high density $scCO_2$, the ρ_w/ρ_{CO_2} range from 9.5 to 1.3. Experiment 4 was made at the same condition as 3 (50°C, 20 MPa) with the exception of doping the water with 5 wt% Nal to enhance the contrast between the fluids for the CT image.

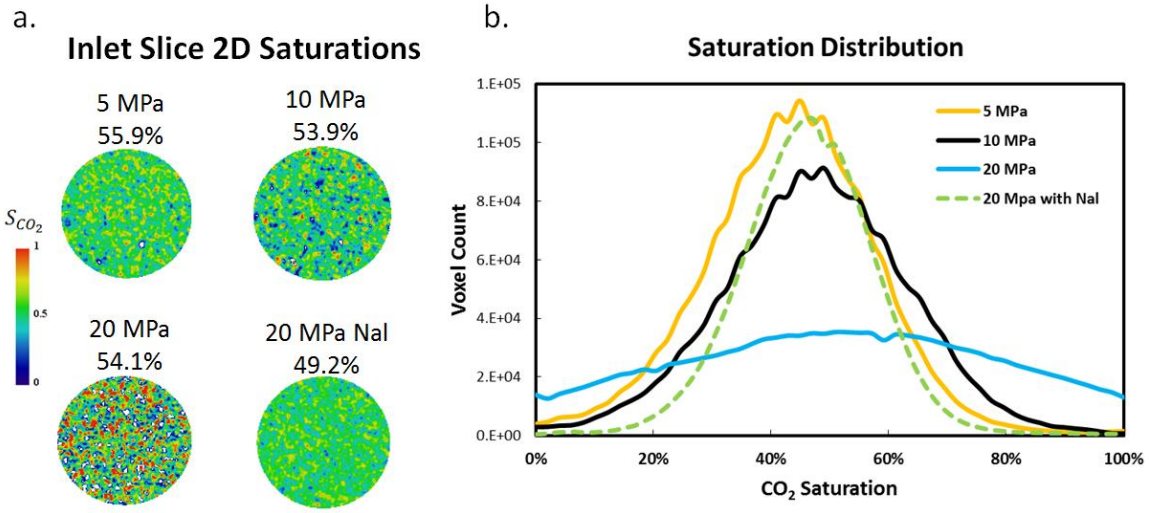

Figure 4. a. 2D saturation map of the inlet slice for 4 different experiements examining the impact of pressure on multiphase flow properties. The 2D slices have similar average saturations. b. Saturation distributions of the 2D inlet slices are directly proportional to experimental pressure and as CO_2 becomes denser. This is not representing insitue saturations but rather noise in CT measurements due to low water/CO_2 density ratio. This was confirmed by observing the saturation distribution at the high density CO_2 experiment after dopping water with Nal.

This test proves that the actual saturation distribution in the core sample remains unchanged and that the difference in the saturation distribution between experiments 1 to 3 is mainly due to the noise associated with lower density contrast. This noise has random nature and is irrelevant to the experimental conditions, as shown in Figure 5a. By subtracting two CT images at same conditions and location, the noise at voxel by voxel level was obtained. Usually, the noise has normal distribution and no relationship with fluid density. The uncertainty on calculated saturation induced by random noise for CO_2-brine system can be calculated by [21].

$$\sigma_S = \frac{\sigma_\Delta}{CT_{brine} - CT_{CO_2}} \sqrt{1 + \left(\frac{CT_{brine} - CT_{brine+CO_2}}{CT_{brine} - CT_{CO_2}}\right)^2} \quad (2)$$

where σ_S is the uncertainty on saturation, and σ_Δ is the standard deviation of random noise. The average uncertainty at various experiment ranges from 0.115 to 0.379, which is large enough to influence the comparison of saturation maps at different conditions. Therefore, different coarsening schemes have been applied to images from 1x1 to 15x15, as shown in Figure 5b. With increasing degree of coarsening, the level noise can be reduced. Therefore, the images at different experimental conditions have been processed with proper coarsening scheme before the reconstruction of saturation maps. By using the above approach, the range of the average uncertainty on saturation at various experiments has been reduced to 0.115~0.129, which is acceptable for the comparison between saturation maps.

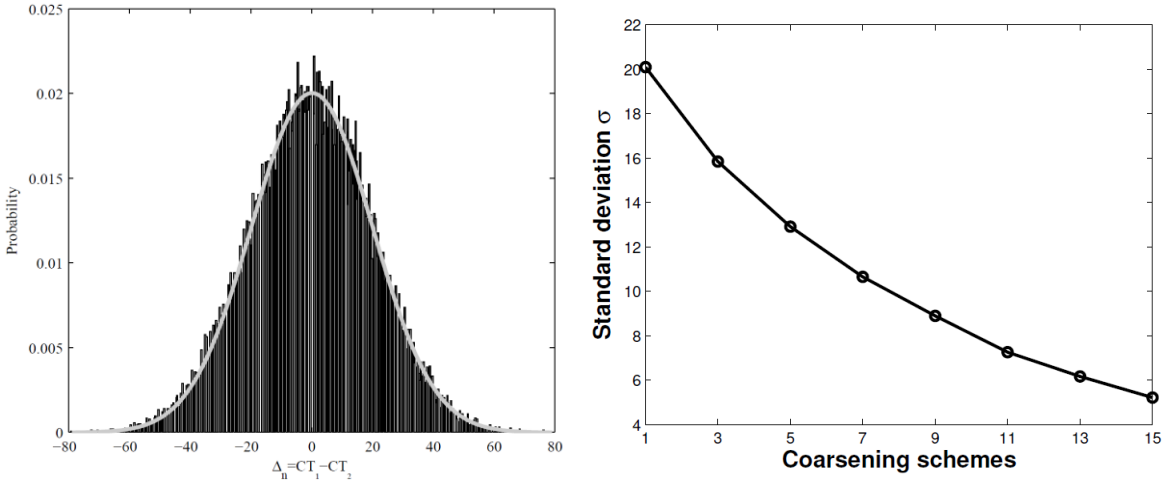

Figure 5. a. A histogram of CT numbers obtained by taking the difference of two scans of the same location. Various shades of grey represent difference values obtained at various conditions of pressure and temperature but they are indistinguishable indicating that the nature of the noise was intrinsic to the x-ray scanner. From light to dark the histogram bars are taken from: CT images of CO_2 saturated core at 5MPa-50ºC, 10MPa-25ºC, and 20MPa-50ºC respectively, Grey line: fitted normal distribution curve with mean value μ = 0.04 and standard deviation σ_Δ = 19.9. b. Random noise vs. coarsening schemes.

Quantify the impact of density ratio on error from image noise is crucial for studies targeting voxel resolution saturations from CT x-ray scanning. In this study, coarsening the images is not necessary for obtaining accurate saturation values as the slice average saturation remains unaffected. This analysis was made to inspect dissolution or gravity segregation and assure that the experiments were performed as designed by visualizing comparable images with less noise. This was also useful to confirm that the saturation distribution remains unaffected with different experimental conditions.

CONCLUSION

Wettability determines the efficiency of enhanced oil recovery operations as well as our ability to inject and store CO_2 in geological formations. This study investigated the effective core-scale wetting properties at a wide range of reservoir conditions to observe the impact of pressure, temperature and brine salinity on the wetting properties of the CO_2-brine system in siliciclastic rocks during primary drainage. Core-flood semi-dynamic capillary pressure were measured to observe the impact of different reservoir conditions on effective wettability from observations of multiphase flow properties. This allowed for measuring the core-scale effective and dynamic wetting properties representative of CO_2 injection processes such as EOR and carbon storage. No significant change in capillarity observed with regard to pressure even with different CO_2 phases (gaseous and supercritical). The saturation distribution of the fluids remained similar within the core sample with varying water/CO_2 density ratios. This was confirmed by a repeat of high density supercritical CO_2 and doped brine measurement. The error associated with noise from density ratio has to be considered in studies looking into voxel size saturations from CT imaging or spatial saturations distribution and up scaling resolution is advised. Analogue fluids can be used for characterising multiphase flow properties when reservoir conditions cannot be replicated. In general, reservoir conditions are not having a major impact on the wettability of CO_2-brine-sandstone system during CO_2 injection process and the system remains strongly water-wet during primary drainage for the experimental conditions investigated in this study.

ACKNOWLEDGEMENT

We gratefully acknowledge funding from the Qatar Carbonates and Carbon Storage Research Centre (QCCSRC), provided jointly by Qatar Petroleum, Shell, and Qatar Science & Technology Park.

REFERENCES

1. Espinoza, D., and J. Santamarina. "Water-CO_2-Mineral Systems: Interfacial Tension, Contact Angle, and Diffusion—Implications to CO_2 geological Storage." *Water Resources Research* 46, no. 7 (2010).
2. Chiquet, P., D. Broseta, and S. Thibeau. "Wettability Alteration of Caprock Minerals by Carbon Dioxide." *Geofluids* 7, no. 2 (2007): 112-22.
3. Jung, J., and J. Wan. "Supercritical CO_2 and Ionic Strength Effects on Wettability of Silica Surfaces: Equilibrium Contact Angle Measurements." *Energy & Fuels* 26, no. 9 (2012): 6053-59.
4. Wang, S., I. Edwards, and A. Clarens. "Wettability Phenomena at the CO_2–Brine–Mineral Interface: Implications for Geologic Carbon Sequestration." *Environmental Science & Technology* (2012).
5. Kim, Y., J. Wan, T. Kneafsey, and T. Tokunaga. "Dewetting of Silica Surfaces Upon Reactions with Supercritical CO_2 and Brine: Pore-Scale Studies in Micromodels." *Environmental science & technology* 46, no. 7 (2012): 4228-35.

6. Krevor, S., R. Pini, L. Zuo, and S. Benson. "Relative Permeability and Trapping of CO_2 and Water in Sandstone Rocks at Reservoir Conditions." *Water Resources Research* 48, no. 2 W02532 (2012).
7. Golding, M., J. Neufeld, M. Hesse, and H. Huppert. "Two-phase gravity currents in porous media." *Journal of Fluid Mechanics* 678:248-270 (2011).
8. Golding, M., H. Huppert, and J. Neufeld. "The effects of capillary forces on the axisymmetric propagation of two-phase, constant-flux gravity currents in porous media." *Physics of Fluids 1994-present*, 25 (3):036602 (2013).
9. Niu, B., A. Al-Menhali, and S. Krevor. "The Impact of Reservoir Conditions on the Residual Trapping of Carbon Dioxide in Berea Sandstone." *Water Resources Research* (2015).
10. Al-Menhali, A., B. Niu, S. Krevor. "Capillarity and Wetting of Carbon Dioxide and Brine During Drainage in Berea Sandstone at Reservoir Conditions" [in preperation] *Water Resources Research* (2015).
11. Al-Menhali, A., and S. Krevor. "Pressure, Temperature and Ionic Strength Effects on the Wettability of CO_2-Brine-Sandstone System: Core-Scale Contact Angle Measurements." *Society of Core Analysts Symposium* SCA2013-003, no. Paper presented at the 2013 SCA in Napa Valley, California (2013).
12. Li, X., E. Boek, G. Maitland, and J. Trusler. "Interfacial Tension of (Brines + CO_2): (0.864 Nacl + 0.136 KCl) at Temperatures between (298 and 448) K, Pressures between (2 and 50) Mpa, and Total Molalities of (1 to 5) Mol·Kg–1." *Journal of Chemical & Engineering Data* 57, no. 4 (2012).
13. Yan, W., G. Zhao, G. Chen, and T. Guo. "Interfacial Tension of (Methane + Nitrogen) + Water and (Carbon Dioxide + Nitrogen) + Water Systems." *Journal of Chemical & Engineering Data* 46, no. 6 (2001): 1544-48.
14. Lemmon, E., M. McLinden, and D. Friend. "Thermophysical Properties of Fluid Systems in Nist Chemistry Webbook; Nist Standard Reference Database No. 69, Eds. P. Linstrom and W. Mallard, National Institute of Standards and Technology, Gaithersburg Md, 20899, Http://Webbook.Nist.Gov." (retrieved May 6, 2013).
15. Kestin, J., H. Khalifa, and R. Correia. *Tables of the Dynamic and Kinematic Viscosity of Aqueous Nacl Solutions in the Temperature Range 20-150 C and the Pressure Range 0.1-35 Mpa*. American Chemical Society and the American Institute of Physics for the National Bureau of Standards, 1981.
16. Al-Menhali, A., C. Reynolds, P. Lai, B. Niu, N. Nicholls, J. Crawshaw, and S. Krevor. "Advanced Reservoir Characterization for CO_2 Storage." *International Petroleum Technology Conference*, (2014).
17. Hassanizadeh, S., and W. Gray. "Thermodynamic Basis of Capillary Pressure in Porous Media." *Water Resources Research* 29, no. 10 (1993): 3389-405.
18. Lenormand, R., A. Eisenzimmer, and C. Zarcone. "A Novel Method for the Determination of Water/Oil Capillary Pressures of Mixed-Wettability Samples." Paper presented at the SCA, (1993).
19. Ramakrishnan, T., and A. Cappiello. "A New Technique to Measure Static and Dynamic Properties of a Partially Saturated Porous Medium." *Chemical Engineering Science* 46, no. 4 (1991): 1157-63.

20. Pini, R., and S. Benson. "Simultaneous Determination of Capillary Pressure and Relative Permeability Curves from Core-Flooding Experiments with Various Fluid Pairs." *Water Resources Research* (2013): 49, doi:10.1002/wrcr.20274.
21. Pini, R., S. Krevor, and S. Benson. "Capillary Pressure and Heterogeneity for the CO_2/Water System in Sandstone Rocks at Reservoir Conditions." *Advances in Water Resources* 38 (2012): 48-59.
22. Brooks, R., and A. Corey. "Hydraulic Properties of Porous Media, Hydrology Papers, No. 3, Colorado State University, Ft." *Collins, Colo* (1964).
23. Wiebe, R. "The Binary System Carbon Dioxide-Water under Pressure." *Chemical Reviews* 29, no. 3 (1941): 475-81.
24. Wiebe, R., V. Gaddy, and C. Heins. "The Solubility of Nitrogen in Water at 50, 75 and 100° from 25 to 1000 Atmospheres." *Journal of the American Chemical Society* 55, no. 3 (1933): 947-53.

THE IMPACT OF RESERVOIR CONDITIONS ON MULTIPHASE FLOW IN THE CO_2-BRINE SYSTEM IN PERMEABLE SANDSTONE

Samuel Krevor, Catriona Reynolds, Ali Al-Menhali, Ben Niu
Department of Earth Science & Engineering
Qatar Carbonates and Carbon Storage Research Centre
Imperial College London

This paper was prepared for presentation at the International Symposium of the Society of Core Analysts held in St. John's Newfoundland and Labrador, Canada, 16-21 August, 2015

ABSTRACT

Capillary strength and multiphase flow are key parameter inputs for modeling CO_2 injection processes for enhanced oil recovery and CO_2 storage. Experimental observations of the multiphase flow properties in this system reported over the past 10 years have raised important questions about the impact of reservoir conditions on flow through effects on wettability, interfacial tension and fluid-fluid mass transfer. In this work we report the results of a three year investigation aimed at resolving many of these outstanding questions for flow in sandstone rocks. The capillary pressure, relative permeability and residual trapping characteristic curves have been characterized in Bentheimer and Berea sandstone rocks across a pressure range 5 – 20 MPa, temperatures 25 – 90 C and brine salinities 0-5M NaCl. In total over 30 reservoir condition core flood tests were performed evaluating these properties with techniques including the steady state relative permeability test, the semi-dynamic capillary pressure test and a novel test for the rapid construction of the residual trapping initial-residual (IR) curve. Test conditions were designed to isolate effects of interfacial tension, viscosity ratio, density ratio and salinity. The results of the tests show unequivocally that reservoir conditions have minimal impact on relative permeability and residual trapping, consistent with continuum scale multiphase flow theory for water wet systems. The invariance of the characteristic curves is observed across the range of conditions, including transitions of the CO_2 from a gas to a liquid to a supercritical fluid, and in comparison with N_2-brine systems. Variations in capillary pressure curves are generally well explained by corresponding changes in IFT although some further variation may reflect small changes in wetting properties that have been observed in sessile drop experiments. As with gas-brine systems, the low viscosity of CO_2 at certain conditions results in particular sensitivity to rock heterogeneity. We show that (1) heterogeneity is the likely source of much of the uncertainty around relative permeability observations for this system and (2) that appropriate scaling of the driving force for flow by a quantification of capillary heterogeneity allows for the selection of core flood parameters that eliminate this effect. Similarly this scaling can be used to approximate the effect of small scale heterogeneity on flow for real reservoir systems.

INTRODUCTION

Fluid flow during CO_2-injection processes, for enhanced oil recovery and CO_2 storage, is governed by the multiphase flow properties - capillary pressure, relative permeability, hysteresis and residual trapping. A sketch of fluid flow during buoyant CO_2 migration in a reservoir is shown in Figure 1. The leading edge and upper portions of a plume maintain high capillary pressures and CO_2 saturation is high in these regions – leading to high values of relative permeability. In the lower and distal sections of the plume a capillary fringe will appear as saturation tapers to the residual. The disconnection of CO_2 ganglia results in hysteresis in the multiphase flow functions.

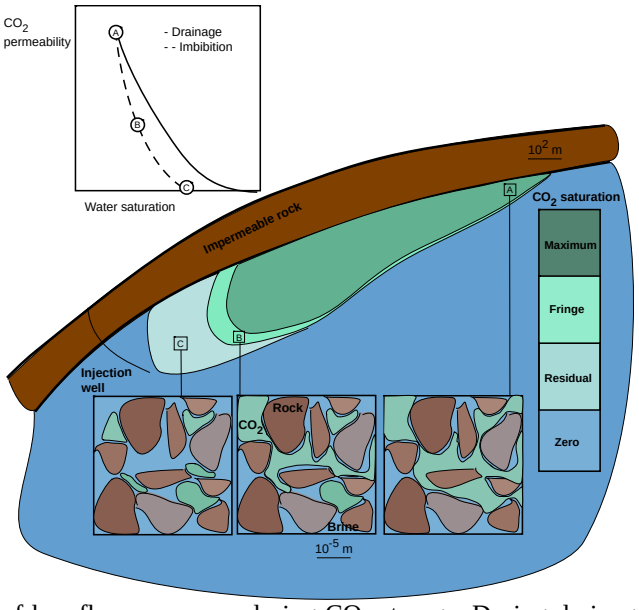

Figure 1. A sketch of key flow processes during CO_2 storage. During drainage, at the leading edge of the plume, CO_2 displaces resident brine to near the connate water saturation and relative permeability is high. Where the CO_2 plume is receding, brine imbibes and results in a disconnected fluid saturation. Ultimately, the saturation is lowered to residual immobile CO_2 which remains trapped. Figure from [25]

These relationships between the capillarity of a geologic system, and the saturation and permeability of the fluids have a direct bearing on the migration speed and reservoir sweep of a CO_2 plume (Figure 2, [1]), immobilisation through capillary trapping [2] and are used directly in assessments of the capacity of a storage site to contain CO_2 over geologic timescales [3].

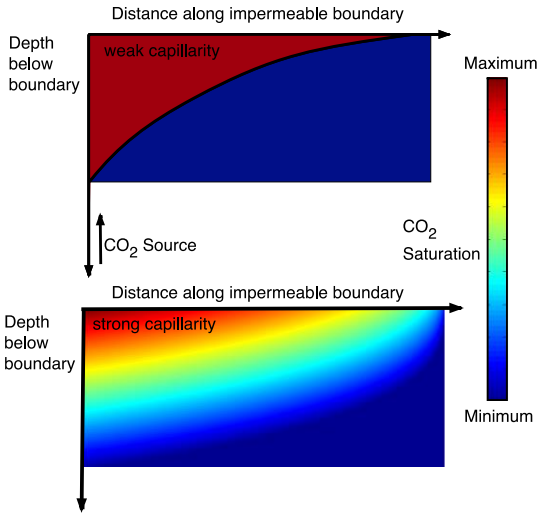

Figure 2. The impact of capillarity on multiphase flow – in systems with strong capillarity, i.e. strongly water wet systems, there is a larger plume sweep and lower forward propagation of CO_2 compared to systems with weaker capillarity, i.e. less strongly water wet systems. Figure adapted from [1].

Previous and ongoing experience with industrial scale carbon dioxide injection has come mostly from operations of enhanced oil recovery in the United States although there are pilot CO_2 storage projects around the world [4].

Despite the long history of the use of CO_2 for enhanced oil production there are longstanding uncertainties about the multiphase flow properties underlying descriptions and predictions of CO_2 migration and trapping in the subsurface. Major outstanding uncertainties include the impact of reservoir conditions of pressure, temperature and brine salinity on the wetting state and the relative permeability characteristic curve.

A large number of studies using sessile drop observations to characterise wetting have observed effects of pressure, temperature and brine salinity on wetting in this system with silicate and carbonate minerals, but the direction of the effects (increasing or decreasing wetting strength) and the magnitude have at times been contradictory [5-10]. A review of this issue has recently been published by [11].

Similarly, there are a large number of relative permeability curves reported in the literature (Figure 3, [12]). Based on these observations studies have variously described the CO_2-brine system as both less [13] and equivalently [14, 15] water wetting than hydrocarbon systems, to have relative permeabilities sensitive to variation in reservoir conditions [16], and for the system to have unusually low endpoint CO_2 relative permeabilities [17].

The work of [14] stands alone as a comprehensive evaluation of the sensitivity of the multiphase flow properties of the CO_2-brine system to reservoir conditions. In this approach, capillary pressure and relative permeability curves of rocks were characterised

with mercury-air and nitrogen-water observations respectively. These properties were shown to lead to accurate modelled predictions of observations of unsteady state drainage, CO_2 displacing brine, at various temperatures and pressures. This lead to the conclusion that the CO_2-brine-rock system was water wet and the multiphase flow characteristics insensitive to reservoir conditions.

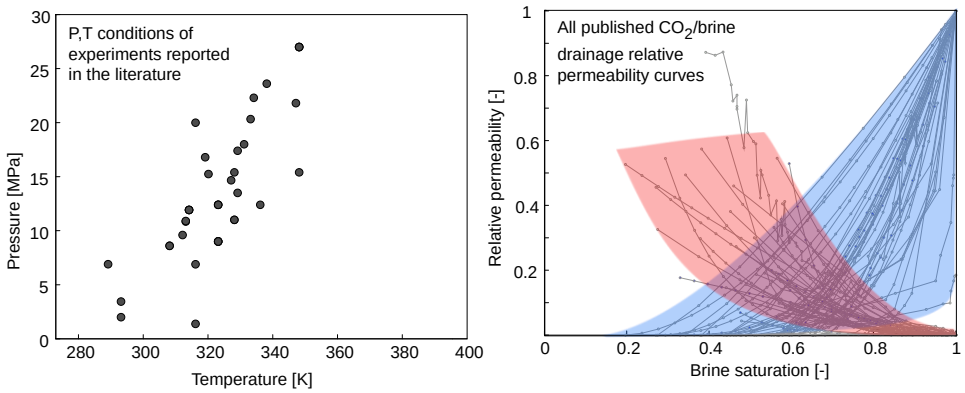

Figure 3. Compilation of drainage relative permeability curves published for CO_2-brine systems. From [12].

Characterisation of the capillary pressure characteristic curve can provide useful insight into the wetting state of a system and its impact on multiphase flow. Figure 4 shows sketches of capillary pressure primary drainage and secondary imbibition curves for water and mixed-wet CO_2-brine systems. In the mixed wet system during drainage there is a lower capillary entry pressure, a lower range of pressures required for full brine desaturation compared with the water wet system. During imbibition, there is more trapping in the water wet system and the residual is approached at capillary pressures close to zero. In the mixed-wet system, significant desaturation occurs at negative capillary pressures.

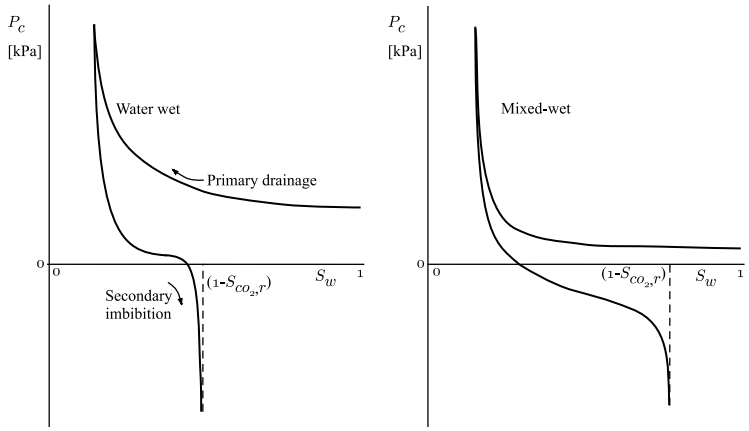

Figure 4. Primary drainage and secondary imbibition capillary pressure characteristic curves for water wet (left) and mixed-wet systems (right).

The residual trapping characteristic of a rock can thus be used partly as a diagnostic for the wetting state of the system. As described above, it is also a key reservoir characteristic, with primary controls on plume migration and storage capacity. The characteristic curve – described by the initial residual relationship shown in Figure 5 – is also often used to parameterise hysteresis models for capillary pressure and relative permeability, i.e. the Land model shown in Figure 5 [18].

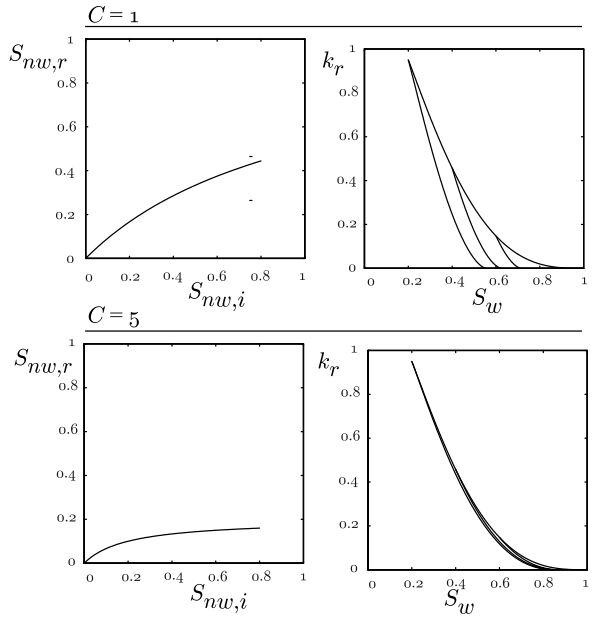

Figure 5. Initial-residual characteristic curves are shown on the left, constructed from the Land model with various values of the constant *C* [18]. On the right are the corresponding relative permeability curves with hysteresis tracking curves constructed with the Land model.

In this study we have sought to address outstanding questions around the response of multiphase flow properties in the CO_2-brine-sandstone rock system to reservoir conditions. We have evaluated the drainage capillary pressure, steady state relative permeability, and initial-residual curves characterising residual trapping at a range of reservoir conditions. These curves were compared with observations of the characteristic curves using the N_2-water system, known to be water-wet.

MATERIALS AND METHODS

A homogenous Berea sandstone rock core was used for the studies on capillary pressure and residual trapping. The homogeneity of the rock was most evident in the highly uniform saturation distribution of CO_2 and brine during multiphase flow displacement. The core was 3.8cm in diameter and 20cm in length and had a porosity and permeability of 0.19 and 210 mD respectively. The rock core was heated in an oven at 700˚C to stabilise mobile clays. A Bentheimer sandstone sample was used for the observations of relative permeability. The rock core was 3.8 cm diameter, 23 cm in length and had a porosity and permeability of 0.22 and 1.8 D respectively.

The ranges of pressures, temperatures and brine salinities for all of the tests are summarised in Table 1.

Table 1. Conditions and rock samples used in the multiphase flow experiments.

Observation	**Pressures [MPa]**	**Temperature [ºC]**	**Salinity [M NaCl]**	**Rock core**	**Technique**
Capillary pressure (drainage)	5-20	25, 50	0,1,3,5	Berea sandstone	Semi-dynamic Pc
Relative permeability (drainage)	10 – 21	30 - 90	0,1,3,5	Bentheimer sandstone	Steady state
Residual trapping	5- 20	25, 50	0,1,3,5	Berea sandstone	[19]

We used a variation of the semi-dynamic capillary pressure method [20-22] to measure the capillary pressure characteristic curves. A detailed description of the procedure is included in another paper in this symposium [23].

A steady state technique was used to characterise relative permeability. The saturation in the core sample was controlled by the ratio of injected phases, i.e. the fractional flow. In-situ saturation was measured along the entire sample with x-ray CT for each fractional flow once a constant pressure drop (i.e. steady state) was achieved. Evaluating the impact of reservoir conditions on multiphase flow in the CO_2-brine system is not a trivial task given that multiple fluid properties (density, viscosity) are changing over the same conditions of pressure, temperature and brine salinity**.** Experiments were designed to make observations of the relative permeability by varying interfacial tension while holding one or more of these parameters constant.

To construct the initial-residual capillary trapping characteristic curve, a core flood test was used to exploit the presence of capillary end effects to rapidly observe the relationship across a wide range of saturations at reservoir conditions [19]. In a given test, a range of initial CO_2 saturations along the length of the core were created by performing drainage at a flow rate that maximised the capillary end effect. Subsequently, imbibition was performed at a flow rate representative of reservoir conditions until the CO_2 saturation reduced to the residual. A range of residual saturations observed along the length of the core corresponded to the range in initial saturation existing prior to imbibition. As a result, a single core flood could be used to parameterise the initial-residual curve along a range of saturations.

RESULTS

One group of capillary pressure characteristic curves for tests evaluating the impact of pressure on capillarity are shown in Figure 6. In the right graph of the figure, the capillary

pressures are scaled by the respective interfacial tensions for each condition. Variation in the capillary pressure characteristic curves are accounted for by the variation in interfacial tension for each condition suggesting that any variation in wettability is not making an impact on capillarity for this system. This was generally the case for all of the conditions tested, although there was some variation in the scaled curves. The consistency with the N_2-water system indicates that the CO_2-brine system is water wet during drainage. Further results are detailed in another paper in this symposium, [23].

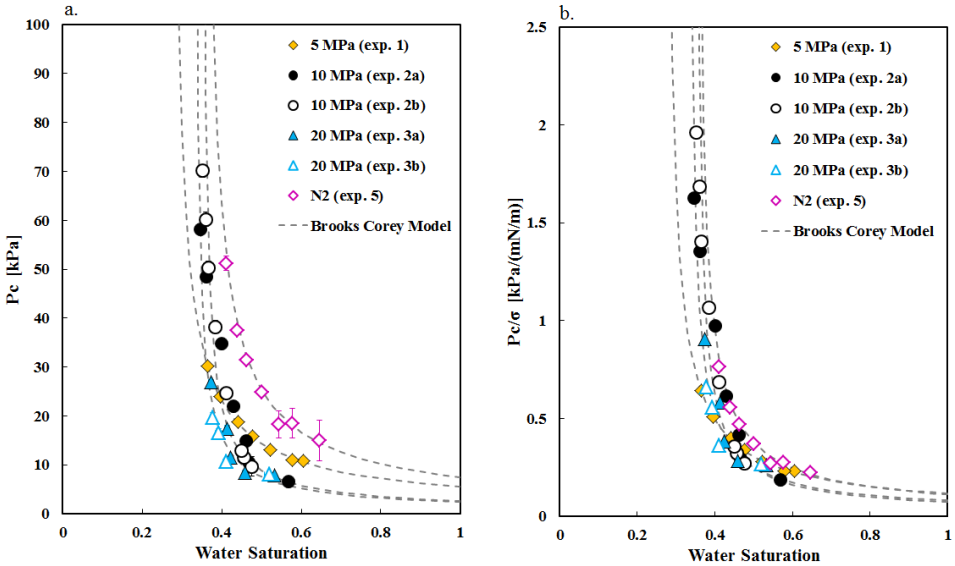

Figure 6. Capillary pressure characteristic curves evaluating the impact of pressure variation on capillarity in the system. Curves measured at pressures ranging from 5 MPa to 20 MPa are shown on the left and scaled by interfacial tension on the right. [23].

In the relative permeability tests the relative permeability of the rock core obtained when fluid saturations were unaffected by end effects, gravity segregation, and rock heterogeneity, was found to be invariant with reservoir conditions and equivalent to the N_2-water relative permeability. This will be referred to as the *intrinsic* relative permeability.

One group of results is shown in Figure 7. Two of the tests were performed with CO_2 and brine at reservoir conditions of pressure, temperature and brine salinity, while a third test was performed using a nitrogen-brine system at ambient conditions. The range of interfacial tension spanned from 37 mN m^{-1} to 62 mN m^{-1}. The results show little variation in the relative permeability between the tests.

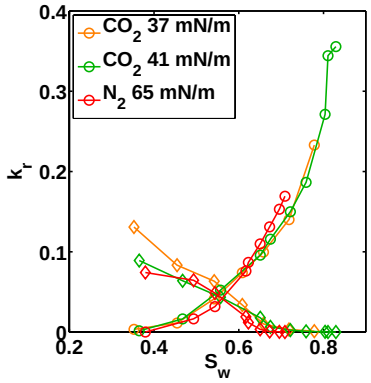

Figure 7. The intrinsic relative permeability of the rock core obtained from CO_2 and N_2 systems.

At conditions that resulted in CO_2 viscosities less than 30 μPa s, the fluid distributed heterogeneously throughout the core due to natural heterogeneity in the rock. Under these conditions, the derived relative permeability will be referred to as the *effective* relative permeability. We use this as the observational counterpart of a pseudo relative permeability. See [24] for a study in which pseudos have been applied to investigate core scale rock heterogeneity.

The effective relative permeability was observed to be sensitive to the test conditions, pressure, temperature, brine salinity and fluid flow rate. This is consistent with past observations and modelling of the impact of rock heterogeneity on observed flow properties [24]. Figure 8 shows one example of the intrinsic curve measured compared with an effective curve in which the interfacial tension was constant, but the viscosity of the CO_2 was less than 30 μPa s in the measurement affected by rock heterogeneity.

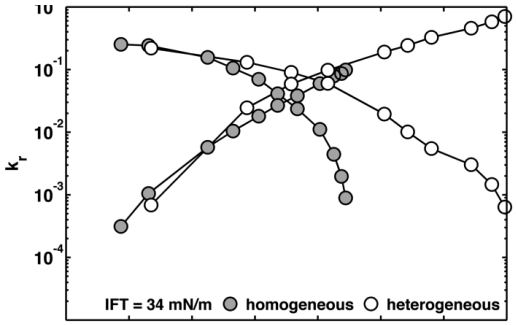

Figure 8. An intrinsic relative permeability curve (grey) and an effective relative permeability curve (white) measured at the same interfacial tension but distinct values of pressure and temperature. The difference in CO_2 viscosity led to homogenous and heterogeneous fluid distributions in the rock core.

The relative permeability core floods were all performed at a constant total flow rate of 20 ml min^{-1}, this being sufficient to minimise capillary end effects. Thus the total viscous pressure differential across the core, $\Delta\Phi = P_{inlet} - P_{outlet}$, varied primarily depending on

the viscosity of CO_2 for a given test. When the viscous force was high enough to support the capillary pressure gradients prevalent at constant saturation (Figure 9), a homogenous saturation was obtained and the intrinsic relative permeability was achieved. When the viscous force was low compared with the capillary heterogeneity in the core, capillary driven flow redistributed fluid towards a system with constant *Pc*, but heterogeneous saturation distribution and an effective relative permeability was observed.

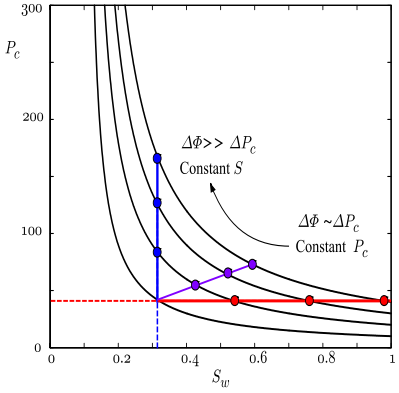

Figure 9. Conceptualising heterogeneity in the rock core with distinct capillary pressure characteristic curves. Low viscous force leads to a system of constant capillary pressure, but heterogeneous saturation distribution. A high viscous force leads to a system of homogenous saturation but capillary pressure gradients.

This study confirms the importance of evaluating the capillary heterogeneity in reservoir rock cores. We recommend in particular a characterisation of spatial heterogeneity in capillary pressure characteristic curves, e.g. [22]. A comparison of this with the estimated driving force for flow – e.g., pressure gradients, buoyancy - in a reservoir allows for one to design laboratory experiments either so that (1) an intrinsic relative permeability curve may be obtained or (2) effective flow functions representative of reservoir conditions can be observed. If capillary heterogeneity is significant, this provides quantitative guidance as to the conditions at which core tests should be operated to obtain representative effective relative permeabilities.

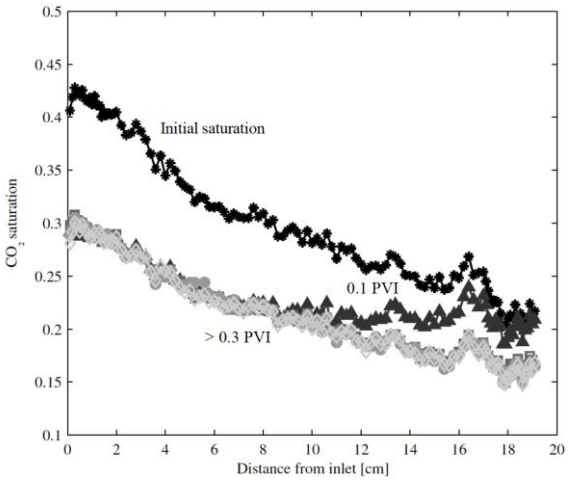

Figure 10. In-situ saturation profiles of CO_2 saturation after drainage (Initial saturation), after 0.1 pore volume of brine injection (PVI) and greater than 0.3 PVI showing the residually trapped saturation. From [19].

Observations of the saturation profile in a residual trapping experiment after drainage and during imbibition is shown in Figure 10. A compilation of the initial-residual data from all of the floods reported in [19] is shown in in Figure 11, along with the data obtained with an N_2-water system. There was little, if any, impact of reservoir conditions on the residual trapping characteristics of this system. The N_2-water curve was also indistinguishable from the CO_2-brine curves suggesting that this system was water wet during imbibition.

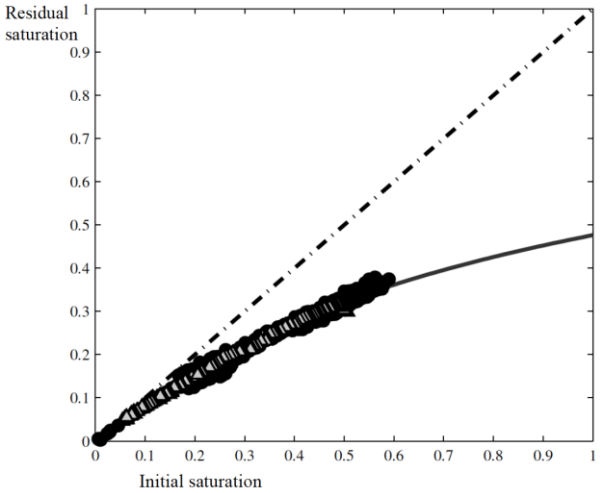

Figure 11. Initial-residual data from CO_2-brine core floods at all of the conditions are shown in black. Light colored symbols show trapping data obtained from a N_2-water system. From [19].

CONCLUSION

The body of observations demonstrate definitively that (1) the CO_2-brine system is water wet, and (2) the intrinsic multiphase flow properties of this system are invariant across the range of pressure, temperature and brine salinity in subsurface reservoirs worldwide. These two conclusions are consistent with the findings of [14] where a comprehensive evaluation of CO_2-brine multiphase flow was evaluated in carbonate rocks. It was also observed that (3) relative permeability in the CO_2-brine system may be sensitive to the presence of rock heterogeneity. In this case effective relative permeabilities should be obtained with appropriate scaling to reservoir conditions by comparing capillary heterogeneity to the viscous flow force representative of the reservoir system.

ACKNOWLEDGEMENTS

The authors gratefully acknowledge funding support for this work from the Qatar Carbonates and Carbon Storage Research Centre provided jointly by Shell, Qatar Petroleum and the Qatar Science and Technology Park.

REFERENCES

1. Golding, M.J., H.E. Huppert, J.A. Neufeld (2013) The effects of capillary forces on the axisymmetric propagation of two-phase, constant-flux gravity currents in porous media. *Physics of Fluids*. **25**, 3, 036602
2. Hesse, M.A., F.M. Orr Jr., H.A. Tchelepi (2008) Gravity currents with residual trapping. *Journal of Fluid Mechanics* **611**, 35-60
3. Szulczewski, M.L., C.W. MacMinn, H.J. Herzog, R. Juanes (2012) Lifetime of carbon capture and storage as a climate-change mitigation technology. *Proceedings of the National Academy of Sciences of the United States of America*. **109**, 14, 5185-5189
4. Global CCS Institute (2014) The Global Status of CCS: 2014
5. Chiquet, P., D. Broseta, S. Thibeau (2007) Wettability alteration of caprock minerals by carbon dioxide. *Geofluids*. 7, 112-122
6. Espinoza, D.N. and J.C. Santamarina (2010) Water-CO_2-mineral systems: Interfacial tension, contact angle, and diffusion – Implications to CO_2 geological storage. *Water Resources Research* **46**, 7, W07537
7. Jung, J-W. and J. Wan (2012) Supercritical CO_2 and Ionic Strenght Effects on Wettability of Silica Surfaces: Equilibrium Contact Angle Measurements. *Energy & Fuels*. **26**, 9, 6053-6059
8. Wang, S., I.M. Edwards, A.F. Clarens (2013) Wettability Phenomena at the CO_2-brine-mineral interface: Implications for Geologic Carbon Sequestration. *Environmental Science & Technology*. **47**, 1, 234-241
9. Kim, Y., J. Wan, T. J. Kneafsey, T. K. Tokunaga (2012) Dewetting of Silica Surfaces upon Reactions with Supercritical CO_2 and Brine: Pore-Scale Studies in Micromodels. *Environmental Science & Technology*. **46,** 7, 4228-4235
10. Broseta, D., N. Tonnet, V. Shah (2012) Are rocks still water-wet in the presence of dense CO_2 or H_2S? *Geofluids*. **12**, 4, 280-294
11. Iglauer, S., C. Pentland, A. Bush (2015) CO_2 wettability of seal and reservoir rocks and the implications for carbon geo-sequestration. *Water Resources Research*. **51,** 1, 729-774
12. Benson, S., Pini, R., Reynolds, C., and Krevor, S. (2013) Relative permeability analyses to describe multiphase flow in CO_2 storage reservoirs. Global CCS Institute

13. Berg, S., Oedai, H., Ott, H. (2011) Displacement and mass transfer between saturated and unsaturated CO_2-brine systems in sandstone. *International Journal of Greenhouse Gas Control*. 12, 478-492.
14. Egermann, P., Chalbaud, C., Duquerroix, J.-P., Gallo, Y.L. (2006) An Integrated Approach to Parameterize Reservoir Models for CO_2 Injection in Aquifers. *SPE Annual Technical Conference and Exhibition, San Antonio, Texas, 24-27 September 2006.* SPE 102308
15. Krevor, S.C.M., R. Pini, L. Zuo, S.M. Benson (2012) Relative Permeability and Trapping of CO_2 and Water in Sandstone Rocks at Reservoir Conditions. *Water Resources Research*. **48**, 2, W02532
16. Bachu, S. and B. Bennion (2008) Effects of in-situ conditions on relative permeability characteristics of CO_2-brine systems. *Environmental Geology*. **54**, 1707-1722
17. Levine, J., Goldberg, D.S., Lackner, K.S., Matter, J.M., Supp, M.G., Ramakrishnan, T.S. (2014) Relative permeability Experiments of Carbon Dioxide Displacing Brine and Their Implications for Carbon Sequestration. *Environmental Science & Technology*. 48, **1**, 811-818.
18. Land, C. (1968) Calculation of Imbibition Relative Permeability for Two- and Three-Phase Flow From Rock Properties. *SPE Journal*. 8, **02,** 149-156
19. Niu, B., Al-Menhali, A., Krevor, S.C. (2015) The impact of reservoir conditions on the residual trapping of carbon dioxide in Berea sandstone. *Water Resources Research*. In Press. doi: 10.1002/2014WR016441
20. Ramakrishnan, T.S., Cappiello, A. (1991) A New Technique to Measure Static and Dynamic Properties of a Partially Saturated Porous Medium. *Chemical Engineering Science.* 46, **4,** 1157-1163
21. Lenormand, R., A. Eisenzimmer, C. Zarcone (1993) A Novel Method for the Determination of Water/Oil Capillary Pressures of Mixed-Wettability. *Society of Core Analysts Conference Paper*. SCA 1993-9322
22. Pini, R., S.C.M. Krevor, S.M. Benson (2012) Capillary pressure and heterogeneity for the CO_2/water system in sandstone rocks at reservoir conditions. *Advances in Water Resources.* **38**, 48-59
23. Al-Menhali, A., Niu, B., Krevor, S. (2015) The Impact of Reservoir Conditions on Wetting and Multiphase Flow Properties Measurements for CO_2-Brine-Rock System During Primary Drainage. *International Symposium of the Society of Core Analysts, Newfoundland and Labrador, Canada, 16-20 August, 2015*. SCA-A058
24. Yokoyama, Y., Lake, L.W. (1981) The Effects of Capillary Pressure on Immiscible Displacements in Stratified Porous Media. *56th Annual Fall Technical Conference and Exhibition of the Society of Petroleum Engineers of AIME, San Antonio, Texas, Oct. 5-7, 1981*. SPE 10109
25. Krevor, S, Blunt, M.J., Benson, S.M., Pentland, C.H., Reynolds, C, Al-Menhali, A., Niu, B (2015) Capillary trapping for geologic carbon dioxide storage – From pore scale physics to field scale implications. *International Journal of Greenhouse Gas Control*. In Press

IMPROVED CORE ANALYSIS MEASUREMENTS IN LOW PERMEABILITY TIGHT GAS FORMATIONS

S. Kryuchkov[1,2], J. Bryan[1,2], L.Yu[1], D. Burns[3] and A. Kantzas[1,2]
[1]PERM Inc., Calgary, Canada; [2]University of Calgary, Canada
[3]TAQA North Ltd, Calgary, Canada

This paper was prepared for presentation at the International Symposium of the Society of Core Analysts held in St. John's Newfoundland and Labrador, Canada, 16-21 August, 2015

ABSTRACT

Recovery of hydrocarbon gas in micro-Darcy rock is now becoming more common-place for gas producers. As part of the reservoir characterization associated with these systems, it is required to understand parameters such as the total porosity and permeability of the system, but also the initial water saturation and the effective gas permeability at this connate water saturation. This is still under the realm of what is termed "routine core analysis", but in these tight formations it is imperative to understand that these tests are actually very non-routine by nature. Current work presents a case study of core analysis that was run on plugs from a tight gas producing formation, and illustrates some of the pitfalls and corrections associated with measurements of this low permeability rock.

The case study combines low field NMR measurements with core flooding measurements of porosity and permeability. Cores are initially tested at their connate water saturations: NMR measures the initial water present in each core, and effective porosity and permeability to gas are measured through different core analysis techniques. By considering the time scales required for pressure to propagate within the cores, it is shown that "routine" measurement of permeability through multi-rate Darcy flow of gas is simply not adequate to properly characterize the core. Instead, core properties are measured through analysis of transient pressure data. Cores are then run through a Dean-Stark cleaning process, and NMR measurements are used to verify the ability of Dean-Stark to remove all water out of the cores. In this manner, post-cleaning measurements of porosity and permeability can be understood as effective values rather than their assumed absolute properties. This case study illustrates the challenges in making accurate measurements in micro-Darcy rock systems, and helps end-users to understand the dangers in using routine data without knowing how the data was collected.

INTRODUCTION

The objective of this test was to measure effective porosity and permeability in tight cores containing some residual water content. These values were then to be compared to measured porosity and permeability after attempting to clean water out of the cores. In order to assess the objective of this project, six core plugs from the Ferrier field operated by TAQA North Ltd. were cut from as received (pseudo-native-state) core and were sent

to PERM Inc. The field is a dry gas field with water present. The mineralogy is primarily carbonate.

The following work plan was defined at the start of the project:

- Measure dimensions of cores.
- Measure NMR spectra of initial cores with parameters of 0.16ms TE, 5000 Echoes, 12,000ms waiting time, and 128 trains.
- Measure pore volume and porosity with gas expansion and effective permeability to gas under 14.9MPag (2160psig) overburden pressure and near ambient pore pressure for the cores.
- Dean-Stark the cores, making sure to spend sufficient time to try to remove all water from the samples.
- Measure NMR spectra of cores after Dean Stark extraction with parameters of 0.16ms TE, 5000 Echoes, 2,000ms waiting time, and 128 trains.
- Measure pore volume and porosity with gas expansion and effective permeability to gas under 14.9MPag (2160psig) overburden pressure and near ambient pore pressure for the cores.
- Dual-energy CT scanning of the cores.

PROCEDURE

1) In order to execute the work plan, the following steps/modifications were carried out: Cut both ends of "as received" cores and obtain cylindrical plugs. The cylindrical plugs were thereafter named as "initial cores".
2) Re-measure dimensions and mass of initial cores.
3) Make up brine that is 125,000ppm (12.5%) of NaCl, and measure its density at 25°C. This is the expected salinity of the connate water in the cores.
4) NMR measurement of initial cores, as well a known amount of water to establish the amplitude index of the brine.
5) Place the cores under 14.9MPag (2160psig) overburden pressure and measure effective permeability to gas and porosity with gas expansion.
6) Again weigh the cores and measure NMR spectra of the cores after permeability and porosity measurement.
7) Dean-Stark the cores with Toluene for two weeks and then Acetone / Methanol for one week. Dry the cores in a conventional oven for 2 days at 105°C.
8) Take the mass of cores after extraction, and measure the NMR spectra of the cores.
9) Record the saturation values (S_w) before and after Dean-Stark extraction for all plugs.
10) Put the cores back to core holder under 14.9MPag (2160psig) overburden pressure and measure permeability to gas and porosity with gas expansion. Based on the post-cleaning NMR spectra, this step is either an absolute permeability or an effective permeability at lower water saturations.

Please note that the Dean Stark extraction had to be extended much longer than the standard method of 48 hours per solvent to ensure maximum contact of the solvents with

resident fluids. When comparing the results with routine core analysis measurements, care must be taken to reconcile the methodology used by the routine core analysis laboratory.

The porosity and permeability measurements were done following the methodologies of gas expansion and steady state permeability measurement. However, the results were analyzed with two different methods. One was the traditional approach. The second method relied on conducting a history matching of the pressure decay data as observed in the gas expansion method and by fitting different values of permeability until a match was found. The results were compared for all the plugs and all conditions.

Equations for the non-stationary gas flow are nonlinear, which calls for numerical solution for calculation of permeability. The total pressure change from initial state to final stationary state is used to characterize the porosity of the core.

The slope of the pressure curve as a function of square root of time at the origin depends on gas parameters, the geometry of the system, and the core porosity and permeability. This simplifies the formulation of the algorithm for finding permeability from the history match of the pressure decay data.

EXPERIMENTAL RESULTS AND DISCUSSION

Tested Core Properties

Tabulated values for all measured properties are included as well as sample graphs for individual plug measurements along with summary graphs that show trends.

Figure 1 shows the setup for porosity and permeability measurements. Tests were run at ambient temperature. Due to the relatively high permeability range measured in the core plugs (i.e. micro-Darcies compared to nano-Darcies expected for shale), pressure decay tests can be run relatively quickly and a more thorough temperature control was not considered necessary. In these small pore volume systems, the key to being able to measure pressure changes is to keep all dead volumes small, on the same order of magnitude as the pore volumes of the core. Traditional gas expansion core analysis equipment will not register an accurate change in pressure as gas enters the core, since the dead volumes are so much larger than that of the pores.

Table 1 summarizes the dimensions of each plug. The grain density numbers are estimated from bulk density and porosity calculations with liquid saturation included.

Table 2 summarizes the porosity and apparent permeability results for the “as received” cores. The term effective porosity refers to the porosity measured with gas expansion, i.e. the pore space that is saturated with gas only. The term total porosity is the sum of the gas saturated porosity (measured by gas expansion) and the liquid-filled porosity measured by NMR. Total porosity is then taken to be the sum of the gas expansion (effective) porosity and the bound water porosity, and fluid saturations are also calculated

on this basis. Without any additional information about the drilling mud used and the pressure conditions while drilling it is uncertain whether the determined liquid saturation values represent the true irreducible wetting saturation numbers; in the absence of any other data, the liquid in the core is assumed to be the saline brine present for this system (125,000 ppm salt).

Table 3 summarizes the porosity and apparent permeability results for the core after Dean Stark extraction. Despite the extended cleaning and drying there are still some notable amounts of liquid left in the core samples. This is due to the presence of small pores that hold water or solvent through capillary forces. In small pores the vapor pressure starts dropping because of the high curvature of the concave interfacial surfaces. This slows down the evaporation rate. In addition, surface area of pores with small radii is increasingly important, because of its relatively high contribution to the total surface area and because of the water films, which are hard to evaporate due to the surface forces.

Drying this remaining trapped water would require substantially higher temperatures for the cores to dry. This cannot be allowed because drying at extreme temperatures would damage the clays and the pore structure of the core would change. Thus the residual liquid volume has to be considered when the porosity is calculated. Once again, these liquid volumes are measured through NMR analysis of the cores; the effective porosity measured through gas expansion is still lower than the true porosity of the core. Estimates of total porosity are similar in Tables 2 and 3, indicating that this methodology is accurate.

The other significance of the remaining water saturation after cleaning is that the measured permeability values are not absolute permeability, but rather are still effective gas permeability measurements at some (albeit reduced) liquid saturation. Table 4 presents the apparent vs. Klinkenberg corrected permeability values for all plugs, all conditions for reference purposes. There is very little difference between apparent and Klinkenberg corrected permeability for the samples and pressure ranges tested here.

Discussion

Figure 2 shows a typical NMR spectrum for plug SP16A at the different stages of the experimental process. Figure 3 shows the effective porosity change before and after the Dean Stark extraction process. Figure 4 shows the total porosity before and after the extraction process. The fact that the total porosity measurements match is very encouraging and justifies the use of the NMR technology in compiling supplementary measurements even for routine purposes in the calculation of total porosity.

Figure 5 presents the permeability data before and after cleaning. An increase in permeability is seen for the cleaned core. Figure 6 presents rudimentary relative permeability curves for gas for different plugs lumped together based on their extrapolated absolute permeability values. It is fascinating that the data are lumped into three sets that can be fitted by straight lines. Extrapolation of these line to zero

permeability provides predictions for critical gas saturation that appears to be inversely proportional to permeability. In Figure 7 the permeability data are compared against the history matching predictions of the pressure transient data. The agreement is fairly good, although it becomes worse as the 1μD value is reached.

Figure 8 and Figure 9 show samples of the permeability measurements for plug SP16. They are presented as examples in order to illustrate the linearity of the steady state results. Note that routine core analysis will not be conducted under the steady state mode. For cores with permeability larger than 1μD, the steady state method remains the most reliable method for permeability measurement. However, the transient approach for cores with permeability below 1μD appears to be quite reliable.

Figure 10 and Figure 11 are examples of the pore volume measurement and the transient data used in the complex transient permeability predictions. The line in red is the pressure transient match if the steady state permeability is used and the black line is the permeability obtained by better history matching with permeability being the adjustable parameter.

As discussed above, the slopes of the pressure transient curves at short times are directly related to the permeability of the core and help to accelerate the history match procedure for permeability. Straight lines on the graph are trend lines based on few initial experimental and calculated points.

Some mismatch of the fitted curve and the observed pressures is due to the variation of the sample temperature during this experiment.

The combination of NMR and Dean Stark was very useful in calculating the saturations in the core. Table 5 summarizes the residual saturation after Dean Stark as calculated from mass balance and NMR. The agreement is good. It should be noted that there is no evidence of hydrocarbons in the reservoir (it is considered a dry gas reservoir).

However, the NMR could pick up the presence of residual hydrocarbons. Discriminating hydrocarbons from water in small pores and pore wedges or physically trapped in clay structures would require NMR with gradients. This can be done but it was not addressed in this paper.

Furthermore it should be noted that the reservoir cores were quite heterogeneous. Image examples of the different plugs are shown in Figure 12. The whole plugs are used for the testing under net overburden pressure. Thus core heterogeneity is maintained and it is utilized in the calculations.

PERM has developed numerous algorithms for the determination of special core analysis information from limited data through pore network modelling and pore level multi-physics programs [1-3]. This Digital Core Analysis approach would be ideal to provide

estimates of capillary pressures, resistivity indices, and relative permeability curves. The analysis can be extended to the utilization of NMR spectra as input [4]. However, this was deemed outside the scope of this project and will be pursued as future research.

CONCLUSIONS

- Deviations from routine methods (steady state testing) increase when permeability falls below the 1μD range.
- Transient methodology becomes more accurate and it can be used to measure permeability values below 1μD.
- The combined porosity measurements from gas expansion and NMR converge to the same total porosity value, irrespective of the saturation conditions of the core.

ACKNOWLEDGEMENTS

Funding of this project from TAQA North, as well as permission to publish this paper are gratefully appreciated.

REFERENCES

1. Ghomeshi, S., Bashtani, F., Bryan, J., Kryuchkov, S. and Kantzas, A. "Determination of Physical Properties of Tight Porous Media Using Digital Core Physics/Analysis", accepted to Society of Core Analysis Symposium 2015, St. John's, NL, Canada, August 16-21, 2015.
2. Ghomeshi, S., Bashtani, F., Taheri, S., Skripkin, E., Kryuchkov, S., Bryan, J. and Kantzas, "Predicting Physical Properties of Porous Media at Sub-Pore Scales from Natural to Complex Heterogeneous Systems: Application in Tight Reservoirs", GeoConvention 2015, Calgary, AB, Canada, May 4-8, 2015.
3. Rubin M., Wickens S., Leung S., Akinbobola O., Kent T. and Kantzas A. "Network Modeling and Two-Phase Flow in Tight Reservoirs" GeoConvention 2014, Calgary, Canada, 12–14 May 2014.
4. Talabi, O. and Blunt, M.J. "Pore-Scale Network Simulation of NMR Response in Two-Phase Flow", *J. Pet. Sci. Eng.*, (2010), **72**, 1-9.

Table 1: Core ID and Dimensions

Sample ID	Depth (m)	Diameter (cm)	Length (cm)	Grain Density (kg/m^3)
SP16A	2565.70	3.81	6.05	2788.1
SP18A	2566.74	3.81	7.21	2779.4
SP19A	2567.70	3.81	7.53	2811.5
SP30A	2578.68	3.81	7.17	2750.8
SP33A	2580.30	3.81	7.27	2748.1
SP34A	2581.30	3.81	7.03	2992.1

Table 2: Initial Core Properties

Sample ID	Mass (g)	Effective Porosity (%)	Total Porosity (%)	k_{gas} (µD)		S_{liquid}	S_{gas}
				Steady state	Transient		
SP16A	175.68	5.57	10.62	0.81	2.07	0.48	0.52
SP18A	220.77	1.29	4.68	0.12	0.41	0.73	0.27
SP19A	226.34	3.75	7.70	0.09	0.89	0.51	0.49
SP30A	204.47	6.17	10.82	1.60	1.60	0.43	0.57
SP33A	210.82	4.84	9.18	2.36	2.36	0.47	0.53
SP34A	229.53	1.63	5.82	0.32	0.42	0.72	0.28

Table 3: Core Properties after Cleaning with Dean-Stark Extraction

Sample ID	Mass (g)	Effective Porosity (%)	Total Porosity (%)	k_{gas} (µD)			
				Steady state	Transient	S_{liquid}	S_{gas}
SP16A	172.82	10.10	10.59	6.71	7.56	0.05	0.95
SP18A	218.15	4.17	4.72	1.10	1.70	0.12	0.88
SP19A	222.99	7.42	7.92	1.03	1.84	0.06	0.94
SP30A	200.75	10.29	10.52	7.71	11.82	0.02	0.98
SP33A	207.41	8.86	9.26	12.51	13.60	0.04	0.96
SP34A	227.02	4.86	5.73	2.88	3.45	0.15	0.85

Table 4: Core Apparent and Klinkenberg Corrected Permeability Data

Sample ID	Before Cleaning (µD)		After Cleaning (µD)	
	k_g (µD)	k_∞ (µD)	k_g (µD)	k_∞ (µD)
SP16A	0.81	0.73	6.71	5.38
SP18A	0.12	0.10	1.10	0.91
SP19A	0.09	0.05	1.03	0.79
SP30A	1.60	1.59	7.71	6.54
SP33A	2.36	2.35	12.51	10.71
SP34A	0.32	0.29	2.88	2.52

k_∞ is Klinkenberg corrected permeability.

Table 5: Post Dean-Stark Water Mass Balance

Sample ID	Water Extracted (cm^3)	Residual water in core (cm^3)	NMR Residual water in core (cm^3)
SP16A	2.27	0.32	0.34
SP18A	1.68	0.53	0.45
SP19A	2.70	0.43	0.44
SP30A	3.17	0.17	0.19
SP33A	2.57	0.31	0.33
SP34A	1.62	0.71	0.70

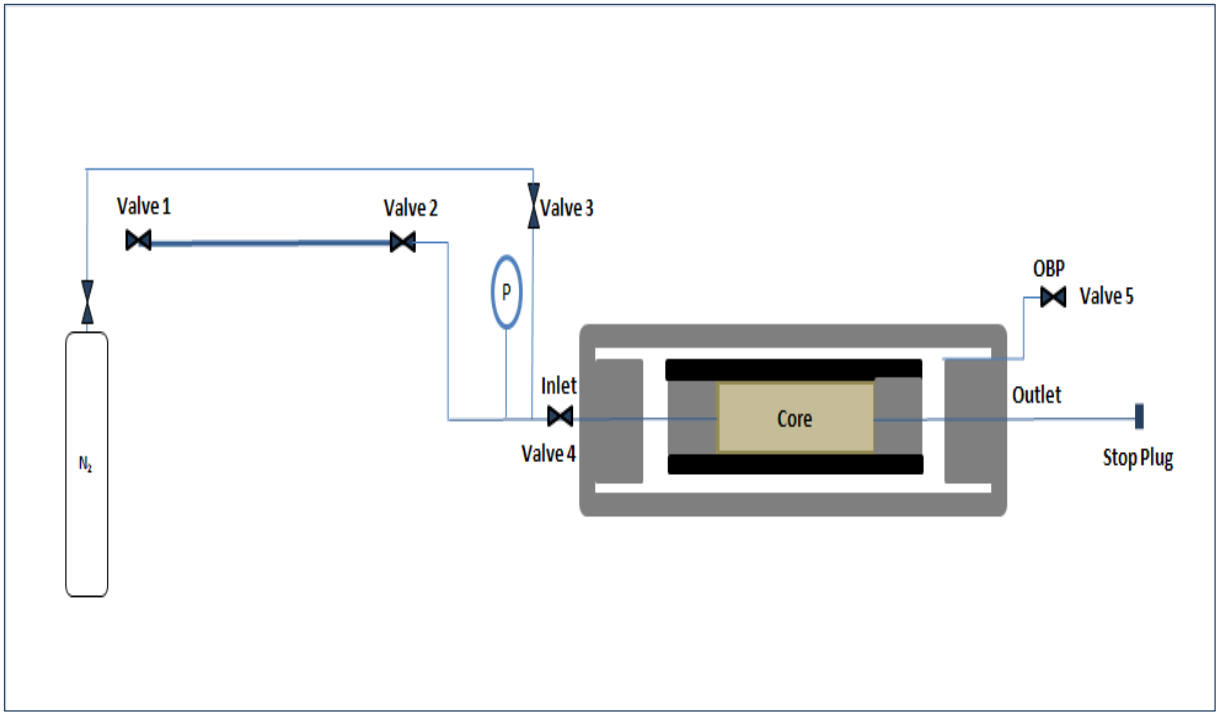

Figure 1: Core Testing Apparatus Rig Setup

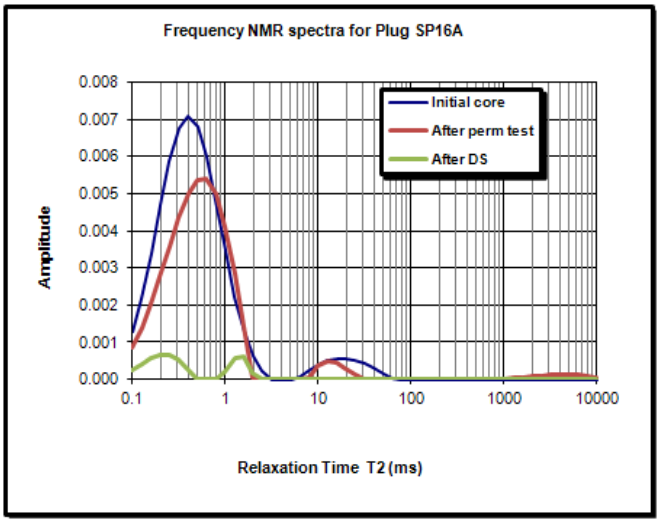

Figure 2: NMR Spectra for Plug SP16A

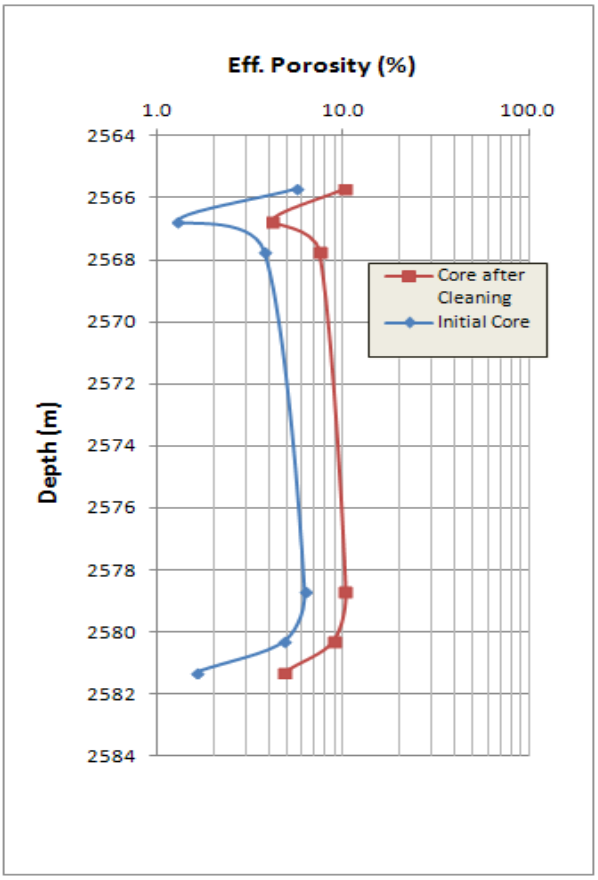

Figure 3: Effective Porosity of Initial Core and Core after Cleaning with Dean-Stark

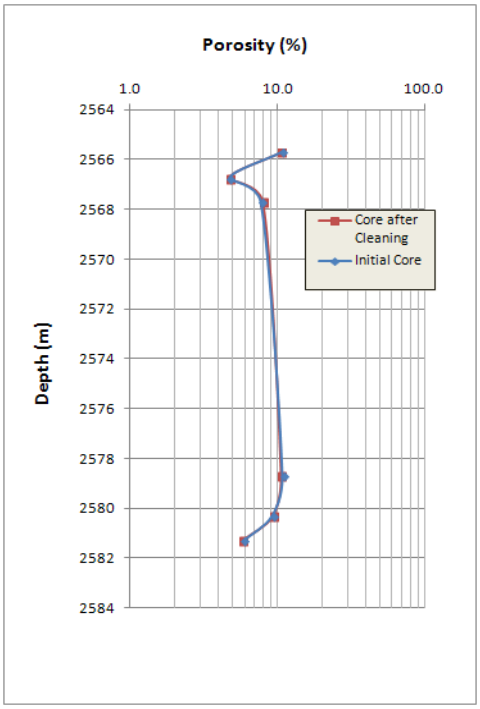

Figure 4: Total Porosity of Initial Core and Core after Cleaning with Dean-Stark

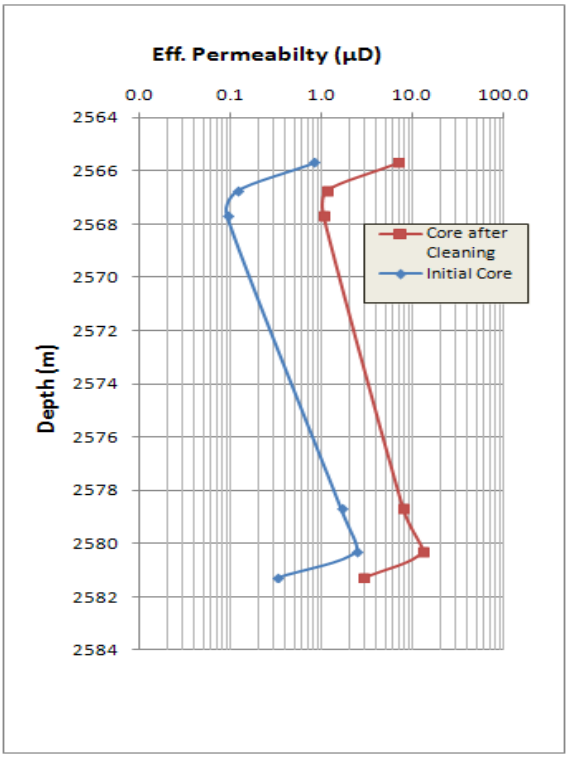

Figure 5: Gas Permeability of Initial Core and Core after Cleaning

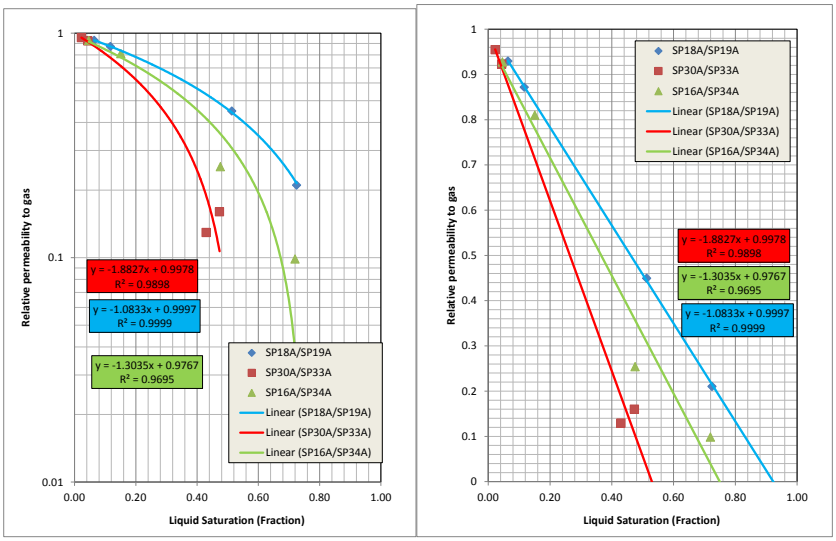

Figure 6: Gas Relative Permeability with Liquid Saturation for Each Core

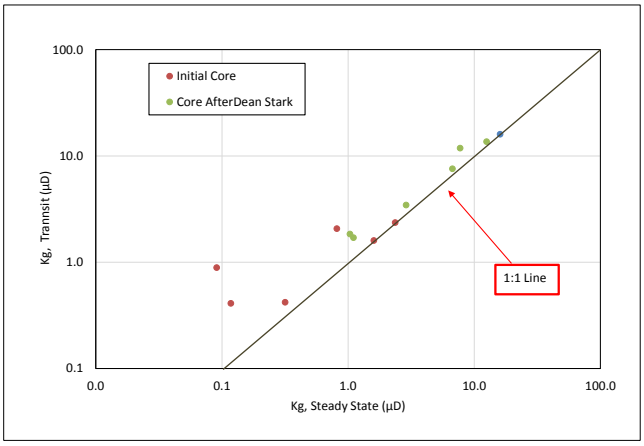

Figure 7: Comparison of Gas Permeability of Steady State with Transient Pressure Method

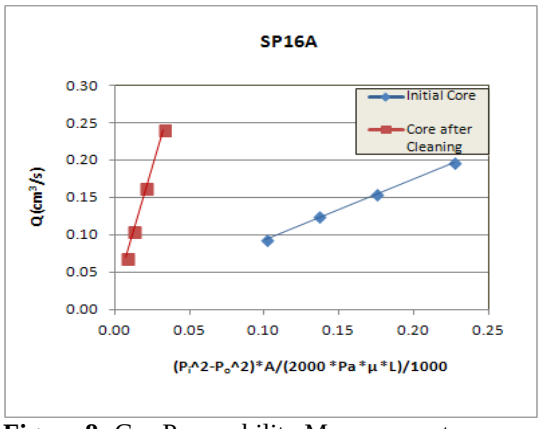

Figure 8: Gas Permeability Measurement Sample

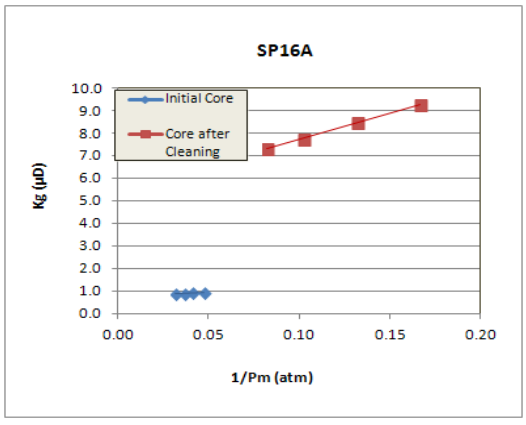

Figure 9: Klinkenberg Correction for Gas Permeability Measurement

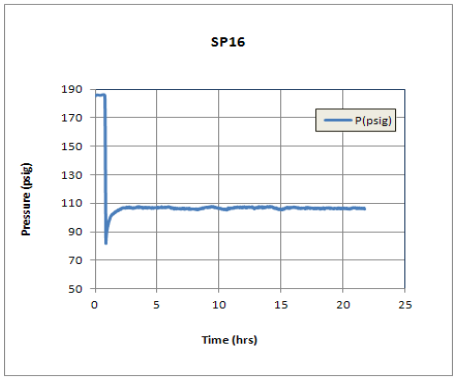

Figure 10: Porosity Measurement with Gas Expansion with Transient Data

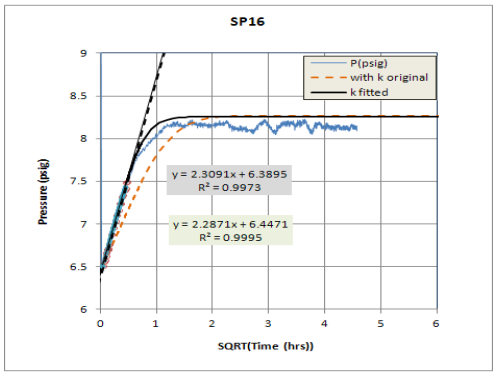

Figure 11: Permeability Calculation from Transient Pressure Data

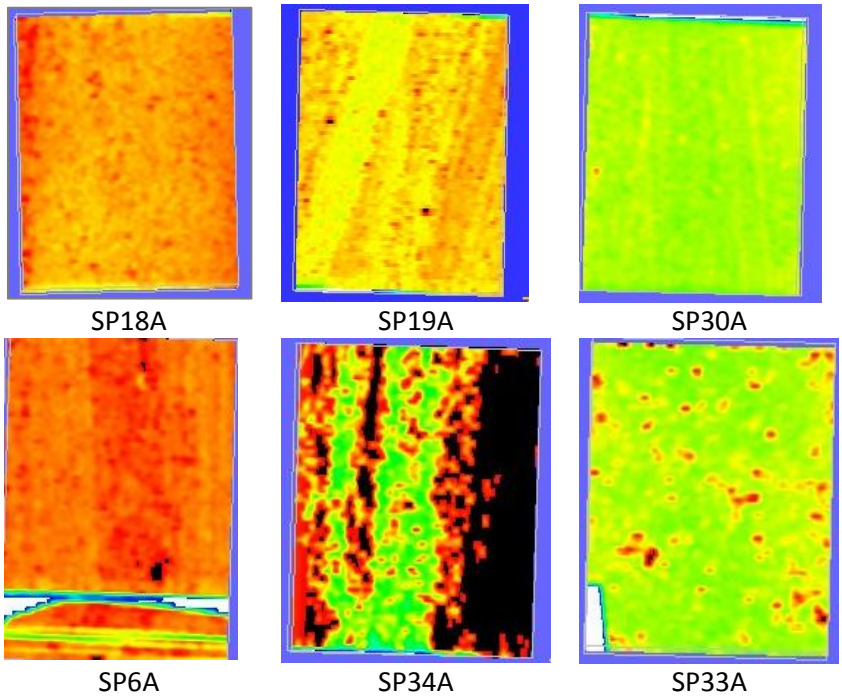

Figure 12: CT image reconstructions of the tested plugs. Plug 6A includes more than one pieces. Plug 34A is the most heterogeneous (tightest) of all samples

LOW PERMEABILITY MEASUREMENTS: INSIGHTS

Sandra Profice, Gérald Hamon and Benjamin Nicot
TOTAL CSTJF – Avenue Larribau – 64018 Pau Cedex – France

This paper was prepared for presentation at the International Symposium of the Society of Core Analysts held in St. John's Newfoundland and Labrador, Canada, 16-21 August, 2015

ABSTRACT

An accurate determination of the intrinsic permeability k_l is essential for characterizing hydrocarbon production from shale. However, recent studies have reported unacceptable discrepancies (up to several decades) between k_l measurements obtained by different laboratories. These discrepancies could be explained by:

i. The diversity of experimental protocols, since no standards of measurement have been clearly defined for poorly permeable samples.
ii. The validity of interpretative models, which are rarely published.

Firstly, this paper presents the results of an experimental study comparing:

i. Values of the intrinsic permeability k_l from Step Decay (gas), Pulse Decay (gas) and steady-state (both gas and liquid) tests
ii. Values of the Klinkenberg coefficient b from Step Decay and steady-state tests
iii. Values of the porosity ϕ from Step Decay and pycnometry tests.

On a homogeneous material principally composed of clay (pyrophyllite, 10 nD < k_l < 60 nD), no matter which property is being measured (k_l, b or ϕ), different testing techniques achieve similar results. Thus, our Step Decay method provides simultaneous and accurate estimations of low porosities (ϕ down to 2 %) and permeabilities (k_l down to 10 nD). Besides, the accurate prediction of gas flow behavior by the Step Decay and steady-state interpretative models proves the relevance of the Darcy-Klinkenberg equation. In other words, gas flows in tight rock can be described as viscous flows with slippage at pore walls. To check these conclusions for reservoir rocks, the study was repeated on shale.

Secondly, we provide the results of a Round-robin test where Total and three commercial laboratories performed unsteady-state and, when possible, steady-state measurements on identical plugs of pyrophyllite. All laboratories chose their techniques and experimental conditions but had to work on the whole plugs at a given effective pressure, to provide estimations of k_l. Furthermore, no prior treatment was carried out on the plugs in order to prevent any bias in the results due to preparation. The comparison of the collected series of k_l values reveals that the results agree in a satisfactory manner.

Thus, after showing the validity of the classical interpretative models through preliminary studies on pyrophyllite and shales, the results of the round robin test emphasize the need to properly define experimental procedures in order to provide a framework in which to compare low permeability results produced by different laboratories.

INTRODUCTION

Oil and gas shales have become over the past ten years a topic of real interest due to the large amounts of hydrocarbons they could potentially produce. Their characterization is a challenging task since these unconventional reservoirs have tight pore throats (a few tens of nanometers) and low permeabilities (from microdarcies to nanodarcies). Consequently, shales require careful identification of tractable and reliable methods to identify their one-phase flow properties.

Steady-state techniques are the oldest and simplest ones. They allow the determination of the intrinsic permeability k_l and, when applied with gas at different mean pore pressures, provide the Klinkenberg coefficient b in addition [1, 2]. Until recently, the principal drawback of such methods lay in the time needed to achieve steady-state at each new measuring point. The sample characterization used to be a long process, requiring several hours or even days when the material was extremely tight. Alternative methods dedicated to a faster analysis of ultra-low permeable porous media have been developed since the early 50's. Bruce *et al.* [3] were the first authors to propose in 1953 an unsteady-state technique commonly referred to as "Pulse Decay". This pioneering work gave birth to numerous other studies on the technique, mainly aiming at deriving interpretative models [4, 5, 6]. To summarize, in most of the studies, k, apparent permeability, or k_l is estimated separately from the porosity ϕ and, in rare cases, simultaneously with b. The Pulse Decay technique is still widely used in the petroleum industry, either on core plugs or on drill cuttings. This cheaper and faster option consisting in working on cuttings, known as "Gas Research Institute (GRI) technique", was first described by Luffel and Guidry in 1992 [7]. Even if unsteady-state methods relying on the application of a pulse of pressure are popular, they are not the only methods enabling a rapid and accurate characterization of low permeable rocks. Indeed, some oil and gas companies have made the choice to be equipped with different in-house techniques such as the improved steady-state technique proposed by IFPEN [2], the "Step Decay technique" [8] developed by Total or the "Pore Pressure Oscillation technique" [9] adopted by Shell. The first technique allows a fast estimation of k_l with a liquid. The second one delivers k_l, b and ϕ simultaneously using a series of pulses of pressure to excite the plug while the last one provides k and ϕ (b too if several tests are done) using a sinusoidal pressure wave.

All techniques presented in the previous paragraph involve interpretative models based on the first assumption that Darcy's law is still valid when modeling fluid flows in poorly permeable porous media. The second assumption that Klinkenberg's law [10] is valid too is made when b is determined. However, many publications question these assumptions since the Knudsen numbers typical of shales are out of the range of validity of the Darcy-Klinkenberg law. Karniadakis and Beskok [11] and also Javadpour [12], who worked on networks composed of micropores and nanopores respectively, rejected Darcy's law and suggested new formulations of the gas flow rate. Javadpour even derived an expression of k depending not only on the material specificities but also on the fluid properties at given values of temperature and pressure. In his approach, the notion of intrinsic permeability is completely lost. Using Karniadakis and Beskok's theory, Civan [13] found a relationship

between k and k_l applicable to the whole Knudsen number range. More recently, Fathi *et al.* [14] have determined a similar relationship by theorizing the phenomenon of double molecular slippage at the pore scale.

From these last studies, a natural question arises. Are interpretative models relying on the Darcy-Klinkenberg law well-suited for shales? This is the first question this paper will try to answer. The second question regards the great number of methods used in the industry for routine measurements. Are the discrepancies between the results found on an identical sample by different laboratories explained by the diversity of their interpretative models? Indeed, several authors [15, 16] recently mentioned discrepancies between permeability estimations up to several decades. The question remains whether this wide dispersion of results is due to interpretation or to sample preparation.

STUDY

Three experimental studies were devised to answer the questions above. Study 1 aimed at comparing the values of k_l, b and ϕ estimated for homogeneous plugs of pyrophyllite with common methods of the industry to those estimated with our Step Decay method. To be more precise, the comparison was made between:

i. The values of k_l given by a Step Decay test, a Pulse Decay test, a steady-state test with gas and a steady-state test with oil
ii. The values of b given by a Step Decay test and a steady-state test with gas
iii. The values of ϕ given by a Step Decay test and a pycnometry test.

The same approach was then applied in Study 2 to two shale plugs sourced from an actual development target area, in order to check whether the results from the pyrophyllite study could be corroborated by a similar study with reservoir rocks. Study 3 was a Round-robin test involving three commercial laboratories and Total. Its goal was to identify the main cause of the discrepancies often observed between the k_l estimations found by different laboratories for an identical sample.

Plugs

Study 1 was carried out on five plugs of pyrophyllite named Pyro 1, Pyro 2, Pyro 3, Pyro 4 and Pyro 5 respectively. Pyrophyllite is a homogeneous quarry rock sourced from the United States. It is mostly composed of clay and consequently has a low permeability. All plugs were successively subjected to Step Decay tests, Pulse Decay tests and steady-state tests using gas and. Pyro 5, the least permeable of the five plugs, was also analysed with a liquid at steady-state, at the end of the experiments with gas. No special treatment, such as cleaning or drying, was performed on the pyrophyllite prior to the measurements with gas, which were conducted therefore on plugs containing some water. Before starting the steady-state experiment with liquid, Pyro 5 was saturated at 400 bar during two weeks, after having created a vacuum over a period of four days. Pyro 1, Pyro 2, Pyro 3 and Pyro 4 were the four plugs sent to each of the three commercial laboratories selected for the Round-robin test of the Study 3.

The two shales involved in Study 2, Shale 1 and Shale 2 respectively, are of different origins. Shale 1 comes from a wet gas well and Shale 2 from an oil well. Both samples were subjected to all the gas tests in native state. Step Decay, Pulse Decay and steady-state. No steady-state analysis with liquid was undertaken since the oil phase existing in the plug would have probably moved with the flow. This would have led to an estimation of k_l that was not comparable with the results derived with gas.

A Mercury Injection Capillary Pressure (MICP) analysis was carried out on a fragment of rock from the same block that provided Pyro 1. Figure 1, which shows the pore throat size distribution from the MICP analysis, reveals that the most represented pore throat radius in the material is around 20 nm. This result is in line with the range of pore radius of 10 to 40 nm found by using the Density Functional Theory (DFT) method on a crushed sample taken from the Pyro 1 block. Pores in shales are likewise characterized by radii of several tens of nanometers.

Methods and Interpretative Models

The Pulse Decay technique [4] consists in applying a pulse of pressure on one face of the plug and recording the differential pressure ΔP calculated from measurements taken at both extremes of the plug. As shown on Figure 2, the plug is confined in a Hassler sleeve core holder connected to two tanks. The pulse of pressure is prepared in the upstream tank V_0 and released at the plug entrance by opening the valve v_0. The recording of ΔP is triggered simultaneously with the pulse emission. The downstream tank V_1 collects the gas flowing out of the plug. All Pulse Decay experiments were conducted with the "Pulse Decay Permeameter 200", an automated device manufactured by Corelab, which works with nitrogen and at high mean pore pressure P_p to eliminate the Klinkenberg effect. P_p was initially stabilized at:

- Shale 1: 31 bar (450 psi)
- Plugs of pyrophyllite and Shale 2: 69 bar (1000 psi).

The gas flow from V_0 to V_1, which are both around 20 cm^3, is started by depressurizing V_1 until ΔP reaches 3 bar (40 psi). The effective pressure P_{eff}, defined as the difference between the confining pressure P_c and P_p, was:

- Plugs of pyrophyllite: 60 bar
- Shales: 100 bar.

The temperature was fixed at 20 °C for all our tests (unsteady-state and steady-state). The interpretation of ΔP is based on Jones' approach described in reference [5]. Jones devised a method of calculating k_l by using an approximate analytical solution of the Pulse Decay problem that combines the traditional equations of fluid mechanics in porous materials (including Darcy's law) and excludes the Klinkenberg effect. The solution is an infinite sum of exponentials decreasing over time. At long times, the first term predominates over the other terms. As a consequence, the curve of the logarithm of ΔP evolves linearly over time, allowing the derivation of k_l from the slope.

In the Step Decay technique [8], the plug is subjected to a series of pulses of pressure. In terms of the device, the Step Decay differs from the Pulse Decay only by the existence of an additional buffer tank V_b located at the plug entrance, as represented in Figure 3. The first pulse of pressure is prepared by filling V_0 and V_b with nitrogen. Once the selected pressure setpoint is reached, valve v_b is closed to isolate V_b from V_0. The pulse is then emitted by opening v_0. This operation triggers the simultaneous recording of upstream and downstream pressures, P_0 and P_1 respectively. All pulses of pressure from the second pulse are produced by pressurizing V_b and are liberated by briefly opening v_b. The pulse pressures and waiting time intervals used for the Step Decay tests were the following:

- Plugs of pyrophyllite: 6 bar – 16 min / 10 bar – 30 min / 31 bar – 5 to 15 hours
- Shale 1: 3 bar – 1 hour / 5 bar – 1.5 hours / 9 bar – 2 hours
- Shale 2: 6 bar – 15 min / 13 bar – 2 hours / 22 bar – 20 hours

For each plug, the same P_{eff} was applied for both Pulse Decay and Step Decay tests. The values of V_1 were of:

- Pyro 1, Pyro 2, Pyro 3 and Pyro 4: 8.43 cm^3
- Pyro 5, Shale 1 and Shale 2: 12.46 cm^3.

In terms of the interpretation of the raw data, the Step Decay model assumes the validity of the Darcy-Klinkenberg law, as do most Pulse Decay models found in existing studies of experiments at low pore pressure. The Step Decay provides k_l, b and ϕ by matching a numerically simulated P_1 profile with the recorded P_1 data. Note that a particular strength of the method resides in the fact that the P_0 profile acts as an input for the interpretation. One consequence of that is the removal of V_0 from the series of parameters required for the inversion. As a result, the interpretation is only concerned with the measurement of V_1. Regarding ϕ, as evoked in reference [8], an increase in the sensitivity of P_1 to ϕ was necessary to ensure its accurate estimation by history matching. This was achieved thanks to the technique's major strength resulting from the fact that P_0 is an input of the history matching: the modulation of the excitation. By emitting successive pulses of pressure, the phenomenon of gas accumulation occurring right after the pulse emission and creating sensitivity to ϕ is generated several times, compared to only once in a Pulse Decay test.
The results from unsteady-state experiments were compared to the results from a steady-state analysis carried out with nitrogen. In the case of Pyro 5, characterization at steady-state was also repeated with Isopar L. Figure 4 shows a diagram of a typical steady-state device. Regardless of the fluid used, one point of measurement was made by regulating P_0 and recording at steady-state P_0, P_1 and the volume flow rate Q_v. For all tests involving nitrogen, several points were taken at increasing mean pore pressures to derive k_l and b independently. For the test with Isopar L, only one point was needed to determine k_l. The parameters chosen for the characterization with nitrogen were:

- Plugs of pyrophyllite: 40 bar $\leq P_0 \leq$ 70 bar, $P_1 = P_{atm}$ (atmospheric pressure), P_{eff} = 60 bar
- Shale 1: 40 bar $\leq P_0 \leq$ 70 bar, $P_1 = P_{atm}$, P_{eff} = 100 bar
- Shale 2: 6 bar $\leq P_0 \leq$ 11 bar, $P_1 = P_{atm}$, P_{eff} = 100 bar.

In the steady-state test with Isopar L on Pyro 5, P_0 was set at 80 bar, P_1 at 2 bar and P_{eff} at 60 bar. The interpretation of the steady-state raw data recorded with nitrogen relies on:

$$k = k_l \left(1 + \frac{b}{P_m}\right) \quad (1)$$

In this relationship presented first by Klinkenberg [10], *k* is calculated from Equation 2, which was derived for an isothermal steady-state gas flow by integrating the differential form of Darcy's law including the Klinkenberg effect.

$$k = \frac{\mu L}{S} \frac{P_1 Q_V}{P_m \Delta P} \quad (2)$$

Note that μ is the viscosity, L the length, S the cross-section area and P_m the mean pore pressure. According to Klinkenberg's law, it appears that the separate estimation of k_l and *b* requires the plot of *k* versus $1/P_m$. Indeed, this plot displays a linear behaviour with a slope equal to k_l**b* and an intercept with the Y-axis equal to k_l. For the characterization with Isopar L, the calculation of *k* is immediate with Darcy's law:

$$k = \frac{\mu L}{S} \frac{Q_V}{\Delta P} \quad (3)$$

Across all tests carried out with gas on a given plug, P_p varied approximately between 1 bar and 70 bar. For these extreme values of P_p, the mean free path λ defined by Equation 4 is in the range [1 nm - 94 nm].

$$\lambda = \frac{\mu}{P} \sqrt{\frac{\pi \mathcal{R} T}{M}} \quad (4)$$

$\mathcal{R}$ is the ideal gas constant, T the absolute temperature and M the molecular mass. For such a range of λ and for pyrophyllite mean pore radius R_p of 25 nm (10 nm ≤ R_p ≤ 40 nm), the Knudsen number Kn derived from Equation 5 is between 0.04 and 3.8.

$$Kn = \frac{\lambda}{R_p} \quad (5)$$

Consequently, in pores having radii of a few tens of nanometers, either a slip flow regime or a transition flow regime arises, depending on the level of pressure [17]. For the latter, both Darcy's law and Klinkenberg's law are seriously put into question knowing that gas molecules collide principally with pore walls and no longer with other molecules.

Round-Robin Test

After characterization, Pyro 1, Pyro2, Pyro 3 and Pyro 4 were sent successively to three different commercial laboratories for a round Robin-test comprising unsteady-state and, when possible, steady-state experiments. The specifications emphasized conducting them with nitrogen, on the whole plugs (no crushing), by regulating P_{eff} at 60 bar and without carrying out any treatment on the plugs (cleaning or drying) in order to prevent any bias

in the results due to preparation. The laboratories were free to choose their own methods and experimental conditions (pressures, flow rates, temperature...).

Laboratory 1 performed unsteady-state tests with the Pulse Decay technique and steady-state tests following a procedure similar to ours. The interpretation of the Pulse Decay raw data relied on the methodology implemented in the Pulse Decay Permeameter 200, except that the analytical solution was not Jones' but Brace *et al.*'s [4]. The unsteady-state measurements were started by increasing P_0 by a few bars (between 2.5 and 3.5 bar), after the stabilization of P_p between 15.5 and 18 bar. V_0 and V_1 were of 58 cm^3 and 47 cm^3 respectively. Estimations of k_l were deduced from the tests. Each analysis at steady-state involved several points of measurement to enable the separate identification of k_l and b. The mean P_p chosen for a given plug varied between a few bars (from 1.5 to 4 bar) and 20 bar. Both types of test were carried out at a temperature of 24 °C.

Laboratory 2 delivered values of k_l and b from unsteady-state experiments done with the "Automated Permeameter - 68" manufactured by Coretest Systems. P_p was initially set at 14 bar. Once equilibrium was achieved, the gas flow was started by opening v_1. Hence, P_1 was kept at P_{atm} and P_0, recorded in V_0 of 6 cm^3, was the only signal introduced in the history matching procedure to obtain k_l and b. The numerical model assumed as usual the validity of Darcy's law and Klinkenberg's law. The temperature was of 20 °C.

Laboratory 3 provided estimations of k_l from steady-state and unsteady-state analyses. Steady-state tests relied on a unique point of measurement obtained by applying a similar procedure to our own, P_1 and ΔP being of 6 bar and 5 bar respectively. The value of k was then corrected with an unknown empirical correlation to derive k_l. Unsteady-state tests used the Pulse Decay method. The plug was first pressurized at 40 bar and the pulse of pressure was then prepared by increasing P_0 to 60 bar. V_0 and V_1 were of 15 cm^3 and 13 cm^3 respectively. The model, assumptions and procedure on which the interpretation was based were not given. All tests were carried out at a temperature of 22 °C. At the moment of writing the present paper, the results of Laboratory 3 were not available but will be presented during the conference.

RESULTS AND DISCUSSION

Results of the Comparative Studies

Table 1 lists the results of all measurements conducted on the five plugs of pyrophyllite. The estimations of ϕ given by the Step Decay method were compared to those provided by pycnometers employing helium at low pressure. The subscripts "PD", "SD", "SSG", "SSO" and "Pyc" refer to: "Pulse Decay", "Step Decay", "Steady-State Gas", "Steady-State Oil" and "Pycnometry" respectively, in Table 1 as below. Moreover, the deviation indicator $D\xi$ quantifying the discrepancy between ξ_1 and ξ_2, both estimations of ξ (= k_l, b or ϕ), and used throughout the present development has been defined as:

$$D\xi = 100\,\frac{|\xi_1 - \xi_2|}{(\xi_1 + \xi_2)/2} \qquad (6)$$

For Pyro 1 to Pyro 5, Dk_l derived for $k_{l,SD}$ and $k_{l,PD}$ is in the range [5 % - 17 %], against [19 % - 40 %] when calculated for $k_{l,SSG}$ and $k_{l,PD}$. Consequently, the values of k_l from experiments performed with gas, i.e. $k_{l,PD}$, $k_{l,SD}$ and $k_{l,SSG}$, agree in a satisfactory manner. As highlighted in Table 1, this agreement can be extended to estimations of k_l from tests carried out with gas and oil, at least for pyrophyllite. Indeed, in the case of Pyro 5, Dk_l determined for $k_{l,SSO}$ and $k_{l,SSG}$ is about 26 %. Regarding b and ϕ, b_{SD} compares well with b_{SSG} as well as ϕ_{SD} with ϕ_{Pyc}, Db ranging from 10 % to 43 % and Dϕ from 0 % to 19 %.
Figure 5.a presents, for Pyro 1, the normalised difference $(P_{1,rec} - P_{1,sim}) / P_{1,rec}$ where $P_{1,rec}$ is the recorded profile P_1 and $P_{1,sim}$ the profile P_1 simulated with the Step Decay model. Similar graphs were obtained for Pyro 2 to Pyro 5. The signal is flat and centered on 0, excepted during a period of less than half an hour right after the pulse emission. Figure 6 gives an example of k plotted against $1/P_m$. This graph results from the processing of the steady-state raw data collected for Pyro 1. A similar linearity was observed for Pyro 2 to Pyro 5.

Table 2 provides the results from the experiments conducted on Shale 1 and Shale 2. As emphasized for pyrophyllite plugs, the same gas-based techniques used on shale plugs to identify a given property, k_l or b, lead to consistent estimates. Dk_l is about 9 % for Shale 1 and about 19 % for Shale 2, when comparing $k_{l,SSG}$ and the mean of $k_{l,SD}$ and $k_{l,PD}$, while Db is about 21 % for Shale 1 and about 26 % for Shale 2. The estimations of ϕ_{SD} are not available since the characterization of ϕ with the Step Decay technique is uncertain when dealing with shales. The bias in ϕ is mainly due to the fact that one major assumption of the Step Decay model, which is the homogeneity of the studied rock, is rarely respected in the presence of shales. In the case where the rock is highly heterogeneous, it has been proven with numerical simulations and practical tests that the method delivers an accurate estimation of k_l, an acceptable estimation of b and an unreliable estimation of ϕ [18].

Results of the Round Robin Test

Table 3 lists the values of k_l obtained for Pyro 1, Pyro 2, Pyro 3 and Pyro 4 by Total and by the two laboratories (Laboratory 1 and Laboratory 2) which participated in the Round-robin test and could deliver their results in time for the writing of the paper. Estimations of b were provided by some of the laboratories but are not reported here since focus was primarily on the characterization of k_l. Regarding the values of k_l measured by Laboratory 1 and by Laboratory 2 for a given plug, those obtained at unsteady-state were compared to $k_{l,SD}$ while those obtained at steady-state were compared to $k_{l,SSG}$. Dk_l ranges from 31 % to 118 % at unsteady-state and from 9 % to 27 % at steady-state, leading to a maximum discrepancy factor of 3.8. Therefore, the discrepancies noted here are much more modest than the two decades reported in the literature [15].

Discussion

As demonstrated by the first series of comparative measurements performed on the plugs of pyrophyllite, our in-house Step Decay method enables the simultaneous and accurate estimation of k_l, b and ϕ, in the case of homogeneous and low permeable media. From the tests on both pyrophyllite and shale plugs, it results that a satisfactory agreement between

the estimations of k_l found with different methods used in the industry can be achieved. This conclusion is also applicable to estimations of k_l determined by different laboratories working with their own protocols and interpretative models, as highlighted by the Round-robin test. Therefore, the discrepancies of several decades reported in references [15, 16] and noted between values of k_l derived for a same plug by different laboratories cannot be explained by the diversity of the experimental conditions selected for the design and use of the devices (pressures, flow rates, volumes...). Similarly, these discrepancies cannot be justified by the diversity of the interpretative models and of their assumptions: negligible ϕ, no Klinkenberg effect, constant gas compressibility… Consequently, the main cause of divergence of the results delivered for an identical sample by several laboratories is likely the sample preparation. This last conclusion is supported by reference [19] where Tinni *et al.* evidence the great variability of k_l according to the sample specificities when dealing with cuttings. In addition, Darcy's law and Klinkenberg's law remain usable in the case of nanoporous rocks, like pyrophyllite or shale. This is clearly proven by the linear behavior observed in Figure 6. In Figure 5.b are shown the discrepancies at short times between the recorded and simulated P_1 signals. They are due to the poor quality of the recorded response P_1 and probably to the inability of the Darcy-Klinkenberg model to predict the gas flow since the values of P_p of a few bars at short times induce Knudsen numbers higher than 0.1, i.e. out of the range of validity of the Darcy-Klinkenberg law. However, despite the fact that the model is not well-adapted to predict the flow during a short period, $k_{l,SD}$ remains reliable and accurate. Thus, the need to revise classical fluid mechanics when testing rocks of low permeability is not justified in the unsteady- and steady-state ranges of P_p considered in this paper.

CONCLUSION

Redundant estimations of k_l can be determined for an identical poorly permeable plug, by using different techniques of the industry. More precisely, steady-state and unsteady-state methods applied with gas lead to results in excellent agreement on pyrophyllite and shale. The convergence of the results from all measurements with gas and from a measurement at steady-state with a liquid is true for pyrophyllite. The verification of this last point in the case of shale is ongoing. Moreover, comparable estimations of k_l can be determined by different laboratories working with their own techniques, experimental conditions and interpretative procedures, provided that sample preparation is carefully defined. Knowing the numerous difficulties tied to the characterization of cuttings, we recommend carrying out permeability measurements on whole plugs as much as possible. Finally, Darcy's law and Klinkenberg's law remain valid when modeling gas flows in nanoporous rocks such as pyrophyllite and shale. In other words, gas flows in tight formations can be described as viscous flows with slippage at pore walls.

ACKNOWLEDGEMENTS

The financial support from Total is gratefully acknowledged. Besides, we thank Ghislain Pujol, Jean-Michel Kluska, Frédéric Plantier, Sonia Vincent-Gill and Antoine Delafargue for their contribution to the work presented in this paper.

REFERENCES

1. Rushing, J. A., Newsham, K. E., Lasswell, P. M., Cox, J. C., Blasingame, T. A., "Klinkenberg-Corrected Permeability Measurements in Tight Gas Sands: Steady-State Versus Unsteady-State Techniques", SPE Annual Technical Conference and Exhibition, Houston, Texas, USA, 26-29 September 2004.
2. Boulin, P. F., Bretonnier, P., Gland, N., Lombard, J. M., "Contribution of the Steady-State Method to Water Permeability Measurement in Very Low Permeability Porous Media", *Oil and Gas Science and Technology - Rev. IFP Energies nouvelles*, (2012) **67**, 3, 387-401.
3. Bruce, G. H., Peaceman, D. W., Rachford Jr., H. H., Rice, J. D., "Calculations of Unsteady-State Gas Flow Through Porous Media", *Journal of Petroleum Technology*, (1953) **5**, 3, 79-92.
4. Brace, W. F., Walsh, J. B., Frangos, W. T., "Permeability of Granite Under High Pressure", *Journal of Geophysical Research*, (1968) **73**, 6, 2225-2236.
5. Jones, S. C., "A Rapid Accurate Unsteady-State Klinkenberg Permeameter", *SPE Journal*, (1972) **12**, 5, 383-397.
6. Hsieh, P. A., Tracy, J. V., Neuzil, C. E., Bredehoeft, J. D., Silliman, S. E., "A Transient Laboratory Method for Determining the Hydraulic Properties of 'Tight' Rocks - 1. Theory", *International Journal of Rock Mechanics and Mining Sciences & Geomechanics Abstracts*, (1980) **18**, 3, 245-252.
7. Luffel, D. L., Guidry, F. K., "New Core Analysis Methods for Measuring Reservoir Rock Properties of Devonian Shale", *Journal of Petroleum Technology*, (1992) **44**, 11, 1184-1190.
8. Lasseux, D., Jannot, Y., Profice, S., Mallet, M., Hamon, G., "The 'Step Decay': A New Transient Method for the Simultaneous Determination of Intrinsic Permeability, Klinkenberg Coefficient and Porosity on Very Tight Rocks", International Symposium of the Society of Core Analysts, Aberdeen, Scotland, 27-30 August 2012.
9. Wang, Y., Knabe, R. J., "Permeability Characterization on Tight Gas Samples Using Pore Pressure Oscillation Method", International Symposium of the Society of Core Analysts, Halifax, Nova Scotia, Canada, 4-7 October 2010.
10. Klinkenberg, L. J., "The Permeability of Porous Media to Liquids and Gases", *API Drilling and Production Practice*, (1941), 200-213.
11. Karniadakis, G., Beskok, A., Aluru, N., *Microflows and Nanoflows, Fundamentals and Simulation*, Springer-Verlag, New-York, 2005, 818 p.
12. Javadpour, F., "Nanopores and Apparent Permeability of Gas Flow in Mudrocks (Shales and Siltstones)", *Journal of Canadian Petroleum Technology Distinguished Author Series*, (2009) **48**, 8, 16-21.
13. Civan, F., "Effective Correlation of Apparent Gas Permeability in Tight Porous Media", *Transport in Porous Media*, (2009) **82**, 2, 375-384.
14. Fathi, E., Tinni, A., Akkutlu, I. Y., "Shale Gas Correction to Klinkenberg Slip Theory", America's Unconventional Resources Conference, Pennsylvania, USA, 5-7 June 2012.
15. Passey, Q. R., Bohacs, K. M., Esch, W. L., Klimentidis, R., Sinah, S., "From Oil-Prone Source Rock to Gas-Producing Shale Reservoir - Geologic and Petrophysical

Characterization of Unconventional Shale Gas-Reservoirs", CPS/SPE International Oil & Gas Conference and Exhibition, Beijing, China, 8-10 June 2010.
16. Sondergeld, C. H., Newsham, K. E., Comisky, J. T., Rice, M. C., Rai, C. S., "Petrophysical Considerations in Evaluating and Producing Shale Gas Resources", SPE Unconventional Gas Conference, Pittsburgh, Pennsylvania, USA, 23-25 February 2010.
17. Ziarani, A. S., Aguilera, R., "Knudsen's Permeability Correction for Tight Porous Media", *Transport in Porous Media*, (2012) **91**, 1, 239-260.
18. Profice, S., *Mesure de Propriétés Monophasiques de Milieux Poreux Peu Perméables par Voie Instationnaire*, PhD Thesis, Université de Bordeaux, France, 2014.
19. Tinni, A. O., *Permeability Measurements of Nanoporous Rocks*, Master Thesis, University of Oklahoma, USA, 2012.

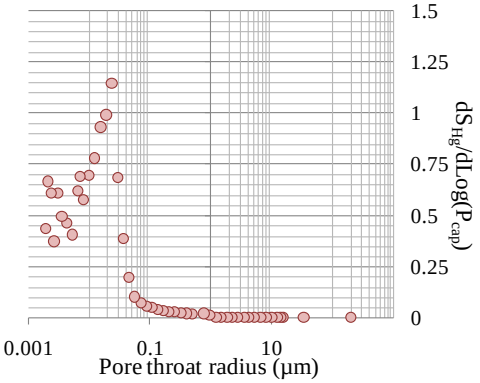

Figure 1 : Pore throat size distribution

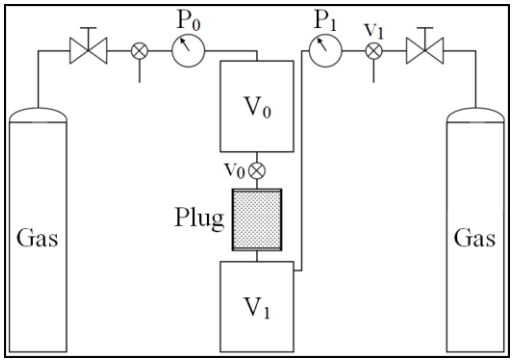

Figure 2 : Pulse Decay device

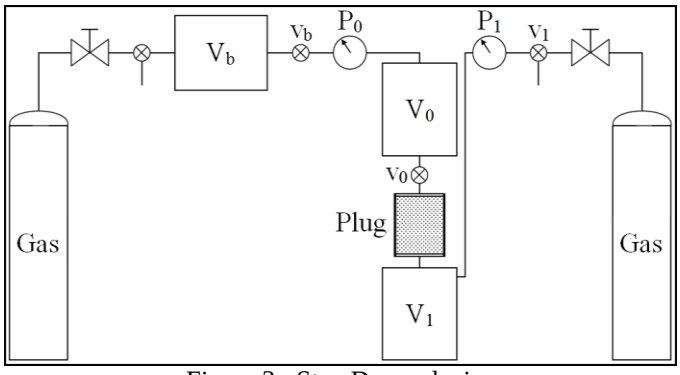

Figure 3 : Step Decay device

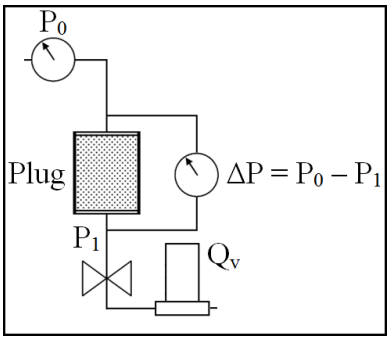

Figure 4 : Steady-state device

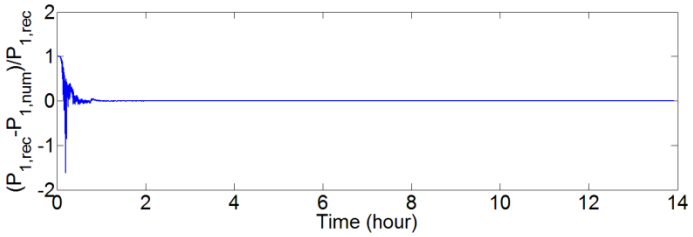

Figure 5.a : Normalised difference between $P_{1,rec}$ and $P_{1,sim}$ versus time

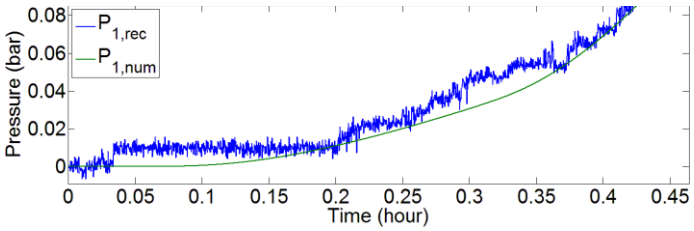

Figure 5.b : $P_{1,rec}$ and $P_{1,sim}$ signals at short times

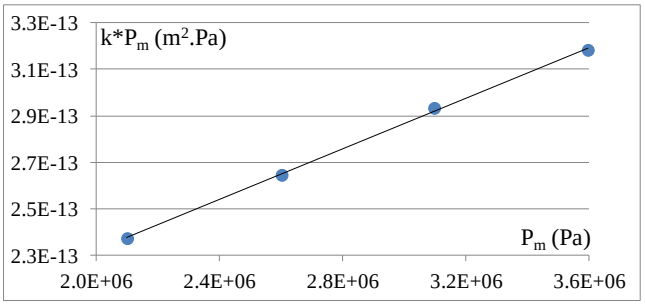

Figure 6 : $k*P_m$ versus P_m

Table 1 : Results of the comparative measurements for the plugs of pyrophyllite

Plug	k_l (nD)				b (bar)		ϕ (%)	
	$k_{l,PD}$	$k_{l,SD}$	$k_{l,SSG}$	$k_{l,SSO}$	$b_{,SD}$	$b_{,SSG}$	$\phi_{,SD}$	$\phi_{,Pyc}$
Pyro 1	70	59	56	-	19.6	22.4	4.2	4.1
Pyro 2	35	33	24	-	24.0	26.6	3.8	3.5
Pyro 3	67	56	53	-	18.5	23.0	4.0	4.0
Pyro 4	51	46	42	-	20.2	24.6	3.7	3.5
Pyro 5	11	10	14	8	33.3	21.5	2.5	2.1

Table 2 : Results of the comparative measurements for the shales

Plug	k_l (nD)				b (bar)		ϕ (%)	
	$k_{l,PD}$	$k_{l,SD}$	$k_{l,SSG}$	$k_{l,SSO}$	$b_{,SD}$	$b_{,SSG}$	$\phi_{,SD}$	$\phi_{,Pyc}$
Shale 1	2031	2222	2303	-	4.3	3.5	-	10.1
Shale 2	46	58	43	-	7.4	9.6	-	0.7

Table 3 : Results of the round robin test

Plug	Total				Laboratory 1		Laboratory 2	
	k_l (nD)							
	$k_{l,PD}$	$k_{l,SD}$	$k_{l,SSG}$	$k_{l,SSO}$	$k_{l,PD}$	$k_{l,SSG}$	$k_{l,PD}$	$k_{l,SSG}$
Pyro 1	70	59	56	-	115	48	203	-
Pyro 2	35	33	24	-	45	22	127	-
Pyro 3	67	56	53	-	121	59	185	-
Pyro 4	51	46	42	-	78	55	104	-

UNCONVENTIONAL TIGHT OIL RESERVOIRS: A CALL FOR NEW STANDARDIZED CORE ANALYSIS WORKFLOWS AND RESEARCH

Gary A. Simpson and Neil S. Fishman
Hess Corporation

This paper was prepared for presentation at the International Symposium of the Society of Core Analysts held in St. John's, Newfoundland and Labrador, Canada, 16-21 August 2015

ABSTRACT

Recommended Practices for Core Analysis is firmly established in the American Petroleum Institute's RP 40 Second Edition, February 1998 document. Standardized workflows for the core analysis of unconventional shale reservoirs are deeply rooted in analytical techniques that were originally developed for coal bed methane, shale gas and tight gas reservoirs. These techniques were researched and developed by the Gas Research Institute (GRI) and are outlined in the GRI final report: GRI-95/0496, "Development of Laboratory and Petrophysical Techniques for Evaluating Shale Reservoirs." These methodologies were extremely successful in evaluating cores from gas shale reservoirs. As operators shifted their development focus from gas shale reservoirs to unconventional oil producing reservoirs, these same gas core analytical techniques were used to analyze unconventional tight oil cores.

This paper will discuss the results of tests and experiments that were made on core from the Bakken petroleum system's Middle Bakken and lower Three Forks formations. These series of tests were made following a very poor core-to-log data water saturation comparison. The core analysis measured 40% to 60% water saturation, and the logs showed the reservoir to be 100% water saturated.

This investigation started by looking closely at the solvent extraction methods with Dean and Stark [3] using toluene followed by chloroform/methanol azeotrope extraction. Preliminary tests focused on the possibility of anhydrite dissolution, which would have created excess porosity, thus making the core analysis incorrect. Additional investigation of the problem included measurements with nuclear magnetic resonance (NMR), retort extraction methods and possibilities of errors in the computations due to extremely high water salinities. While this investigation has resulted in applying some new protocols in the analysis of tight oil cores, it has also demonstrated that more research is needed and new standard core analysis workflows need to be developed for unconventional tight oil reservoirs.

INTRODUCTION

One of the most important aspects in the development of unconventional reservoirs is a comparison of core measurements with wireline logging measurements. This comparison primarily accomplished by cutting whole core and completing extensive wireline logging in pilot hole wells, is particularly important in the development of unconventional tight oil reservoirs. Unconventional tight oil reservoirs typically have a porosity of less than 10% and a permeability of less than 0.01 mD.

The Bakken petroleum system, one of the largest tight oil deposits in the world, is situated in the Williston Basin [Fig. 1]. The Bakken petroleum system is generally considered a hybrid type of unconventional tight oil reservoirs: it consists of two layers of organic-rich shale (the Upper and Lower shales) sandwiching a dolomitic-siltstone interval called the Middle Bakken [Fig. 2]. Included in the Bakken petroleum system below the Lower shale is the Three Forks formation, composed of laminations of dolostone and dolomitic-mudstone. Developing large acreage positions in the Bakken petroleum system to maximize hydrocarbon production requires a thorough understanding of the reservoir parameters across the play and an understanding of the individual reservoirs of the system.

To evaluate the production potential more accurately, a series of five wells [Fig. 3] were cored and logged in the Bakken petroleum system starting at the end of 2013 and through 2014. The wells were positioned over a broad section of leases that represented the acreage being developed. During this process, routine core analysis (RCA) saturation data from parts of the middle Bakken and the lower Three Forks formations were compared with wireline logging data. The workflows recommended by API RP 40 [1] were implemented to acquire the RCA saturation data. The comparison revealed obvious discrepancies between the core and log data sets.

Advanced logging measurements using dielectric and NMR logs had been run and analysed over these formations. The NMR logging tools measure total porosity, while the dielectric logging tools measure the total water-filled porosity. Therefore, by plotting the NMR total porosity with the dielectric water-filled porosity, the difference between the two measurements is a hydrocarbon-filled porosity. A plot of the porosities from the log measurements is shown in Fig. 4 in the second log track from the right, labeled "Porosity." The dark green shading between the two curves represents oil-filled porosity. The teal blue color represents water-filled porosity. The maroon dots are core porosity measurements.

Due to these log measurements, there was a high level of confidence that log data in the lower portion of the Three Forks formation indicated 100% water saturation, as represented in Fig. 4 by the blue curve in the middle log track labeled "Water Saturation." In the same intervals, water saturations from the RCA data, shown as maroon dots, largely ranged from 40% to 60% and as such were highly questionable.

This discrepancy triggered an inquiry into its sources, with a focus on the core data. The authors started with the core service company working on the core in which a large discrepancy in the data sets was observed; a second inquiry began into other cores from the same formations in process at a second core service company. Additionally, the authors examined historic core data. It was concluded that this was probably not the first time that a discrepancy between the data sets existed.

Research into the reliability of the core data led, over time, to a more comprehensive understanding of analytical procedures and lab workflows for data acquisition from the Bakken petroleum system. A series of lab visits, detailed discussions with lab analysts and a review of industry-accepted protocols were all-necessary to define the scope of the problems and develop tests to address analytical procedures and lab workflows. The authors' focus has been on the following:

- Solvent extraction procedures during RCA on both core plugs [1]; as well as crushed rock using the GRI method [2], or a modified version of GRI (following a proprietary lab workflow that diverges from the original GRI workflow), which itself was developed for characterizing reservoir properties of gas shales.
- NMR as an independent check of plug porosity and fluid saturations.
- The possibility of anhydrite dissolution during solvent extraction. In the absence of resolution to this investigation, processing of previously unanalyzed core materials has been suspended. Cores 1 and 2 had already been analyzed, Core 3 had had plugs cut and Dean Stark had been started on some, and Cores 4 and 5 were being evaluated for sampling intervals. [Fig. 3]

DISCUSSION

Solvent Extraction

Cleaning of core materials was undertaken on both 1.5 x 2-inch core plugs and on material that was crushed. Cleaning of the core plugs followed the procedures originally developed by Dean and Stark [3] and a workflow outlined in API RP 40 [1]. For both Dean Stark and GRI, the samples are subjected to extraction using toluene at 110^{o}C. Questions were raised regarding the efficacy of the Dean Stark workflow because it was developed for conventional reservoir rocks, but applied here to the Bakken and Three Forks formations, considered unconventional tight oil reservoirs [4].

A quick test of the Dean Stark method was made on six plug samples of Bakken and Three Forks rocks from Core 4 [Fig. 3]. Core plugs were first subjected to RCA and Dean Stark cleaning. Lab protocols for cleaning required no measurable increase in water level in the extraction apparatus after at least 24 hours. Upon completion of the cleaning process, the plugs, still saturated with toluene, were removed from the extractor and immediately crushed. The crushed material was placed back into the extractor, and additional hydrocarbons and water were removed during this second episode of extraction [Figs. 5A and 5B]. Preliminary results from this quick test indicate that as much as 15% more water was removed from the crushed material, which would suggest

that there was incomplete cleaning of the core plugs through the normal RCA Dean Stark process. Additional testing is currently underway to confirm the degree to which the Dean Stark procedures on the Bakken and Three Forks rocks are inadequate to fully clean core plugs, and to verify the volume of water left in the core plugs after the normal RCA workflow.

While attempting to understand the efficacy of RCA on plugs from the Bakken and Three Forks formations, an unexpected error was uncovered in calculating water saturations from the volume of extracted distilled water using Equation 1:

$$Sw = (V_{DW} * V_{Brine}/V_{Pure\ Water})/V_{Pore} \quad (1)$$

Where the brine volume is calculated as follows:

$$V_{Brine} = [(V_{PureWater} * \rho_{Pure\ Water})/\rho_{Brine}][1{,}000{,}000/(1{,}000{,}000 - C_{salinity})] \quad (2)$$

(Sw, water saturation; V_{DW}, volume of distilled water; V_{Brine}, volume of brine; $V_{Pure\ Water}$, volume of pure water; V_{Pore}, pore volume; ρ, density)

In the absence of client guidance, two labs used different default salinity values in Equation 2 to calculate water saturations in Equation 1: one lab applied a default salinity value of 50,000 ppm (density of ~1.03 g/cc); and the second lab applied a default salinity value of 30,000 ppm (density of ~1.02 g/cc). Pore waters in the Bakken petroleum system are extremely saline, with salinities measured on produced waters at the surface ranging up to 360,000 ppm (density of ~1.29 g/cc) or greater. As a result, using the correct values for water salinity resulted in as much as a 15.34% difference in the calculated water saturations, especially in rock intervals that are dominantly water-wet. Therefore, the simple matter of using correct values for pore water salinity allowed for a significant change in calculated saturation values, and thereby 'corrected' core data to match log data more closely. Use of the appropriate salinity affected saturation calculations for samples subjected to either RCA or GRI. Fig. 6 is a plot of water saturation for 350 core plugs. The blue line is computed water saturation assuming a formation water salinity of 50,000 ppm; the red line is computed water saturation assuming a formation water salinity of 350,000 ppm.

Given the extreme salinity of formation waters in the Bakken petroleum system, there was a suspicion that salt (halite) precipitation was a possibility in core material. Analysis confirmed the presence of halite occluding pores in core material [Fig. 7] as well as in at least some X-ray diffraction analyses. The authors now believe that the halite precipitated after the core was brought to the surface and subjected to ambient conditions. (Formation temperatures are approximately 250°F, and pressures are as high as 7,000 psi.) The halite not only occludes pores but also occurs as a partial coating on diagenetic minerals in the rocks. This conclusion corroborates the assumption that the halite is a 'contaminant' formed after the cores were retrieved. The presence of halite in the rocks calls into question whether salt can be completely removed during the chloroform/methanol azeotrope and subsequent methanol cleaning steps of RCA, especially given that

incomplete cleaning of water and hydrocarbons during RCA toluene extraction had been observed [Figs. 5A and 5B]. Further, because the GRI protocol as written [2] does not include either a methanol/chloroform or methanol cleaning after toluene extraction, incomplete removal of halite can be expected in crushed rock analyses. Indeed, initial lab tests showed that both post-toluene cleaning steps are required on crushed rock samples to remove the 'contaminant' halite completely from the rocks; the methanol/chloroform azeotrope cleaning proved insufficient to remove all halite, and a methanol cleaning was required. Because incomplete removal of halite will affect subsequent measurements of materials, it is likely that the core measurements are in error from the lack of thorough salt removal. The significance of this source of error is being evaluated.

Comparison of Nuclear Magnetic Resonance and Extraction Saturation Analysis

Core NMR measurements were run to attempt an independent analysis of the core saturations without using an extraction method. The NMR measurements required a 1-inch diameter core plug. This was accomplished by under coring preserved 1.5-inch diameter plugs that were twins to original core analysis. These 1-inch plugs were measured in native saturation using a high field 20 MHz NMR spectrometer by acquiring both T2 and T1 datasets. From these measurements, porosity, oil and water saturations were calculated. Following NMR measurements, the 1-inch plugs were placed in Dean Stark apparatus and normal Dean Stark measurements were made on the plugs. The remnants from this core were used to make retort extraction analysis measurements. Table 1 shows a comparison of the retort, NMR and Dean Stark measurements for porosity, oil saturation, and water saturation. The water and oil saturations calculated from Dean Stark uses water salinity of 360,000 ppm and oil gravity of 45 API.

Fig. 8 contains plot of all of the data in Table 1. Fig. 8A is a plot of porosity and shows that Dean Stark and NMR porosities are similar whereas Retort porosities are generally lower in value. Fig. 8B is a plot of oil saturations for all of the methods and shows that Retort gives lower values, Dean Stark the highest values and NMR is generally in between the other two. Fig. 8C, is a plot of the water saturations and shows that Dean Stark has the lowest saturation values, Retort the highest and the NMR saturations values varying both higher and lower when compared to the other two methods. Therefore, the variation in the results of this data would seem to indicate that there is uncertainty as to which method is more accurate in determining saturations in unconventional tight oil.

It should be mentioned that the current version of API RP 40 protocol for retort procedures does not include a brine-density volume correction factor as required in the Dean Stark procedures using Equations 1 and 2. Additionally, this protocol does not have any procedures for the removal of salts from the sample during the test.

Anhydrite Dissolution

Early in the deliberations about possible sources of error in core measurements, the likelihood of gypsum dissolution by methanol during RCA was discussed. This question arose from the observation that the interval where the difference in log and core saturations was occurring started where anhydrite was appearing in the log mineral analysis. Although little or no indication of gypsum was observed in the samples,

anhydrite is present, particularly in the Three Forks. That gypsum is methanol soluble is expected based on relevant literature [5, 6]. Although lab experiments have shown that anhydrite solubility is higher than that of gypsum [6], it was unclear whether some of the anhydrite in the Three Forks rocks was dissolving during the cleaning process when methanol was used. Thus, the service labs were instructed to perform bench top tests; anhydrite from the Three Forks was carefully weighed and then bathed in methanol. After approximately two weeks, the samples were carefully removed from the beakers, dried and reweighed, with little to negligible weight loss from the beginning of the experiment. From these test results, the concerns regarding anhydrite dissolution during the Dean Stark cleaning process seem unfounded.

CONCLUSION

An ongoing evaluation to understand possible reasons why core data are mismatched to log data from the Bakken and Three Forks formations has uncovered several issues that are being considered as sources of errors in the original core data. Most notable is the problem with core analysis that may have roots in the salinities of the pore waters in these rocks. The very high salinities require special attention in the calculations of water saturation. In addition, salt precipitation in the cores on retrieval to the surface can lead to porosity occlusion and therefore to incomplete cleaning during routine core and crushed rock analysis. The salt precipitation may be considered a principal hurdle to overcome when performing lab tests on either core plugs or crushed samples. Diligence is required to inform core service labs of formation water salinity and produced oil density values before commencing lab work, and to ensure that errors are minimized in calculating water and oil saturations.

The characteristically low porosity and permeability of Bakken and Three Forks rocks, coupled with the concerns regarding salt precipitation, calls into question the use of existing core analytical approaches and workflows to obtain accurate core data from unconventional tight oil rocks. Existing methods were developed for conventional reservoir rocks (RCA) and gas shales (GRI). Consequently, the authors propose research and development of analytical protocols and workflows specific to unconventional tight oil reservoirs (low porosity/permeability) and associated rocks. Finally, our studies suggest that the API RP 40 is due for a review and revision, and should be updated to include detailed analytical techniques suitable for unconventional reservoirs.

ACKNOWLEDGEMENTS

The authors thank Hess Corporation and the Bakken Asset Team for permission to publish this paper, and the service company representatives for putting up with relentless questioning and insistence to try different tests to evaluate the nature and degree of the problems. Specifically, the authors sincerely thank Pat Lasswell and Ron Martino at Weatherford, and John Dacy, Craig Merritt, Michael Long, Stacy McWhorter, Greg Salter, Tom Swisher and Wayne Sealey at Core Laboratories.

REFERENCES

1. API RP 40, *Recommended Practices for Core Analysis*. 1998. Washington, DC: API.
2. Luffels, D. L. and F. K. Guidry. 1992, New core analysis methods for measuring reservoir rock properties of Devonian shale. *Journal of Petroleum Technology* **44**: 1184-1190.
3. Dean, E. W. and D. D. Stark, 1920. A convenient method for the determination of water in petroleum and other organic emulsions. *Industrial and Engineering Chemistry* **12**: 486-490.
4. Gaswirth, S. B. and K. R. Marra, 2015. U.S. Geological Survey 2013 assessment of undiscovered resources in the Bakken and Three Forks Formations of the U.S. Williston Basin Province. *American Association of Petroleum Geologists Bulletin* **99**: 639-660.
5. Marshall, W. L. and R. Slusher, 1966. Thermodynamics of calcium sulfate dehydrate in aqueous sodium chloride solutions, 0-110°. *Journal of Physical Chemistry* **70**: 4015-4027.
6. Kan, A. T., R. Gongmin, and M. Tomson, 2003. Effect of methanol and thylene glycol on sulfates and halite scale formation. *Industrial and Engineering Chemistry Research* **42**: 2399-2408.

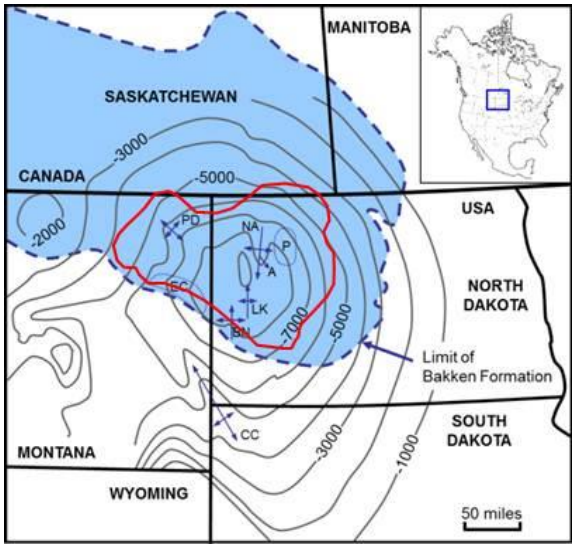

Fig. 1 - Map showing Williston Basin (outlined in red) in North America

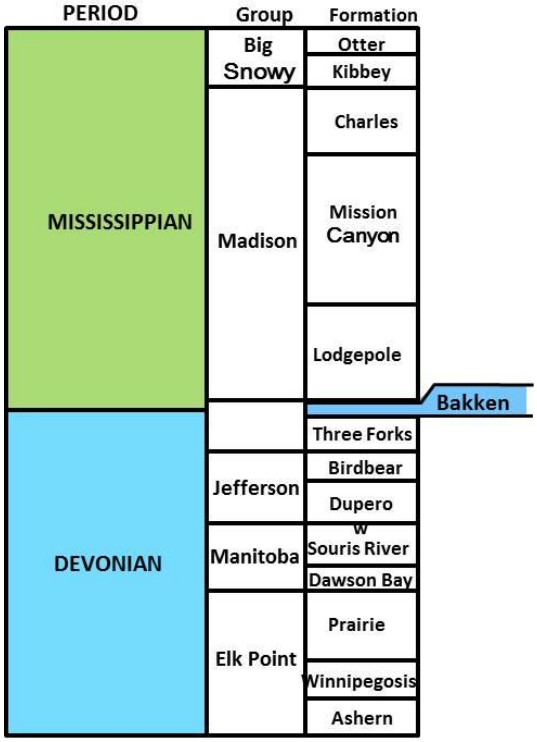

Fig. 2 - Generalized stratigraphic column of the Williston Basin

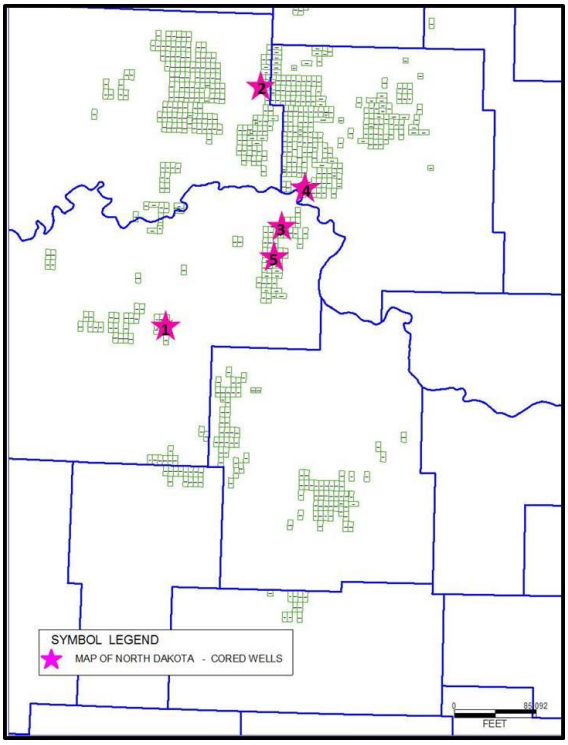

Fig. 3 - Map showing the location of five cored wells in the Bakken petroleum system taken in 2013 - 2014

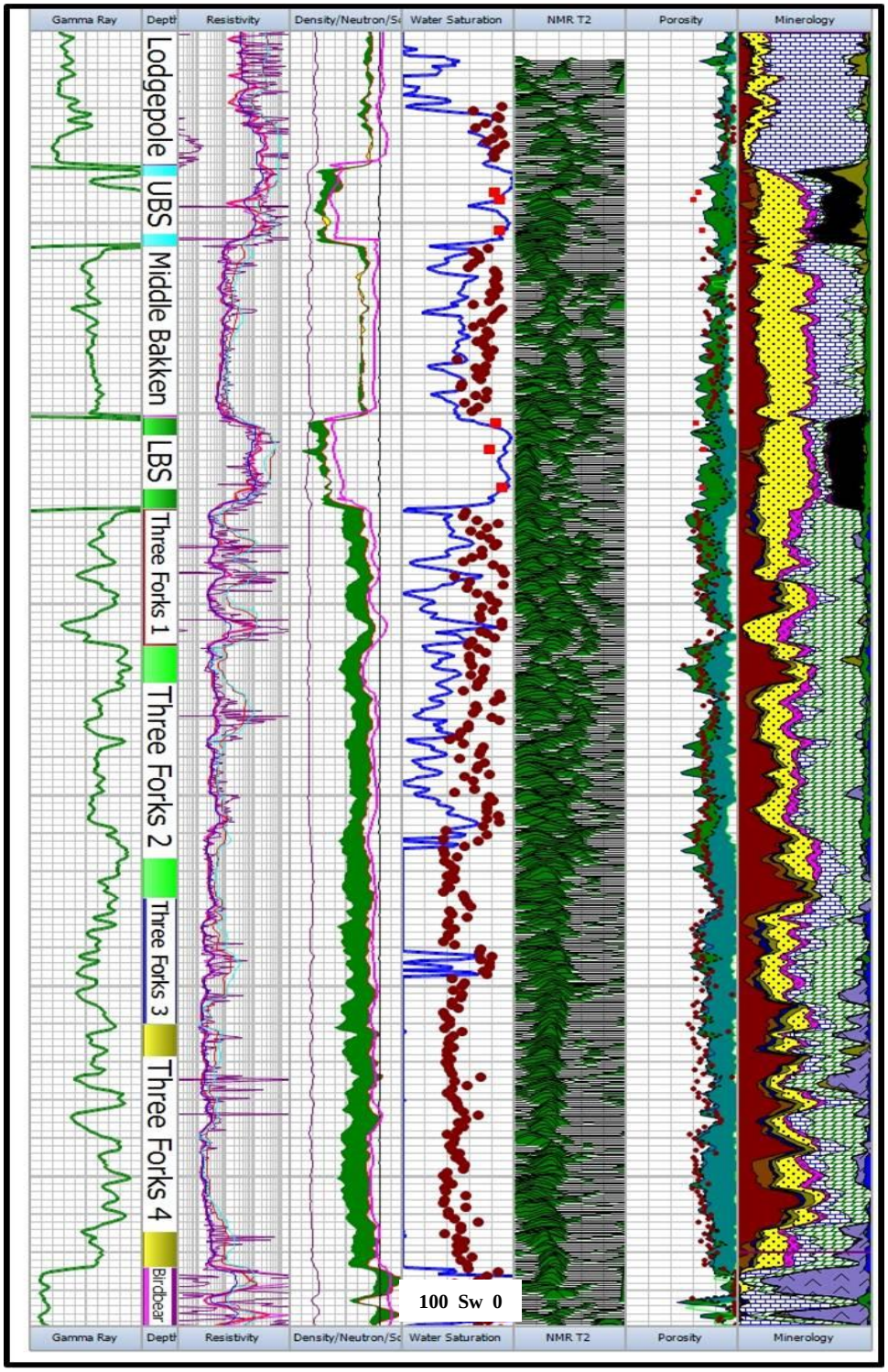

Fig. 4 - This example shows a poor log to core water saturation comparison in the middle water-saturation log track, primarily over the Three Forks Zones 3 and 4

Fig. 5A - Dean Stark extraction apparatus showing orange discoloration of toluene in boiling flask. The discoloration resulted from hydrocarbons released after crushing a core plug that had already been subjected to RCA Dean Stark cleaning

Fig. 5B - Water level in the calibrated receiver of the Dean Stark extraction apparatus. This additional water was extracted from the sample after crushing a core plug that had already been subjected to 'complete' RCA Dean Stark cleaning

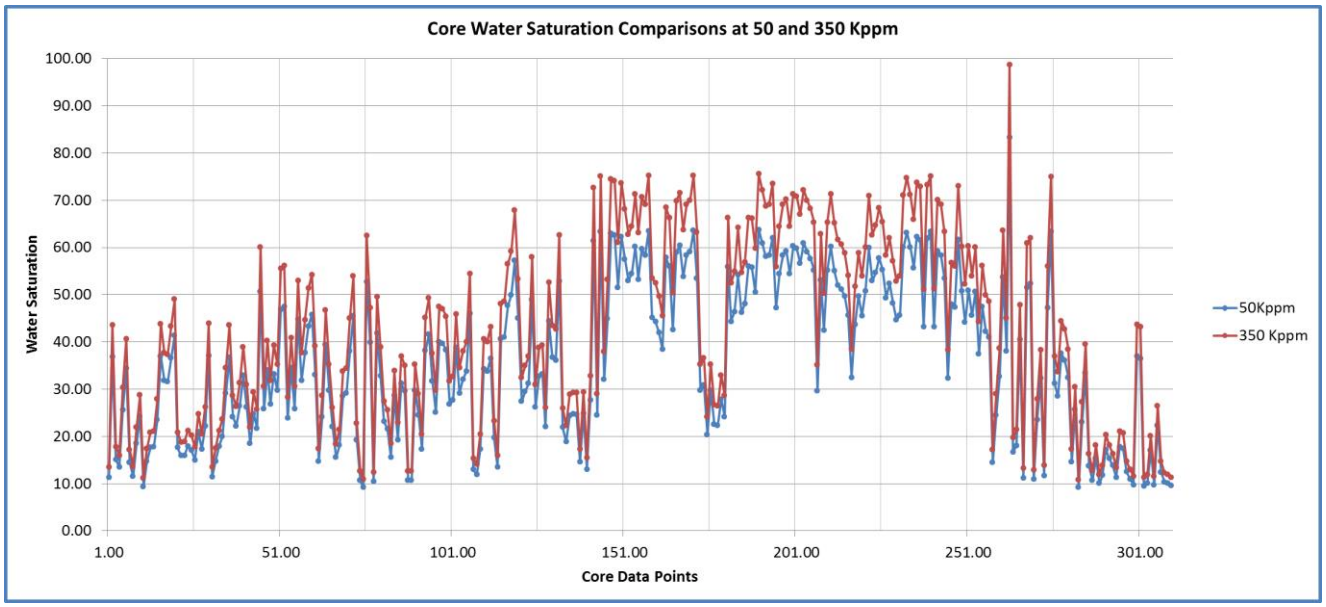

Fig. 6 - Comparison of 350 RCA cores, changing formation water salinity from 50,000 ppm to 350,000 ppm

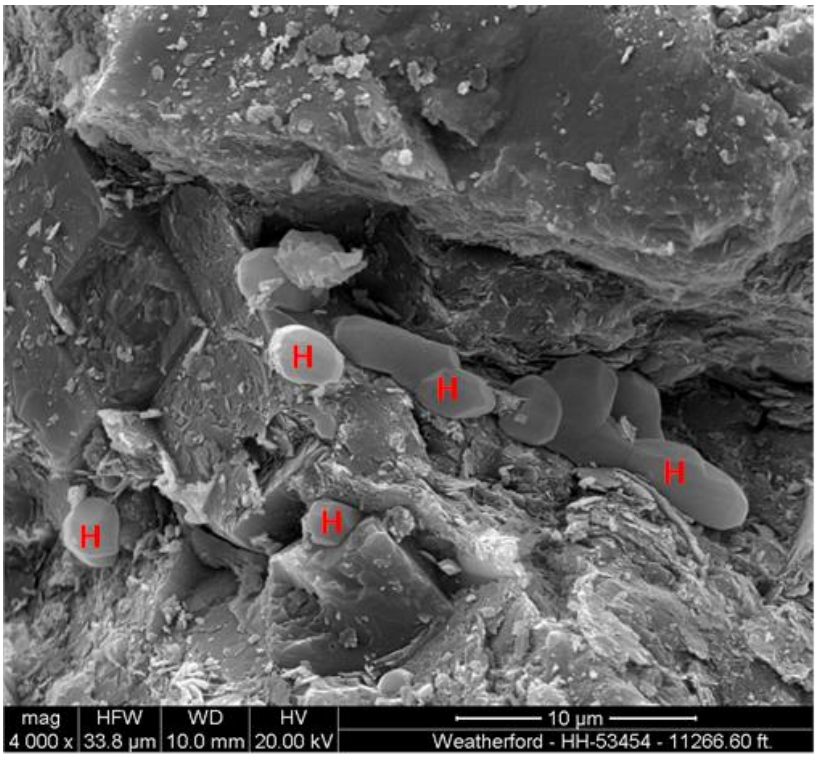

Fig. 7 - Scanning electron micrograph showing halite crystals (H) that partly occlude pores and coat diagenetic minerals

	Porosity			Oil Saturation			Water Saturation		
	Retort	NMR	DeanStark	Retort	NMR	DeanStark	Retort	NMR	DeanStark
Sample	Porosity	Total				360K & 45API			360K
Number		Porosity	Porosity	Oil	Oil	Oil	Water	Water	Water
	%	%	%	% PV	% PV	% PV	% PV	% PV	% PV
30Rb	2.14	2.2	1.94	0.00	9.4	28.7	52.45	42.7	21.3
48Rb	3.22	4.9	4.91	4.48	13.9	20.1	77.87	32.5	31.2
53RB	4.60	6.0	5.58	13.57	18.3	27.3	68.91	52.8	43.5
58RB	2.58	2.5	1.98	12.67	18.4	9.7	44.33	69.0	44.5
62Rb	6.45	8.4	8.74	19.62	18.0	11.3	71.39	25.7	39.7
84Rb	4.69	6.1	7.20	0.00	10.6	10.1	79.88	40.3	56.0
108Rb	3.46	4.6	5.54	3.64	14.2	11.0	76.97	22.6	33.4
139Rb	2.82	6.4	7.89	3.67	19.5	20.2	58.47	18.8	8.2
161RB	5.75	5.4	4.91	2.71	3.5	41.5	85.08	94.9	69.0
183Rb	5.86	4.6	10.69	0.00	2.6	9.2	80.46	48.6	54.9
195RB	3.09	3.8	4.26	0.00	5.6	29.6	72.58	90.3	63.4
207Rb	3.91	1.2	2.25	0.00	10.2	20.2	72.58	36.9	50.8
216Rb	6.59	4.7	6.29	2.71	6.7	17.7	66.17	44.2	42.6
241RB	5.72	7.0	6.84	2.95	2.7	17.9	90.37	74.3	58.2
247Rb	4.95	4.9	3.88	0.00	6.0	12.8	76.06	45.5	28.9

Table 1 – Comparison of porosity, oil saturation and water saturation measured on preserved core plugs using three different analysis techniques. Values in the green columns were from retort extraction methods; values in blue were from a 20 MHz lab NMR spectrometer; and values in yellow were computed from Dean Stark solvent extraction methods

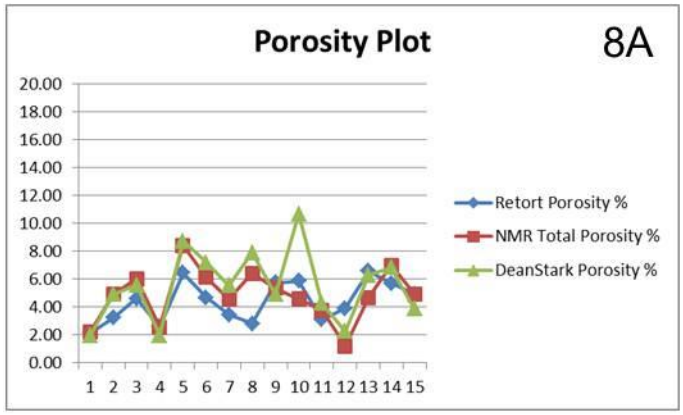

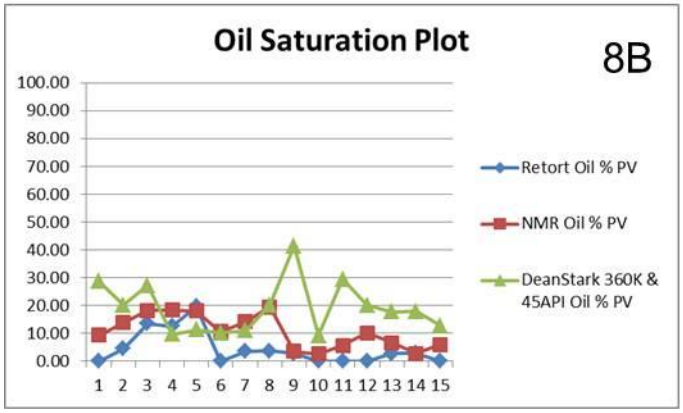

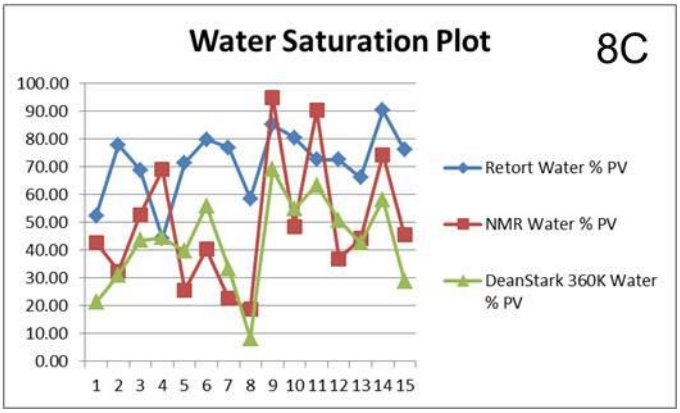

Fig. 8 – Porosity, Oil and Water Saturation plots from Retort, NMR and Dean Stark

COMPUTERIZED X-RAY MICROTOMOGRAPHY OBSERVATIONS AND FLUID FLOW MEASUREMENTS OF THE EFFECT OF EFFECTIVE STRESS ON FRACTURED LOW PERMEABILITY POROUS MEDIA

Nathan J. Welch[1], John P. Crawshaw[1], and Edo S. Boek[2]
[1]Department of Chemical Engineering, Qatar Carbonates and Carbon Storage Research Centre, Imperial College London, South Kensington Campus, London SW7 2AZ, U.K.
[2]Department of Chemistry, Cambridge University
e-mail: n.welch12@imperial.ac.uk

This paper was prepared for presentation at the International Symposium of the Society of Core Analysts held in St. John's Newfoundland and Labrador, Canada, 16-21 August, 2015

ABSTRACT

This work shows the observed changes in sample permeability and fracture geometry that occur within a fractured piece of low permeability shale with different effective stress gradients applied to the plug sample. These observations were made using an in-situ micro-CT fluid flow imaging apparatus with a carbon fibre Hassler-type core holder. Changes within the preferential fluid flow path under different stress regimes as well as physical changes to the fracture geometry are reported. Lattice-Boltzmann single phase permeability flow simulations were performed on the extracted flow paths and compared to experiment permeability measurements.

Experimental flow measurements showed significant changes in the permeability of the fractured system with varying stress states. Imaged fracture apertures were also used in simple parallel plate flow calculations, and compared to results from fluid flow simulations on segmented sample void space and experimental fluid flow measurements.

INTRODUCTION

Ensuring the long-term safe geologic storage of carbon dioxide has become an important scientific and political issue for wide spread implementation of carbon dioxide sequestration operations. An intact and substantial seal formation above a storage reservoir is required for a significant portion of the initial sealing mechanisms believed to occur during carbon dioxide storage operations [1]. Shales and evaporites are common seal formation rock types found above numerous hydrocarbon reservoirs, as well as potential saline aquifer storage locations [2]. These seals are known for having very low permeabilities, however, some also have the tendency to be quite fissile, and the formation of fractures within these seals can have a significant detrimental effect on the sealing potential of a reservoir and amount to large areas of high permeability and low capillary pressures compared to the surrounding intact rock [3].

Work has continued to progress the rapid determination of these sealing parameters in the selection of suitable sequestration sites. A recent review of all available literature for capillary entry pressure measurements in an attempt to predict sealing characteristics of these seal formations shows the substantial lack of data available for interpretation [4]. Numerous experimental techniques have been developed for quickly determining these properties [5-9] with an overall comparison of each method presented by Boulin et al. [10]. Intact seal samples typically have nanometre sized pores as well as very low permeabilities, and fluid flow through fractures would largely dominate any observed fluid behaviour in the system. Fractures in these systems therefore allow for application of more traditional core analysis techniques [11] due to the rise in permeability and decrease in capillary pressure.

In this work, we were able to image the individual fractures found to be present in a fractured sample using our recently developed in-situ microtomography fluid flow apparatus. The purpose of this work is to attempt to relate observed changes in the sample fracture network geometry with varying system stress to changes in recorded fluid flow behaviour, and also to compare predicted fluid flow behaviour using simple equations for fluid flow between parallel plates and numerical fluid flow simulations, to experiment results.

EXPERIMENT DESIGN

The fractured sample used in all of these observations was a cored plug sample taken from a large carboniferous shale quarry sample received from Todhills Long Lane Quarry in the UK. The sample was extracted via bulldozer from one of the working benches of the quarry and shrink-wrapped to try and prevent loss of natural pore fluid during shipping. The approximately 20 kg sample arrived after 2 days of shipping still in the original packaging material. Upon removal, the sample remained in one large roughly cube-shaped mass. The sample was then immediately wrapped in several layers of heavy black plastic and stored for later use.

High pressure mercury intrusion (Micromeritics AutoPore IV 9500, Cup and stem penetrometer) measurements were recorded on oven dried fragments collected from the larger mass shown in **Figure 1**. After drying, these fragments were further broken down into pieces no longer than 6 mm of any side length to fit into the mercury cup of the penetrometer. The majority of pores of the intact sample pore structure were <100nm in size, with a total porosity of 9.77%.

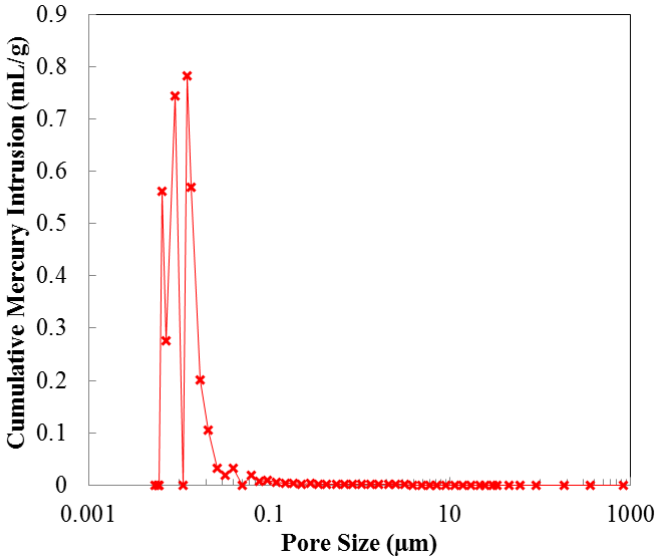

Figure 1: HPMI results for Long Lane Quarry shale

Large chunks of the original sample were broken away by hand with little force along natural cleavage planes of the sample for plug drilling. The sample's reactivity to water was immediately apparent on contact with tap water used for drilling. The sample began to fail along multiple parallel cleavage planes due to clay swelling and resulted in laminate sheets of about 1 cm in thickness. These smaller cleaved sheets still had a fairly high strength to them, and could not be broken by hand. In order to avoid the clay swelling, later plugs were instead drilled using compressed air to remove debris and cool the coring bit. The sample used in this study was drilled and then came into contact with untreated water resulting in the observed fracture network. This caused the sample to immediate begin to break apart due to swelling and it was then wrapped in PTFE tape to maintain the original configuration of fractured pieces.

Fluid flow measurements and x-ray microtomography observations were collected in our [12] micro-CT fluid flow apparatus designed for high resolution in-situ imaging of fluid flow behaviour in porous samples. Tomograms were collected with an Xradia XRM-500 computerized microtomography apparatus. A specially designed Hassler-type flow cell was used for this system designed by Airborne International. The flow cell has a maximum internal diameter of 19 mm, and can accommodate samples up to 212 mm in length. The flow cell is constructed of high strength carbon fibre for low x-ray absorbance, and sealed with stainless steel end caps. ISCO 260D syringe pumps were used to maintain all fluid pressures and record flow rates.

The fractured sample was then carefully removed from the PTFE tape and placed inside Viton tubing, while maintaining the original alignment of the fractured pieces. Current capabilities of the core holder system limits the system to only applying uniform confining pressure around the whole of the sample with no other axial stress provided.

SINGLE PHASE PERMEABILITY OBSERVATIONS

After loading the sample into the fluid flow cell, water was used the annulus of the flow cell as the system's confining fluid. This was done to try to ensure the x-ray transmission of the dry scan was similar to that during fluid flow. A dry tomogram was recorded to show the zero-stress geometry of the system.

Avizo 9.0 produced by FEI [13] was used for initial tomogram visualization and manipulation. Orthogonal slices of the dry fractured sample can be seen in **Figure 2**. To avoid interference with image segmentation and later analyses, a region similar to the one represented with the white cornered rectangles in each plane was extracted from each 3D reconstruction recorded. This region of interest was selected to exclude end piece artefacts and the core sleeve, being the largest inscribed rectangular shape that could be fit within the sample. Registration and exact extraction of a similar region would have been more feasible if not for the rather high anisotropy of compressibility exhibited by the sample.

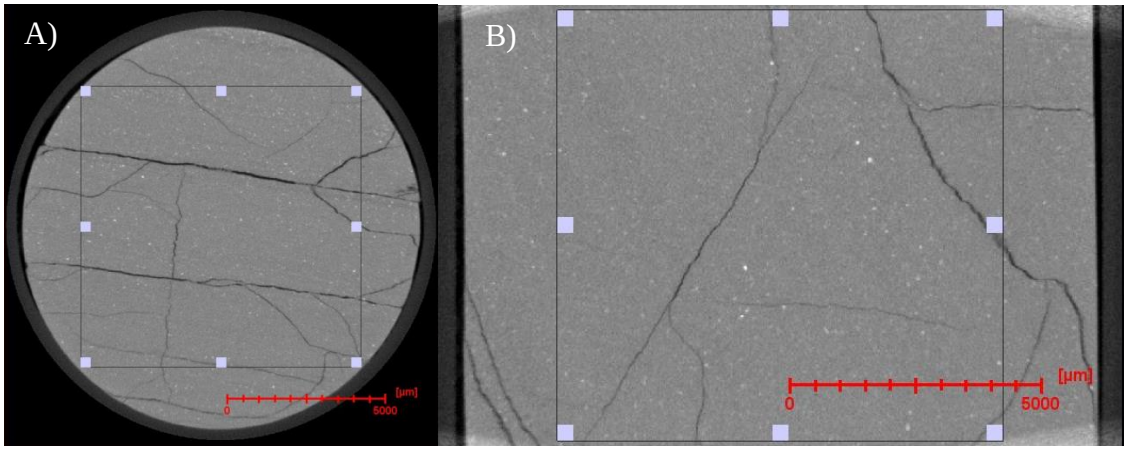

Figure 2: Orthogonal slices of the dry scan tomography highlighting the region of interest extracted avoiding x-ray artefacts in full 3D space. A) x-y and B) x-z orthogonal slice. All scale bars shown are a length of 5000 µm.

Following the extraction of the region of interest, a noise-reducing, edge-preserving non-local means filter [14] was applied to the image data set to assist in image segmentation and analysis for the dry scan. Following dry scan imaging, 5wt% NaCl, 1wt% KCl brine was introduced to the sample and pressurized to an initial system pressure of 6 bar confining pressure, 5 bar upstream pressure, and 4 bar downstream pressure. This brine was selected to try and reduce further reactivity with changes in ion concentration within the shale matrix and pore fluid. No further fracturing was observed from the introduction of this wetting phase brine.

System stress was then varied, initially holding a constant pressure drop of 1 bar across the fractured sample, and incrementally increasing confining pressure of the system from 6 bar to 120 bar. After each change in system stress, a tomogram was recorded for the

system and permeability measurements recorded based on volume displacement in system pumps over the course of the scan. System scan times took on average 90-120 minutes for a 13.2-13.7 µm cubic voxel side length tomogram.

A slice orthogonal to the flow direction from approximately the same location in the fractured system can be seen in **Figure 3** under no-stress, a low confining stress of 5 bar, and a high confining stress of 120 bar. The plane parallel to the major fractures has a much lower resistance to stress than those opposing the major fractures. This change in overall sample geometry also caused issues with direct visual comparison as the overall geometry of the system had changed between each change in system stress.

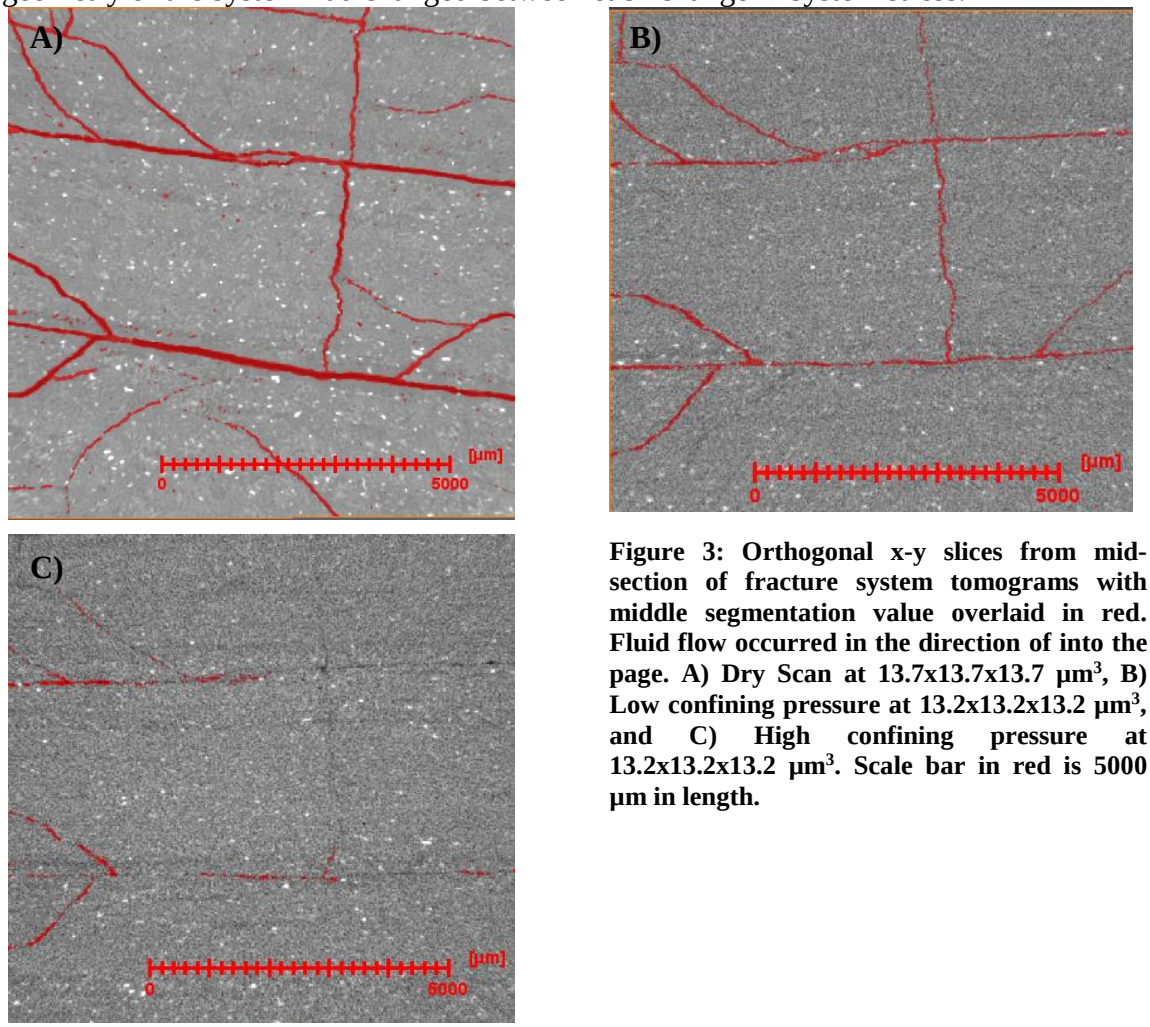

Figure 3: Orthogonal x-y slices from mid-section of fracture system tomograms with middle segmentation value overlaid in red. Fluid flow occurred in the direction of into the page. A) Dry Scan at 13.7x13.7x13.7 µm^3, B) Low confining pressure at 13.2x13.2x13.2 µm^3, and C) High confining pressure at 13.2x13.2x13.2 µm^3. Scale bar in red is 5000 µm in length.

Sample permeabilities were also recorded with changes in system stress with a varying pressure drop across the core. Finally, system permeabilities and tomograms were recorded for decreasing effective stress, or rising pore pressure. The permeability results for each different system stress can be seen in **Figure 4**. Initially confining fluid pressure was increased in logarithmic intervals from 6 to 120 bar. Then, only the upstream pressure was increased from 5 to 119 bar, with the maximum pressure selected to remain

just below the confining pressure of the system. Finally the downstream pressure was increased in similar intervals until a final pressure of 118 bar was reached.

The effective pressure of the system is defined in this work as the confining pressure minus the average of the inlet and outlet pore pressures. Error bars are reported as discrepancies found between upstream and downstream measurements, with minimal contribution to error with the in terms of the volume resolution of the pumps. One set of error bars on the highest stress data point for the rising confining pressure data series was omitted due to non-realistic flows found in the downstream pump. This non-realistic flow behaviour may have been due to either compression of gases trapped in the pore space or thermal variations within experimental environment.

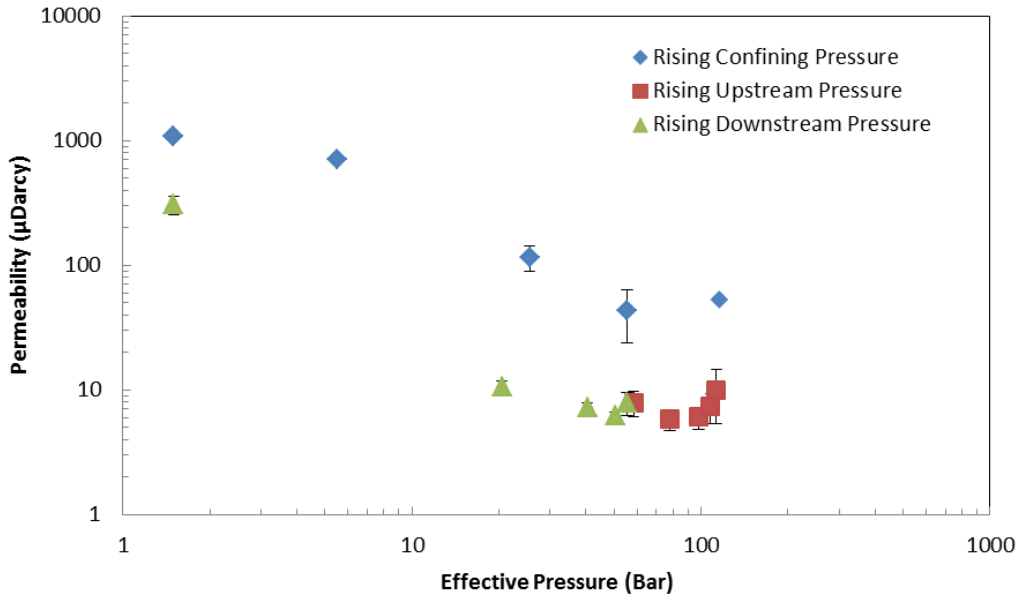

Figure 4: Changes in permeability of the fractured system due to changes in system stress.

The initial changes in permeability with increased confining pressure are expected as the overall aperture of the observed fractures was seen to decrease as the effective pressure of the system increased. During increasing upstream pressure, and overall differential pressure, permeability was seen to initially decrease with increasing pressure drop across the sample. This decrease in permeability may be caused by further narrowing of downstream fractures under the new stress of the high upstream pressure. There also exist several cross bedding fractures within the sample that may have been closed, decreasing permeability, due to the new stress applied from the increased inlet pressure.

Finally, while raising the downstream pressure of the sample, a recovery of the sample's initial permeability is seen. This shows that the decrease in permeability recorded for the increasing pressure drop across the sample was not caused by fines migration. The final recovered permeability in a stress state similar to that of the first recorded permeability is

expectedly lower, as some of the larger features holding the fracture open for fluid flow may have been compacted over the course of the tests.

The fracture void space from each tomogram was then segmented from the rest of the solid material. This segmentation was accomplished using a simple thresholding method instead of a more advanced watershed based algorithm, since the selection of appropriate phase label seeds within narrow near- or sub-resolution features proved to yield erroneous results due to an insufficient gradient between phases. Label seeds would also propagate inappropriately far into solid phase regions due to the lack of a significant greyscale gradient between suspected void space and solid. To assess the significance of the selected threshold value, three segmented images were created and used for flow simulations using a subjective optimal threshold value and deviations ±200.

This segmentation method was first applied to the dry scan images followed by the low confining pressure, and then high confining pressure system tomographies. As the stress applied to the system is increased, the aperture of the imaged fractures decreases and the accuracy of the segmentation of the fracture void became increasingly challenging as seen in **Figure 3**. Threshold segmentation was still found to yield the most representative of fracture segmentations, but the inclusion of numerous regions of noise within the solid regions of the sample significantly decreased the accuracy of the void space in each tomogram.

These erroneous regions were largely eliminated from the final fracture segmentation by computing the connected flow path along the flow direction of the sample using a neighbourhood selection allowing segmented voxels to be considered connected across edges, but not through vertexes. This analysis module then removes all disconnected components that are smaller than 10 voxels in a given volume. This greatly reduces the inclusion of non-connected, improperly segmented noise regions, but incorrect regions near the connected fracture space remain problematic. Previous work has attempted to tackle this issue of selecting a proper threshold value for features below image resolution [15] with the inclusion of looking at the connectivity factor or Euler-Poincaré number for 2D and 3D systems [16]. However, the distinction between erroneous regions attributed to the void space segmentation and simply void space regions below image resolution may have a significant effect and the analysis was not implemented here.

The high stress system proved to be beyond segmentation capabilities, as once a threshold segmentation value was found that had connectivity through the sample in the direction of flow, large errors were evident in the segmentation and excluded. A different greyscale value was selected for each tomography as the reconstruction bit scaling was different for each system based on how much overall resolvable fracture void space could be observed in the final reconstruction, as well as known x-ray source issues.

The segmented fracture void space data sets from the zero and low effective pressure conditions were processed using a Lattice-Boltzmann based flow simulation for the

determination of local velocity fields and single phase absolute permeability as shown in Error! Reference source not found.. The calculations were performed by mirroring the geometry about the flow face and using a constant uniform fluid body-force [17]. Experiment fluid flow and flow simulations were performed along the axial direction of the sample, the direction into the page for the shown images in **Figure 3**.

The preferential fluid flow path for the most conservative threshold image of the dry scan system can be seen in **Figure 5** following the results of the fluid flow simulation. The fluid flow path appears to be rather uniform throughout the fractured system flow network, with slight cross-bedding fluid exchange via smaller interlayer fractures. The two largest of fractures running through the sample appear to contribute the most to all fluid flow through the sample.

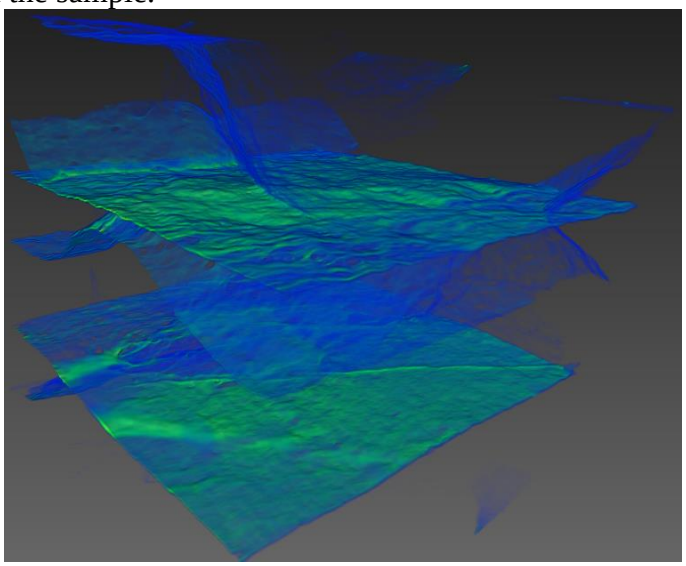

Figure 5: 3D representation of single phase fluid flow through segmented fracture system. Fluid flow occurred from the left front face to the rear right face of the extracted void space. Lighter colours represent areas of higher flow velocity with the darker blue being areas of lower velocity.

The two major lateral fractures running through the entire length of the observed region highlighted in **Figure 5** were extracted for analysis compared to the known solution for a system of two infinite parallel plates.

The flow rate between parallel plates is given by [18]:

$$\frac{Q}{l} = -\frac{\alpha^3 \Delta P}{12 \mu L} \tag{1}$$

Where Q is the volumetric flow rate, l is the length normal to flow, ΔP is the pressure difference across the length of the system, α is the distance between the two plates, μ is the fluid viscosity, and L is the length of the sample in the direction of flow. Then by

equating with Darcy's Law and solving for permeability, the following relation can be found:

$$k = -\frac{\alpha^3 l}{12A} \quad (2)$$

Where k is the sample permeability, and A being the sample area normal to flow. Predicted permeabilities for both the upper and lower major fractures as seen in the fluid flow representation are presented below in **Table 1** based on this calculation using the measured mean aperture from the original greyscale images. Crack apertures are a calculated mean value measured from greyscale images across 6 different orthogonal slices along the length of the sample.

Table 1: Predicted permeability of fractured system using parallel plate model and Lattice-Boltzmann flow simulations compared to measured values. Note: The values presented for the flow simulation permeability calculations are based on the range of threshold values used for fracture segmentation.

System		Crack Aperature (μm)	Crack Permeability (Darcy)	Combined Predicted Permeability (Darcy)	Flow Simulation Permeability (Darcy)	Measured Permeability (Darcy)
Dry Scan	Top Crack	101.5	10.16	14.7	15.3-44.6	N/A
	Bottom Crack	77.2	4.46			
Low Stress	Top Crack	23.8	0.14	0.71	0.63-2.52	0.001
	Bottom Crack	38.4	0.57			

These results show that the resulting permeabilities from the fluid flow simulations and those predicted by the parallel plate model correspond quite well. However, the predicted permeability at the low stress condition was much higher than that measured in the experiment. This was due to the fracture width being below the voxel size of the tomograms. To obtain a permeability of 1 mDarcy, the estimated aperture width of a planar fracture is 3.7 μm, well below the 13.2 μm voxel size of the scan. The fracture segmented from the scan has a width of at least one voxel, much too large to correctly represent the actual fracture system.

The effect of the matrix between fractures was assumed to be negligible, although fluid flow experiments on intact samples could not be completed as no unfractured plugs could be obtained. This assumption is supported by considering the orders of magnitude difference that exists between the imaged fracture apertures and the first major pore size peak appearing near 100 nm as seen in **Figure 1**. The lower values of measured permeability approaching the 1 μDarcy magnitude may be approaching that of the intact

matrix, and then would need to consider the effect of flow within the porous matrix structure.

A technique was then developed to measure qualitatively changes in overall fracture aperture along the length of the sample, making use of changes within the greyscale values for features below the resolvable limit. The mean greyscale value for the entire volume of interest (660x635x600 μm^3) at each effective pressure was calculated and used to normalize the mean grey value for each slice in the plane orthogonal to flow along the length of the sample. Fluid flow occurs in direction of increasing slice number, or left to right in **Figure 6**. This analysis gives a qualitative analysis of sample void space for both above and below resolvable fracture features.

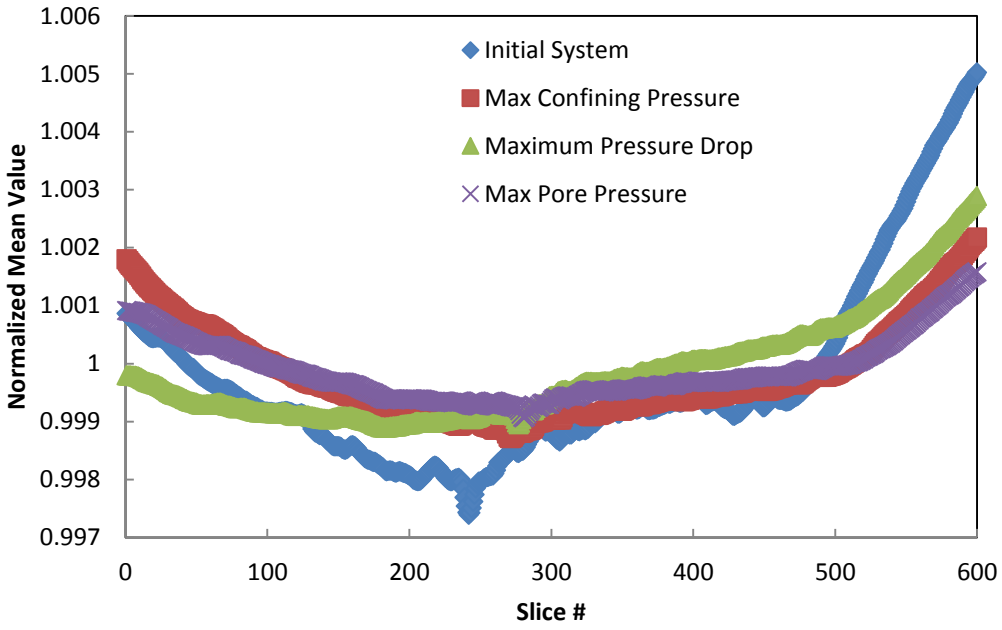

Figure 6: Normalized mean grey scale value of x-y plane orthogonal slices along length of sample for different stress systems.

The initial profile shows a high level of fluctuations with each advancing slice. These are caused by the large open and fully resolved fractures observed, which contribute a large portion of the potential fluid flow path. The profile at maximum confining pressure shows the homogenisation along with a smaller total spread of values caused by the closure of the fracture system. The maximum pressure drop data set shows the widening of upstream fractures with the slight dip seen in the left hand side of the figure compared to that of the maximum confining stress system, but with still a highly closed downstream portion. The final maximum pore pressure profile was similar to the maximum stress system, but has noticeably higher amounts of void space in the initial upstream and final downstream portions of the sample leading to the higher permeabilities. This final state also shows the unrecoverable change in system geometry following compaction by not returning to the level of fluctuations seen initially in the system.

The overall “U” shape of the final curves may be a result of beam hardening or lack of uniform x-ray delivery from the source cone shape leading to slight deviations from an overall mean value. This shape may also have been an effect of the compression in the axial direction of the sample caused by the unrestrained fluid inlets of the core-holder assembly, dissipating with depth into the fractured sample.

CONCLUSIONS AND FUTURE WORK

The measurement of fractured system permeability under varying systems stresses was successfully recorded in a hassler type flow cell. Fractured sample permeability was found to decrease with increasing confining pressure under a constant, small pressure gradient. The near complete recovery of initial permeability was found to be possible by raising fluid pore pressure to the same initial effective pressure state. Full 3D x-ray micro-tomograms were collected after each change of system stress, and used to show qualitative changes in fracture void space. The fractured system was observed to exhibit no major change in permeability under a rising pressure gradient, despite evidence showing the widening of initial upstream fracture apertures. Upon raising pore pressure to reduce the effective pressure to close to the initial value, the sample recovered most of its initial permeability, with a slight decrease thought to be due to sample compaction. The limitations of system resolution for imaging the entire diameter of the sample limited the effectiveness of segmenting the fracture void space. The actual fracture aperture for even the lowest confining pressure was estimated to be well below the voxel size of the CT scan, and the image segmentation technique therefore overestimated the fracture width subsequently used in the Lattice-Boltzmann simulations.

ACKNOWLEDGEMENTS

The authors would like to acknowledge the support of the Qatar Carbonates and Carbon Storage Research Centre (QCCSRC) for the funding of this project, as well as Shell, Qatar Petroleum, and Qatar Science and Technology Park for the funding of this program. The authors would also like to acknowledge to fellow PhD candidate Farrel Gray for his contribution of the Lattice-Boltzmann fluid flow simulation results.

REFERENCES

1. S. M. Benson and D. R. Cole, "CO2 sequestration in deep sedimentary formations," *Elements*, vol. 4, pp. 325-331, 2008.
2. F. K. North, *Petroleum Geology*, 2nd ed. Winchester, Mass. 01890, USA: Allen & Unwin, 1985.
3 K. Edlmann, S. Haszeldine, and C. McDermott, "Experimental investigation into the sealing capability of naturally fractured shale caprocks to supercritical carbon dioxide flow," *Environmental earth sciences*, vol. 70, pp. 3393-3409, 2013.
4 A. Busch and A. Amann-Hildenbrand, "Predicting capillarity of mudrocks," *Marine and Petroleum Geology*, vol. 45, pp. 208-223, 2013.

5 A. Amann, M. Waschbüsch, P. Bertier, A. Busch, B. M. Krooss, and R. Littke, "Sealing rock characteristics under the influence of CO2," *Energy Procedia*, vol. 4, pp. 5170-5177, 2011.
6 A. Hildenbrand, S. Schlömer, and B. Krooss, "Gas breakthrough experiments on fine‐grained sedimentary rocks," *Geofluids*, vol. 2, pp. 3-23, 2002.
7 P. Egermann, J. Lombard, and P. Bretonnier, "A fast and accurate method to measure threshold capillary pressure of caprocks under representative conditions," *SCA2006 A*, vol. 46, 2006.
8 N. J. Welch, J. P. Crawshaw, and E. S. Boek, "COMPARISON OF THE CHANGE OF CAP ROCK PERMEABILITY AND CAPILLARY ENTRY PRESSURE WITH VARYING EFFECTIVE STRESS," *SCA2014*, 2014.
9 S. Li, M. Dong, Z. Li, S. Huang, H. Qing, and E. Nickel, "Gas breakthrough pressure for hydrocarbon reservoir seal rocks: implications for the security of long‐term CO2 storage in the Weyburn field," *Geofluids*, vol. 5, pp. 326-334, 2005.
10 P. Boulin, P. Bretonnier, V. Vassil, A. Samouillet, M. Fleury, and J. Lombard, "Entry Pressure Measurements Using Three Unconventional Experimental Methods," presented at the International Symposium of the Society of Core Analysts, Austin, TX, USA, 2011.
11 A. RP40, "Recommended practices for core analysis," *Feb*, 1998.
12 M. Andrew, B. Bijeljic, and M. J. Blunt, "Pore-scale contact angle measurements at reservoir conditions using X-ray microtomography," *Advances in Water Resources*, vol. 68, pp. 24-31, 2014.
13 V. S. Group, "Avizo," 9.0 ed: FEI 2015.
14 A. Buades, B. Coll, and J.-M. Morel, "A non-local algorithm for image denoising," in *Computer Vision and Pattern Recognition, 2005. CVPR 2005. IEEE Computer Society Conference on*, 2005, pp. 60-65.
15 A. Samouëlian, H.-J. Vogel, and O. Ippisch, "Upscaling hydraulic conductivity based on the topology of the sub-scale structure," *Advances in water resources*, vol. 30, pp. 1179-1189, 2007.
16 H.-J. Vogel, "Topological characterization of porous media," in *Morphology of condensed matter*, ed: Springer, 2002, pp. 75-92.
17 S. M. K. Shah, J. P. Crawshaw, O. Gharbi, E. S. Boek, and J. Yang, "Predicting Porosity and Permeability of Carbonate Rocks From Core-Scale to Pore-Scale Using Medical CT Confocal Laser Scanning Microscopy and Micro CT," in *SPE Annual Technical Conference and Exhibition*, 2013.
18 R. W. Fox, A. T. McDonald, and P. J. Pritchard, *Introduction to Fluid Mechanics* 8th ed.: John Wiley & Sons, Inc., 2010.

ESTIMATING SATURATIONS IN ORGANIC SHALES USING 2D NMR

Benjamin NICOT[1], Nopparat VORAPALAWUT[2], Berengere ROUSSEAU[1], Luis F. MADARIAGA[1], Gerald HAMON[1], Jean-Pierre KORB [3]
[1] Total E&P, Pau, France, [2] WellStaff, Pau, France
[3] PMC, Ecole Polytechnique-CNRS, Palaiseau, France

This paper was prepared for presentation at the International Symposium of the Society of Core Analysts held in St. John's Newfoundland and Labrador, Canada, 16-21 August, 2015

ABSTRACT

Tight organic shales are a challenge to the oil industry in several ways. An accurate petrophysical evaluation of these rocks includes porosity, permeability, hydrocarbon saturation and fracability. The evaluation of these petrophysical parameters has appeared more challenging in tight organic shales than in conventional reservoirs. In this paper, we describe a non destructive method allowing the measurement of hydrocarbon saturation based on two dimensional T_1-T_2 NMR.

First, we give the experimental evidence of an NMR contrast between oil and water in organic shales. Contrary to the conventional reservoirs, the contrast between oil and water in shales is not based on diffusion, but on T_1/T_2. Various imbibition tests with water/light oil/D_2O were performed. These tests prove unambiguously that the oil and water NMR signals can be assigned unambiguously in 2D T_1-T_2 NMR maps. They also prove that the high T_1/T_2 in organic pores is not due to bitumen (high viscosity), and that it can be achieved by light oil (isopar L). The high T_1/T_2 observed is only due to confinement in the organic pores. In order to understand how confinement only can lead to such a high T_1/T_2, multi-frequency NMR dispersion (NMRD) experiments were performed. These experiments allow us to propose an interpretation that explains the unexpected dynamical behavior of the light oil in organic pore leading to high T_1/T_2.

Hydrocarbon saturation in organic shales is commonly measured by Dean Stark, or retort method. Saturation is the ratio between a volume of fluid and a total pore volume. If thermal method may be good at estimating the volume of fluid produced, its major drawback is that it is destructive, therefore preventing the direct measurement of total pore volume. The total pore volume is then estimated by adding water, oil and gas volumes: this leads to an accumulation of errors in the estimation of hydrocarbon saturation in shales. The NMR method being non destructive, it allows performing a total porosity measurement afterwards; therefore providing a much more accurate saturation estimation. The porosity estimation being challenged for the thermal method, we compare water volumes measured by NMR and a thermal method for validating the NMR approach.

INTRODUCTION

Petrophysical properties including porosity, permeability, fracability and hydrocarbon saturation are crucial for hydrocarbon producibility and economic assessment in tight organic shales. Therefore, a technique to evaluate these petrophysical properties in tight organic shales has become more challenging. It has been demonstrated extensively that porosity measurement could have significant bias in these rocks [1-2]. Therefore, a proper experimental protocol is a required to obtain usable data. The saturation is the ratio between fluids (water or hydrocarbon) volume and a total pore volume. Standard methods for evaluating water saturation are Dean Stark and retort fluid extraction. Dean Stark can be time consuming while the Retort method can be relatively fast. However, the hydrocarbon saturation estimated by retort method may be erroneous because the total pore volume is a summation of gas, water and oil volumes [3]. Nuclear magnetic resonance (NMR) is a non destructive method that is commonly used in the industry to provide the porosity. Advanced NMR techniques such as 2D D-T_2 maps are also commonly used to estimate saturations in conventional reservoirs. There is an effort to apply this technique in unconventional rocks [6] and they have shown the difficulty to measure diffusion coefficients in nanoporous materials. Recently, 2D T_1-T_2 NMR has been used by different authors to characterize the fluids contained in shale samples [5-9]. To summarize the finding of these different authors: (1) oil exhibits a high T_1/T_2, (2) water exhibits a low T_1/T_2, (3) bitumen is identified by Singer P.M. et al. [7] and Washburn K.E. et al [8] on their samples (Eagle Ford and Green River formation) and, (4) bitumen is not found in samples used by Korb J-P et al. [10].

Here, we use 2D T_1-T_2 NMR to estimate water and hydrocarbon saturation in tight organic shales. A contrast between water and oil signals in 2D T1-T2 maps is proved by spontaneous imbibitions test in cleaned and as received shales by various liquids, i.e. heavy water (D_2O), light oil (isopar L) and water (70 g/L NaCl). Moreover, dynamic behavior of light hydrocarbon confined in organic pore leading to high T_1/T_2 is proposed. This model is confirmed by multi-frequency NMR dispersion (NMRD) and 2D T_1-T_2 maps at 2.5 MHz and 23 MHz. We therefore propose a comprehensive approach, combining experiment and theory, allowing us to estimate accurately water and oil saturations by NMR. The saturation from 2D T_1-T_2 NMR is then compared to gravimetric method for the imbibitions test and by Thermo Gravimetric Analysis coupled to a mass spectrometer (TGA) for 15 shale samples (as received) from the Vaca Muerta formation in Argentina.

EXPERIMENTAL

Our samples were source rocks from the Vaca Muerta formation in Argentina. We worked with two different wells, shale A which comes from the oil window, and shale B which comes from the wet gas window.

On these samples we performed different types of measurements: NMR, mass balance and Thermo Gravimetric Analysis (TGA):

- 2D T_1-T_2 maps were acquired at 2.5 MHz and 23 MHz on Oxford Instrument spectrometers with TE = 200 μS and inversion recovery varying from 70 μs to 1 s in 200 values. The results were processed using an in-house 2D inverse Laplace transform. The temperature of the samples was 21 ± 1 °C. 2.5 MHz measurements were performed on cylindrical samples of 30 mm diameter by 50 mm height, while the samples for 23 MHz measurements were 10 mm in diameter by 15 mm height.
- Multi-frequency NMR dispersion (NMRD) was performed on a fast field cycling spectrometer from *Sterlar s.r.l., Mede, Italy*. The measurements were performed on samples of 9mm in diameter and 15mm height. At each frequency (varying from 10kHz to 35MHz), a full T_1 measurement is performed, and processed using an in-house 1D inverse Laplace transform.
- A TGA instrument (NETZSCH-STA 449) coupled with mass spectrometer (Aeolos-OMS 403 D) was used. Thermo gravimetric analysis (TGA) is an analytical technique used for accurately measuring mass changes as a function of increasing temperature, while the MS is used to analyze the produced gases. The 10 x 15 mm samples were placed in the TG furnace and heated under helium gas. The samples were heated from 25 °C to 315 °C at 5 °C/min heating rate and held at this temperature for 30 min. Final temperature of 315 °C was chosen after previous tests in order to evaporate all the water and the mobile oil, while minimizing the cracking of kerogen and the production of structural water. This temperature is consistent with retort method for total oil extraction [3-4]. The water molecule at mass 18 was monitored by mass spectrometer. An integrated area of water mass peak allows us quantifying the water mass. The oil mass was calculated by mass subtraction between total mass loss and water mass. Samples used for TGA were 10 mm in diameter by 15 mm.

SPONTANEOUS IMBIBITION TESTS: EVIDENCE OF AN NMR CONTRAST BETWEEN WATER AND OIL

Samples of 30 x 50 mm were used for imbibition tests. Firstly, shale A followed the following experimental procedure (detailed in Figure 1):

- As Received NMR measurement (Fig. 1a)
- Cleaning by chloroform for 4 days and iso-propanol for 4 days.
- Drying at 60 °C for 1 day.
- Spontaneous imbibition by water (70 g/L NaCl) (Fig. 1b and Fig. 2)
- Cleaning 4 days isopropanol and drying (60°C)
- Spontaneous imbibition by mineral oil (isopar L) (Fig. 1c and Fig. 2)

Figure 1 shows the 2D T_1-T_2 maps for shale A: as received (a), cleaned and imbibed by water (b), and cleaned and imbibed by isopar L (c). In as received shale A (Fig. 1a), we noticed two separated signals. We have already shown [10] that the signal at low T_1 and T_2 was water and the other elongated signal with T_1/T_2 varying from 5 to 10 was oil. During imbibition by water, the signal at low T_1 and T_2 increased. On the contrary, during imbibition by isopar L, it was the signal with high T_1/T_2 that increased.

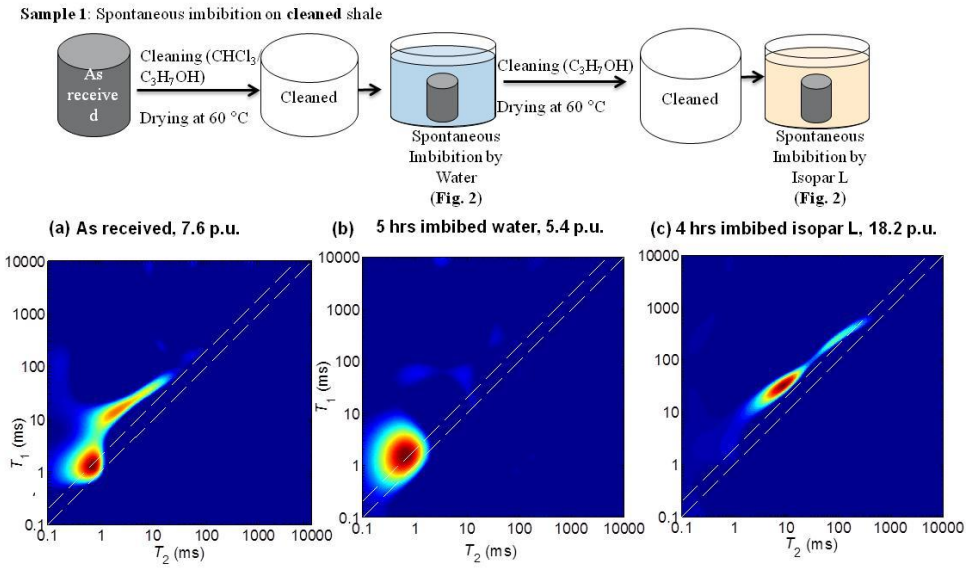

Fig. 1: 2D T_1-T_2 2.5 MHz NMR for shale A: as received (a), cleaned/dried and imbibed by water (b) and cleaned/dried and imbibed by isopar L (c). The diagonal lines correspond to T_1/T_2=1 and T_1/T_2=2.

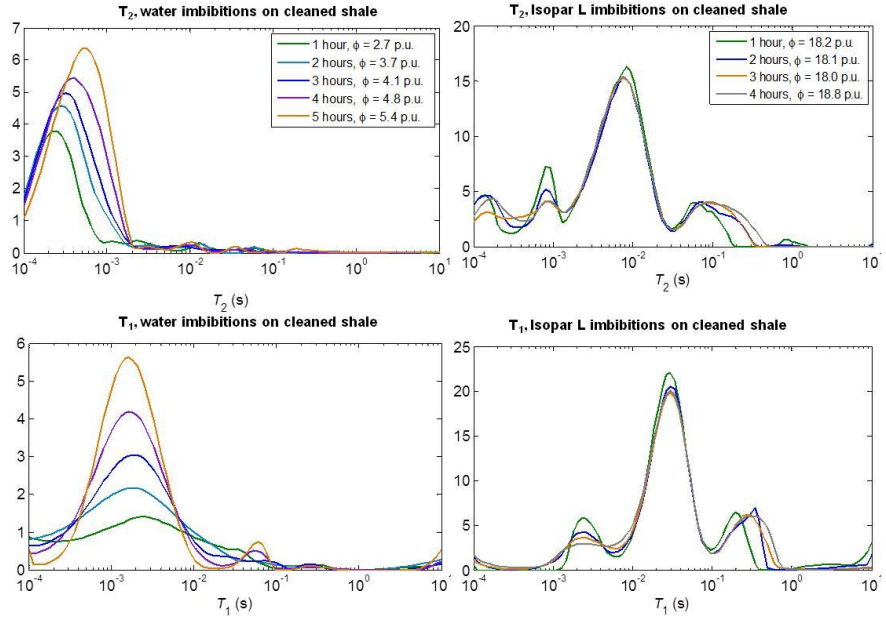

Fig.2: 2.5 MHz T_1 and T_2 projections of 2D T_1-T_2 maps for cleaned shale A imbibed by water (Fig 1b) and isopar L (Fig 1c).

Figure 2 shows T_1 and T_2 projections of the 2D T_1-T_2 maps obtained for shale A during spontaneous imbibitions by water (left) and isopar L (right). During imbibition by water, the T_2 distribution is shifted to longer T_2s, while the T_1 distribution seems stable. Basically such a net difference can be explained by the basic relaxation features of T_2 and T_1. Intrinsically, T_2 is dominated by the slow surface dynamical contributions driven by the dipolar fluctuations at zero Larmor frequency, while T_1 is only due to the much faster

volume dynamical contributions driven by the dipolar fluctuations at the Larmor frequency. T_2 is thus more sensitive than T_1 to the slow surface relaxation processes. Owing to the biphasic fast exchange conditions, the evolution of the T_2 distribution to longer T_2s thus reveals the progressive enhancement of the volume contributions in the relaxation. On the contrary, the T_1 distribution which is less sensitive to the surface contributions mainly reveals the enhancement of the volume contributions with the imbibition processes.

One can wonder if these results from spontaneous imbibitions are affected by the partial saturation of the rock *i.e.* by the presence of gas in the sample. To answer that question we performed NMR T_1-T_2 maps on another sample of shale A, and compared the results for as received and 100% saturated with water and isopar L (Fig. 3). Fluid saturations were performed by vacuuming the sample for 4 days, then saturating it with the fluid under 100 bars of pressure.

First, the as received NMR T_1-T_2 map (Fig. 3a) of sample 2 is very similar to the one obtained for sample 1 (Fig. 1a). Second, when saturating the shale sample with 100% water (Fig 3b), we notice that water penetrates pores that were not penetrated under spontaneous imbibition, and exhibit an elongated NMR signal along the T_1/T_2=1-2. Third, when saturating the shale with 100% isopar L (Fig 3c), we notice that the NMR signature is very similar to the one obtained after spontaneous imbibition of isopar L (Fig 1c).

One can interpret that water spontaneously imbibes only in the mineral porosity, corresponding to the signal observed on Figure 1b (rounded signal at T_1/T_2=1-2). When water is forced into the organic porosity, it appears as an elongated signal at T_1/T_2=1-2 (Fig. 3b). For isopar L, it always exhibits an elongated signal at high T_1/T_2.

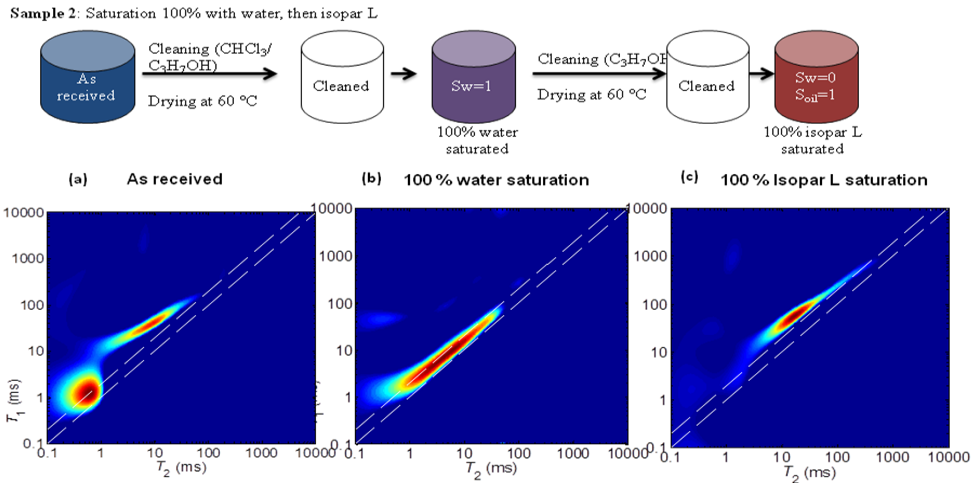

Fig.3 2D T_1-T_2 2.5 MHz NMR for shale A: as received (a), 100 % water saturation (b) and 100 % isopar L saturation (c).

Additionally, we confirm the contrast between water and oil signal in 2D T_1-T_2 maps by other imbibition tests: shale A (sample 3) was submitted to imbibition tests directly from the "as received" state. The 2D T_1-T_2 maps for as received shale A imbibed by D_2O (for 9 hours) and by isopar L (for 8 hours) are presented in Figure 4. The 2D T_1-T_2 map of the as received sample is very similar to the one presented in Figure 1a. In fact, most of our samples exhibit such 2D T_1-T_2 contrast between oil and water in the as received state. The imbibition test by D_2O (D_2O has no NMR signal) shows that the signal of water at low T_1 and T_2 has disappeared. However, the resolution of the oil signal (elongated signal at high T_1/T_2) seems to be lost. After 9 hours of D_2O imbibitions, isopar L was then imbibed. During oil imbibition, it is clear that only the oil signal (elongated signal at high T_1/T_2) increased.

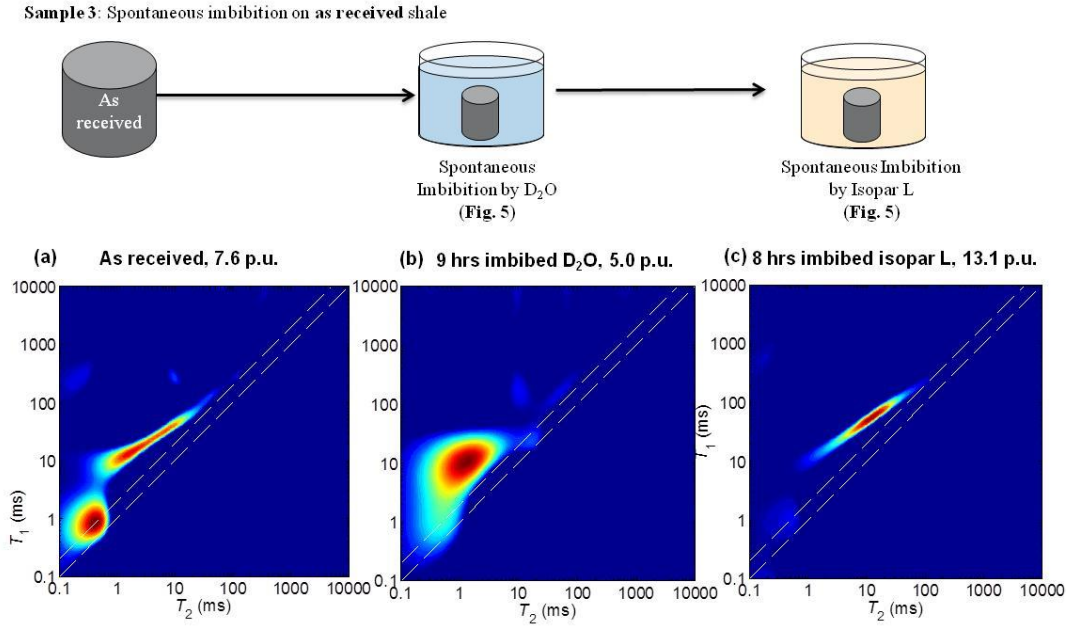

Fig. 4: 2D T_1-T_2 2.5 MHz NMR for as received shale A (a) and imbibed by D_2O (b) and isopar L (c).

Figure 5 shows T_1 and T_2 projections of the 2D T_1-T_2 maps for as received shale A imbibed by D_2O and isopar L. It obviously shows a continuous decrease of the signal at low T_1 and T_2 when imbibed by D_2O. During D_2O imbibition, the peak of the T_2 distribution is slightly shifted to longer T_2 whereas the T_1 distribution remains centered en the same value. This was already observed in Figure 2 during H_2O imbibition. These different behaviors in the ^1H T_2 and T_1 distributions have already been explained above on the basis of the origin of the ^1H T_2 and T_1 relaxation processes. The progressive imbibition by the heavy water (with quadrupolar ^2H nuclei) also explains the net decrease of the ^1H T_1 and T_2 intensities.

Moreover, T_1 and T_2 projections for isopar L imbibitions present only an increase of oil signal at high T_1 and T_2. The water signal at low T_1 and T_2 was stable.

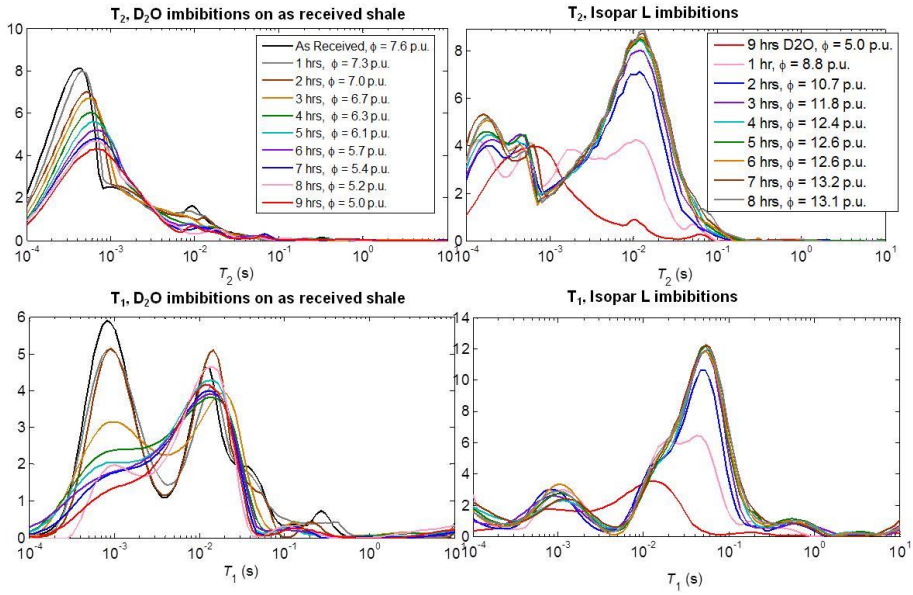

Fig. 5: 2.5 MHz T_1 and T_2 projections for as received shale A imbibed by D_2O (Fig 4b) and isopar L (Fig 4c).

Isopar L could imbibe very fast into both cleaned and as received shales. Particularly in the case of as received shale, an equivalent of 8.1 p.u. of isopar L imbibed the rock, and only air was expelled from the sample, no water was produced. This demonstrates that isopar L imbibed pores that were not accessible to water. This could be explained by a well connected network of strongly oil-wet organic pores.

Moreover, from isopar L (light oil) imbibitions test in cleaned shale A, we still observed a high T_1/T_2 for oil signal. Therefore, we proved that such a high T_1/T_2 is not due to bitumen (as reported in Green River formation [7]) but due to light oil confined in organic pore.

UNDERSTANDING THE NMR CONTRAST BETWEEN OIL AND WATER IN 2D T1-T2 MAPS

Using NMR 2D T_1-T_2 maps at 2.5 MHz, we have identified a contrast between water and oil. The water appears at short T_1 and T_2 with T_1/T_2 ~1, while oil exhibit a surprisingly high T_1/T_2 ratio. In order to understand why such a high T_1/T_2 ratio can be achieved with light oil like isopar L we performed multi-frequency NMR dispersion (NMRD).

At each frequency, a T_1 measurement is performed and the T_1 distribution is calculated. The T_1 distribution appears bimodal at all the frequencies. The peak corresponding to the water signal is identified by performing the same experiment on a 100% water saturated sample. A typical multi-frequency NMR dispersion plot is made by plotting the relaxation rates R_1 ($R_{1\_oil}=1/T_{1peak\_oil}$ and $R_{1\_water}=1/T_{1peak\_water}$).

The multi-frequency NMR dispersion obtained on an as received sample of shale A (Figure 6) clearly shows a very different frequency behavior for oil and water: we observe a very strong frequency dependence of the relaxation of the oil (red squares) compared to the one for the water (blue circles). We have proposed theoretical models [10] for oil (red dash line) and water (blue solid line) allowing us to fit the experimental data. The details of the theory are not the purpose of this article and are explained in details in ref [10].

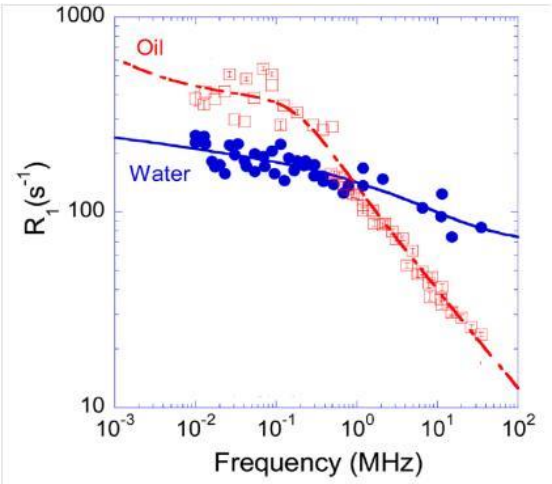

Fig. 6: Multi-frequency NMR dispersion plot showing the relaxation rates $R_1=1/T_1$ as a function of the Larmor frequency for as received shale A. (Figure taken from [10]).

We have applied our relaxation theory for T_1 and T_2 relaxation for the two different cases. We found a constant value of T_1/T_2 ~1.36 for water. While we found T_1/T_2 for oil varies with frequency. According to this theory, we display in Figure 7 the evolution of the ratio T_{1oil}/T_{2oil} with frequency, showing that the T_1/T_2 ratio for oil is expected to increase linearly with the square root of the frequency.

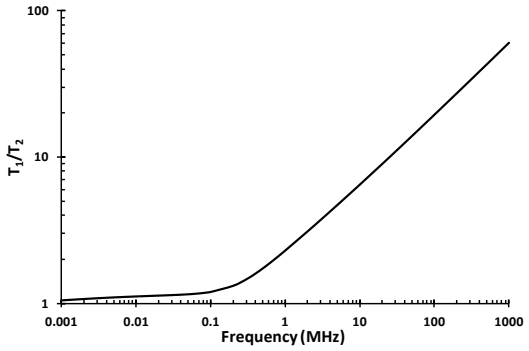

Fig. 7: T_{1oil}/T_{2oil} versus frequency, showing that the T_1/T_2 for oil is expected to increase with frequency.

Since the oil-water contrast we observed in the previous section is based on the T_1/T_2 ratio, this suggests that this contrast should increase with frequency. This led us to investigate higher frequencies and to perform NMR measurements at 23MHz.

Figure 8 shows 2D T_1-T_2 maps obtained at 2.5 MHz and 23 MHz for cleaned shale A imbibed by isopar L and as received shale B. We observe that the T_1/T_2 ratio for oil (isopar L) obtained at 2.5 MHz is around 4 to 5. On the other hand the T_1/T_2 ratio for oil obtained at 23 MHz is the order of 10. The theoretical predictions T_1/T_2 for oil (Figure 7) are in excellent agreement with the experimental values found: T_1/T_2(oil@2.5MHz)~4-5 while T_1/T_2(oil@23MHz)~10.

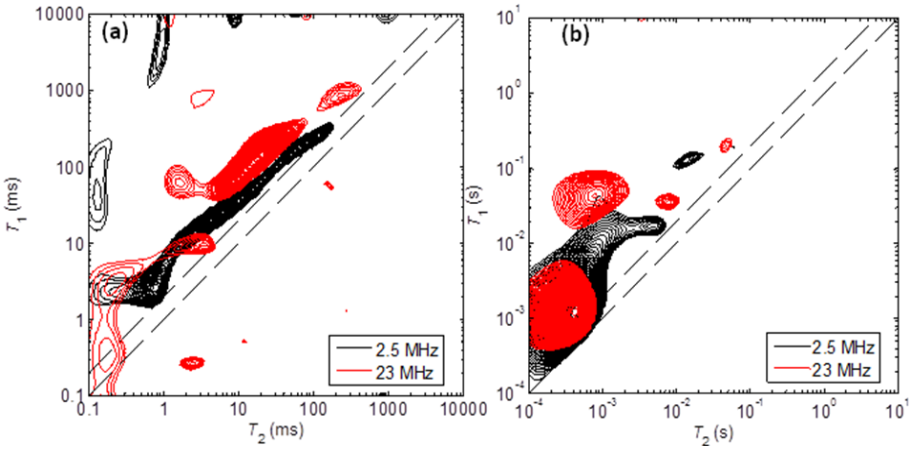

Fig.8: 2D T_1-T_2 2.5 MHz and 23 MHz NMR for cleaned shale A imbibed by isopar L (a) and as received shale B (b).

High T_1/T_2 is usually attributed to the presence of bitumen. In this case we prove that a signal with very high T_1/T_2 ratio can be obtained only by putting light oil (isopar L) inside a nanoporous system. On the other hand, the high T_1/T_2 ratio observed on as received samples (Fig. 1a) completely disappeared after cleaning with chloroform (Fig. 1b). While the definition of what is called "bitumen" is still highly debated [11], this confirms that the high T_1/T_2 ratio comes from a fluid that is soluble in chloroform. While previous authors observed bitumen at high T_1/T_2 ratio[7] we demonstrate that in our case, high T_1/T_2 ratio is only due to light oil in a high confinement. We also show that after cleaning and imbibing with isopar L (Fig. 1c) the signal at low T_1 and T_2 has disappeared; this proves that our samples do not contain bitumen as described in [7].
In other words:

- The T_1/T_2 for water is almost constant with frequency.
- The T_1/T_2 for oil varies strongly with frequency.
- Therefore, the higher the frequency the stronger the contrast between oil and water in 2D T_1-T_2 maps.

We thus recommend using 23 MHz NMR 2D T_1-T_2 data in order to measure the quantity of water and oil contained in a given sample. The next section aims at comparing water and oil volumes obtained by NMR and other techniques (mass balance and TGA).

COMPARISON OF WATER AND OIL VOLUMES BETWEEN NMR AND OTHER TECHNIQUES

Several imbibition tests have been performed on shale A samples and were reported in the previous section. For two imbibition test (water imbibition from Fig. 2 and isopar L imbibition from Fig. 5), the amount of fluid imbibed was monitored using NMR and also by weighting the sample (mass balance). In Figure 9, we compared the water and isopar L imbibed volume calculated from 2D T_1-T_2 2.5 MHz NMR with mass balance. Water and oil volumes obtained from 2D T_1-T_2 maps have been calculated by integrating the NMR signal attributed to each fluid in the 2D T_1-T_2 map. The excellent agreement between NMR and mass balance measured volumes for both water and oil shows that 2D T_1-T_2 NMR could be an accurate technique to estimate volumes of fluids confined in porous media.

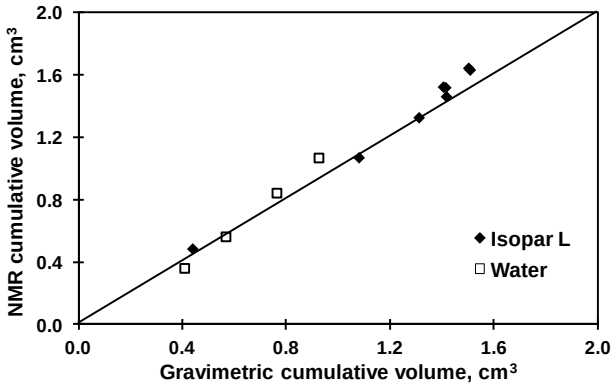

Fig. 9: Cross plot of water and isopar L volumes obtained from gravimetric and 2D T_1-T_2 NMR methods.

The performance of the NMR approach was tested versus TGA on a set of as received samples from a different well (shale B). The water and oil volume of 15 as received samples from shale B obtained from 2D T_1-T_2 23 MHz NMR were compared with TGA. The 2D T_1-T_2 maps at 23 MHz acquired before and after TGA measurement are shown in Figure 10. Before TGA (Fig. 10a) the 2D T_1-T_2 map is characteristic of a shale sample containing water (low T_1/T_2) and oil (high T_1/T_2). After TGA (Fig. 10b) the measured NMR porosity is less than 1 p.u., meaning that water and oil were almost totally lost after TGA analysis. This could confirm that high T_1/T_2 in our samples is not due to bitumen because boiling point of bitumen is higher than 315 °C [12].

Since TGA measures the mass loss, the density of water and oil is needed in order to convert the mass to volume unit. We used the following values for the density: 1.05 g/cm^3 for water (70 kppm NaCl brine) and 0.85 g/cm^3 for oil (light crude oil). The cross plot between volumes calculated from TGA and 2D T_1-T_2 NMR is presented in Figure 11a. The water, oil and total volumes obtained from 2D T_1-T_2 NMR and TGA are in very good agreement. In order to estimate saturations, one needs to measure porosity. TGA being a destructive measurement, we had to measure porosity on a set of twin samples. 15 twin samples were saturated by 100 % water to measure total porosity. Then, water

and oil saturation were estimated by dividing fluid volume with total pore volume. We present the water and oil saturation for 15 as received shales in Figure 11b.

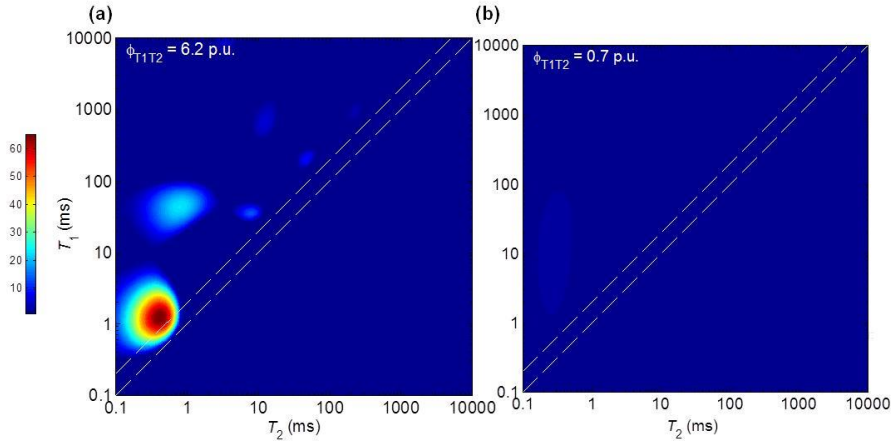

Fig. 10: 2D T_1-T_2 maps at 23 MHz for as received shale B before (a) and after (b) TGA analysis.

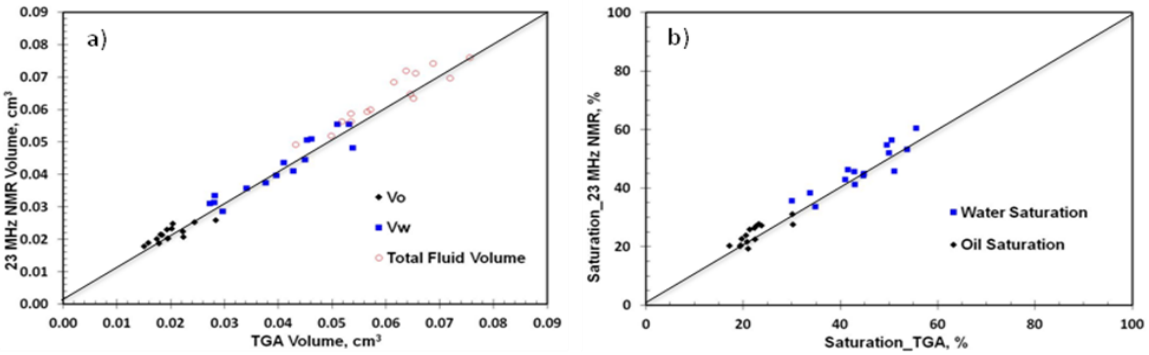

Fig. 11: Comparison of the results obtained by TGA and 23MHz NMR: a) volumes and b) saturations.

CONCLUSION

We proposed the 2D T_1-T_2 NMR technique as a non destructive technique to estimate the water and oil saturation in tight organic shales. We interpreted the contrast between water and oil in 2D T_1-T_2 maps on the basis of excellent agreement between experimental and theoretical arguments (multi-frequency NMR dispersion). According to our theory of NMRD in shales, oil and water are undergoing completely different dynamics, leading to a high T_1/T_2 ratio for oil, and a low T_1/T_2 ratio for water. We also showed in our samples that such a high T_1/T_2 ratio is not due to bitumen but comes from light oil (isopar L) confined in organic pore. The T_1/T_2 ratio of oil depends on the frequency whereas T_1/T_2 of water is invariant with frequency. Therefore, using 23 MHz NMR water and oil signals could be easily separated in 2D T_1-T_2 maps. The water and oil volumes obtained from 2D T_1-T_2 maps were compared with Thermo Gravimetric Analysis. The fluid volumes obtained from both techniques are in excellent agreement. Furthermore, the volume of

imbibed isopar L from 2D T_1-T_2 maps is also correlated well with gravimetric method (mass balance). The water and oil saturation is calculated by dividing water or oil volume with total pore volume. Because NMR is a non destructive method, the total pore volume could be directly determined after 2D T_1-T_2 maps acquisition. In our case, because the thermal method is destructive, the total pore volume was determined by T_2 measurement of 100 % water saturated twin samples. If NMR only was performed, one could even measure saturation and porosity (NMR acquisitions on as received and 100% water saturated sample) on the same sample. This would be a strong advantage compared to commonly used thermal methods (retort). Therefore, our proposed technique could give more accurate determination of water and oil saturation in tight organic shales.

ACKNOWLEDGEMENTS

The authors would like to thank J.F. Perrette and Gregory Dubes for their help.

REFERENCES

1. Sondergeld C.H., Newsham K.E., Comisky J.T., Rice M.C., Rai C.S., "Petrophysical Considerations in Evaluating and Producing Shale Gas Resources", SPE, (2010), 131768.
2. Le Bihan A., Nicot B., Marie K., Thébault V., Hamon G., "Quality Control of Porosity and Saturation Measurements on Source Rocks", SPWLA, (2014).
3. Handwerger, D. A., Keller, J., & Vaughn, K. "Improved Petrophysical Core Measurements on Tight Shale Reservoirs Using Retort and Crushed Samples", SPE, (2011), 147456
4. Handwerger D.A., Willberg D., Pagels M., Rowland B., Keller J.F., "Reconciling Retort versus Dean Stark Measurements on Tight Shales", SPE, (2012), 159976.
5. Kausik R., Cao Minh C., Zielinski L., Vissapragada B., Akkurt R., Song Y., Liu C., Jones S., Blair E., "Characterization of Gas Dynamics in Kerogen Nanopores by NMR", SPE, (2011), 147198.
6. Ozen A.E., Sigal R.F., "T1/T2 NMR Surface Relaxation Ratio for Hydrocarbons and Brines in Contact with Mature Organic-Shale Reservoir Rocks", *Petrophysics*, (2013), **54** no. 1, pp. 11-19.
7. Singer P.M., Rylander E., Jiang T., McLin R., Lewis R.E., Sinclair S.M., "1D and 2D NMR Core-Log Integration in Organic Shale", SCA, (2013), 018.
8. Washburn K.E., Birdwell J.E., "A New Laboratory Approach to Shale Analysis Using NMR Relaxometry", SPE, (2013), 168798.
9. Fleury, M. "Characterization of Shales with Low Field NMR", SCA, (2014), 014
10. Korb J-P., Nicot B., Louis-Joseph A., Bubici S., Ferrante G., "Dynamics and Wettability of Oil and Water in Oil Shales", *The Journal of Physical Chemistry C* (2014), **118**, pp. 23212-23218.
11. Landis C.R., Castano J.R., "Maturation and Bulk Chemical Properties of a suite of solid hydrocarbons", *Org. Geochem.*, (1995), **22** no. 1, pp. 137-149.
12. Etherington J.R., McDonald I.R., "Is Bitumen a Petroleum Reserve?", SPE, (2004), 90242.

COMPARISON OF PORE SIZE DISTRIBUTION BY NMR RELAXATION AND NMR CRYOPOROMETRY IN SHALES

M. Fleury[1], R. Fabre[1], J.B.W. Webber[2]
[1]IFP Energies nouvelles, 1 avenue de Bois-Préau, 92852 Rueil-Malmaison, France.
[2]Lab-Tools Ltd, Lakesview International Business Park, Hersden, Canterbury, Kent CT3 4JZ, UK

This paper was prepared for presentation at the International Symposium of the Society of Core Analysts held in St. John's Newfoundland and Labrador, Canada, 16-21 August, 2015

ABSTRACT

The characterization of shales is challenging due to their very small pore sizes. In a previous paper, we have shown that Nuclear Magnetic Resonance relaxation techniques are well suited for detecting and quantifying water in nanopores. However, the distribution of relaxation times does not necessarily represent the distribution of pore sizes in the sample due to pore diffusive coupling. Indeed, all pore sizes below the diffusion length will be averaged around a single relaxation time representing an average volume to an average surface ratio. We illustrate the above-mentioned effects by comparing NMR relaxation and cryoporometry data on the same sample. The NMR cryoporometry experiment relies on the shift of the melting temperature of the saturating liquid, which is itself a function of pore size according to Gibbs-Thomson theory. The experiments were performed first on a model system made of a mixture of two calibrated porous glass (15 and 139 nm) and secondly on a shale. On the model system, the cryoporometry results are in quantitative agreement with the expectations but the T_2 distribution is strongly modified by pore coupling and only the 15nm pore size population can be identified. Pore coupling is also clearly identified by T_2-store-T_2 experiments. On the shale sample, the pore size distribution obtained from cryoporometry experiments is quasi uniform from 2 up to 100 nm, while the T_2 distribution is log-normal and relatively narrow. The disagreement between these two results is also explained by pore coupling.

INTRODUCTION

The characterization of shales requires revisiting petrophysical techniques. For example when considering porosity, strong disagreement between standard techniques can result if inappropriate protocols are used [1]. For the pore size distribution, the mercury injection technique may also fail to capture the very small range of pore sizes below ∅ 6nm. Also, the sample drying can interfere with the PICP measurement in the presence of clays. For this point of view, NMR techniques requiring saturated samples are non-disturbing and well suited for pore sizes down to nanometers. For example we have shown that NMR relaxation techniques are adequate for detecting and quantifying water in the interlayer of smectites [2].

For the range of pore size considered, 1nm up to 1µm, other techniques routinely used in the field of catalysis are available. Gas adsorption and thermo-porometry are some examples. NMR cryoporometry is not new [3] but has not been widely used although it has several advantages. In low field systems, it only requires a device to control the temperature of the sample very accurately. Very few results have been published so far about this technique for characterizing shales and we believe it has a great potential.

In this work, we emphasize that standard T_2 distribution cannot always capture the true pore size distribution due to strong pore coupling effects. These effects are ideally demonstrated by comparing NMR cryoporometry and relaxation results on the same sample. For this purpose, we used calibrated porous glasses as a model system, and a shale sample from a tight clayey formation.

BACKGROUND: NMR CRYOPOROMETRY

NMR cryoporometry is based on the shift of the freezing or melting point of the fluid saturating the porous media according to:

$$\Delta T_m(x) = -\frac{k_{GT}}{x} \quad (1)$$

where k_{GT} is the so-called Gibbs-Thomson constant and x is the pore size. The above equation has been established rigorously in the case of a cylinder, hence x may correspond to the diameter of this cylinder. However, when the shape is undefined, the pore size x will rather correspond to a curvature $\partial V/\partial S$ in the melting cycle [4]. In this work, we only consider the melting cycle to avoid hysteresis problems and to allow a large pore size to be explored given the capabilities of our instrument. If one detects the amount of liquid volume V(T) present in the sample at a function of temperature T, one can obtain the pore size distribution P(x) from the derivative of the V(T) curve using the following equation:

$$P(x) = \frac{dV}{dx} = -\frac{k_{GT}}{x^2}.\frac{dV}{dT} \quad (2)$$

Since pore size distributions are usually plotted using logarithmic scales, it is more useful to plot the following distribution:

$$P^*(x) = \frac{dV}{dln(x)} = -\frac{k_{GT}}{x}.\frac{dV}{dT} \quad (3)$$

in a similar way as in mercury intrusion experiments for example.

The constant k_{GT} actually contains complex and multiple physical phenomena but it has been shown that coherent values are obtained on a series of model materials characterized by other experimental techniques, such as gas adsorption [5]. In this work we will take the value k_{GT}=58.2 K.nm for water. With this value and the range of temperatures available in our instrument, the range of pore sizes that can be explored is about 2 to 600

nm (Figure 1). For the upper value, we assumed that a temperature resolution of 0.1°C is achieved. Due to a 1/x sensitivity, the method has a non-uniform resolution (excellent around 10 nm and potentially very poor around 500nm) if the temperature is increased linearly, as explained later.

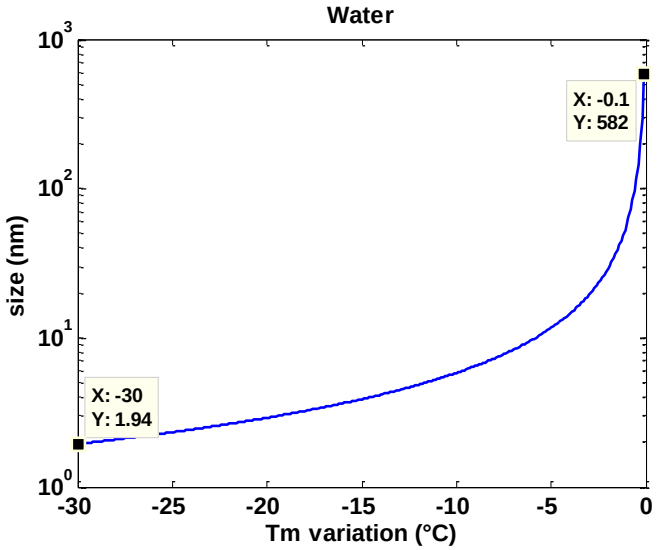

Figure 1: range of pore sizes that can be explored with water considering a variation of the melting temperature Tm from 0 down to -30°C.

A very common interrogation is whether the pore size is modified during the freezing cycle due to the formation of ice with a smaller density. NMR cryoporometry is actually only one branch out of many cryoporometry techniques and freezing-melting cycles are used routinely for example in Differential Scanning Calorimetry (DSC) techniques without any damage to samples. A key aspect is certainly to avoid freezing by nucleation and this can be achieved by surrounding the sample with bulk water and performing a freezing-melting-freezing cycle prior to the main melting cryoporometry experiment, without melting the bulk phase at the second step [4]. Also, the ice formed in pores has a different structure referred as plastic ice [6].

MATERIALS AND NMR METHODS

NMR Relaxation Methods

The experiments have been carried out on a Maran Ultra proton spectrometer from Oxford Instruments with a proton Larmor frequency of 23.7 MHz. Beside standard CPMG measurements, 2D T_2-store-T_2 exchange maps were measured using the methodology presented elsewhere [7].

For the cryoporometry experiments, the liquid volume quantity is measured using a single Hahn echo chosen at an appropriate echo spacing τ to avoid detecting ice. Indeed, although normal ice has a T_2 relaxation time of 8 µs (and T_1=70 s), some of the ice

formed in pores may have different characteristics. The τ value is also selected as a function of the sample in order to maintain an adequate signal to noise ratio. For the calibrated porous glass, τ=500µs, and for the shale, τ=100µs (i.e. the NMR amplitude is taken at 1ms and 0.2ms respectively). Unfortunately, a CPMG sequence in which one would choose any appropriate time cannot be used because the radio-frequency pulses produce a significant and measurable heating of the sample, interfering with the imposed temperature ramps.

NMR Cryoporometry Device

The cryoporometry device (Figure 2) designed by Lab-Tools Ltd is composed of a special probe that can be inserted inside the magnets, replacing standard probes from the manufacturer of the NMR instrument. In this probe, a glass tube of diameter 5mm o.d. can be inserted, and the sample can have a maximum height of about 20 mm. This tube is in close contact with a copper tube connected to a Peltier system for regulating very precisely the temperature. Heat resulting from the cooling of the sample is evacuated from the Peltier system using water circulating at a temperature of 5°C. Temperature is measured using thermocouples constantly calibrated with a reference bath at 0°C. They are placed at two locations : as closed as possible to the sample above the NMR antenna, and close to the Peltier system. With a maximum current of 3A at 12V, the temperature can decrease down to -31°C. A software controlling the power supply allows programming temperature ramps as small as 0.002 °C/min. Such small ramps are only set close to the bulk melting point and non-linear temperature ramps are generally used to speed up experiments (Figure 3). Since a NMR measurement may take 2 minutes and temperatures are also averaged over 2 minutes, the corresponding NMR signal may be averaged over a temperature gradient of 0.004°C. From this principle, a theoretical resolution curve can be calculated as a function of pore size (Figure 3). For example, at 600 nm, the resolution is limited to about ±11nm.

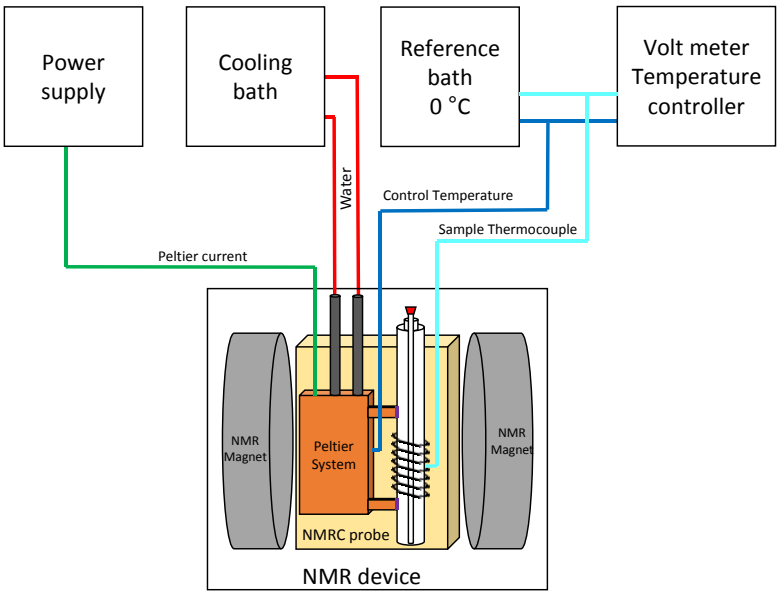

Figure 2: Schematic of the NMR cryoporometry probe and associated control components.

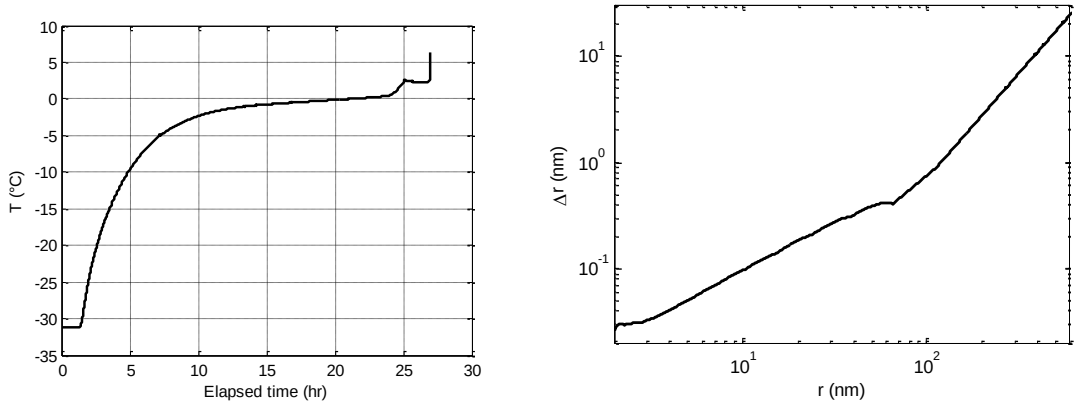

Figure 3: Typical temperature profiles for shale samples (left). Temperature increase is reduced to 0.002°C/min close to the bulk melting point. Theoretical pore size resolution assuming a measuring time of 120 s (right).

Samples

We used a model system composed of calibrated porous glass (CPG from BAM, Federal Institute for Materials Research and Testing, Germany) of mean pore sizes d_{50}=15.1±0.2nm (ERM-FD121, pore volume 624.6mm^3/g) and d_{50}=139±3.7nm (ERM-FD122, pore volume 924.4mm^3/g) as measured by high pressure mercury injection experiments. Taking a glass density of 2.5, the porosity of these medium are 25% and 37% respectively. The shape of the pores in these medium are tubular like. These reference materials are delivered as grains of mean diameter 55µm (ERM-FD121) and

90µm (ERM-FD122). We made a grain pack from these materials by mixing 80.5 mg of ERM-FD121 and 55.0mg of ERM-FD122 in a 5mm tube (Figure 4).

The shale sample originates from the Callovo-Oxfordian (COx) formation at a depth of 604m (EST433 borehole of Montiers-sur Saulx, France). At this depth of the COx formation, a high clayey unit is present with carbonate nodules dispersed in the medium (20%wt) playing a minor role in terms of porosity or permeability [8]. On a plug size, the porosity measured by NMR and water permeability measured by steady-state were respectively 14.8% and 7.3nD. We extracted from the plug a small cylinder of diameter 4mm and length 20mm for the cryoporometry experiments.

RESULTS

We show the results obtained on the above-mentioned samples. For the CPG medium, the objectives are to test the cryoporometry device as well as comparing the measured pore size distributions with NMR relaxation.

Calibrated Porous Glass

The cyoporometry experiments on the CPG mixture gave the expected results (Figure 5); we observe 3 plateaus that correspond to the successive melting of the 15nm CPG, the 139nm CPG and finally the inter-grain phase surrounding the CPG grains. Each plateau value allows calculating the fraction of each phase as detailed later. Then, the curve was fitted with spline functions in order to extract the derivative and obtain the pore size distribution, as detailed in equation 3. The pore sizes obtained fall very close to the values given by the manufacturer using MICP measurements: 14 nm and 147 nm (Figure 6). First, although we compare two measurements with different physical mechanisms, the good agreement comes from the fact that both techniques use a cylinder shape for the pores. Second, the pore size values obtained from cryoporometry depend (i) on the constant k_{GT} that can vary from one author to another, (ii) on the fine adjustment of the bulk melting temperature which is not known very precisely (although thermocouples are calibrated very accurately). The increase of temperature vs. time is a minor source of uncertainty, as shown above. Qualitatively, the narrow width of the 15nm CPG medium is in agreement with the MICP distribution given by the manufacturer (not shown), and the width of the 139nm CPG is larger. Concerning the fraction of each population, cryoporometry results are in good agreement with simple weight measurement of water and CPG materials inserted in the tube (Table 1)

The T_2 distribution measured for the CPG mixture at 30°C is essentially bimodal (Figure 7). At first glance, the peak at T_2~30ms corresponds to the 15nm population, whereas the wider peak centered around T_2~220ms correspond to the 139nm population. However, the inter-grain water is not identified and the tail at T_2>1s correspond in fact to a small amount of supernatant water at the top of the CPG grain pack in the tube (it was later removed for performing the T_2-store-T_2 exchange experiments). Given the weak surface relaxivity of this clean material (~0.25 µm/s), the inter-granular water is expected close

the bulk value. In fact, the T_2 distribution is strongly influenced by pore coupling, i.e. molecules are diffusing in and out of the porous glass and exchange with inter-granular water. Hence, none of the peaks are representative of the different population fractions. A strong evidence is given by the T_2-store-T_2 map (Figure 8) measured separately at a temperature of 30°C. On such map, pore coupling is unambiguously indicated by the presence of off-diagonal peaks located symmetrically on both sides. The exchange time was chosen here at 300ms but other smaller values give similar (but weaker) off-diagonal peaks. However, the details of the exchanges cannot be known precisely. Taking a diffusion coefficient of water of 0.5x 10^{-9} m^2/s, the diffusion length at 300ms is about 30µm. Therefore, inter-granular water can partially exchange with the porous grains for each size. Most probably, exchanges between grains are also possible. Further evidence is given by the T_2 distribution measured at -0.15°C (Figure 5) when the inter-granular water is frozen but the 15nm and 139nm CPG are melted (Figure 9). We obtain in this case two narrow peaks that are truly representative of the relaxation time and fraction of each population. Focusing at the fraction of each population (Table 1), we retrieve the appropriate values measured by cryoporometry and weight.

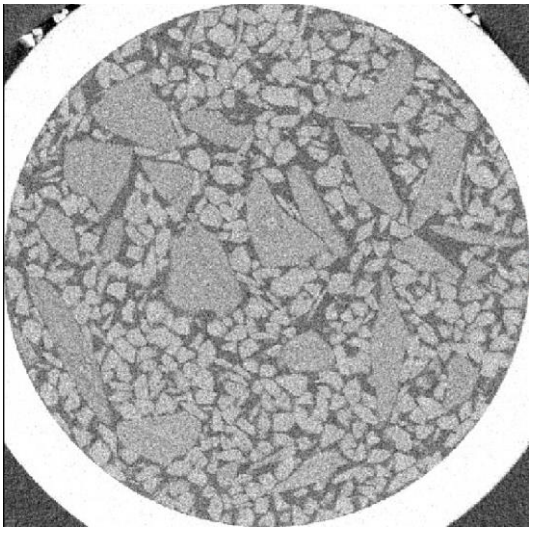

Figure 4: Micro-CT image of the CPG mixture. The diameter is 4 mm. Small grains: 15 nm, large grains: 139nm

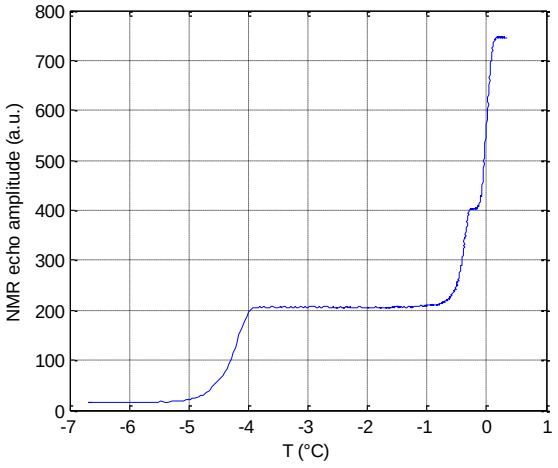

Figure 5: Hahn echo amplitude at 1ms as a function of temperature. The 3 plateaus correspond to the successive melting of the 15nm CPG, the 139nm CPG and finally the bulk phase surrounding the CPG grains around 0°C.

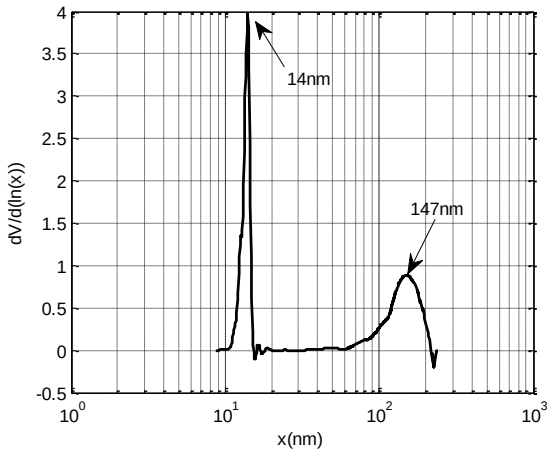

Figure 6: Pore size distribution on the CPG mixture obtained from the cryoporometry experiment (raw data shown in Figure 5).

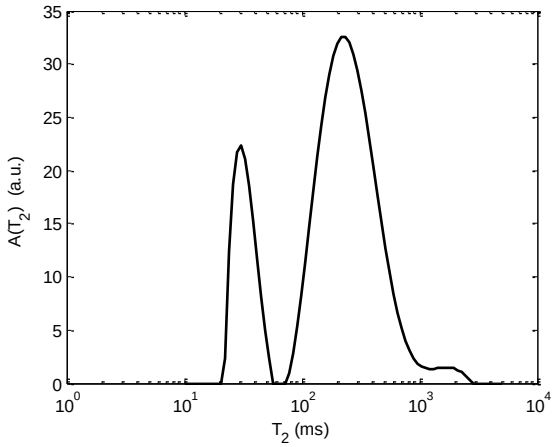

Figure 7: T_2 distribution of the CPG mixture at 30°C.

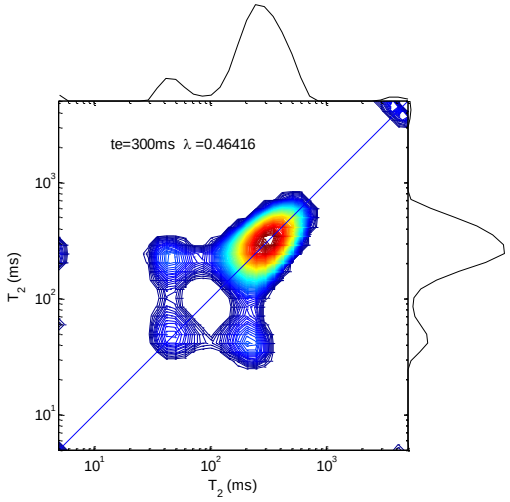

Figure 8: T_2-store-T_2 exchange experiment t 30°C on the CPG mixture performed at an exchange time te=300 ms.

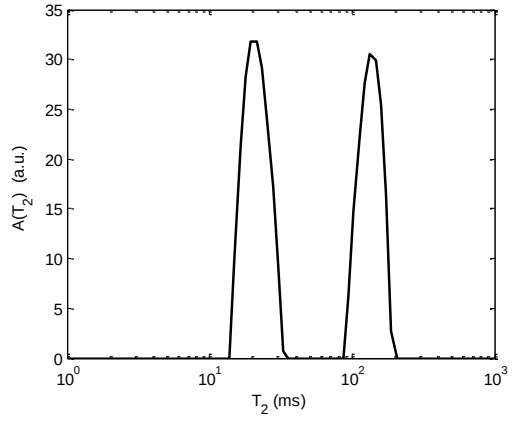

Figure 9: T_2 distribution obtained when the inter-grain water is frozen at -0.15°C, inhibiting diffusive exchange. The two narrow peaks are located at T_2=20ms and 138ms.

Shale Sample

The cryoporometry experiment was performed on the shale sample using the largest possible range of temperature (-31°C). The measured pore size distribution (Figure 10) is relatively uniform from 2 up to 100nm, in qualitative agreement with results obtained on a Barnett shale [9]. Due to the low permeability of this sample (7 nD), pore sizes larger than 100nm are not expected. As opposed to this large distribution, the T_2 distribution

(Figure 11) has a more classical shape close to log-normal (note here that no shape is imposed in the data processing). Compared to the model system, the T_2 values are much shorter due to a larger surface relaxivity (typically of the order of 5 µm/s) but also due to a much larger surface to volume ratio generated by pore size as small as 2 nm. The strong disagreement with cryoporometry results can be explained by pore coupling as discussed further later. We also measured the T_2 distribution at several temperature (but in a separate experiment) and found that the distribution is simply shifting as the temperature is increasing and the largest pore sizes gradually melting. The small pores are not described by the tail at small values inside the T_2 distribution at full saturation.

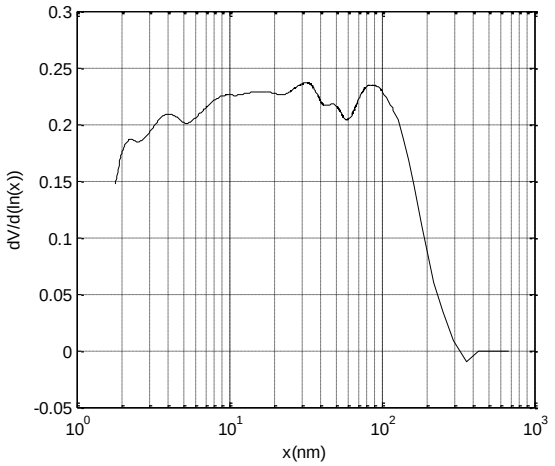

Figure 10: Pore size distribution obtained on the shale sample, cryoporometry technique.

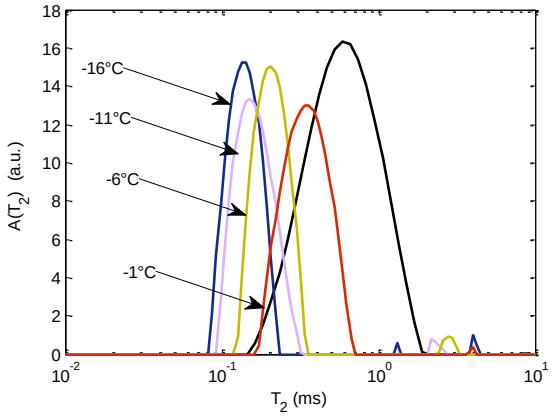

Figure 11: T_2 distribution obtained from relaxation measurements (black curve at 30°C) and at different temperature during melting.

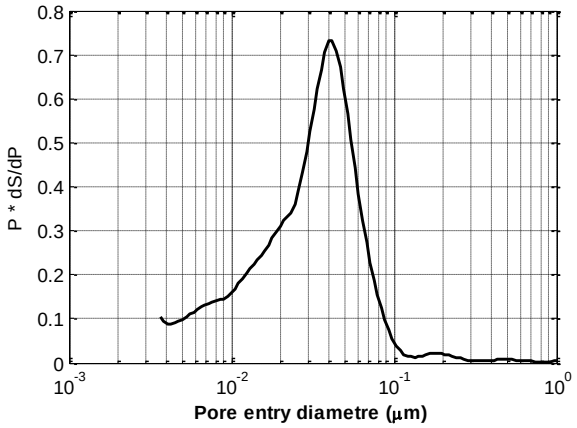

Figure 12: Pore size distribution obtained on the shale sample, high pressure mercury injection technique.

DISCUSSION

Pore size distribution deduced from NMR relaxation measurements relies on a diffusion process of molecules interacting with the pore surface yielding the well-known relationship with the surface to volume ratio. However, when molecules diffuse over distances that are larger, the surface to volume ratio is averaged over several pores. For standard reservoir samples in the mD or D permeability range, pore coupling is inherently present in many NMR relaxation measurement, especially at high temperature, but to a relatively small degree, except in certain cases. Hence, MICP measurements are often in agreement with NMR T_2 distributions and their direct comparison allows the calculation of an apparent surface relaxivity. Indeed, very often, the different pore size populations are grouped in well-defined regions of the porous media and therefore, the pore coupling is very limited. For example in carbonates, microporosity may be due to intra-grain porosity and these grains are large enough to avoid diffusive coupling. In shales, the pore sizes are roughly 2 or 3 orders of magnitude smaller. The permeability is then reduced to the nD range but this not the case for the diffusion coefficient. Indeed the latter primarily depends on porosity at first order. Indeed, from several measurements of diffusion in caprocks [10] and shales [11], we found that a reasonable estimation of the effective diffusivity can be made using an Archie relationship $D_{eff}/D_m = \Phi^{m-1}$ where D_m is the molecular diffusion coefficient of bulk water, with m varying between 1.8 and 2.5, as observed for electrical measurements. Hence, the diffusion coefficient decreases roughly linearly with porosity and the diffusion length $(6D_{eff}t)^{1/2}$ calculated at the peak relaxation time is still large. However, if the sample is heterogeneous at the micron scale (e.g. thin laminations or organic matter channels), one may find large T_2 distributions representing indeed the different pore populations. The correct interpretation of T_2 distributions in shales must be complemented by high resolution visualization of the pore network structure.

For the homogeneous shale sample studied here, the diffusion length at 0.7ms is about 1.4µm when taking a diffusion coefficient of 0.5×10^{-9} m^2/s,. Since we have a pore size distribution extending up to 100 nm, a strong coupling effect exist. Furthermore, in such case, a T_2-store-T_2 experiment cannot further demonstrate the coupling because an intermediate level of coupling is needed in such experiment (i.e. a bimodal or wide distribution is needed). Also, as suggested during the review of this manuscript, heterogeneous surface relaxivities within the porous media could also be a source of discrepancy when comparing different pore size distribution measurements. This effect would create larger T_2 relaxation distribution and to some degree compensate for the coupling effect. In the present situation the width of the distribution obtained by cryoporometry is about 2 decades, whereas it is about 1 decade or less for T_2 relaxation time distribution.

Interestingly, the pore entry size distribution obtained by high pressure mercury injection (HPMI) on a sister sample is relatively narrow with a peak at 40 nm, unlike the cryoporometry result (Figure 12). Although we often observe a correlation between pore size and pore throats, this correspondence is not necessarily true and is highly dependent

on the pore structure and geological history. At least, in terms of maximum size, the two distributions agree: the largest throat size is about 100 nm, while the largest pore size is about 300 nm (a ratio of 3 is the theoretical result for a sphere pack).

CONCLUSION

We show that pore size distribution obtained from NMR cryoporometry and relaxation experiments on the same sample can strongly disagree. While the cryoporometry technique is able to give accurate results from 2nm up to about 1µm, T_2 relaxation is strongly influenced by pore coupling. As a result, the distribution obtained from relaxation is representative on an average volume to surface ratio; in shales, this distribution also depends on the length scales of the heterogeneities present in the porous medium, compared to the diffusion length.

AKNOWLEDGEMENTS

We thank F. Norrant for providing the calibrated porous glasses, Elizabeth Rosenberg for performing the microCT images, and J. Labaume for the HPMI experiments.

REFERENCES

1 B. Lalanne, A. Le-Bihan, E. Elias, R. Poyol, L. Martinez, How to Cope with some of the Challenges Associated with Laboratory Measurements on Gas Shale Core Samples, in: Proceeding Soc. Pet. Eng. SPE 167709, 2014: pp. 1–17.

2 M. Fleury, E. Kohler, F. Norrant, S. Gautier, J. M'Hamdi, L. Barré, Characterization and Quantification of Water in Smectites with Low-Field NMR, J. Phys. Chem. C. 117 (2013) 4551–4560.

3 J. Strange, M. Rahman, E. Smith, Characterization of porous solids by NMR, Phys. Rev. Lett. 71 (1993) 3589–3591. doi:10.1103/PhysRevLett.71.3589.

4 O. V. Petrov, I. Furó, NMR cryoporometry: Principles, applications and potential, Prog. Nucl. Magn. Reson. Spectrosc. 54 (2009) 97–122. doi:10.1016/j.pnmrs.2008.06.001.

5. J. Mitchell, J. Webber, J. Strange, Nuclear magnetic resonance cryoporometry, Phys. Rep. 461 (2008) 1–36. doi:10.1016/j.physrep.2008.02.001.

6 J.B.W. Webber, Studies of nano-structured liquids in confined geometries and at surfaces, Prog. Nucl. Magn. Reson. Spectrosc. 56 (2010) 78–93. doi:10.1016/j.pnmrs.2009.09.001.

7 M. Fleury, J. Soualem, Quantitative analysis of diffusional pore coupling from T2-store-T2 NMR experiments., J. Colloid Interface Sci. 336 (2009) 250–9. doi:10.1016/j.jcis.2009.03.051.

8 P. Cosenza, J.C. Robinet, D. Prêt, E. Huret, M. Fleury, Y. Géraud, et al., Indirect estimation of the clay content of clay-rocks using acoustic measurements: New insights from the Montiers-sur-Saulx deep borehole (Meuse, France), Mar. Pet. Geol. (2013). doi:10.1016/j.marpetgeo.2013.07.004.

9 J.B.W. Webber, P. Corbett, K.T. Semple, U. Ogbonnaya, W.S. Teel, C. a. Masiello, et al., An NMR study of porous rock and biochar containing organic material,

Microporous Mesoporous Mater. 178 (2013) 94–98. doi:10.1016/j.micromeso.2013.04.004.
10 M. Fleury, S. Gautier, N. Gland, P. Boulin, B. Norden, C. Schmidt-Hattenberger, Advanced and integrated petrophysical characterization for CO2 storage: application to the Ketzin site., Oil Gas Sci. Technol. (2013).
11 M. Fleury, Characterization of shales withlow field NMR, in: Proceeding SCA Annu. Conf., 2014.

Table 1: Fraction in % of the different water populations from different methods (CPG sample).

Method	*15 nm*	*139nm*	*Inter-granular+bulk*
Weight	27.0	27.3	45.6
Cryoporometry	26.0	27.0	47.0
Relaxation	21.5	88.5	
Relaxation (-0.15°C)	28.4	24.6	-

MULTI-SCALE AND UPSCALING OF DIGITAL ROCK PHYSICS WITH A MACHINE THAT CAN LEARN ABOUT ROCKS

R. Sungkorn, A. Morcote, G. Carpio, G. Davalos, Y. Mu, A. Grader, N. Derzhi, J. Toelke
Ingrain Inc., 3733 Westheimer Rd., Houston, Texas, 77027, U.S.A.

This paper was prepared for presentation at the International Symposium of the Society of Core Analysts held in St. John's Newfoundland and Labrador, Canada, 16-21 August, 2015

ABSTRACT

Digital rock physics (DRP) is becoming a standard tool for rock characterization. DRP utilizes 2D and 3D digital images of rock samples to analyze petrophysical and geological properties. The ability to apply DRP to a large rock sample opens a way for economic exploration and recovery of hydrocarbon. Nevertheless, due to the well-known multi-scale nature of rocks and limitations in imaging technology, less than 1% by volume of a rock sample will be digitally acquired and analyzed. Undoubtedly, relevancy and representativeness of DRP remain hotly debated topics in oil and gas industry.

Machine learning (ML) has recently accelerated advances in many industries. ML brings together multiple disciplines such as computer science, statistics, and natural science to create algorithms that can learn from data. DRP can harness the power of ML to learn from its data, the digital image of rocks, to generate breakthroughs in the oil and gas industry.

In this paper, we present a framework that combines advances in DRP and ML to characterize rock samples at a large scale, not only a tiny part of it. The framework is based on an understanding that a rock consists of multi-scale rock fabrics intermixed spatially. These rock fabrics are captured as groups of patterns within a digital image when they are smaller than the image resolution being used. We developed ML algorithms that can automatically learn about rock fabrics and their patterns. This learning process can be iteratively repeated down to an image resolution that resolves the smallest or the most significant rock fabrics. Thus, the framework integrates DRP paradigm to achieve a truly multi-scale analysis. Also, DRP and ML analysis determine the optimum number and optimum locations for further acquisition and analysis of rock fabrics at a higher resolution.

INTRODUCTION

Rocks are well-known to inherit complex heterogeneous structures with a broad spectrum of scales. For example, pores within a rock sample can range in size from nanometers to millimeters. Ehrenberg [1] carried out laboratory measurements of porosity and permeability of the same rock at different sample scales; the smaller plug samples were

drilled from the larger cores. The study found that the larger core samples had generally lower porosity but higher measured permeability values than the plugs. It can be implied that small-scale rock samples do not adequately represent all features found in large-scale samples. In addition, it is rarely feasible to perform laboratory measurements of large-scale rock samples and, measurements of small-scale rock samples are typically limited to a small amount of samples due to extensive time and cost.

Digital rock physics (DRP) aims at providing qualitative and quantitative understanding of flow transport units as well as geometrical properties of rocks. Some of the rock properties are extremely difficult, if not impossible, to measure in the laboratory. Thus, DRP in conjunction with laboratory measurements, will compliment and complete well log analysis with not only detailed information but also with new kinds of insights. Such well logs enhance analysis of reservoirs and will open a way for economic exploration and better recovery of hydrocarbons.

The use of DRP involves three steps: (a) *digital imaging* to create a digital representation of a rock in 2D and 3D at a scale and resolution that will resolve rock features such as pores, organics, and grains; (b) *digital image processing* to categorize pixels/voxels in 2D and 3D respectively, with similar properties, and (c) *digital rock analysis* to digitally model desired rock properties using the digital image of the rock [2, 3, 4].

The following discussions are applicable for both 2D and 3D images. For the sake of simplicity, the term “image” refers to 2D and 3D images and “pixel” refers to both image pixel and voxel, unless otherwise stated.

Scientists and researchers have been analysing rock properties using multi-scale DRP [5] [6, 7, 8, 9]. Figure 1 shows on the left a typical multi-scale DRP paradigm and on the right the DRP paradigm introduced in this paper. The main differences are the use of rock fabrics instead of rock features and the recursive process to obtain information from the small-scale rock fabrics. A rock fabric is defined as a combination of rock features. Similar rock fabrics have similar properties or follow similar property trends.

The process begins with an image of a large rock sample acquired at a relatively coarse resolution to cover a large field of view. At this stage, rock fabrics larger than the image resolution are resolved while smaller ones are unresolved. A rock fabric is considered resolved when it is represented, in every direction, by at least two pixels. Then, the unresolved rock fabrics are segmented into groups. Information concerning the unresolved rock fabrics is analyzed from additional images acquired at a finer resolution and smaller field of view. The information from resolved and unresolved rock fabrics are fused and populated back into the large-scale image. DRP analysis, of desired properties, is carried out using the large-scale image.

Multi-scale DRP provides a promising method to characterize rocks. Nevertheless, due to limitations in imaging technology, currently available multi-scale DRP methods still suffer from shortcomings. They can be roughly summarized as follow:

- ***Image scale***: despite advances in image processing and imaging technology, the size of a "*large*" rock sample is still limited, at best, to several centimeters and often only to a few millimeters range. Properties derived from a large sample provide higher reliability and relevancy.
- ***Image resolution***: in rocks, pore size may span several orders of magnitudes. For complex rocks, such as shales small scale pores play an important role in transport properties as well as in the total porosity of the rock. Therefore, an image resolution adequately small to resolve these small pores should be used. However, such image will have a drastic reduction in the field of view.
  Lemmens & Richards [10] created an impressive high-resolution, 12 mm in length 2D-SEM image. 12800 images where stitched and tiled together. It resolved pores from millimeter to nanometer-scale. Their approach accurately provides detailed rock properties with extensive time and resources requirements. Set aside the practical aspect in 2D imaging, the approach is undoubtedly infeasible for 3D imaging.
- ***Representative elementary area/volume (REV)***: REV is defined as the size of sub-samples in which a measured property is approximately independent from location. The definition is arguably invalid when a rock has a mild level of heterogeneity.
- ***Unresolved rock fabrics sampling locations***: unresolved rock fabrics are divided into groups of similar properties, e.g. pixel intensity and CT number. Images of these groups are acquired at a higher-image resolution to determine their properties. The image locations are typically chosen manually and qualitatively. However, it is extremely difficult to make a reasonable and consistent selection in 3D due to complex process in human perception of volume from texture [11].

Recent advances in computing hardware and machine learning (ML) have accelerated innovations and breakthroughs in many industries. ML brings together multiple disciplines such as computer science, statistics, and natural science to create algorithms that can learn from data. These algorithms have the ability to build a model from data and/or training data without strict instructions. Detailed discussion regarding ML can be found in [12] and [13]. Examples of ML-based computer vision applications include autonomous vehicle technology [14], automatic tumor detection [15], and object recognition [16]. Digital images produced in DRP can be also considered as data. Based on this perspective, DRP can harness the power of ML to discover and learn from its data.

In the computer vision community, a texture is loosely defined by complex visual patterns formed by distinct features. Such features can be extracted using various mathematical models such as intensity histogram, co-occurrence matrix, and Gabor filter. Detailed discussion regarding texture analysis can be found in [17].

A paradigm for texture analysis usually involves four steps: (a) *keypoint detection* to limit the analysis only to meaningful areas, (b) *feature extraction* to quantitatively represent texture using appropriate models, (c) *feature classification* defines clusters of keypoints corresponding to a perceptually homogeneous texture, and (d) *texture segmentation* to construct area/volume based on the feature clusters. Texture in computer vision is similar to the rock fabrics in DRP. Therefore, the texture analysis paradigm can be used with some modifications to discover rock fabrics in DRP.

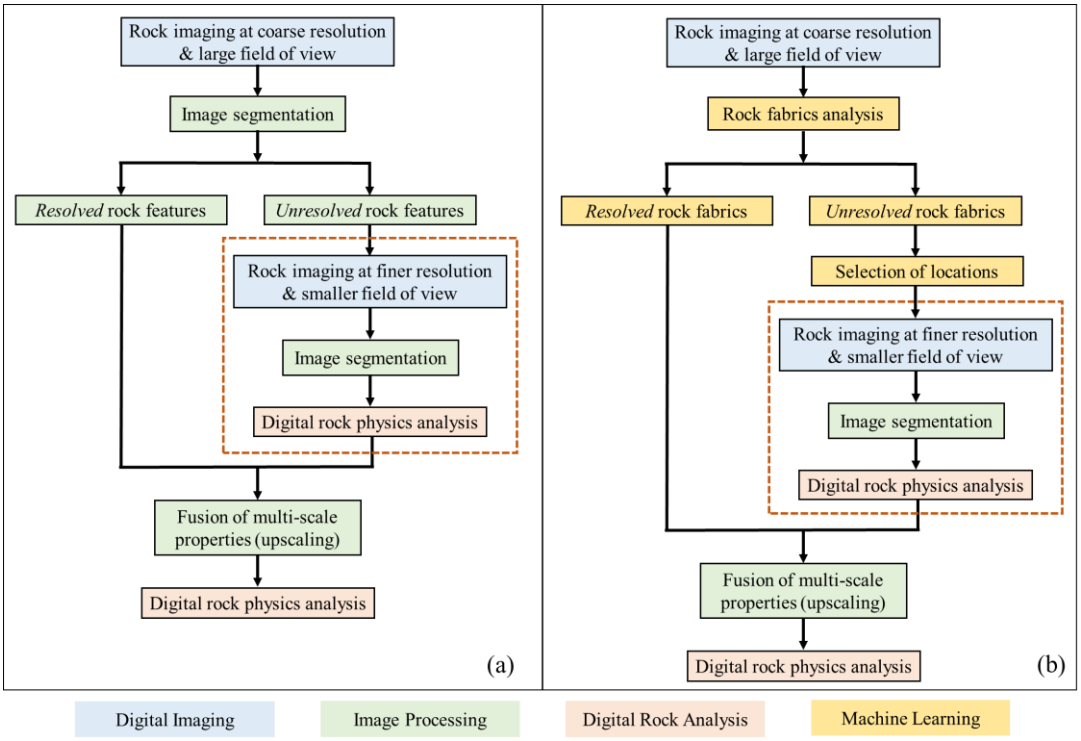

Figure 1: Left: generalized paradigm for multi-scale digital rock physics. Right: generalized paradigm for multi-scale digital rock physics using machine learning. Steps are highlighted according to the tasks shown in the bottom. Dotted block indicates a nested digital rock physics paradigm for unresolved rock features.

ROCK IMAGING

Rocks inherit complex multi-scale heterogeneous structures. A variety of imaging and detection techniques have been used to gain insights into rocks. Ideally, the image resolution being used should resolve all significant rock features and provide a reasonably large field of view (i.e. image scale). Due to limitations in imaging technology both image resolution and image scale are overly compromised.

Figure 2a shows a schematic image with multi-scaled objects. Overlaying the objects, we have grid cells. Large objects encompass significant amount of grid cells and will be resolved. In contrast, small objects are significantly smaller than the grid cells and will be unresolved. Figure 2b shows a digitized representation of Figure 2a image. The gray

scale (i.e. intensity) of the grid cells directly relates to the object area covered by the grid cell. A grid cell has low intensity (dark gray) when completely covering a feature while high intensity (light gray) is presented in a grid cell that covers only a tiny part of a feature. It can be seen that larger objects are fairly well represented by digitized grid cells. On the other hand, small objects are smeared out in digitized grid cells and are unrecognizable.

Nevertheless, digitized grid cells are generated based on the interaction between an object and the physics of the imaging technique being used. A group of unresolved grid cells contains information regarding patterns of unresolved objects. A sophisticated mathematical model which quantifies patterns of grid cells intensity, e.g. co-occurrence matrix, local binary patterns and Gabor filter, must be used [15] [17]. Since averaged intensity of these patterns is approximately similar, the widely used averaging approach cannot distinguish them. Figure 3 shows an example of multi-scale rock image. A large-scale rock image, in the center, contains unresolved rock fabrics which have different image intensity patterns. On the sides, we have high-resolution images

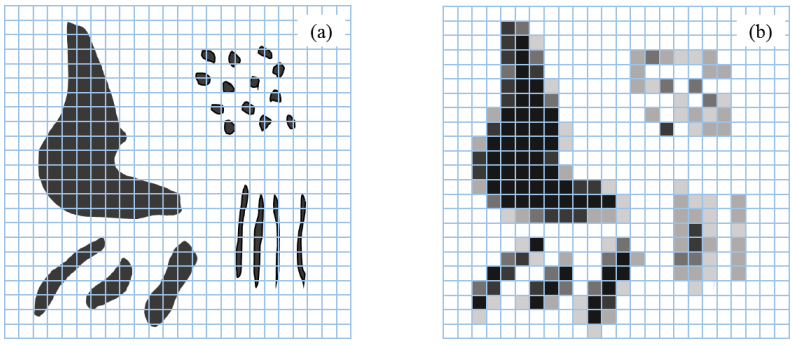

Figure 2: Illustration of a comparison between image resolution (grid size) with resolved rock features on the left of (a) and unresolved rock features on the right of (a). Illustration similar rock features acquired and digitized (b).

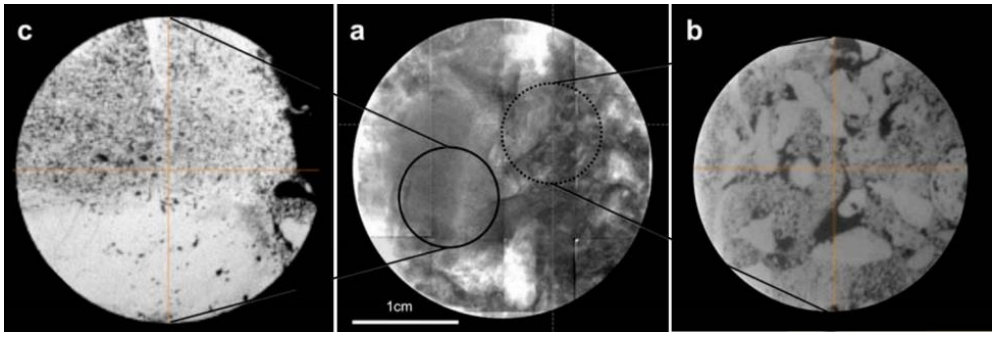

Figure 3: An example of unresolved rock fabrics in a large-scale image (a). Image of the unresolved rock fabrics are acquire at higher resolution (b) and (c). Image courtesy of ADCO Ltd.

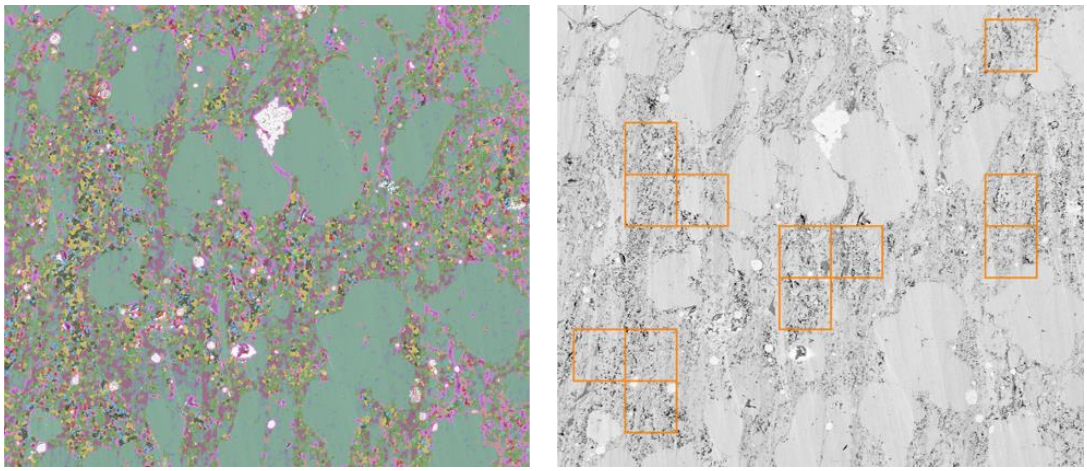

Figure 4: Eagle Ford sample. Segmented rock fabric overview (left) with optimum size and number of areas to capture all rock fabrics (right).

MULTI-SCALE DRP WITH ML

DRP has been improved significantly in recent years. Variations of multi-scale DRP (Figure 1a) are widely adopted [5] [6] [7] [8] [9]. However, applications of DRP for reservoir characterization are still limited due to shortcomings discussed earlier. In this section, we discuss a scalable multi-scale DRP paradigm with ML techniques for rocks. The differences from previous multi-scale DRP are the use of ML to learn about resolved and unresolved rock fabrics presented in a rock sample. We also use ML to identify optimum size and location for further analysis of the unresolved rock fabrics.

The present multi-scale DRP paradigm (Figure 1b) begins with a digital imaging of a rock sample at a large scale. This image will be called overview throughout this section. The overview (Figure 4, right) might contain resolved and/or unresolved rock fabrics.

In the second step, rock fabrics (Figure 4, left) in the overview are detected and segmented using the texture analysis method discussed earlier. However, rock fabrics are different from image texture commonly encountered in computer vision. The main difference is that rock fabrics tend to have pattern at individual pixel level not at edge or blob level [13] [14] [15] [16] [17].

We developed a novel *rock fabric analysis* method, based on the texture analysis paradigm (Figure 1b). Rock fabrics key-points are detected using the method discussed in Appendix A. They are mostly located within an area with a rock fabric.

Then, *rock fabric features* of the area around the keypoints are computed using the method discussed in Appendix B. In this method, four rock fabric features or attributes are used: contrast, homogeneity, entropy, and variance.

Consequently, keypoints are clustered using the four rock fabric features. We developed an unsupervised ML method for clustering high-dimensional data. It automatically learns data and finds an appropriate number of clusters. Based on the understanding of rock images, it is reasonable to postulate that keypoints within similar clusters have similar rock fabrics. For example, in Figure 5, green represents areas with medium to high intensities (unresolved organics and pores) while magenta represents areas only with medium intensities (might be unresolved organics or very small pores). These clusters can be used as a model for segmentation of the whole overview. During segmentation, rock fabric attributes for every pixel/voxel are computed. Distance from clusters is computed using, for example, Euclidean and Mahalanobis distance. A general discussion regarding data clustering can be found in [12].

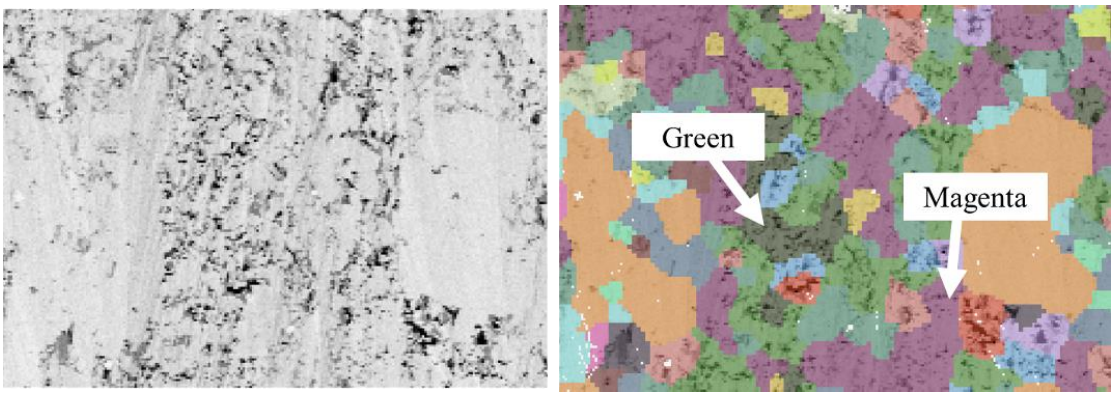

Figure 5: Close-up view of overview image (left) and its corresponding segmented fabrics (right).

The goal of rock fabric segmentation is to gain knowledge about unresolved rock fabrics. Detailed information of the unresolved fabrics is needed in order to characterize the large-scale image. This can be done by sub-sampling unresolved rock fabrics. An optimum amount of sub-sampling is desired to minimize expenses while keeping high level of accuracy and reliability. We developed an optimization algorithm for spatial data analysis which it determines the most suitable locations for further analysis (Figure 4). The algorithm finds a combination of areas that contains all fabrics with broadest variety within the fabric. Information from sub-sampling areas can be used in fusion of multi-scale information later.

An illustration of an extraction of multi-scale correlation extraction is shown in Figure 7. We give an example of 2D porosity upscaling in this paper. The method can be used directly to upscale properties in 2D and 3D. The suggested area within an overview image is acquired at a resolution that adequately resolved rock features and segmented into phases (e.g. pore and organic matters). A multi-scale correlation is obtained by correlating, for each fabric, the intensity of the overview image pixels to the porosity obtained from the area cover by the pixel in the high-resolution image. Examples of the extraction are shown as plots in Figure 7. A multi-scale correlation for each fabric is

derived by fitting a function to the data (shown as solid lines in the plots). Then, the porosity is upscaled by populating information from the multi-scale correlations for each fabric to all pixels in the overview image (Figure 7).

A truly multi-scale DRP is achieved by repeating the procedure above recursively on the unresolved rock fabrics until all rock fabrics are resolved. A method designed for upscaling and fusion of multi-scale rock properties is discussed in [9]. It is noted that, the multi-scale DRP with ML technology discussed here can be directly applied to multi-dimensional rock images. We use 2D images in this paper only for the sake of simplicity. It is also worth to note that, the methods present in this paper are implemented using graphics processing unit (GPU), which results in a computational time of approximately 100 seconds for a 2D image with a dimension of 2000 x 3000 pixels.

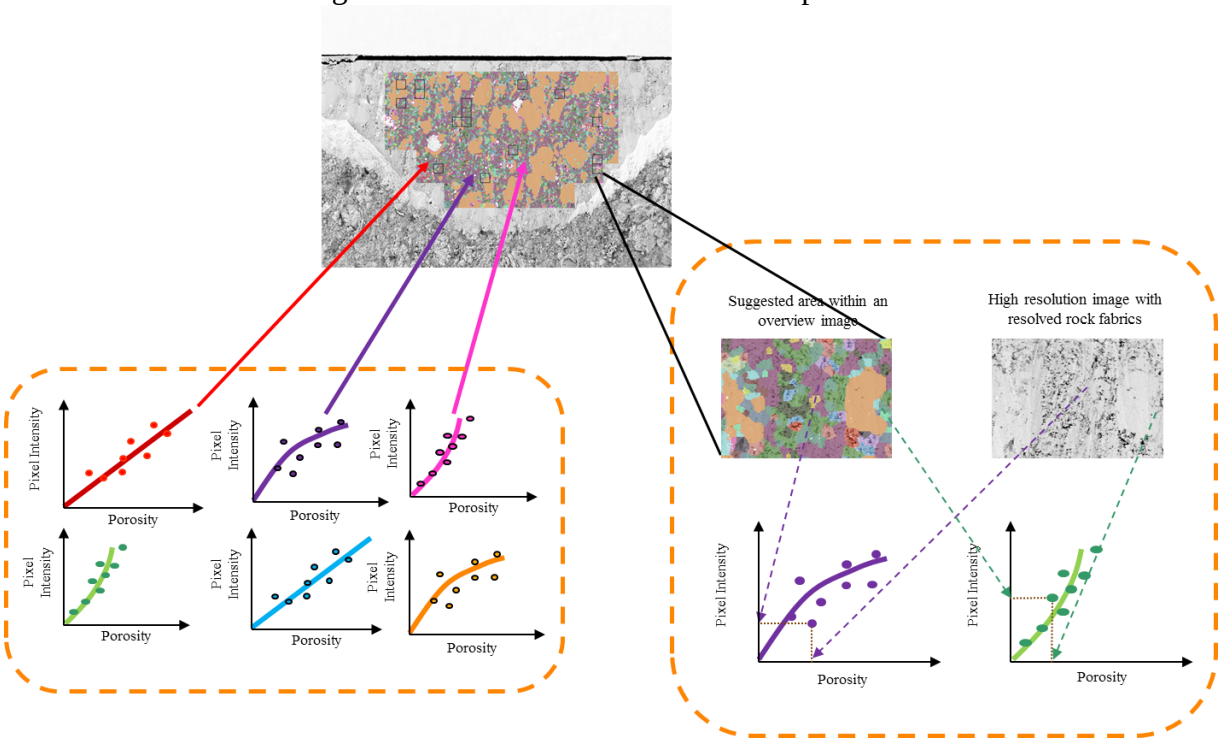

Figure 7: Illustration of multi-scale correlation extraction based on fabrics (bottom right) and population of the multi-scale correlation back on the overview image (bottom left).

CONCLUSION

We present a multi-scale digital rock physics (DRP) method using machine learning (ML) for rock fabrics characterization and scaling of rock properties. The method integrates knowledge in geology, physics, and computer science. We developed new algorithms based on the ones used in computer vision and pattern recognition communities. The rock fabric analysis discovers rock fabrics both resolved and unresolved by the image resolution being used. Also, it has the capability to characterize large-scale rock images by iteratively learning about fabrics.

Additionally, it can be applied for selecting optimum number of meaningful areas/volumes for laboratory measurements using whole core and cuttings.

It is also important to note that, despite the use of unsupervised ML methods, we designed the method based on the concept of intelligence augmentation (IA) [21]. Thus, experts can integrate their knowledge into the analysis to maximize benefits.

REFERENCES

1. Ehrenberg, S.N., "Whole core versus plugs: Scale dependence of porosity and permeability measurements in platform carbonates," *AAPG Bulletin*, (2007) **91**, pp. 835-846.
2. Dvorkin, J., Derzhi, N., Diaz, E., Fang, Q., "Relevance of computational rock physics," *Geophysics*, (2011) **76**, pp. E141-E153.
3. Andrä *et al*, "Digital rock physics benchmarks – Part I: Imaging and segmentation," *Computers & Geosciences*, (2013) **50**, pp. 25-32.
4. Andrä *et al.*, "Digital rock physics benchmarks – Part II: Computing effective properties," *Computers & Geosciences*, (2013) **50**, pp. 33-43.
5. Øren P.E., Bakke, S., "Process based reconstruction of sandstones and prediction of transport properties," *Transport in Porous Media*, (2002) **46**, pp. 311-343.
6. Grader, A.S., Clark, A.B.S., Al-Dayyani, T., Nur, A., "Computations of porosity and permeability of sparic carbonate using multi-scale CT images," *Society of Core Analysis International Symposium 2009*, SCA2009-10.
7. Sok, R.M., Vaslot, T., Ghous, A., Latham, S., Sheppard, A.P., Knackstedt, M.A., "Pore scale characterization of carbonates at multiple scales: Integration of micro-CT, BSEM and FIBSEM," *Society of Core Analysis International Symposium 2009*, SCA2009-18.
8. Khalili, A.D., Arns, C.H., Arns, J.-Y., Hussain, F., Cinar, Y., Pinczewski, W.V., "Permeability upscaling for carbonates from the pore-scale using multi-scale Xray-CT images," *SPE/EAGE European Unconventional Resources Conference and Exhibition 2012*, pp. 606-622.
9. Sungkorn, R., Gundepalli, V.A., Mu, Y., Grader, A., Sisk, C., Bhakta, S., Dvorkin, J., Toelke, J., "Multiscale permeability trends using digital rock physics," *Society of Core Analysis International Symposium 2014*, SCA2014-43.
10. Lemmens, H., Richards, D., "Multiscale imaging of shale samples in the scanning electron microscope," in Camp, W., Diaz, E., Wawak, B., *Electron microscopy of shale hydrocarbon reservoirs: AAPG Memoir*, (2013) **102**, pp. 27-35.
11. Tory, M., Möller, T., "Human factors in visualization research," *IEEE Transactions on Visualization and Computer Graphics*, (2004) **10**, pp. 1-13.
12. Bishop, C.M., *Pattern Recognition and Machine Learning*, Springer, Cambridge U.K., (2006).
13. Bengio, Y., "Learning deep architectures for AI," *Foundations and Trends in Machine Learning*, (2009) **1**, pp. 1-127.

14. Li, Q., Chen, L., Li, M., Shaw, S.-L., Nüchter, A., "A sensor-fusion drivable-region and lane-detection system for autonomous vehicle navigation in challenging road scenarios," *IEEE Transactions on Vehicular Technology*, (2014) **63**, pp. 540-555.
15. Menze *et al*., "The multimodal brain tumor image segmentation benchmark (BRATS)," *IEEE Transactions on Medical Imaging*, (2014), pp. 33.
16. He, K., Zhang, X., Ren, S., Sun, J., "Delving deep into Rectifiers: Surpassing human-level performance on ImageNet Classification," *arXiv:1406.4729*, (2015).
17. Materka, A., Strzelecki, M., *Texture Analysis Methods – A Review*, Technical University of Lodz, Institute of Electronics, COST B11 report, Brussels, (1998).
18. Lowe, D.G., "Distinctive image features from scale-invariant keypoints," *International Journal of Computer Vision*, (2004) **60**, pp. 91-110.
19. Yang, J., Yu, K., Gong, Y., Huang, T., "Linear spatial pyramid matching using sparse coding for image classification," *Proceedings of CVPR*, (2009).
20. Haralick, R.M., "Statistical and structural approaches to texture," *Proc. IEEE*, (1979) **67**, pp. 1786-804.
21. Licklider, J.C.R., "Man-computer symbiosis," *IRE Transactions on Human Factors in Electronics*, (1960) **1**, pp. 4-11.

APPENDIX

A. Rock keypoint detection

Natural rock images inherit highly heterogeneous arrangements of rock features. Dividing images into tiles leads to an overestimation and classification of rock fabrics. In order to (1) limit further analysis only to meaningful areas, (2) keep computational expense tractable and (3) obtain reasonable number and classification of rock fabrics, keypoints are detected. Concepts of keypoint detection are widely used in computer vision community [18] [19]. Since rock fabrics have different characteristics from commonly encountered image texture, previous methods for keypoint detection are not applicable. Our rock keypoint detection algorithm (step b in Figure A1) begins with (a) *discrete wavelet decomposition* of the image up to desired level. This step ensures that rock fabrics at multiple scales will be captured. Then, (b) pixel/voxel *gradient of images* obtained from previous step is computed. (c) *Laplacian of Gaussian* (LoG) is computed on the gradient images to locate points of variation of pixel/voxel intensity. (d) *Keypoints detection* within rock fabrics are detected by locating maxima in LoG images. Keypoints at the edges of rock features are eliminated by limiting keypoints within certain value of maxima (e.g. 80% of maxima).

B. Rock fabric features

There are models for image texture available in literature [17]. It is known that features of rock fabrics, especially the unresolved rock fabrics, are in pixel/voxel level. Additionally, similar rock fabric may have different orientations in an image. Therefore, a model that quantitatively describes rock fabric features and is rotation invariance must be selected. Note that, for the sake of naming consistency, rock fabric features (in DRP) are used interchangeably with texture features (in computer vision). We use Haralick texture

features [20] which based on gray-level co-occurrence matrix (GLCM). They can be used to quantify spatial distribution and auto-correlation of pixel/voxel pairs. The GLCM, $P_{i,j}$, is constructed from probability of intensity j next to intensity i in defined directions and distance. In this paper, we select an appropriate set of Haralick texture features to obtain maximum separation between rock fabrics (for following features classification) namely, (1) contrast, (2) homogeneity, (3) entropy, and (4) variance. Their mathematical description can be found in [20].

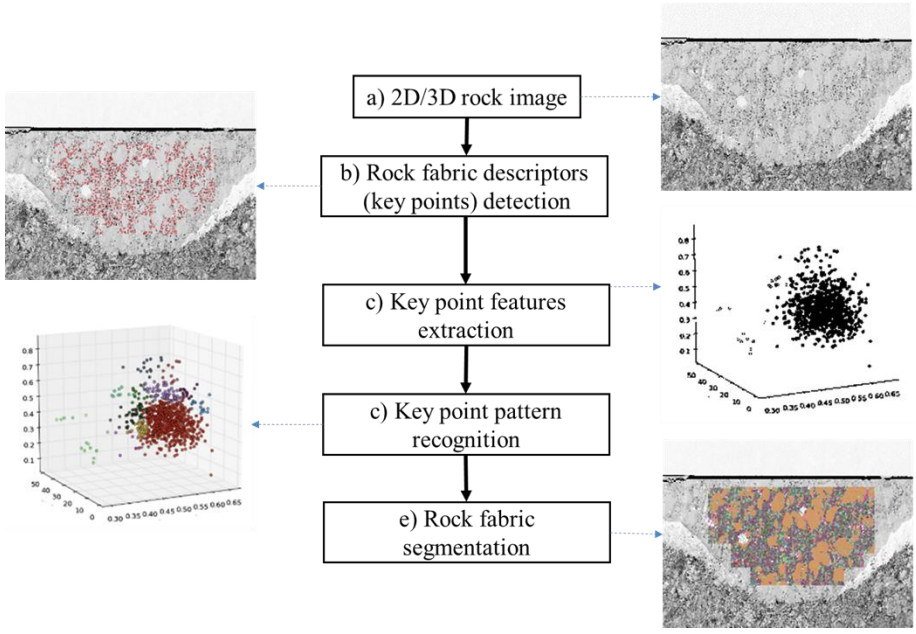

Figure A1: Flow diagram for rock fabric recognition and segmentation.

A MULTI-SCALE, IMAGE-BASED PORE NETWORK MODELING APPROACH TO SIMULATE TWO-PHASE FLOW IN HETEROGENEOUS ROCKS

Tom Bultreys[1], Wesley De Boever[1], Luc Van Hoorebeke[2] and Veerle Cnudde[1]
[1]UGCT/PProGRess, Dept. of Geology and Soil Science, Ghent University, Krijgslaan 281 (S8), 9000, Ghent, Belgium
[2]UGCT/Radiation Physics, Dept. of physics and astronomy, Ghent University, Proeftuinstraat 86, 9000 Ghent, Belgium

This paper was prepared for presentation at the International Symposium of the Society of Core Analysts held in St. John's Newfoundland and Labrador, Canada, 16-21 August, 2015

ABSTRACT

Despite the large interest in the multi-phase flow properties of rocks with broad pore size distributions, most digital rock physics approaches struggle with the presence of multiple pore scales. In this work, we present a method to estimate relative permeability (K_r) and resistivity index (RI) curves of such heterogeneous rocks during drainage. In our dual pore network model (DPNM), macropores are represented as pores and throats , while unresolved microporosity is treated as a continuous porous medium. The scales are coupled by including microporosity as symbolic network elements in the DPNM, based on 3D image analysis. The validity of the method is investigated by treating two carbonate rocks (Estaillades and Savonnières limestone). We present a sensitivity analysis of the drainage behaviour of these networks on the microporosity's petrophysical properties, which are provided as input. While a number of challenges persist, the presented examples show how DPNM can help increase the understanding of two-phase flow in complex carbonate rocks.

INTRODUCTION

Pore scale modeling is becoming an important tool to study how multi-phase transport properties of core samples depend on the rock's microstructure and on the rock-fluid system (e.g. wettability). Thanks to the recent developments in imaging techniques like micro-computed tomography (micro-CT) [1], the pore space of many rock types can be imaged in 3D. In pore network modeling, a simplified network of pores and throats is extracted from these images. For low capillary numbers, two-phase flow can then be simulated on the pore network model (PNM) by applying quasi-static invasion percolation. The loss in detail caused by the simplification of pore space geometry and fluid mechanics is compensated by the method's high computational efficiency. Despite the large interest in image-based pore scale modeling, modeling multi-phase flow in heterogeneous materials (e.g. many carbonates and clay-bearing sandstones) with broad pore sizes remains problematic. The difficulties are mostly related to the sample size/resolution trade-off in both imaging and modeling. PNM are the most likely candidate for this type of modeling, due to their high computational efficiency and their

infinite resolution. In some dual pore network modeling (DPNM) approaches, individual pores from the different scales are coupled into one multi-scale network [2,3]. This approach offers a detailed description of the microporosity present, but quickly becomes computationally infeasible when pore sizes span several orders of magnitude. In contrast, the sub-resolution porosity can be treated as a continuous porous medium, characterized by upscaled properties (e.g. [4]). In the method presented here, we use the continuum approach for the microporosity to generate image-based multi-scale networks which allow simulations even when the macroporosity does not percolate.

MATERIALS AND METHODS

We present simulations performed on two monomineralic, calcitic French limestones. Estaillades limestone has a porosity of about 25 %, which contains intergranular macropores and intra-granular micropores in fossil grains [5]. Savonnières limestone is a layered oolithic limestone belonging to the Oolithe Vacuolaire, a stratigraphical unit which also includes Brauvilliers stone (among other varieties) [6]. Its pore structure contains 4 types of porosity: inter-granular and intra-oolithic microporosity, and inter-granular and micro-connected macroporosity (hollow ooliths) [7]. The hollow ooliths are only connected to the other macro-pores by microporosity in the oolith-shells. Depending on local variations, the permeability ranges from 115 mD to more than 2000 mD (based on TinyPerm mini-permeameter measurements), and porosity ranges from 22% to 41%.

Imaging

The pore space of an Estaillades sample of 7 mm and a Savonnières sample of 6 mm diameter were imaged with UGCT's HECTOR micro-CT scanner (developed in collaboration with XRE, Belgium) [8]. The former sample was scanned at an accelerating high voltage of 100 kV and a target power of 10W. 2800 projections (2s illumination each) were reconstructed with Octopus Reconstruction software (Inside Matters, Belgium). The scan had a voxel size of 3.1 µm. A 1000x1000x1001 section of the scan was treated with a binormal noise filter and segmented into 3 phases (pore, solid and microporous voxels) with a hysteresis thresholding algorithm in Octopus Analysis. The Savonnières sample was scanned at an accelerating voltage of 120 kV and a target power of 10W. 2400 projections (illumination time 1s) were acquired, resulting in a scan with 3.8 µm voxel size. A 1000x1000x1000 subsection was segmented with a gradient watershed thresholding algorithm in Avizo (FEI, France), after performing an anisotropic diffusion filter.

DPNM Extraction

To extract a DPNM, a single-scale PNM was first extracted from the macroporous voxels with a maximal ball algorithm [9]. Then, microporous voxels in the micro-CT image were clustered into connected regions. Any two nodes in the macropore network which touch the same microporous cluster were connected by adding a special network element, henceforth called "micro-link". The multi-scale PNM thus consist out of three types of network elements: macroporous nodes, macroporous links and micro-links.

For each micro-link, the contact surface area of the microporous region with the connected macropores is calculated by applying a marching cubes (MC) algorithm on the 3D three-phase image. Micro-link lengths are defined as the corresponding pore-to-pore distances. Figure 1 illustrates the imaging and network extraction workflow. Note that due to the applied network extraction method, microporous connections both parallel and in series to macroporous links are automatically taken into account. This is important, as serial microporous conductivity (dominant in rocks with pore-filling microporosity due to e.g. clay) was found to have different effects on the transport properties than parallel microporous conductivity (dominant in rocks with grain-filling microporosity due to e.g. partial grain dissolution) [10].

DPNM Simulations

To calculate capillary pressure (P_c) curves, K_r-curves and RI-curves on multi-scale networks, we modified the quasi-static network simulator developed at Imperial College [11]. This model performs an invasion-percolation algorithm to simulate the pore filling sequence during drainage, while neglecting the influence of viscous forces. At several points during this invasion simulation, the flowrates of both fluid phases are calculated separately by imposing a pressure difference over the network and assuming mass conservation of the fluids in each pore. This leads to a set of linear equations which can be solved for the pressure:

$$q_{ij} = g_{ij} \frac{P_i - P_j}{L_{ij}}$$
$$\sum_j q_{ij} = 0, \forall i \quad (1)$$

With q_{ij} the flow from pore i to pore j, g_{ij} the electrical or hydraulic conductance between pores i and j, L_{ij} the distance from pore i to pore j and P_j the pressure in pore j. Network elements have square, triangular or circular cross-sections and retain wetting films in the corners, which is important to correctly model the wetting phase connectivity.

The multi-scale PNM simulation extends this framework by taking into account micro-links. Flow through the microporosity is taken into account by assigning upscaled transport properties to these network elements. Therefore, the multi-scale simulations take a number of variable parameters of the microporosity as input rather than calculating them: porosity, P_c-curve, (relative) permeability, breakthrough capillary pressure (BCP) at a certain micro-link length, formation factor and saturation exponent. The advantage is that the model does not have to take each separate micropore into account, allowing to simulate larger volumes and thus incorporate more rock heterogeneity in the simulations. The transport properties of the coupled network are then calculated as described in the rest of this section (more details provided in [12]).

The saturation is calculated by summing the macroporous and the microporous saturation, the latter is extracted from the microporosity's P_c-curve. The porosity of the microporous phase is supplied as input, while the total volume of microporosity is

calculated on the micro-CT image. Macropores can be invaded with non-wetting fluid through a micro-link if a BCP is exceeded. This type of invasion is usually only important for macropores which are only connected to the inlet face of the network by taking into account microporous connectivity, as other macropores can be invaded through macro-throats (which have larger radii than the throats in the microporosity). If one would assume one single BCP for all micro-links, each macropore would be invaded instantaneously and simultaneously at a certain capillary pressure. To come to a more realistic drainage behavior, we try to mimic the behavior that a network with individual micropores would display. Each microlink is therefore regarded as a cuboid domain filled with a regular network of micropores. The hight of the cuboid is determined as the pore-to-pore distance, while the square base is set to match the average pore-microporous contact surface area of the micro-link. Scaling relations can then be deduced from percolation theory to find the breakthrough saturation at which the non-wetting phase percolates through this geometry, if a breakthrough saturation for a certain domain size is provided as input. This input value can be calculated from a representative single-scale network for the microporosity, informed by e.g. SEM imaging. The percolation threshold saturation is translated to a BCP for each micro-link by using the input capillary pressure curve for the microporosity. It should be noted that the approach followed here does not take correlated heterogeneity in the microporous network into account.

Permeabilities and electrical resistivities of the multi-scale network are calculated in the classical way (equation 1, [11]), but micro-links are also assigned a conductivity. Since the microporosity is treated as a continuous porous medium with known upscaled properties (which are provided as input), these conductivities can be calculated if a geometric shape is assigned to each micro-link. Micro-links are treated as truncated cones: the surface areas of the bases are set equal to the pore-micropore contact surface areas, and the length of the cone is set equal to the pore-to-pore distance. The electrical or hydraulic conductivity of the micro-link can then be calculated by taking into account this geometry, in combination with the microporosity's effective electrical conductance or effective permeability at its current wetting phase saturation:

$$g_{ij} = \frac{\sqrt{A_i \cdot A_j}}{\rho_{micro}(S_w) \cdot L_{ij}} \tag{2}$$

With A_i the contact surface area of the microporosity cluster to pore i, L_{ij} the distance from pore i to pore j, and $\rho_{micro}(S_w)$ the hydraulic or electric resistance of the microporosity at the current wetting saturation:

$$\rho_{hydr,p}(S_w) = \frac{\mu_p}{k \cdot k_{r,p}(S_w)} \tag{3}$$

$$\rho_{elec}(S_w) = R_w \cdot FF_{micro} \cdot S_w^{-n} \tag{4}$$

In these equations, μ_p and $k_{r,p}(S_w)$ are the viscosity and the relative permeability of fluid phase p (wetting or non-wetting), k is the absolute permeability, R_w is the resistivity of the wetting fluid, FF_{micro} the formation factor, and n the saturation exponent.For computational reasons, a maximum length for micro-links has to be set. All micro-links larger than this length are removed. This cut-off length also influences the results, as the simplifications made in the network model cause an overestimation of the microporous conductivity in long micro-links. Therefore, the cut-off length is chosen as the shortest length for which all micro-connected macropores can be drained appropriately. Eliminating this user-defined parameter is the subject of further research.

RESULTS AND DISCUSSION

For Estaillades, the microporosity's input P_c-curve was deduced from a mercury intrusion porosimetry (MIP) experiment. For Savonnières, this P_c-curve was based on the pore size distribution in [7]. For both cases, the input K_r-curve and BCP were assessed by simulations on an artificial network with a pore throat size distribution representative for the microporosity in each rock. The other microporosity input properties (Table 2) were based on [4] and [7], respectively.

Estaillades Limestone

In the Estaillades model, all macro-pores and throats were scaled with a factor 1.25 to correct for an overestimation of intrusion capillary pressure (likely due to segmentation uncertainty). Single-phase transport results calculated on the DPNM can be found in Table 1. K_r and RI results are compared to experimental measurements from [13,14] in Figure 2. DPNM simulations match the experimental trends better than single-scale PNM, showing the importance of including microporosity in the simulations. Differences between the experimental measurement and our results can be explained by sample scale, heterogeneity, and by the difficulty of assessing the input parameters. In this sample, the microporosity conducts mainly in parallel to the macroporosity. The model presented here and the model in [4] mainly differ in their treatment of serial microporous conductivity. As can be expected then, the RI results are in good agreement with the results presented in [4] and show double-bending behavior [14]. The K_r-results agree with the observations in [16] that added microporous pathways increase $K_{r,nw}$ and decrease $K_{r,w}$, and that this effect is stronger for higher microporous conductivities (see further).

Savonnières Limestone

In the investigated sample, the macropores in the hollow ooliths make up 30% of the macropore space. As these pores are only connected through microporosity, they are not taken into account when calculating transport properties with conventional, single-scale PNM. The P_c-curve simulated with the DPNM therefore matches the experimental P_c-curve (scaled from an MIP experiment on a different Savonnières sample) better than the single-scale PNM (Figure 3). The hollow ooliths start to drain at $S_w = 0.61$, when nearly all inter-granular macropores have been filled with non-wetting phase. The Kr-curve (Figure 3) is in qualitative agreement with measurements on Brauvilliers limestone [15],

which has a similar lithology than Savonnières but is tighter. The saturations at the cross-over K_r and at the onset of non-wetting phase flow are matched better with the DPNM than with the PNM, mostly due to the inclusion of the wetting saturation in microporosity. In the multi-scale network, the inter-granular macropores dominate the $K_{r,nw}$ behavior ($K_{r,nw}$ = 0.83 at S_w = 0.61). At S_w < 0,61, $K_{r,nw}$ bends down due to the lower importance of the microporosity/hollow ooliths pore system for the conductivity. In the RI-simulation (Figure 3), the bending-up behavior at S_w=0.3 in the single-scale simulation contradicts the classification of Brauvilliers as a texture III rock characterized by a double bending RI [14]. In the DPNM simulation however, the curve weakly bends up until reaching the macropores' percolation threshold (S_w = 0.61), and bends down when the pressure is further increased because the wetting films in the macropores become the dominant electrical pathways when the microporosity drains. The weakness of the bending-up may be an artifact of the selection of the length cut-off parameter. The simulations on Savonnières illustrate how our DPNM can be used when microporosity provides both parallel and serial connectivity to macroporosity.

Sensitivity study of P_c and K_r on microporosity properties

In this section, the influence of the microporosity's permeability, breakthrough saturation and capillary pressure curve on the relative permeability behavior of the multi-scale networks is investigated. Varying these properties helps to better understand the influence of microporosity on petrophysical properties of complex rocks. Furthermore, it allows to probe the sensitivity of the model to the microporosity's input properties which are often difficult to assess.

Influence of the microporosity's permeability

The microporosity's permeability was varied over 4 orders of magnitude for the Estaillades and the Savonnières network (Figure 4), while keeping all other parameters constant. With increasing microporous permeability, the non-wetting phase relative permeability decreases and the wetting phase relative permeability increases. This is due to the increasing importance of fluid flow through microporosity, which is only invaded by the non-wetting phase at S_w < 0.5 for Estaillades and S_w < 0.6 for Savonnieres. The behavior fits well with the observation that non-wetting phase mobility is enhanced and wetting phase mobility decreased by the existence of high-permeability pathways [16], in this case caused by the macroporous network.

Influence of the microporosity's breakthrough saturation

To test the influence of the input breakthrough saturation (and equivalently BCP) on a network where a significant amount of micro-links conduct in series to macro-throats, this parameter (defined for a 100x100x100 µm geometry) was varied for simulations with the Savonnières network. Drainage results for the different breakthrough saturations (Figure 5) show identical P_c-curves and K_r-curves for S_w down to 0.6, as macro-pores cannot be invaded through micro-links as long as the capillary pressure is below the microporosity's intrusion capillary pressure. The well-connected macropores are thus drained first. Below S_w = 0.6, P_c and K_r curves show minor differences, related to the fact

that disconnected macro-porosity (mostly hollow ooliths) start to fill at different capillary pressures for different microporous breakthrough saturations. The results show that this parameter is of particularly minor importance to the K_r-calculations in this network, if the pore sizes of the microporosity and the macroporosity do no significant overlap.

Influence of the microporosity's input capillary pressure curve

To assert how the microporosity's pore size distribution affects the drainage behavior in a multi-scale carbonate, the input capillary pressure curve in the Savonnières simulation was varied while keeping the other input parameters constant. Results with input capillary pressure curves corresponding to a scaling of the microporous throat sizes with factors 0.1, 2, 3, 4 and 5 were compared. Size distributions for micro-and macroporosity are shown in Figure 6. When microporous throat sizes are scaled with a factor 3 or more, there is significant overlap with the throat sizes of the macroporous network. This is an interesting test case, as it indicates how the model responds to situations where there is no clear distinction between the peaks in a rock's multimodal pore size distribution, or when the resolution of the imaging method (in this case micro-CT) cannot be tuned to a value in between the peaks. Scaling factors larger than 5 were not tested, as microporosity with throat sizes larger than the macroporosity would be unphysical.

When microporosity is scaled with a factor 0.1, all well-connected macropores are filled before the microporosity is invaded. This is clearly reflected in the P_c-curve by a strong increase in the capillary pressure at $S_w = 0.6$. The new flow paths which are opened to non-wetting phase flow below this saturation are less efficient, as they are associated with drainage of macropores which only contribute to the flow through connections with low-permeability micro-links. In the $K_{r,nw}$-curve (Figure 7), this point in the drainage sequence is characterized by a sharp bend. The influence on $K_{r,w}$ is much smaller, as the wetting phase flow is already limited by passage through wetting films in the (fully drained) well-connected macro-pore network.

For scaling factors larger than 1, the rise in the $K_{r,nw}$-curve shifts to lower wetting saturations (Figure 7). This behavior can be analyzed by looking at the relative permeability behavior of the macro-pore network separately ("classical network" in Figure 3). Due to its heterogeneous nature, the relative permeability of the macro-network has a sharp increase at a (macroporous) wetting saturation of 0.5. At this point, 70% of the well-connected macro-pore space has been drained. The slight shift for the multi-scale simulation with scaling factor 2 (Figure 7) can then be explained by taking into account that the microporosity's invasion capillary pressure is reached at $S_w = 0.72$ for this simulation. Therefore, at a given total wetting saturation below 0.72, the wetting saturation of the well-connected macro-network is higher than in the multi-scale simulation with the original microporosity's throat sizes (due to drainage of microporosity and, at lower saturation, of isolated macropores). For larger scaling factors, the microporosity also starts to significantly affect the invasion sequence of the well-connected macropores, due to the increased overlap in microporous and macroporous throat sizes. For scaling factor 3, the strong increase in permeability (at total $S_w = 0.65$)

only happens when 82% of the well-connected macropore space has been drained (compare to 70% in the original multi-scale network). This means that the well-connected macroporosity is drained through macro-throats and micro-links concurrently, and suggests that pores are not strictly drained in order of decreasing size of their connected macro-throats. More validation work is needed to investigate the physical relevance of the model in such situations.

CONCLUSION

In this work, we show a method to perform DPNM simulations with upscaled microporosity properties based on micro-CT scans of heterogeneous rocks. The employed method takes microporous conductivity into account by the concept of microlinks, and allows pores to be drained through microporous connectivity in the drainage simulation. While the method cannot be considered truly predictive yet, the presented simulations on real carbonates illustrate how the model can help to understand the influence of microporosity on transport properties, by investigating the influence of microporosity properties. Major remaining challenges are the current need to include a user defined micro-link cut-off parameter and the difficulty of assessing the upscaled petrophysical parameters for the microporosity.

ACKNOWLEDGEMENTS

Prof. Dr. M. Blunt and Dr. A.Q. Raeini are thanked for helping with the maximal ball code and the microPoreFlow code. Dr. H. Derluyn and Dr. M.A. Boone are acknowledged for their help with the Savonnières sample and its micro-CT scan, and Dr. J. Dils and Prof. Dr. G. Deschutter for the MIP measurements on Estaillades. The agency for Promotion of Innovation by Science and Technology in Flanders (IWT) is acknowledged for T. Bultreys' PhD grant.

REFERENCES

1. Cnudde V., M.N. Boone, "High-resolution X-ray computed tomography in geosciences: A review of the current technology and applications", *Earth-Science Rev.* (2013) **123**, 1–17.
2. Jiang Z., M.I.J. van Dijke, K.S. Sorbie, G.D. Couples, "Representation of multiscale heterogeneity via multiscale pore networks", *Water Resources Res.* (2013) **49**, 5437–5449.
3. Prodanović M., A. Mehmani, A.P. Sheppard, "Imaged-based multiscale network modelling of microporosity in carbonates", *Geol. Soc. London, Spec. Publ.* (2014) **406**, SP406–9.
4. Bauer D., S. Youssef, M. Fleury, S. Bekri, E. Rosenberg, O. Vizika, "Improving the Estimations of Petrophysical Transport Behavior of Carbonate Rocks Using a Dual Pore Network Approach Combined with Computed Microtomography", *Transp. Porous Media*. (2012) **94**, 505–524.

5. Youssef S., M. Han, D. Bauer, E. Rosenberg, S. Bekri, M. Fleury, O. Vizika, "High resolution µ-CT combined to numerical models to assess electrical properties of bimodal carbonates", (2008) 37, in: Int. Symp. Soc. Core Anal., Society of Core Analysts, Abu Dhabi UAE.
6. Derluyn H., M. Griffa, D. Mannes, I. Jerjen, J. Dewanckele, P. Vontobel, A. Sheppard, D. Derome, V. Cnudde, E. Lehmann, J. Carmeliet, "Characterizing saline uptake and salt distributions in porous limestone with neutron radiography and X-ray micro-tomography", *J. Build. Phys.* (2013) **36**, 353–374.
7. Roels S., J. Elsene, J. Carmeliet, H. Hens, "Characterisation of pore structure by combining mercury porosimetry and micrography", *Mater. Struct.* (2001) **34**, 76–82.
8. Masschaele B., M. Dierick, D. Van Loo, M.N. Boone, L. Brabant, E. Pauwels, V. Cnudde, L. Van Hoorebeke, "HECTOR: A 240kV micro-CT setup optimized for research", *J. Phys. Conf. Ser.* (2013) **463**, 012012.
9. Dong H., M. Blunt, "Pore-network extraction from micro-computerized-tomography images", *Phys. Rev. E*. (2009) **80**, 036307.
10. A. Mehmani, M. Prodanović, "The effect of microporosity on transport properties in porous media", *Adv. Water Resources*. (2014) **63**, 104–119.
11. Valvatne P.H., M.J. Blunt, "Predictive pore-scale modeling of two-phase flow in mixed wet media", *Water Resources Res.* (2004) **40**, W07406.
12. Bultreys T., L. Van Hoorebeke, V. Cnudde, "Multi-scale, micro-computed tomography-based pore network models to simulate drainage in heterogeneous rocks", *Adv. Water Resources*. (2015) **78**, 36–49.
13. Ott H., C.H. Pentland, S. Oedai, "CO2–brine displacement in heterogeneous carbonates", *Int. J. Greenh. Gas Control*. (2015) **33**, 135–144.
14. Han M., M. Fleury, P. Levitz, "Effect of the pore structure on resistivity index curves", (2007) 34, in: Int. Symp. Soc. Core Anal., Society of Core Analysts, Calgary CA.
15. Moctezuma-Berthier P., O. Vizika, P. Adler, "Water-oil relative permeability in vugular porous media: experiments and simulations", (2002) 06, in: Int. Symp. Soc. Core Anal., Society of Core Analysts, Monterey USA.
16. Bekri S., C. Laroche, O. Vizika, "Pore-network models to calculate transport properties in homogeneous and heterogeneous porous media", *Computational Methods in Water Resources, Proceedings of the XIVth International Conference*, Elsevier, Delft, Holland, (2002) **2**, 1115, Hassanizadeh, Schotting, Gray and Pinder, Elsevier

TABLES AND FIGURES

Table 1. Single phase flow properties of the two carbonates calculated with single-scale PNM, with DPNM and measured experimentally (experimental values for Estaillades from [4]).

	Estaillades	Savonnières
K PNM (mD)	281	244
K DPNM (mD)	289	268
K Exp. (mD)	273	903 (but heterogeneous)
FF PNM	36.8	85.7
FF DPNM	19.3	13.5
FF Exp.	24	-

Table 2. Input parameters for the DPNM.

	Estaillades	Savonnières
φ_{micro}	0.36	0.35
K_{micro}(mD)	8	4.1
FF_{micro}	7.72	8.2
BCP	0.3 for $(300\mu m)^3$ network	0.3 for $(100\mu m)^3$ network
Cut-off length (µm)	67.5	160

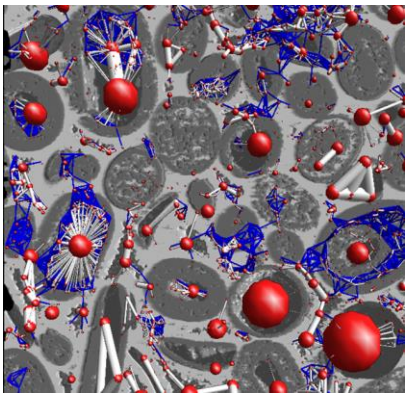

Figure 1. Illustration of DPNM extracted from avonnières limestone. Microporous zones are in dark grey, micro-links in blue.

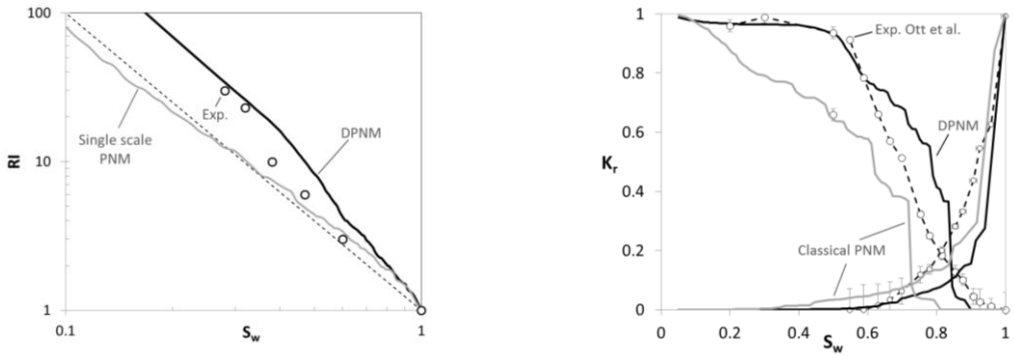

Figure 2. RI and Kr-curves for drainage of Estaillades calculated with a single scale maximal ball based PNM and with a DPNM, compared to experimental results from resp. [14] and [13] (the former estimated from the graph).

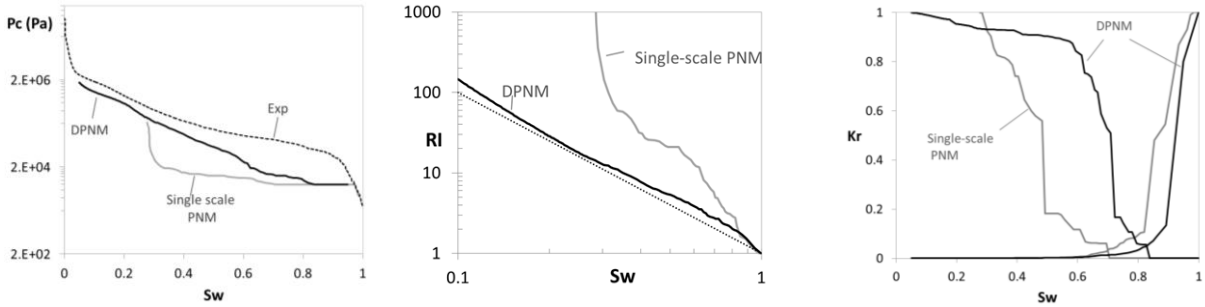

Figure 3. Pc-curve (left), RI-curve (middle) and K_r-curves (right) for drainage of Savonnières, calculated with a single scale maximal ball based PNM and with the proposed DPNM. The experimental Pc-curve is obtained from an MIP measurement.

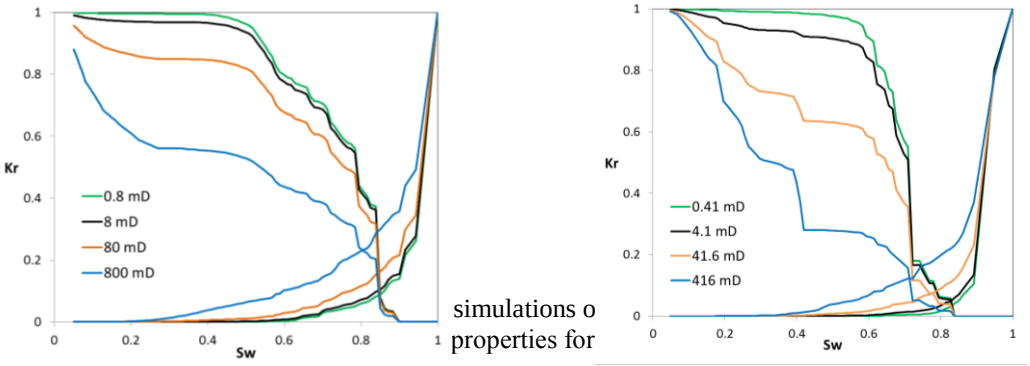

Figure 4. R simulations o the Savonni properties for

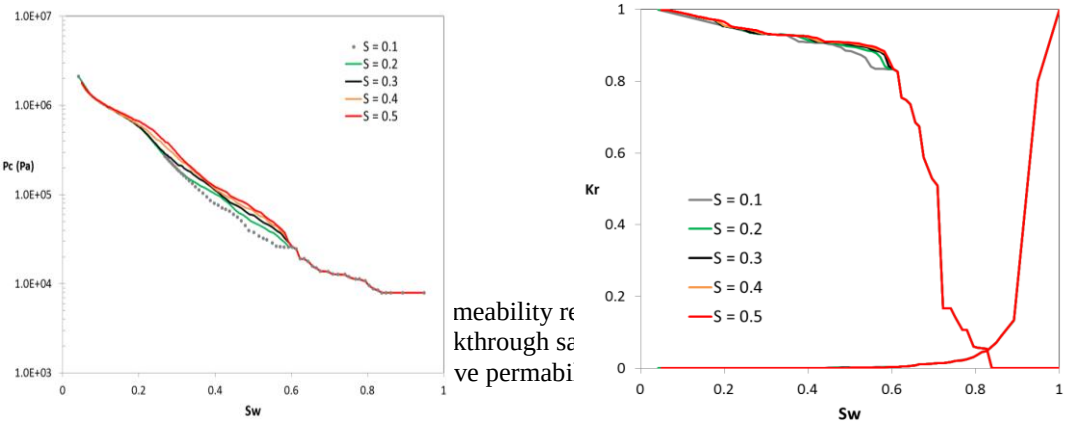

Figure 5. D meability re Savonnière kthrough sa geometry). ve permabi

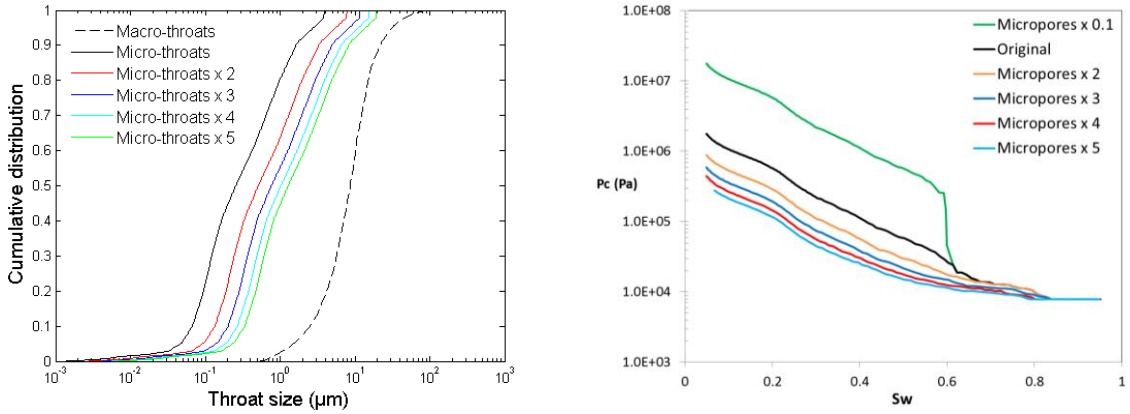

Figure 6. Cumulative pore size distributions and multi-scale drainage capillary pressure curves for different input microporosity Pc-curves in Savonnières.

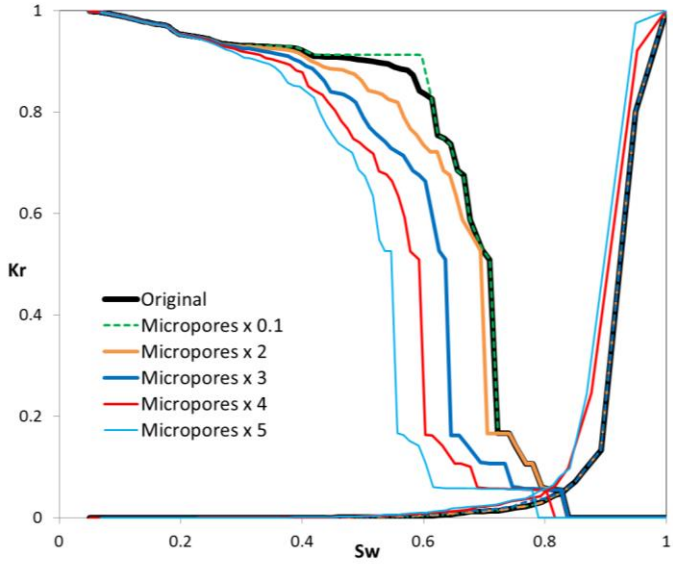

Figure 7. Drainage relative permeability curves calculated on the multi-scale Savonnières network with different microporosity P_c-curves as input. These input P_c-curves correspond to scaling of the throat sizes in the microporosity with different factors. The permeability of the microporosity was kept constant, to allow better interpretation of the results.

NANOFLUID ENHANCED OIL RECOVERY – MOBILITY RATIO, SURFACE CHEMISTRY, OR BOTH?

A. Khezrnejad, L.A. James, T.E. Johansen
Memorial University of Newfoundland

This paper was prepared for presentation at the International Symposium of the Society of Core Analysts held in St. John's Newfoundland and Labrador, Canada, 16-21 August, 2015

ABSTRACT

The goal of enhanced oil recovery (EOR) is to manipulate the fluid-fluid properties and fluid-rock properties between the injected fluid and the residual oil phase to improve recovery efficiency. Water enhanced with nanoparticles (nanofluids) has recently gained research interest for enhanced oil recovery because of the possible physical and chemical properties imparted by the nanoparticles. The application of nanofluids in enhanced oil recovery is strongly dependent on the resulting nanofluid properties. The research question asked is whether oil recovery using nanoparticle enhanced water is due to a more favorable mobility ratio (increased water phase viscosity) or is it due to the effect of the enhanced surface chemistry? In this study, we examine the role of increased viscosity of the water phase on oil recovery using nanoparticle enhanced water and polymer enhanced water with similar viscosity. First, the nanoparticle enhanced water is characterized. A statistical design of experiments technique, Response Surface Methodology, is used to investigate the effect of the type of nanoparticles (silicon oxide and aluminum oxide nanoparticles), concentration of the nanoparticles, pressure, and temperature on viscosity. The effect of interactions between the factors on viscosity is also studied. Second, the viscosity measurement results are used to plan micromodel and coreflooding laboratory scale enhanced oil recovery experiments at low pressure and temperature conditions. The results can be used to help elucidate the role of increasing viscosity versus surface chemistry on oil recovery.

INTRODUCTION

The two main forces controlling fluid flow in porous media are viscous and capillary forces. Literature suggests that recovery efficiency can be improved for waterflooding by increasing the viscosity of injected fluid (improving the macroscopic sweep efficiency) or through improving the microscopic efficiency via wettability alteration or interfacial tension reduction [1, 2, 3].

Polymers are commonly used to increase viscosity of the injected phase [4, 5, 6, 7]. However, challenges such as the stability of polymers in harsh reservoir conditions, cost, and required facilities hinder the wider use of polymer flooding [8, 9]. Adding nanoparticles to water increases the viscosity; hence, improves the mobility ratio [10, 11]. Nanofluids have been shown to be very effective in terms of wettability alteration and interfacial tension reduction [12, 13, 14]. Moreover, Zhang et al. [15] along with other

researchers demonstrated that specially designed nanoparticles are significantly more stable than polymers or surfactants in harsh reservoir conditions [16, 17]. All these features make nanofluids a very promising EOR technique for improving both microscopic and macroscopic sweep efficiency.

In this study, nanoparticle enhanced water flooding is compared to polymer enhanced water flooding to examine the role of mobility ratio, surface chemistry or both on oil recovery efficiency. Two different types of nanoparticles were added to deionized (DI). The results of the nanoparticle enhanced water flooding experiments are compared to polymer flooding using a polymer solution with the same viscosity as the nanofluid. Moreover, response surface methodology, a statistical design of experiment technique, was used to investigate the effect of nanoparticle concentration, pressure, and temperature on the viscosity of DI water. The effect of interactions between the factors on the viscosity was also studied. Interfacial tension between the nanofluid and oil, and the polymer solution and oil were also measured to better understand the possible mechanisms of oil recovery.

MICROMODEL EXPERIMENTS

Etched micromodels were used to examine the effectiveness of injecting nanoparticle enhanced water and polymer water solutions on oil recovery. The properties of the dispersed nanoparticles (manufactured by US Research Nanomaterials, Inc.) are tabulated in Table 1. It should be noted that the silica (SiO_2) nanoparticles used in the experiments were amorphous, and the alumina (Al_2O_3) nanoparticles were gamma type. In order to completely disperse the nanoparticles in the DI water, an ultrasonic device was used. The sonication process was performed on the nanofluid for 30 minutes. Homogeneity and stability of the prepared solution were confirmed by placing the nanofluid solution in a closed transparent bottle away from degrading factors such as light and heat for two weeks. Visual inspection showed neither precipitation nor other visible alterations indicating a stable nanoparticle suspension. The polymer used in these set of experiments was Flopaam 3430S (manufactured by SNF Floerger). The hydrocarbon fluid used in the experiments was stock tank crude oil from offshore Newfoundland with approximately 32-35 ^{o}API.

Table 1: Properties of nanoparticles

Type	Description	Average Particle Size (nm)	Purity (%)	pH value
Al_2O_3	Gamma	10	99.9	2-5
SiO_2	Amorphous	5-35	99.9	8-11

A micromodel fabricated from polymethyl methacrylate (PMMA) was used as the porous medium. Figure 1 shows a photo of the micromodel saturated with oil. Table 2 shows the properties of the micromodel. Different scenarios of waterflooding were performed on the glass micromodel using: DI water, polymer solution, silica nanofluid (5 wt%), and alumina nanofluid (5 wt%). Figure 2 shows a schematic of the micromodel visualization setup. The different injection scenarios are defined in Table 3.

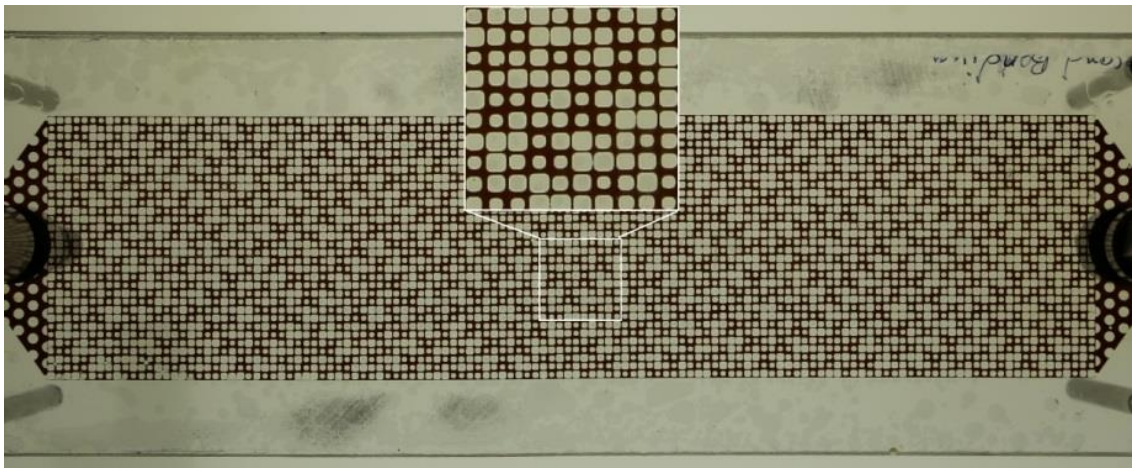

Figure 1: PMMA Micromodel

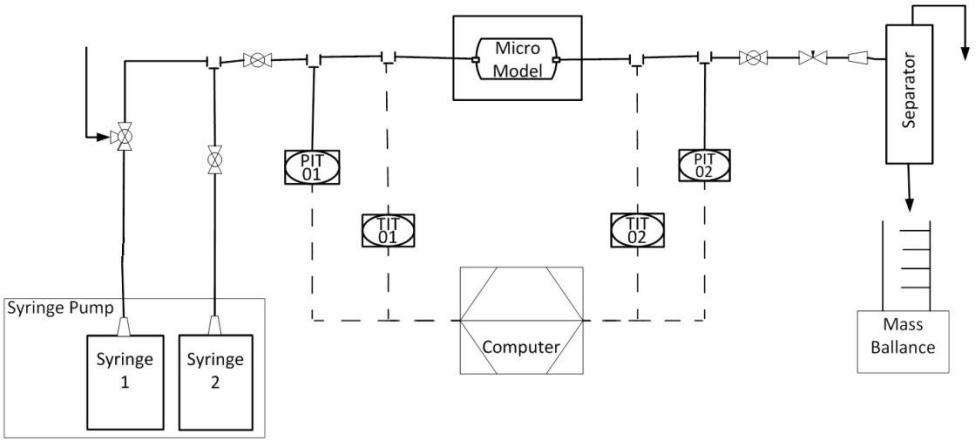

Figure 2: Schematic diagram of micromodel visualization setup

The following procedure was used to conduct the nanofluid/polymer solution/DI waterflooding experiments in the low pressure (ambient conditions) micromodel system:

1. The micromodel was cleaned by flushing with hexane (2 pore volumes).
2. The micromodel was completely dried using compressed air.
3. The injection fluids were loaded in the syringe pumps.
4. DI water was injected up to the inlet through the temporary line.
5. The micromodel inlet valve was closed.
6. The micromodel and downstream tubing were vacuumed to remove any air and reduce the probability of trapping air during the primary imbibition.
7. The outlet valve was closed.
8. By opening the inlet, the system was drained by DI water.
9. The outlet valve was opened.
10. Oil was loaded into a temporary line.
11. Oil was injected into the micromodel to the outlet.
12. Slugs of desired fluid were injected in the micromodel.

Table 2: Micromodel dimensions and characteristics

Description	Dimension
Length (cm)	25.6
Width (cm)	6.4
Average depth (μm)	160
Porosity	0.43
Pore Volume (cm^3)	1.15
Permeability (Darcy)	2.9

Table 3: Micromodel Experimental Conditions

Test #	Injected Fluid	Viscosity (cP)	Injection flow rate (ml/min)
1	DI water	1.00	0.010
2	Polymer (10 ppm)	1.75	0.010
3	Polymer (10 ppm)	1.75	0.005
4	Polymer (10 ppm)	1.75	0.010
5	Polymer (20 ppm)	2.30	0.010
6	Polymer (20 ppm)	2.30	0.005
7	SiO_2 nanofluid (5 wt%)	1.06	0.010
8	Al_2O_3 nanofluid (5 wt%)	1.75	0.010

Oil saturation in the micromodel experiments can be measured at any time by image analysis. Standard image analysis using Matlab software® was used to determine the oil recovery. The difference between the initial state of the black pixels and the final state was interpreted as oil recovery.

Figure 3 shows the oil recovery at different pore volumes injected. The recovery values used for the polymer 10 ppm case are the average value of test # 2 and 4. The standard deviation was measured to be 1.89% recovery according to recovery values measured for these two tests. The standard deviation is also shown in Figure 3. As shown in the figure, the recovery values for alumina, silica and DI water are outside of this standard deviation giving us confidence in the experimental results. Comparing the recovery of alumina nanofluid and polymer solution (10 ppm) both with μ = 1.75 cP at experimental conditions, we can see that the oil recovery for the alumina nanofluid is higher. Moreover, we can see that silica nanofluid with μ=1.06 cP but the lowest interfacial tension (will be discussed more) has the highest oil recovery. This higher oil recovery might result from improvement of microscopic sweep efficiency. Nanoparticles have the ability to decrease the interfacial tension between oil and water and improve microscopic efficiency, which will be discussed in detail in IFT measurements section later.

Figure 4 shows the ultimate oil recovery, oil recovery at breakthrough, and breakthrough time for different injection scenarios. As shown in the figure, oil recoveries obtained for the alumina and silica nanofluids are 8 and 11% higher than the oil recovery by DI water injection respectively, showing a significant improvement of oil recovery. Moreover, the recoveries from injecting alumina and silica nanofluids were 5 and 8% higher respectively than the recovery from injecting 10 ppm polymer. The oil recovery from injecting 10 ppm polymer compared to DI water injection was approximately 3% higher, which illustrates the effect of the increased viscosity of the injected fluid on oil recovery. As shown in Figure 4, injected fluids with the same viscosities have approximately the same breakthrough time.

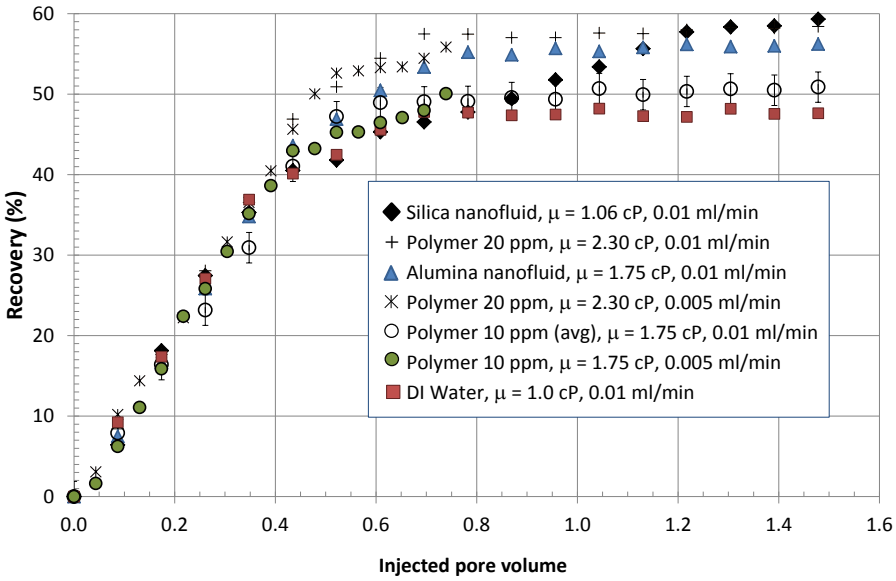

Figure 3: Oil Recovery vs. injected pore volume

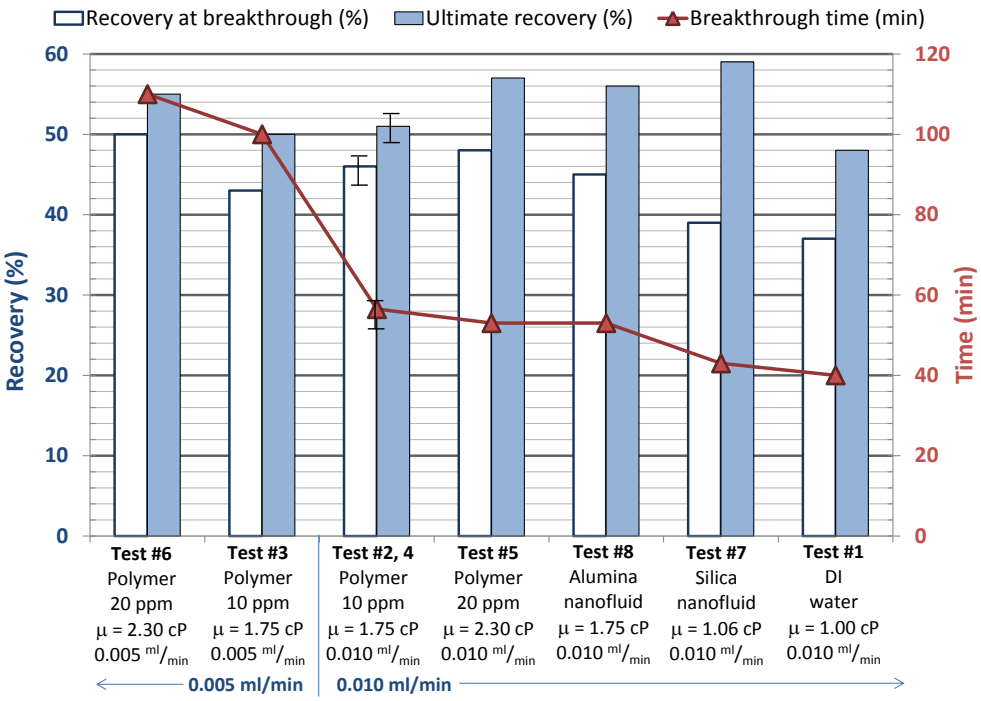

Figure 4: Ultimate recovery, recovery at breakthrough, and breakthrough time for the experiments

One replicate test was performed for the polymer (10 ppm) solution to better estimate the error in the experiments. The difference in recovery of tests two and four with a polymer concentration of 10 ppm at 0.010 ml/min was approximately 2%. This difference in recoveries might be due to experimental errors or image analysis errors. An additional experiment at half flow rate was also performed to see the effect of flow rate on

breakthrough time and ultimate recovery. Decreasing the injection flow rate causes a more stable front movement, which increases the breakthrough time significantly. However, ultimate recovery did not change by decreasing the flow rate.

Overall, nanofluid injection has higher recovery compared to polymer waterflooding. The fact that nanoparticles are surface active at the oil-water interface might be the reason for this improvement. Therefore, we measured the interfacial tension between the nanofluid and oil as well as the interfacial tension between the polymer solution and oil to better understand the role of nanoparticles in possibly reducing the interfacial tension between the immiscible phases. This is discussed in more detail subsequently. Mobility control might be another reason for enhanced oil recovery of nanofluid or polymer injection over simple water flooding. In the next section the viscosity measurements for nanofluid, polymer solution and DI water are discussed.

NANOFLUID VISCOSITY MEASUREMENTS

As discussed in the introduction, nanoparticles are capable of increasing the viscosity of water. However, most of these viscosity measurements were conducted under fixed pressure and temperature. In order to understand the behavior of viscosity with respect to different factors and their interactions, we need to change all the factors at the same time. Response surface methodology (optimal design) was employed to investigate the effect of each factor: concentration of nanoparticles, pressure, temperature, nanoparticle type, and their interaction on the response (viscosity).

In this study, Design Expert Software® was used for the design of experiments. Table 4 shows the 24 viscosity measurements based on optimal design. Concentration, pressure, and temperature are quantitative factors varying from 0 to 5 wt%, 20 to 8000 psia, and 20 to 80°C respectively.

The VISCOlab PVT viscometer (manufactured by Cambridge Viscosity) was used for measuring the viscosity. A billet for the range of 0.25 to 5 cP was used for the experiments. After loading the pump, the system was set to the desired temperature and pressure. Before measuring any data, the system was bled through the relief valves to rid the system of any air. Then, viscosity was measured under stable pressure and temperature conditions. After running each test, the system was flushed with an appropriate solvent to clean all the lines and fittings, and then vacuumed. Bias was avoided by performing the experiments in random order. As shown in the table, * indicates replicate runs. A standard deviation of 0.01cP was calculated based on the replicate values. The viscometer was calibrated using DI water. As shown in Table 4, the viscosity measured for the DI water at ambient condition was 1.07 cP (run #15), which is slightly different than available data for DI water viscosity in literature. This discrepancy might be due to experimental errors.

Table 4: Optimal design of viscosity measurements (* denotes replicate runs)

Run	Concentration (wt%)	Pressure (psia)	Temperature (°C)	Nanoparticle type	Viscosity (cP) ± 0.01
*1	5.00	8000	55.4	Al_2O_3	0.78
*2	5.00	8000	55.4	Al_2O_3	0.80
*3	2.50	4010	50.0	SiO_2	0.66
*4	2.50	4010	50.0	SiO_2	0.66
5	0.00	4110	79.8	DI water	0.36
6	5.00	20	80.0	Al_2O_3	0.53
*7	2.50	4010	50.0	SiO_2	0.66
8	5.00	20	20.0	SiO_2	1.06
9	0.00	4848	22.4	DI water	0.86
10	5.00	4010	24.4	Al_2O_3	1.82
11	5.00	5207	79.8	SiO_2	0.40
*12	2.90	8000	80.0	Al_2O_3	0.40
13	1.85	20	33.8	SiO_2	0.81
14	0.00	8000	22.6	DI water	0.84
15	0.00	20	20.0	DI water	1.07
16	3.80	3611	61.6	Al_2O_3	0.74
17	5.00	8000	21.3	SiO_2	0.92
18	1.00	4010	38.0	Al_2O_3	0.75
*19	2.90	8000	80.0	Al_2O_3	0.43
20	1.43	20	61.7	Al_2O_3	0.51
21	0.00	8000	79.5	DI water	0.34
22	0.00	20	80.4	DI water	0.37
23	0.55	7880	42.5	SiO_2	0.57
24	5.00	4010	27.8	Al_2O_3	1.69

Table 5 shows the analysis of variance (ANOVA) results for the viscosity measurements. The prediction interval provides the upper and lower levels for 95% confidence level. The p-value represents the probability of the occurrence of a given event. When the p-value is less than 0.05 (1-95% confidence) the factor is considered significant. The analysis of variance is model dependent, so it is up to the user to suggest models that describe the data. We systematically tried and compared several different models (linear, quadratic, etc.) with the inclusion and elimination of higher order and interaction terms. The goal was to find the simplest model to best fit the results. The results of the ANOVA table demonstrate that all the individual factors have significant effect on viscosity (p-value < 0.05). Moreover, the interaction between concentration and nanoparticle type and second order terms of pressure and temperature were shown to be important and should be considered in the model.

Figure 5 shows how the viscosity predicted by the model matches the actual experimental data. As shown in the figure, the data points fall very close to the 45° slope line, which confirms that lack of fit is not significant as it was shown in the ANOVA table.

Figure 6 shows the effect of nanoparticles concentration on the viscosity. The black points are indicating the experimental measurements. Figure 6a demonstrates that by

increasing the concentration of alumina (Al_2O_3) nanoparticles in the DI water, the viscosity increases. However, Figure 6b shows that adding silica (SiO_2) nanoparticles to DI water does not change the viscosity significantly. As shown in the figure, viscosity decreases with increasing temperature. The effect of pressure on the viscosity of nanofluid is slightly more significant at lower temperatures. In fact, the viscosity values at high temperature (80°C) are almost the same for different states of pressure, which is showing the insignificance of pressure effect on viscosity at high temperature. The dashed lines indicate the 95% confidence interval bands for the predictive model.

Table 5: Analysis of variance for viscosity experiments

Source	**Sum of Squares**	**Mean Square**	**F Value**	**p-value**
Model	2.320	0.330	359.11	<0.0001
Concentration (C)	0.160	0.160	176.93	<0.0001
Pressure (P)	0.023	0.023	25.09	<0.0001
Temperature (T)	1.840	1.840	1990.49	<0.0001
Nanoparticle type (N)	0.079	0.079	85.15	<0.0001
Concentration x Nanoparticle Type (CN)	0.069	0.069	74.98	<0.0001
Pressure^2 (P^2)	0.011	0.011	12.14	0.0021
Temperature^2 (T^2)	$4.323x10^{-3}$	$4.323x10^{-3}$	4.68	0.0416
Lack of fit	0.019	$1.096x10^{-3}$	3.26	0.0976

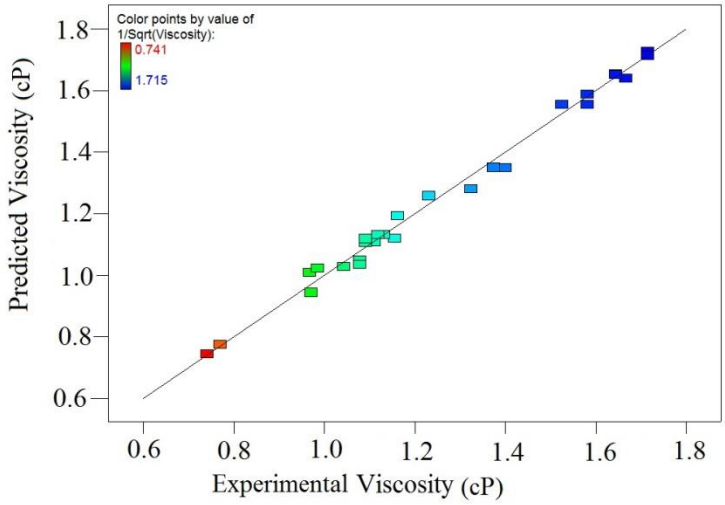

Figure 5: Predicted viscosity vs. experimental viscosity measurements

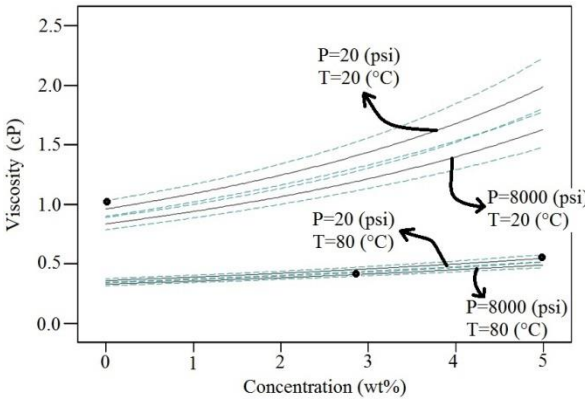

Figure 6a: Effect of nanoparticles concentration on Alumina (Al_2O_3) nanofluid viscosity

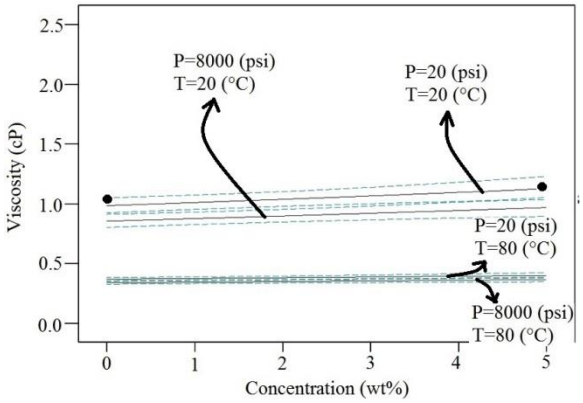

Figure 6b: Effect of nanoparticle concentration on Silica (SiO_2) nanofluid viscosity

Figure 7 shows the effect of interaction between pressure and temperature on the measured viscosity of nanofluid. As shown in the ANOVA table, the effect of second order terms of pressure and temperature are significant. We can see this non-linearity effect in Figure 7. Again, pressure is shown to have little effect. Figure 7b indicates that viscosity behaves more non-linear while using alumina nanoparticles at higher concentration. Moreover, by looking at Figure 7b, we can see that the maximum viscosity was obtained while using alumina nanoparticles at medium pressure, low temperature, and high concentration. For silica nanofluid increasing the concentration of nanoparticles in DI water does not affect the viscosity significantly. However, viscosity increases significantly by increasing the concentration of alumina nanoparticles in DI water. Increasing the concentration of alumina nanoparticles increases the effect of non-linearity behavior of viscosity (Figure 7a and 7b). Overall, the model predicts that the viscosity of DI water can be increased to a maximum value of approximately 2 cP using alumina nanoparticle.

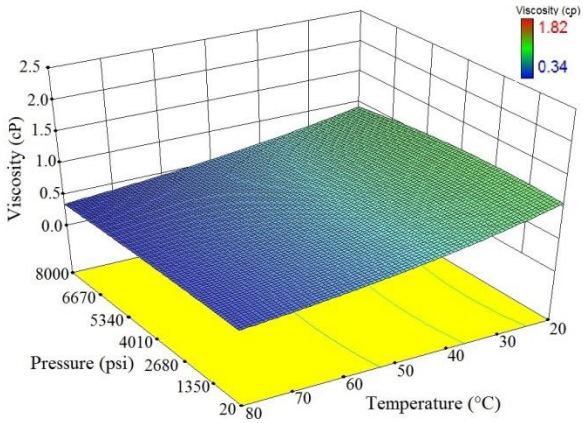

Figure 7a: 3D map of viscosity vs. pressure and temperature (Al_2O_3, 1 wt%)

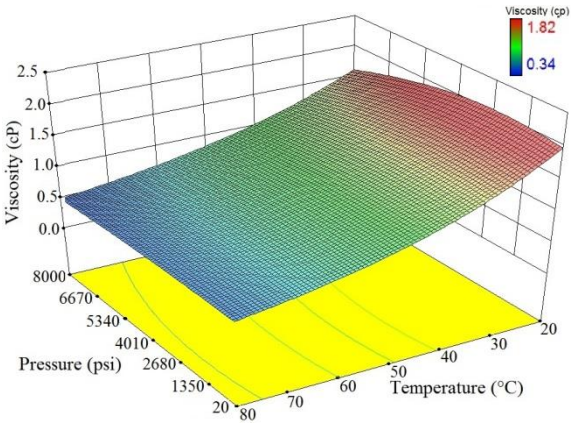

Figure 7b: 3D map of viscosity vs. pressure and temperature (Al_2O_3, 5 wt%)

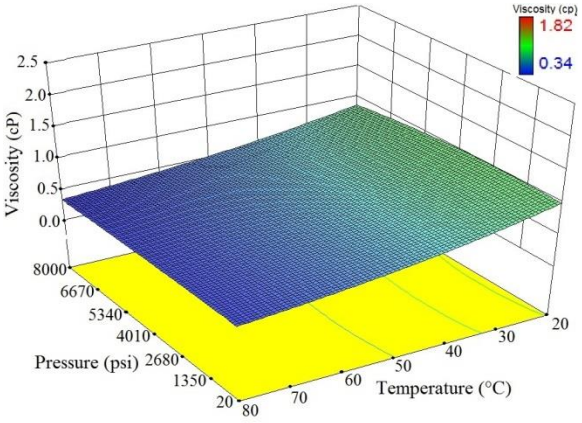

Figure 7c: 3D map of viscosity vs. pressure and temperature (SiO_2, 1 wt%)

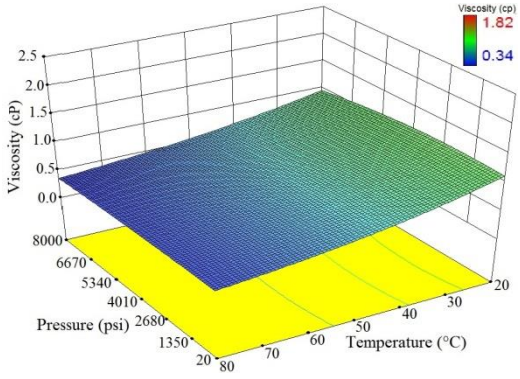

Figure 7d: 3D map of viscosity vs. pressure and temperature (SiO_2, 5 wt%)

INTERFACIAL TENSION (IFT) MEASUREMENTS

An Interfacial Tension Meter (IFT 700, manufactured by Vinci Technologies) was used to determine interfacial tension between the oil and DI water, polymer solution, and the nanofluid (liquid-liquid interface) at ambient (experimental) conditions. The pendant drop method was used for IFT measurements. An oil drop was created and put in contact with the nanofluid in a cell. A camera connected to a computer records the shape of the oil droplet to derive the interfacial tension. The results of IFT measurements are tabulated in Table 6 where the value reported is the average value for approximately 70 runs. The standard deviation was calculated for each test separately. As shown in the table, interfacial tension decreases significantly by adding nanoparticles to DI water. Moreover, the minimum IFT was obtained while using silica nanoparticles.

Table 6: Interfacial tension measurements

Fluid	**IFT (mN/m)**
DI Water and Oil	29.00
Silica nanofluid (5 wt%) and Oil	6.56 ± 1.06
Alumina nanofluid (5 wt%) and Oil	12.71 ± 0.35
Polymer Solution (10 ppm) and Oil	21.47 ± 1.30

CONCLUSIONS

In conclusion, the results of this experimental work shows that nanoparticle have the ability to increase oil recovery by improving both microscopic and macroscopic sweep efficiencies. The results of viscosity measurements demonstrated that alumina nanoparticles can increase the viscosity of deionized water. The viscosity of the silica and alumina nanofluids was measured at different conditions of pressure, temperature and nanoparticle concentration. Interfacial tension (IFT) experiments show that surface chemistry plays an important role when using nanoparticle enhanced water compared to polymer water solutions of the same viscosity in micromodel water flooding experiments. The results of IFT measurements indicate that the IFT between oil and DI water can decrease from 29 to 6.56 and 12.71 for silica (5 wt%) and alumina (5 wt%), respectively.

The results of micromodel experiments show that this IFT reduction causes higher oil recovery using nanofluid injection compared to polymer flooding with the polymer solution having the same viscosity as the nanofluids. Oil recoveries using polymer injection with concentrations of 10 and 20 ppm were 3 and 9% higher respectively than oil recovery using DI water injection, which shows the effect of viscosity improvement on oil recovery. The recoveries obtained from silica and alumina nanofluid injection were also higher than the recovery of DI water injection by 11 and 8% respectively. More investigation is required but our results indicate that surface chemistry does seem to play a role in oil recovery using nanofluids. This experimental work shows that nanoparticles are very promising for EOR purposes due to their specific chemical and physical properties, and the fact they have the ability to improve oil recovery through viscosity improvement and surface chemistry.

ACKNOWLEDGEMENTS

The authors thank the Hibernia Management and Development Company (HMDC), Chevron Canada, the Natural Sciences and Engineering Research Council of Canada (NSERC), and the Research and Development Corporation (RDC) for their support, without which this work could not have been performed.

REFERENCES

1. Chatzis, I., and Morrow, N. R., "Correlation of Capillary Number Relationships for Sandstone," *SPE Journal*, (1984) **24,** 05.
2. Lake, L. W., *Enhanced Oil Recovery*, Prentice Hall, New Jersey, USA, (1989).
3. Nguyen, P. T., Do, B. P. H., Pham, D. K., Nguyen, Q. T., Dao, D. Q .P., and Nguyen, H. A., "Evaluation on the EOR Potential Capacity of the Synthesized Composite Silica-Core/ Polymer-Shell Nanoparticles Blended with Surfactant Systems for the HPHT Offshore Reservoir Conditions," Paper presented at the SPE International Oilfield Nanotechnology Conference and Exhibition, 12-14 June, Noordwijk, The Netherlands, (2012).
4. Wang, J., Wang, D., Sui, X., Bai, W., "Combining Small Well Spacing with Polymer Flooding To Improve Oil Recovery of Marginal Reservoirs," SPE-96946-MS Paper presented at SPE/DOE Symposium on Improved Oil Recovery, 22-26 April, Tulsa, Oklahoma, USA, (2006).
5. Wang, Y., Zhao, F., Bai, B., "Optimized Surfactant IFT and Polymer Viscosity for Surfactant-Polymer Flooding in Heterogeneous Formations," SPE-127391-MS Paper presented at SPE Improved Oil Recovery Symposium, 24-28 April, Tulsa, Oklahoma, USA, (2010).
6. Morelato, P., Rodrigues, L., Romero, O. L., "Effect of Polymer Injection on the Mobility Ratio and Oil Recovery," SPE-148875-MS Paper presented at SPE Heavy Oil Conference and Exhibition, 12-14 December, Kuwait City, Kuwait, (2011).
7. Fletcher, A. J. P., Weston, S., Haynes, A. K., Clough, M. D., "The Successful Implementation of a Novel Polymer EOR Pilot in the Low Permeability Windalia Field," SPE-165253-MS Paper presented at SPE Enhanced Oil Recovery Conference, 2-4 July, Kuala Lumpur, Malaysia, (2013).

8. Kurenkov, V. F., Hartan, H. G., Lobanov, F. I., "Degradation of Polyacrylamide and Its Derivatives in Aqueous Solutions," *Russian Journal of Applied Chemistry*, (2002) **75**, 07, 1039-1050.
9. Ayatollahi, S. and Zerafat, M. M., "Nanotechnology-assisted EOR techniques: New solutions to old challenges," Paper SPE 157094 presented at the SPE International Oilfield Nanotechnology Conference and Exhibition, Noordwijk, 12-14 June, (2012).
10. Fei, D., Dingtian, K., and Alexandru, C., "Viscosity affected by nanoparticle aggregation in Al2O3-water nanofluids," *Nanoscale Research Letters*, (2011) **6**, 1, X1-5.
11. Zhi-Yong, L., Dong-Jian, S., Zhong-Qiang, Z., Jian-Ning, D., Guang-Gui, C., Long, Q., and Rui, Z., "Effect of temperature and nanoparticle concentration on the viscosity of nanofluids," *Gongneng Cailiao/Journal of Functional Materials*, (2013) **44**, 1, 92-95.
12. Maghzi, A., Mohebbi, A., Kharrat, R., and Ghazanfari, M. H., "Pore-scale monitoring of wettability alteration by silica nanoparticles during polymer flooding to heavy oil in a five-spot glass micromodel," *Transport in Porous Media*, (2011) **87**, 3, 653-664.
13. Roustaei, A., Moghadasi, J., Bagherzadeh, H., and Shahrabadi, A., "An Experimental Investigation of Polysilicon Nanoparticles Recovery Efficiencies through Changes in Interfacial Tension and Wettability Alteration," Paper SPE 156976 presented at the SPE International Oilfield Nanotechnology Conference and Exhibition, Noordwijk, 12-14 June, (2012).
14. Khezrnejad, A., James, L. A., and Johansen, T. E., "Water Enhancement Using Nanoparticles in Water Alternating Gas (WAG) Micromodel Experiments," Paper SPE 173484-STU presented at the SPE Annual Technical Conference and Exhibition, 27-29 October, Amsterdam, The Netherlands, (2014).
15. Zhang, T., Espinosa, D., Yoon, K. Y., Rahmani, A. R., Yu, H., Caldelas, F. M., Ryoo, S., Roberts, M., Prodanovic, M., Johnston, K. P., Milner, T. E., Bryant, S. L., and Huh, C., "Engineered Nanoparticles as Harsh-Condition Emulsion and Foam Stabilizers and as Novel Sensors," OTC-21212-MS Paper presented at Offshore Technology Conference, 2-5 May, Houston, Texas, USA, (2011).
16. Jafari, S., Khezrnejad, A., Shahrokhi, O., Ghazanfari, M. H., and Vossoughi, M., "Experimental Investigation of Heavy Oil Recovery by Continuous/WAG Injection of CO2 Saturated with Silica Nanoparticles. *International Journal of Oil, Gas and Coal Technology*, (2015) **9**, 2, 169-179.
17. Yu, J., Wang, S., Liu, N., and Lee, R., "Study of Particle Structure and Hydrophobicity Effects on the Flow Behavior of Nanoparticle-Stabilized CO2 Foam in Porous Media," Paper SPE-169047-MS presented at the SPE Improved Oil Recovery Symposium, 12-16 April, Tulsa, Oklahoma, USA, (2014).

AN EXPERIMENTAL INVESTIGATION OF NANOPARTICLES ADSORPTION BEHAVIOR DURING TRANSPORT IN BEREA SANDSTONE

Shidong Li, Miaolun Jiang and Ole Torsæter,
Norwegian University of Science and Technology (NTNU)

This paper was prepared for presentation at the International Symposium of the Society of Core Analysts held in St. John's Newfoundland and Labrador, Canada, 16-21 August, 2015

ABSTRACT

Nanoparticles fluid (nanofluid) has shown its potential for increasing oil recovery during last few years. Due to very small size (D~ 1 to 100 nm), nanoparticles can pass through reservoir, while the huge specific surface area of porous media and nanoparticles result in significant adsorption of nanoparticles inside reservoir. The behavior of this adsorption plays very important role for enhanced oil recovery (EOR) mechanisms of nanofluid, it can alter reservoir wettability and change permeability. Investigation of nanoparticles adsorption behavior leads to better understanding of nanofluid EOR process.

The objective of this experimental study is to investigate nanoparticles adsorption behavior during transport in Berea sandstone, analyses of pressure drop and nanoparticles concentration of effluent fluid were used to evaluate nanoparticles adsorption. Three different wettability core plugs (water, oil, and neutral wet) with 8cm length and 3.8 cm diameter were employed. Hydrophilic nano-structure particle and colloidal nanoparticle were used in this experiment and they were dispersed in 3 wt. % brine. Nanofluid was injected into each core plug saturated with brine for several pore volumes, and brine was injected afterwards for post-flush. Pressure drop across core was recorded during whole injection process. Nanoparticles concentration of effluent fluid was measured to plot adsorption curve.

The results showed that nano-structure particle and colloidal nanoparticles undergo adsorption during transport inside core, but nano-structure particle has larger adsorption amount than colloidal nanoparticle. For nano-structure particle more nanoparticles can be adsorbed if the core is neutral wet, nanoparticles desorption was not observed inside water wet cores. Injection of high concentration of nano-structure particle fluid can block core channels and result in permeability impairment, while for colloidal nanoparticles fluid injection does not reduce permeability dramatically, on the contrary it makes core more permeable for some cases.

INTRODUCTION

During last decade nanotechnology was proposed can be utilized in oil and gas industry for different disciplines [1]. Particles can show some special properties when size reduce down to nanoscale, like surface activity and huge specific surface area, so nanoparticles

have promising future to be a new EOR agent. The nanoparticles suspension fluid, so called nanofluid, is a fluid containing nanometer-sized particles, and the dispersing liquids can be water for hydrophilic nanoparticles. Based on many publications [2, 3, 4, 5] addressed on this topic, nanofluid has already been proven to have good potential for EOR.

Miranda et al. [6] have mentioned that silica nanoparticle has many advantages as EOR agent, for instance, 1) 99.8% of silica nanoparticle is silicon dioxide (SiO_2), which is main component of sandstone, so silica nanoparticle is an environmentally friendly material compared to chemical substance; 2) nanoparticles dispersion has good stability because surface forces easily counterbalance the force of gravity; 3) the properties of thermal, stress–strain and rheology strongly depend on size and shape of the nanoparticles, and can be tailored during their production; 4) the chemical behavior of the nanoparticle is correlated to the chemical substance of surface coating, the chemical properties of nanoparticle can be easily controlled by changing surface coating chemical; 5) the price of silica nanoparticle is cheaper than chemical, which makes silica nanoparticle can be widely applied for EOR at oil field.

The EOR mechanisms for nanofluid have already been discussed in previous author's papers [7, 8], which include disjoining pressure, interfacial tension reduction, wettability alteration, pore channels plugging and emulsification. The effect of nanoparticle adsorption inside core on wettability alteration is highlight of these mechanisms, since hydrophilic nanoparticles can alter oil wet and neutral wet core to water wet [9, 10]. The adsorption of nanoparticles might also affect permeability of core, so this paper focuses on adsorption behavior of hydrophilic silica nanoparticles inside different wettability core and its effect on permeability.

Adsorption and Transport of Nanoparticles inside Porous Medium

After hydrophilic nanofluid is injected into porous medium, five phenomena will occur: adsorption, desorption, blocking, transportation and aggregation of nanoparticles. Since the particle size of nanoparticle is less than 1 micron, so they are Brownian particles, and five forces dominate the interactions between nanoparticles and pore walls: the attractive potential force of van der Waals, repulsion force of electric double layers, Born repulsion, acid-base interaction, and hydrodynamics. When the total force of five forces is negative, the attraction is larger than repulsion between nanoparticle and pore walls, which leads to adsorption of nanoparticle on the pore walls. Otherwise desorption of nanoparticle from the pore walls will occur at the same time. Adsorption and desorption is a dynamic balance process controlled by the total force between nanoparticle and pore walls. Zhang et al., [11] discussed that both reversible and irreversible adsorption of nanoparticles occurs during transport through porous medium. Blocking will take place if the diameter of the particle is larger than the size of pore throat, or when some nanoparticles aggregate to form bigger particle at the pore throat. The aggregation of nanoparticles happens if the previous equilibrium of the nanoparticle dispersion system breaks up and nanoparticles

form clusters to block some pore channels. Some images of adsorption and aggregate of nanoparticles in porous medium are shown in Figure 1.

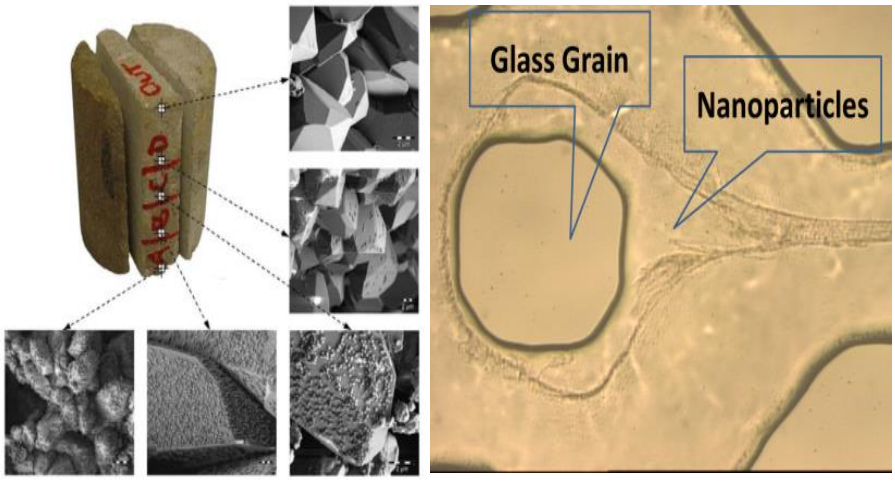

Figure 1 Nanoparticles adsorption inside porous medium.
Left: ESEM image of nanoparticle adsorption inside core [12]; right: Microscope image of nanoparticles adsorption in glass micromodel

Transportation of nanoparticles in porous medium is governed by diffusion, convection and hydrodynamics. After adsorption and desorption reach the equilibrium state, nanofluid can flow through the porous medium without too much adsorption and retention. The equilibrium adsorption is estimated to be 1.27 mg/g for 5000 ppm nanofluid [13].

EXPERIMENTAL MATERIALS

Nanoparticle

Both hydrophilic silica Nano-Structure Particles (NSP) and hydrophilic silica Colloidal NanoParticles (CNP) were employed in this experimental study. They are produced by Evonik Industries. NSP and CNP are supplied as powder and highly concentrated dispersion fluid respectively. They have been characterized by Transmission Electron Microscope (TEM) and TEM images are shown in Figure 2. NSP have average primary particle size of 7 nm and specific surface area of 300 m^2/g, but they can aggregate to form bigger particles, where particle size might be higher than 100nm. CNP have average single particle size of 18 nm and specific surface areas of 350 m^2/g, and this type of nanoparticles don't aggregate in dispersion due to adding of special stabilizer. The reason for NSP and CNP looking similar in Figure 2 is that CNP dispersion fluid was dried before TEM imaging, so nanoparticles reaggregated and formed soft agglomerate, while NSP always form hard agglomerate both in dispersion and powder status.

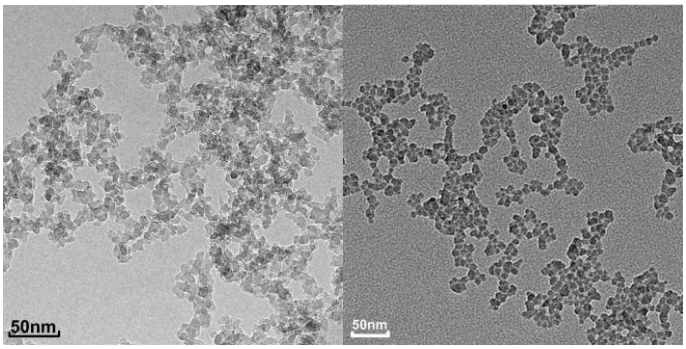

Figure 2 TEM images for NSP (left) and CNP (right) (Provided by Evonik)

Nanofluid

Three nanoparticles concentrations (0.05 wt. %, 0.2 wt. % and 0.5 wt. %) were utilized for nanofluid, and 3 wt. % NaCl brine was used as dispersion fluid. NSP was weighed and dispersed in brine by sonicator, while CNP nanofluid was diluted from concentrated dispersion. Two types of nanofluid with different concentration are shown in Figure 3, as we can see there is no big difference between different concentrations of CNP nanofluid due to good nanoparticle dispersion, but for NSP the higher concentration the milkier nanofluid will be. Fluid properties of each fluid are shown in Table 1.

Table 1 Fluid properties

Fluid	Density, g/cm^3	Viscosity, cP
Brine Nacl 3 wt. %	1.022	1.0026
NSP Nanofluid 0.05 wt. %	1.021	1.0858
NSP Nanofluid 0.2 wt. %	1.022	1.1550
NSP Nanofluid 0.5 wt. %	1.022	1.5627
CNP Nanofluid 0.05 wt. %	1.022	1.0331
CNP Nanofluid 0.2 wt. %	1.022	1.0342
CNP Nanofluid 0.5 wt. %	1.022	1.0372

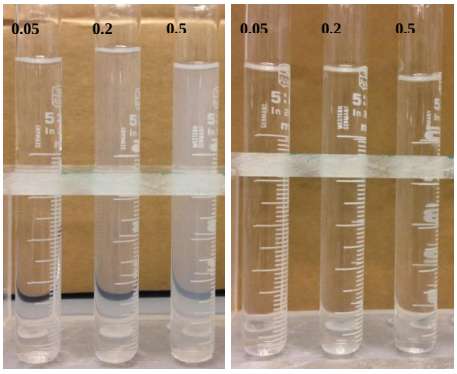

Figure 3 Nanofluid for NSP (left) and CNP (right)

Porous Medium

In total, 18 long core plugs drilled from one block of Berea Sandstone were used for this nanoparticles transport experiment. The average porosity and permeability are 19.5% and 352 mD respectively. The diameter is 3.83cm and length is 8 cm. The pore volume (PV) is about 16ml. Two groups (6 cores for each) were aged to be oil wet and neutral wet under the same condition and the wettability index for oil wet core and neutral wet core is -0.39 and -0.09 respectively. The wettability index for original water wet core is 0.8.

Flooding Setup

Figure 5 shows schematic of flooding setup. The pump injected Exxol D-60 as pumping fluid to push the piston located inside the reservoir. There are 3 reservoirs filled with brine, oil and nanofluid respectively. The pressure drop across the core plug during nanoparticle transport experiments was recorded by precision pressure gauge.

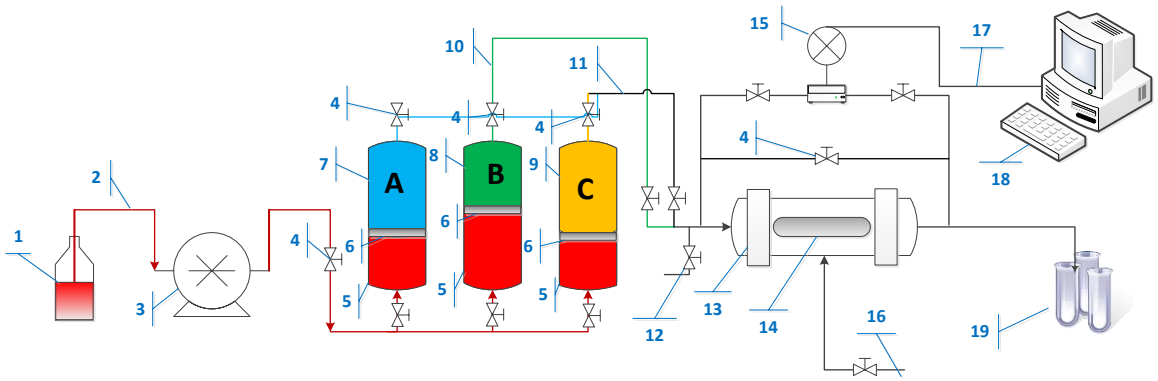

1) Pump fluid (Exxol D60); 2) injection line; 3) Quzix Pump; 4) Valve; 5) Pump Fluid in reservoir; 6) Piston plate; 7) Brine in reservoir-A; 8) Oil in reservoir-B; 9) Nanofluid in reservoir-C; 10) Oil line; 11) Brine/Nanofluid line; 12) Bypass Valve; 13)Hassler Core Cell; 14) Core plug ; 15) Pressure gauge; 16) Sleeve pressure; 17) connection cable; 18) Computer; 19) Accumulator

Figure 4 Schematic of flooding setup

EXPERIMENTAL METHODS

The core plugs were saturated by 3 wt. % brine using a vacuum pump to ensure there was no trapped air inside. Firstly, about 1 PV of brine was injected to measure core absolute permeability, and then about 4 or 5 PVs NSP or CNP nanofluid injection with different concentrations was followed to evaluate effect of nanoparticles adsorption and retention on permeability. Finally, brine injection was conducted as post-flush to observe desorption of nanoparticles, flow rate of 2 ml/min was utilized. Pressure drop across the core was recorded during whole injection process. Effluent fluid was collected every 4ml (1/4 PV) for NSP nanofluid flooding experiments, nanoparticles concentration was measured by using UV Spectrophotometer afterwards, 4-5 measurements were conducted for one sample to get average result.

RESULTS AND DISCUSSION

Oil Wet Core

Figure 5 shows the pressure drop of oil wet core flooding experiments for NSP and CNP nanofluid with different concentrations. There is big difference of pressure drop curve between NSP and CNP nanofluid injection cases. For NSP injection case pressure drop increased rapidly after nanoflud injection and the higher concentration the higher pressure drop, at end of nanofluid injection pressure was still continuing to climb and far away from equilibrium. During post-flush brine injection of NSP case pressure drop decreased gradually for all of three cores. Compared to adsorption process desorption process is slow but quite significant, pressure drop decreased about 30% during post-flush injection. CNP nanofluid injection showed different pressure drop curves, as Figure 5 right shows. There is no rapid pressure increase after CNP nanofluid injection and pressure still kept the same during post-flush period. The different nanoparticles adsorption behavior indicates the adsorption of NSP nanoparticles is multilayer while CNP might be monolayer.

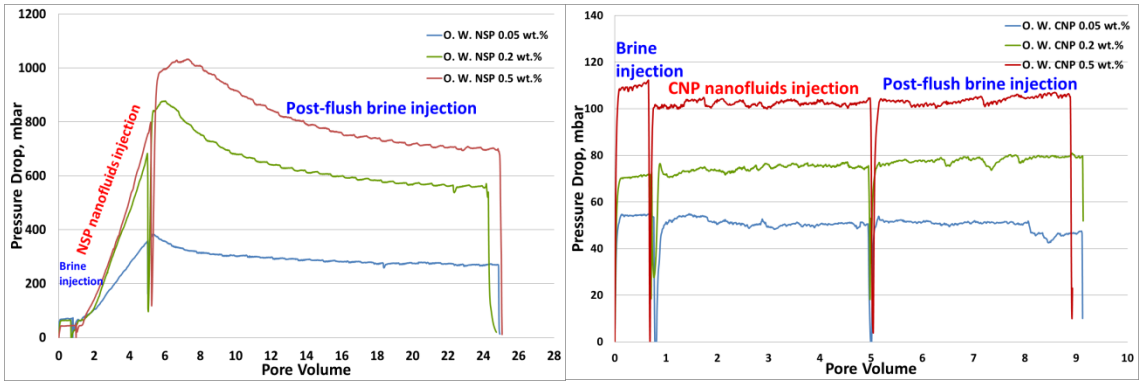

Figure 5 Pressure drop curves for oil wet cores (left: NSP, right: CNP)

Figure 6 shows dimensionless nanoparticles concentration curve of NSP nanoparticles transport through oil wet core plugs, the dimensionless nanoparticles concentration is defined as the ratio of effluent nanoparticles concentration to the injection nanoparticles concentration. As shown in Figure 6, 0.05 wt. % NSP nanofluid have earliest breakthrough while 0.5 wt. % NSP nanofluid have latest breakthrough. Effluent nanoparticles concentration can stay on plateau for about 3 to 4 PV and the lower concentration the longer plateau will be. For 0.2 and 0.5 wt. % cases concentration vibration is observed during plateau, the reason might be due to discontinuous adsorption and desorption, which means for injection of higher concentration nanofluid large amount of nanoparticles adsorbed and trapped inside core and resulted in blocking of pore channels as well as increase of pressure drop. While when pressure drop increased high enough adsorption or retention of nanoparticles can be detached and flushed out of core and then more adsorption and retention will happen again to recover previous balance until next breakthrough, this lead to decline of the effluent concentration. Similar vibration was also observed in pressure drop curve. The effluent concentration of three

cases decreased at about 5 PV during post-flushing. A "tail" of concentration curve was shown up after brine breakthrough, which means desorption of nanoparticles during post-flush injection.

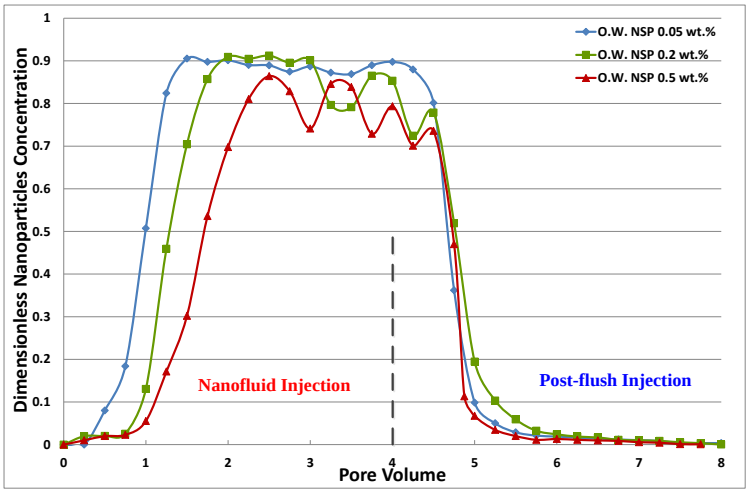

Figure 6 Effluent NSP nanoparticles concentration curves for oil wet cores

Neutral Wet Core

Pressure drop curves were plotted in Figure 7 for neutral wet core NSP nanofluid injection, three curves were plotted separately due to big scale difference. Similar with previous case, pressure drop increase very fast after nanofluid injection. The higher concentration the faster pressure drop increase will be. For 0.5 wt. % case both nanofluid injection and post-flush injection were terminated earlier because pressure almost reached to maximum limit of pressure gauge. Pressure drop decline result from nanoparticles desorption was observed. Permeability change before nanofluid and after post-flush was list in Table 2.

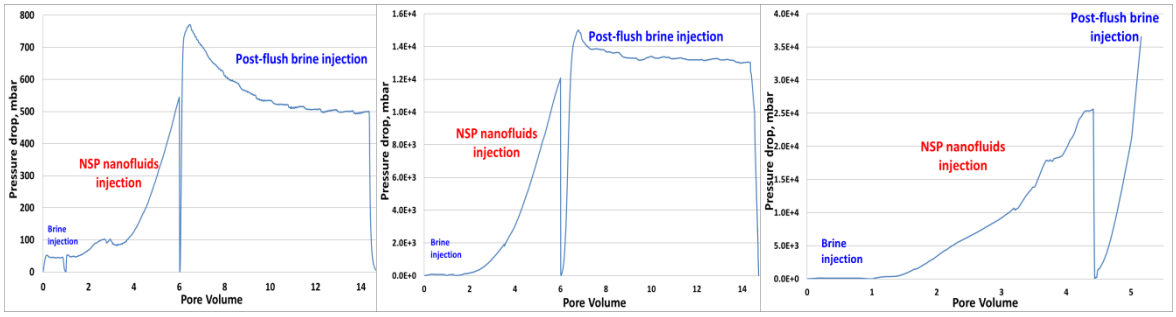

Figure 7 Pressure drop for neutral wet cores NSP nanofluid (left: 0.05 wt.%, middle: 0.2 wt.%, right: 0.5 wt.%)

Figure 8 shows pressure drop for neutral wet CNP injection, the pressure drop didn't change too much before and after nanofluid injection. Which means for neutral wet core adsorption of CNP is still monolayer while NSP adsorption is multilayers. For 0.2 and 0.5

wt. % cases after nanofluid injection pressure drop decrease somehow, which might mean that permeability increased. Table 2 shows that percentage of permeability change.

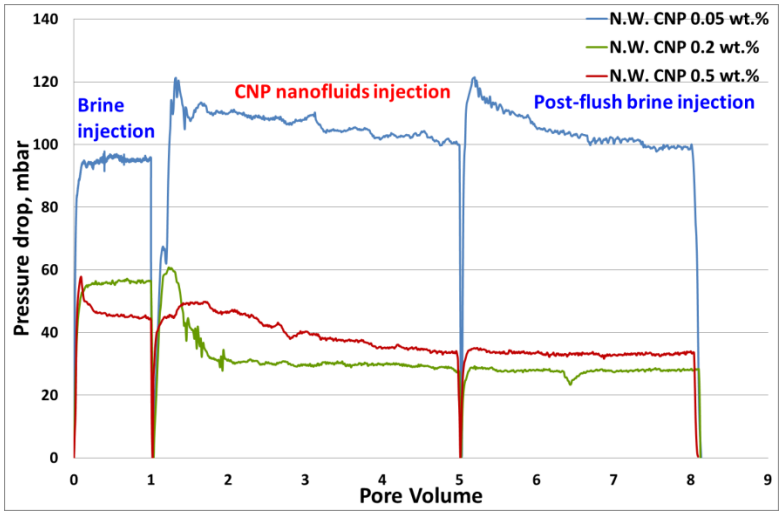

Figure 8 Pressure drop for neutral wet cores CNP nanofluid

Table 2 Permeability of core plugs

Injection scenario	K1, mD (before NP injection)	K2, mD (after NP injection)	K2/K1, %
O.W. NSP 0.05 wt.%	326.2	85.5	26.20
O.W. NSP 0.2 wt.%	361.8	41.1	11.37
O.W. NSP 0.5 wt.%	526.3	33.0	6.27
O.W. CNP 0.05 wt.%	428.9	509.0	118.70
O.W. CNP 0.2 wt.%	321.6	303.2	94.26
O.W. CNP 0.5 wt.%	210.5	228.8	108.66
N.W. NSP 0.05 wt.%	511.4	47.1	9.20
N.W. NSP 0.2 wt.%	326.7	1.8	0.55
N.W. NSP 0.5 wt.%	232.9	0.7	0.29
N.W. CNP 0.05 wt.%	247.6	237.6	95.96
N.W. CNP 0.2 wt.%	427.7	871.3	203.70
N.W. CNP 0.5 wt.%	522.8	691.9	132.35
W.W. NSP 0.05 wt.%	269.3	18.1	6.72
W.W. NSP 0.2 wt.%	463.2	5.9	1.28
W.W. NSP 0.5 wt.%	326.2	1.6	0.48
W.W. CNP 0.05 wt.%	367.6	361.8	98.44
W.W. CNP 0.2 wt.%	165.4	171.5	103.70
W.W. CNP 0.5 wt.%	308.8	361.8	117.19

Figure 9 shows effluent concentration of NSP nanoparticle for neutral wet core, 0.5 wt. % was not presented because not enough effluent samples were collected. 0.05 wt. % case

have earlier breakthrough than another one and for both of curves' effluent concentration started to decrease slowly when it reach to the peak. The dimensionless concentration reached only to about 40% maximally, which means most of nanoparticles were trapped inside core. During post-flush large amount of nanoparticles can be measured even at late of post-flush for 0.2 wt. % case.

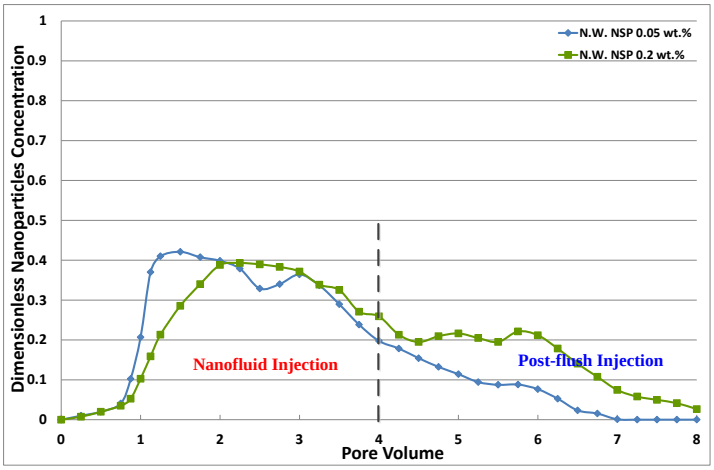

Figure 9 Effluent NSP nanoparticles concentration curves for neutral wet cores

Water Wet Core

Figure 10 left shows NSP nanofluid injection for water wet core, after nanofluid injection pressure drop behavior is similar with previous flooding cases. At end of nanofluid injection pressure curves of 0.5 wt. % case is much higher than another two cases. During post-flush pressure drop increased to plateau and kept constant until end of flooding for all of three concentrations nanofluid cases, which might mean that for water wet core there is no significant desorption of nanoparticles. Figure 10 right indicates that there is no significant pressure drop difference between CNP nanofluid injection and post-flush injection, meaning CNP adsorption is monolayer and will not impair permeability of core. Detail data of effect of nanoparticles adsorption on permeability change can be found in Table 2.

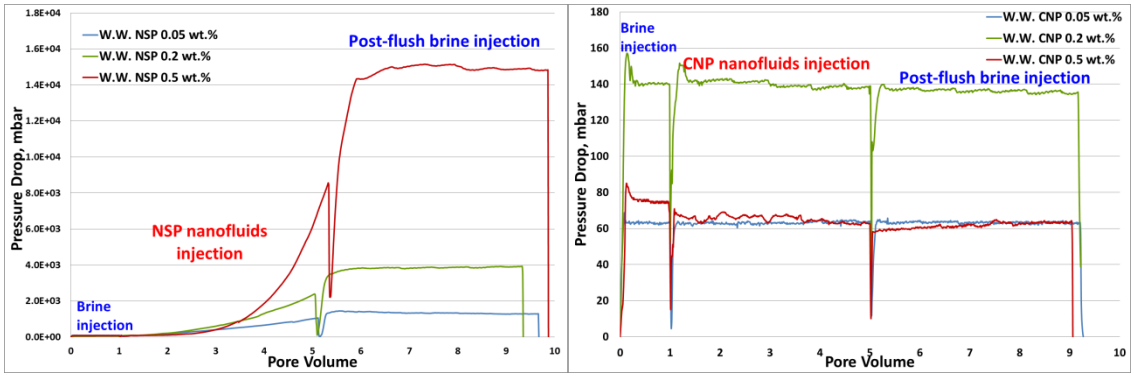

Figure 10 Pressure drop curves for water wet cores (left: NSP, right: CNP)

Effluent NSP nanoparticles concentration curves were plotted versus time and shown in Figure 11. Higher concentration nanofluid case had earlier breakthrough than lower concentration cases, but lower concentration nanofluid curve reached to peak faster than higher cases. The effluent concentration of all the curves decreases immediately after reaching the peak and concentration almost reduced to 0 at 5 PV, which shows a big amount of adsorption and retention of nanoparticles inside the core. The possible reason might be "self-adsorption" of nanoparticles, which means that the previous adsorbed nanoparticles can adsorb nanoparticles injected afterwards, so when adsorbed nanoparticles accumulate more enough the following injected nanoparticles cannot pass through core easily as before. During post-flush injection almost no desorption of nanoparticles after 5 PV, this is consistent with the conclusion from pressure drop.

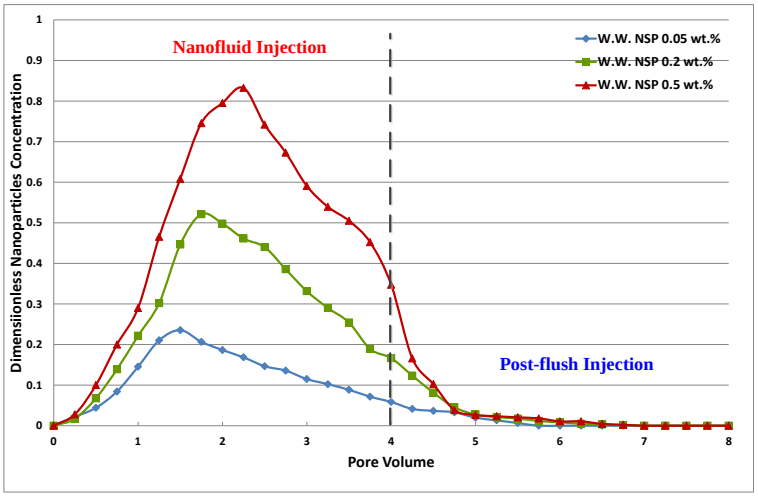

Figure 11 Effluent NSP nanoparticles concentration curves for water wet cores

Comparison of Nanoparticles Adsorption Behavior Against Different Wettabilities

As shown in above figures nanoparticles adsorption behavior is different for different wettability core. First of all, for higher concentration NSP nanofluid injection, neutral wet cores have higher pressure drop than other wettability cores at the same injection volume, while oil wet cores have lowest pressure drop during nanofluid injection. As shown in Figure 12 oil wet cores have highest recovery for nanoparticles, 80 to 90% nanoparticles can pass through core plug. Water wet cores have different recovery for various concentrations of nanofluid, the higher concentration of nanofluid the more nanoparticles can be recovered. While the neutral wet cores have lower dimensionless concentration, the maximum value is only 40%. Based on all of pressure drop data and effluent concentration curves, we can conclude that oil wet cores have lowest adsorption ability for nanoparticles and for higher concentration nanofluid neutral wet cores have highest adsorption ability of nanoparticles but for lower concentration of nanofluid water wet core can adsorb more than others. Desorption of nanoparticles was observed in oil wet and neutral wet cases, but was not presented in water wet cores as discussed above. The core permeability for each core at end of post-flush injection was calculated and listed in Table 2. The permeability for all of core plugs injected by NSP nanofluid has been

impaired dramatically, some of them reduced to less than 1% compared with original value.

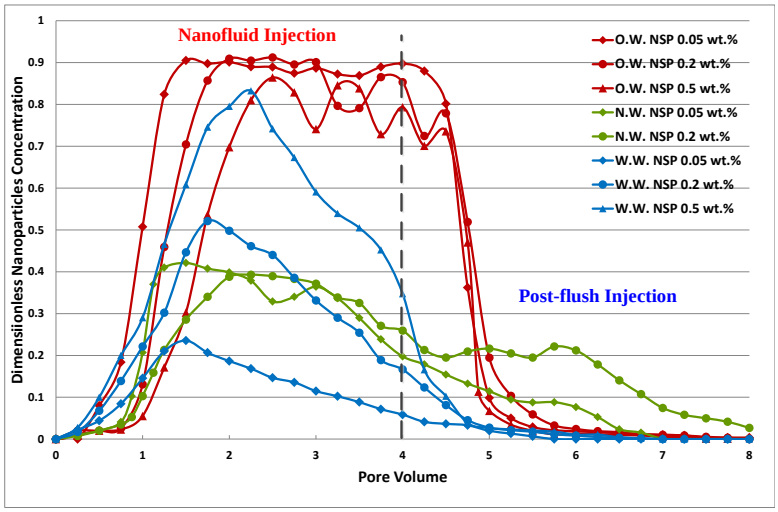

Figure 12 Comparison of effluent nanoparticles concentration curves for different wettability

For CNP nanofluid injection, nanoparticles adsorption is monolayer and will not impair core plug's permeability significantly, which means that after nanoparticles breakthrough most of particles can recovered. During post-flush pressure drop didn't change too much meaning desorption of CNP might be minor. There is no significant difference of CNP adsorption for all three different wettability core plugs. Permeability of cores was calculated and shown in Table 2, as we can see for some core plug permeability increased significantly, especially for neutral wet 0.2 wt. % case permeability double increase. The reason is still unclear, more experiments need to be done to find out the mechanism.

CONCLUSION

1. NSP and CNP have different adsorption behavior inside core plug. Adsorption of NSP is multilayer while CNP adsorption is monolayer. Amount of NSP adsorption is much larger than CNP and result in permeability impairment.
2. Adsorption behavior of NSP is various with different wettability of core. For oil wet core, most of nanoparticles can pass through core and plateau was present in concentration curves. However, neutral wet core adsorbs a large amount of nanoparticles resulting in high pressure drop. For water wet the higher nanoparticles concentration the more nanoparticles can be recovered, and nanoparticles "self-adsorption" was observed.
3. NSP has different desorption behavior against different wettability core plug, desorption happened during post-plush for both oil wet and neutral wet core, but there is no significant desorption of nanoparticles was observed for water wet core.
4. CNP adsorption is independent of wettability and nanoparticles concentration. Injection of CNP nanofluid will not impair core permeability, on the contrary it will increase permeability for some cores.

REFERENCES

1. Xiangling, K. and Ohadi, M.M. 2010. Applications of Micro and Nano Technologies in the Oil and Gas Industry - Overview of the Recent Progress. Paper presented at Abu Dhabi International Petroleum Exhibition and Conference, 1-4 November, Abu Dhabi.
2. Binshan, J., Tailiang, F. and Mingxue, M. 2006. Enhanced Oil Recovery by Flooding with Hydrophilic Nanoparticles. China Particuology 4, 41-46.
3. Suleimanov, B. A., Ismailov, F.S., and Veliyev, E.F. 2011. Nanofluid for enhanced oil recovery. Journal of Petroleum Science and Engineering 78, 431-437.
4. Hendraningrat, L., Li, S., and Torsæter, O. 2013. Enhancing Oil Recovery of Low-Permeability Berea Sandstone through Optimized Nanofluid Concentration. Paper presented at SPE Enhanced Oil Recovery Conference, Kuala Lumpur, Malaysia, 2-4 July.
5. Skauge, T., Spildo, K., and Skauge, A. 2010. Nano-sized Particles For EOR. Paper SPE 129933-MS presented at SPE Improved Oil Recovery Symposium, 24-28 April, Tulsa, Oklahoma, USA
6. Miranda, C.R., De Lara, L, S., and Tonetto, B, X. 2012. Stability and Mobility of Functionalized Silica Nanoparticles for Enhanced Oil Recovery Application. Paper presented at SPE International Oilfield Technology Conference, 12-14 June, Noordwijk,
7. Li, S., Hendraningrat, L., and Torsæter, O. 2013. Improved Oil Recovery by Hydrophilic Silica Nanoparticles Suspension 2-Phase Flow Experimental Studies. Paper IPTC-16707 presented at the International Petroleum Technology Conference held in Beijing, China, 26–28 March 2013.
8. Li, S., and Torsæter, O. 2014. An Experimental Investigation of EOR Mechanisms for Nanoparticles Fluid in Glass Micromodel. Paper SCA2014-022 was prepared for presentation at the International Symposium of the Society of Core Analysts held in Avignon, France, 8-11 September, 2014
9. Li, S., Torsæter, O. The Impact of Nanoparticles Adsorption and Transport on Wettability Alteration of Intermediate Wet Berea Sandstone. Published on SPE Middle East Unconventional Resources Conference held 26 – 28 January, 2015 in Muscat, Oman.
10. Li, S., Torsæter, O. Experimental Investigation of the Influence of Nanoparticles Adsorption and Transport on Wettability Alteration for Oil Wet Berea Sandstone. Published on 19th MEOS held 8 – 11 March, 2015 in Manama, Kingdom of Bahrain
11. Zhang, T., Murphy, M., Yu, H., Bagaria, H. G., Huh, C., and Bryant, S.L. Investigation of Nanoparticle Adsorption during Transport in Porous Media. Paper was prepared for presentation at the SPE ATCE held in New Orleans, 30 Sept.–2 Oct. 2013.
12. Kanj, M.Y., Funk, J. J., and Yousif, Z. A. 2009. Nanofluid Coreflood Experiment in the ARAB-D. Paper SPE-126161 was prepared for presentation at the SPE Saudia Arabia Section Technical Symposium, 9-11 May, AlKhobar, Saudi
13. Yu, J., An, C., Mo, D., Liu, N., Lee, R. Study of Adsorption and transportation behavior of Nanoparticles in Three Different Porous Media. Paper was prepared for presentation at the SPE Improved Oil Recovery Symposium, 14-18 April, Tulsa, USA (2012).

EFFECT OF HYDROSTATIC LOADING ON THE PORE STRUCTURE AND TRANSFER PROPERTIES OF A TIGHT GAS SANDSTONE

Yi WANG[(1)], Catherine DAVY[(1)], Franck AGOSTINI[(1)], Frédéric SKOCZYLAS[(1)], Laurent JEANNIN[(2)]
(1): LML UMR CNRS 8107/Ecole Centrale de Lille, CS20048,
59651 Villeneuve d'Ascq Cedex, France
(2): GDFSUEZ E&P International SA, 1 place Samuel de Champlain,
92930 Paris La Défense cedex - France

This paper was prepared for presentation at the International Symposium of the Society of Core Analysts held in St. John's, Newfoundland and Labrador, Canada, 16-21 August, 2015

ABSTRACT

Our study focuses on tight gas sandstones from a field located in North Africa and explored by GDFSUEZ E&P. This rock is characterized by its low porosity (below 10%) and its low absolute permeability (below 0.1mD i.e. $10^{-16}m^2$ under ambient conditions). A dedicated experimental setup has been designed to allow simultaneous measurements of gas permeability, connected porosity and poro-elastic properties, under given hydrostatic loading (up to 60 MPa). In the dry state, the decrease in accessible porosity is demonstrated experimentally: for one sample, accessible porosity is reduced by more than 10% (relative value) under 40 MPa hydrostatic loading. Simultaneously, gas permeability reduction is observed of a factor 8. In the partial water saturation state, the decrease in accessible porosity and effective gas permeability is enhanced. This shows an important stress sensitivity of the petrophysical properties of the sandstone: it is interpreted as pore entrapment under hydrostatic loading.

INTRODUCTION

Tight gas reservoirs are unconventional gas reservoirs constituted of low permeability sandstones, which are characterized by low connected porosity (lower than 10%), low absolute permeability (below 0.1mD i.e. $10^{-16}m^2$ under ambient conditions), and strong sensitivity to *in situ* stress as compared to conventional reservoirs [1-3]. Although these unfavorable properties make them more complicated to explore than conventional ones, tight reservoirs have a great potential in terms of gas production [4,5].

For their economical exploitation, characterization of the petrophysical properties of tight reservoirs is necessary. This paper presents the assessment of the effect of hydrostatic stress on the petrophysical properties of a particular sandstone, in both dry state and partially water-saturated state. We also relate the effect of hydrostatic stress to the changes in pore structure, by assessing the changes in connected pore volume.

Firstly, gas permeability and connected pore volume are investigated in the dry and in the partially water saturated state, under different confining pressures. Secondly, we compare variations in pore volume during loading and unloading to sample deformation, in order to confirm our interpretation of pore entrapment. Thirdly, we measure sandstone poro-elastic properties, in order to obtain a relationship between the externally applied stress and the drained bulk modulus K_b (or the solid matrix bulk modulus K_s). This allows getting further insight into the pore structure changes.

EXPERIMENTAL METHODS

Sample Preparation And Water Porosity Measurement

The samples of tight gas sandstone used in this study originate from a field located in North Africa [6], from depths between -2000 m and -2550 m. They are received by our laboratory as cylinders with a diameter of 37 mm, and a length cut to 60 mm.
Water porosity ϕ_w is defined as:

$$\phi_w = \left(m_{sat} - m_{dry}\right)/\left(\rho_w V_{sample}\right) \quad (1)$$

where m_{sat} and m_{dry} are respectively the water-saturated mass and the dry mass, ρ_w is water density and V_{sample} is the sample bulk volume. m_{dry} is obtained by oven-drying the sample at 105ºC, and regular weighing until the mass does not change by 0.01g for one whole week. Similarly, for m_{sat}, samples are water-saturated under vacuum until mass stabilization.

Partial Water Saturation State And Sample Conditioning

Partial water saturation S_w is defined as:

$$S_w = \left(m - m_{dry}\right)/\left(m_{sat} - m_{dry}\right) \quad (2)$$

In order to achieve a given S_w, a specific method is used, which corresponds to that recommended by RILEM [7], as follows. Firstly, sample water-saturated and dry masses are assessed; the dry sample is then water saturated until reaching the desired mass m. It is then sealed in three aluminium layers, and one layer of paraffin. Following this, it is kept in a climatic chamber at 40 ºC for at least 14 days, to allow water to have a homogeneous distribution in the sample.

Gas Permeability Measurement

Gas permeability of each sandstone sample is measured with the quasi-stationary fluid flow method [8,9]. The test is performed in a hydrostatic cell where the sample is sealed in a Viton Jacket (Figure 1). A buffer reservoir with a manometer is set up outside the hydrostatic cell between the source of gas and the sample. At first, when valve V_3 is closed and V_1, V_2 and V_4 are open, gas flows from the source of gas, *via* the buffer reservoir, until reaching a steady state. At steady state, the upstream side of the sample is

at pressure P_1, while the pressure on the downstream sample side P_0 is equal to the atmospheric pressure. Then, valve V_1 is closed at time $t = 0$, and we measure the time necessary for upstream gas pressure to decrease by ΔP_1 (ΔP_1 is less than one 1% of P_1). During Δt, gas is assumed to flow steadily at an average pressure $P_{mean} = P_1 - \Delta P_1 / 2$ on the upstream side, and the average volume flowrate is given by:

$$Q_{mean} = \frac{V_1 \Delta P_1}{P_{mean} \Delta t} \tag{3}$$

where V_1 is the buffer reservoir volume. Finally, gas permeability is given by simplified Darcy's law [10]:

$$K_x = \frac{\mu Q_{mean}}{A} \frac{2LP_{mean}}{\left(P_{mean}^2 - P_0^2\right)} \tag{4}$$

where L is sample length, A is its sectional area and μ is the dynamic viscosity of gas (here Argon is used with $\mu = 2.2 \cdot 10^{-5} Pa \cdot s$).

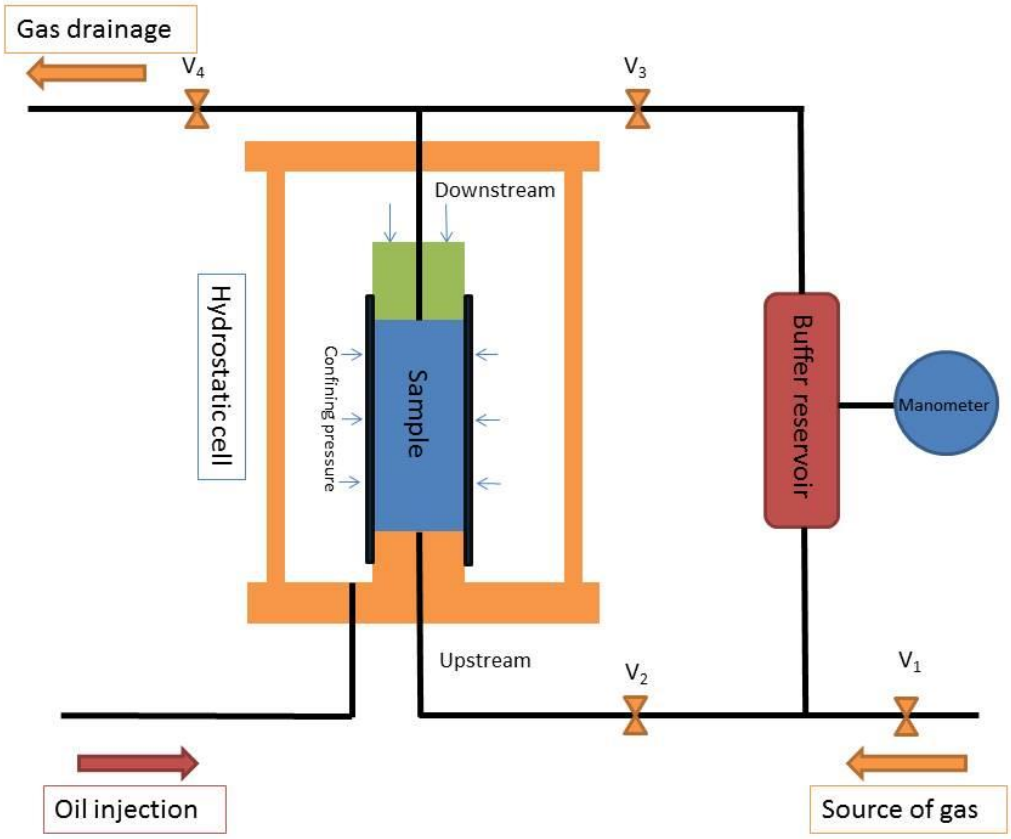

Figure 1 Principle for the quasi-stationary fluid flow method for gas permeability measurement

Measurement of Gas-accessible Pore Volume

This test quantifies the accessible pore volume under a given confining pressure [11,12]. The interpretation of this method is based on the ideal gas law:

$$PV = nRT \tag{5}$$

As shown in Figure 1, the sample is placed in the hydrostatic cell under given confining pressure. The buffer reservoir, of known volume Vr, is isolated from the rest of the circuit (by closing valves V_2 and V_3), and it is filled with gas at an initial pressure $P_{initial}$ (this is achieved by closing valve V_1 when reaching the desired pressure) while the sample is at atmospheric pressure. While valve V_4 is closed, the opening of valves V_2 and V_3 connects the buffer reservoir to the sample by both ends, while all other valves (V_1 and V_4) remain closed. From this moment, gas enters the sample connected pores and pressure P measured in the buffer reservoir decreases until reaching stabilization at a value P_{final}. Owing to the conservation of the gas mass initially located in the buffer reservoir, the relationship between $P_{initial}$ and P_{final} writes:

$$P_{initial}Vr = nRT = P_{final}\left(Vr + V_{pore}\right) \tag{6}$$

So that the accessible pore volume is determined by:

$$V_{pore} = \left(\frac{P_{initial}}{P_{final}} - 1\right)V_r \tag{7}$$

If the sample is in the dry state, the porosity accessible to gas is deduced as:

$$\phi_g = \frac{V_{pore}}{V_{sample}} \tag{8}$$

where V_{pore} is calculated by Equation (7) and sample volume V_{sample} is determined by hydrostatic weighing (using Archimedes' law): first, the dry sample is weighted, then it is submerged in water, and its weight under water (equal to its dry weight minus the weight of water occupying the volume of the sample) is measured. Sample volume is the difference between the two weights divided by the density of water.

Poro-Elastic Property Measurement

The measurement of poro-elastic properties is based on the theory of Biot [14]. The saturated porous material is considered as the superposition of two continua: the solid matrix and the fluid present in the pores. In the following, in a first approach, the porous medium (solid matrix+pores) is considered isotropic.

The drained bulk modulus K_b represents the deformability of the whole material i.e. of the so-called solid skeleton. The solid skeleton is constituted of connected and non-connected pores, and of the solid matrix [13]. K_b is measured under constant pore pressure (often equal to atmospheric pressure, as used here), by varying the hydrostatic stress by a small ΔP_c, so that K_b is given by:

$$K_b = \frac{\Delta P_c}{\Delta \varepsilon_{v1}} \tag{9}$$

where $\Delta\varepsilon_{v1}$ is the volumetric strain variation due to the variation in confining pressure ΔP_c.

The solid matrix bulk modulus K_s represents the rigidity of the solid matrix, which is composed of the solid and of the non-connected porosity alone [14]. In order to determine directly K_s, the variation in sample volumetric strain $\mathrm{D}e_v$ is measured when the same variation in interstitial pore pressure $\mathrm{D}p$ and in confining pressure $\mathrm{D}P_c = \mathrm{D}p$ is achieved:

$$K_s = \frac{\mathrm{D}p}{\mathrm{D}e_v} \tag{10}$$

However, in order to avoid dealing with equal gas and confining oil pressures (which would mean extensive test leakage) , $\Delta p = \Delta P_c$ may be difficult to obtain. K_s is rather calculated from the measurement of modulus *H*, which is by varying pore pressure by an amount Δp when hydrostatic stress is kept constant [11-13], as:

$$H = \frac{\Delta p}{\Delta \varepsilon_{v2}} \tag{11}$$

where $\Delta\varepsilon_{v2}$ is the volumetric strain variation due to the variation in pore pressure Δp.
Finally K_s is given by [11-13]:

$$\frac{1}{K_s} = \frac{1}{K_b} - \frac{1}{H} \tag{12}$$

Generally, strain gauges are used to measure sample longitudinal and radial deformations. In this study, four LVDT sensors are used to measure longitudinal strains (Figure 2). As our sandstone samples are considered isotropic, the volumetric deformation ε_v is calculated by:

$$\varepsilon_v = \frac{3}{4}\left(\varepsilon_1 + \varepsilon_2 + \varepsilon_3 + \varepsilon_4\right) \tag{13}$$

When compared to strain gauges, using LVDT sensors has several advantages:

1) Sample length changes are measured directly without sample surface preparation and the assembly of the hydrostatic cell is simplified.
2) The problem of strain gauge bonding, especially on partially saturated samples is avoided.
3) The bonding of strain gauges and electric wire soldering can suffer from saturation/drying cycles, and from confining pressure changes.

4) By avoiding sample surface preparation and the use of glue, the measurement of sample mass variation before and after the experiment is more accurate.

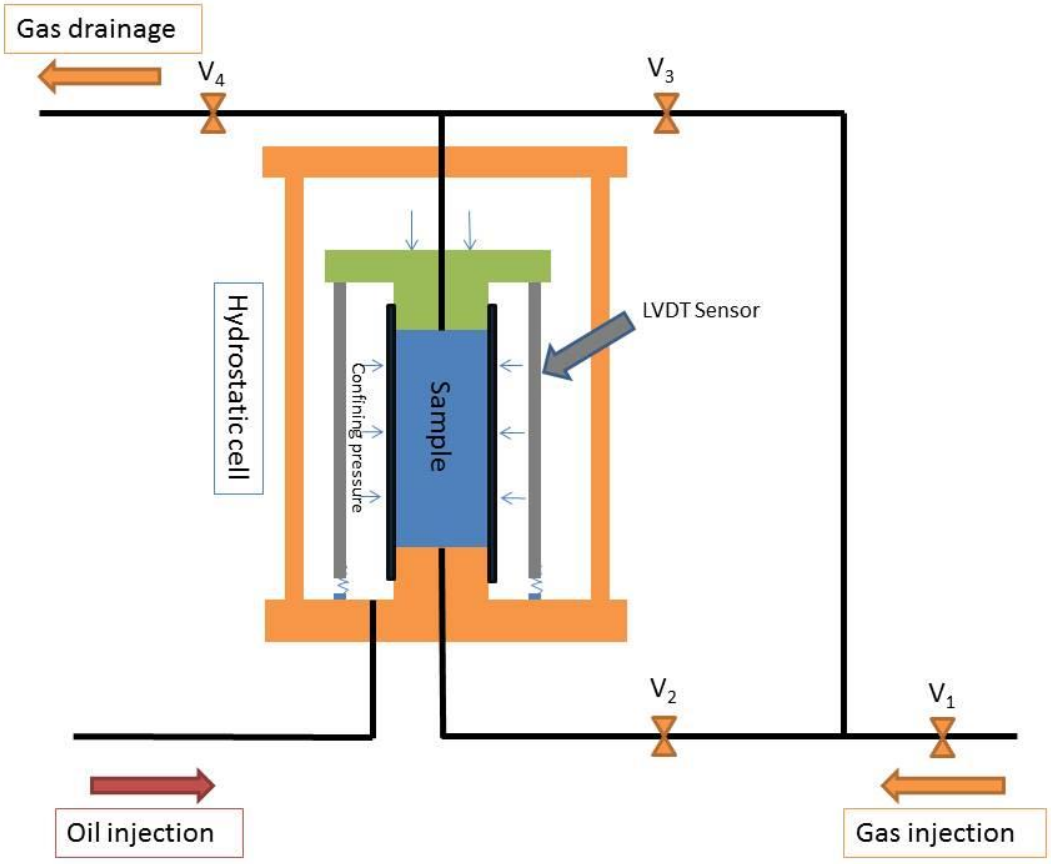

Figure 2: LVDT measurement system

RESULTS AND DISCUSSION

Water porosity

Water porosity results (Table 1) indicate that the tested samples have small water porosity values, with variations from 1.52% to 4.96%. No clear correlation is found between water porosity and drilling depth. This absence of correlation is expected [15, 17, 18]. Drilling depth has some influence on porosity, but it is not the determining factor: porosity also depends on diagenetic conditions (e.g. *in situ* chemical transformations of minerals) [6].

Table 1 Water porosity of tight sandstone samples

Number	2335	3248	3249	3250	3372	3375	3377	3379	4456	4458
Water porosity (%)	4.96	3.37	3.83	3.88	2.05	2.93	1.81	1.52	2.54	2.78
Depth (m)	2359	2181	2080	2197	2501	2496	2511	2516	2312	2311

Gas Permeability In The Dry State

Normalized dry gas permeability is defined as $K_{drynorm} = K(P_c)/K(P_c = 3MPa)$, where $K(P_c)$ is dry gas permeability under confining pressure P_c, $K(P_c = 3MPa)$ is that under confining pressure $P_c = 3MPa$. Figure 3 illustrates the evolution of normalized dry gas permeability over a range of confining pressures from 3 MPa to 40 MPa. A decrease in $K_{drynorm}$ by 90% is observed for the three samples presented in Figure 3, when hydrostatic stress reaches 40 MPa. This underlines the important stress sensitivity of the material. Samples 3249 and 3248 show almost the same type of $K_{drynorm}$ variation while 3379 seems to be more stress-sensitive. This is compared to the accessible porosity of those samples: samples 3249 and 3248 have comparable porosities (3.83% and 3.37% respectively), while sample 3379, which is more sensitive to P_c changes, has a lower porosity (of about 1.52%). This has already been observed in a previous study on tight Rotliegend sandstones from Germany [15].

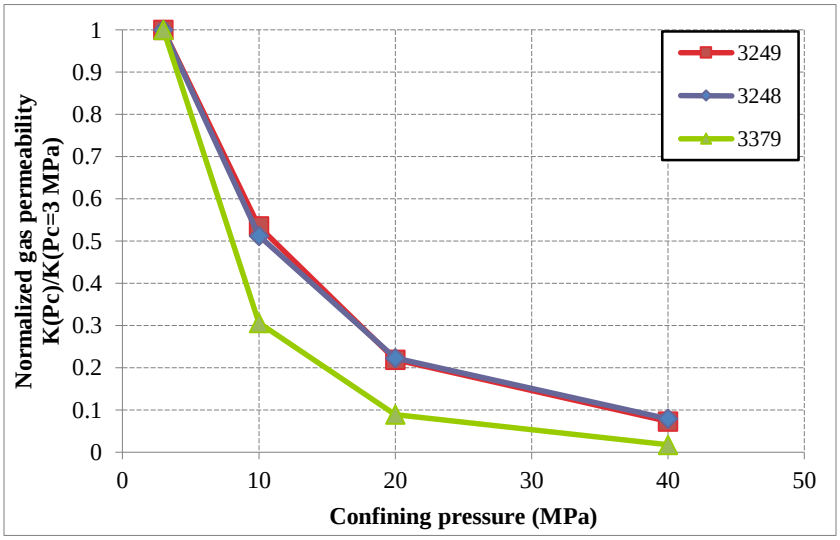

Figure 3: Normalized gas permeability for dry sandstone samples

Porosity And Pore Volume Variation In The Dry State

Similar stress-sensitivity is observed with normalized porosity, which is defined as $\phi_{norm} = \phi(P_c)/\phi(P_c = 3MPa)$ (Figure 4). Samples 3249 and 3248 lose nearly 10% of their porosity when confining pressure varies from 3 MPa to 40 MPa, while sample 3379 loses 25% of porosity. The loss of porosity is so large, that it is difficult to explain by the poro-elastic behaviour of the sandstone in terms of volume changes. It may well be indicative of the entrapment of pores in the solid skeleton.

To confirm this assumption, let us take sample 3248 as an example. The variation of pore volume as a function of sample volume variations (given by LVDT sensors) is shown in Figure 5. According to the poro-mechanics theory for isotropic media, a value of Biot coefficient equal to 1 implies that the variation in pore volume is identical to the variation

in sample volume: this is generally observed for granular media. For cohesive rocks such as tight sandstones, Biot's coefficient is smaller than 1, so that the variation in sample volume is greater than the variation in pore volume [14]. However, the reduction in pore volume is greater than the reduction in sample volume (Figure 5), even for moderate P_c (between 3 MPa and 10 MPa). This is explained by the closing of micro-cracks in the pore structure, which induces an occlusion of pores in the solid skeleton [12,15]. Above P_c = 10 MPa, accessible pore volume variation is parallel to the theoretical line corresponding to Biot's coefficient=1. Our interpretation is that micro-cracks are closed below P_c = 10 MPa: above this value, the material behavior is governed by its poro-elastic properties.

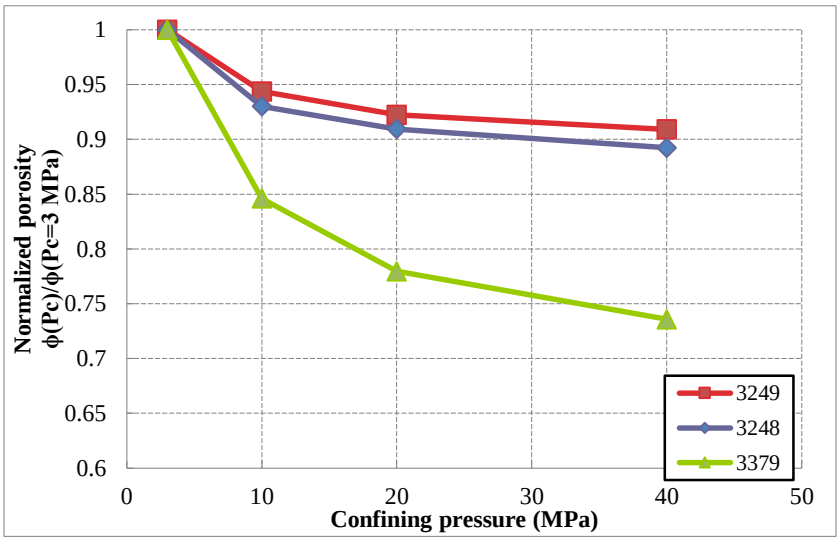

Figure 4 Normalized porosity for dry samples

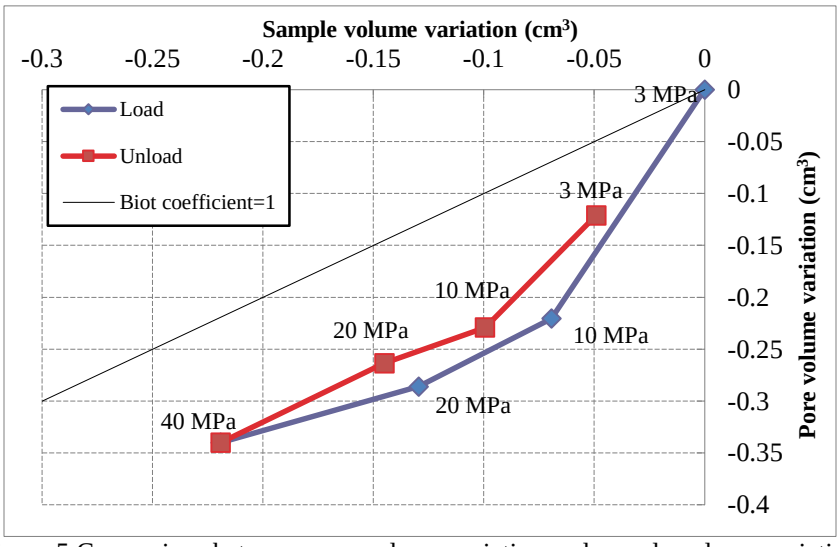

Figure 5 Comparison between pore volume variation and sample volume variation

Poro-elastic Properties In The Dry State

In order to confirm the changes in pore structure (entrapment under increasing P_c), poro-elastic properties K_b and K_s are assessed under different confining pressures. As shown in Figure 6, for the three samples, the effect of P_c is more important for low confinement. Between P_c = 3 and 10 MPa the increase in K_b reaches about 200%, and increases an additional 50% between P_c = 10 and 40 MPa. Finally at P_c = 40 MPa, K_b increases to about 20 GPa. Similar stiffness values are also observed for other such tight sandstones [14].

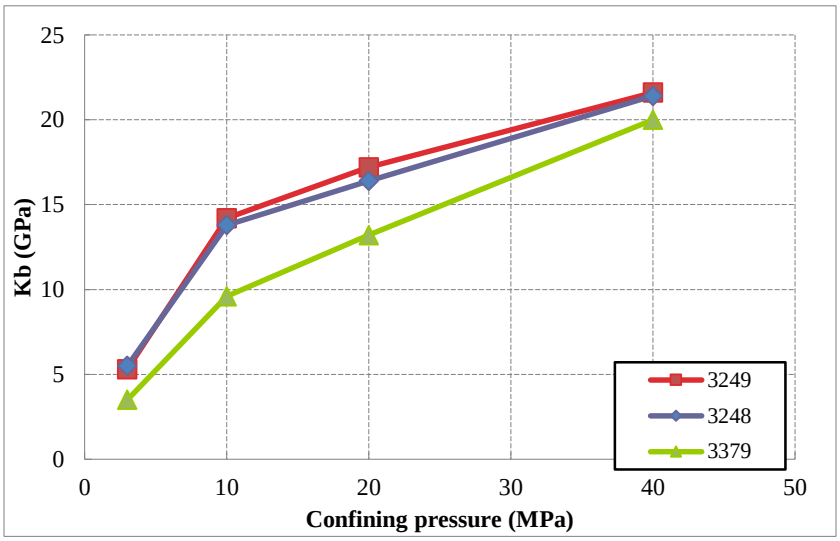

Figure 6 Drained bulk modulus K_b as a function of confining pressure

However, difficulties have been encountered when measuring the solid matrix bulk modulus K_s, which are quite high (above 20 GPa). When an interstitial pore pressure is applied, only small deformations of the solid matrix occur, which induces an important uncertainty to the measurement. Further effort shall be dedicated to accurately assess the value of K_s, as in [14].

Gas Permeability In A Partially Water Saturated State

In the partially water saturated state, normalized gas permeability is the ratio between gas permeability in the partially water saturated state at given P_c and gas permeability in the dry state at P_c =3MPa: $K_{norm} = K(P_c)/K(P_c = 3MPa)$. It is plotted under increasing confining pressure for sample 3249 in Figure 7. It is observed that K_{norm} is more stress-sensitive than in the dry state. For Sw = 25.6%, between P_c = 3 and 10MPa, normalized permeability has decreased significantly, by 70%. The sharp decrease continues until confining pressure reaches P_c = 20 MPa. Above this confining pressure value, normalized permeability shows little variation. This behavior is highly dependent on the structure of the pore network and on pore size distribution. The decrease in K_{norm} when P_c increases indicates that the pores, which have closed under increasing P_c, were significantly

participating in gas flow, so that they were not filled with water, although the material is in a partial water saturated state. Further interpretation will be conducted on this aspect with the help of Mercury Intrusion Porosimetry (MIP), Scanning Electron Microscopy (SEM) investigations and micro mechanical modelling [16].

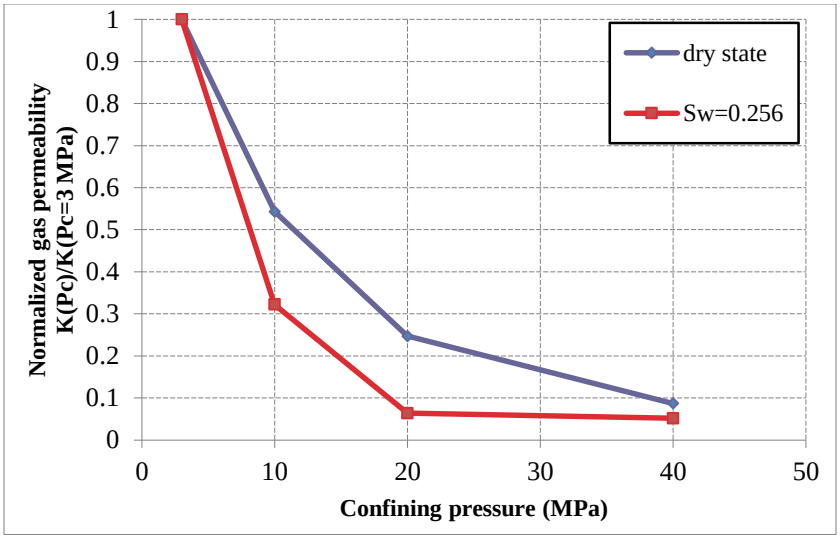

Figure 7 Normalized gas permeability of sample 3249 in the dry and partially water saturated states

Gas Accessible Pore Volume In A Partially Water Saturated State

The water saturation has a greater influence on gas-accessible pore volume, than on normalized permeability (
Figure 8). Large reductions are observed for Sw = 25.6%, especially when confining pressure P_c increases from 10 MPa to 20 MPa: a large portion of nearly 30% of the gas-accessible pore volume is lost.

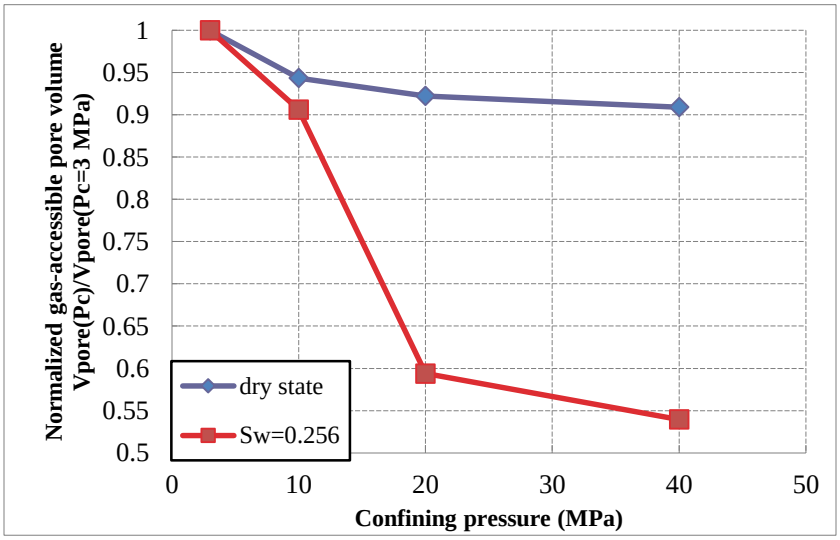

Figure 8 Normalized gas-accessible pore volume of sample 3249 in the dry and partially water saturated states

From Figure 7 and
Figure 8, we conclude that in the partially water saturated state, the evolution of permeability and gas-accessible pore volume do not evolve so smoothly as in the dry state: in the partially water saturated state, the major decrease in permeability occurs at the beginning of loading, while relative pore volume decreases mainly under intermediate confining pressures (10MPa to 20MPa). Further investigations and a dedicated micro-mechanical model are required for a proper interpretation.

CONCLUSION

This experimental study deals with samples from a tight gas reservoir. First, gas permeability is investigated under different confining pressures. For samples in the dry state, we show a great stress-sensitivity of normalized gas permeability. Additionally, sample 3379, with a smaller initial porosity, is more sensitive to external stress than the other two samples. The partial water saturation of the samples increases the sensitivity of permeability to changes in P_c. Secondly, gas accessible pore volume is measured under confining pressure. Large losses in pore volume are observed in dry state, which is attributed to pore entrapment, which occurs when micro-cracks close under increasing confining pressure. This phenomenon is more visible in a partially water saturated state. The variation in pore volume is compared with that of sample volume: under increasing P_c, a large loss of pore volume is observed, which is also an evidence of pore entrapment. Thirdly, poro-elastic experiments are conducted to provide further information on sample structure: it is observed that the drained bulk modulus K_b increases steadily under increasing P_c loading.

The interpretation of those tests requires further investigation. Rock micro-structure shall be assessed by Scanning Electron Microscopy (SEM) and Mercury Intrusion Porosimetry (MIP). The use of a micromechanical model will provide a prediction of petrophysical properties for the reservoir.

ACKNOWLEDGEMENTS

We gratefully acknowledge financial support by GDFSUEZ E&P International SA.

REFERENCES

1. Cluff, R. M., and A. P. Byrnes. "Relative Permeability In Tight Gas Sandstone Reservoirs-The ‘Permeability Jail’ Model." *SPWLA 51st Annual Logging Symposium*. Society of Petrophysicists and Well-Log Analysts, (2010).
2. Blasingame, T. A. "The characteristic flow behavior of low-permeability reservoir systems." *SPE Unconventional Reservoirs Conference. Keystone, Colorado, USA*. (2008).
3. Ward, J. S., and N. R. Morrow. "Capillary pressures and gas relative permeabilities of low-permeability sandstone." *SPE Formation Evaluation*, (1987) vol.2, no.03, 345-356.

4. Jiang, L. Z., J. Y. Gu, and B. C. Guo. "Characteristics and mechanism of low permeability clastic reservoir in Chinese petroliferous basin." *Acta Sedimentologica Sinica*, (2004) vol.22, no.1, 13-18.
5. Kang, Y. l., and P. Y. Luo. "Current status and prospect of key techniques for exploration and production of tight sandstone gas reservoirs in China." *Petroleum Exploration and Development*, (2007) vol.34, no.2, 239.
6. Tournier, F., et al. "Relationship between deep diagenetic quartz cementation and sedimentary facies in a Late Ordovician glacial environment (Sbaa Basin, Algeria)." *Journal of Sedimentary Research*, (2010) vol.80, no.12, 1068-1084.
7. Hilsdorf, H. K., and J. Kropp. "Permeability of Concrete as a criterion of its durability." *Report of RILEM Technical Committee TC*, (1992) vol.116.
8. Skoczylas, F., *Ecoulements et couplages fluide-squelette dans les milieux poreux: études expérimentales et numériques*., Dissertation, (1996).
9. Meziani, H., and F. Skoczylas, "An experimental study of the mechanical behaviour of a mortar and of its permeability under deviatoric loading." *Materials and structures*, (1999) vol.32, no.6, 403-409.
10. Davy, C. A., F. Skoczylas, P. Lebon, Th. Dubois, "Permeability of macro-cracked argillite under confinement: gas and water testing." *Physics and Chemistry of the Earth*, (2007) vol.32, no.8, 667-680.
11. Chen, X. T., *Effet du chauffage sur le comportement mécanique et poro-mécanique de matériaux cimentaires: propriétés hydrauliques et changements morphologiques*., PhD Dissertation, (2009).
12. Chen, X. T., G. Caratini, C. A. Davy, D. Troadec, F. Skoczylas, "Coupled transport and poro-mechanical properties of a heat-treated mortar under confinement." *Cement and Concrete Research*, (2013) vol.49, 10-20.
13. Coussy, O., *Poromechanics*. John Wiley & Sons, Chichester, (2004).
14. Duan, Z., C. A. Davy, F. Agostini, L. Jeannin, D. Troadec, F. Skoczylas "Gas recovery potential of sandstones from tight gas reservoirs." *International Journal of Rock Mechanics and Mining Sciences*, (2014) vol.65, 75-85.
15. Fu, X., *et al.* "Effect of mechanical loading and water saturation on the gas recovery of tight gas: experimental study." *2012 International Symposium of the society of Core Analysts*. Aberdeen, SCA, (2012), 27-30.
16. Dormieux, L., L. Jeannin, and N. Gland. "Homogenized models of stress-sensitive reservoir rocks." *International Journal of Engineering Science*, (2011) vol.49, no.5, 386-396.
17. Ramm, M., and K. Bjørlykke, 1994, Porosity/depth trends in reservoir sandstones: Assessing the quantitative effects of varying pore-pressure, temperature history and mineralogy, Norwegian shelf data: Clay Minerals, v. 29, p. 475 – 490.
18. Ehrenberg S. N., Nadeau P. H., Sandstone vs. carbonate petroleum reservoirs: A global perspective on porosity-depth and porosity-permeability relationships, AAPG Bulletin, v. 89, no. 4 (April 2005), pp. 435 – 445.

MICRO-SEISMIC EVALUATION OF FRACTURING IN CORES DURING TRIAXIAL COMPRESSION TESTS

Y. Xiao, A. Abugharara and S.D. Butt
Advanced Drilling Laboratory, Memorial University of Newfoundland, St. John's, NL, Canada

This paper was prepared for presentation at the International Symposium of the Society of Core Analysts held in St. John's Newfoundland and Labrador, Canada, 16-21 August, 2015

ABSTRACT

This study is an evaluation of rock cracking and failure by means of laboratory standard strength tests and real time micro-seismic or acoustic emission (AE) monitoring. Three groups of rock-like materials were cast using fine aggregate and Portland cement, out of which standard test specimens were cored. Confined compression strength (CCS) tests were conducted on those cores while two non-destructive testing (NDT) sensors were placed in end platens used to compress the core. Conventional rock mechanics results were obtained such as stress-strain response. Hundreds of micro-seismic events were recorded in the process of rock deformation and especially when the core failed. Seismic data processing indicated the synchronization of event occurrence rate with correlated material deformation. Also, micro-seismic properties were analyzed such as dominant frequency (DF), event energy and cumulative AE counts. Event energy was found closely related to the peak amplitude of seismic waves. Under the same confining pressure, DF was prone to decrease with increase of deformation until the core failed. This correlated with the higher AE event rate when deformation increased. High strength material tended to generate higher DF than that of low strength material. For the same strength material, increasing confining pressure played different roles on the dominant frequency. Finally, AE event occurrence locations were determined along the core length which was compared with the observation of core surface cracks.

INTRODUCTION

Micro-seismic events or AE are the elastic waves produced when rock undergoes internal change, such as micro-crack initiation and propagation. Piezoelectric transducers are commonly employed in detecting and monitoring micro-crack propagation [1]. As an alternative way to 'see' micro-crack initiation and propagation, AE detection was applied in triaxial compression tests to monitor the whole deformation process [2]. Some AE parameters such as DF, event energy and cumulative AE counts are related to the different deformation stages [3, 4]. Source location was conducted to identify the approximate location of AE events applied in hydraulic fracturing researches [5, 6, 7]. Numerical simulation was used to simulate the deformation process and predict the failure [8, 9]. Crack type was also classified based on detected acoustic emissions for failure prediction [10, 11, 12, 13].

EXPERIMENTAL SETUP

Monitoring AE during the CCS test was scheduled. The CCS tests were conducted using a servo-controlled axial loading frame and a Hoek triaxial pressure cell. AE were recorded using a two-sensor AE system.

Axial Loading Frame

During the CCS test, axial load was applied by the Instron load frame (Figure 1). The maximum loading could be 250 kN. By setting the loading rate of 1 mm/min, extension and load were recorded until the core specimen failed. The core was put into the Hoek triaxial cell and specific confining pressure was loaded by a manually operated pump.

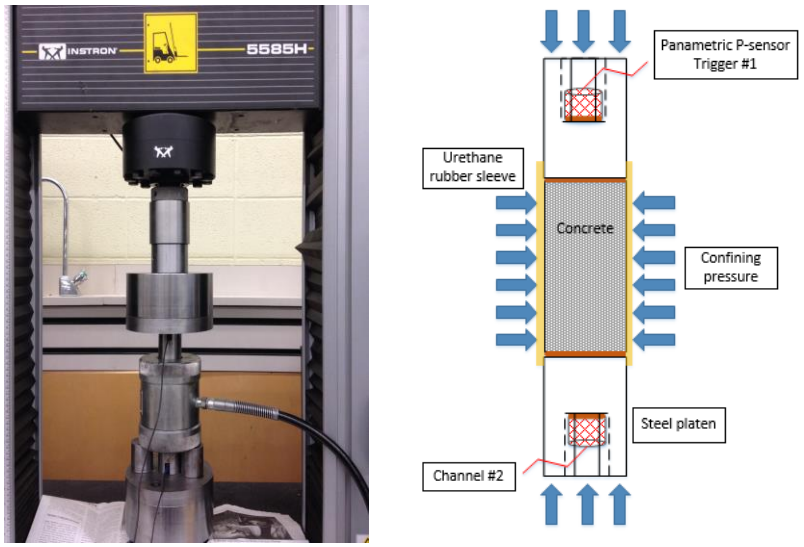

Figure 1. Strength test apparatus with the Hoek triaxial cell (left) and working schematic (right).

Monitoring Acoustic Emission

Two Panametrics p-wave sensors were placed into steel platens on both ends of core specimens (Figure 1). Sponge material was put between the sensors and the loading frame for complete contact assurance and p-wave couplant was put between the steel platens and core ends and between sensors and steel platens to make better signal transmittal. The central frequency of the p-wave sensors was 1.14 MHz with working bandwidth of from 0.65 to 1.63 MHz at -6dB attenuation. Two PAC 2/4/6 preamplifiers were utilized and gain selection of 40dB. Two customized power supply adapters were connected to the preamplifiers with output voltage of 20 volt. The DAQ system was comprised of GaGe CompuScope 8280 eight-channel board and its included DAQ software. The trigger sensor was always located on the top of cores. Inputs for AE detection are listed in Table 1.

Table 1. Inputs for monitoring acoustic emission.

Sampling frequency	P-wave sensors #	Gain	Peak-peak input	Trigger level
10 MHz	2	40 dB	10 V	0.15 V

Test Materials

Three groups of rock-like materials were used with UCS (0 confining pressure) at 20, 55.5 and 87.5 MPa, designated as low, medium and high strengths (L, M and H) in Figure 2. These materials were made of fine aggregate, Portland cement and water. This type of rock-like materials has been used in all previous lab tests in this project based on the ability of the reproducibility. Such tests were performed to study the drill-ability including AE. In this paper, AE tests were conducted to investigate the deformation and cracking properties which were valuable for future bit-rock interaction investigation, but petroleum cores were not involved. Standard NQ cores were drilled with core diameter of 47.6 mm and the minimum ratio of height to diameter was 2:1. All the coring process and requirements were done in accordance to ASTM D4543 [14]. Averaged core dimensions and the loading plan are given in Table 2. To be consistent with the investigation of rock-like material's properties and mechanical response, confining pressures were chosen in accordance to previous rock characterization tests.

Figure 2. Tested concrete cores (low, medium and high strength).

Table 2. Loading plan for triaxial compression test and CCS results.

Core #	Length (mm)	Diameter (mm)	P-wave velocity (m/s)	Conf. Pres. (MPa)	CCS (MPa)
L1	111.64	47.23	4304.0	2	33.90
L2	105.04	47.22	4304.0	4	41.48
M1	100.79	47.38	4785.4	2	59.84
M2	103.47	47.18	4785.4	4	75.36
H1	108.39	47.43	4710.4	2	105.65
H2	104.88	47.51	4710.4	4	116.11

Overall Workflow

The overall flow chart for this test is shown in Figure 3. Acoustic emission signals from cracking were automatically detected and saved to the AE computer disk. At the same

time, CCS test was being conducted and the stress and strain data were recorded into the other computer. Both the computers were synchronized before each test began.

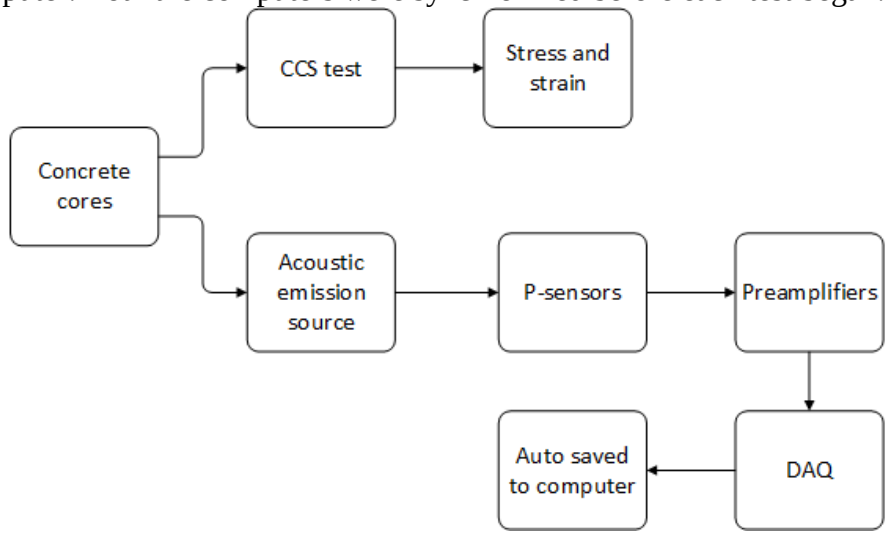

Figure 3. Flow chart of CCS test with monitoring acoustic emissions.

RESULTS

The CCS tests [15] were conducted with the results in Table 2 and acoustic responses were also obtained. Analysis of events includes DF, event energy, peak amplitude, cumulative AE number and event location interpretation from the relative travel time was numerically processed.

Single Acoustic Emission

A single event from a CCS test was obtained in Figure 4. The top sensor was always set as the trigger channel and two bursts of signals were captured at both sensors. The different first arrival time demonstrated that the AE source located closer to the top sensor. AE parameters were calculated based on methodology previously developed [3].

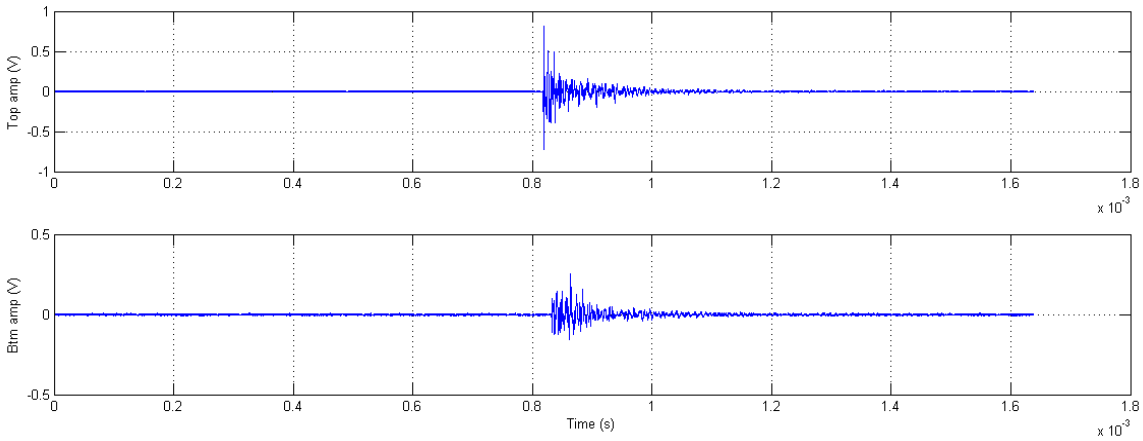

Figure 4. One burst event from top sensor (upper) and bottom sensor (lower) detected from the high strength material with 4 MPa confining pressure.

Single Test Inspection

AE event locations were determined and only those from inside the cores were kept. The mechanical response and acoustic properties of low, medium and high strength cores were plotted together for comparison in Figure 5-7. Stress and cumulative AE counts were plotted on the same time base. Before the linear loading section, few AE events were detected. AE events initiated at the end of the linear loading sections and the number increased within non-linear ductile deformation section. This was explained by the initiation of micro-cracks and micro-crack connection. AE rate dramatically increased before and after the core failed. This was due to the micro-crack propagation and crack nucleation that was continuously generated.

Event energy and peak amplitude were also investigated from both sensors. Event energy was found closely correlated with peak amplitude. And energy from both sensors correlated with each other. This indicated that a single channel of signals could be used for AE analysis.

For medium strength cores, limited AE events were detected due to less capability of signal transmittal between core surfaces and sensors.

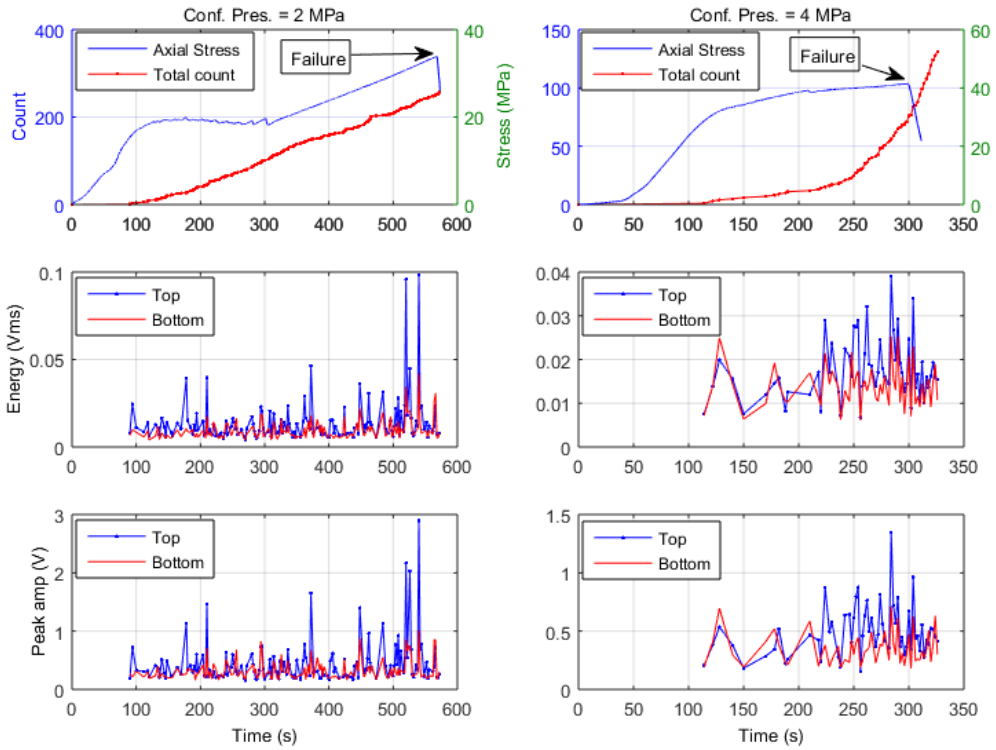

Figure 5. Mechanical and acoustic responses of low strength cores with acoustic properties comparison from both sensors.

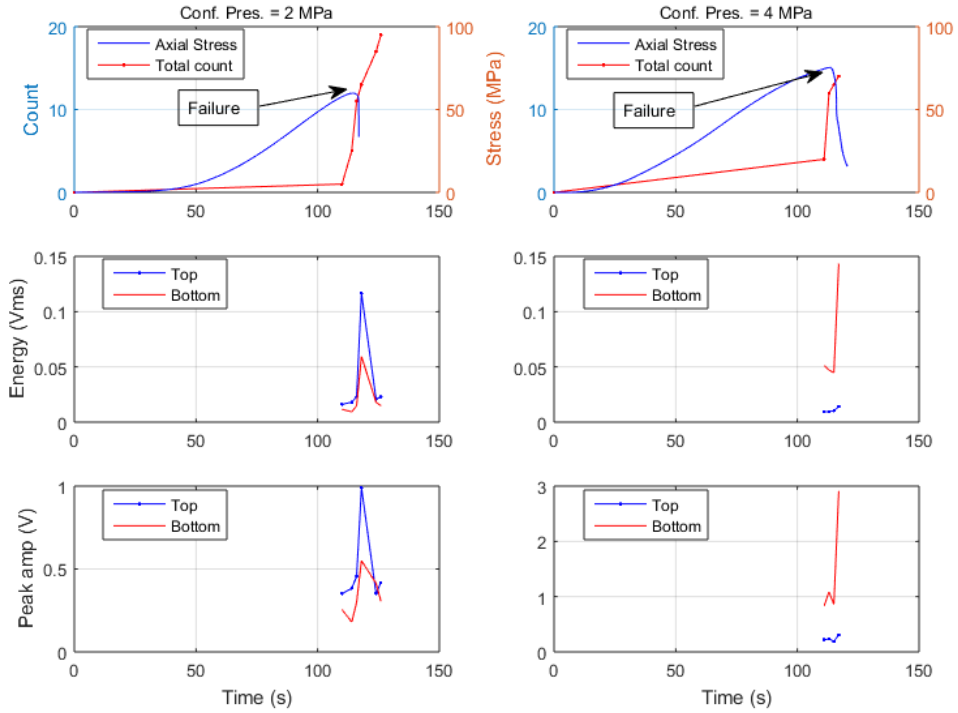

Figure 6. Mechanical and acoustic responses of medium strength cores with acoustic properties comparison from both sensors.

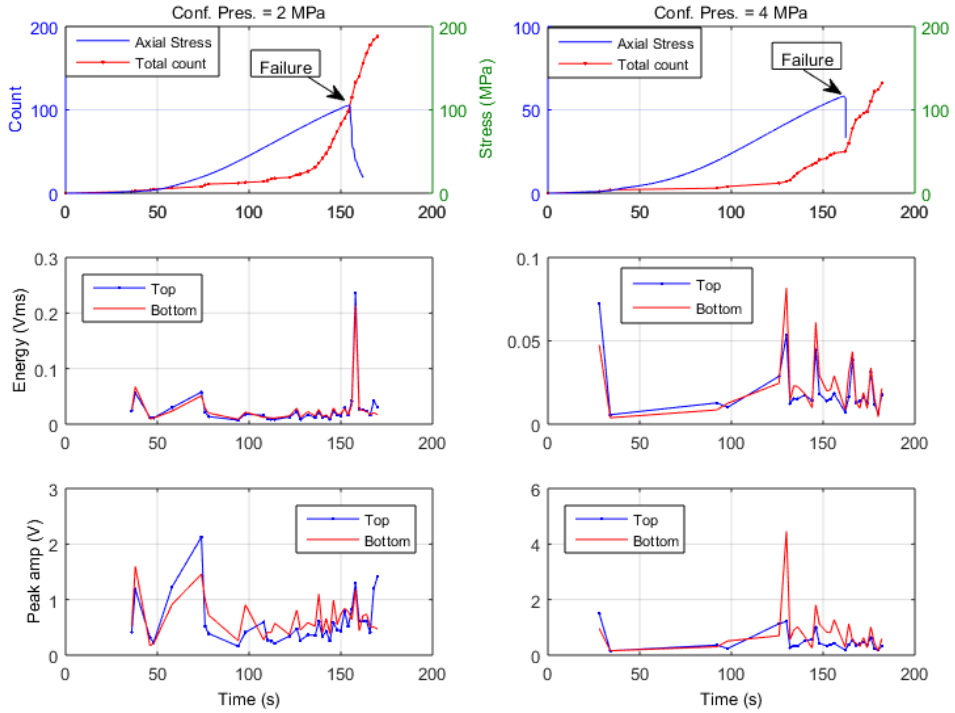

Figure 7. Mechanical and acoustic responses of high strength cores with acoustic properties comparison from both sensors.

Dominant Frequency and Source Energy

DF and AE event energy of signals from the top trigger sensor were compared for all tests in Figure 8 and Figure 9, separately. Linear fit was plotted for each group of scattered points to the test time. Under the same confining pressure, DF tends to decrease with the increase of core deformation. For the low strength material, DF stays constant during the rock deformation process. There is no evidence to show the relation of material strength and the DF level.

AE event energy generally decreases with increased DF under the same confining pressure. An exception exists that event energy increases with increased DF for the medium strength material under the confining pressure of 2 MPa.

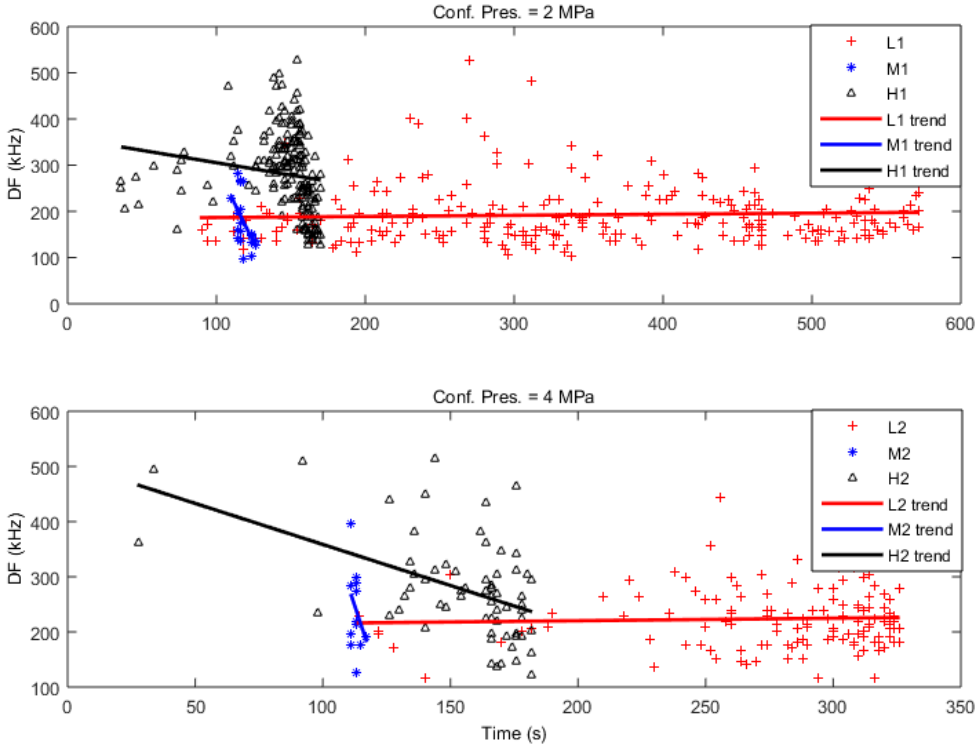

Figure 8. DF versus time for low, medium and high strength cores under confining pressure of 2 MPa (upper) and 4 MPa (lower). Linear fit was provided for each group of scattered points.

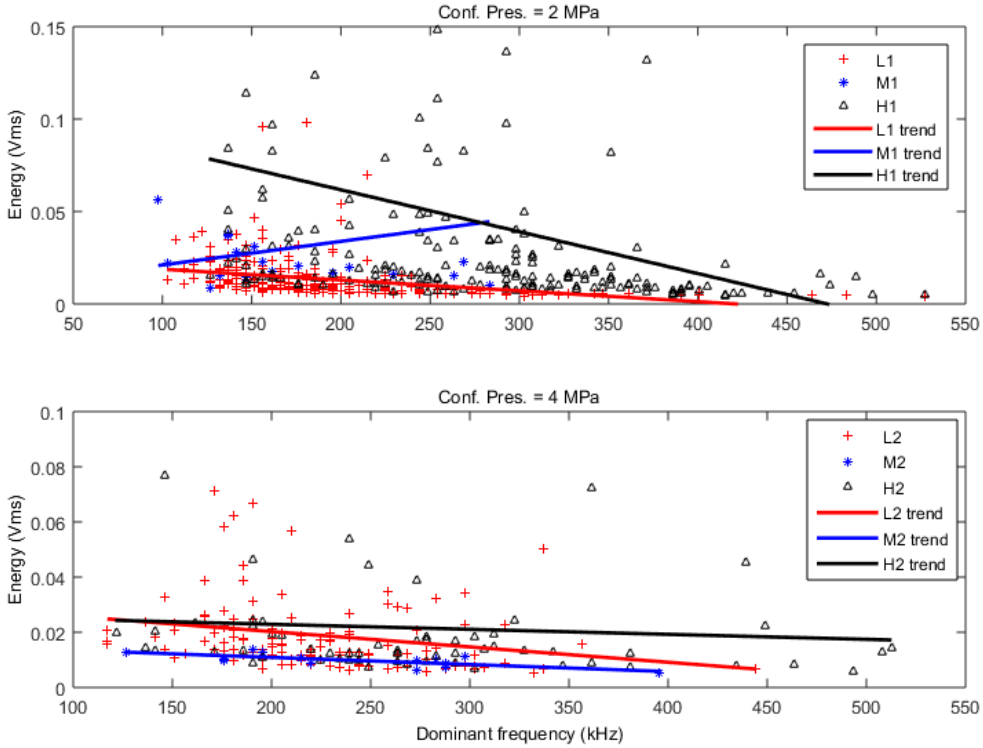

Figure 9. AE energy versus dominant frequency for low, medium and high strength cores under confining pressure of 2 MPa (upper) and 4 MPa (lower). Linear fit was provided for each group of scattered points.

Source Location and Failure Observation

The AE source location was obtained and plotted versus the test time in Figure 10. The vertical axes are scaled to the actual core lengths. For low strength material, the majority of AE events were located in the upper half of the core under both confining pressures. This coincides with the observed results. For medium strength material, there was limited number of AE sources due to lack of good sensor contact. For high strength material, AE sources were distributed more uniformly along the length of the core.

The above AE distribution characteristics or cracks were observed from the post failure demonstration in Figure 11. The cores failed due to shear cracking and macroscopic cracks propagate along all the length of the cores. Cracks mainly distributed along one portion of core length for low strength material, which was possibly due to unevenly distributed axial stress.

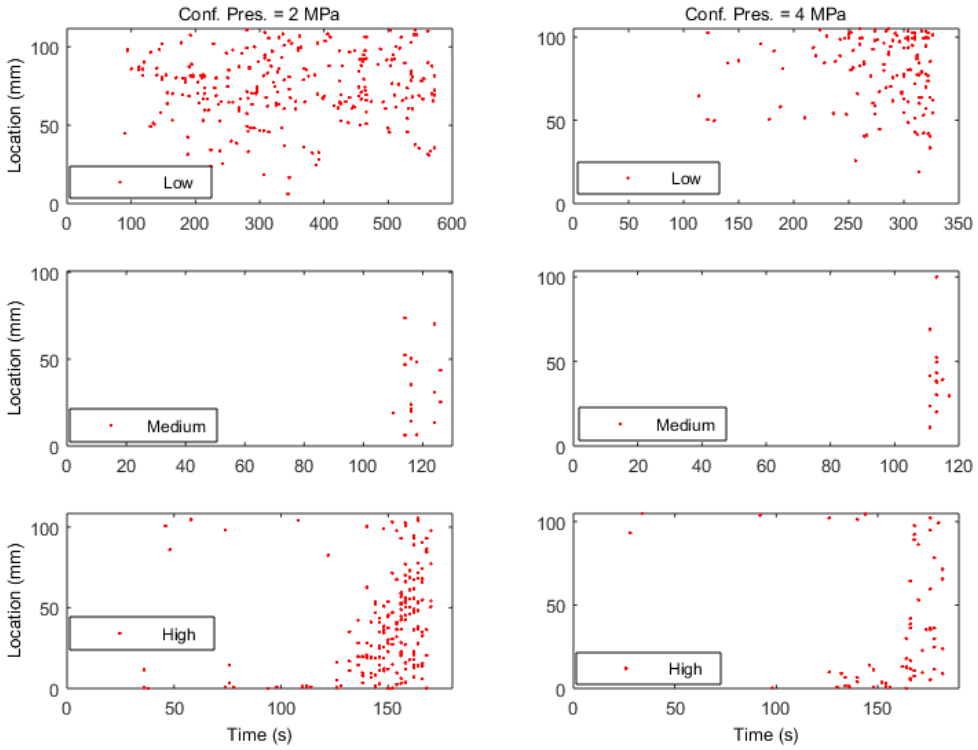

Figure 10. One dimensional acoustic source distribution versus test time for low, medium and high strength cores. Vertical axes were scaled to actual core heights.

CONCLUSIONS

AE provides one feasible technique of characterizing rock deformation and failure in the laboratory. AE event rates correlate with the rock failure.

AE event DF tends to decrease with increased deformation. Also, event energy tends to decrease with increased dominant frequency. There is no evident relationship between DF and CCS.

AE source location was plotted versus time along the length of the cores. For low strength cores, AE sources were mainly distributed on one end which was observed in the failed specimens. For medium strength and high strength cores, AE sources were more uniformly distributed along the core length.

Figure 11. Post failure illustration for low, medium and high strength cores under confining pressure of 2 MPa.

ACKNOWLEDGEMENTS

The project is funded by Atlantic Canada Opportunity Agency, Husky Energy, Suncor Energy and Research and Development Corporation (RDC) of Newfoundland and Labrador under AIF contract number: 781-2636-1920044.

REFERENCES

1. Hardy, H.R. Jr., "Applications of Acoustic Emission Techniques to Rock and Rock Structures: A State-of-the-Art Review", *Acoustic Emissions in Geotechnical Engineering Practice, American Society for Testing and Materials*, (1981), 4-92.
2. Lockner, D., "The role of acoustic emission in the study of rock fracture", *Int. J. Rock Mech. Min. Sci. & Geomech. Abstr*., (1993) **30**, 7, 883-899.
3. Butt, S.D. and P.N. Calder, "Experimental Procedure to Measure Volumetric Changes and Microseismic Activity During Triaxial Compression Tests", *Int. J. Rock Mech. Min. Sci.*, (1998) **35**, 2, 249-254.
4. Keshavarz, M., F.L. Pellet and K.A. Hosseini, "Comparing the effectiveness of energy and hit rate parameters of acoustic emission for prediction of rock failure",

in *ISRM International Symposium on Rock Mechanics,* 2009, The University of Hong Kong, China.
5. Damani, A., A. Sharma, C.H. Sondergeld and C.S. Rai, "Mapping of Hydraulic Fractures under Triaxial Stress Conditions in Laboratory Experiments using Acoustic Emissions", In *SPE Annual Technical Conference and Exhibition*, 2012, San Antonio, Texas.
6. Chitrala, Y., C.H. Sondergeld and C.S. Rai, "Microseismic Studies of Hydraulic Fracture Evolution at Different Pumping Rates", in *SPE Americas Unconventional Resources Conference*, 2012, Pittsburgh, Pennsylvania.
7. Fortin, J., S. Stanchits, G. Dresen and Y. Gueguen. "Acoustic Emissions Monitoring during Inelastic Deformation of Porous Sandstone: Comparison of Three Modes of Deformation", *Pure and Applied Geophysics*, (2009).
8. Cai, M., P.K. Kaiser, Y. Tasaka, H. Kurose, M. Minami and T. Maejima, "Numerical Simulation of Acoustic Emission in Large-scale Underground Excavations", in *The 42nd US Rock Mechanics Symposium*, 2008, San Francisco, CA.
9. Tang, C., P.K. Kaiser and G. Yang. "Numerical Simulation of Seismicity In Rock Failure", *2nd North American Rock Mechanics Symposium*, 1996, 19-21 June, Montreal, Quebec, Canada.
10. Zang, A., C. Wagner, F., S. Stanchits, G. Dresen, R. Andresen, and M.A. Haidekker. "Source analysis of acoustic emissions in Aue granite cores under symmetric and asymmetric compressive loads", *Geophysical Journal*, (1998) **135**, 3, 1113-1130.
11. Aggelis, D.G. "Classification of cracking mode in concrete by acoustic emission parameters", *Mechanics Research Communications*, (2011) **38**, 3, 153–157.
12. Ohno, K. and M. Ohtsu. "Crack classification in concrete based on acoustic emission", *Construction and Building Materials*, (2010) **24**, 12, 2339–2346.
13. Chow, T.M. "Concurrent ultrasonic tomography and acoustic emission in solid materials", Doctoral dissertation, Queen's University at Kingston, 1992.
14. ASTM D4543-08, *Standard Practices for Preparing Rock Core as Cylindrical Test Specimens and Verifying Conformance to Dimensional and Shape Tolerances*, ASTM International, West Conshohocken, PA, 2008, www.astm.org.
15. ASTM D7012-14, *Standard Test Methods for Compressive Strength and Elastic Moduli of Intact Rock Core Specimens under Varying States of Stress and Temperatures*, ASTM International, West Conshohocken, PA, 2014, www.astm.org.

SIMULATING IN-SITU CONDITIONS FOR DIGITAL CORE ANALYSIS

S. Linden[1,2], T. Cvjetkovic[2], E. Glatt[2], J.-O. Schwarz[2] and A. Wiegmann[2]
[1]Fraunhofer ITWM, Fraunhofer-Platz 1, 67665 Kaiserslautern, Germany
[2]Math2Market GmbH, Stiftsplatz 5, 67655 Kaiserslautern, Germany

This paper was prepared for presentation at the International Symposium of the Society of Core Analysts held in St. John's Newfoundland and Labrador, Canada, 16-21 August, 2015

ABSTRACT

Digital rock physics (DRP) for routine and special core analysis is usually based on 3D digital images acquired under ambient conditions. Hence it does not account for the pressure release the rocks suffer during the uplift from reservoir to laboratory conditions. The resulting change in the pore space affects all physical properties significantly. In this paper we present an efficient workflow to perform the full digital core analysis under in-situ conditions. The in-situ conditions are modeled by numerically compressing a scan taken under ambient conditions rather than performing the scan under in-situ conditions. The workflow is illustrated using a segmented 3D image of a Berea sandstone derived from a CT-scan under ambient conditions. Our results confirm that high geostatic pressures lead to significant changes of the physical rock properties.

INTRODUCTION

In the oil and gas industry, digital rock physics (DRP) on 3D images is a fast growing research topic. It is a standard tool to supplement and replace routine core analysis (RCA) and special core analysis (SCAL). However, most simulations are performed on 3D images taken under ambient conditions by µCT or FIB-SEM. The uplift of rocks from high geostatic pressures to ambient conditions enlarges the overall pore space. This change in pore space affects all physical properties significantly and has to be taken into account. Another challenge for DRP is the need to work on representative elementary volumes (REV) and hence very large images due to the inhomogeneity of the samples. In this paper we study the influence of increasing the geostatic pressure on

1. Porosity & pore size distributions,
2. Absolute & relative permeability,
3. Electrical conductivity, resistivity index & formation factor and
4. Capillary pressure.

There are two approaches to simulate in-situ conditions: (i) performing a scan under in-situ conditions or (ii) numerically compressing a scan taken under ambient conditions. We present an efficient workflow that allows computing these properties under in-situ conditions by numerically compressing a scan. The simulations are performed using the digital material laboratory GeoDict. Its built-in highly optimized numerical solvers are

capable of performing simulations on very large REVs (e.g. 1000^3 voxels). The workflow is illustrated using a segmented 3D image of Berea sandstone [1, 2] derived from a CT-scan under ambient conditions.

METHODS

The physical properties mentioned above are computed on 3D digital images that may stem from µCT-scans, FIB-SEM, or virtual rock models. The outline of the proposed workflow is

1. Acquisition of µCT-scans or FIB-SEM images under ambient conditions
2. Segmentation of the image into solid phases and pore space
3. Numerical compression of the 3D image (NEW STEP)
4. Computation of single-phase properties
    a. Porosity & pore size distributions
    b. Absolute permeability
    c. Electrical conductivity and formation factor
5. Computation of the distribution of the two liquid phases in the pore space
6. Computation of two-phase properties on varying saturation states
    a. Capillary pressure
    b. Resistivity index
    c. Relative permeability

The calculations are performed by highly optimized numerical solvers that work directly on 3D digital images, without additional meshing. It is also not required to assemble matrices that describe discretized physical equations. That approach reduces the memory consumption dramatically. All but one solver use Fourier transforms to reduce the number of iterations, and thus achieve very low runtimes.

Numerical compression

The prediction of mechanical properties and the geostatic correction, i.e. uniaxial compression of the sample, is computed with the FeelMath [3,4] solver. The input parameter for the compression step is the compression rate in percent or a given geostatic pressure. In this section we summarize the basic ideas of the implemented algorithms.

The equations of linear elasticity for a constant macroscopic strain S are defined by

$$\begin{aligned} \nabla \cdot \sigma &= 0 && \textit{Equilibrium} \\ \sigma &= C : \epsilon && \textit{Hooke's law} \\ 2\epsilon &= 2S + \nabla u^* + (\nabla u^*)^T \end{aligned} \qquad (1)$$

for the stress-field σ, strain-field ϵ, and the displacement-field u^*. By introducing a reference material of homogeneous stiffness C^0 these equations can be reformulated into the Lippmann Schwinger equation

$$\epsilon + \Gamma^0 * \left((C - C^0) : \epsilon\right) = S \quad (2)$$

where the convolution of the Green operator Γ^0 can be solved by using Fast Fourier transforms. The solver is able to handle linear and non-linear (i.e. replacing Hooke's law with a non-linear formulation) material laws assigned to mineral phases. The number of iterations required for computation depends on the largest phase contrast in the structure.

Then the displacement field u^* is used to predict a compressed structure [5]. The voxels of the original image are moved along the displacement field and cut with a reduced boxel image. The size of the boxel image can be derived from the input parameters. The result of that procedure is a gray-value image where a global threshold is used to perform a segmentation of the different phases. The threshold is chosen such that either mass or volume is preserved. Then the boxel image is resampled to a voxel image again.

For the mechanical properties it is important to capture the complete mineralogy in the segmentation process to predict representative results. Another important aspect to improve the validity is the correct modelling of contacts between grains. The stiffness at grain-to-grain interfaces is much lower compared to the stiffness within the grains. We approximate that aspect with an increased uniaxial macroscopic stress. The compressed 3D image is then used in further computations of the workflow.

Distribution of the Two Liquid Phases

The pore morphology method [6], also known as method of maximal inscribed spheres [7] predicts the distribution of a wetting phase (WP) and a non-wetting phase (NWP) inside a porous medium. The method distributes the phases by using morphological operations rather than solving partial differential equations. For drainage, spheres that represent the NWP are placed inside the pore space where the pore size is greater than a certain radius. The radius is decreased in an iterative process, i.e. the capillary pressure is increased. Additional connectivity checks with respect to NPW and WP reservoirs can be used to increase the validity of the distributions. These connectivity checks allow the algorithm to introduce residual phases where parts of the NWP are trapped and cannot leave the simulated domain.

The output of the algorithm is a finite sequence of quasi-stationary states. Each state is a 3D image again that encodes the solid phase, WP and NWP. In a post-processing step the Young-Laplace equation based on the radii of the inscribed spheres and the interfacial tension is used to predict the capillary pressure curve. The sequence of 3D images is then the input data to predict relative properties.

Absolute and Relative Permeability

Absolute and relative permeability on the WP and NWP are computed with the SIMPLE-FFT and LIR-Stokes [8] methods. The SIMPLE-FFT is an enhancement of the original SIMPLE algorithm that solves the pressure correction within a single step using Fourier transforms. The LIR-Stokes solver uses an adaptive tree structure and solves the

discretized Stokes equations at once for each cell. The methods are very fast and in particular the latter has very low memory requirements.

Both methods assume no-slip boundary conditions at pore-solid interfaces for the absolute permeability and also no-slip boundary conditions at WP-NWP interfaces for the relative permeability. At the domain boundaries we assume periodic boundary condition with inlet (e.g. 16 voxel) in flow direction. This flow boundary condition connects all pores from inlet and outlet and predicts permeabilities between those of purely periodic boundary conditions and symmetry boundary conditions.

Electrical Conductivity and Resistivity Index

The electrical conductivity, resistivity index and formation factor are computed with the Explicit Jump Immersed Interface Method [9, 10]. Additional jump variables at material interfaces are introduced to represent discontinuities inside the flux. The physical problem can be reformulated from a three-dimensional to a two-dimensional problem where the method solves for the jump variables. The number of iterations depends on the number of interfaces. The chosen boundary conditions for the electrical properties are similar to the flow properties. For the resistivity index we also assume that the NWP is non-conductive.

RESULTS

In our experiments we use a binary segmented 3D image of a computed tomography scan from a Berea sandstone under ambient conditions. The image consists of 720 x 720 x 1024 voxels, has a resolution of 0.74 µm, and is shown in Figure 1 together with the original gray value image. The origin and segmentation of the dataset is described in the first part of the benchmark study [1]. The second part of the benchmark study [2] includes the numerical computation of physical properties but considers permeability, electric conductivity and elastic moduli only.

Table 1 shows runtimes and memory consumptions for single computations of the numerical solvers. Depending on the available computational resources, all simulations can be performed in a couple of days. Figure 5 shows the graphs of porosity, pore sizes, formation resistivity factor, absolute permeability, capillary pressure, and resistivity index with respect to the pressure states.

Mechanical Properties and Numerical Compression

First, we compute a sequence of images which have been corrected for different geostatic pressures, i.e. numerical compression with the states: 0.0, 0.12, 0.24, 0.48, 0.71, 0.95, and 1.43 GPa. Pores are assumed to be filled with air ($E = 0$ GPa and $\nu = 0$) and the solid phase is assumed to be quartz ($E = 94.5$ GPa and $\nu = 0.074$). Then the core analysis is performed on each compression step. The pressures correspond to the compression ratios: 0.0, 0.25, 0.5, 1.0, 1.5, and 3.0%. The computed isotropic elastic modulus is E = 45.9 GPa and the Poisson ratio is $\nu = 0.108$ for the uncompressed Berea sandstone. The visible

difference of the uncompressed and compressed image can be seen in Figure 2 and indicates a significant change of effective physical properties.

Porosity and Pore Size Distribution
The porosity of the uncompressed sample is 18.4 % and decreases linearly to 15.7 %. The (relative) pore size distribution (PSD) obtained by maximum inscribed spheres does not change significantly under increasing geostatic pressure. In contrast to the Porosimetry simulation where the most frequent pore diameter 8.8 µm is decreased to 7.4 µm. A reduction between 2% and 3% is a reasonable value for sandstone and agrees with measured values in literature [12].

Absolute Permeability
The absolute permeability is 108 mD under ambient conditions and decreases with a high slope to 66 mD under in-situ conditions. This decline of permeability agrees with the relation of velocity and pore diameter. Figure 3 shows the velocity field of a Stokes flow under ambient conditions. The trend agrees to the measured stress dependence of permeability reported in [12].

Absolute Electrical Conductivity and Formation Factor
The electrical conductivity of the fully Brine saturated Berea sandstone is simulated to 0.17 S/m, assuming that Brine has a conductivity of 5 S/m and Quartz is non-conductive.
Figure 3 shows the potential field for the fully saturated medium under ambient conditions. The corresponding formation resistivity factor increases almost linear from 27 to 39 when air drains brine as illustrated in Figure 4. That behavior coincides with the linear decrease of the pore diameters.

In contrast to the permeability, the number of iterations for computing electrical properties is almost the same from ambient to in-situ conditions. This can be explained by the fact that the number of iterations depends on the brine surface area which does not change significantly during the numerical compression.

Two-Phase Distribution
The pore morphology method is used to perform a drainage simulation. Figure 4 shows different stationary saturation states of the drainage process where air drains brine. In that experiment we assumed a non-wetting phase (Air) reservoir at the top and a wetting phase (Brine) reservoir at the bottom of the domain.

Since that method does not solve a partial differential equation the computation is much faster compared to the computations of single-phase flow, mechanical, and electrical properties. A subset of these quasi stationary states is used to predict relative properties.

Capillary Pressure
Similar to the pore size distribution, the capillary pressure curve computed from the two-phase distribution does not change significantly within the investigated geostatic pressure

range. The irreducible wetting phase saturation is 17.3% but the displacement pressure increases from 24 kPa to 29 kPa.

Relative Permeability
The relative permeability of the wetting phase is almost the same for ambient and in-situ conditions other than the relative permeability of the non-wetting phase. Figure 6 shows the relative permeability of both phases with respect to the normalized wetting phase. The decline occurs more early and can be explained by delayed breakthrough of the non-wetting phase.

The relative permeability is the most expensive property to compute depending on the number of saturation states. The number of iterations increases significantly in lower saturation states even though the number of computational cells decreases. The SIMPLE-FFT method cannot profit from the decreasing number of cells while the LIR method can and hence the runtime per iteration decreases.

The number of iterations needed until the same stopping criterion is reached increases by 25% for computing the absolute permeability from ambient to in-situ conditions. This can be explained by the increased complexity of the pore space. That behavior can be observed for the SIMPLE-FFT, LIR, and also other flow solvers.

Resistivity Index
The electrical conduction simulation is performed for the wetting phase on 8 saturation states from 0.3 to 1.0. Figure 5 shows the resistivity index for the Berea sandstone under ambient and in-situ conditions together with an exponential fitting curve. The saturation exponents of Archie's law are 2.38 and 2.04, respectively. Similar to the relative permeability, the absolute resistivity of the wetting phase under ambient condition is greater compared to the in-situ conditions.

CONCLUSION

The integrated approach of highly optimized solver technologies allows performing the full digital core analysis under in-situ conditions in a short amount of time and memory. Our results confirm that high geostatic pressure leads to different physical rock properties. The impact is significant on the single-phase properties: porosity, the most frequent pore diameter, permeability, and formation factor. The capillary pressure, resistivity index, and relative permeability are also influenced by increasing pressure but to a lesser extent. The next step is a comparative study of digital and laboratory in-situ conditions, also for other types of rocks. In addition, numerical simulations and modelling will be improved in at least three ways: 1. segmentation of all mineral phases, 2. modelling and consideration of grain contacts, and 3. improving the computational runtimes for relative properties.

REFERENCES

1. H. Andrä, N. Combaret, J. Dvorkin, E. Glatt, H. Junehee, M. Kabel, Y. Keehm, F. Krzikalla, M. Lee, C. Madonna, M. Marsh, T. Mukerji, E. Saenger, R. Sain, N. Saxena, S. Ricker, A. Wiegmann and X. Zhan, "Digital rock physics benchmarks Part I: Imaging and segmentation," Computers & Geosciences, 2013 (43), pp. 25-32.
2. H. Andrä, N. Combaret, J. Dvorkin, E. Glatt, H. Junehee, M. Kabel, Y. Keehm, F. Krzikalla, M. Lee, C. Madonna, M. Marsh, T. Mukerji, E. Saenger, R. Sain, N. Saxena, S. Ricker, A. Wiegmann and X. Zhan, "Digital rock physics benchmarks Part II: Computing effective properties," Computers & Geosciences, 2013 (43), pp. 33-43.
3. M. Kabel and H. Andrä, Fast numerical computation of precise bounds of effective, Report of Fraunhofer ITWM, 2013 (224).
4. M. Kabel, T. Böhlke and M. Schneider, "Efficient fixed point and Newton-Krylov solvers for FFT-based homogenization of elasticity at large deformations," Computational Mechanics, 2014 (54), pp. 1497-1514.
5. M. Kabel, H. Andrä, F. Hahn and M. Lehmann, "Simulating the Compression of Filter Materials," Proceedings of FILTECH, 2013
6. M. Hilpert and C. T. Miller, "Pore-morphology-based simulation of drainage in totally wetting porous media," Advances in Water Resources, 2001 (24), pp. 243-255.
7. D. Silin, L. Tomutsa, S.M. Benson and T.W. Patzek, "Microtomography and Pore-Scale Modeling of Two-Phase Distribution," Transport in Porous Media, 2011 (86), pp. 495-515.
8. S. Linden, A. Wiegmann and H. Hagen, "The LIR space partitioning system applied to the Stokes equations," Dagstuhl Geometric Modelling 2014 Special Issure of Graphical Models, to be published.
9. A. Wiegmann and K. P. Bube, "The Explicit-Jump immersed interface method: Finite difference methods for PDE with piecewise smooth solutions," SIAM Journal on Numerical Analysis, 2000 (37 No 3), pp. 827-862.
10. A. Wiegmann and A. Zemitis, "EJ-Heat: A fast Explicit-Jump harmonic averaging solver for the effective heat conductivity of composite materials," Fraunhofer ITWM Technical Report No 94, 2006.
11. J.J. Dong, J.Y. Hsu, W.J. Wu, T. Shimamoto, J.H. Hung, E.C. Ye, Y.H. Wu and H. Sone, "Stress-dependence of the Permeability and Porosity of Sandstone and Shale from TCDP Hole-A," International Journal of Rock Mechanics and Mining Sciences, 2010 (47), pp. 1141-1157
12. S. Linden, T. Cvjetkovic, E. Glatt and A. Wiegmann, "An integrated approach to compute physical properties of core samples," Proceedings of SCA Avignon, 2014, Paper 057.

FIGURES AND TABLES

Table 1 Runtime and Memory requirements of the solvers on a computer with 16 cores and 128 GB RAM. The runtimes account for a single simulation on the uncompressed Berea sandstone.

Method	Flow (SIMPLE-FFT)	Flow (LIR)	Electrical Conduction (Explicit Jump)	Two-Phase Distribution (Pore Morphology)	Mechanics (FeelMath)
Runtime [h]	3.6	3.1	0.6	0.8	8.3
Memory [GB]	42.3	5.4	9.4	5.0	97.1

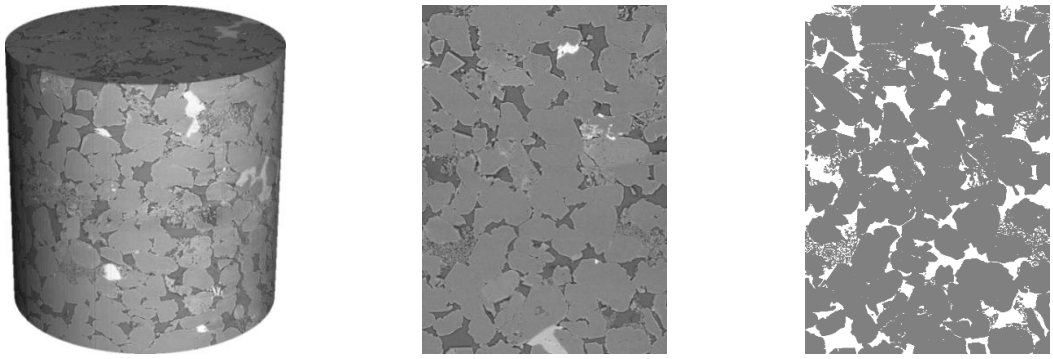

Figure 1 Gray value image from the Berea sandstone (left and center) with a binary segmentation (right). The gray value image consists of 1024x1024x1024 voxel and the cropped segmentation consists of 720x720x1024 voxel.

Figure 2 Cut-out from the segmented image of Berea sandstone before (left) and after (right) numerical compression (1.43 GPa). The pore diameter in the blue region is visibly decreased while even the connectivity of the pores is reduced in the two red regions.

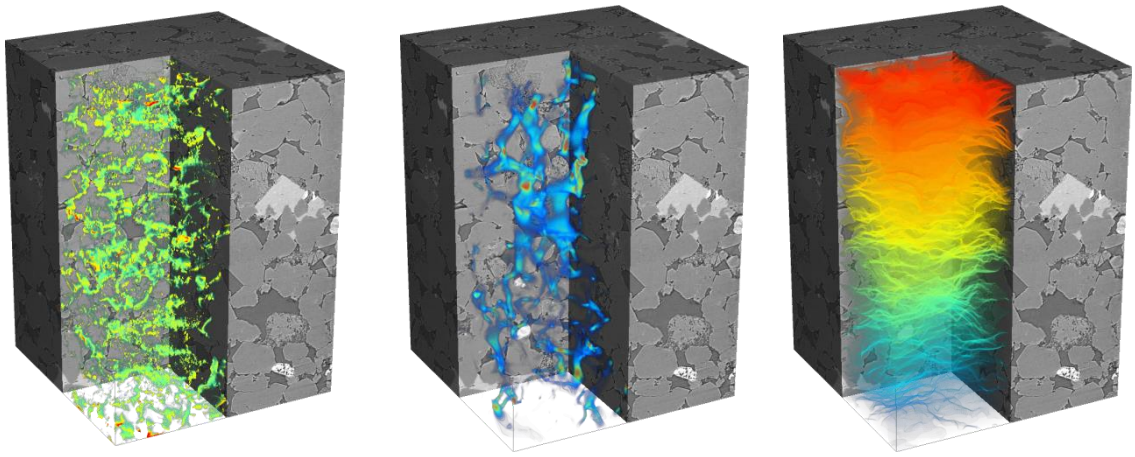

Figure 3 Visualization of the von-Mises stress (left), the velocity field of a Stokes flow (center) and electrical potential (right) on a smaller cut-out. A compression, drop in pressure, and potential difference are applied in y-direction from top to bottom.

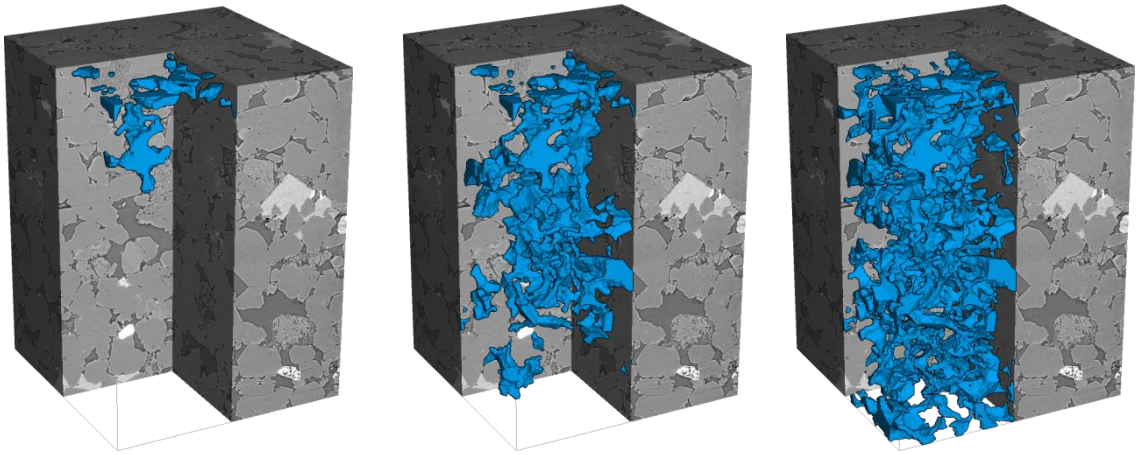

Figure 4 Air drains brine and we visualize air saturations of 25%, 50% and 75% respectively.

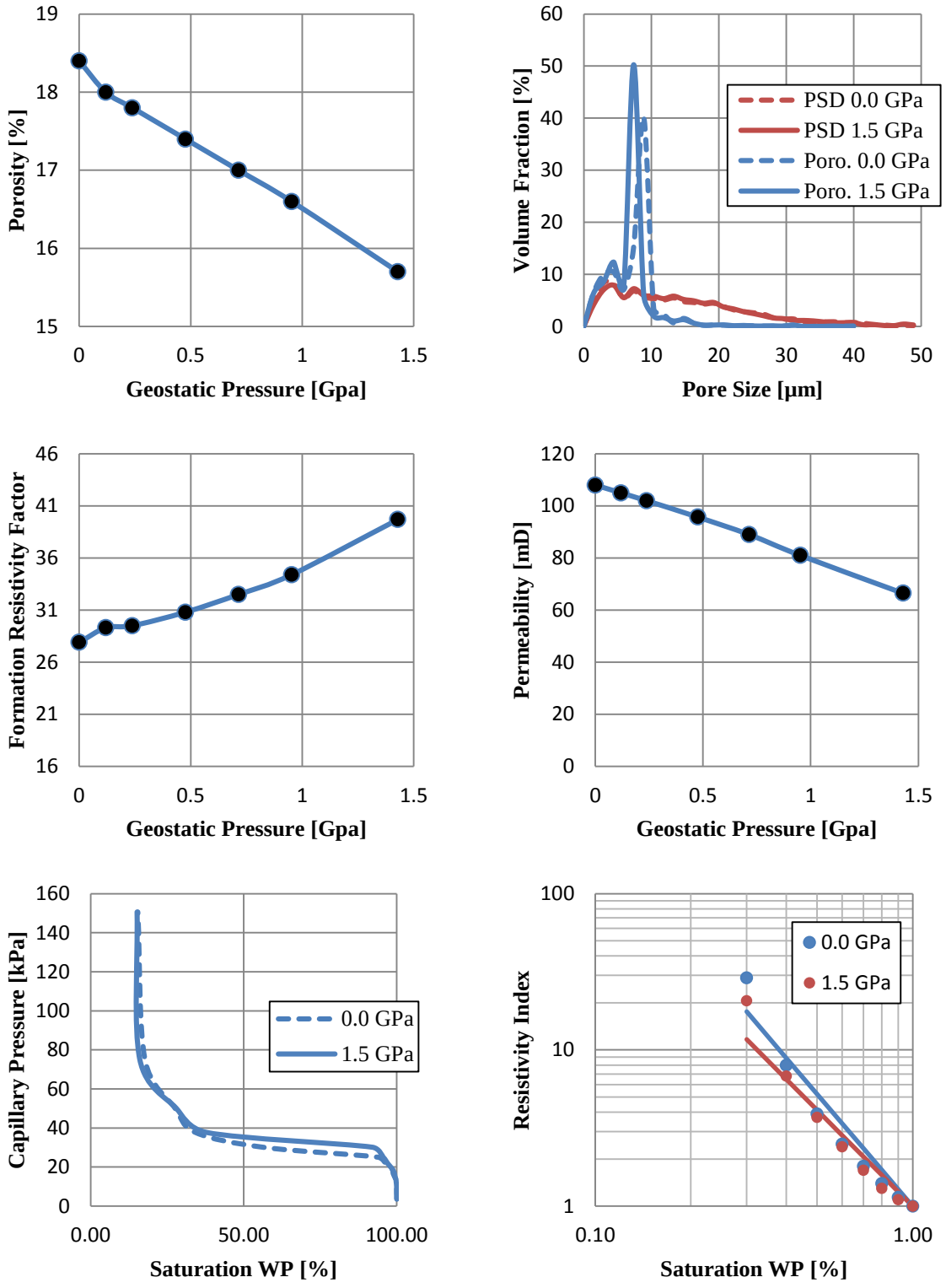

Figure 5 Porosity, pore size distribution, porosimetry, formation resistivity factor, absolute permeability, capillary pressure, and resistivity index for different applied geostatic pressures.

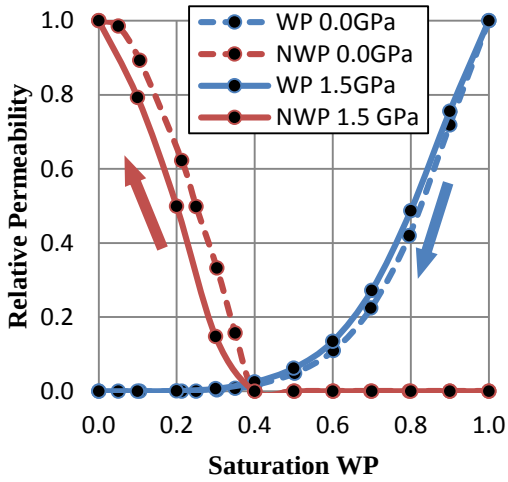

Figure 6 Relative permeability of the WP and NPW for ambient and in-situ conditions.

CARBONATE NMR MEASUREMENTS IN A COMBINED AMOTT-USBM WETTABILITY METHOD

Edmilson Helton Rios, National Observatory; Vinicius de França Machado, Bernardo Camilo Coutinho dos Santos, Willian Andriguetto Trevizan, André Luiz Martins Compan, Dario Abilio Cruz, Rodrigo Skinner, Petrobras; Felipe Moreira Eler, Gorceix.

This paper was prepared for presentation at the International Symposium of the Society of Core Analysts held in St. John's Newfoundland and Labrador, Canada, 16-21 August, 2015

ABSTRACT

NMR measurements were performed along with the stages of a combined Amott-USBM method for some Brazilian deep-water carbonates. Guided by the T_2 signature of non-confined brine and dead crude oil, monophasic and biphasic T_2 distributions were interpreted revealing pore occupancy and wettability of micro and meso-to-macro pores. Consistent T_2 shifts were observed after core aging, imbibition and second drainage. The results indicate that simple 1D-NMR shall support standard methods that cannot resolve saturation and wettability per porosity type.

INTRODUCTION

Shortly after NMR phenomenon discovery in the late forties, the enhancement of relaxation time rates for the wetting phase was noticed [1]. Since then, many studies have been performed on NMR wettability based either on modeling or experimental approaches [2-4]. Although most of these works introduce NMR indices and compare them to the industry standard indices, they do not necessarily must have the same response because these techniques rely on different physical grounds. Instead, for improving conventional methods response, this work evaluates transverse relaxation times (T_2) in the different saturation and wettability conditions availed from the stages of a combined Amott-USBM method [5,6]. As indicated in Figure 1a, T_2 measurements were acquired after 1) total water saturation (S_w=100 %), 2) first drainage with dead crude oil up to irreducible water saturation (S_{wi}), 3) three-months aging in the crude oil, 4) spontaneous plus forced water imbibition up to residual oil saturation (S_{or}) and, 5) spontaneous plus forced drainage with crude oil up to final water saturation (S_{wf}).

As indicated in Figure 1b, the water Amott index (I_w) measures the displacement-by-water ratio, which is the oil volume displaced by spontaneous water imbibition (ΔS_{ws}), relative to the total oil volume displaced by spontaneous and forced water imbibition ($1-S_{wi}-S_{or}$). The oil index (I_o) is analogously defined and the difference between water an oil indices is known as the Amott-Harvey index (I_{AH}) which is bound by $-1< I_{AH}<+1$, Figure 1b. In contrast, the US Bureau of Mines (USBM) index is calculated with the areas under the capillary pressure curves that describes displacement of oil by water A_i (forced imbibition) and the displacement of water by oil A_d (second forced drainage), Figure 1c.

For example, a carbonate with index -1 would require 10 times more energy for imbibition than for drainage (and vice versa for index +1). Although the USBM index is more sensible to neutral wettability, it cannot differ between neutral (I_w and I_o are equal and low) and mix (I_w and I_o are equal and high) wettability.

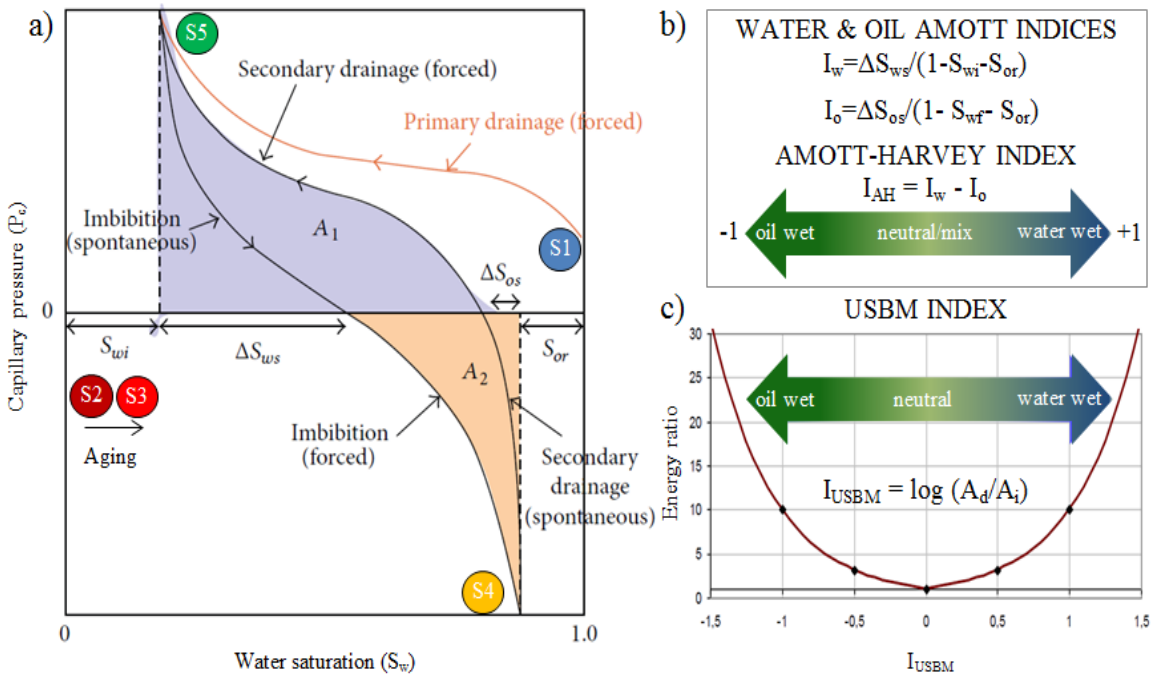

Figure 1: a) Complete cycle of the Amott-USBM method showing the five stages where T_2 measurements were aquired. The classical wettability indeces are also defined: a) Amott-Harvey and c) USBM.

EXPERIMENTAL

X-ray microtomography (μCT) and routine core analyses (RCAL) were used for selection of seven representative core plugs from a Brazilian Pre-Salt carbonate reservoir. Special core analyses (SCAL) were performed at the reservoir temperature of 60 °C. Brine salinity in NaCl equivalent was 182 g/l; brine density and viscosity was 1.09 g/cm^3 and 0.65 cP, respectively, and dead crude oil density and viscosity was 0.86 g/cm^3 and 11.23 cP, respectively. Spontaneous imbibition and drainage volumes were acquired until production stabilization, between 25 and 75 days. Without confinement, forced imbibition and drainage were performed with a centrifuge in 15 increasing capillary pressure steps up to 100 psi (at the face of the core plug). The Carr-Purcell-Meiboom-Gill (CPMG) pulse sequence were used for measuring T_2 in a 2.2 Mhz (for ^{1}H) benchtop NMR analyzer (Maran DRX-HF, Oxford instruments, UK). A full polarization time and a minimum signal to noise ratio of 100:1 were used. T_2 distributions were inverted in the WinDXP program (the Maran accompanying software) using 256 bins which were then normalized to a unitary sum of amplitudes. Further details on NMR phenomenon, data acquisition and inversion can be found in the reference [7].

RESULTS AND DISCUSSION

Bulk transverse relaxation time T_{2b} of the brine and the crude oil are shown in Figure 2a (non-confined in the rock). In brine, ^1H is present only in the molecules of water and thus T_{2bw} distribution is quite narrow. In contrast, dead crude oil presents a very broad T_{2bo} distribution due to the diversity of hydrocarbon molecules (between tens and hundreds of thousands) that contains ^1H. Long T_{2bo} is related to light components (e.g. paraffins and aromatics) holding small molecules with high mobility. Short T_{2bo} is associated to heavy components (e.g. resins and asphaltenes) holding big molecules with low mobility. However, if water and oil are confined in a porous media, relaxation time rates are enhanced due to the interaction with pore surface. Considering a fast diffusion regime and assuming no diffusional relaxation effects due to magnetic field gradients nor diffusion pore coupling [7], T_2 of water and oil confined in a pore can be described as follows [3]:

$$\frac{1}{T_2} = \frac{1}{T_{2bw}} + \rho_w \frac{A_w}{S_w V_p} + \frac{1}{T_{2bo}} + \rho_o \frac{A_o}{S_o V_p}, \quad (1)$$

Where ρ_w and ρ_o are the T_2 surface relaxivity for water and oil, respectively; V_p is the pore volume; S_w and S_o are the fractional water and oil pore saturation ($S_w+S_o=1$), respectively and; A_w and A_o are the fractional water and oil pore surface area ($A_w+A_o=A$), respectively. From equation 1, the characteristic length (R) of a spherical pore site ($R/3 = V/A$) occupied by a fluid which has a single T_{2b} is $R(T_2) = 3\rho(T_2 T_{2b}/T_{2b} - T_2)$. Figure 2b plots $R(T_2)$ for brine and each of the three crude oil components with $\rho_w = 0.006\ \mu m/ms$ (average values based on mercury-injection data comparison) and assuming $\rho_o = \rho_w/3$ as in reference [8]. Characteristic lengths of 1 and 10 μm were considered as thresholds among micro, meso and macro pore types.

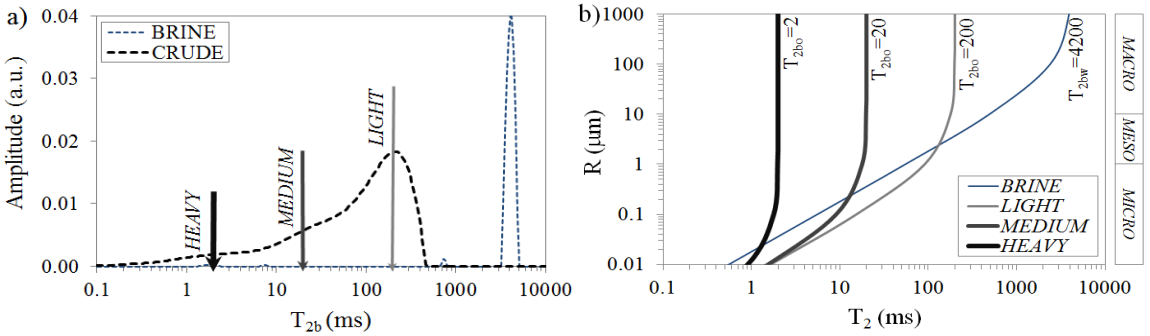

Figure 2: a) Bulk T_2 for brine (T_{2bw}) and crude oil (T_{2bo}). b) Characteristic length (R) of spherical pore sites as a function of monophasic T_2 for brine and crude (although the oil components cannot be separated, their relaxation behavier is illustrated separately, as if they were three different oils).

The studied carbonates are high quality reservoir facies with good porosities (15-20 %) and permeabilities (8-1552 mD) responding with long monophasic (brine) T_2 distributions, Figure 3a. Higher T_2 are associated with higher permeabilities which is explained by the bigger characteristic lengths (brine curve of Figure 2b). When these

carbonates were desaturated by crude oil (S_{wi} ranging from 13 to 25 %), previous T_2-based differences in pore structure became less evident and all biphasic T_2 distribution reduce to a similar shape of the crude oil bulk response, black dotted curve in Figure 3b. This indicates that crude is in meso-to-macro pores relaxing almost like T_{2bo} distribution (Figure 2b shows that surface relaxation is low in such pore types even for light oil components). After brine imbibition (S_{or} ranging from 3 to 29 %), some previous features of macropores (300 to 3000 ms in Figure 3a) are clearly recovered in Figure 3c between 600 and 4000 ms. The observed shift towards T_{2bw} indicates a decrease of the brine surface relaxation component (less contact with the pore walls) compared to the bulk relaxation component (Equation 1). Although residual oil ocuppies smaller sites after brine imbibition, characterist lengths of theses sites would be in the same order of magnetude (lets say, for instance, a quarter of the meso-to-macro pore sizes). Imbibed brine may also reduce contact with pore walls further explaining why it still relaxes as T_{2bo} distribution (which is sumed with the irreducible brine signal from micro pores, T_2<500 ms). Imbibed brine is not totaly drived out after second drainage (S_{wf}-S_{wi}>0) and its portion more isolated from the pore walls, responding in the T_2 range of 600 to 2000 ms (Figure 3d), prevents hysteresis back to the distribution shapes of Figure 3b.

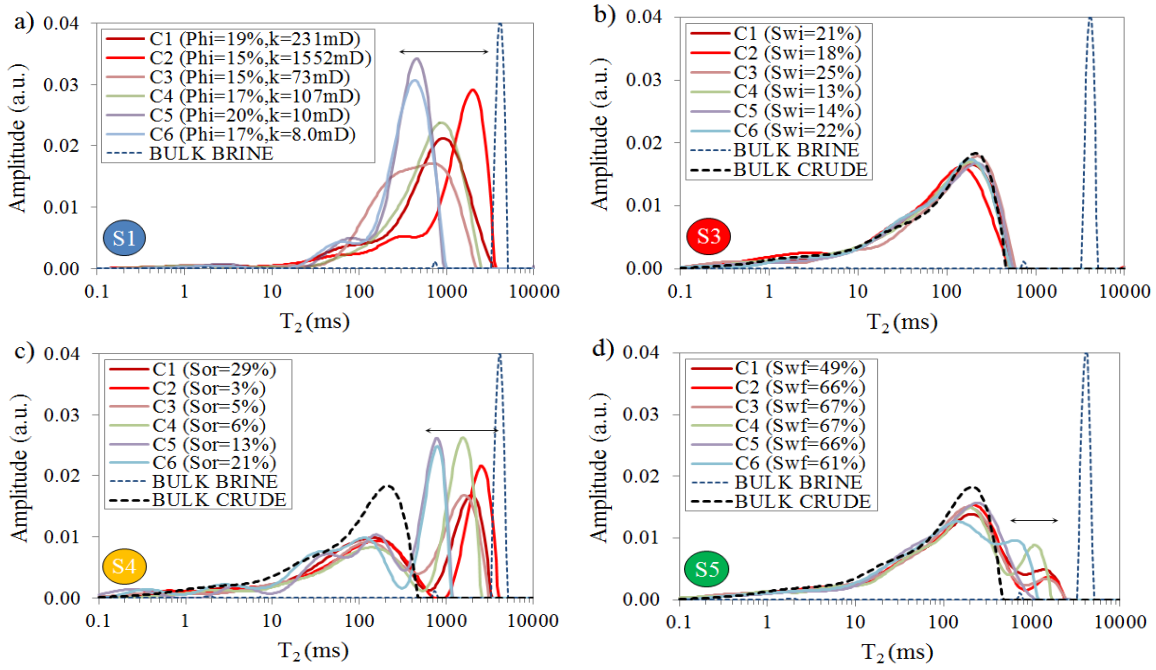

Figure 3: T_2 distributions for the carbonate plugs (continuous curves) after: a) fully water saturation, b) drainage up to S_{wi} and aged, c) imbibition up to S_{or} and d) drainage up to S_{wf}. T_{2b} distribution of non-confined brine and crude oil are also shown as reference (black and blue dotted curves, respectively).

The curves for the three first stages are plotted together for samples C4 and C5 in Figure 4a and 4b, respectively. Strictly, the standard wettability methods started only after native wettability restoration, which was performed by aging the samples in crude oil for three months. The bigger shift to short T_2 agrees with the more oil-wet conditions indicated by

the Amott and USBM methods of sample C4. After aging, the surface wetted by crude oil in meso-to-macro pores (A_o) increases and so does T_2 rates (Equation 1). The four stages presented in Figure 3 are plotted all together in Figure 5. Partial exchange between oil and water is highlighted in black shading for sample C4 after imbibition (Figure 5a) whereas the opposite exchange is highlighted in blue shading for sample C5 after second drainage (Figure 5b). The biphasic distributions of Figure 5 are shown in Figure 6 subtracted by the oil signal which was considered to have the same shape of T_{2bo} distribution (sum of amplitudes normalized to 1-S_{wi}, S_{or} and 1-S_{wf} for stages 3, 4 and 5, respectively). According to the classical cutoff interpretation, calculated with the S_{wi} value on the monophasic T_2 distribution, irreducible brine is in micro pores and free brine is in meso-to-macro pores. While subtracted irreducible brine in stage 3 is within the monophasic T_2 distribution agreeing especially for shorter T_2, its apparent increase in the stage 4 and 5 is probably brine coating the walls of meso-to-macro pores or occupying reduced sites in such pore types. In contrast, free brine in pore sites with less contact with the pore walls can have longer T_2 than the monophasic response which is due to a decrease of surface relaxation and consequent bigger influence of bulk brine components.

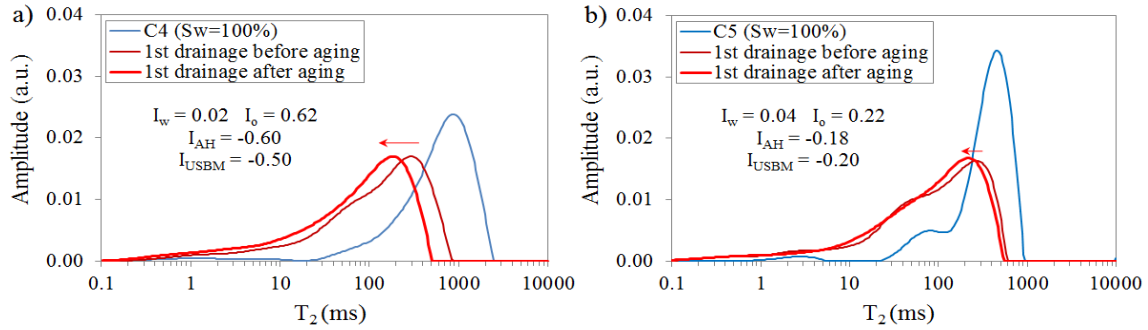

Figure 4: Monophasic (S1) and biphasic (S2 and 3) T_2 distribution for carbonates plugs a) C4 and b) C5.

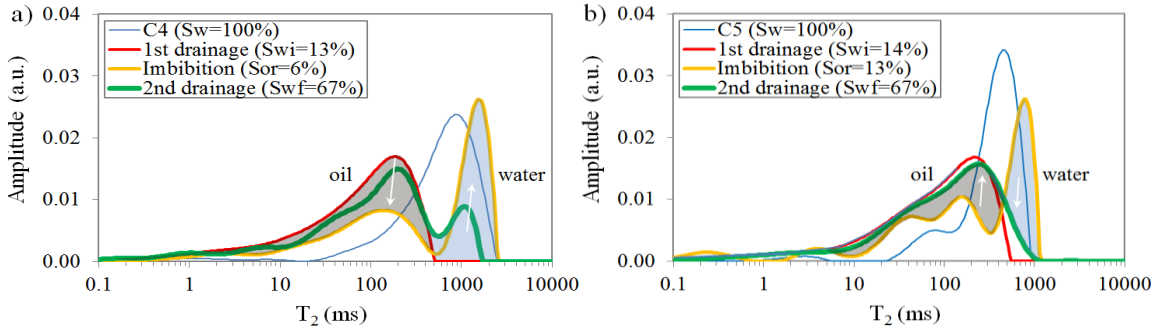

Figure 5: Monophasic (S1) and biphasic (S3,4 and 5) T_2 distribution for a) C4 and b) C5.

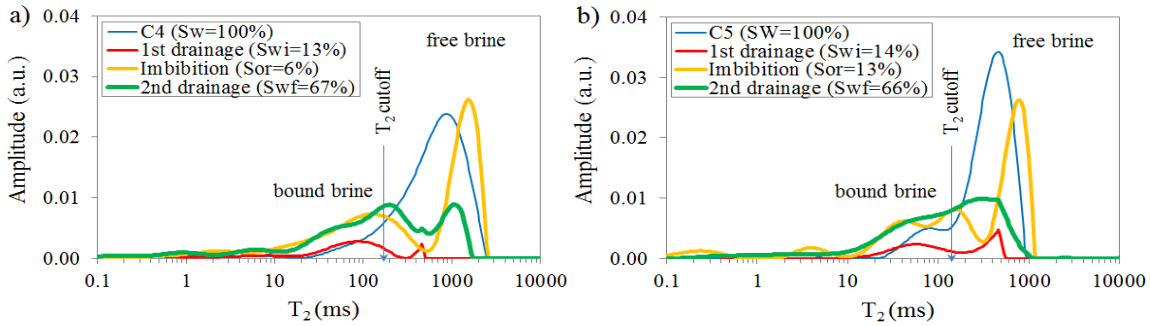

Figure 6: Monophasic (S1) and brine signal of biphasic (S3,4 and 5) T_2 distribution for a) C4 and b) C5.

CONCLUSION AND PERSPECTIVES

NMR transverse relaxation times (T_2) were interpreted for some Brazilian deep-water carbonates under the different saturation and wettability conditions of a combined Amott-USBM method. While monophasic T_2 distribution was more sensible to the samples variation in characteristic pore lengths, the biphasic T_2 distributions had signals overlapped from the fully-brine-saturated micro pores (thus water-wet) and the brine and crude oil presence in meso-to-macro pores. Several arguments were presented showing that the crude oil relax quite close to its bulk T_2 signature which allowed a simple signal separation in T_2-domain. Samples with the Amott-USBM indices indicating a preferably oil-wet condition presented T_2 distributions shifted to shorter values after restoring native wettability. With the aging, crude oil increased its contact with the surface of the meso-to-macro pores. After imbibition and second drainage, the presence of residual crude oil makes brine relax in different sites with more or less contact with the pore walls (i.e. shorter or longer T_2, respectively). This work is been extended for different carbonate reservoirs with a bigger number of samples. The evaluation shall be improved with others NMR techniques such as spatial T_2 and difusion-T_2 measurements.

ACKNOWLEDGEMENTS

The authors thank Petróleo Brasileiro SA (PETROBRAS) for releasing publication. Edmilson Helton Rios is grateful to CNPq and Petrobras for his research fellowship.

REFERENCES

1. Brown, R.J.S and Fatt, I.: “Measurement of Fractional Wettability of Oilfield Rocks by the Nuclear Magnetic Relaxation Method”, *Trans. AIME*, (1956) Vol. 207, p.262–264.
2. Al-Mahrooqi, S.H., Grattoni, C.A., Muggeridge, A.H. and Jing, X.D.: “Wettability Alteration During Aging: The Application of NMR to Monitor Fluid Redistribution”, *Society of Core Analyst*, (2005) Toronto, August 21-25.
3. Looyestijn, W. and J. Hofman, “Wettability Index Determination by Nuclear Magnetic Resonance,” Proceedings of SPE Middle East Oil and Gas Show and Conference, (2005).
4. Al-Muthana, A.S., Hursan, G.G., Ma, S.M., Valori, A., Nicot, B. and Singer, P.M., “Wettability as a function of pore size by NMR,” (2012) SCA2012-31.

5. Donaldson, E., R. D. Thomas, and P. B. Lorenz, "Wettability Determination and Its Effect on Recovery Efficiency," SPE Journal, (1969), 9, pp. 13-20.
6. Anderson, W.G. "Wettability Literature Survey - Part 1 to 6," *Journal of Petroleum Technology*, (1986-1987), vol. 38-39.
7. Dunn, K.J., Bergman, D.J. & Latorraca, G.A., 2002. Nuclear Magnetic Resonance-Petrophysical and Logging Applications, Pergamon Press, Oxford.
8. Machado, V.F., Ramos, P.F.O., Netto, P., Azeredo, R.B.V., Boyd, A., Souza, A.A., Zielinski, L. & Junk, E., 2012. Carbonate Petrophysics in Wells Drilled with Oil-Based Mud, Petrophysics, 53(4), 285-292.

MULTI-SCALE ROCK ANALYSIS FOR IMPROVED ROCK TYPING IN COMPLEX CARBONATES

Moustafa Dernaika, Yasir Naseer Uddin, Safouh Koronfol, Osama Al Jallad and Gary Sinclair, Ingrain Inc-Abu Dhabi

This paper was prepared for presentation at the International Symposium of the Society of Core Analysts held in St. John's, Newfoundland and Labrador, Canada, 16-21 August, 2015

ABSTRACT

The evaluation of carbonate reservoirs is a complex task because of the inherent heterogeneities that occur at all length scales. Rock types may be defined differently at different scales and this introduces a challenge in capturing heterogeneity in a single rock volume. Heterogeneities at smaller length scales must be upscaled into larger scale volumes to better predict reservoir performance. The objective in this study is to define carbonate rock types at multiple scales and then upscale those rock types to the whole core level.

Representative core plugs were selected in a heterogeneous reservoir interval based on statistical distribution of litho-types in the core. The litho-types were described by porosity and mineralogy variations along the core length using advanced dual energy XCT imaging. Plug-scale rock types were defined on the basis of petrophysical data and geological facies. High-resolution micro to nano XCT images were integrated in the rock typing scheme. Those rock types were upscaled to the whole core level by linking the core litho-types to the plug data.

The core litho-types (porosity and mineralogy) gave good representation of the whole core heterogeneity and were reliable for selecting representative samples. This was qualified by X-ray diffraction mineralogy and plug porosity measurements. This allowed establishing the link between plugs and whole cores and hence upscaling rock type information to the whole core scale. The high-resolution digital images emphasized the different pore geometries in the samples and improved the definition of the rock types. Accurate porosity and permeability logs were derived along the core length and gave very good match with the plug data.

The paper presents an advanced and quick tool for representative sample selection and statistical core characterization in heterogeneous reservoirs. The identified rock types at multiple scales provided new insights into carbonate heterogeneity and gave upscaling options for rock types and petrophysical data. The upscaled rock types at the whole core level enhance the prediction of dynamic imbibition data along the reservoir column for improved reservoir performance.

INTRODUCTION

Proper core characterization is often overlooked in rock typing and sample selection studies. Random core sampling is usually performed and the selected plugs are not associated to the heterogeneity at the whole core level. This leads to unrepresentative selection of the core samples and their rock types, and hence raises questions about the effectiveness of the core data in reservoir models and their calibrations.

In this study, rock typing was first established at the whole core level by advanced dual energy CT scanning. Three main lithologies were identified that appeared to be the main control of the petrophysical variations along the core length. Representative plugs were selected from each lithology and analysed to confirm the rock types at the micro level. This was performed by Poro-Perm measurements, thin-section photomicrograph description, mercury injection analysis and high resolution XCT imaging.

DETAILED WHOLE CORE CHARACTERIZATION

X-ray CT imaging is a powerful non-destructive method used in the oil industry to evaluate the internal structures of reservoir cores. When the core is imaged by the Dual Energy technique it provides two distinct 3D images by using a high- and a low- energy setting. The high-energy images are more sensitive to bulk density (Compton Scattering effect) and the low-energy images are more sensitive to mineralogy (Photoelectric Absorption effect). The bulk density (RHOB) and effective atomic number (Zeff) values are computed independently for each CT slice along the core length [1].

Lithology Log and Statistical Analysis

In this study, 300 feet of reservoir core was imaged by the dual energy technique, and the bulk density (BD) and Zeff were calculated at 0.5 mm spacing. Figure 1(a) shows the bulk density and Zeff variations with three-color mineralogy log. The detected minerals were calcite (for Zeff larger than 14), dolomite (at Zeff around 13) and partially dolomitized core (at Zeff around 14) [2]. This mineralogical variation was also confirmed by XRD analysis performed on rock samples taken from each Zeff response along the core length. The identification of these minerals was obtained at very early stage of the study while the core was still in the barrel, hence providing a quick tool for detailed core characterization and representative sample selection. The volume percent of each mineralogy with respect to the total core volume was quantified from the whole core CT data and is presented in the pie chart in figure 2(a). The core is mainly composed of calcite with 66 vol%, 15 vol% dolomite and 19 vol% partially dolomitized core.

Core-Scale Porosity and Permeability

Representative samples were taken from each mineralogy along the core and were measured for helium porosity and gas permeability. The poro-perm data for the acquired plugs are plotted in figure 2(b), and shows two distinct correlations that are controlled by the different characteristics of the mineralogy in the reservoir. The dolomite and partially dolomitised plugs gave single trend with the dolomite samples at the higher poroperm range. Porosity ranges from 12 to 30 porosity unit and the permeability varies from 5 mD

to 1000 mD. On the other hand, the calcite samples gave a lower permeability trend varying from 0.02 mD to 4 mD, while the porosity ranging from 8 to 25 porosity unit.

Figure 1(b) compares the plug porosity data with the core porosity log derived from the XCT bulk density data along the core length. The core porosity was calculated from the bulk density log and by using different grain density (GD) values for each mineralogy (GD: 2.71 g/cc for calcite, 2.85 g/cc for dolomite and 2.79 g/cc for partially dolomitized (dol/cal) intervals). There is an overall reasonable match between the plug helium porosity and the XCT-derived whole core porosity. Many plugs were taken in the core and gave different porosity values at almost the same depth intervals because of the core heterogeneity that cannot normally be characterized properly by plug-scale measurements. The comparison shows better matches for lower porosity range (i.e. <15%) at which the core shows less heterogeneity. In direct conventional comparison studies between whole core and plug helium porosity measurements, the whole core porosity data would normally be lower than the plug porosity [3,4], confirming our findings in this study.

Figure 1(c) compares the plug gas permeability with a permeability log derived along the core length from the porosity log and by using the plug poro-perm relations from figure 2(b). A very good comparison is observed between the core permeability log and the plug data. Very heterogeneous plugs overestimate core permeability by short-circuiting flow either because of fractures or vuggy porosity channels that do not represent the full diameter core [3,4]. Around two to three order of magnitude increase in permeability is seen in the dolomite intervals, which suggests large improvement in the rock transport properties with dolomitization for this reservoir under study.

ROCK TYPING

In order to understand the structure and porosity type of the rock types, thin-section and MICP wafers were cut from selected representative locations along the plug lengths. Figure 3 represents typical rock types identified from the different mineralogical variations at the whole core level. The figure presents (from left to right, in each RRT) 2D whole core XCT image, high-resolution micro CT image, mercury-derived pore-throat size distribution (PTSD) from mercury injection experiments and thin-section photomicrograph. The whole core image represents the location from which the plug was taken. The high-resolution micro images for the three rock types are taken at different resolutions to resolve the pore system. The dolomite rock type needed lower resolution at 4 micron/voxel where the corresponding mercury peak is at 10 micron pore throat radius and thin-section photomicrograph shows a complete dolomitised grainy system with inter-crystalline porosity. On the other hand, the pore system of the calcite rock type was only resolved by nano imaging at a voxel resolution of 0.064 micron. This muddy calcitic rock type is almost completely made of micrite with inter-particle porosity and a mercury peak at 0.7 micron. The partially dolomitized rock type gives the mercury peak at 3 micron pore throat radius and was imaged at 2 micron/voxel. Both the thin-section photomicrograph and the micro CT image show the dolomitized rock with precursor

limestone as micritic particles. This integration of data confirms the rock types and enhances our understanding of these rock types at the micro level that can be upscaled to the whole core by the link of mineralogy.

The rock typing scheme presented in figure 3 can be populated in the whole core by the identified mineralogy as depicted in figure 1(a). In this perspective, the different minerals in this core are the main control of the petrophysical and fluid flow in the reservoir. The dolomitization that occurred has been a great improvement in the rock properties in the core, which is mainly composed of low permeability calcite. The dolomitization and partial dolomitization in the core have enhanced the permeability by 2 to 3 orders of magnitude and this was crucial for reservoir modeling and field development plan.

SUMMARY AND CONCLUSION

Dual Energy CT scanning was used to identify three different lithological variations along the core length by bulk density and effective atomic number. The core was mainly composed of low permeability calcite and higher permeability dolomitized intervals, which were crucial for enhanced petrophysical and fluid flow properties. Representative plugs were cut from the different lithologies and were grouped in three different rock types based on micro CT imaging, MICP analysis and thin-section description. The following can be concluded from this study:

1. Dual Energy CT scanning is a quick and powerful tool to accurately identify porosity and mineralogy variations along reservoir core lengths at early stages of the analysis.
2. The identified mineralogy in this core was found to be the main control of transport properties and fluid flow.
3. The CT-derived porosity and permeability logs at the core level showed good match with the plug data and gave averaged properties in more heterogeneous intervals.
4. Two distinct poro-perm correlations were established for the calcite and dolomitized rock types.
5. Rock typing was attempted at the following different scales, and was shown to give an excellent tool for improved understanding and upscaling:
    a. Whole core RRT by porosity and mineralogy logs
    b. Plug RRT by poro-perm
    c. Micro-level RRT by high-resolution CT, MICP and thin-section

ACKNOWLEDGEMENTS

The authors wish to acknowledge Ingrain Inc for the permission to publish the results of this study.

REFERENCES

1. Wellington, S.L. and Vinegar, H.J.(1987): “X-Ray Computerized Tomography,” J. Pet Tech 39 (8): 885-898. SPE-16983-PA.

2. Dernaika, M.R., Basioni, M., Dawoud, A., Kalam, M.Z., and Skjæveland, S.M. (2013):"Variations in Bounding and Scanning Relative Permeability Curves with Different Carbonate Rock Types" J. Res. Eval. & Eng. (August 2013) paper SPE-162265-PP presented at the Abu Dhabi International Petroleum Exhibition & Conference held in Abu Dhabi, UAE, 11–14 November (2012).
3. Dernaika, M., Serag, S. and Kalam, M.Z., (2011): "The Impact of Heterogeneity and Multi-Scale Measurements on Reservoir Characterisation and STOOIP Estimations" paper SCA2011-46 presented at the International Symposium of the Society of Core Analysts held in Austin, Texas, USA 18-21 September.
4. Ehrenberg, S.N., 2007, Whole core versus plugs: Scale dependence of porosity and permeability measurements in platform carbonates: AAPG Bulletin, V. 91, NO. 6 (June 2007), pp. 835 – 846.

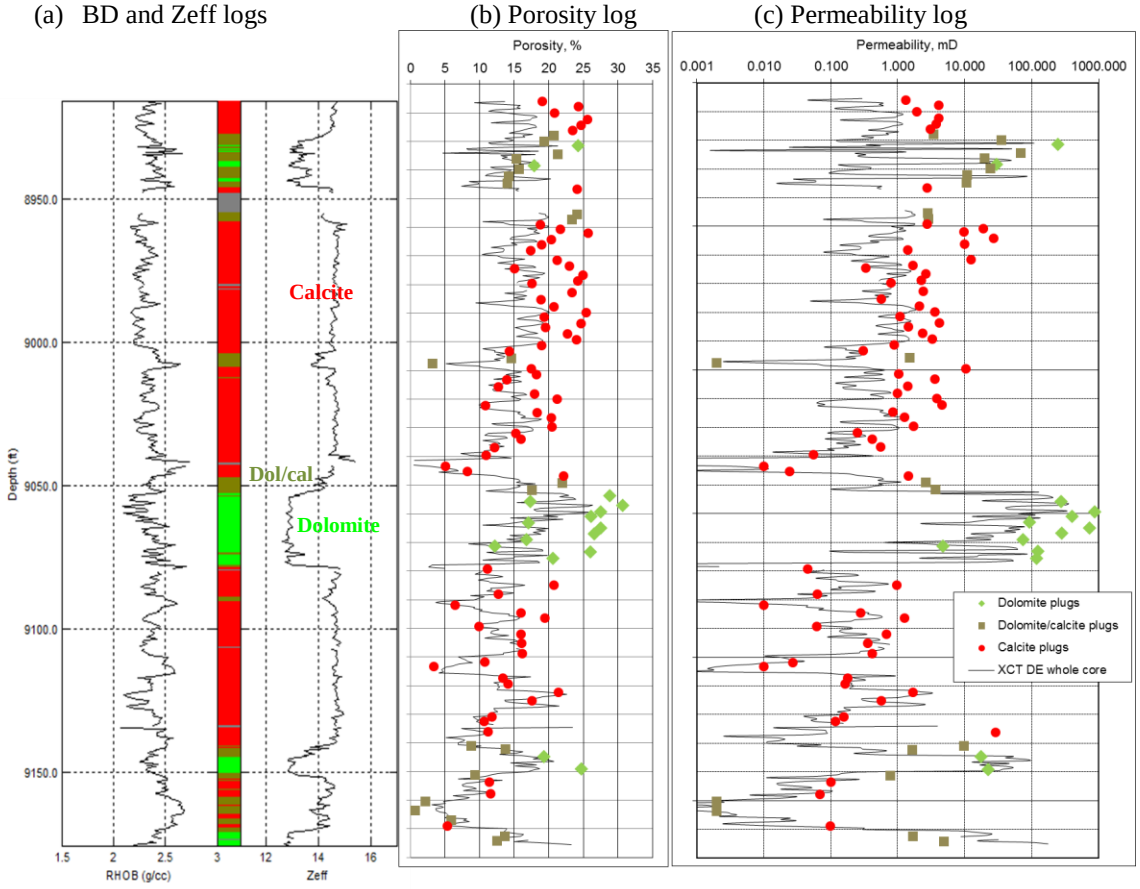

Figure 1 (a) XCT Dual Energy-derived bulk density and Zeff logs along the core length with colored mineralogy log based on Zeff variation. (b) Comparison of DE-derived porosity with plug porosity. (c) Comparison of DE-derived permeability with plug permeability.

(a) (b)

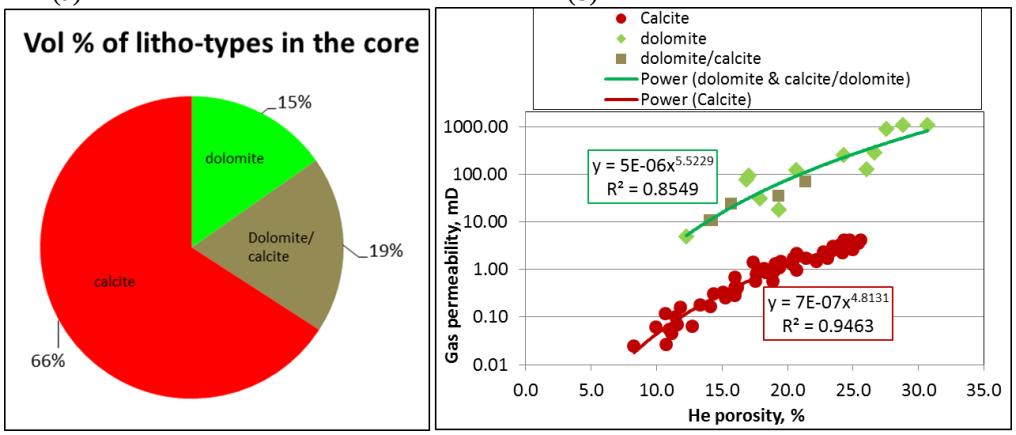

Figure 2 (a) Dual Energy-derived statistical analysis of the litho-types in the core (data from figure 1a). (b) Poro-perm relations for the calcite and the dolomitized plugs.

(a) Dolomite RRT

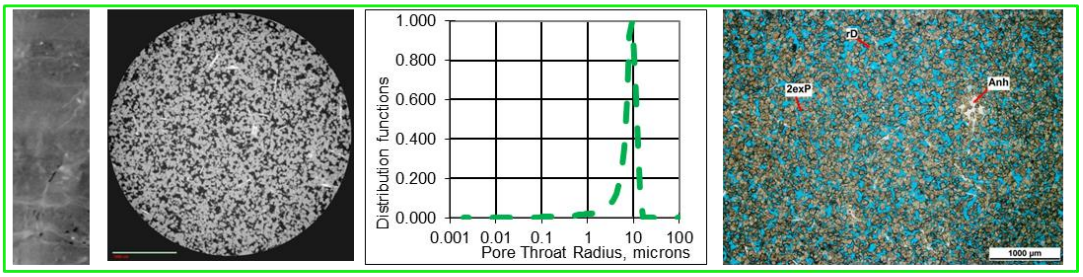

(b) Dolomite/calcite RRT

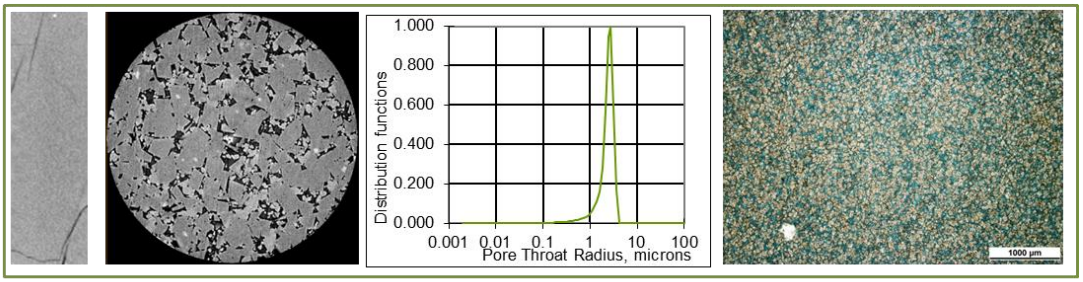

(c) Calcite RRT

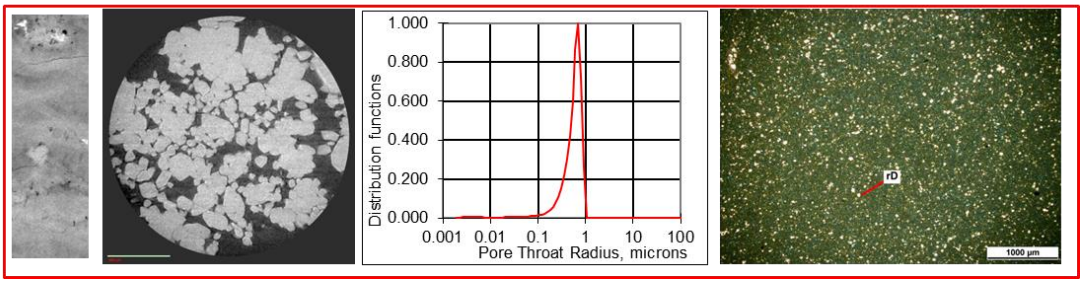

Figure 3 From left to right (in each RRT): 2D whole core XCT image, high resolution micro CT image, mercury-derived pore-throat size distribution (MICP) and thin-section photomicrograph.

ASSESSMENT OF SIDEWALL CORES FOR ROUTINE AND SPECIAL CORE ANALYSES

F. Pairoys[1], A. Nadeev[1], K. Kirkman[1], G. Poole[1], K. Bohn[1], M. Alexander[1], N. Radwan[1], W. Abdallah[2], M. Akbar[3]

[1]Schlumberger Reservoir Laboratories, Houston, Texas, 77041, United States
[2]Schlumberger Dhahran Carbonate Research, Dhahran Techno Valley, Saudi Arabia
[3]Ex Schlumberger - Independent O&G Consultant, Toronto, Canada

This paper was prepared for presentation at the International Symposium of the Society of Core Analysts held in Newfoundland and Labrador, Canada, 16-20 August, 2015

ABSTRACT

This paper assesses the authenticity of the petrophysical measurements made on core plugs taken with a new downhole sidewall coring tool that can acquire core-plugs of 1.5" diameter and lengths of 2.5", 3.0" and 3.5". For this purpose, one block of Indiana limestone and one block of Berea sandstone were used. These blocks were characterized with a minipermeameter through acquisition of minipermeability grid points.

Two types of twin plugs were cut from each block at locations having similar permeability range. The first set of plugs was cut from each block using the new downhole rotary sidewall coring tool with a dimension of 1.5" diameter and 2.5" length. The second, twin set of plugs was cut with a conventional rotary core-plugging device used by commercial core laboratories. Both types of plugs were full-size scanned using micro-CT and measured for routine core properties. Resistivity and NMR measurements were also made after brine saturation.

The results of the measurements made on the new sidewall-coring plugs were found to be comparable with the measurements made on the plugs acquired with the conventional core-plugging device. It can be concluded that the new sidewall cores are suitable for RCA and further SCAL analyses.

INTRODUCTION

Routine (RCA) and Special Core Analyses (SCAL) are important for field development projects. One of the main sources of data for this purpose comes from rock samples which are acquired in the form of drill cuttings, continuous whole cores and sidewall cores. The most established and well accepted of these rock sample sources is the continuous whole core - sidewall cores have not gained such acceptance yet. The most probable reasons may include non-standard dimensions of such cores and their potential alteration in the process of acquisition.

In the past, the samples from rotary sidewall coring were limited in size, resulting in limited laboratory evaluation. Recently, a new coring tool has been developed to obtain

1.5” diameter sidewall core samples equivalent to standard laboratory core plugs. With this new coring capability, operators can fully characterize an extended reservoir interval in a single sidewall coring descent instead of multiple sidewall coring descents or multiple stands of whole core retrieval. There are no published documents proving that these core samples can provide good routine core analysis data. The purpose of this study is to compare core analysis data from samples obtained from a conventional lab plugging machine and from the rotary sidewall coring tool (Figure 1):

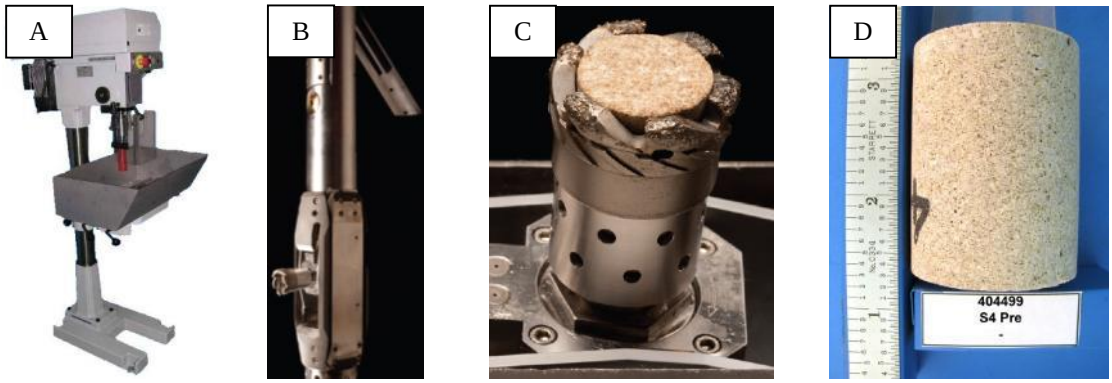

Figure 1: Conventional laboratory plugging machine (A), rotary sidewall coring tool (B), 1.5” diameter core within the drill bit (C) and 3.5” length sidewall core (D)

ROCK SAMPLES

Two rectangular cross section outcrop blocks were selected for the study: one block of Indiana limestone and one block of Berea sandstone. These blocks were indexed into a grid system (rows R and columns C (Figure 1). For each grid section local gas permeability data were obtained with a mini-permeameter in a first step with the objective to identify several zones with similar permeability prior to coring. This ensured the reliability of the comparisons between the core analysis data obtained from twin samples plugged with the two different techniques.

The permeability range for the Berea sandstone block was found to be between 500 and 800 mD whereas the permeability for the Indiana limestone block ranged from 15 to 150 mD. Figure 2 shows a picture of the Indiana limestone block which was plugged with both laboratory plugging machine and rotary sidewall coring tool:

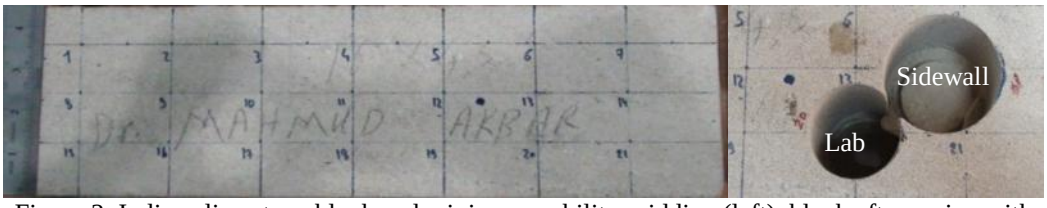

Figure 2: Indiana limestone block and mini-permeability gridding (left), block after coring with conventional laboratory plugging machine and rotary sidewall coring tool (right)

Four core plugs were cut from each block (Berea and Indiana): on each block, two core

plugs were cut using the conventional laboratory plugging machine, two using the rotary sidewall coring tool. They were all drilled in zones of close permeability. Tap water was used as drilling fluid.

The integrity of the plugs did not seem to be affected by the way the plugs were drilled (Figure 1, D), at least qualitatively. Results of additional measurements are described in detail below to prove that the properties of plugs cut with the rotary sidewall coring tool and with conventional plugging machine are not affected by the coring method.

EXPERIMENTAL RESULTS

All outcrop samples were first Soxhlet cleaned and dried before being measured for routine core properties.

Grain density ρ, ambient helium porosity ϕ (based on Boyle's law), gas and Klinkenberg permeabilities Kg and Kkl (using the pressure falloff method), were performed on all samples. Data results are listed in Table 1:

Block	Mineralogy	Sample Id	Coring type	ρ_g g/cc	ϕ %	Kg mD	Kkl mD	ε_m
Berea	sandstone	BS1	lab	2.64	25.09	704	696.6	4.77
Berea	sandstone	BS2	lab	2.65	25.95	706	698.0	---
Berea	sandstone	BS3	sidewall	2.65	24.84	592	585.2	---
Berea	sandstone	BS4	sidewall	2.65	25.32	699	690.9	4.68
Indiana	limestone	IL4	lab	2.69	15.75	22.4	21.2	8.13
Indiana	limestone	IL10	sidewall	2.69	15.65	58.2	56.21	---
Indiana	limestone	IL14	sidewall	2.70	16.48	29.10	27.74	8.18
Indiana	limestone	IL20	lab	2.69	15.74	33.46	31.97	---

Table 1: Dry core plug properties

Grain density and dry matrix permittivity cannot highlight the presence or absence of micro-fractures. The measured grain density ranges from 2.64 g/cc to 2.65 g/cc for the sandstone samples and from 2.69 g/cc to 2.70 g/cc for the limestone samples. The dry matrix permittivity of four samples was also measured and was found to be in the expected range (around 4.7 for pure quartz and 8.5 for pure calcite from literature – values in dielectric unit).

As to porosity and permeability, the presence of induced fractures can increase both values. The porosity ranges from 24.8% to 25.3% for the sandstone samples and from 15.4% to 17.2% for the limestone samples, gas permeability from 585 mD to 728 mD for the sandstone samples and from 30.4 mD to 56.2 mD.

While three out of the four samples within a group (group BS for Berea Sandstone, group IL for Indiana Limestone) show very good agreement in permeability and porosity, the

overall range of porosity and permeability data obtained within the group can be attributed to natural anisotropy. No evidence is apparent that the sidewall coring tool has damaged the rock during the coring process.

The core plugs were then scanned using X-ray micro-Computed Tomography (micro-CT) techniques. Figure 3 shows typical 2D cross-sections of two Indiana limestone samples, one obtained from the conventional laboratory plugging machine (IL4), one from the rotary sidewall coring tool (IL14):

Figure 3: Typical 2D micro-CT cross-sections obtained from conventional sample IL4 (A) and from sidewall sample IL14 (B)

Micro-CT was used to image core plugs with resolution of 42µm/voxel. A high voltage X-ray tube and different zoom-in objectives allow samples with higher resolution to be scanned (5µm/voxel without physical core mini-plug cutting). Micro-CT image processing and analysis were carried out by using commercial software and in-house developments. 3D pore structure representations of samples IL4 and IL14 are shown in Figure 4:

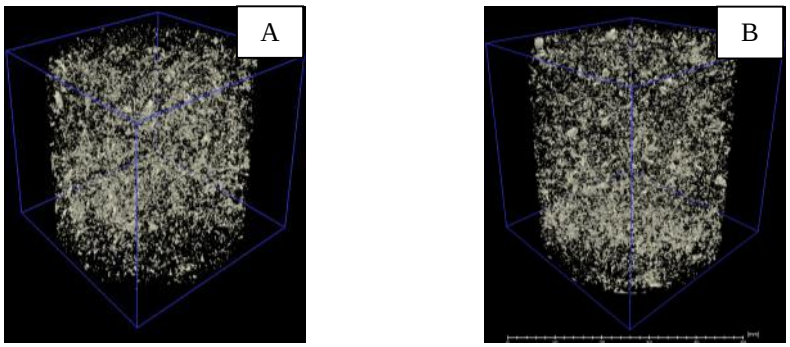

Figure 4: 3D volume rendering from conventional sample IL4 (A) and from sidewall sample IL14 (B)

Both images and 3D volumes in Figure 3 and Figure 4 are very similar. There is no visual evidence of rock structural alterations such as mini-fractures induced by the coring method.

MICP data can also highlight the presence of tiny fractures due to the coring process: tests were run on four end trims from rocks drilled with the two different methods. Figure 5 represents both capillary pressure and pore throat size distribution of two Indiana

limestone and two Berea sandstone rock chips obtained from the end-trims of the samples cut from the conventional laboratory plugging machine (IL4 and BS1) and from the rotary sidewall coring tool (IL14 and BS4):

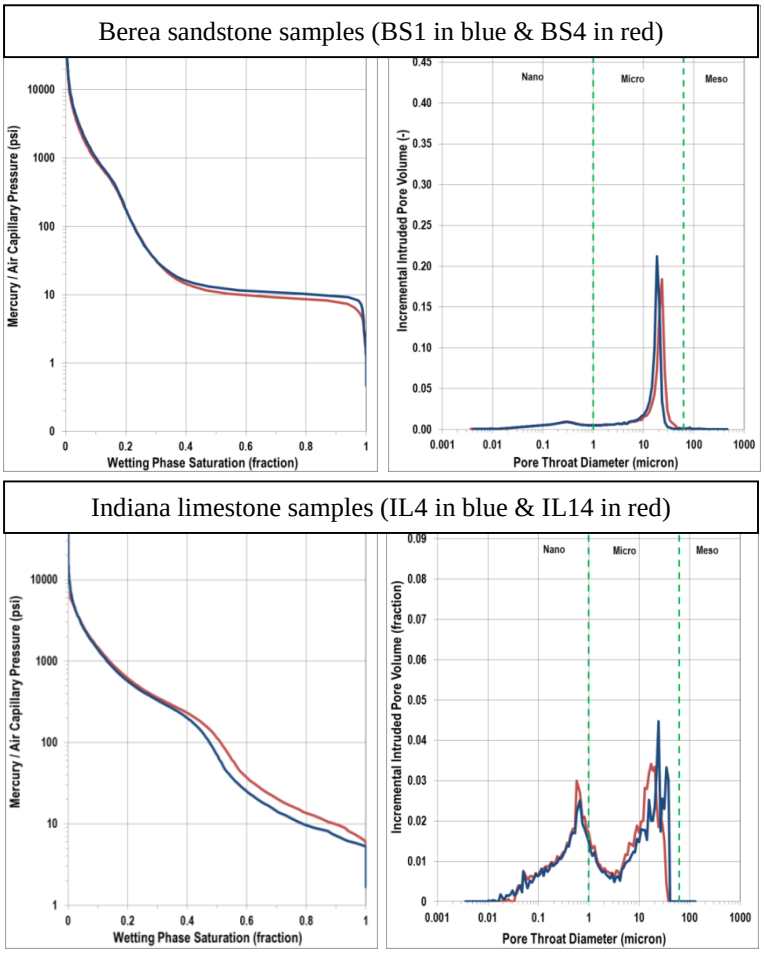

Figure 5: Mercury injection capillary pressure (MICP) and pore throat size distribution

Figure 5 shows that capillary pressure curves Pc and pore throat size distribution curves of sidewall and laboratory samples are very similar - there is no evidence of potential micro-fracture or rock damage due to the coring process.

The MICP parameters obtained from both types of curves are presented in Table 2:

Sample Id	Hg ϕ (%)	Nanopores 1nm<Dia.<1µm (%PV)	Micropores 1nm<Dia.<1µm (%PV)	Mesopores 62nm<Dia.<4µm (%PV)	Hg/air Pe (psi)	Swanson Kg (mD)
IL4	15.8	42.7	57.3	0	6.24	35.7
IL14	16.7	41.0	59.0	0	5.55	38.3
BS1	26.3	19.3	80.0	0.74	1.68	518
BS4	25.4	19.0	80.1	0.85	1.34	616

Table 2: MICP data results

Note that MICP porosity and permeability are close to the ones obtained on core plugs.

Four core samples were then saturated with brine (200 kppm equivalent NaCl). Brine permeability was run on the samples in addition to resistivity and NMR measurements.

Block	Sample Id	Coring type	Brine perm mD	FF @ 1 KHz	m @ 1 KHz	NMR ϕ %
Berea	BS1	lab	536	13.5	1.96	24.2
Berea	BS4	sidewall	532	13.4	1.96	24.0
Indiana	IL4	lab	24.0	53.0	2.16	14.8
Indiana	IL14	sidewall	33.2	48.5	2.10	14.3

Table 3: Brine saturated core plug properties

Table 3 shows that all values (sidewall versus laboratory) are essentially the same for each couple of cores, with cementation factors equal to 2.0 for sandstone and 2.1 for limestone. If fractures would have been induced, the permeability and cementation factor on sidewall cores would have been found respectively higher and lower.

The NMR porosity was obtained from T_2 distribution measurements (Figure 6).

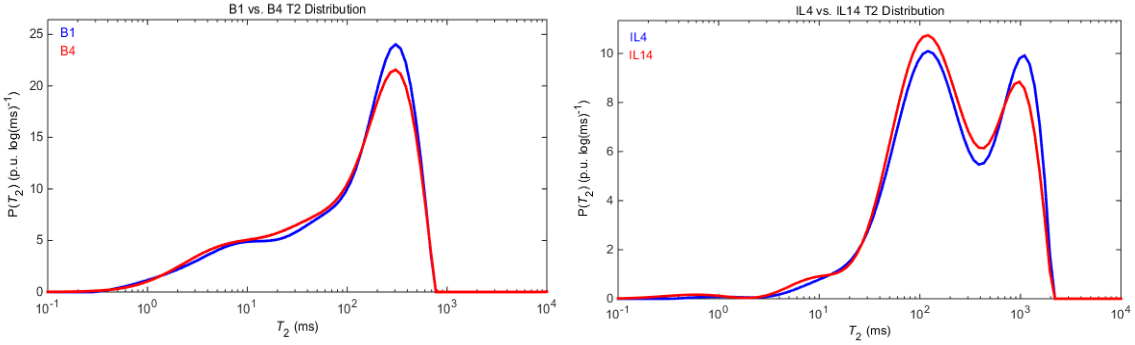

Figure 6: NMR T_2 distributions of BS1 and BS4 (left), and IL4 and IL14 (right)

The NMR porosity is slightly lower than the helium porosity, maybe due to some evaporation during the ambient NMR tests. However, the results are still in agreement with the laboratory porosity. T_2 distributions do not show a difference between sidewall and conventional samples, showing again that the rocks were not altered by the way they were cut.

CONCLUSIONS

Core plugs of different rock types were cut using both a standard laboratory plugging machine and a new rotary sidewall coring tool. All samples were full-size scanned using micro-CT and measured for routine core properties, resistivity, NMR and dielectrics. The results of the measurements made on the new sidewall-coring plugs were found to be comparable with the measurements made on the plugs acquired with the conventional

core-plugging device. It is concluded that the sidewall cores are suitable for RCA and SCAL analyses. The SCAL work is in progress at the Houston Schlumberger Reservoir Laboratory; the preliminary results confirm the good quality of the sidewall cores. To summarize, the new rotary sidewall coring tool is now an alternative for acquiring high quality downhole core samples with proper core size for laboratory analyses.

MAGNETIC SUSCEPTIBILITY OF DRILL CUTTINGS IN A NORTH SEA OIL WELL: A RAPID, NON-DESTRUCTIVE MEANS OF CHARACTERIZING LITHOLOGY

[1]Arfan Ali, [2]David K. Potter and [3]Andrew Tugwell
[1]Shell UK Limited, Aberdeen, UK
[2]Department of Physics, University of Alberta, Edmonton, Canada
[3]Advanced Downhole Petrophysics Limited, Aberdeen, UK

This paper was prepared for presentation at the International Symposium of the Society of Core Analysts held in St. John's, Newfoundland and Labrador, Canada, 16-21 August, 2015

ABSTRACT

Magnetic susceptibility measurements provide a non-destructive method to rapidly characterize drill cuttings at the wellsite or laboratory. Our previous studies on core plugs, slabbed core and whole core have demonstrated that magnetic measurements can identify lithological variations, estimate mineral content, and correlate with key petrophysical properties (such as permeability) and with downhole gamma ray data. In the present study volume magnetic susceptibility measurements were undertaken on drill cuttings from a North Sea oil well using a portable low field magnetic susceptibility sensor. The values were then converted to mass magnetic susceptibility by dividing by the bulk density of each sample. The results clearly indicated the main lithological zonations in the well, and provided estimates of basic mineral type (diamagnetic versus paramagnetic or ferrimagnetic) significantly quicker and cheaper than undertaking XRD measurements. The magnetic results also showed a correlation with the downhole LWD (logging while drilling) gamma ray profile. Interestingly, the correlation was the opposite way round to that observed in most other reservoirs we have studied. However, this provided additional mineralogical information for the well in the present study. Normally a low gamma ray signal (e.g., in a clean sandstone interval) would give a low or negative magnetic susceptibility due to diamagnetic quartz, whereas a high gamma ray signal (e.g., in shale) would give a higher magnetic susceptibility signal due to paramagnetic clays etc. In the present study many of the low gamma ray sandstone intervals exhibited a higher magnetic susceptibility signal, which indicated that there are additional paramagnetic and/or ferrimagnetic minerals present in those intervals in addition to the main diamagnetic matrix mineral (quartz). These additional higher magnetic susceptibility minerals can, for example, be due to a strongly paramagnetic mineral such as siderite, small amounts of a ferrimagnetic mineral such as magnetite or the canted antiferromagnetic mineral hematite. These minerals can affect the permeability, and may explain why productivity has been lower in this well.

INTRODUCTION

Drill cuttings have generally been a highly under utilized resource in the petroleum industry. Apart from some exceptions, such as the Darcylog™ method to determine permeability [1] and porosity from drill cuttings, there have been very few published studies that have derived mineralogical or petrophysical properties from drill cuttings. Our previous magnetic susceptibility work on conventional core plugs [2], slabbed core [3,4] and whole core [5] proved fruitful in demonstrating correlations between magnetic susceptibility, mineralogy (especially clay content) and key petrophysical properties such as permeability. For instance, our work on North Sea oilfields [2,3] showed strong correlations between magnetically derived illite content and permeability. The present paper describes how magnetic susceptibility measurements on drill cuttings can rapidly and non-destructively identify mineralogical / lithological variations. In the present study we made 421 measurements from 157 bags of drill cuttings from a North Sea oil well. We were told by the operating company that there was an issue in this well, in that the oil production was lower than expected compared to other wells in the same field. We were therefore asked to see if the drill cuttings measurements might provide a possible reason for the lower production.

METHODS

The drill cuttings measurements were performed at Iron Mountain in Dyce, Aberdeen, UK. The sample boxes containing bags of drill cuttings were arranged in order of depth (**Figure 1 (a)**). Each sample bag contained drill cuttings from a particular depth interval. 10cc plastic vials were used as sample pots and were filled with randomly selected "spoonfuls" of cuttings from each sample bag (**Figure 1 (b)**). Volume magnetic susceptibility measurements were undertaken on the vials containing the drill cuttings using a small portable low field Bartington MS2B magnetic susceptibility sensor connected to laptop via an MS3 meter (**Figure 2**). Each sample vial containing drill cuttings was also accurately weighted. Volume magnetic susceptibility measurements were then simply converted into mass magnetic susceptibility as follows:

$$\chi = \kappa / \rho \quad (1)$$

where χ is the mass magnetic susceptibility, κ is the measured volume magnetic susceptibility, and ρ is the bulk density of the drill cuttings in the vial. The advantage of using mass magnetic susceptibility is that it removes any small effects due to porosity, which can affect the volume magnetic susceptibility measurements. This includes the intrinsic porosity of the individual drill cuttings and also the "porosity" between individual drill cuttings. This ensures that drill cuttings with an identical mineralogy will give exactly the same mass magnetic susceptibility value (whereas they would give different volume magnetic susceptibility values if the amount of those cuttings is different in each sample vial). During the measurement procedure a calibration sample was also measured every hour to check whether there was any drift in the sensor.

RESULTS AND DISCUSSION

The results showed that the mass magnetic susceptibility was positive throughout the 9,000 ft section of the well. Moreover, an analysis of the magnetic results with the LWD (logging while drilling) gamma ray data (**Figure 3**) shows that the sandstone intervals identified by the low gamma ray sections (shaded yellow on the gamma ray log) have anomalously high mass magnetic susceptibility values (shaded yellow on the mass magnetic susceptibility data). This was very unexpected, since pure quartz sandstone should have a very low, negative mass magnetic susceptibility (since quartz is diamagnetic). The large positive mass magnetic susceptibility values immediately tell us that there are additional paramagnetic and /or ferrimagnetic minerals contained within the sandstones. Possible candidates for these minerals are siderite (a strongly paramagnetic iron carbonate), the ferrimagnetic mineral magnetite, or the canted antiferromagnetic mineral hematite. The additional minerals in the sandstone intervals are not likely to be paramagnetic clays such as illite or chlorite, otherwise they would have given a much higher gamma ray signal. Whilst there was no X-ray diffraction (XRD) data available in this well, there was XRD data for just 10 samples from another well in the same oilfield. The XRD data indicated average values of around 85% quartz, around 4% K-feldspar, 1-2% plagioclase, 1-2% pyrite, around 6% kaolinite (which is diamagnetic) and only trace amounts of illite. No evidence for siderite was seen in this data. Of course the XRD data from the other well may not necessarily be representative of the mineralogy in the present studied well. However, it seems more likely that the observed high mass magnetic susceptibility values are due to a mineral like magnetite or hematite. Small amounts of these minerals would not necessarily be readily identified by XRD, yet would give the observed high magnetic susceptibility values.

The additional minerals identified by the magnetics in the sandstone intervals may have important implications for the petrophysical properties. We have previously demonstrated [6] that small amounts of fine-grained hematite, for instance, can have a very dramatic effect on reducing the permeability. The additional minerals in the sandstones may therefore help to explain why the well in our present study was not as good a producer as other wells in the same oilfield. It is also important to be able to readily identify additional paramagnetic and ferrimagnetic minerals, since nuclear magnetic resonance (NMR) log data can be significantly affected by these minerals.

CONCLUSIONS

1. The drill cutting measurements gave generally high positive mass magnetic susceptibility values in the sandstone intervals (low gamma ray). This is very unusual since pure quartz sandstone is diamagnetic with a low, negative magnetic susceptibility. The magnetic measurements demonstrated that there must be significant additional paramagnetic and/or ferrimagnetic minerals in the sandstone intervals. Potential candidates could be the paramagnetic mineral siderite, the ferrimagnetic mineral magnetite, or the canted antiferromagnetic mineral hematite.

2. The presence of these additional minerals in the sandstones is likely to affect the permeability of the sandstones, and this may in turn be responsible for the lower productivity that has been observed by the operating company in this well.
3. The study demonstrated that magnetic measurements on drill cuttings provide a rapid means of identifying of mineralogical variations over large intervals and are a potentially important supplement to XRD data.

FUTURE WORK

Either high field magnetic susceptibility or magnetic remanence measurements would enable us to determine whether the additional minerals in the sandstones were due to, for instance, small amounts of magnetite or hematite (note that XRD would not necessarily be helpful in this respect). Also it would be useful to undertake magnetic susceptibility measurements on drill cuttings in one of the good producing wells in the same field. If we obtained a normal diamagnetic signal in the sandstones of the good producer then it would be further evidence to suggest that the additional minerals identified in the present well were responsible for its lower productivity. We are waiting for permission from the operating company to undertake these extra studies.

REFERENCES

1. Lenormand, R., Bauget, F., Ringot, G., 2010. Permeability measurement on small rock samples. *2010 International Symposium of the Society of Core Analysts***,** Halifax, Nova Scotia, Canada. Paper SCA2010-32 (12 pages).
2. Potter, D. K., 2007. Magnetic susceptibility as a rapid, non-destructive technique for improved petrophysical parameter prediction. *Petrophysics*, **48** (issue 3), 191-201.
3. Ali, A., Potter, D. K. and Tugwell, A., 2014. Correlation between magnetic properties and permeability: results from a new case study in the North Sea. *2014 International Symposium of the Society of Core Analysts***,** Avignon, France. Paper SCA2014-077 (6 pages).
4. Agbo, B. C. and Potter, D. K., 2014. Novel high resolution probe magnetic susceptibility and comparison with wireline gamma ray and grain size in an Albertan oil sand well. SEG Technical Program Expanded Abstracts: pp. 2590-2594. doi: 10.1190/segam2014-1140.1.
5. Potter, D. K., Ali, A., Imhmed, S. and Schleifer, N., 2011. Quantifying the effects of core cleaning, core flooding and fines migration using sensitive magnetic techniques: implications for permeability determination and formation damage. *Petrophysics*, **52** (issue 6), 444-451.
6. Potter, D. K., Ali, A. and Ivakhnenko, O. P., 2009. Quantifying the relative roles of illite and hematite on permeability in red and white sandstones using low and high field magnetic susceptibility. *2009 International Symposium of the Society of Core Analysts***,** Noordwijk aan Zee, The Netherlands. Paper SCA2009-11 (12 pages).

Figure 1. (a) Bags of drill cuttings arranged in order of their depth in the well. (b) Samples of drill cuttings being put into the vials for measurement.

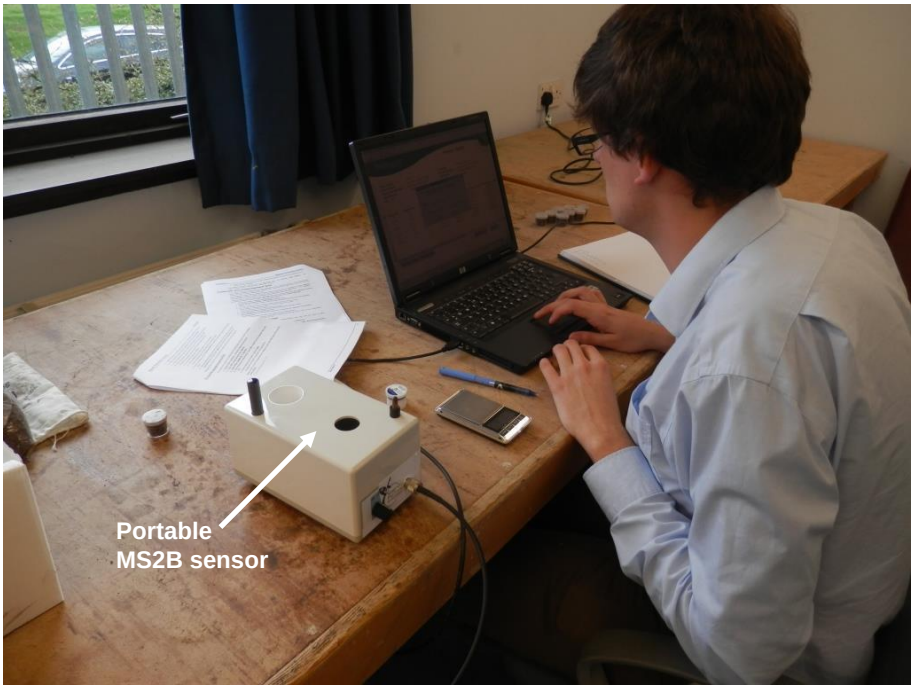

Figure 2. View of the portable MS2B magnetic susceptibility sensor, connected to a laptop.

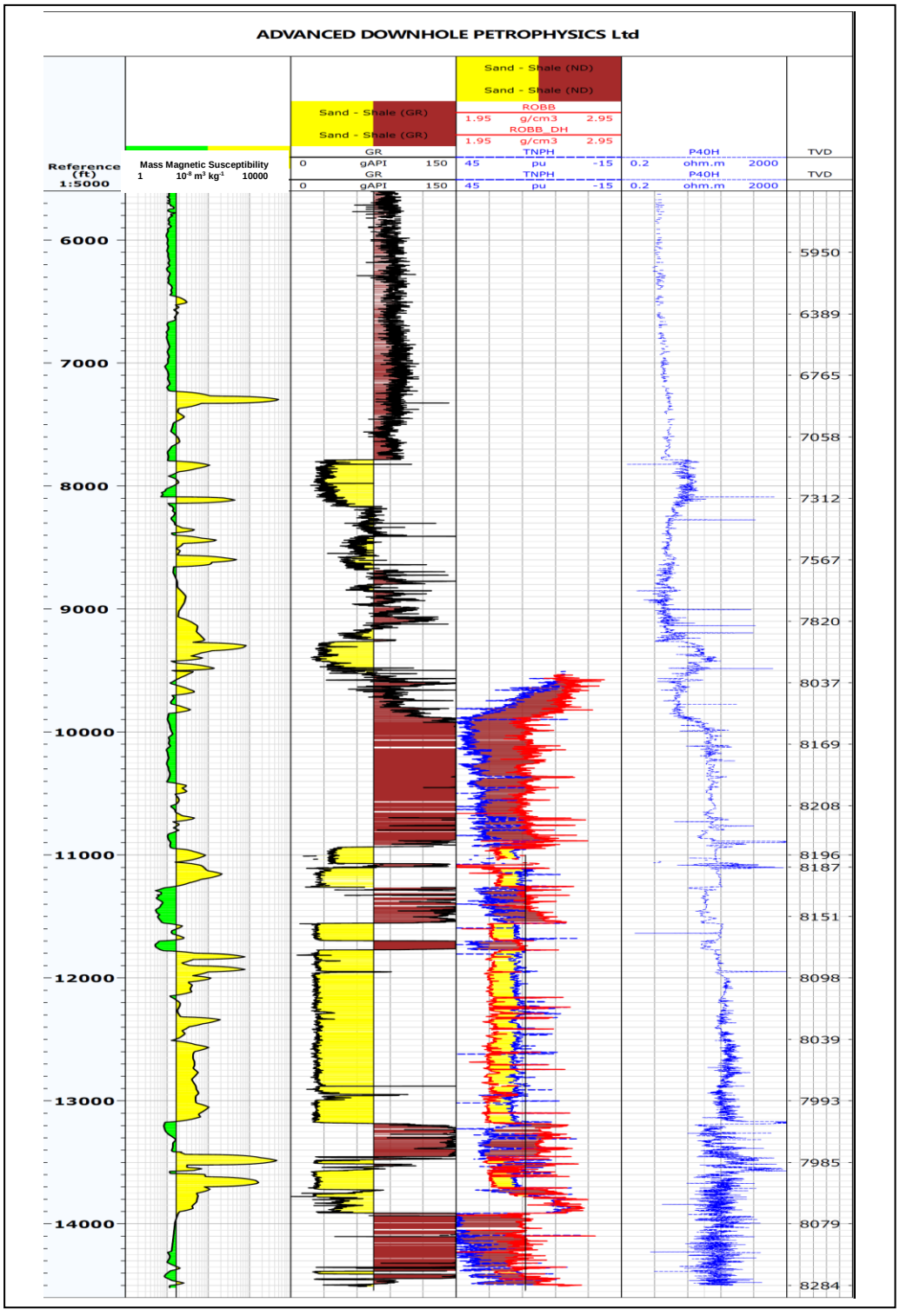

Figure 3. Mass magnetic susceptibility results for 421 measurements over 9,000 ft are shown in the left hand column (scale runs from 1–10,000 x 10^{-8} m^3 kg^{-1}). An arbitrary cut-off (green/yellow) is given at around 17 x 10^{-8} m^3 kg^{-1} to compare easily with the low gamma ray (yellow) values in the adjacent column.

CARBONATE NMR PERMEABILITY ESTIMATES BASED ON THE WINLAND-PITTMAN MICP APPROACH

Edmilson Helton Rios[1], Adam Keith Moss[2], Timothy Neil Pritchard[2], Ana Beatriz Guedes Domingues[2] and Rodrigo Bagueira de Vasconcellos Azeredo[3]
[1]National Observatory
[2]BG Group plc
[3]Fluminense Federal University

This paper was prepared for presentation at the International Symposium of the Society of Core Analysts held in St. John's Newfoundland and Labrador, Canada, 16-21 August, 2015

ABSTRACT

Nuclear magnetic resonance (NMR) logging is widely used for continuous downhole permeability estimates. But long before NMR, laboratory measurements of capillary pressure curves were used for the same purpose. Remarkably, the mercury injection capillary pressure (MICP) technique was developed for predicting the permeability of small and irregular-shaped samples, such as drilling cuts. In the Winland-Pittman MICP approach, pore-throat radii corresponding to different Hg saturations were individually correlated with porosity and permeability. The saturation where the best correlation is found defines the critical aperture. By adapting this methodology for NMR context, this work introduces a novel concept of cumulative saturation cutoff applied on the transverse relaxation time (T_2) distributions. The performance and the fitting coefficient as a function of saturation cutoff were graphically analyzed for a group of North Sea and Middle East Carbonate core plugs. Critical saturation cutoffs for both pure and size-scaled NMR distributions delivered better permeability estimates when compared with the standard logarithmic mean estimator.

INTRODUCTION

Kozeny developed a theory, later improved by Carman, in which porous rocks are regarded as bundles of capillary tubes [1]. The so-called Kozeny-Carman equation takes many forms, including the following:

$$k_{kc} = a' \phi_b \left(\frac{V}{S}\right)^c, \quad (1)$$

where a', b and c are general coefficients for adjustment, ϕ is porosity, V/S is volume-to-surface-area ratio, also known as the hydraulic radius. For simple pore geometries, V/S can be written as R_p/γ, where R_p is the pore radius and γ is a pore shape factor (e.g. 1 represents flat or flake-like pores, 2 represents open-ended cylindrical pores and 3 represents spherical pores). From Equation 1, Winland [2]

and then Pittman [3] related MICP-derived pore-throat radius R_t with permeability and porosity, as following:

$$logR_t = a_1 logk + a_2 log\phi + a_3, \quad (2)$$

where $a_1 = 1/c$, $a_2 = -b/c$ and $a_3 = (\log a')/c + log(\delta/\gamma)$, with δ being the pore body-to-throat ratio (R_p/R_t). $R_t = -2\sigma cos\theta/P_c$, with σ and θ being the air-mercury interfacial tension and the surface contact angle, respectively, and P_c is the capillary pressure, selected for a specific saturation of the MICP curve $S(P_c)$. The best-performing correlation defines the aperture that best describes permeability.

Seevers [4] and then Kenyon [5] showed that nuclear magnetic resonance (NMR) porosity and an average of the longitudinal T_1 or transverse T_2 NMR relaxation times could be indirectly used as the independent variables of Equation 1 if considered the fast diffusion regime and assuming no diffusional relaxation effects due to magnetic field gradients nor diffusion pore coupling [6]. The Seevers-Kenyon NMR estimator can be written for T_2 (the widely used in modern NMR logging) as follows:

$$k_{SK} = a\phi_{NMR}^b (T_{2lm})^c, \quad (3)$$

where $a = a'\rho_2^c$ is a pre-multiplier factor that includes the T_2 surface relaxivity (ρ_2), $\phi_{NMR} = \sum \phi(T_2)$ is the NMR-derived total porosity and $T_{2lm} \approx (1/\rho_2)(V/S)$ is the logarithmic mean of the $\phi(T_2)$ distribution such that $T_{2lm}^{\phi_{NMR}} = \prod T_2^{\phi(T_2)}$. Literature coefficients are commonly used in the logging suites under an estimator usually called as Schlumberger-Doll-Research model, $k_{SDR} = a\phi_{NMR}^4 T_{2lm}^2$. In this work, the Winland-Pittman approach was adapted for the NMR context as follows:

$$k_{sat} = a\phi_{NMR}^b (T_{2sat})^c, \quad (4)$$

where $a = a'\rho_2^c = (10^{a_3}\rho_2\gamma/\delta)^c$, $b = -a_2 c$ and $c = 1/a_1$ are fitting coefficients, the T_{2sat} is a relaxation time selected for a fixed point in the cumulative saturation curve. The saturation cutoff is applied to the cumulative curves computed from the normalized (or saturation-based) NMR distributions $S(T_2)$, such that $\sum S(T_2) = 1$. Several cutoffs are tested using Equation 6 and the sat-based estimates are compared to the standard k_{SK} estimator.

NMR carbonates are generally less sensitive to variations in pore body size, thus T_2 distributions were size-scaled based on a NMR-MICP data integration. Because true surface relaxivity is very complex to be determined and depends on the method used, a simple scaling factor defined as the ratio of the logarithmic means between MICP and NMR distributions were employed. This size-scaling factor

encompasses both the surface relaxivity and the geometry of the pore system (both assumed to be constant within all pore-size families) as follows:

$$S_{MICP} \equiv \frac{R_{tlm}}{T_{2lm}} \approx \frac{R_{plm}/\delta}{R_{plm}/\gamma\rho_2} = \frac{\gamma}{\delta}\rho_2, \quad (5)$$

where R_{plm} is the logarithmic mean of the pore radius distribution, γ is a pore shape factor for simple geometries and δ is the pore body-to-throat ratio. By solving for ρ_2 in Equation 5 and inserting it into Equations 3 and 4, size-scaled NMR permeability estimators can be obtained where the pre-multiplier a incorporates the geometry of the pore system such that $a = a'(\delta/\gamma)^c$.

EXPERIMENTAL

Carbonates rocks from Cretaceous chalk fields were studied: 14 from Norwegian reservoirs in North Sea (the Valhall, Hod and Tommeliten fields) and 15 diagenetic chalks from Middle East (the Thamama C Formation, Bu Hasa Field, Abu Dhabi). Core plugs (1.5' x 1.8') and small core-end trims (visually representative of the plugs) were cleaned of native fluids via Soxhlet extraction and then dried in an oven [7]. The MICP measurements were performed in an AutoPore II 9220, with a "filling pressure" of 0.1 bar followed by one hundred pressure steps with maximum pressure of 4,130 bar. Plugs were routine core analysed (RCAL) using helium gas at an overburden pressure of 20 bars and then they were fully saturated with a 50,000 ppm brine solution for NMR measurements. The ^{1}H NMR T_2 measurements of core samples were performed on a bench-top NMR analyser at 2 MHz and 30^{o}C using the Carr–Purcell–Meiboom–Gill (CPMG) technique [8], with 4,050 spin echoes spaced by 700 μs (Te). Under sufficient time for fully spin polarization 10s (Tw), signal averages were performed until a minimal signal-to-noise ratio (SNR) of 100. A distribution window with one hundred relaxation-time bins logarithmically spaced from 0.1 to 10,000 ms was set for T_2.

RESULTS

The normalized MICP, NMR, and size-scaled NMR distributions are shown on Figure 1a, b and c, respectively. Left side is the incremental curves and right side is the cumulative curves (two saturation cutoffs are showed as examples), respectively. For MICP and size-scaled NMR, micro-, meso- and macro-porosity ranges are outlined with the 0.3 and 3 μm threshold, in accordance with [9]. All the curves are labelled based on the increasing k_{RCAL} values of the plugs. Small apertures and pores corresponds to plugs with low k_{RCAL} (predominantly North Sea Chalks), whereas large apertures and pores corresponds to plugs with high k_{RCAL} (predominantly Middle East Chalks). The similarity between routine and special core analysed porosity in Figure 2a, indicates that gas, Hg and brine probed representative pore spaces and that isolated fluid-filled pores may not have been present. Figure 2b well illustrate that a simple power regression cannot

simultaneously handle the different pore-perm trends exhibited by the chalk groups. Additional information such as apertures and pore sizes may help in obtaining a global permeability estimator.

The r-squared and the fitting coefficients for the estimators k_{SK} and k_{sat} (with 50 and 85%) are presented in Table 1 for pure and size-scaled T_2. Figure 3 plots the R-square and multiple linear regression coefficients obtained with saturation cutoffs from 5 to 85% under increments of 5%. The y-axis lower limit (0.37) corresponds to the particular case where coefficient c is null (Figure 2b). The performance of k_{SK} for each case is also indicated in the plot. Size scaling improved permeability estimation considerably for all case, producing lower b (for porosity) and higher c (for $S_{MICP}T_2$) coefficients values. It indicates that the size-scaled T_2 distributions are more effective to explain permeability and maybe can mitigate some of the difficulties encountered in carbonate NMR, such as variations in surface relaxivity and diffusive pore coupling. Figure 5 shows the response curves for the k_{sk} and $k_{85\%}$ before and after size scaling. In their original works with sandstones, Winland and Pittman described an equivalent cumulative saturation (from micro to macro) of 65% and 75%, respectively.

CONCLUSION

Inspired by the work of Winland and Pittman on MICP data, a novel NMR permeability estimator was introduced based on new concept of cumulative saturation cutoffs. T_2 associated with macroporosity reveals much better results than the standard T_2 logarithmic mean estimator. To overcome the lower sensitivity of carbonate NMR to pore and throat variation, this new approach was also evaluated after T_2 distribution size scaling. The results exceeded the performance compared to the estimators with pure T_2. The study confirms the potentiality of saturation-based NMR permeability estimator and further evaluation is in course for logging application.

ACKNOWLEDGEMENTS

ANP (*Compromisso com Investimentos em Pesquisa & Desenvolvimento*) and BG Group plc. for funding and providing the database. Derrick Green for reviewing and suggesting improvements in the manuscript. Edmilson Helton Rios is grateful to CNPq and Petrobras for his research fellowship.

REFERENCES

1. Carman, P.C., 1956. Flow of gases through porous media, Butterworths Scientific Publications, London.
2. Kolodzie Jr., S., 1980, Analysis of pore throat size and use of the Waxman–Smits equation to determine OOIP in spindle field, Colorado, SPE 55th Annual Fall Technical Conference.

3. Pittman, E.D., 1992. Relationship of porosity and permeability to various parameters derived from mercury injection-capillary pressure curves for sandstone, American Association of Petroleum Geologists (1992), 76 (2), 191–198.
4. Seevers, D.O., 1966. A nuclear magnetic method for determining the permeability of sandstones, Trans. 7th Ann. SPWLA Logging Symp.,Tulsa.
5. Kenyon, W.E., 1992. Nuclear magnetic resonance as a petrophysical measurement, Nucl. Geophys., 6(2), 153-171.
6. Dunn, K.J., Bergman, D.J. & Latorraca, G.A., 2002. Nuclear Magnetic Resonance—Petrophysical and Logging Applications, Pergamon Press, Oxford.
7. American Petroleum Institute, 1998. Recommended Practice for Core Analysis Procedure, 2nd edn, API RP 40, (Washington, DC:API)
8. Meiboom, S. & Gill D., 1958. Modified spin-echo method for measuring nuclear relaxation times, Rev. Scien. Inst., 29, 688-691, doi:10.1063/1.1716296.
9. Marzouk, I., Takezaki, H., & Suzuki, M., 1998. New classification of carbonate rocks for reservoir characterization, 8th SPE Inter. Petrol. Exhib. Confer.,10p

Table 1: Performance and regression coefficients for pure and size-scaled NMR permeability estimators.

k_{NMR}	Pure T_2				Size-scaled T_2			
	R^2	a	b	c	R^2	a	b	c
k_{SK}	0.70	4E-05	2.82	1.33	0.89	7.65	0.01	2.54
$k_{50\%}$	0.71	3E-05	2.76	1.35	0.88	7.65	-0.04	2.53
$k_{85\%}$	0.81	1E-05	2.87	1.37	0.95	7.14	1.01	2.10

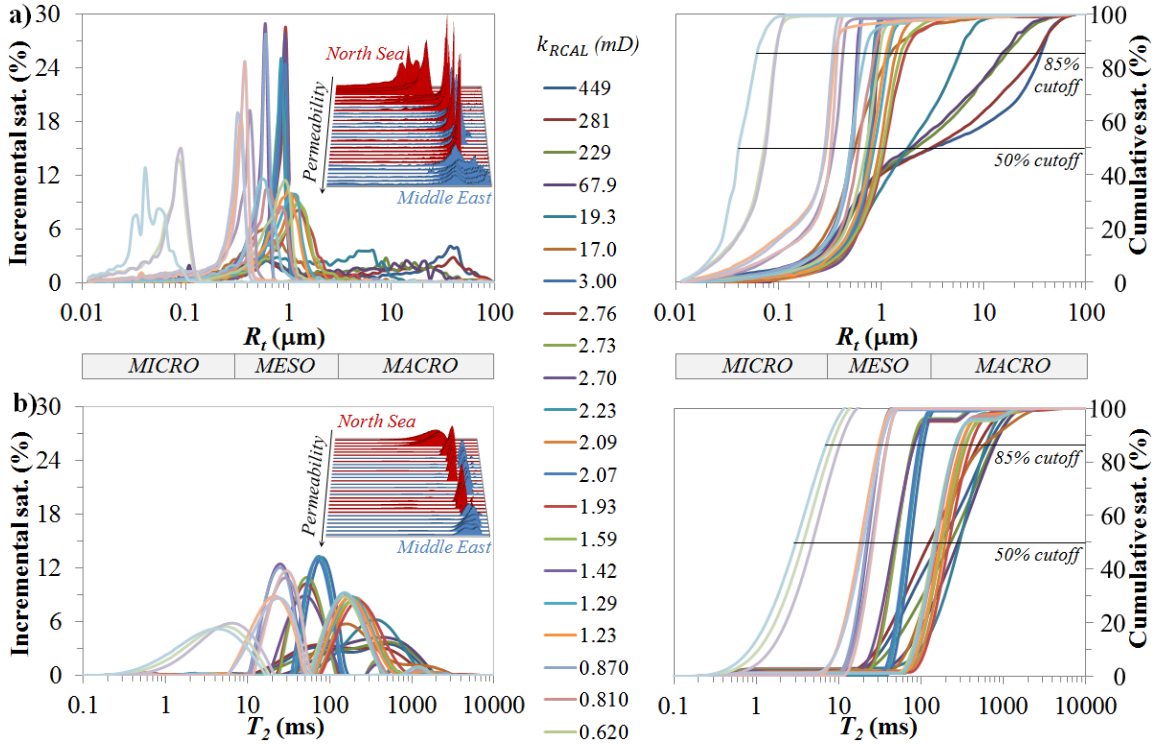

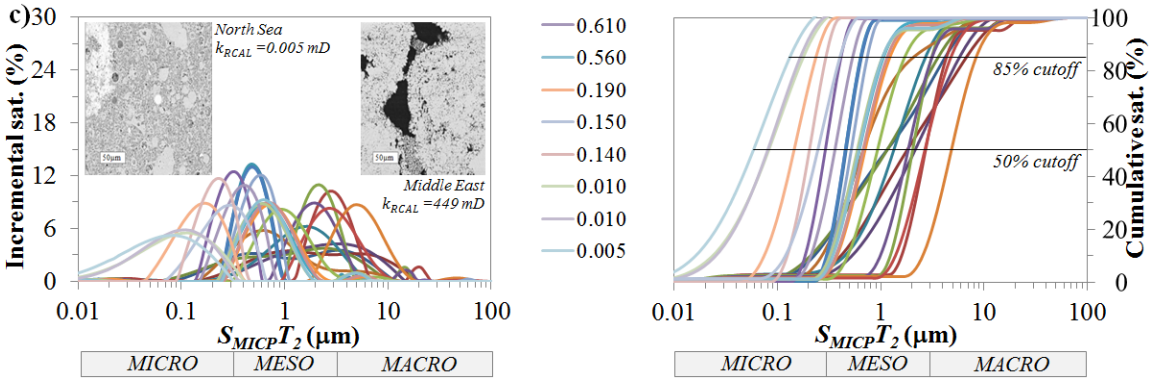

Figure 1: a) $S(R_t)$ and b) $S(T_2)$ with 3D plots showing each chalk group as inserts. c) Size-scaled NMR distribution $S(S_{MICP}T_2)$ with the thin section of the lower and higher permeability chalks as inserts.

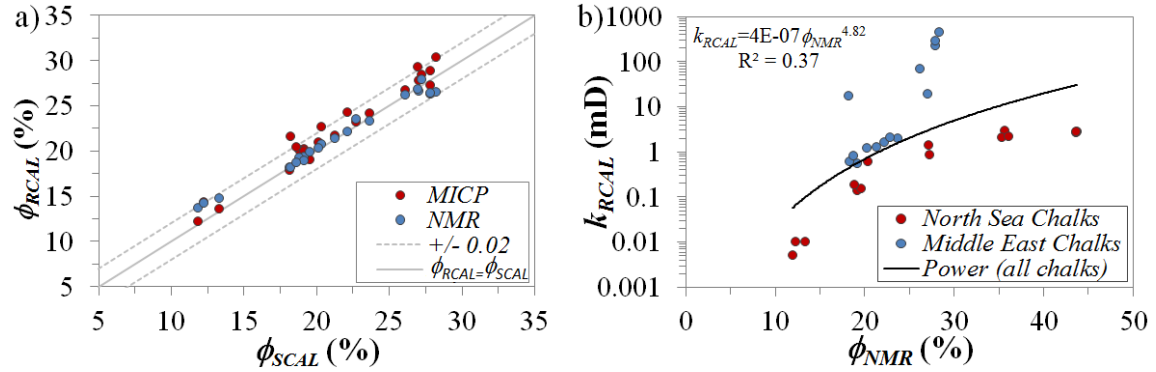

Figure 2: a) Routine core analysed porosity (standard reference) versus special core analysed porosities (MICP & NMR). b) RCAL permeability (standard reference) versus NMR porosity.

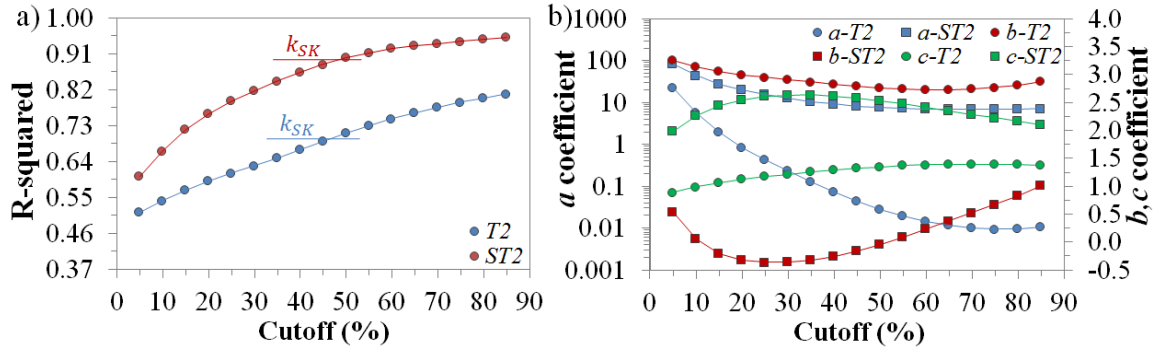

Figure 3: a) Performance and b) regression coefficients of the saturation-based estimator for both pure and size-scaled T_2 distribution.

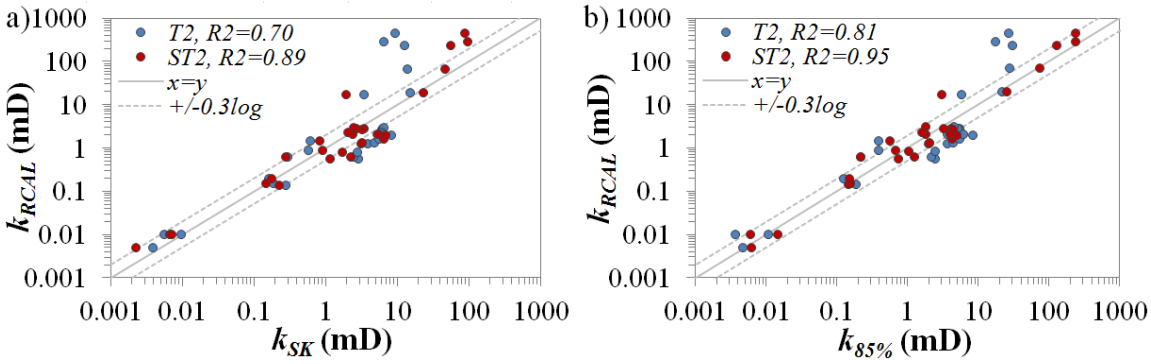

Figure 4: a) Standard log mean estimator and b) the best saturation–based estimator response curves.

ON THE MEASUREMENT OF PORE GEOMETRY: A COMPREHENSIVE PETROPHYSICAL STUDY OF CONVENTIONAL ROCKS

Babak Salimifard[1]; Douglas W. Ruth[1]; Derrick Green[2]; Brent Nassichuk[3]
[1]University of Manitoba, [2]Green Imaging Technologies, [3]Trican Geological Solutions

This paper was prepared for presentation at the International Symposium of the Society of Core Analysts held in St. John's, Newfoundland and Labrador, Canada, 16-21 August, 2015

ABSTRACT

Various techniques have been developed over the years for characterizing pore structure beyond a simple visual description. These tests provide qualitative data for both reservoir evaluations in the short run and reservoir simulation in the long run. In this study, mercury porosimetry (MP), low field (2MHz) nuclear magnetic resonance (NMR) relaxometry, centrifuge drainage tests and flow tests were run on 11 plugs of a mix of sandstones, limestones, dolomites and chalk. Initially, a representative elemental volume (REV) which uses pore size distribution (PSD) data and porosity to simulate the pore network is discussed. The model is later used to predict permeability and predictions were compared with gas flow measurements. NMR and centrifuge data are coupled to derive capillary pressure curves and the results are compared with MP derived capillary curves. The results indicate that there is significant difference between the two capillary curves based on the degree of heterogeneity of the samples. NMR and centrifuge data are also used to come up with a method to study the degree of heterogeneity of the plugs based on which it was decided which PSD (MP, NMR or centrifuge) would be the better representative of the pore network. This PSD is then used to make new permeability predictions using the REV model and the results show significant improvement over previous predictions. This study proves that MP, NMR and centrifuge tests provide complimentary information that is crucial to pore network simulation and analysis. This study also highlights the fact that rocks are complex and one test cannot represent the properties of the pore network, making it is necessary and beneficial to run complimentary tests to better understand the pore network. It also verifies the applicability of methods that combine results of these tests to assess the rock pore network.

INTRODUCTION

Pore network simulation and reservoir rock characterization have been of interest to researchers for almost a century. Initial approaches were mainly focused on permeability prediction. There is a vast literature that deals with permeability prediction; however most pioneering methods were based on experimental correlations [1]. Porosity-permeability cross plots are a good example of these approaches. Later researchers tried to predict permeability by simulating the pore network and applying fluid flow principles to the simulated network. Carman and Kozeny suggested that the porous network can be simulated using a bundle of non-interconnected tubes of varying radii [2]. This work has been the bedrock for future modeling by various researchers. Berg and Van Baaren used the same mentality and tried to correlate tube diameter with grain size distributions [3, 4]. Works of Leveret, Purcell, Thomeer and Swanson on the other hand dealt directly with pore entry pressures derived through Mercury Porosimetry (MP) [5, 6, 7, 8]. Following the work of Purcell, Ruth *et al.* suggested that the pore network can be simulated using a single REV,

correlating permeability with an average diameter and an average length of the conduit as follows [9]:

$$k = \frac{\emptyset\ \delta^2}{32\ \tau^2} \tag{1}$$

Here k is permeability, ∅ is porosity, δ is the representative diameter and τ is tortuosity. In their model they used Purcell's mean tube diameter as follows:

$$\delta^2 = (4\sigma\cos\theta)^2 \int_0^1 \frac{dS_v}{(P_c)^2} \tag{2}$$

Here, Sv is vacuum saturation, Pc is capillary pressure and σ and θ are surface tension and contact angle in the MP experiment respectively. They also incorporated electrical properties to account for the extended length of the mean flow path due to tortuosity. Archie's formation factor was used to define tortuosity as a function of porosity, cementation factor (m) and lithology factor (a) as follows:

$$\tau^2 = \frac{a}{\emptyset^{m-1}} \tag{3}$$

Eventually, they rewrite their model as:

$$k = \frac{\emptyset^m(\sigma\cos\theta)^2}{2\ a} \int_0^1 \frac{dS_v}{(P_c)^2} \tag{4}$$

PRELIMINARY WORK

This REV model was initially tested against a mix of 25 sandstone and carbonate samples from an offshore Ghana formation of Turonian age. Once provided with the mercury intrusion and formation factor data, the method was able to predict permeability with a mean error of less than 35%. Results of this study are presented in Figure 1. The two dashed lines represent the 50% and 100% error bars and the solid line is the one-to-one line where prediction matches measurement.

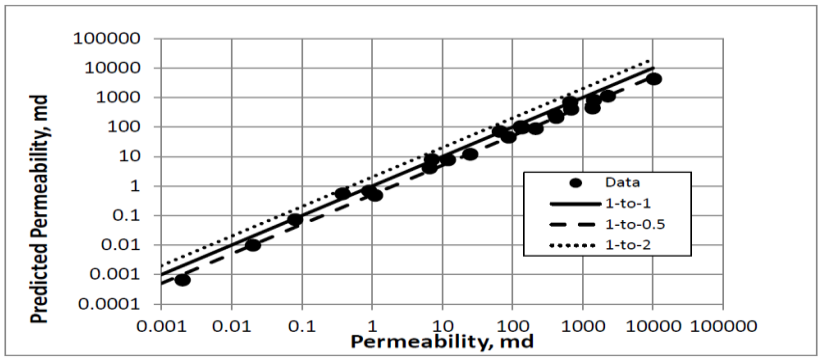

Figure 1 - Comparison between the calculated permeability and the measured permeability

In two other attempts, the REV model's predictions were compared with predictions of Carman-Kozeny, Swanson, Timur-Coates and Schlumberger-Doll-Research (SDR) methods [10, 11]. In

all cases except Swanson's, predictions made using the REV model outperforms predictions made using other methods. Swanson's however, makes better predictions than the REV method because it is optimized for the data set, thus making it less reliable when not optimized for the specific data set or formation.

After all, out of all the compared models, the REV model is the only one that solely relies on petrophysical properties of the rock and does not incorporate any fitting parameter. However, a claim cannot be made about the general applicability of this method particularly because the mean diameter of the conduit is calculated based on MP measurements done on small samples which are not always representative of the pore network. To start with, MP data is representative of the pore volumes accessible through specific pore throat sizes. In clean, homogenous sandstones where pore throats are supposed to be the main obstacles against fluid flow, and when pore throat to pore body ratios are not large, using throat size distribution (TSD) instead of pore size distribution (PSD) would not result in misinterpreting the pore network. However, in carbonates, where there is a wider variety of pore throat to pore body ratios using TSD would result in unreliable predictions.

Also, when it comes to field applications, MP is not the most applicable method because it's not easy to generate a continuous TSD profile for the entire height of the reservoir. However, logging techniques such as Nuclear Magnetic Resonance (NMR) can produce a continuous PSD profile for the entire height of the reservoir adjacent to the well bore.

RESULTS AND DISCUSSION

Techniques have been developed to derive capillary pressure from NMR data [12, 13]. Green [14] developed a model to produce capillary pressure data by coupling centrifuge tests with low field NMR measurements. In their method they calculated the capillary pressure distribution at each centrifuge spin by using Hassler-Brunner boundary conditions and applying it to Darcy's law to end up with the following formula:

$$P_c(r) = \frac{1}{2}\Delta\rho\omega^2(r_0^2 - r^2) \tag{5}$$

Here Pc(r) is the capillary pressure at each point along the sample, $\Delta\rho$ is the different in the densities of saturating and displacing fluids, ω is the spin velocity and r_0 is the distance from center of rotation. After each spin the sample is removed from the centrifuge and brine saturation along the sample is measured using low field NMR. Finally saturation at each r is coupled with capillary pressure at that point and a global capillary pressure curve is plotted for the sample. This test was run on the 11 samples used by Salimifard *et al.* [11] and results show that for the more homogeneous samples, MP capillary pressure curves match with the NMR capillary pressure curves. However, for the less homogeneous samples, i.e. samples E and J, the two capillary pressure curves differ. Figure 2 shows the results of the comparison. It should be mentioned that choosing the right contact angle for analyzing centrifuge capillary pressures is of utmost importance. In this study a fixed value of zero degrees was used for brine-air system which might not be the case for some rocks.

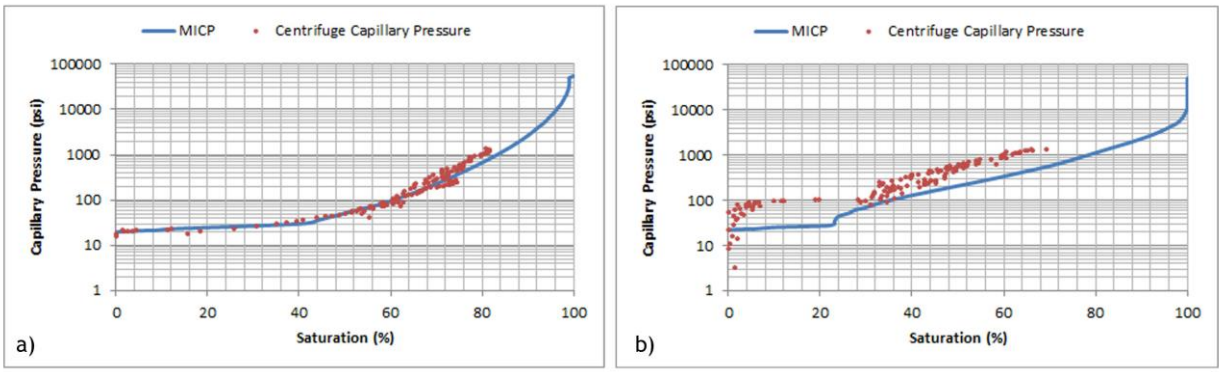

Figure 2 – a comparison between capillary pressures derived from MP and Centrifuge tests. Figure a (on the left) shows how MP and centrifuge capillary pressures match for a homogeneous sample while Figure b (on the right) highlights the fact that for less homogeneous samples, proper sampling can play an important role in capillary pressure determination.

Results of the same test are used to quantify the degree of inhomogeneity of the 11 samples. Each sample is divided in 4 segments and the total change in brine volume in each segment is monitored after each centrifuge spin. An average capillary pressure was calculated for each segment using Green's approach and the change in brine volume was coupled with that capillary pressure to construct the capillary pressure curve for each segment. The inhomogeneity of the sample then can be analyzed based on how well the capillary pressure curves for the four segments match. Obviously a good match means the sample is fairly homogenous and indicates that the end piece used for mercury porosimetry is a good representative of the core plug. As expected, capillary pressures for the four segments of samples E and J do not match which highlights the degree of inhomogeneity of the two samples.

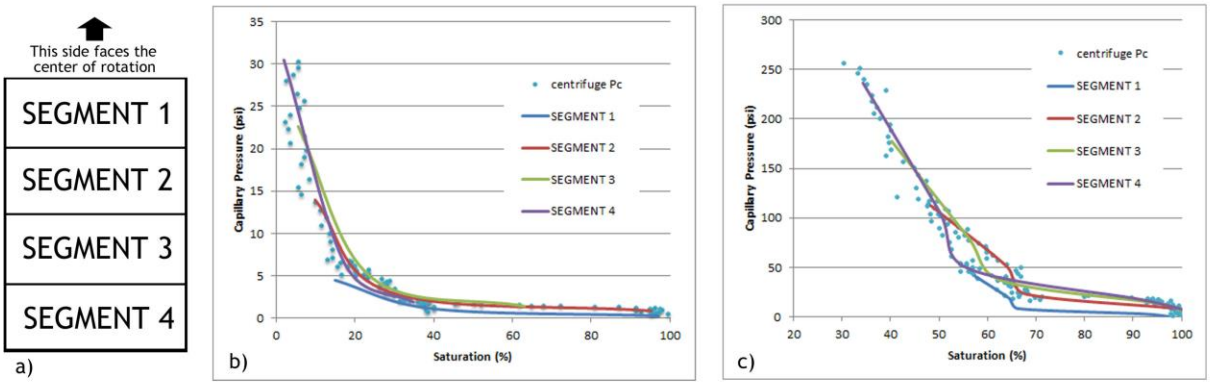

Figure 3 – a comparison between capillary pressures calculated for the four sections of a homogenous and a less homogenous sample. Figure a (far left) shows how the four segments are arranged on the core plug, segment 1 being the closest to the center of rotation and segment 4 being the farthest. Figure b (middle) shows capillary pressures of the four segments of a homogenous plug compared with centrifuge capillary pressure of the plug. Figure c (far right) shows the same results for a less homogenous sample.

In presence of heterogeneity, it is believed that the NMR derived PSD is a better representative of the pore network as it sees the entire plug, not just an end piece. Marschall's and Kleinberg's methods are used to convert NMR T2 distributions to capillary pressure data by matching the NMR T2 distribution curves with MP capillary pressure curves. As Marschall explained, NMR

data can be correlated with pore size when the plug is 100% brine saturated using the following equation:

$$\frac{1}{T_2} = \rho \frac{S}{V} \tag{6}$$

Here ρ is relaxivity and $\frac{S}{V}$ is the surface to volume ratio, which can be replaced by $\frac{2}{r}$ when a cylindrical pore network (a bundle of capillary tube) is assumed. Here ρ is calculated using

$$\rho = \frac{\sigma \cos\theta}{PT_2} \tag{7}$$

where ρ is defined as the effective relaxivity to account for the fact that NMR responds to pore bodies whereas MP responds to pore throats. An effective relaxivity is calculated for all 11 samples by finding the best match between the NMR T2 and MP capillary pressure distributions. These relaxivities match with the values reported by Marschall and Kleinberg and are tabulated in Table 1. Relaxivities are used to produce capillary pressure curves from NMR T2 distributions and permeability is recalculated using the REV method based on the new capillary pressure curves.

Table 1 – a compilation of sample properties and prediction results using different techniques

Sample Name	A	B	C	D	E	F	G	H	I	J	K
Porosity (%)	17.3	22.1	19.9	19.9	28.8	15.5	23.3	22.3	25.9	9.2	18.3
Measured Permeability (mD)	62.8	1060	7050	107	58.9	106	52.3	3810	1150	0.45	283
MP-Predicted Permeability (mD)	210	1090	2500	908	123	336	52	1220	892	6.13	302
Calculated Relaxivity (μm/s)	12.8	17.1	21.3	2.7	13.1	2.7	24.0	12.8	17.6	2.4	15.5
NMR-Corrected Permeability (mD)	180	1780	3960	184	590	250	86.9	3030	1030	4.38	295

CONCLUSION

Results shown in the table above clearly show that excluding sample E, using NMR derived capillary pressure curves improves the predictions for less homogeneous samples, namely for samples D and J. Even though the NMR T2 distributions are calibrated with MP capillary pressure curves, this approach improves the predictions by 113% (from 245% using MP data to 132% using NMR data, excluding sample E for both cases). Also, the T2 distribution curve was recalibrated with centrifuge capillary pressures for sample J and a new permeability prediction of 1.07 mD was achieved.

Sample E is a chalk sample which is highly compressible and sensitive to confining pressure. This is confirmed both by pressure-adjusted flow tests and by the NMR inhomogeneity test. As a result, because permeability tests are performed under confining pressure, NMR PSD might not be the best representative of the pore network when compared to confined flow tests, because NMR tests are done under no overburden pressure. Using NMR PSD would result in over estimating the pore sizes and over estimating the resultant permeability.

In conclusion NMR derived capillary pressures have proven to be properly representative of the pore network and are capable of making reliable permeability predictions. However, there's still a need for calibrating the T2 relaxation times with either centrifuge or MP capillary pressures. N2 adsorption techniques on the other hand can provide a direct measurement of surface to volume ratios, through which relaxivity values for each sample can be calculated [15]. In another approach, Fleury discussed a novel method to directly measure relaxivity values from NMR diffusion curves and concluded that the results compare with values derived through N2 adsorption measurements [16]. Unfortunately there wasn't sufficient data to apply these methods to the current set of samples. Once relaxivity is obtained for a formation, T2 relaxation times can directly be converted to PSD data and a continuous PSD profile can be generated for the entire height of the reservoir from NMR logs.

REFERENCES

1. Nabovati A. and A. C. M. Sousa, "Fluid Flow Simulation in Random Porous Media At Pore Level Using Lattice Boltzman Method," *Journal of Engineering Science and Technology,* vol. 2, no. 3, pp. 226-237, 2007.
2. Carman P. C., Flow of Gasses Through Porous Media, NewYork: Academic Press Inc., 1956.
3 Berg R. R., "Method for Determining Permeability From Reservoir Rock Properties," *Transactions - Gulf Coast Association of Geological Societies,* vol. 20, pp. 303-335, 1970.
4 Van Baaren J. P., "Quick-Look Permeability Estimates Using Sidewall Samples and Porosity Logs," in *6th Annual European Logging Symposium, Society of Professional Well Log Analysts*, 1979.
5 Leverett M. C., "Capillary Behavior in Porous Solids," *Transactions of AIME,* vol. 142, pp. 152-169, 1941.
6 Purcell W. R., "Capillary Pressure - Their Measurement Using Mercury and the Calculation of Mercury Therefrom," *Journal of Petrleum Technology,* vol. 1, no. 2, 1949.
7 Thomeer J. H. M., "Introduction of a Pore Geometrical Factor Defined by the Capillary Pressure Curve," *Journal Of Petroleum Technology,* vol. 12, no. 3, 1960.
8 Swanson B. F., "A Simple Correlation Between Permeability and Mercury Capillary Pressure," *Journal of Petroleum Technology,* vol. 33, no. 12, pp. 2488-2504, 1981.
9 Ruth D. W. , C. Lindsay and M. Allen, "Combining Electrical Measurements and Mercury Porosimetry to Predict Permeability," in *International Symposium of the Society of Core Analysts*, Aberdeen, Scotland, 2012.
10 Salimifard B., D. W. Ruth, M. Allen and C. Lindsay, "Applicability of Carman-Kozeny Equation for Well-Consolidated Samples," in *International Symposium of the Society of Core Analysts*, Napa, California, 2013.
11 Salimifard B., D. W. Ruth, D. Green and D. Veselinovic, "Developing a Model to Estimate Permeability from Other Petrophysical Data," in *International Symposium of the Society of Core Analysts*, Avignon, France, 2014.
12 Marschall D., J. S. Gardner, D. Mardon and G. R. Coates, "Method for Correlating NMR Relaxometry and Mercury Injection Data," in *Annual Simposium of the Society of Core Analysts*, 1995.
13 Kleinberg R. L., "Utility of NMR T2 Distributions, Connection with Capillary Pressure,

Clay Effect, and Determination of the Surface Relaxivity Parameter," *Magnetic Resonance Imaging,* vol. 14, no. 7/8, pp. 761-767, 1996.

14 Green D. P., "Capillary Pressure Curves Determined by Direct Measurement of the Saturation using Magnetic Resonance Imaging," *Canaadian Well Logging Society,* vol. 28, no. 1, pp. 20-25, May 2009.

15 Saidian M., U. Kuila, S. Rivera, L. J. Godinez and M. Prasad, "Porosity and Pore Size Distribution in Mudrocks: A Comparative Study for Haynesville, Niobrara, Monterey and Eastern European Silurian Formations," in *Unconventional Resources Tecnology Conference*, Denver, Colorado, 2014.

16 Fleury, M. "NMR Surface Relaxivity Determination Using NMR Apparent Diffusion Curves and BET Measurements" in *International Symposium of the Society of Core Analysts,* Calgary, Canada, 2007

ANALYTICAL INTERPRETATION METHODS FOR DYNAMIC IMMISCIBLE CORE FLOODING AT CONSTANT DIFFERENTIAL PRESSURE

Jie Cao, Xiaolong Liu, Lesley James, Thormod Johansen
Memorial University of Newfoundland

This paper was prepared for presentation at the International Symposium of the Society of Core Analysts held in St. John's Newfoundland and Labrador, Canada, 16-21 August, 2015

ABSTRACT

Relative permeabilities are usually determined from unsteady state immiscible core flooding experiments under constant differential pressure or constant flow rate conditions. In the latter case, the classical fractional flow theory can be applied to interpret the results. Recently, a new analytical interpretation method was presented for core flooding experiments under constant differential pressure. This new interpretation method is based on an analytical solution published recently. The analytical nature improves the accuracy of the interpretation. It eliminates the need of using numerical differentiation, and therefore reduces the overall numerical error. Under constant differential pressure, the new theory determines the flow rate as a function of time, which is used to interpret core flooding experiments under constant differential pressure conditions. In this paper, we will first briefly review the interpretation method. Next, unsteady state core flooding experiments are conducted under constant differential pressure conditions; the results from different interpretations are compared and analyzed in terms of accuracy and efficiency.

INTRODUCTION

Core flooding experiments are essential to Special Core Analysis (SCAL). These experiments provide valuable information such as relative permeabilities and recovery factors. Interpretation of the experimental results is generally based on fractional flow theory of an immiscible fluid flow system. Combining Darcy's Law and a material balance equation for each phase, the general fractional flow model can be written as

$$\frac{\partial S_w}{\partial t} + \frac{u_T}{\emptyset}\frac{\partial F_w(S_w)}{\partial x} = -\frac{1}{\emptyset}\frac{\partial}{\partial x}\left[\frac{\lambda_w \lambda_o}{\lambda_T}\frac{dP_c(S_w)}{dS_w}\frac{\partial S_w}{\partial x}\right], \qquad (1)$$

where S is the phase saturation; w means the water phase; P_c is capillary pressure; u_T is the total volumetric flux; the water fractional flow function is given by $F_w = \lambda_w/(\lambda_o + \lambda_w)$; where the water mobility is $\lambda_w = Kk_{rw}/\mu_w$ and the oil mobility $\lambda_o = Kk_{ro}/\mu_o$, $\lambda_T = \lambda_w + \lambda_o$. In analytical solutions to fractional flow theory, capillary pressure is ignored, i.e. the right hand side of Eq. (1) equals zero. The classical fractional flow theory by Buckley and Leverett [1] assumes that the total volumetric flux u_T is

constant. A similar theory was recently presented by Johansen and James [2] assuming that the inlet and outlet pressures are constant rather than the flow rate. In the latter solution, the total flow rate is a function of time, which is determined analytically.

Johnson *et al*. [3] first presented an analytical method (JBN method) to determine relative permeabilities based on the fractional flow theory developed by Buckley and Leverett [1] and Welge [4]. This interpretation method is based on the assumption that the total flow rate is constant during the core flooding experiments. However, core flooding experiments are sometimes conducted under constant differential pressure conditions. One of the main inaccuracies using JBN method is from the numerical calculation of the differentiation of the cumulative water injection terms. Jones and Roszelle [5] provided a similar method to JBN method. In the Jones-Roszelle method, the "reciprocal relative mobility" at the outlet is determined by the intercepts of the tangent of the effective viscosity curves. Since the tangent is determined from the discrete effective viscosity data points, this introduces numerical instability and inaccuracy. Recently, Cao et al. [6] presented a new analytical interpretation method for core flooding experiments under constant differential pressure conditions. This method applied the novel solution to fraction flow theory under constant pressure boundaries by Johansen and James [2]). Contrary to the assumption of constant total flow rate, the total flow rate is a function of time under constant differential pressure conditions and it is determined analytically as part of the generalized solution. In the formulation by Cao et al. [6] pressure and saturation profile at each point in time are solved analytically, hence this new method eliminates numerical differentiation and provides stable and accurate results.

In this paper, the new interpretation method for unsteady state core flooding experiments under constant pressure boundaries is first briefly reviewed. Then, it is applied to determine relative permeabilities from the core flooding experiments. The main purpose of this paper is to verify the accuracy of the new interpretation method and compare it to the JBN and Jones-Roszelle interpretation methods. Two cases are presented in this paper: Case 1: high viscosity oil in a low permeability core; and Case 2: low viscosity oil in a high permeability core. In both cases, the core flooding experiments are conducted under constant pressure condition and interpreted by the new method and JBN and Jones-Roszelle methods. The results show that the new method is more accurate and stable as a consequence of eliminating numerical differentiation.

METHODOLOGY

The core flooding experiments used two sandstone cores, synthetic oil, filtered crude oil (from Hibernia oil field offshore Newfoundland, Canada), and brine. The experiments were performed at room temperature. The schematic of the core flooding experiment is shown in Fig. 1.

The pressure differential on the core was held constant by running the Quizix 20K pump at constant pressure delivery mode for the inlet and using a back pressure regulator (BPR) at the outlet. A calibrated density meter was connected to the outlet of the core holder to

monitor the density change in real time in order to determine the fraction of each producing phase.

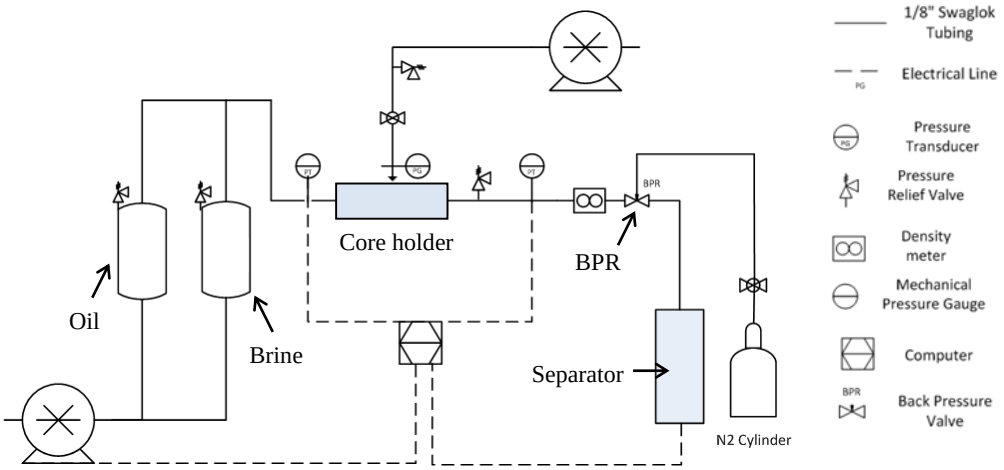

Fig. 1 Schematic of the core flooding experiment

The interpretation methodology for core flooding experiments under constant differential pressure conditions was presented by Cao et al. [6]. During the core flooding experiments, differential pressure, total fluid density at the outlet and cumulative production were recorded in time. Basic information of the core dimension and fluid properties (viscosity and density) are shown in Table 1. The methodology involves determining the pressure and saturation profiles analytically along the core length at the time of water breakthrough analytically using the method in Johansen and James [2]. The saturation profile is calculated when each saturation point arrives at outlet. In this process, the total flow rate as a function of time can also be determined analytically and injection accumulation is easily integrated. The new method for relative permeability calculation in this paper can be summarized in the steps described below with the detailed procedures and equations described by Cao et al. [6].

1. Calculate the saturation at the outlet at selected times post water breakthrough: calculate the water fractional flow function for each saturation point.
2. Determine the saturation and pressure profiles along the length of the core at the time of water breakthrough analytically using Johansen and James [2].
3. Calculate the spatial pressure derivative (pressure gradient) throughout the core.
4. Calculate the relative permeability.
5. Calculate the absolute permeability with brine when the single phase flow is steady state. End points of the relative permeability curves are determined by continuing the steady state two phase flow until connate water and residual oil saturation is reached.

RESULTS

In both cases (Case 1: high viscosity oil and low permeability core; and Case 2: low viscosity oil and high permeability core), the core flooding experimental results are interpreted using the JBN method, the Jones-Roszelle method and the new method. The experimental data is shown in Table 1. The lack of data regularity in both cases stems from the fact that the core floods are performed under unsteady state conditions.

Case 1. High viscosity oil and low permeability core

In Case 1, a viscous crude oil (32 cP) and a tight sandstone (10 mD) core were used. As shown in Fig. 2, the relative permeability results calculated from different methods are compared. It is shown in Fig. 2. that the water relative permeability results from the new method have a good agreement with most of the data points with the results from Jones-Roszelle method, where oil relative permeability results are perfectly matched in the water saturation range from 0.68 to 0.80. Water relative permeability results from JBN methods shows minor deviation from the new method in the water saturation ranged from 0.20 to 0.58. The results from both the JBN and Jones-Roszelle methods show a non-monotonic derivative variation deviating from the new method curve ranged from water saturation of 0.55 to 0.75, while the results from the new method gives a smooth relative permeability curve.

Table 1 Experimental data

Parameter	Symbols	Case 1 Value	Case 2 Value
Oil viscosity (cP)	μ_o	32.0	3.0
Brine viscosity (cP)	μ_w	1.0	1.0
Core sample length (cm)	L	30.48	30.48
Core cross-section area (cm^2)	A	10.01	10.01
Core sample porosity	ϕ	0.24	0.24
Absolute oil permeability (mD)	K	10	876
Connate water saturation	S_{wc}	0.35	0.29
Differential Pressure (psi)	ΔP	243.0	1.0

Case 2 Low viscosity oil in a high permeability core

The comparison of the results of Case 2 using a low viscosity oil (3 cP) in a high permeability core (876 mD) from the three methods is shown in Fig. 3. It is shown that the relative permeability curve obtained from the new method still shows a smooth continuous curve. Similar to Case 1, the results from both the JBN and Jones-Roszelle methods show a non-monotonic derivative variation deviating from the new method curve in the water saturation range of 0.45 to 0.55, where the non-monotonic derivative variation is more significant compared to Case 1. During the calculation using the Jones-Roszelle method, the effective viscosity calculated for Case 2 is scattered as shown in Fig. 4 which makes it difficult to calculate the tangents on the curve numerically and leads the instability of the relative permeability curve. It is relatively easier to calculate the tangents for the smooth effective viscosity curve in Case 1 compared with Case 2 as

shown in Fig. 4, but the calculation of the tangents using discrete points numerically still introduces errors.

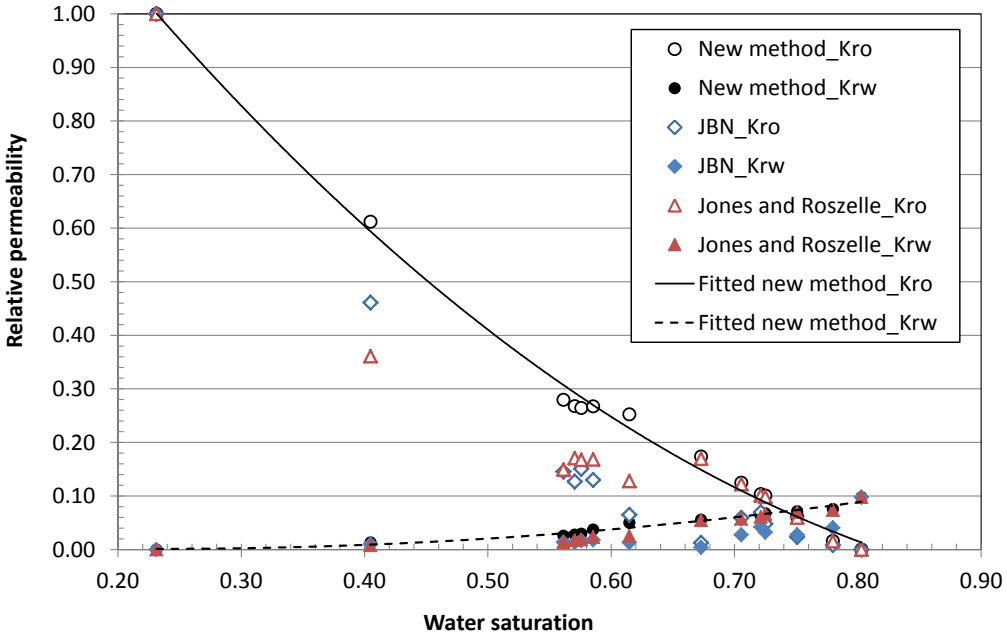

Fig. 2 Relative permeability for Case 1: 32 cP oil and 10 mD rock

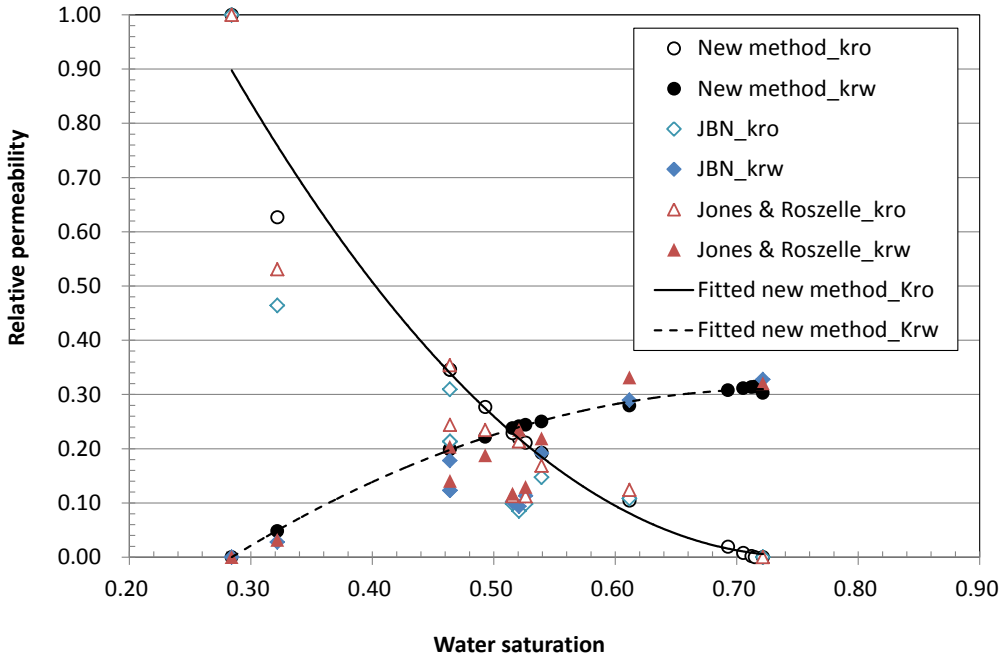

Fig. 3 Relative permeability for Case 2: 3.0 cP oil and 876 mD rock

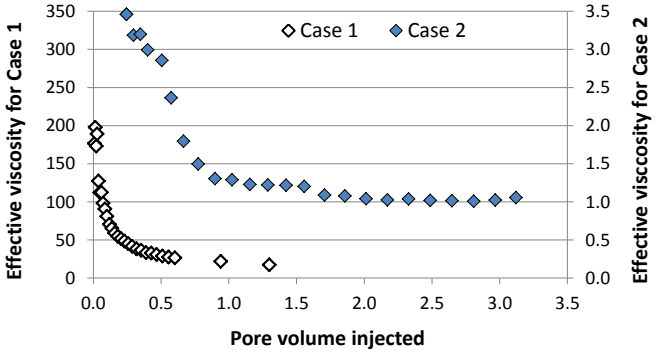

Fig. 4 Effective viscosity for the Jones-Roszelle method

CONCLUSIONS

As discussed in the comparison of the results using different methods, both JBN and Jones-Roszelle methods give instable relative permeability results shown as non-monotonic derivative variation on the curves due to numerical differentiation. By eliminating the numerical differentiation calculation, relative permeability results from the new method yield smooth curves for both cases. We show that the new method provides a robust and stable methodology to interpret unsteady state core flooding data for determining relative permeability. The superiority of the new method is that the numerical differentiation is eliminated and the overall numerical errors are reduced.

ACKOWLEDGEMENTS

The authors thank the Hibernia Management and Development Company (HMDC), Chevron Canada, the Natural Sciences and Engineering Research Council of Canada (NSERC), and the Research and Development Corporation (RDC) for their support without which this work could not have been performed.

REFERENCES

1. Buckley, S. E. and Leverett, M. C.: Mechanism of Fluid Displacement in Sands, Trans. AIME 146 (1942), 107-116.
2. Johansen, T. E. and James, L. A.: Fractional Flow Analysis for Multi-Component Problems with Constant Pressure Boundaries, To appear in Journal of Engineering Mathematics, Springer Verlag. 2015.
3. Johnson, E. F., Bossler, D. P. and Naumann, V. O.: Calculation of Relative Permeability from Displacement Experiments, *Trans. AIME* 216 (1959), 370-372.
4. Welge, H.G.: A Simplified Method for Computing Oil Recovery by Gas or Water Drive, Petrol. Trans AIME 195(1952), 91.
5. Jones, S.C. and Roszelle, W.O.: Graphical Techniques for Determining Relative Permeability From Displacement Experiments. Society of Petroleum Engineers of AIME. 1978.
6. Cao, J., James, L.A. and Johansen, T.E.: Determination of Two Phase Relative Permeability from Core Floods with Constant Pressure Boundaries. Society of Core Analysis Symposium, Avignon, France. 2014.

ANALYZING THE OPEN FACE CONDITION AND NON-EQUILIBRIUM EFFECTS IN CO- AND COUNTER-CURRENT SPONTANEOUS IMBIBITION WITH EXPERIMENTS AND NUMERICAL SIMULATION

Rasoul Arabjamaloei[1], Douglas W. Ruth[1], Derrick Green[2], Dragan Veselinovic[2]
[1]Centre for Engineering Professional Practice and Engineering Education, University of Manitoba, Canada
[2] Green Imaging Technologies INC., Fredericton, NB, Canada

This paper was prepared for presentation at the International Symposium of the Society of Core Analysts held in St. John's, Newfoundland and Labrador, Canada, 16-21 August, 2015

ABSTRACT

In this work a set of co- and counter-current spontaneous imbibition experiments were conducted on a sandstone core sample using Decane and D_2O as displacing/displaced fluids. Using an Oxford Maran DRX-HF instrument, the saturation profiles of the fluids inside the core were measured and recorded during the experiments. The capillary pressure-saturation curves for the sample rock were obtained by MICP and centrifuge tests. The accumulative production of non-wetting phase, determined by integrating the obtained saturation profiles, shows a square root of time behavior while the whole process was seen to be affected by non-equilibrium effects at the inlet. It was assumed that all the production was from the upstream face in the counter-current case, and from the downstream face in co-current test. The experiments also showed an inlet water saturation of around 50%, which is in contradiction with the assumption of capillary continuity at the core face. The results were analyzed using an explicit simulator to obtain Corey-type relative permeability functions. It was found that the counter-current experimental results showed a close match between the simulated and the experimental results. Further, the relative permeability curves obtained by history matching of counter-current imbibition test results were used to simulate and predict the results for co-current imbibition test.

INTRODUCTION

Both co-current and counter-current spontaneous imbibition are complicated two phase processes which are not yet well understood. One of the main processes involved in oil production from fractured reservoirs is spontaneous imbibition (SI) which is driven by capillary forces [1]. Experimental work has been done to study SI processes and obtain relative permeability and capillary pressure curves; however exact measurements of saturation distribution profiles are not very common [1, 2, 3]. The SI process could be modeled analytically if the proper sets of relative permeability curves are known for the porous medium. However, it is not yet known with certainty if a unique set of relative

permeability curves can be implemented for the mathematical modeling of all the processes happening in a porous medium. In the present work, experiments were run to measure the saturation distribution profiles in the sample core during co-current and counter-current spontaneous imbibition processes. The experimental data was then input to an explicit numerical simulator to achieve relative permeability curves by history matching. The core properties and the capillary pressure curves are taken from a previous study [4].

THE EXPERIMENTAL STUDY

In this study two co- and counter-current SI tests were performed on a core sample of tight rock. Table 1 shows the rock type and properties.

Table 1: Rock properties of the sample used for co-current and counter-current experiments

Rock type	Porosity (%)	Permeability (md)	Length (cm)	Cross Section (cm^2)
Sandstone	23	2	2.5	9.61

Teflon tape was wrapped tightly around the cylindrical sample plug and then the plug was sealed with heat shrink plastic tubes. Figure 1 shows how the core was prepared before the experimental work and figure 2 shows a diagram of experiment set-up. A constant volume D_2O reservoir is always maintained at the top of the sample by adding droplets. The length to diameter ratio of the sample might be small, that was due to the limitations of accessibility to big range of samples.

The two ends of the plug were open in co-current experiments while one end of the sample was sealed with liquid glue for counter-current test. The sample was fully saturated with decane by using centrifuge before the start of the experiment. That leads to zero initial water saturation which might affect the results of the experiment. To study the effect of initial water saturation another broad study is needed. Deuterium oxide (D_2O) was used as the injected fluid because this substance is not "seen" by the NMR apparatus. The NMR measurements were done using an Oxford Maran DRX-HF instrument at 30℃ and 2MHz frequency. Green Imaging Technologies (GIT) software was used to measure the decane saturation distribution. By proper design of the core holder it was possible to continue the experiment in the machine while the measurements were done.

The simulator uses 50 central grid blocks system with equal distances except for the boundary node which is a zero width block. The saturation change at each grid is calculated based on the flow rate difference across the block boundaries. The flow rates are calculated by modified Darcy's law and gravity is ignored. The saturation profiles, the capillary pressure curves and rock and fluid properties were provided to the simulator as inputs. The program uses those data to find the best Corey-type relative permeability curves for the sample. The simulation was fully explicit and the upstream saturation of each grid block was used to calculate the Corey-type relative permeability of the corresponding block. Further details of the model may be found in [6].

History matches were achieved by minimizing the error between the experimental and simulated saturation profiles. Neither production data nor pressure data were used for the process of history matching.

DATA ANALYSIS

Figure 3 shows the counter-current SI experimental data and the best fit curves resulting from the simulations. As observed in figures 3 and 4, there is a very good match between the experimental and simulation results, especially for the production curve. However, the measured saturation profiles might not show the well-known patterns expected for this displacement process. It is seen that water imbibes through the core very fast and compensate for the zero initial water saturation. It is also observed that the NMR readings don't show a strong water front during the co-current process at the early times. But it is seen that a front forms at latter times. The non-wetting phase production was calculated from NMR outputs. The relative permeability curves found for counter-current imbibition were next used to predict the results for the co-current imbibition test. Figure 5 shows the calculated relative permeability curves.

The objective was to determine if the history matched relative permeability curves are suitable for the co-current imbibition process. The simulator was used to produce and compare the saturation distribution and production curves. Figures 6 and 7 show the comparison of results.

DISCUSSIONS AND CONCLUSIONS

As observed in figures 6 and 7, a Corey-type relative permeability curve can be used to numerically simulate the counter-current spontaneous imbibition. The predicted saturation distribution curves do not perfectly match the experimental results; however the predicted production has an excellent match with the experimental results. Because the NMR measurements take 1-2 minutes each time, this is a potential source of error in the saturation profiles and might cause the difference between experimental and simulation results. It is also observed in the experimental results that the inlet face saturation is changing with time and is not a unique value. This shows the role of non-equilibrium effects in a spontaneous imbibition process. However, at later times the saturation values stabilize and agree approximately with results predicted by the method of Arabjamaloei *et al* [7].

The co-current experimental production results did not show as close a match as for the counter-current case. This problem is likely related to the fact that in these experiments the two faces were open and production was happening at both faces as it was observed in the experiments; in the present experiments only the total production could be determined. Parts of the saturation curves show reasonable agreement; however, the upstream face saturation is not well predicted. This is further evidence that the face condition during spontaneous imbibition is poorly understood. It should be noticed that

the produced decane floating on the top of the water reservoir in counter-current experiment or collected at the bottom in co-current experiment might affect the readings, but the effect was reduced by taking the decane out of the set-up every once in a while.

The results are encouraging since they show that, at least for one case, a single set of relative permeability curves based on counter-current test can be used to approximately predict the co-current test results.

ACKNOWLEGEMENTS

This work was supported in part by a grant from the Natural Sciences and Engineering Research Council of Canada. The simulator used in this study was PORLAB and is used by permission of D&B Ruth Enterprises Inc.

REFERENCES

1. Mason, G. and N.R. Morrow, "Developments in Spontaneous Imbibition and Possible Future Work", *Journal of Petroleum Science and Engineering*, (2013).
2. Baldwin, B.A., Spinler, B.A., 2002. In situ saturation development during spontaneous imbibition. Journal of Petroleum Science and. Engineering, 35 (1-2), 23–32.
3. Li, Y., Ruth, D., Mason, G., and Morrow, N.R., 2004, "Pressures acting in counter-current spontaneous imbibition", Proceedings of the 8th International Symposium on Reservoir Wettability, Houston, TX, May 17-18.
4. Mason, G., Ferno, A., Morrow, N.R., Ruth, D.W., 2012, "Spontaneous Counter-Current Imbibition Outward from a Hemi-Spherical Depression", Journal of Petroleum Science and. Engineering, 90-91 (July), pp.131-138.
5. Babak Salimifard, Douglas Ruth, Derrick Green, Dragan Veselinovic, "Developing a Model To Estimate Permeability from Other Petrophysical Data", SCA2014-063, *International Symposium of the Society of Core Analysts*, (2014), Avignon, France, 8-11 September.
6. Ruth, D.W., Mason, G., Fernø, M.A., Haugen, A., Morrow, N.R., Arabjamaloei, R., "Numerical Simulation of Combined Co-Current/Counter-Current Spontaneous Imbibition", International Symposium of the Society of Core Analysts, (2015), St.John's, Newfoundland and Labrador, Canada, 16-21 August.
7. Arabjamaloei, R. and Shadizadeh, S. R., "A New Approach for Specifying Imbibition Face Boundary Condition in Countercurrent Spontaneous Imbibition", *Petroleum Science and Technology*, (2010), 28(18): 1855-1862.

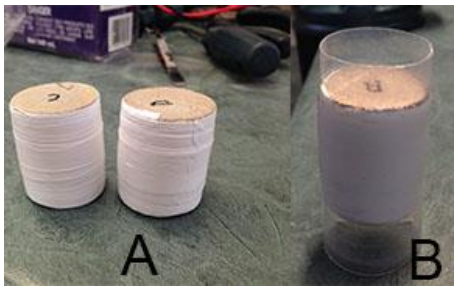

Figure 1: A: first step, the plugs are wrapped with Teflon tape, B: at the second step the cores are fitted inside a plastic tube

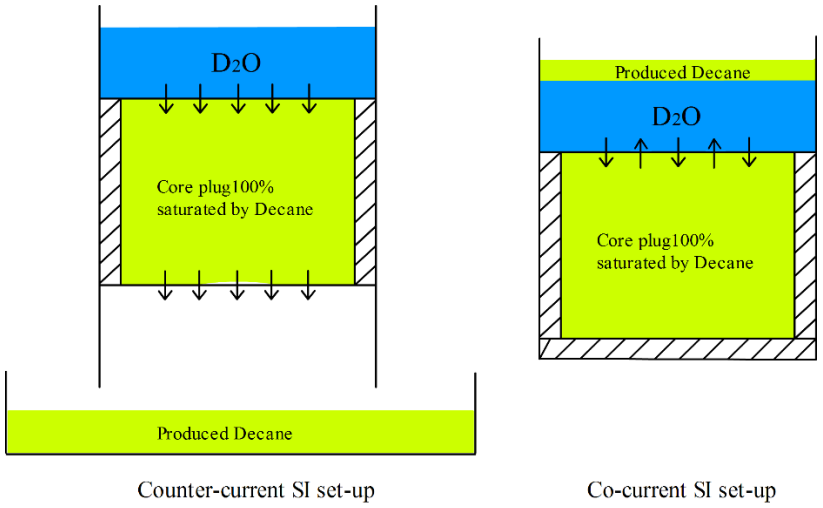

Figure 2: Diagram of the experimental set-up

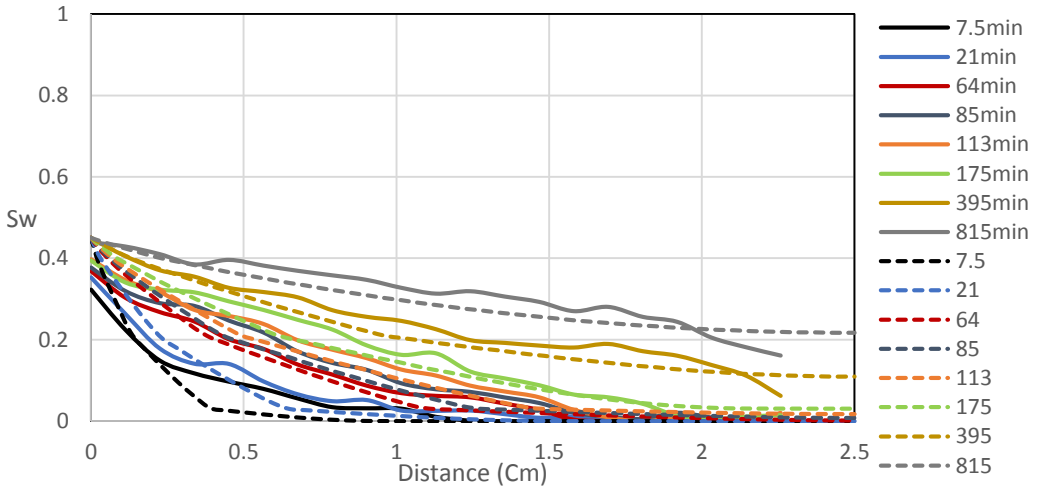

Figure 3: Comparison of the simulated (dash lines) and experimental (solid lines) saturation profiles for the counter-current spontaneous imbibition test

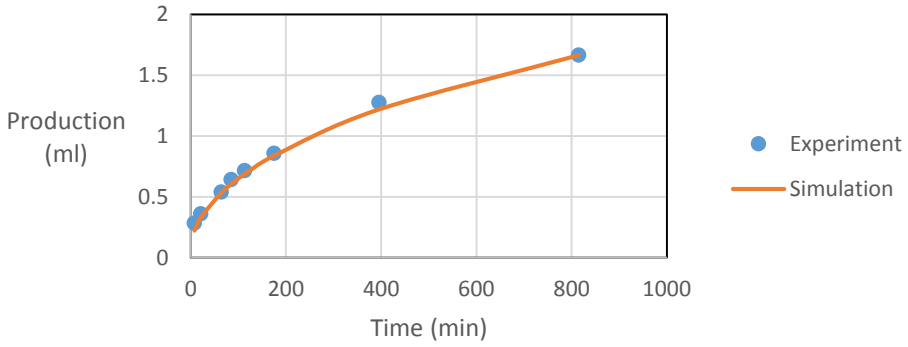

Figure 4: Comparison of non-wetting phase production data of experiments and simulation for counter-current test

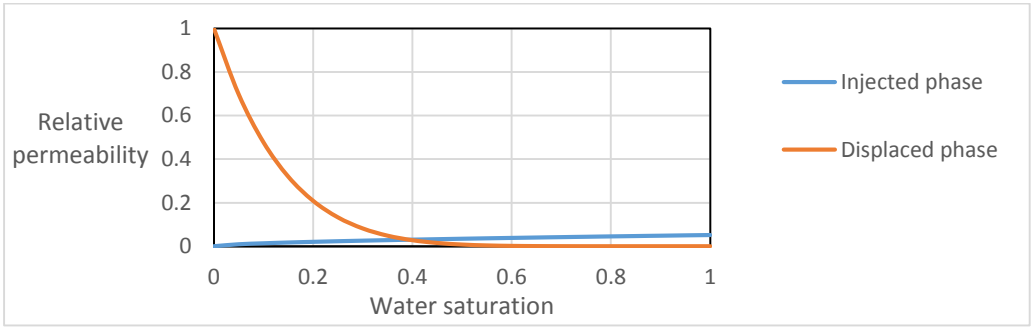

Figure 5: Relative permeability curves obtained by history matching the Counter-current imbibition test results. These relative permeability curves were also used to simulate non-wetting phase production of the co-current imbibition test.

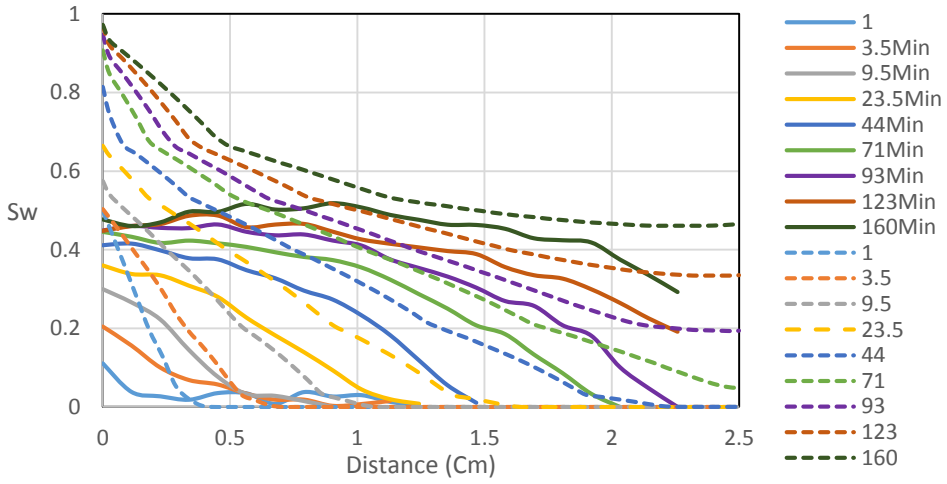

Figure 6: Comparison of the simulated (dash lines) and experimental (solid lines) saturation profiles for co-current spontaneous imbibition test

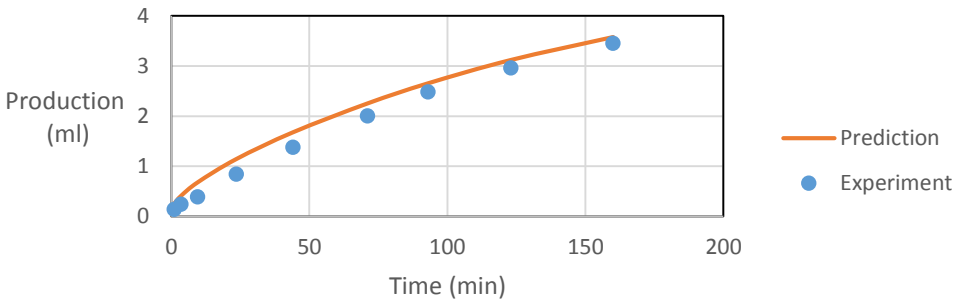

Figure 7: Comparison of non-wetting phase production data of experiments and simulation for co-current test

APPLICATION OF COMPRESSED SENSING MRI TO LABORATORY CORE-FLOODS

N.P. Ramskill, I. Bush, A.J. Sederman, M.D. Mantle, L.F. Gladden
Department of Chemical Engineering and Biotechnology, University of Cambridge, New Museums Site, Pembroke Street, Cambridge, Cambridgeshire, CB2 3RA.

This paper was prepared for presentation at the International Symposium of the Society of Core Analysts held in St. John's, Newfoundland and Labrador, Canada, 16-21 September 2015

ABSTRACT

Imaging of fluid distributions is essential to enable the unambiguous interpretation of core flooding data. In the present study, a rapid and robust magnetic resonance imaging (MRI) approach to provide 3D images of the fluid saturation in rock core samples during laboratory core floods has been demonstrated. MRI has been widely used to image fluid saturation in rock cores; however, the conventional acquisition strategies are typically too slow to capture the dynamic nature of the displacement processes that are of interest. Using Compressed Sensing (CS), it is possible to reconstruct a near-perfect image from significantly fewer measurements than was previously thought necessary, and this can result in significant reductions in the image acquisition times. Using a CS-MRI approach, 3D images of the fluid saturation in the rock core have been acquired in minutes as opposed to hours, as is the case with the conventional methods.

As a proof-of-principle, the CS-MRI technique has been applied to image the residual water saturation in the rock during a water-water displacement core flood. The enhancement in the temporal resolution that has been achieved using the CS-MRI approach will enable dynamic transport processes pertinent to laboratory core floods to be investigated on a time-scale that, until now, has not been possible.

INTRODUCTION

Laboratory-scale displacements in rock core-plugs (core floods) are widely used to develop the understanding of oil recovery mechanisms [1,2]. Magnetic resonance imaging (MRI) and X-ray tomography (CT) are the most widely used techniques for imaging *in situ* core flood fluid distributions – of which both can non-destructively image multiphase fluid systems in porous media [3-6]. CT images bulk densities and effective atomic numbers, distinguishing multicomponent systems based on atomic density differences. While this enables detection of both the rock matrix and imbibed fluids, this presents a challenge in providing contrast between fluids within the pore space, *i.e.* oil and brine, which, without the addition of dopants, the difference in atomic densities is small. In contrast, MRI has the advantage that there are numerous contrast mechanisms that can be implemented to provide contrast between different chemical species, namely: chemical selectivity of NMR-active nuclei detected (e.g. ^{1}H, ^{23}Na), spectroscopic

chemical shift, relaxation time (T_1 and T_2) weighting, diffusivity contrast and use of lower gyromagnetic species, such as D_2O water [7].

However, conventional 3D MRI suffers low temporal resolution and hence, the dynamic nature of core flood displacements cannot be effectively monitored. In conventional MRI, data are uniformly sampled at the Nyquist rate (at a rate of at least twice the frequency of the highest frequency components present in the signal of interest). This is determined by the desired field of view (FOV) and image resolution. Therefore, when multi-dimensional and high spatial resolution images are sought, this can result in long acquisition times. It has been shown that using Compressed Sensing (CS), a near-perfect reconstruction can be obtained from a number of measurements sampled below the Nyquist rate. Therefore, by applying CS to MRI, reducing the number of data points sampled would lead to a reduction in the image acquisition time [8].

CS has previously been applied to pure phase-encoding techniques for the study of porous materials [9,10]. Due to their robustness in the presence of paramagnetic impurities and magnetic susceptibility gradients, the pure phase encode methods have proven to be suitable for providing quantitative measurements of the fluid content in particularly challenging systems, such as rock cores. However, even with under sampling, these techniques are too slow for studying dynamic displacement processes, particularly when 3D images are required. Depending on the system under investigation and the information sought, the choice of MRI pulse sequence is a trade-off between how quantitative it is and its achievable temporal resolution. In this work, Rapid Acquisition with Relaxation Enhancement (RARE) [11] with CS has been used to image the residual fluid saturation during a laboratory core flood.

PROCEDURE

In the present study, a Bentheimer sandstone plug, 38 mm in diameter and 68 mm in length has been used. The pore volume of the rock was determined to be 18 ml corresponding to a porosity of ~24 %. The rock was initially saturated with deionised water, which was displaced by a gadolinium chloride ($GdCl_3$) doped-water solution during the core flood. The concentration of the $GdCl_3$ (aq) solution (~8 mM) was chosen to ensure that the transverse relaxation time (T_2) was sufficiently short that it could not be detected in the images. The sample was held in-place by an Aflas sleeve within a PEEK rock core holder (ErgoTech, Conwy, UK). A constant confining pressure was applied to the outside of the Aflas sleeve by per-fluorinated oil (Fluorinert FC-43) using a Gilson 307 (Gilson Inc., USA) HPLC pump maintained at 250±25 psig by a back pressure regulator (Idex Health and Science, USA). The injectant was pumped through the rock at a flow rate of 0.025 ml min^{-1} using a Quizix QX1500 (Chandler Engineering, USA) dual-syringe pump. The corresponding interstitial pore velocity was ~0.4 ft day^{-1}.

The MRI experiments were carried out on a 2 T (85 MHz for ^1H) horizontal bore magnet controlled by a Bruker AV spectrometer. Prior to the start of the core flood, a fully-sampled 3D image was acquired as a reference and has been used for CS simulations.

During the core flood, under-sampled 3D images were acquired. For the acquisition of both fully and under-sampled 3D images, the RARE pulse sequence has been used. The field of view (FOV) was 80 mm × 50 mm × 50 mm in the *z*, *x* and *y* directions respectively. Correspondingly, for a data matrix size of 256 × 128 × 128 pixels in the read (*z*) direction and first (*x*) and second (*y*) phase encoding directions, the image resolution is 0.31 × 0.39 × 0.39 mm pixel^{-1}. For the fully-sampled 3D RARE images, the acquisition time was 2 hours and 9 minutes whereas for the 3D CS-RARE images, with 25 % sampling the acquisition time was approximately 16 minutes.

RESULTS AND DISCUSSION

Three-dimensional Compressed Sensing Simulations

In order to demonstrate the performance of CS, a qualitative comparison has been made between an image reconstructed from the fully-sampled data set and that from a CS reconstruction. For details on the CS reconstruction method used herein, the reader is directed to [12]. A more detailed description of the CS acquisitions and reconstructions employed in the present study will be reported in a future publication. Figure 1 a) shows a 2D *xz* slice taken from the reconstruction of the fully-sampled 3D reference image. For the CS simulation, a 30 % sampled data set was created by replacing 70 % of the data points, from the fully-sampled data, with zeros. Figure 1 b) and c) show 2D *xz* slices taken from the 3D images obtained from the zero-filled Fourier transform and CS reconstructions of the simulated under-sampled data, respectively.

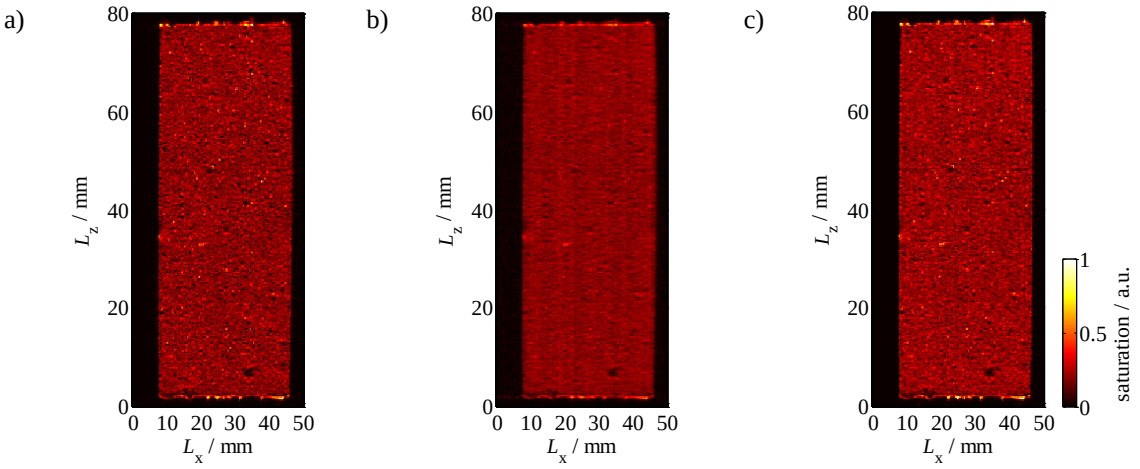

Figure 1. 2D *xz* slices taken from the centre of 3D images of the water-saturated Bentheimer rock prior to the core flood obtained by a) Fourier transform of the fully-sampled data, b) Fourier transform of the 30 % sampled data and c) CS reconstruction of the 30 % sampled data.

It can be seen that, due to the aliasing artefacts that arise from under-sampling, the contrast in the image the reconstruction from the zero-filled Fourier transform (Figure 1 b)) is somewhat reduced with respect to the fully-sampled case (Figure 1 a)). However, due to the bias towards a 'sparse' solution in the CS reconstruction (Figure 1 c)), an image with greater contrast than the zero-filled Fourier transform is obtained and is, visually, much closer to the fully-sampled image. A quantitative assessment of the CS

methodology that has been implemented in the present study will be discussed in detail in a future publication. However, the qualitative comparison shown in Figure 1 has demonstrated that a near-perfect image has been recovered from data sampled significantly below the Nyquist rate, and would therefore allow for significant improvements in the temporal resolution for the acquisition of 3D images.

Application of 3D CS-MRI Imaging to a Water-Water displacement core flood

The fully and under-sampled 3D images of the initially water-saturated rock cores, prior to the start of the core flood, are shown in Figure 2 a) and b), respectively.

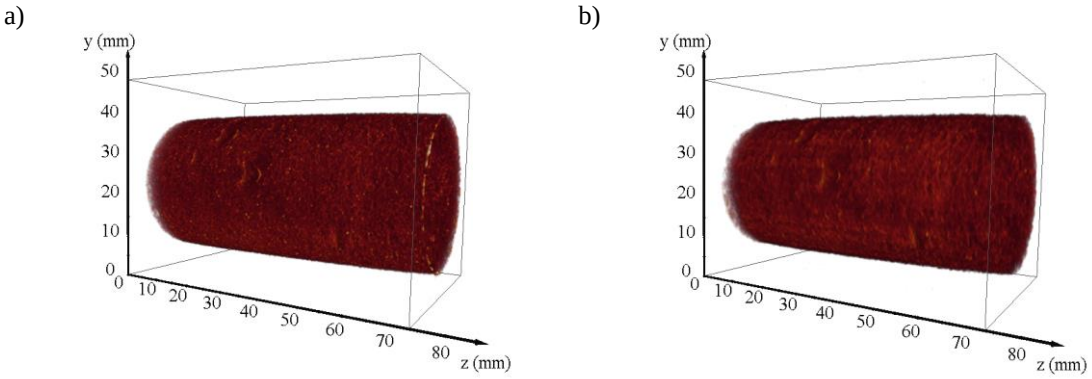

Figure 2. 3D images of the initially water-saturated Bentheimer rock from a) fully-sampled and b) 25 % sampled data set for which the acquisition times were 2 hours 9 minutes and 16 minutes, respectively.

By using CS combined with RARE, an enhancement in the temporal resolution by a factor of 8 has been achieved. It should be noted that the reduction in acquisition times relative to a standard spin-echo sequence or purely phase-encoded would be significantly greater. For instance, a 3D image of the same resolution as those presented herein acquired with a standard spin-echo sequence would take around 60 hours to acquire.

Figure 3 shows the 3D CS images of the residual saturation of the water that was *initially* present in the rock at various times following injection of the injectant solution. The flow of the injectant is from right-to-left, *i.e.* in the –*z* direction.

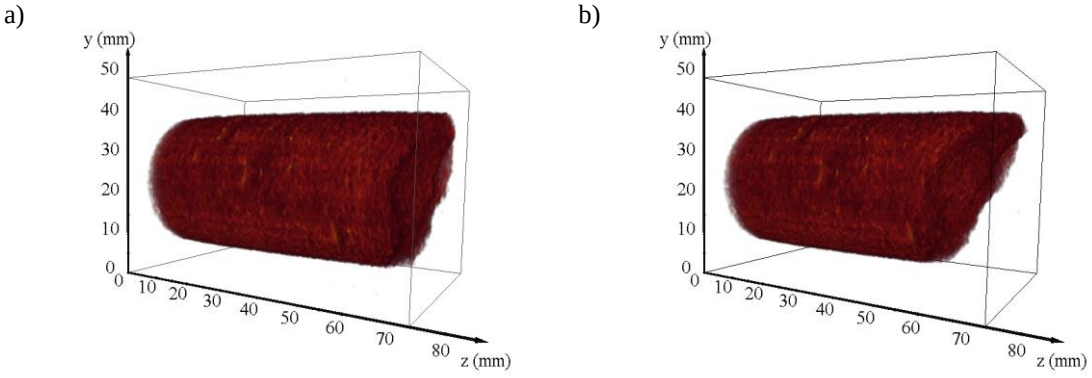

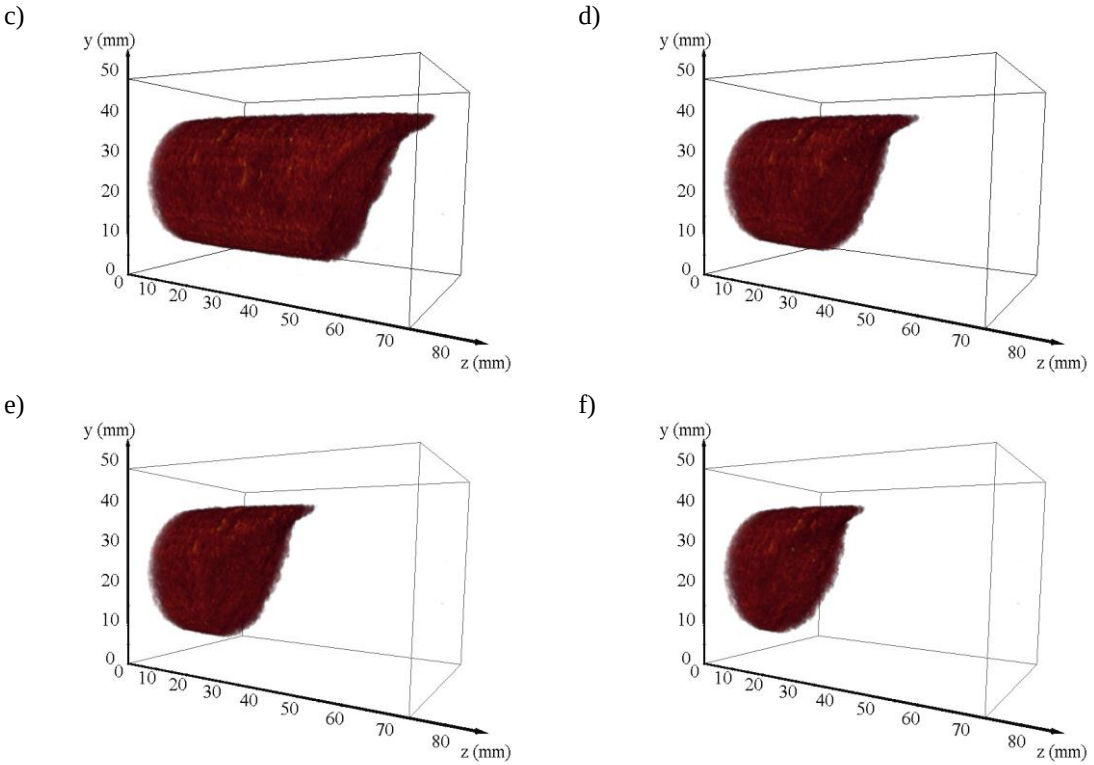

Figure 3. 3D CS images of the residual water in the Bentheimer rock core after a) 82, b) 180, c) 279, d) 377, e) 476 and f) 574 minutes of flowing a ~8 mM $GdCl_3$ (aq) solution at 0.025 ml min^{-1}. The flow of the injectant is from right-to-left, in the –*z* direction. The concentration of the $GdCl_3$ (aq) solution was chosen as such to ensure that the transverse relaxation time (T_2) was sufficiently short thus it was 'invisible' in the images. From the series of images, the invasion front throughout the core flood is evident.

From the series of images presented in Figure 3, the progress of the displacement front through the rock during the core flood can be clearly observed.

CONCLUSIONS

In this paper, a CS MRI method for 3D imaging of the fluid saturation in rocks during a laboratory core flood has been demonstrated. Firstly, it has been shown that, visually, a near-perfect image can be reconstructed from data sampled in violation of the Nyquist criteria, thus allowing for significant reductions in the acquisition times. Using CS with RARE, an eight-fold improvement in the temporal resolution has been achieved, relative to the fully-sampled RARE acquisition. However greater time savings are possible over more standard pulse sequences. Secondly, the CS-RARE technique has been applied to image the residual water saturation during a water-water displacement core flood.

The enhancement in the temporal resolution obtained with CS will unlock the potential to observe phenomena during a core flood on a time scale that would not be possible using conventional MRI protocols. It is therefore the aim of future work that this method will be applied to investigate pertinent issues such as ganglion dynamics [6] and the influence of capillary end effects [13] during an oil recovery core flood.

REFERENCES

1. Mitchell, J., Staniland, J., Chassagne, R. and Fordham, E.J., 2012a. Quantitative In Situ Enhanced Oil Recovery Monitoring Using Nuclear Magnetic Resonance. *Transport in Porous Media*, **94**, pp. 683-706.
2. Mitchell, J., Wilson, A., Howe, A., Clarke, A., Fordham, E.J., Edwards, J., Faber, R. and Bouwmeester, R., 2012c. Magnetic Resonance Imaging of Chemical EOR in Core to Complement Field Pilot Study. SCA 2012-30. In Proc: *International Symposium of the Society of Core Analysts*. Aberdeen, Scotland, UK, 27-30 August 2012. Society of Core Analysts.
3. Vinegar, H.J., 1986. X-ray CT and NMR Imaging of Rocks. *Journal of Petroleum Technology*, (March), pp. 257-259.
4. Yuechao, Z., Yongchen, S., Yu, L., Lanlan, J. and Ningjun, Z., 2011. Visualization of CO_2 and oil immiscible and miscible flow processes in porous media using NMR micro-imaging. *Petroleum Science*. **8**(2), pp. 183-193.
5. Fernø, M. A. Ersland. G., Haugen, Å, Johannesen, E., Graue, A., Stevens, J. Howard, J., 2007. Impacts from fractures on oil-recovery mechanisms in carbonate rocks at oil-wet and water-wet conditions – visualizing fluid flow across fractures with MRI. In Proc: *International Oil Conference and Exhibition*. Veracruz, Mexico, 27-30 June 2007. Society of Petroleum Engineers.
6. Youssef, S., Rosenberg, E., Deschamps, H., Oughanem, R., Maire, E. and Mokso, R., 2014. Oil ganglia dynamics in natural porous media during surfactant flooding captured by ultra-fast X-ray microtomography. SCA paper 2014-023. In Proc: *International Symposium of the Society of Core Analysts*. Avignon, France, 11-18 September 2014. Society of Core Analysts.
7. Mitchell, J., Chandrasekera, T.C., Holland, D.J., Gladden, L.F. and Fordham, E.J., 2013a. Magnetic resonance imaging in petrophysical core analysis. *Physics Reports*, **525**, pp. 165-225.
8. Holland, D.J. and Gladden, L.F., 2014. Less is More: How Compressed Sensing is Transforming Metrology in Chemistry. *Agewandte Chemie Int. Ed.* **53**, 2-13.
9. Xiao, D., Balcom., B.J., 2012. Two-dimensional T_2 distribution mapping in rock core plugs with optimal *k*-space sampling. *Journal of Magnetic Resonance*, **220**, pp 70-78.
10. Xiao, D., Balcom., B.J., 2014. *k*-t Acceleration in pure phase encode MRI to monitor dynamic flooding processes in rock core plugs. *Journal of Magnetic Resonance*, **243**, pp 114-121.
11. Hennig, J., Nauerth, A., Friedburg, H., 1986. RARE imaging: A Fast Imaging Method for Clinical MR. *Magnetic Resonance in Medicine*, **3**, pp 823-833.
12. Benning. M., Gladden, L.F., Holland, D.J., Schönlieb, C.B., Valkonen, T., 2014. Phase reconstruction from velocity-encoded MRI measurements – A survey of sparsity-promoting variational approaches. *Journal of Magnetic Resonance*, **238**, pp 26-43
13. Huang, D.D., Honarpour, M.M., 1996. Capillary end effects in coreflood calculations. SCA 1996-34. In Proc: *International Symposium of the Society of Core Analysts*. Montpellier, France, 8-10 September 1996. Society of Core Analysts.

STUDY OF ROCK PORE SPACE BY COMBINATION OF DIRECT AND INDIRECT TECHNIQUES

Aleksandr Denisenko, Ivan Yakimchuk, and Boris Sharchilev
Schlumberger

This paper was prepared for presentation at the International Symposium of the Society of Core Analysts held in St. John's Newfoundland and Labrador, Canada, 16-21 August, 2015

ABSTRACT

During the last few decades, Nuclear Magnetic Resonance (NMR) has become known in the petrophysics community as a convenient and efficient technique for studying pore space structure. NMR is an indirect method of pore size evaluation based on a proportionality between relaxation times and surface-to-volume ratio for each pore. The coefficient of proportionality (surface relaxivity) reflects the ability of mineral pore surfaces to increase the relaxation rates. It is common to use a single value of relaxivity for each core, which assumes that the pore surface properties within a small sample are sufficiently homogeneous [1]. However, in some cases the sample might contain pores with different surface properties that result in a range of relaxivity values characterizing the rock. Induced magnetic susceptibility arising from different sources, for instance metal ions, paramagnetic (Cu2+, Mn2+, Fe2+, Fe3+) or, in a worst-case scenario, ferromagnetic metallic iron (Fe), leads to interpretation uncertainty of T_2 spectra due to the influence of the internal gradient effects on the transverse relaxation rate. Fortunately, constructed T_1–T_2 2D dependences help to monitor the discrepancies in T_1 and T_2 spectra, which are affected by surface property changes and magnetic susceptibility contrast within the sample structure.

In this study, we implemented several proven techniques designed to evaluate pore structure directly. This approach allows for checking consistency of pore size distribution obtained by NMR T_1 at each pore scale. The results of X-ray microtomography (XmCT) imaging validated the large pore scale or slow T_1-decays and Scanning Electron Microscopy (SEM) results confirmed the small pores described by the fast NMR responses. The repeatability of all calculated distributions indicates similar abilities of all pore surfaces with the sample to relax the hydrogen nuclei or close relaxivity values responsible for T_1-relaxation in large and small pores for the observed sandstone rock.

INTRODUCTION

One of the fundamental pieces of information derived from laboratory core analysis is the pore size distribution. The classical and widespread methods used for pore size distribution are thin-section petrography and mercury intrusion porosimetry. Recently, a number of alternative technically complicated approaches have been proposed by the scientific community, including nuclear magnetic resonance (NMR), X-ray microtomography (XmCT), and scanning electron microscopy (SEM). Each of these

methods, as with any experimental technique, has its advantages and drawbacks. For example, the modern nano-CT devices provide resolution down to 50 nm, but the small field-of-view for such scanners raises concerns whether the imaged volume is representative of the overall sample. In contrast to XmCT, laboratory NMR machines detect hydrogen nuclei of fluid molecules constrained in pores of any geometry. Therefore, NMR is an indirect method for pore size evaluation based on a nearly linear relation between relaxation times and surface-to-volume ratio of a pore NMR distribution covers the broadest range of pore sizes, up to 5 orders of magnitude, far greater than any one direct technique.

Every pore-scale measuring method has its own specific limitation to the size range each can detect. A possible solution that eliminates the limitations of individual method is to perform the study by using a combination of methods instead. The key questions in such a combination of techniques are the analysis accuracy and defining the roles for each method. Research scientists have to understand the interpretation workflow and justify the applicability of each method for the particular case. In other words, the combination of different methods should lead to collaborative and consistent results instead of loosely combined data fragments.

METHODS AND APPARATUS

NMR – All of the NMR measurements were carried out using an Oxford Instruments low-field spectrometer, which includes a MARANi-Pharmasence magnet block equipped with a 22×22 mm probe, and DRX-HF electronic control system. The resonance frequency of 20.6 MHz corresponds to hydrogen nuclei spin precession in a ~ 0.5 T magnetic field. The T_2 and T_1 relaxation decays were recorded by ordinary Carr-Purcell-Meiboom-Gill (CPMG) and inversion-recovery with echo detection. We used an echo time of 100 μs and numbers of echoes sufficient to complete a decay, 48 logarithmically spaced delay times over the range 10^{-4} to 10^{1} s, and a relaxation delay of 10 s. The measurement temperature was 34°C. Methodically, all NMR procedures and consequent collation with XmCT data were performed in accordance with our previous work [2].

XmCT – We used two laboratory table-top micro-CT scanners in this study [3], [4]. The Using a 100-keV radiation energy for both systems a pixel size of 2.2 μm was obtained for the Bruker SkyScan 1172 and 0.5 μm for the ZEISS XRadia Versa XRM 500 on studied 8 mm diameter plug without contrast agents. The reconstructed 3D image of a core sample was segmented into two classes of objects: pores and minerals. The most intuitively obvious approach for individual pore analysis consists of separating a whole pore space into a set of individual pores and analyze each pore separately. General algorithms for pore separation are based on watershed techniques [2]. The equivalent spherical diameter is one of the most commonly used quantities for estimating the effective size of the object body. Finally, the histogram of the size values can be constructed.

An alternative method for calculation of the object size distribution is based on sphere fitting inside of the 3D structure [2]. The approach is also applicable for 2D images by using circles instead of spheres. In our opinion, this algorithm more accurately describes the pore space and more correctly fits with the physical phenomena in support of the NMR method, as the magnetic spin relaxation dominated by the nuclei diffusion and subsequent collisions with the grain surfaces. Therefore, the limits of molecules spreads correspond to spherical areas at any time and the sizes of spheres are constrained with the pore body ones.

SEM – In comparison with XmCT the SEM method provides much higher image resolution (up to 1 nm per pixel), but only the surface of the sample is investigated. For accurate studying of pore space structure, a special sample preparation procedure should be performed. This special procedure includes epoxy filling, mechanical cutting, multistage polishing and final coating of the surface by a conductive material. Using an image-stitching option makes it possible to cover rather large surfaces limited only by the SEM chamber and the sample holder. For example, scanning an 8×8-mm area with 1-nm resolution is essentially feasible, but would produce an enormous image of 8 million × 8 million pixels (>50 TB). In the work being reported in this paper, a 100-nm resolution was used (image size = ~80,000 × 80,000; file size = ~8 GB).

Focused Ion Beam coupled with SEM – The focused ion beam inside SEM (FIB-SEM) allows for obtaining a stack of 2D images of the sample's internal structure of some subsurface volume by ion etching of the surface slice-by-slice [5]. Thus, this method produces 3D images with resolution near that of the SEM. Unfortunately, the field of view is rather small (10 — 20 μm).

Sample preparation – The sample for study was cleaned and dried sandstone rock of West Siberia province, 8 mm in diameter and 10 mm long. The plug was saturated with 20 g/l NaCl solution, and placed in hermetically sealed cell for NMR measurements.

EXPERIMENTS AND DISCUSSION

Before consolidation the different pore structure evaluation methods, we analyzed the sample size representativeness and the influence of core preparation techniques on rock integrity and invariance. The comparison of NMR evaluation result on 22-mm and 8-mm samples cut from a single core gave rise to this investigation. The dissimilarity in short relaxation times of T_1–T_2 maps for different cylinder diameters indicated alteration of microporosity structure compared with the consistency and stability of large pores. Plugs drilling and especially a cooling fluid could cause the effect as a tap water was used during the coring. The swelling of clay minerals and consequent dispersion of clay particles along with migration of disrupted small solids at the cylinder near-surface area alter rock properties and consequently, pore size distribution. Using the SEM, we analyzed the structure and elemental alteration near the edges and in the central part of the 22-mm diameter sandstone core (Figure 1). As is clearly shown, the internal core structure is complicated, with rough and sharp points protruding from it. Many clay and

mud particles are observed near the edges of core, although rounded and clean grains prevail in the center.

Therefore, many factors determine the representativeness of cores and we had to be confident with our investigation, even with very homogeneous rock. For that reason, we performed all of the experiments on single-core cylinders or their fragments.

As a result, the study of void space structure was performed on 8-mm diameter by 10 mm in length cylindrical samples. This core size allows for performing experiments on the same sample using the NMR, XmCT and 2D SEM techniques. The FIB-SEM as well as Xradia XmCT scans were conducted on a small part of the rock cylinder. The collation of different methods of observing pore structure was studied on well-sorted sandstone rock samples. Initially, we adjusted the T_1 distribution with two XmCT spectra in terms of relaxation activity value, which was a tuning parameter of NMR and XmCT spectra coincidence.

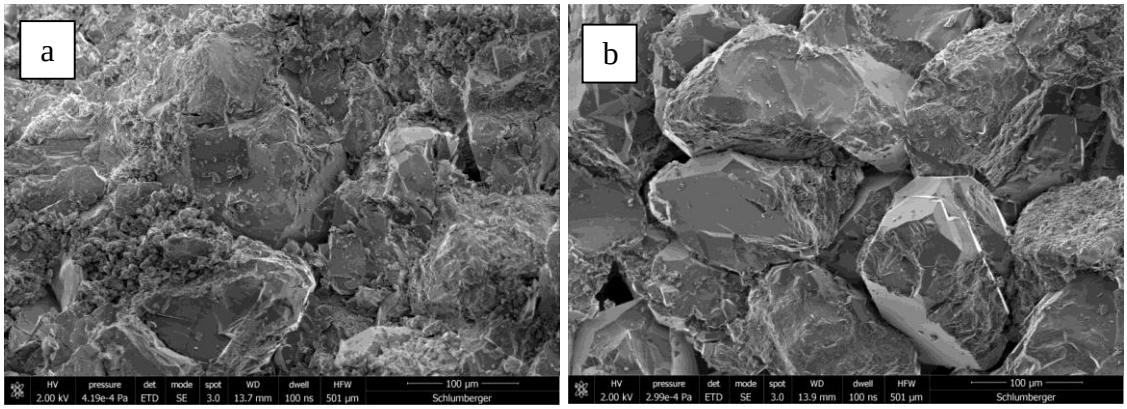

Figure1: SEM images of edge (a) and central parts (b) of granular sandstone core. Note the visible alteration and contamination of pores near the core edges.

Regardless of the applied model, the relaxation activity value mathematically represents the proportionality coefficient between pore sizes and relaxation times. We adopted the spherical pore model assumption: $r = 3\rho T_1$, where r – is a pore radius, ρ – a relaxivity; as the inscribed sphere method used to calculate the pore sizes using XmCT data. It is essential that the coefficient of proportionality between relaxation times and pore diameters, a complicated value, be influenced by pore surface magnetism and wettability, as well as pore shape. Therefore, it is more correct to name the coefficient ρ as being pseudorelaxation activity or cumulative parameter responsible for surface relaxation properties defined by mineralogical composition of rock and a value of specific surface.
The fitting of T_1 with XmCT data (Figure 2) provides a value of tuning parameter, relaxivity ρ_{T1} = 7.4µm/s and a volume of "invisible" microporosity equal to 29.7% of the total capacity; i.e., 8.2 p.u. The microporosity is the amount of the volume, which is below the XmCT scanner resolution (~5µm), i.e., the difference between the NMR and the XmCT porosities.

Combining T_2 spectra with XmCT data leads to a relaxivity value ρ_{T2} = 24 μm/s. Higher values of the relaxation activity of the pore surface in the second case were caused by the various physical mechanisms of longitudinal and transverse relaxation. Overestimation of ρ_{T2} values is caused by the diffusion relaxation mechanism that originated from significant internal magnetic gradients, as T_2 is strongly influenced by echo time. These gradients exert tremendous influence on NMR studies with high-value of magnetic field (20.6 MHz). Differences in T_1 and T_2 spectra are clearly observed on a 2D T_1–T_2 map (Figure 2). Notice the area with an inflated T_1/T_2 ratio in the upper-center region on the map. This separate region can be associated with the presence of the hydrocarbons remaining after extraction and/or contrasting pore surface areas with high-content paramagnetic centers that enhance local diffusion processes, and hence, drastically reduce T_2.

The differences of the T_1 and T_2 spectra described previously forced us to use longitudinal relaxation as internal-free gradients; therefore, a more reliable mechanism for observing pore size characteristics of multimineral rock composition.
The Xradia machine provides enhanced image resolution at the cost of sample size. We use this scanner to verify the consistency of the XmCT results. Both XmCT machines provide similar results; i.e., precisely duplicating large pores (right T_1 mode) in the calculated NMR pore size distribution (Figure 2).

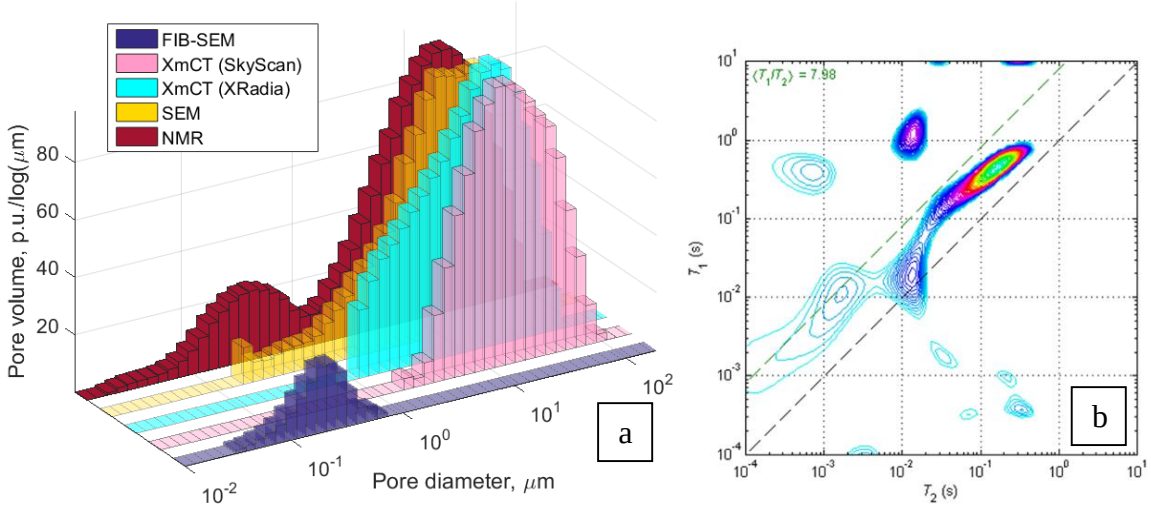

Figure2: (a) Pore size distributions measured by different analysis methods (NMR T_1, XmCT, SEM, and FIB-SEM); (b) T_1–T_2 map for the sandstone rock, West Siberia (Quartz=62%, Feldspar=20%, Clays=18%, Φ=27.8%, Permeability=407mD).

After conducting XmCT and NMR measurements on the cylinder, we obtained a small portion of the sample and performed an FIB-SEM study to characterize microporosity, which is invisible to common XmCT machines. Figure 2 also shows the resulting pore size distribution. The reconstructed image of the sample 3D pore geometry structure helped to visualize and detail small grains, their surfaces, internal structure of feldspars,

and clay mineral skeletons. The high-scale resolution of this method allowed for us to construct the distribution of tiny pores with sizes in the range of 50 nm to 1000 nm. The disadvantage of the FIB-SEM technique is its very small field of view (15×15 μm in our case), which could reduce measurement representativeness of a specimen, making volumetric evaluation difficult. Fortunately, the sample we studied was very homogeneous sandstone rock, and similar to the FIB-SEM field of investigation areas, which could be estimated on the 2D SEM image with a larger scale. The FIB-SEM method was used for an approximate estimation of the volume of rock, which is attributed to microporosity and construct the pore size distribution in porosity units (Figure 3). The sphere fitting technique was also applied during the evaluation of pore size distribution based on SEM data. Suitible repeatability of small pore sizes distributions constructed by NMR and FIB-SEM identified a similarity in the surface abilities to relax the hydrogen nuclei saturating the core. In other words, the pseudorelaxivity value obtained by XmCT and NMR spectra matching is near the small pore region. This result indicates a consistency by combining the input of mineral composition and a specific surface value of the rock matrix.

The SEM image itself contains information about pore scaling. The advantage of the SEM method is the larger field of view compared with the FIB-SEM image, but the data are 2D only.

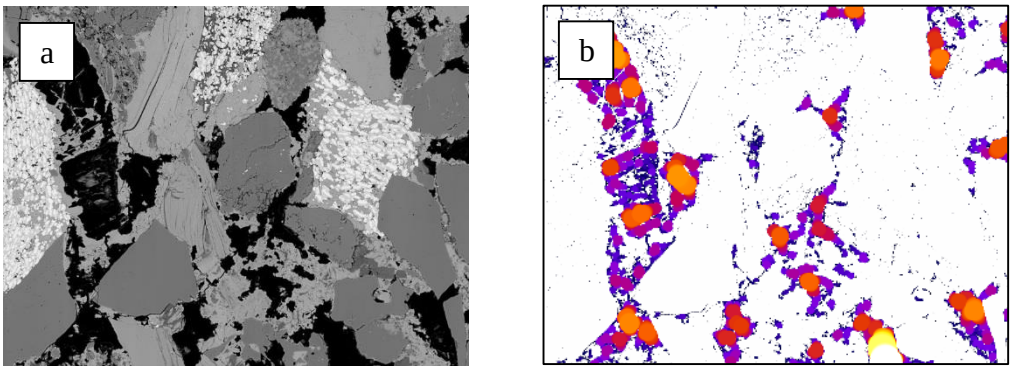

Figure3: (a) SEM slice image examples and resulting pore geometry evaluation technique based on inscribed spheres (b). Each color defines a sphere diameter

This explains why we had to estimate the pore areas instead of volumes and used a circle-fitting technique, which is analogous to previous FIB-SEM technique. Constructed distribution reflects approximate characteristics of pore structure over a wide range of sizes (0.4 — 40 μm).

CONCLUSIONS

The results obtained in this study describe the advantages and drawbacks of different methods of pore structure evaluation. These results point out the necessity for using an integrated study of the pore space structure of rocks by the different methods to investe pore sizes over a wide scale range and resolution. This detailed investigation using

several methods allows for avoiding uncertainties in the interpretation of NMR spectra and consequent evaluation of relaxation activity factors for different pore scales. Sample size as well as core preparation techniques have a strong influence on pore structure and their consistency in different acquisition methods.

ACKNOWLEDGEMENTS

We would like to thank Schlumberger for permission to publish this paper. We also acknowledge Dmitry Korobkov and Igor Varfolomeev for their support in performing the experiments.

REFERENCES

1. Kleinberg, R., 1994, Pore Size Distribution, Pore Coupling, and Transverse Relaxation Spectra of Porous Rocks, Mag.Res.Imag., 12, 2, 271 - 274.
2. Denisenko, A. and Yakimchuk, I., 2014, X-Ray Microtomography and NMR: complimentary tools for evaluation of pore structure within a core, Society of Core Analysts Symposium, 8–11 September, Avignon, France.
3. High-resolution micro-CT. Bruker Micro-CT. SkyScan 1172, http://www.skyscan.be/products/1172.html.
4. High resolution 3D X-ray Microscopes. ZEISS Xradia, http://microscopy.zeiss.com/microscopy/en_de/products/x-ray-microscopy.html
5. Lee, E., et al, 2004, 3D Materials Characterization using Dual-Beam FIB-SEM Techniques. Microscopy and Microanalysis, 10 (Suppl. 02), 1128-1129.

MEASUREMENTS OF MOBILE WATER SATURATION IN OIL SANDS

J. Butron[1], J. Bryan[1, 2], Y. Duan[1] and A. Kantzas[1, 2]
1. PERM Inc.
2. University of Calgary

This paper was prepared for presentation at the International Symposium of the Society of Core Analysts held in St. John's Newfoundland and Labrador, Canada, 16-21 August, 2015

ABSTRACT

The presence of mobile water saturation in heavy oil and bitumen systems is of considerable importance when understanding how different reservoir recovery methods will work. In non-thermal heavy oil production, the presence of mobile water saturation has extreme significance to the production of cold heavy oil (CHOPS) wells. Some wells are able to produce oil under relatively low and constant water cuts, while other wells produce significant water and quickly need to be shut in due to high production water cuts. In this study, an NMR and core analysis approach is used to shed some light into the properties of oil sand with or without mobile water present. Specifically, tests were run in order to study if mobile water is a localized pore scale phenomenon or if it can be understood through a more macroscopic view of the reservoir.

Samples of core are taken from two heavy oil producing wells: one that experienced very high production water cuts, and the other that produced mainly heavy oil with minimal water. The samples (containing heavy oil and connate water) are flooded with water in order to measure effective permeability to water. NMR spectra are also obtained after flooding and after cleaning of the cores, in order to understand the pore-scale location of water in different effective permeability samples. The outcome of this study is insight into what is the difference in core properties between wells with vs. without mobile water. The key conclusion reached is that wells behave similarly at the pore/core scale, but differences are observed macroscopically. The well with high historical water contains thin zones of high water saturation (high water effective permeability) which were missed at the resolution of the logs. Water production may be due to the presence of these heterogeneous zones.

INTRODUCTION

Cold heavy oil production with sand (CHOPS) is a unique non-thermal reservoir recovery strategy that is applied in many unconsolidated oil reservoirs in Alberta and Saskatchewan. This recovery technique involves providing maximum drawdown to pull oil to production wells, and is based on the concepts of process enhancement through foamy oil flow [1,2] and sand production [3]. During CHOPS production, the high pressure drawdowns lead to the generation of discontinuous gas droplets within the oil phase, which keep the differential pressure high in the system and drive foamy oil to the

production wells. Furthermore, sand production creates regions of high permeability (wormholes) throughout the reservoir, which act as conduits for further production of oil. CHOPS production is run in unconsolidated oil sand reservoirs, where sand permeability is on the order of Darcies and oil viscosity is on the order of 1,000 – 50,000 mPa·s at reservoir temperatures. The high oil viscosity is the biggest challenge to production; if there is mobile water present in these reservoirs, water will tend to flow preferentially to oil. Accordingly, oil production will decline and wells will "water out". Identifying if a given heavy oil pool has mobile water is very important for assessing the chance of economic success for CHOPS wells drilled into that pool.

This document is a case study of two CHOPS wells from northern Alberta. The oil in these wells is on the order of 30,000 – 50,000 cP at reservoir conditions, and has an *in-situ* solution GOR on the order of 15 m^3/m^3. In the initial identification of oil pay, the determination for production was made on the basis that both wells have porosity > 30% and measured resistivity (R_t) values greater than 10 ohm·m. In terms of production, **Figure 1** shows that Well 1 produced oil under relatively low and constant water cuts, while Well 2 exhibited much higher water production and, despite attempts to control the production, the water cut spiked again and eventually Well 2 was shut in. This historical production was observed despite the fact that the resistivity (indicative of oil saturation) is higher in Well 2 vs. Well 1 (**Figure 2** and Figure **3**). The goal of this study was to investigate if the differences between these wells can be understood on the basis of pore-scale water location within the sand of the two formations, or if the high water production in Well 2 is due to a more macroscopic phenomenon.

EXPERIMENTAL PROCEDURE

The study of pore-scale water location was made through NMR and permeability measurements in oil sand cores. 1" core plug samples are taken from stored frozen full diameter core intervals from the two heavy oil wells (Well 1 and Well 2), and samples are shown in Table **1**. NMR spectra on the initial cores showed that the samples were partially dried out. The samples were vacuum saturated with brine. The effective steady state permeability to water was measured by running brine through the core at low DP/L values, in order to measure water permeability without producing any oil. The NMR of the cores were then re-measured and Dean-Stark was done to measure the connate water present in each vacuum saturated core. The cleaned sand was saturated with water to measure the true pore size distribution of the sand in each core with NMR.

Furthermore, core analysis (Dean-Stark) water saturations were present over the oil-bearing interval in both wells. Based on correlations of water effective permeability vs. water saturation on the tested samples from Table **1**, a macroscopic study was also run to output profiles of predicted effective water permeability as a function of depth (and water saturation) in each well.

RESULTS

Table **1** shows the core samples that were taken from Wells 1 and 2. The Dean-Stark water saturations are measured on the cores after they have been vacuum saturated and water effective permeability has been measured. These permeability values are also listed in **Table 1**. Effective permeability values are low in the core samples with higher oil saturation, which is expected.

Two types of flow behaviour were observed in the tested cores. One flow type is shown in **Figure 4**, which is the spectra from a low oil saturation lean zone in the reservoir. Water vacuum saturated and flooded through the core is in the same T_2 ranges as the actual NMR pore sizes from this sand. In other words, water exists in the core in direct contact with the sand grains, so water flows as a wetting fluid [3,4]. In contrast, **Figure 5** is a sample containing higher oil saturation. In this case, water from saturation and flooding exists mainly as a slow-relaxing peak at longer T_2 values than the true pore sizes for this sample. In oil-rich samples, water injected even at low injection pressures tends to finger through the oil, i.e. viscous forces dominate flow patterns in high oil saturations. These figures demonstrate that there are two different flow types present in oil sand, and the physics of displacement will be different for both flow types. Unfortunately, both wells exhibited this same behaviour for high S_w vs. low S_w samples. While the NMR shows different flow behaviour in oil rich vs. lean zones, this cannot be used to infer microscopic differences between Wells 1 and 2. Furthermore, Figure **6** shows that both wells have a similar behaviour in terms of effective water permeability vs. water saturation. In other words, the high water production in Well 2 is not a pore-scale difference in wettability or water location within this formation.

A macroscopic view of the wells provides better insight into the production response of the two wells. **Error! Reference source not found.** is the resistivity log (calculated) and core (measured) water saturation profile over the producing zone of this well. The black box at the left of the figure indicates the perforation zone within the oil formation. Water saturations from log and core were used to estimate effective permeability to water by applying the trend line from the core measurements in Figure **6**. **Error! Reference source not found.** shows that this well has low effective permeability to water: values are generally 10 mD or less, as predicted from the water saturation profile. In contrast, **Error! Reference source not found.** plots the resistivity log (calculated) and core (measured) water saturation profile for Well 2. The log initially provides a tightened water saturation profile with depth, but from the finer resolution core measurements, it is observed that there are thin intervals present in this formation that have much higher water. When water saturations are used to predict effective water permeability, Figure **7** shows core predictions of water permeability that can be in the range of 100 mD or higher in these thin lean streaks. The actual resistivity data (Figure **3**) was noisy, compared to the more gradual resistivity changes in Well 1 (Figure **2**). These changes were initially smoothed out in the log predictions of saturation, but the inclusion of core Dean-Stark data shows that these R_t variations are physically present, and should be included in the calculated water saturation profile for this well. A better

log R_t model is shown that has higher fidelity to the R_t variations measured in this well, and greater variations in the predicted permeability as a direct result of these R_t heterogeneities.

The results of this study can provide insight into the ability of these unconsolidated reservoirs to flow non-thermal oil. With absolute permeability on the order of 100 – 1000 mD and water permeability only around 10 mD, heavy oil can be produced even though its viscosity is so much higher than that of water. As water permeability increases by an order of magnitude the mobility of water is higher than that of oil, and the well will preferentially start to produce water.

CONCLUSION

Water effective permeability at connate water saturations is on the order of 1 – 10 mD in oil rich zones, and can approach 100 mD or higher in lean oil zones. The response of high vs. low water producing CHOPS wells is not due to microscopic (pore level) differences between the wells. Instead, the high water production can be related to local variations in water saturation within the oil zone. Thin streaks of high water saturation can be quite permeable to water, and these zones may be missed from logging tool interpretations. Proper reservoir description requires an understanding of heterogeneities in fluid saturations, either through the collection of core or by ensuring that the well log models have fidelity to the variations in measured R_t in the producing intervals.

ACKNOWLEDGEMENTS

The authors gratefully acknowledge Devon Canada for providing core samples and logging tool information for these case study wells. Financial support for this work has come partially from the NSERC Chair in Fundamentals of Unconventional Resources (FUR), the University of Calgary, and its industrial sponsors: Laricina Energy, Husky Energy, Athabasca Oil Corp, Suncor, Brion Energy, CNRL, Devon, Foundation CMG and Alberta Innovates.

REFERENCES

1. Maini,B, “Foamy Oil in Heavy Oil Production”, *J. Can. Pet. Tech.*, **35** (6), 21 – 24, Jun 1996.
2. Firoozabadi, A., “Mechanisms of Solution Gas Drive in Heavy Oil Reservoirs”, *J. Can. Pet. Tech.*, **40** (3), 15 – 20, Mar 2001.
3. Tremblay, B., “Cold Flow: A Multi-Well Cold Production (CHOPS) Model”, *J. Can. Pet. Tech*., **48** (2), 22 – 28, Feb 2009.
4. Bryan, J., Mai, A. and Kantzas, A., “Investigation into the Processes Responsible for Heavy Oil Recovery by Alkali-Surfactant Flooding”, SPE 113993, 2008 SPE Improved Oil Recovery Conference, Tulsa, OK USA, Apr 19 – 23, 2008.
5. Al-Mahrooqi, S.H., Grattoni, C.A., Muggeridge, A.H. and Jing, X.D., “Wettability Alteration during Aging: the Application of NMR to Monitor Fluid

Redistribution", SCA 2005-10, International Symposium of the Society of Core Analysts, Toronto, ON Canada, Aug 21 – 25, 2005.

Well No	Sample	kw (mD)	Dean-Stark post waterflood So (fraction)	Sw (fraction)
1	1	46.4	0.284	0.716
	2	150.9	0.524	0.476
	3	162.4	0.509	0.491
	4	1	0.644	0.356
2	1	2.8	0.516	0.484
	2	1	0.682	0.318
	3	1.4	0.712	0.288
	4	42.7	0.012	0.988
	5	1300	0.058	0.942

Table 1: Core Analysis Samples Tested for NMR and Water Permeability

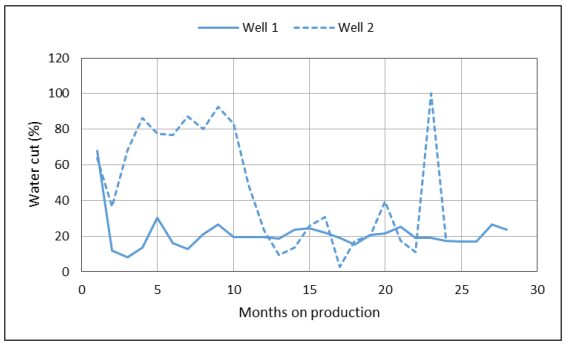

Figure 1: Historical water cuts of Well 1 and Well 2

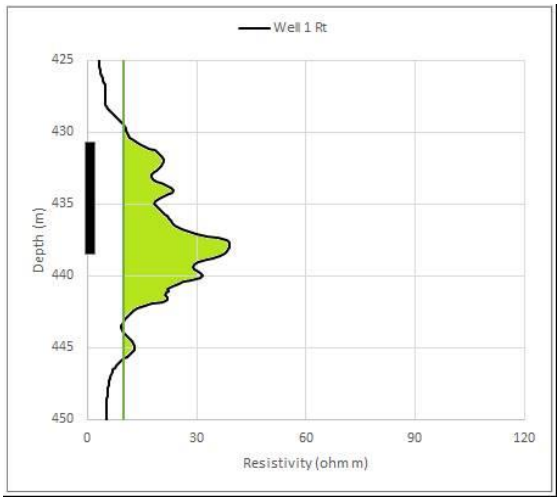

Figure 2: Well 1 Resistivity Profile

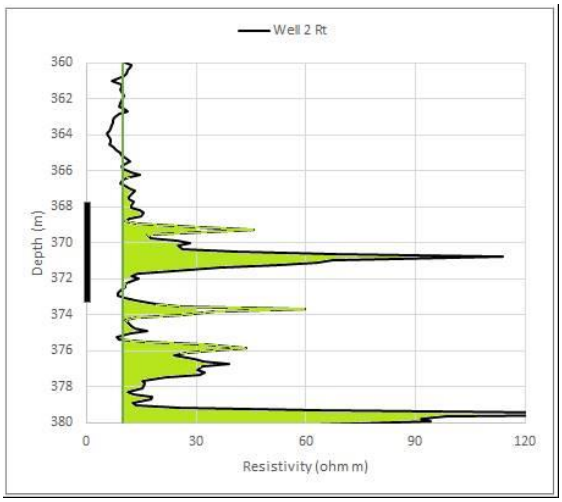

Figure 3: Well 2 Resistivity Profile

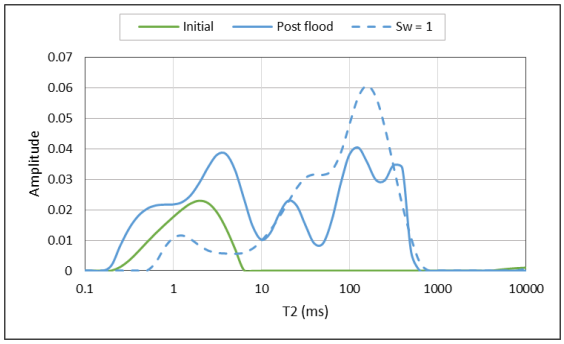

Figure 4: NMR spectra for low oil saturation core

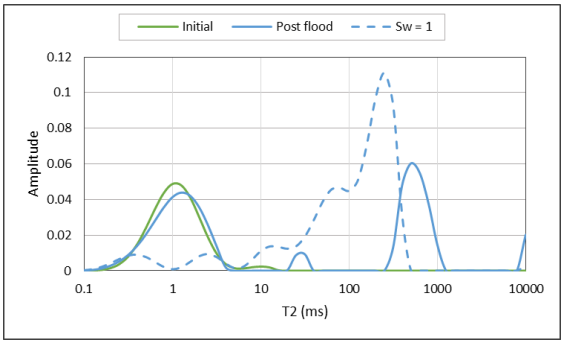

Figure 5: NMR spectra for high oil saturation core

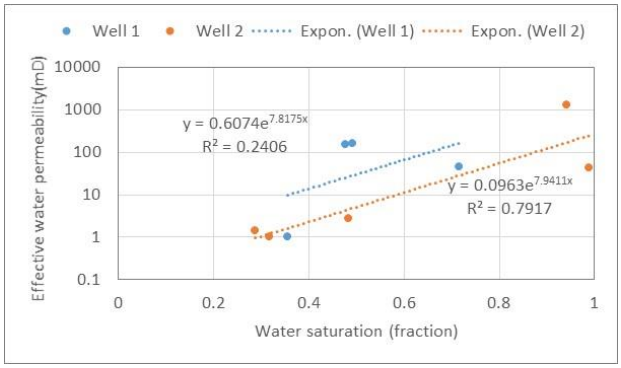

Figure 6: Water effective permeability vs. water saturation

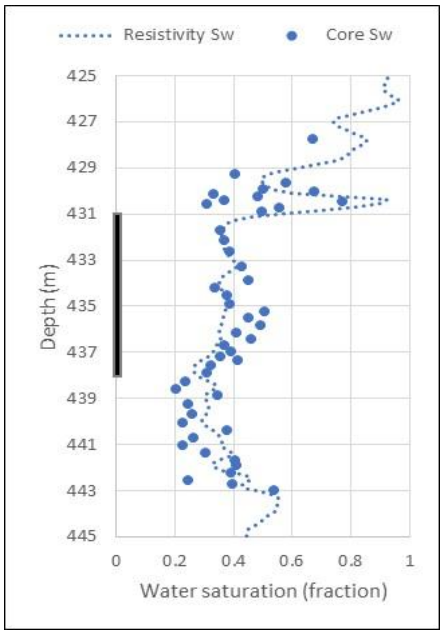

Figure 7: Log and core Sw profile for Well 1

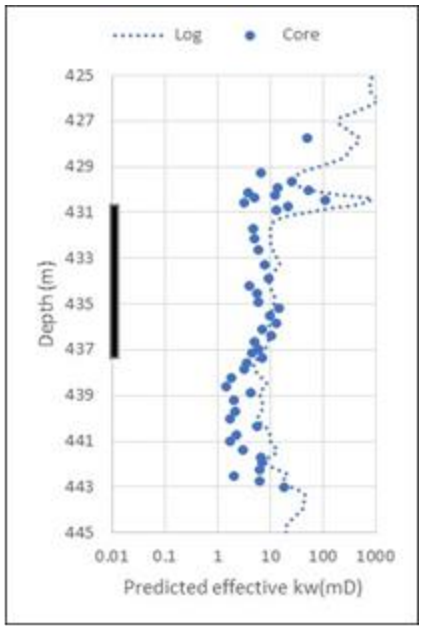

Figure 8: Log and core predictions of effective kw for Well 1

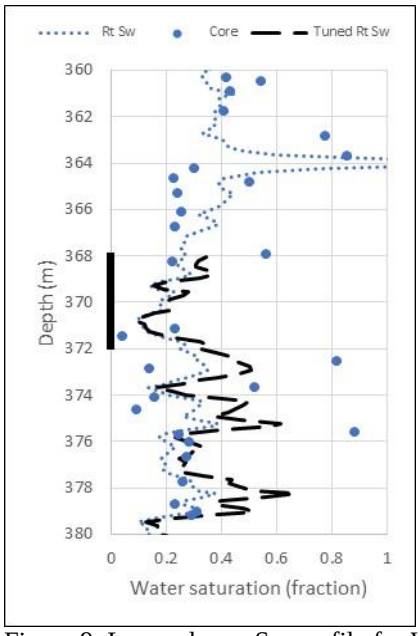

Figure 9: Log and core Sw profile for Well 2

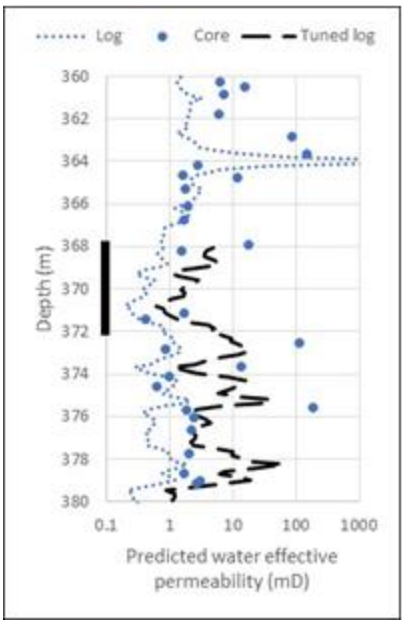

Figure 7: Log and core predictions of effective k_w for Well 2

STUDY OF PETROPHYSICAL PROPERTIES ALTERATIONS OF CARBONATE ROCKS UNDER CARBONATE WATER INJECTION

Eric Yuji Yasuda[1], Erika Tomie Koroishi[2], Osvair Vidal Trevisan[3] and Euclides José Bonet[3].
[1]Mechanical Engineering, State University of Campinas, UNICAMP; [2]Center for Petroleum Studies – CEPETRO; [3] Department of Energy, State University of Campinas – UNICAMP.

This paper was prepared for presentation at the International Symposium of the Society of Core Analysts held in St. John's Newfoundland and Labrador, Canada, 16-21 August, 2015

ABSTRACT

Carbon dioxide (CO_2) injection in reservoirs promotes rock-fluid interactions, which depends on rock nature, brine composition, partial pressure of CO_2, temperature as well as operational conditions. The rock-fluid interactions cause changes in the petrophysical properties, modifying both porosity and permeability of the rock. The present study aims to study the effects of water injection with dissolved CO_2 on the petrophysical properties of carbonate rocks. The effects are evaluated experimentally by displacement runs on a long core of an outcrop coquina. The work emphasizes the evaluation of permeability changes along the length of the core, using a coreholder equipped with multiple pressure taps. The experiments were conducted in dynamic regime, at T=22°C and P=2,000 psi and flow rates of 0.5, 1 and 2 cc/min. X-ray Computerized Tomography (CT) was used to determine porosity alterations during the experiments and the differential pressure drop was used to calculate permeability and its changes along the rock sample. Results show that porosity increased steadily with the accumulated volume of water injected. Permeability increased sharply at the higher flow rates and the changes were unevenly distributed along the core.

INTRODUCTION

The occurrence of reactions between the CO_2 enriched brines and carbonate rocks, has been reported in several applications. The interaction between fluids containing CO_2 and the rock is often found in the literature associated with matters of capture and underground storage of gas. In accordance to Ott et al. 2013 [1] reactions may influence the fluid-flow field, i.e. reactive transport, and the mechanical rock properties, which might degrade, leading to uncertainties with respect to the rock integrity in the affected region. Luquot and Gouze [2] analyzed the dissolution of carbonate rocks submitted to flow of aqueous solutions. In the experiments, measurements of salinity and pH were carried out at different positions along the flow and then it was possible to classify the mass transfer processes both near wellbore and further, where the dissolution becomes increasingly uniform. Zekri et al. [3] observed that the CO_2 injection at supercritical state

alters rock permeability and that the alteration is related to the rock composition. Taking it into account, the changes must be evaluated along time for the particular rock in consideration, due to the heterogeneities present in the reservoirs.
An important characteristic associated to the CO_2 injection in reservoirs is the presence of chemical interaction between the fluid and the rocks. With the CO_2 injection in the reservoir, a fraction of the gas dissolves into the formation brine or into the injection water, producing carbonic acid (H_2CO_3), which dissociates as charged particles with potential to interact chemically with the rock minerals (calcite, dolomite, anhydrite). These reactions are known to geochemists to provoke dissolution or precipitation, depending on the direction they manifest. They are a function of the rock nature, the brine composition, the partial pressure of CO_2 and the thermodynamic conditions. The movement of the fraction of CO_2 dissolved in the formation water is dependent on the transport mechanisms (diffusion or convection) and the reaction kinetics [4]. The mass transfer between the fluid and the rock relies on numerous parameters, such as: partial pressure of CO_2, concentration of cations in the formation water, the injection flow rate, the reactive surface area, porosity, permeability and tortuosity of the medium, among others.

The presence of the rock-fluid chemical interaction may change the pore structure and modify the permeability of the rock, which is a key parameter to the flow in reservoir engineering. The present paper reports an experimental investigation on the permeability and porosity changes of a carbonate rock with the injection of carbonate water.

PROCEDURES

Materials

The carbonate rock used in the study was extracted from a coquina outcrop, from Morro do Chaves formation, in the Sergipe-Alagoas basin, Brazil. Three fluids were employed in the experiment: a sodium chloride (NaCl) brine at 35 kppm concentration as the initial saturation fluid, a sodium iodide (NaI) brine at 35 kppm as the dopant and a sodium chloride brine at 35 kppm saturated with CO_2 at 2,000 psi as injection fluid.

Methods

The experiments were performed on the experimental setup made up basically by the following devices: a positive displacement pump to guarantee a measurable and continuous flow, high pressure vessels for the fluids conditioning, a special coreholder with multiple pressure taps connected to differential transducers referenced at the inlet point and a backpressure system at the outlet port. The coreholder was composed of an aluminum cylinder, with an epoxy and carbon fiber jacket around the sample. The experimental apparatus is schematized in Figure 1.

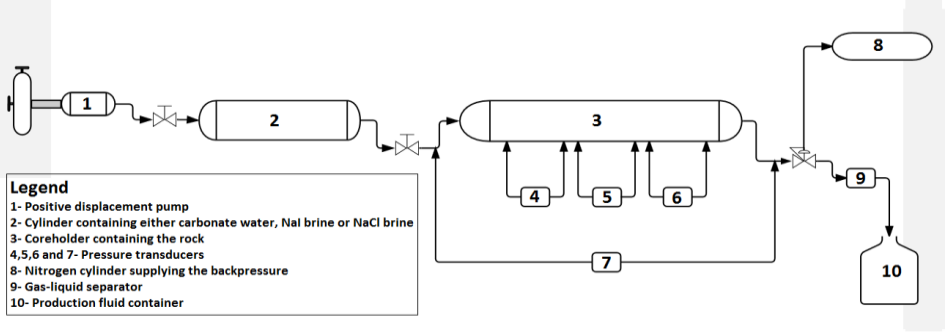

Figure 1. Scheme of the experimental apparatus.

The sample was saturated with the 35 kppm NaCl brine and then flushed with the contrast fluid, the 35 kppm NaI brine. After that, the tests with carbonated water were performed at the flow rates of 0.5, 1 and 2 cc/min. The operating conditions were 2,000 psi and 22°C. Differential pressures were measured at points along the core as shown in Figure 1 by appropriate sensors (nVision Crystal Engineering Corporation). The permeability was evaluated by the pressure drop along the sample. The pressure was measured in six different points along the sample and also on the inlet and outlet valves, resulting in eight pressure taps, as schematized in Figure 2.

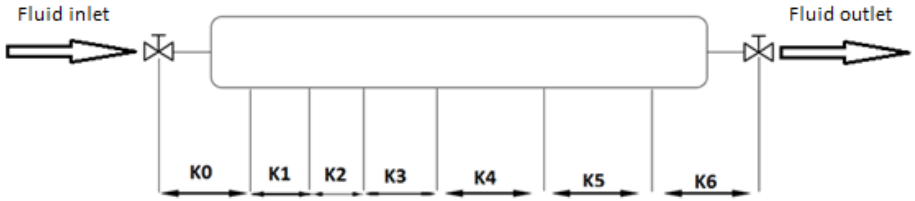

Figure 2. Scheme of the permeabilities evaluated during the test.

Porosity was evaluated by X-ray computerized tomography (Siemens CT scanner model SWFVD30C), using the software Syngo. The images had a 0.5 mm resolution and each scan acquired 69 images along the sample.

RESULTS

Porosity

A MatLab™ routine was used to calculate the porosity of each section. These data were acquired by the continuous CT scan along each test cycle. Porosity was calculated in accordance to Equation 1, where CTn, CTrock and CTfluid represent the mean CT number for the system in a given time, the rock CT number and the fluid CT number respectively.

$$\varphi = \frac{CTn - CTrock}{CTfluid - CTrock} \quad (1)$$

Figure 3 shows the behavior of the mean porosity, which showed a steady increase of its values with the increase of the accumulated volume of water injected. A slightly greater increase was observed at the beginning of the test, when a flow of 1 cc/min was used. The overall increase across the entire test was from 13% to 17%, a substantial change if one considers the volumes of a whole reservoir.

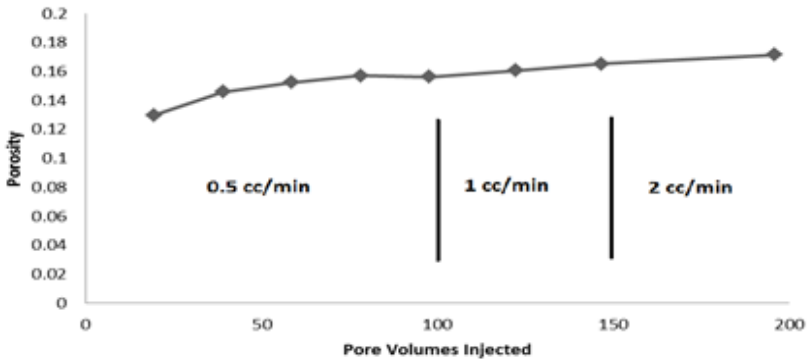

Figure 3. Mean porosity by volume of carbonated water injected.

Using data from each transversal section (69 total slices) of the CT-scan, porosity was calculated at each particular time and position. It was possible to verify porosity evolution through time along the entire core. The evolution and distribution of porosity is depicted in the 3D plot shown in Figure 4.

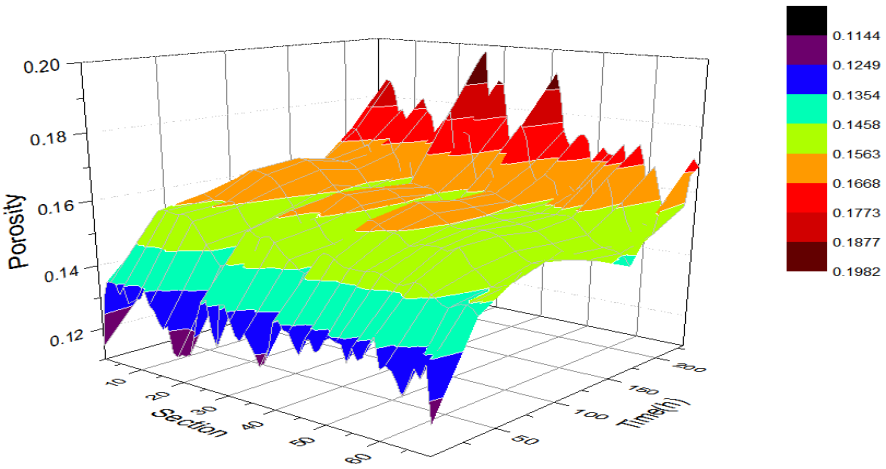

Figure 4. Evolution of porosity along whole sample through time.

During the injection test, small solid white particles were observed to accumulate at bottom of the container of the produced fluids, evidencing the occurrence of dissolution of the rock. In accordance with Grigg et al. 2013 [5], carbonate dissolution caused changes in core permeability and porosity.

Permeability

Figure 5 depicts the variation of the average permeability of the rock sample along the duration of the experiment. Permeability remained basically unchanged up to 120 PVI (pore volumes of water injected). It is important to notice that from the beginning of the test up to 100 PVI the test was carried out at a flow rate of 0.5 cc/min. A steep increase in permeability, from 0.2 D to 12 D, was observed between 120 to 170 PVI. Such remarkable increase is associated to the formation of a preferential path to the flow which was visible at the CT images.

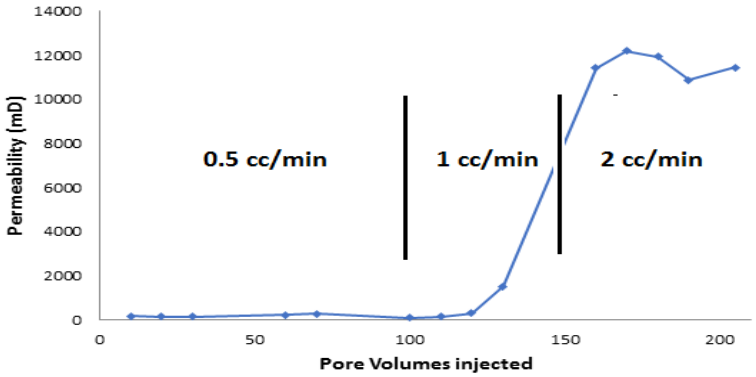

Figure 5. Mean permeability by pore volumes of carbonated water injected.

The significant change in permeability happened soon after the flow rate was raised to 1 cc/min. At 12 D the permeability curve leveled off and remained flat with the continued injection of carbonate water even when the flow rate was increased to 2 cc/min.

Through the experiments, the permeability of all regions from K0 to K6 could be evaluated along the test, and the result is shown in Figure 6. Evolution of permeability was not even through the rock sample. Sections K2 and K6 showed the greatest permeability changes at about 120 pore volumes injected, and it probably occurred due to fluid breakthrough in a wormhole which increased the permeability of the entire core. For these sections, the permeability dropped afterwards probably because of the movement of fine grains of rock which clogged some permeable channels.

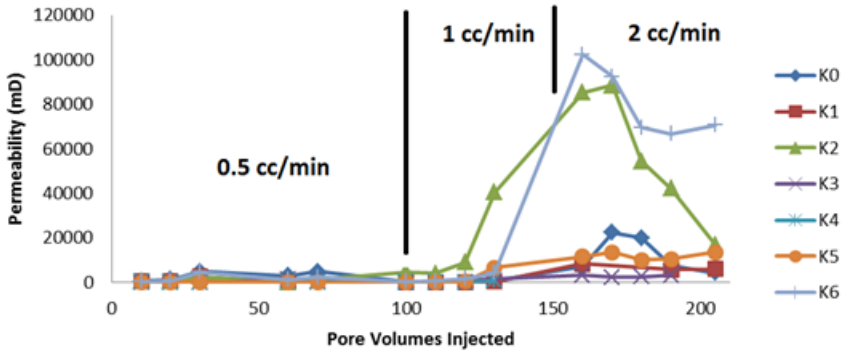

Figure 6. Permeability by sections of the sample against pore volumes injected.

CONCLUSION

It was possible to verify that both injection rate and also the interaction between rock and fluid promoted alterations on the rock petrophysical properties. The porosity showed a progressive increase through the tests. It can be verified the porosity evolution through time along the entire core. The mean porosity performance showed a steady increase of its values with cumulative volume of water injected. Porosity indicated a considerable change along all test. Initially, the outcrop porosity was 13% and in the final test it showed 17% that it represents a considerable change for a whole reservoir.

Permeability remained basically unchanged up to 120 PVI (pore volumes of water injected). It was verified that from the beginning of the test up to 100 PVI the test was carried at a flow rate of 0.5 cc/min. The experiments showed the creation of a preferential path, which increased greatly the rock permeability, showing evident when the flow rate was increased to 1 cc/min.

ACKNOWLEDGEMENTS

The authors acknowledge PETROBRAS and CNPq for financial support of the present study.

REFERENCES

1. Ott, H et al, CO2 Reactive transport in limestone flow regimes, fluid flow and mechanical rock properties. International Symposium of the Society of Core Analysts, 2013, SCA-2013-029.
2. Luquot, L. and Gouze, P., Experimental determination of porosity and permeability changes induced by injection of CO2 into carbonate rocks. Chemical Geology 265, 148-159, 2009.
3. Zekri, A. Y., Shedid, S. A., Almehaided, R. A. Investigation of supercritical carbon dioxide, aspheltenic crude oil and formation brine interactions in carbonate formations. Journal of Petroleum Science and Engineering, v. 69, 63-70, 2009.
4. Grigg, R. and Svec, R., Co-injected CO2-brine interactions with Indiana limestone, International Symposium of the Society of Core Analysts, 2003, SCA-2003-19.
5. Mangane, P. O. Caractérisation des changements dans les propriétés de réservoir carbonaté induits par une modification dans la structure des pores lors d'une injection de CO2: application au stockage géologique du CO2. Tese, Sciences de Techniques du Languedoc-Roussillon, Universite Montpellier II, 2013.

CORNER OIL FILM ELEVATION ABOVE THE GAS-OIL INTERFACE IN WATER-WET CAPILLARIES

Hossein Khorshidian, Lesley James and Stephen Butt
Memorial University of Newfoundland

This paper was prepared for presentation at the International Symposium of the Society of Core Analysts held in St. John's Newfoundland and Labrador, Canada, 16-21 August, 2015

ABSTRACT

In gas assisted gravity drainage, very high oil recovery factors can be obtained when a thin oil film is formed over the water surface in water wet porous media. The formation of an oil film, as an intermediate wetting phase, over the water (wetting phase) surface in the presence of gas (non-wetting phase) is typically linked to the spreading coefficient which is the gas-water interfacial tension subtracted by the sum of the oil-water and oil-gas interfacial tensions. However, the oil film characteristics not only depends on the interfacial tension, but also depend on the geometry of the phase contacts on solid surface which is affected by the geometry and wettability of the solid surface. The oil film, which may exist between the water and gas in the corner of capillaries, can play an important role in oil recovery by gravity drainage during immiscible gas injection. The thin oil film can be the path to transfer the trapped oil in smaller pore-throats, which is left after gas injection, toward the oil bank beneath the gas front. Additional oil recovery can be obtained by gravity drainage if the gas-oil capillary pressure is high enough for the entry of non-wetting phase into the smaller pore-throats. In this article, the oil film characteristics in the corner of a simple square capillary tube are modelled, based on the size of the capillary tube, phase interfacial tension, phase differential density and the distance between the gas front and oil front, through balancing the gravity and capillary pressure under equilibrium condition. The results show that having a higher gas-oil interfacial tension, lower gas-oil differential density and larger oil bank size provides an intermediate phase (oil) with better hydraulic communication over a greater elevation. The proper hydraulic communication above the gas front assists the gravity drainage mechanism to recover more oil from smaller pore-throats in particular scenarios. These scenarios are identified and discussed in this article.

INTRODUCTION

Oil displacement by gas-assisted gravity drainage in a water wet porous media often results in a high recovery factor. In gas-assisted gravity drainage, both gravity and capillary phenomena affect the oil recovery. The conditions that provide an efficient oil recovery factor can be identified by characterizing mechanisms of fluid displacement in gas-assisted gravity drainage. Oren and Pinczewski [1] investigated three phase fluid flow in porous media and drew a relationship between the phase interfacial tensions and the state of the fluids' contacts configuration. In many investigations, it has been stated

that high oil recovery by vertical gas injection in water-wet porous media can be obtained if the oil phase spreads over the water surface in the presence of gas, and the spreading condition of oil over the water surface is only controlled by the interfacial tension between each pair of fluids [2, 3, 4]. Further investigations showed that the oil displacement mechanism is also affected by capillary pressure rather than by interfacial tension alone [5]. The capillary pressure in addition to the fluids' interfacial tensions is a function of the curvature of the interfaces between fluids, which is affected by the capillary geometry and phase contact angle. A stable oil layer over the water surface has also been observed in a system with a negative oil spreading coefficient [5, 6]. Dullien et al. [7] showed that the rate of oil recovery in porous media, when an oil film forms on the smooth glass bead surfaces having positive spreading coefficient, is very low and unmeasurable. Conversely, an oil film that is formed in corners of wedges and crevices on the surface of scratched glass beads is thicker. The thick oil films yielded higher rate of oil recovery that could be measured. Blunt et al. [8] calculated the height of the oil film in porous media for the three phase system. They compared the oil-water and oil-gas contact radii in capillary corners evaluating capillary pressures based on the fluids interfacial tensions and densities. Depending on the fluid interfacial tensions and differential densities, two different types of the oil film are formed in the corner of capillaries. In the first type, the oil film can be present over the water surface at any elevation, and in the second type, the presence of the oil film is limited to a critical elevation. Blunt et al. [8] predicted that for conditions in which the oil height is limited, the oil saturation after vertical gas injection is very low. However, a reverse result was observed for a system in which oil has a negative spreading coefficient.

In this article, the equilibrium height of the oil film in the corner of a water-wet and square shaped capillary tube is calculated varying the fluid characteristics. The relationship between the residual oil saturation after gas breakthrough and the state of the thin oil film is discussed. The results of this study provide insight for the phenomena affecting the gas-assisted gravity drainage oil recovery method.

THEORY

The oil film in a water-wet and square shaped capillary tube with sharp corners can be characterized if the capillary pressure between each pair of phases is known. Fig. 1 schematically shows a square capillary tube containing gas (non-wetting phase), oil (intermediate wetting phase) and water (wetting phase). The equilibrium capillary pressure between oil and water at point 1 in Fig. 1a, (P^*_{cow}), is shown in Eq. 1 [8]

$$P^*_{cow} = \frac{4\sigma_{ow}\cos\theta_{ow}}{D} \quad (1)$$

where, 'σ_{ow}' is the oil-water interfacial tension, 'θ_{ow}' is the oil-water contact angle, and 'D' is the size of the square tube side. The capillary pressure (P_c) at any point inside the tube is the local differential pressure between the non-wet phase (P_{nw}) and wetting phase (P_w) as indicated by Eq.2 [8].

$$P_c = P_{nw} - P_w \tag{2}$$

Oil and water hydrostatic pressure along the corners of the vertical tube vary differently depending on their densities. The water and oil pressure above point 1 (oil-water contact front) in Fig. 1a are calculated by Eq. 3 and 4;

$$P_w = P_w^* - \rho_w g(H+L) \tag{3}$$

$$P_o = P_o^* - \rho_o g(H+L) \tag{4}$$

where, 'P_w' and 'P_o' are water and oil pressures along the tube, 'P^*_w' and 'P^*_o' are the water and oil hydrostatic pressure at point 1 in Fig. 1a, 'ρ_w' and 'ρ_o' are oil and water densities, H is the height of the oil film above the gas-oil contact front (point 2 in Fig. 1a), L is the oil bank length (distance between point 2 and point 1 in Fig. 1a), and g is gravitational constant, which is assumed to be 9.8 m/s^2 in the calculations.

The oil-water capillary pressure at any location above point 1 can be calculated by substituting Eq. 3 and 4 in Eq. 2. Knowing the gas-oil interfacial tension (σ_{go}) and gas-oil contact angle (θ_{go}), the gas-oil capillary pressure above their contact at point 2 in Fig. 1a can be calculated in the same manner. The oil-water and gas-oil capillary pressures, 'P_{cow}' and 'P_{cgo}', are given in Eqs. 5 and 6, respectively;

$$P_{cow} = P_{cow}^* + \Delta\rho_{ow} g(H+L) \tag{5}$$

$$P_{cgo} = P_{cgo}^* + \Delta\rho_{go} gH \tag{6}$$

where, '$\Delta\rho_{ow}$' and '$\Delta\rho_{go}$', are the oil-water and gas-oil differential densities respectively, P^*_{cow}, is the local oil-water capillary pressure at point 1, and 'P^*_{cgo}' is the local gas-oil capillary pressure at point 2. Neglecting the fluid contact curvature along the capillary corner, the oil-water and gas-oil contact radii can be calculated using Eqs. 7 and 8.

$$r_{ow} = \frac{\sigma_{ow}\cos\theta_{ow}}{P_{cow}^* + \Delta\rho_{ow} g(H+L)} \tag{7}$$

$$r_{og} = \frac{\sigma_{go}\cos\theta_{go}}{P_{cgo}^* + \Delta\rho_{go} gH} \tag{8}$$

It can be seen in Fig. 1a and Fig. 1b, the fluids' contact radii become smaller by moving up along the tube corners. In a water-wet capillary tube with sharp corners, depending on fluids' interfacial tensions and differential densities, two different configurations of oil film can be formed. In the first configuration, the oil-water contact radius shrinks toward corner of the tube with a smaller rate rather than the gas-oil contact radius. Since at gas-oil contact front ($H=0$) the gas-oil contact radius is larger than oil-water contact radius, there is an elevation above the gas-oil contact front at which the contact radii of both gas-

oil and oil-water pairs are equal (point 3 in Fig. 1a). The second configuration of the oil film is formed when the gas-oil contact radius along the tube corner remains larger than the oil-water contact radius, as depicted schematically in Fig. 1b. Such a condition is likely to occur when the differential density of the gas-oil pair is lower than the oil-water pair. The elevation of the oil film in this configuration is no longer limited by the oil-water contact radius, and the oil film exists at all heights above the water surface in the tube corners.

The maximum equilibrium oil film height above the gas-oil contact front (H_{max}) for the first configuration is shown by Eq. 9, which is derived by equating the oil-water and gas-oil contact radii.

$$H_{\max} = \frac{(\sigma_{og}\cos\theta_{go}\Delta\rho_{ow}.L)}{(\sigma_{ow}\cos\theta_{ow}\Delta\rho_{go})-(\sigma_{go}\cos\theta_{go}\Delta\rho_{ow})} \quad (9)$$

DISCUSSION

We can see from Eq. 9 that the size of tube has no effect on the maximum oil film elevation. Fig. 2 shows the variation of 'H_{max}' vs. gas-oil interfacial tension and the gas density when the oil-water interfacial tension (σ_{ow}) is 0.03 N.m^{-1}, oil density (ρ_o), is 700 kg.m^{-3}, water density (ρ_w) is 1000 kg.m^{-3}, length of oil bank (L) of 0.05 m, and all contact angles are zero degrees. It can be seen that the

Fig. 3 shows the maximum oil film elevation (H_{max}) vs. the oil bank length when the gas-oil interfacial tension is fixed at 30 mN.m^{-1}, gas density at 300 kg.m^{-3} and other parameters at their previous fixed levels. A greater oil film elevation can be expected for the first configuration when the length of the oil bank is longer. Fig. 4 shows the gas-oil capillary pressure at the top of the oil film in a square tube with the size of 100×100 µm, versus the gas density (ρ_g) and gas-oil interfacial tension (σ_{go}), and keeping all other parameters fixed at their levels, previous indicated in Fig. 3. It is shown that the gas-oil capillary pressure is higher when the gas-oil interfacial tension and gas density are increased. Fig. 3 and 4 also illustrate that the effect of gas density on the oil film elevation and gas-oil capillary pressure is more significant when the gas-oil interfacial tension is higher.

In porous media, a thin oil film can be formed in the crevices and corners between the rock grain and on their surface roughness. During a vertical gas injection, thick oil films are the major paths for both hydraulic communication and recovery of trapped immobile oil. Increasing the gas-oil capillary pressure provides a potential for the gas to enter the small size pore-throats and deplete any residual oil through these paths. Consequently, the overall oil recovery can be higher. Since the fluids' contacts are not under equilibrium conditions during vertical gas injection, the oil recovery from small pores should be studied in a dynamic state of capillary pressure. The dynamic state of the oil film during vertical gas injection is different from the equilibrium state. The non-equilibrium state of

oil film in gravity drainage is currently under experimental investigation at Memorial University of Newfoundland.

CONCLUSIONS

The oil film elevation above the gas-oil contact front in a water-wet, non-circular capillary tube is a function of the oil-water and gas-oil interfacial tensions and their differential densities. Additionally, the oil film elevation can be limited due to the presence of wetting phase in the sharp corners of the capillary tube. It is expected that a longer oil film elevation results in higher oil recovery, since, it yields a higher gas-oil capillary pressure, which allows the gas to enter the small pore-throats that are not swept by primary gas injection. The analysis of the static oil film characteristics implies that the injection of a gas with a higher density and having a greater gas-oil capillary pressure can potentially improve the oil recovery factor in gas-assisted gravity drainage EOR methods.

ACKNOWLEDGEMENTS

The authors would like to thank Petroleum Research Newfoundland and Labrador (PRNL), the Research Development Corporation of Newfoundland (RDC), Hibernia Management and Development Company (HMDC), and the Natural Sciences and Engineering Research Council of Canada (NSERC) for their technical and financial support in this research.

REFERENCES

1. Øren, P.E., & Pinczewski, W.V. 1995. Fluid distribution and pore-scale displacement mechanisms in drainage dominated three-phase flow. *Transport in Porous Media, 20(1-2), 105-133.*
2. Chatzis, I., Kantzas, A., & Dullien, F.A.L. 1988. On the investigation of gravity-assisted inert gas injection using micro models, long Berea sandstone cores, and computer-assisted tomography. *In SPE 18284 Presented at the 1988 SPE Annual Technical Conference and Exhibition, Houston, TX.*
3. Vizika, O., & Lombard, J.M. 1996. Wettability and spreading: two key parameters in oil recovery with three-phase gravity drainage. *SPE Reservoir Engineering, 11(1).*
4. Oren, P. E., & Pinczewski, W.V. 1994. Effect of wettability and spreading on recovery of waterflood residual oil by immiscible gasflooding. *SPE Formation Evaluation, 9, 149-149.*
5. Dong, M., Dullien, F.A.L., & Chatzis, I. 1995. Imbibition of oil in film form over water present in edges of capillaries with an angular cross section. *Journal of Colloid and Interface science, 172(1), 21-36.*
6. Keller, A.A., Blunt, M.J., & Roberts, A.P.V. (1997). Micromodel observation of the role of oil layers in three-phase flow. *Transport in Porous Media, 26(3), 277-297.*
7. Dullien, F.A.L., Zarcone, C., Macdonald, I.F., Collins, A., & Bouchard, R.D. 1989. The effects of surface roughness on the capillary pressure curves and the heights of capillary rise in glass bead packs. *Journal of Colloid and Interface Science, 127(2), 362-372.*

8. Blunt, M., Zhou, D., & Fenwick, D. 1995. Three-phase flow and gravity drainage in porous media. *Transport in Porous Media, 20(1-2), 77-103.*
9. Dullien, F.A.L. 1991. *Porous media: fluid transport and pore structure*. Academic press, 2nd edition.

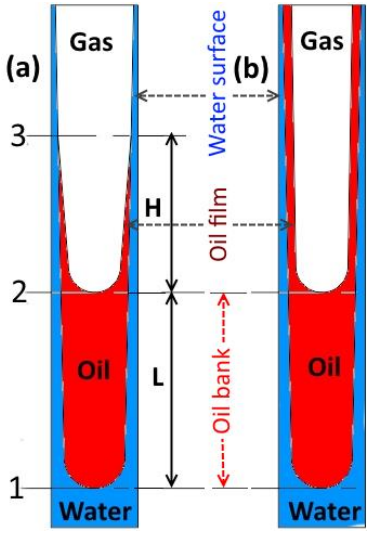

Fig. 1: Water, oil and gas in a non-circular tube a) oil film elevation limited by water film, and b) oil film elevated along the tube corner

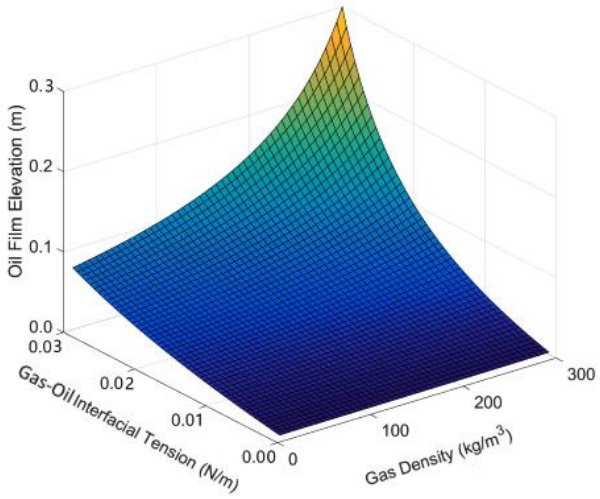

Fig. 2: Oil film elevation above the gas-oil contact front vs. gas density and oil-gas interfacial tension

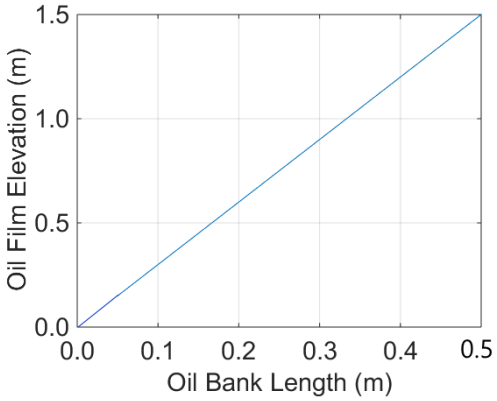

Fig. 3: Oil film elevation vs. oil bank length

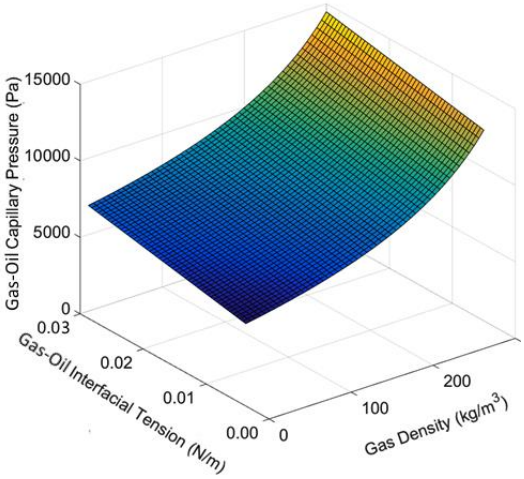

Fig. 4: Gas-oil capillary pressure at the top of the oil film vs. gas density and oil-gas interfacial tension

GAS MIGRATION THROUGH SELF-SEALED OR INTACT CLAYSTONE

Yang Song, C. A. Davy, F. Skoczylas
Ecole Centrale de Lille, LML UMR CNRS 8107, CS20048,
59651 Villeneuve d'Ascq Cedex, France

This paper was prepared for presentation at the International Symposium of the Society of Core Analysts held in St. John's Newfoundland and Labrador, Canada, 16-21 August, 2015

ABSTRACT

This contribution investigates gas migration through fully water-saturated Callovo-Oxfordian (COx) claystone.

Our originality is to evidence the nature of progressive passage through initially macro-cracked and water-saturated (i.e. self-sealed) claystone, or through intact (undisturbed) matter. The sample is subjected to hydrostatic pressure, identical to the mean *in situ* principal stress. We use a mix of gases detected on the sample downstream side by a mass spectrometer accurate to 2-5 ppm (i.e. 2-5 10^{-6} particles). We show that gas breakthrough occurs first, by discontinuous capillary passage, i.e. *snap off*, followed by continuous breakthrough (i.e. permeation), whether the upstream pressure value is increased or kept constant. *Snap off* is characterized by small amounts of gas detected at the outlet at random frequency and amplitude, until all gases in the mix are detected continuously and simultaneously.

At continuous breakthrough, gas permeability is on the order of 10^{-21} m^2 (1nD). For self-sealed claystone, gas breakthrough pressure (GBP) varies hugely in the low range 1.45-3 MPa. For undisturbed claystone, GBP ranges between 4.38 MPa (20 mm thickness) to 5.43 MPa (30 mm thickness), in good accordance with former research. It is concluded that *self-sealed* COx claystone has significantly weaker gas breakthrough properties than undisturbed matter.

INTRODUCTION

This contribution was originally devised for engineering applications related to deep underground nuclear waste storage. In France, the latter is planned at 420-550 m depth, and represents a network of horizontally-drilled galleries of several kms long, starting from a main vertical shaft and an auxiliary vertical shaft [1]. Storage tunnels are made within a claystone of Callovo-Oxfordian age (the so-called COx claystone), which has an undisturbed water permeability of the order of 10^{-21} to 10^{-23} m^2 (0.01 to 1 nanoDarcy). In the Excavated Damaged Zone (EDZ) around the tunnels, macro-fracturing is observed. However, underground water seepage is shown to allow *self-sealing* [2], whereby water permeability recovers values on the order of 10^{-21} to 10^{-23} m^2, similar to undisturbed claystone.

Further, after drilling, filling and closure of storage tunnels, hydrogen gas may develop and progressively pressurize inside the repository, due to varied physico-chemical phenomena (anaerobic corrosion of carbon steel canisters, water radiolysis, etc.).

The industrial issue is to ensure the conditions for proper gas immobilization within the underground site, both in the self-sealed zone and in the undisturbed claystone, away from the repository: this is investigated here by identifying the Gas Breakthrough Pressure (GBP) across fully water-saturated claystone. This study can be extrapolated to the migration of a non wetting fluid (e.g. gas here, or oil in the petroleum engineering context) through a wetting fluid filling the pores (water here, and water too in the petroleum engineering context).

Extensive research has been performed on gas migration (or breakthrough) through COx claystone with the step-by-step method [3, 4, 5] or with quicker, transient techniques [6,7].

With the step-by-step method, progressive gas passage through water-saturated matter is identified, so that both discontinuous and continuous migrations can be observed [8]. Through the test series presented here, our aim is to assess:

1. the difference between discontinuous and continuous gas passage: does the former occur consistently before the latter?
2. is discontinuous passage mainly a feature of our experimental set-up, so that argon gas detected in the downstream chamber is due to argon accumulation by diffusion phenomena, or is discontinuous passage a capillary phenomenon, the so-called *snap off* (or discontinuous capillary digitation)? For this part of our experimental campaign, gas detection on the downstream side uses a mass spectrometer accurate to 2-5 ppm, and gas is either 100% argon or a mix of 50 mol% argon/50mol% helium.
3. is discontinuous or continuous GBP repeatable, *i.e.* after a first breakthrough at a given gas pressure, whenever claystone is re-saturated with water until being self-sealed, does it have the same GBP again?

MATERIALS AND METHODS

Table 1: Main features (sample size, water permeability at saturation) and GBP test results for COx claystone sample series S3.

Sample n.	Core n. EST	direction	H (mm)	Initial state	Pc (MPa)	Water saturation phase (days)	K_{water} at saturation (m^2)	Migration test & GBP (MPa)
n.1	34386	horizontal	10,9	macro-cracked	12	16	$9.3x10^{-21}$	1.64
					12	63	$9.3x10^{-21}$	1.45
n.2	34386	horizontal	10,76	macro-cracked	6	68	7,1 to $7,3x10^{-21}$	2.25
n.3 undisturbed	44331	vertical	19,74	turned	6	35	$3x10^{-20}$	4.5-5.7
					6	49	$2,6x10^{-20}$	4.38
n.4 undisturbed	44140	vertical	30	turned	6	134	6,9 to $7,4x10^{-21}$	5.2-5.3
n.5	44331	vertical	9,5	turned	6	30	$1,9x10^{-20}$	2.2
					6	13	$1,6x10^{-20}$	3.0
					6	96	$1,8x10^{-20}$	2.96
					6	50	$1,7x10^{-20}$	3.6

Sample Origin and Preparation

Each of the five samples tested is cored and macro-cracked by Brasilian test (or splitting test of a circular cylindrical sample), or machined by turning to 37 mm diameter and varying height, from 9.5 to 30 mm, from horizontal core EST34386 or vertical cores EST44331 and EST44140, see Table 1. Turning allows to minimize sample damage and provides us with so-called undisturbed claystone, whereas macro-cracking provides samples similar to damaged claystone from the EDZ.

Water Saturation. Prior to GBP, full water saturation is achieved as follows. The sample is placed in a hydrostatic cell, and subjected to a confining pressure of 12 MPa (on the order of *in situ* principal stress levels). Water is injected on the upstream side at 4 MPa pressure, which is the lithostatic water pressure, until it is fully saturated. Full saturation state is achieved when water permeability K_{water} values fall below 10^{-20} -10^{-21} m^2, see Table 1. Owing to the water flow duration and to the stability in water permeability values, it is thought that either all potentially trapped gas within the pore network has evacuated, or has been dissolved in flowing water.

Single-gas GBP Experiment

Following water saturation, upstream pipes are emptied from water, while the sample is kept at a constant confinement Pc=6 or 12 MPa, in order to avoid its premature failure. The downstream chamber (of a volume of 2 cl) is closed by a dedicated valve, and its pressure $P_{downstream}$ is recorded with a pressure transducer accurate to +/-100Pa. On the upstream side, the argon gas pressure $P_{upstream}$ is increased very slowly, at a rate of 0.5-1 MPa per day (unless otherwise stated in the following), and up to 14 days for a few tests. Upstream gas pressure is given by a pressure transducer accurate to 1 kPa. Gas detection on the downstream side is performed using both the downstream pressure transducer and

a dedicated argon gas detector accurate to +/-10^{-7} l/sec. At constant $P_{upstream}$ value, gas detection is performed every 24 to 72 h as follows: the downstream chamber valve is opened and gas is detected (or not) by placing the detector nozzle at ca. 5 mm from the valve opening. Gas passage is considered discontinuous whenever gas presence is detected for less than 10-60 sec; gas passage is considered continuous when gas outflow is recorded for more than 10 sec, three times every five minutes. This method means that downstream gas pressure goes back to zero after each downstream valve opening. Also, it does not ensure whether gas actually passes through the porous medium by dissolution and diffusion in pore water, or by capillarity. Therefore, both mechanisms are accounted for in the following.

Two-gas GBP Experiment

This test aims at determining what phenomenon is at the origin of gas breakthrough, *i.e.* either percolation or dissolution and diffusion. For this purpose, a mix of gases is injected through water-saturated claystone: it is chosen to ensure a significant difference between both their solubility in water and their diffusivity, *i.e.* a significant difference in the product of their solubility and diffusivity. If the gas with the greatest solubility and diffusion migrates first, these phenomena will be privileged to explain breakthrough.

At 15 °C, the solubility is 3.00×10^{-10} mol/Pa for argon and 7.20×10^{-11} mol/Pa for helium; the diffusion coefficient is 2.00×10^{-9} m^2/sec for argon and 6.30×10^{-9} m^2/sec for helium [9]. The product of solubility and diffusion coefficient at 15 °C is of 5.92×10^{-19} mol/N.sec for argon and 4.48×10^{-19} mol/N.sec for helium: helium has lower solubility and diffusivity by a coefficient of 1.32, when compared to argon. Although this difference may not appear large enough, these gases have been chosen in a first approach given their excellent availability and harmlessness.

After imposing the gas mix on the sample upstream side at given pressure, the presence of each gas is detected individually on the downstream sample side by a mass spectrometer accurate to 2-5 ppm.

RESULTS AND DISCUSSION

In the following, all pressure values are expressed in MPa abs.

Evidence of Discontinuous and Continuous Gas Passage

When the GBP test starts, whatever the initial $P_{upstream}$ value chosen (as low as 0.2 MPa), $P_{downstream}$ increases. This is attributed to water expelled on the downstream side, pushed by gas on the upstream side. Therefore, potentially, gas entry may have begun, yet no device is available in this experiment to check it with adequate accuracy. The argon detector does not record any gas passage after 24 h at $P_{upstream}$ = 2.02 MPa, whereas it detects a discontinuous argon passage after 24 h at $P_{upstream}$ =2.25 MPa. Simultaneously, at each $P_{upstream}$ value, downstream pressure data display a linear increase with time (Fig. 1a), until going back to zero as soon as the downstream valve is opened. Therefore, the rate of increase of downstream pressure is plotted vs. imposed upstream gas pressure (Fig. 1b). An inflexion point is observed in these data, at $P_{upstream}$=2.22 MPa. This is attributed to the start of an additional phenomenon, which induces a greater rate of increase in

downstream pressure. As it occurs at a very close $P_{upstream}$ value as that when the argon detector evidences gas passage, it is attributed to the same phenomenon. This means that we have two independent means of detecting gas passage: the argon gas detector, and the rate of increase in downstream pressure, both occurring due to gas passage from the upstream side (where gas pressure is imposed) and downstream side (where all measurements are made).

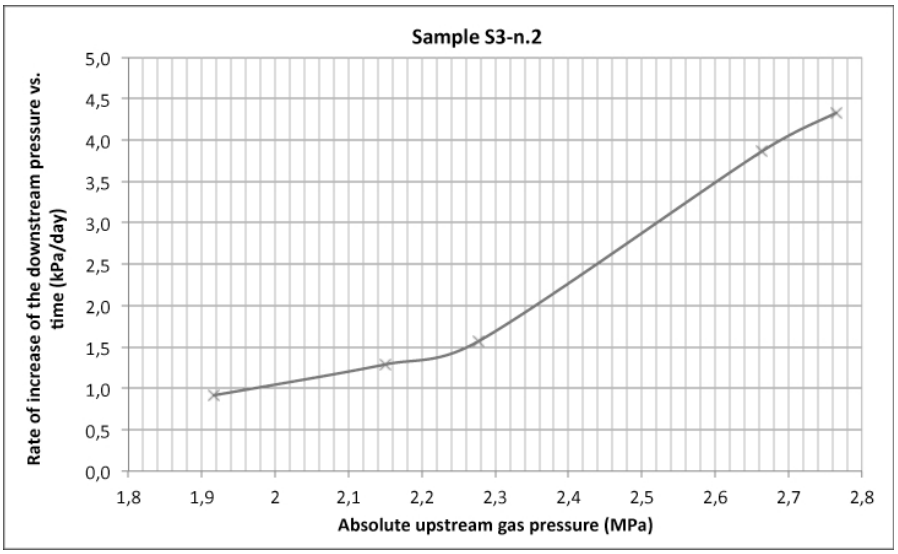

Figure 1 : Sample S3-n.2: rate of increase of downstream pressure (in kPa/day) vs. imposed upstream gas pressure (MPa).

After discontinuous passage has been observed, $P_{upstream}$ is increased regularly until continuous breakthrough (Fig. 2). Continuous breakthrough is measured by (1) the argon detector, (2) the rate of increase of $P_{downstream}$ and also (3) when the rate of decrease in upstream pressure is greater than that due to thermal variations. This second criterion allows for measuring gas permeability K_{gas}, as described in [Davy *et al.* 2007] (with an assumption of quasi-static gas flow). As for discontinuous passage, an inflexion point is observed in the rate of increase in $P_{downstream}$ *vs.* $P_{upstream}$, which occurs at a slightly greater $P_{upstream}$,=3.59 MPa than continuous passage measured by the argon detector (at $P_{upstream}$=3.35 MPa). The upstream pressure transducer allows for gas permeability measurement at an even greater $P_{upstream}$,=4.24 MPa than with the two other devices: K_{gas} is of $1.6x10^{-21}$ m^2 at $P_{upstream}$,=4.24 MPa. Whenever $P_{upstream}$, is increased further, K_{gas} increases monotonously [4].

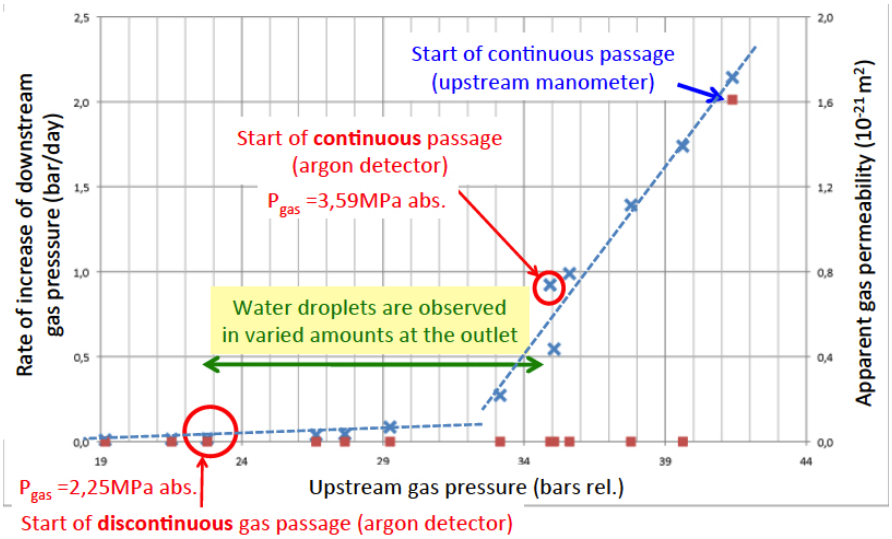

Figure 2. Sample S3-n.2: Evolution of downstream pressure increase rate (red markers) and gas permeability (blue markers) measured on upstream side vs. applied upstream gas pressure

Repeatability of GBP

Samples S3-n.1, S3-n.3 and S3-n.5 have been subjected to several water-saturation phases followed by a GBP test (Table 1). It is observed that GBP values are not repeatable, with greater or lower values after a first GBP test. For instance, for sample S3-n.1, GBP is of 1.6 MPa after a first water saturation phase, whereas it is at a lower 1.45 MPa value after a second water saturation phase. For sample S3-n.5, GBP is of 2.2 MPa after the first water saturation phase, whereas it is at a greater 2.9-3MPa value after the second and third water saturation phases. This is attributed to different gas pathways from one GBP test to the other, in relation with statistically-varying capillary digitation.

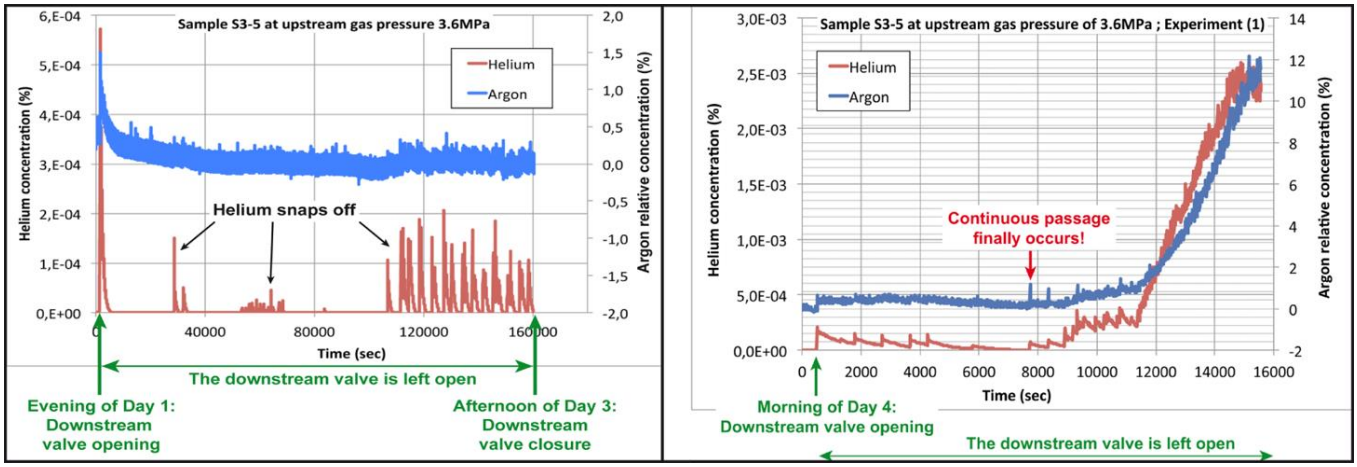

Figure 3 : Sample S3-n.5: (left): Helium and argon concentrations (in %) *vs.* after 24 h at $P_{upstream}$=3.7 MPa and downstream valve opening (at 10 sec); (right): Argon and helium concentrations (in %) *vs.* time, when the downstream valve has been kept closed for 24 h at a value of 3.555 MPa down to 3.504 MPa. The downstream valve is open at time t=500 sec.

Effect of Sample Thickness and Damage State Upon GBP

For test series S3 (Table 1), GBP is below 3 MPa for 9.5-10.9 mm thick samples, below 5.8 MPa for 19.7 mm thick sample, and below 5.4 MPa for 30 mm thickness. Let us compare these results with existing data. GBP results on so-called undisturbed COx claystone have been obtained by BGS (UK) and Laego (France) on 55-85 mm long samples machined by turning, at values ranging between 5.5 and 6 MPa [4]. For 18 mm long COx samples, studies at RWTH (Germany) measure GBP values at 4.8-5.3 MPa, which are also attributed to undisturbed matter [4]. Results by [10] on macro-cracked claystone range between 0.8-2 MPa for 75-103 mm thickness. This means that all the values of our test series S3, and those of test series S1 and S2 (given in [5]) correspond to initially macro-cracked claystone. Higher GBP values observed for thicker samples are attributed to too quick an increase in $P_{upstream}$, which does not allow for sufficient time to record gas breakthrough, rather than to actual unability for gas to breakthrough.

Evidence of the Nature of Discontinuous Gas Passage

After a first GBP test, sample S3-n.5 has been re-saturated with water until $16x10^{-21}$ m^2 water permeability, and further injected with the mix of gases (argon+helium). At $P_{upstream}$=2.96 MPa, the presence of helium is recorded as a peak concentration value upon downstream valve opening, which decreases down to zero after several minutes: it is a first evidence of discontinuous gas passage. Argon concentration is too noisy to show any significant concentration difference upon valve opening. In order to allow for shorter experimental duration, $P_{upstream}$ is then increased slightly, up to 3.7 MPa and kept at that value for 24 h. Fig. 3a shows argon and helium concentrations *vs.* time after valve opening (at 10 sec): a peak in concentration is observed for both gases upon valve opening, with a regular decrease down to zero for helium after 5500 sec (i.e. 1 h 31 min), and with a highly fluctuating decrease for argon, down to ca. 2.8%. After 8 h at $P_{upstream}$ =3.7 MPa with the downstream valve kept open, the mass spectrometer records a peak in helium concentration, which decreases down to zero. This peak in helium concentration is followed by other evenly distributed peaks of varying amplitude, which frequency increases with time. These peaks are attributed to progressive gas passage by a discontinuous phenomenon, which cannot be attributed to progressive dissolution and diffusion through the claystone pore network: no physical reason justifies discontinuity due to dissolution and diffusion (continuous phenomena). Rather, it is the demonstration of capillary *snap off*, *i.e.* of gas passage by a discontinuous progression through pores of sufficiently varying size (gas is regularly blocked in its progression through the pore network by smaller pore throats, which requires an increase in gas pressure to be overcome [11]. Further to this, $P_{upstream}$ is kept at its value of 3.5 MPa +/- 0.05 (no increase back to 3.7 MPa is performed here), and the downstream valve is closed for 24 h. Upon re-opening (Fig. 3b), helium passes again in a discontinuous manner, with several peaks in concentration, which decrease progressively with time, yet not back to zero due to a higher frequency of occurrence. After a total of 64 h 19 min at $P_{upstream}$ =3.7 -> 3.5 MPa, helium finally passes continuously through to the downstream sample side, together with argon (Fig. 3a) again. It is a continuous capillary gas breakthrough.

CONCLUSION

This contribution has shown that gas migration through initially water-saturated and macro-cracked COx claystone occurs consistently by discontinuous capillary *snap off*, followed by continuous passage (*i.e.* percolation) (answer to the first question in the introduction). Discontinuous passage is not related to dissolution and diffusion of gas through to the downstream chamber, which is opened every 24 h (answer to question 2) in the introduction). GBP values are significantly below those of undisturbed claystone, which is evidence of its inability to self-heal, despite excellent self-sealing ability (answer to 3rd question in the introduction).

ACKNOWLEDGEMENTS

The authors are grateful to Andra for financial support of this research.

REFERENCES

1. R. De La Vaissière, G. Armand, J. Talandier, Journal of Hydrology, 521 (2015), 141-156.
2. C. A. Davy, F. Skoczylas, J.-D. Barnichon, P. Lebon, *Physics and Chemistry of the Earth*, pp. 667-680 Vol. 32, Issue 8-14, 2007.
3. S. T. Horseman, J. F. Harrington, P. Sellin, Engineering Geology, 54 (1999), 139-149.
4. G. Duveau, S. M'Jahad, C. A. Davy, F. Skoczylas, J.-F. Shao, J. Talandier, S. Granet, Proceedings of the international conference 45th US Rock Mechanics Geomechanics Symposium ARMA San Francisco, USA, 26-29th, June 2011.
5. C. A. Davy, S. M'Jahad, F. Skoczylas, J. Talandier, M. Ghayaza, *5th International Meeting on Clays in Natural and Engineered Barriers for Radioactive Waste Management*, October 22-25, 2012.
6. P. Egermann, J.-M. Lombard and P. Bretonnier. paper SCA A46, *2006 SCA International Symposium, Trondheim*, Sept. 18-22, 2006.
7. B. M. Krooss, A. Amann-Hildenbrand and A. Ghanizadeh. *Marine and Petroleum Geology*, 31/1 (2012): 90-99.
8. Marschall, P., Horseman, S., Gimmi, T., 2005. *Oil Gas Sci. Technol*. 60 (1), 121-139.
9. P. Marschall and I. Lunati editors, *Technical Report 03-11*, Grimsel Test Site Investigation Phase V, GAM, December 2006.
10. C.-L. Zhang, T. Rothfuchs, *Physics and Chemistry of the Earth*, 33 (2008) S363-S373.
11. W. R. Rossen. *Colloids and Surfaces A*, 166 (2000), 101-107.

ROCK PROPERTY CHANGES FOR CARBONATE RESERVOIR DURING CO_2 INJECTION

M. Shimokawara, S. Takahashi, F. Kono, A. Kato, K. Tsushima
JOGMEC

This paper was prepared for presentation at the International Symposium of the Society of Core Analysts held in Newfoundland and Labrador, Canada, 16-20 August, 2015

ABSTRACT

Carbonate minerals can be dissolved when carbon dioxide CO_2, in presence of aqueous solution, is injected into carbonate rocks. It is therefore known that porosity increases by dissolution as well as porosity decreases by compaction. Porosity changes by dissolution and compaction are one of the most important factors in order to understand fluid flow characteristics and monitor CO2 invasions. Especially, we need to consider that the change of rock properties is affected during CO2 injection into the carbonate reservoirs, when we evaluate seismic data. However it has not been clarified quantitatively.

In this study, we conducted core flooding tests with carbonate rock samples under the cyclic load test to clarify the effects of porosity changes. Carbonate rock samples were collected from a Middle East reservoir. In the core flooding test, CO_2 saturated water was injected into the rock samples for 200 Pore Volume Injected (PVI). Porosity, permeability, and elastic wave velocities were measured every 50 PVI. Porosity was measured using conventional Helium porosimetry and NMR methods. The amount of the dissolved carbonate minerals that is related to porosity increase was evaluated based on the amount of the dissolved cations in the CO_2 saturated water. In addition, the change of carbonate surfaces was also observed with SEM during CO_2 saturated water flooding.

Results show that carbonate dissolution occurred at the early stage of CO_2 saturated water flooding. Porosity decreased under compaction when rock frame was weakened by dissolution. The elastic wave velocities reduce with or without compaction effects when carbonate minerals are dissolved by CO_2 saturated water flooding.

INTRODUCTION

In the field operation of CO_2-EOR as well as carbon capture and storage (CCS), it is important to accurately understand the interaction between rock and fluids in addition to the behavior of the injected CO_2. In crosshole seismic data acquired in the field, cases of significantly decrease of seismic velocity in rocks has been reported after CO_2 was injected [4]. These velocity changes were substantially higher than those due to fluid substitution, as predicted by the Gassmann theory; consequently, it has been argued that these changes were caused by dissolution of carbonate rock minerals.

It is also known that carbonate minerals are dissolved due to CO_2. The effects of mineral dissolution on the rock properties have been investigated by laboratory measurements, and the results have been reported. Vanorio et al. [3] and Kono et al. [2] conducted experiments on carbonate rock samples that were injected with CO_2. Changes in physical properties such as acoustic velocity and porosity were assessed and changes in rock microstructures were observed with SEM images. The results showed that micritic carbonate minerals were dissolved with aqueous solutions of CO_2, leading to increased porosity and decreased acoustic velocity. Grombacher et al. [1] also conducted integrated laboratory measurements including NMR, SEM and CT-scan for carbonate rock samples injected with CO_2. They reported changes in acoustic velocity, permeability, and microstructures.

This paper presents the results of core flooding tests of carbonate rock samples under the cyclic load test to understand the changes of the rock properties and wave velocities during CO_2 injection.

PROCEDURE

1.5-inch-diameter plug samples were used for this study. Samples were carbonate rocks collected from a reservoir in a Middle Eastern oil field. Properties of each plug sample are shown in Table 1.

The laboratory measurement workflow is shown in Figure 1. CO_2 saturated water was prepared by bubbling CO_2 in water. The pH (potential hydrogen) of the distilled water decreased from 6.5 to 3.9. The rock samples were placed inside a pressure vessel to be arranged in series, and the CO_2 saturated water was allowed to be flooded through them. CO_2 saturated water was injected at the rate of 0.1 ml/min. For each 50 PVI flooded, the samples were removed from the pressure vessel. NMR analysis was conducted for the samples fully-saturated with CO_2 saturated water. After drying and basic measurements, elastic wave velocity measurement was conducted. Then, the samples were returned to the pressure vessel, and the experiment procedure was repeated up to 100 PVI. In addition to NMR and elastic wave velocity measurements, observations of carbonate mineral dissolution were performed with a scanning electron microscope (SEM: QUANTA600), and analyses of the amount of dissolved cations in the effluent were also conducted. The data results were used for evaluating effects of dissolution due to CO_2 saturated water on rock properties.

RESULTS

Figure 2 shows the change of the ratio of the pore volume to the initial pore volume (PV/PV0) during the CO_2 saturated water flooding. The porosity of Core_B without the compaction effects increased by 3.6% at the first 50 PVI, and the porosity increased by 6.0% from 50 to 100 PVIs. On the other hand, the porosity of Core_A with the compaction effects decreased by 4.3% at the first 50 PVI, and then the porosity was kept. At the end of 100 PVI, the difference of porosity between Core_A and Core_B was about 8%.

Figures 3 and 4 show the change of normalized elastic wave velocities when CO_2 saturated water was injected. The normalized P-wave velocities decreased by 10% compared to the initial values in the both samples at the first 50 PVI and were constant from 50 to 100 PVIs. The normalized S-wave velocities of Core_B also decreased by 10% as the same as the normalized P-wave velocities whereas the normalized S-wave velocities of Core_A decreased by 5% at 100 PVI of the CO_2 saturated water. Dissolution of carbonate minerals was measured by produced water analysis. The amount of dissolution was confirmed to be substantially equal to the change of porosity.

DISCUSSION

In the case of Core_B without the compaction effects, the change of porosity at the first 50 PVI was greater than after 50 PVI. So the dissolution of the carbonate minerals by CO_2 saturated water flooding occurred at the early stage of flooding. On the other hand, Core_A with the compaction effects showed decrease in porosity. This suggested that the decrease was caused by compaction load because rock frame was weakened by dissolution.

The elastic velocities of Core_B without the compaction effects decreased when the bulk density decreased with porosity increase. Core_A with the compaction effects also showed elastic velocities decrease. This indicates that the elastic wave velocities reduce with or without compaction effects when carbonate minerals were dissolved by CO_2 saturated water flooding.

CONCLUSION

We conducted CO_2 saturated water flooding test for carbonate and evaluated the change of rock properties. Results showed that carbonate dissolution occurred at the early stage of CO_2 saturated water flooding. It is suggested that the porosity decreased under compaction because rock frame was weakened by dissolution. In addition, results showed that the elastic wave velocities reduce with or without compaction effects when carbonate minerals are dissolved by CO_2 saturated water flooding.

ACKNOWLEDGEMENTS

The authors were favored to have the assistance of Yasuyuki Akita, Emiko Shinbo and Akira Hanyu who contributed their experimental skill, sustained effort, and grasp of objectives to the accomplishment of the experimental program.

REFERENCES

1. Grombacher, D., T. Vanorio, and Y. Ebert, 2012, Time-lapse acoustic, transport, and NMR measurements to characterize microstructural changes of carbonate rocks during injection of CO_2-rich water, *Geophysics*, **77**, no. 3, WA169-WA179.
2. F. Kono et al., 2014, Laboratory Measurements on Changes in Carbonate Rock Properties due to CO_2-saturated Water Injection, SPE172013.
3. Vanorio, T., A. Nur, and Y. Ebert, 2011, Rock physics analysis and time-lapse rock imaging of geochemical effects due to the injection of CO_2 into reservoir rocks, *Geophysics*, **76**, no. 5, O23–O33.
4. Wang, Z., M. Cates, and R. Langan, 1998, Seismic monitoring of a CO_2 flood in a carbonate reservoir: A rock physics study, *Geophysics*, **63**, 1604–1617.

Table1 The properties of rock core samples.

Sample ID	Diameter	Length	Dry weight	Pore volume	Grain density	Porosity	Kair	With compaction
	cm	cm	g	ml	g/cm3	fraction	mD	
Core_A	3.804	4.076	89.92	12.56	2.66	0.271	20.9	*yes*
Core_B	3.790	6.154	147.20	15.34	2.72	0.221	28.4	*none*

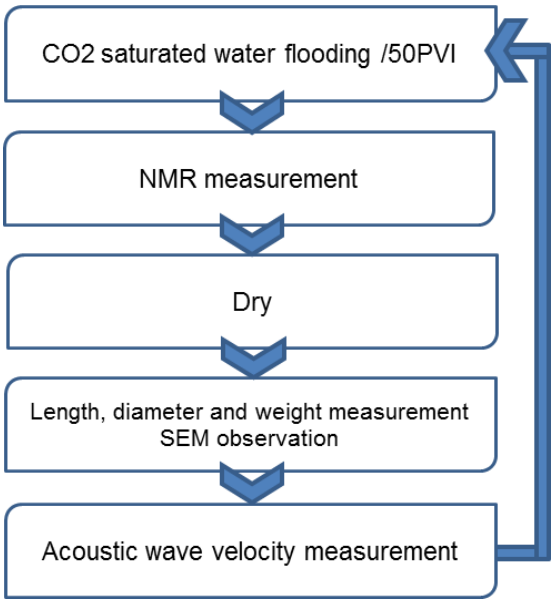

Figure.1 Laboratory measurement flow.

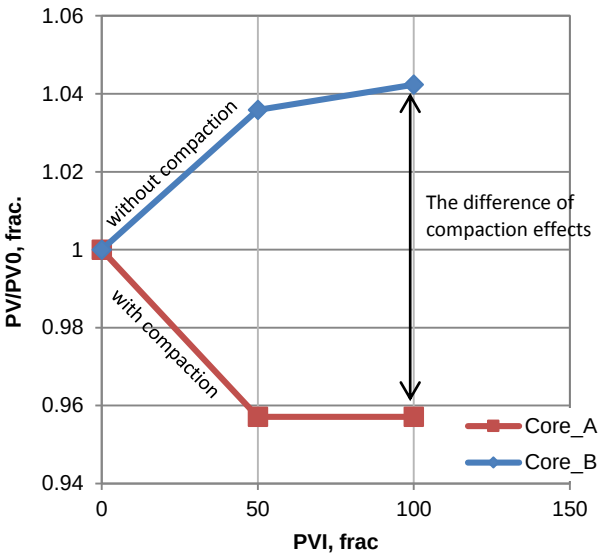

Figure.2 The comparison of PV/PV0 between with compaction effects.

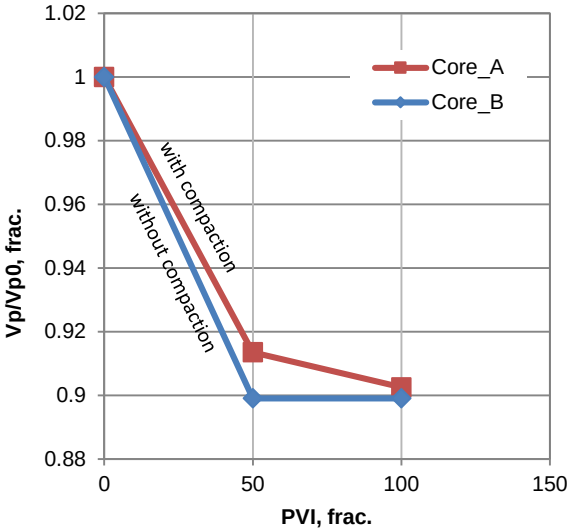

Figure.3 Normalized P-wave velocities.

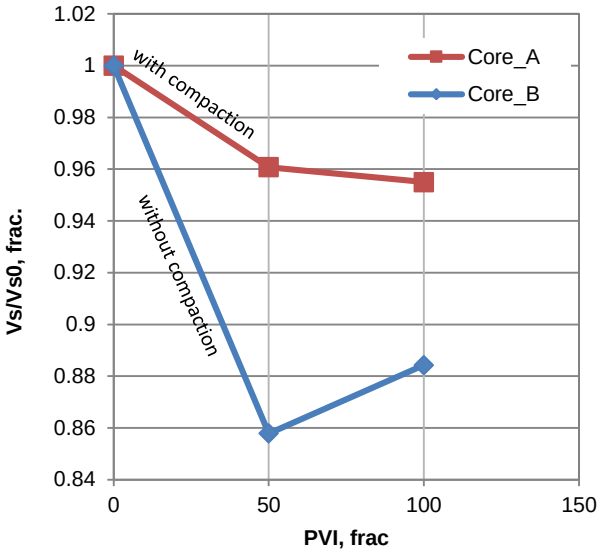

Figure.4 Normalized V-wave velocities.

TWO SCALE PORE ANALYSIS APPLIED TO LOW PERMEABILITY SANDSTONE

C. A. Davy[1], P.M. Adler[2], Yang Song[1], L. Jeannin [3], D. Troadec [4], G. Hauss [1], Thang Nguyen Kim[2]
[1] LML UMR CNRS 8107/Ecole Centrale de Lille, CS20048,
59651 Villeneuve d'Ascq Cedex, France
[2] Metis/UPMC, Paris, France
[3] GDFSUEZ E&P International SA, 1 place Samuel de Champlain,
92930 Paris La Défense cedex - France
[4] IEMN, UMR CNRS 8520, BP60069, 59652 Villeneuve d'Ascq Cedex, France

This paper was prepared for presentation at the International Symposium of the Society of Core Analysts held in St. John's Newfoundland and Labrador, Canada, 16-21 August, 2015

ABSTRACT

The purpose of this research is 1) to predict fluid transport (permeability) from pore structure measurements of a tight gas sandstone and 2) to compare predictions to actual permeability measurements on centimetric plugs. This contributes to explain what is (or are) the relevant pore scale(s) for fluid transport, and should help improve gas production. Tight sandstones are low porosity media, with small fluid transport ability. The sample T-2390-82 used in this contribution has a water porosity of 2.8-3.2%, and a dry gas permeability of the order of 10^{-17} m^2 (10 microDarcy).

The pore size distribution of T-2390-82 is measured by Mercury Intrusion Porosimetry (M.I.P.) with a peak at 350 nm. This justifies the use of Focused Ion Beam/Scanning Electron Microscope (FIB/SEM) to describe the 3D pore structure. FIB/SEM provides the 3D geometry of a single joint (between quartz grains). However, 2D SEM shows the presence of numerous joints of both sub-micrometric and micrometric sizes; 2D SEM is used to describe the joint network topology (density, joint length, etc.). X-ray micro-tomography (micro-CT) is used in an attempt to describe a representative pore network in 3D. If a denotes the voxel size, no connected pore network is measured with a = 13 micron, and it is hardly connected with a = 4.4 micron. A voxel size of 600 nm is necessary to image micrometric joints, yet only individual ones.

In order to predict fluid transport, 2D SEM is used to describe the joint network topology and macroscopic permeability, combined to either (1): micro-CT or (2): FIB/SEM for the individual joint transmissivity. At the joint network scale and at the 3D joint scale, two-scale numerical modelling shows that micrometric joints (observed with micro-CT) control macroscopic permeability, although they have a partial volume contribution to porosity, according to MIP. However, sub-micrometric joints (imaged by FIB/SEM) which contribute significantly to porosity (up to 1.27%) are slow paths for fluid transport

(with permeabilities smaller by two to three orders of magnitude, when compared to that given by micrometric joints).

INTRODUCTION

Low permeability materials are often composed of several pore structures of various scales, which are superposed one to another. It is often impossible to measure and to determine the pore geometry properties relevant for fluid transport in one step, or with a unique experimental device.

In low permeability sandstones, the pore space is essentially made of micro-cracks between grains. These macro-cracks (or fissures) are two dimensional structures, which aperture is roughly on the order of one micron. When considering the grain scale, i.e., on the millimetric scale, fissures form a network.

These two structures (individual crack and fissure network) are measured by using different tools [1]. The density of the fissure network is estimated by trace measurements on the two dimensional images provided by classical 2D Scanning Electron Microscopy (SEM) with a pixel size of about 2 micron. The three dimensional geometry of fissures is measured by both (1) Focused Ion Beam/Scanning Electron Microscopy (FIB/SEM) with voxel size a = 15 nm and (2) X-Ray micro-tomography (micro-CT) in the laboratory (www. http://isis4d.univ-lille1.fr), with a = 0.6 micron, or 4.37 micron or 13 micron.

A two-step methodology is proposed to predict the transport properties of tight sandstones. It is applied on the example of tight sandstone T-2390-82. Transport is characterised on two different scales; the pore network, representative of the macroscopic scale, is imaged by 2D SEM in terms of crack organisation, average length, density, etc.; the aperture b of the individual cracks is characterized on the scale given by FIB/SEM for sub-micrometric joints, and by micro-CT for micrometric joints. Numerical calculations are performed first, for the whole pore network (given by 2D SEM), as a function of network characteristics; they yield a permeability proportional to the fracture transmissivity. This individual crack transmissivity is determined by using the geometry of the individual cracks (given by FIB/SEM and micro-CT).

EXPERIMENTAL

Experiments were performed on a single sample (37.7 mm diameter and 34.6 mm height) of tight sandstone reference T-2390-82, after oven-drying at 105°C until mass stabilization (dry state).

Macroscopic Dry Gas Permeability. Details of the experimental method are given in [3]. The 37.7 mm diameter sample is subjected to a quasi-static argon gas flow, at an upstream gas injection pressure of 2 to 4 MPa. The apparent gas permeability K_{gas} is measured during a small decrease in upstream gas pressure by 0.05 MPa, during two successive cycles of external hydrostatic stress loading up to 45 MPa. For such important gas injection pressures, the Klinkenberg effect is generally negligible [4]. After these

cycles, the sample is over-cored transversely to a sample of 20mm diameter and 30.8 mm height, and tested for gas permeability again.

Fig. 1 shows that gas permeability K_{gas} decreases significantly with increasing hydrostatic stress Pc; this is attributed to the progressive closure of fissures under loading. For further permeability predictions, an average K_{gas} of 2.1+/-0.4 10^{-17} m^2 (21 +/-4 micro Darcy) is considered at low Pc=2.5 to 5MPa.

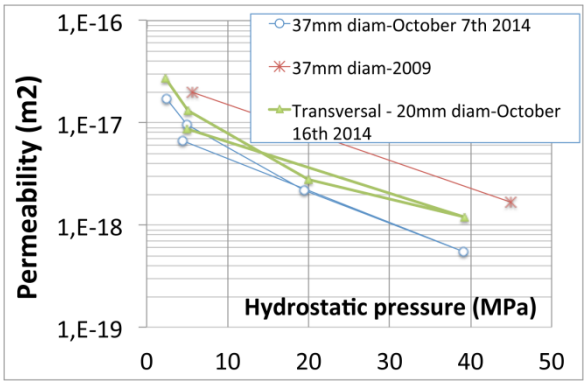

Figure 1: Gas permeability for 37.7mm diameter and perpendicular 20mm diameter T-2390-82 sandstone sample

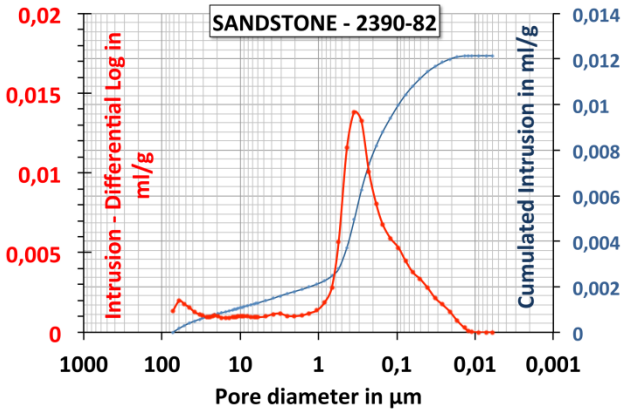

Figure 2: MIP results for T-2390-82 sandstone, plotted after blank cell and conformance corrections [5,6]

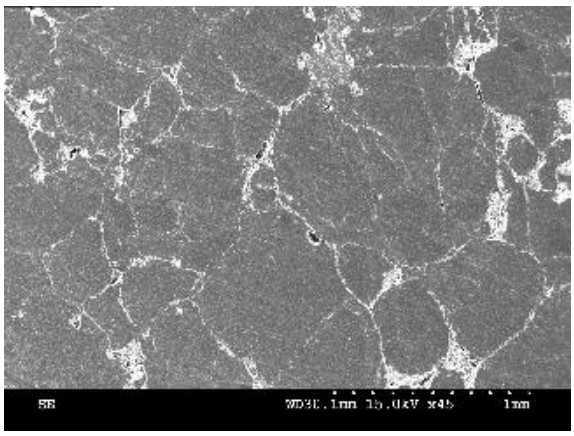

Figure 3: Original 2D SEM image of sample T-2390-82.

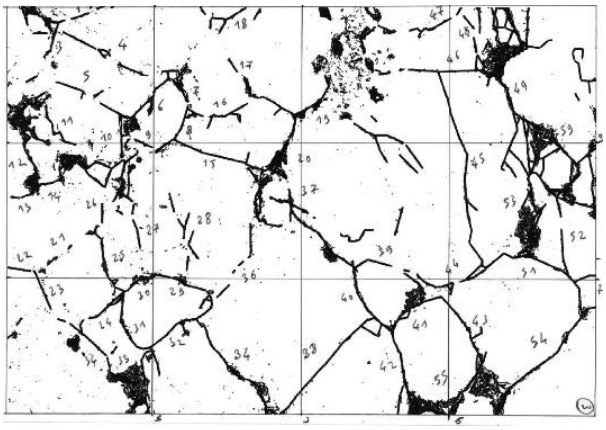

Figure 4: Corresponding trace map of the SEM image (left) used for permeability prediction

Indirect Pore Structure Assessment. Porosity ϕ is measured by the water imbibition method on the 37.7 mm sample and on its 20 mm over-cored part; values of 2.8-3.2% are obtained.

Mercury Intrusion Porosimetry is performed using a MICROMERITICS AutoPore IV 9500 up to 200 MPa, which corresponds to intruded pores down to 4 nm. Results (Fig. 2) show a characteristic pore size of about 350 nm, with a limited contribution of pores

between 1-10 microns to cumulative pore size distribution. This justifies the use of FIB/SEM imaging to describe sub-micrometric pores in 3D.

Direct Characterization of the Pore Structure: 2D SEM. The pore network cannot be characterized by FIB/SEM alone. 2D SEM measures directly the topology (average length, density, connectivity) of the fissure network of T-2390-82 sandstone. SEM images are taken at low magnification (x40-45), with a pixel size of 2.15-2.33 micron, on the top surface of the 37.7 mm diameter sample, where several zones of different fissure densities are observed. A high fissure density zone and a medium density zone are computed in the following. Therefore, a trace map of each individual SEM image is made by manually locating each individual fissure (Figs. 3 and 4).

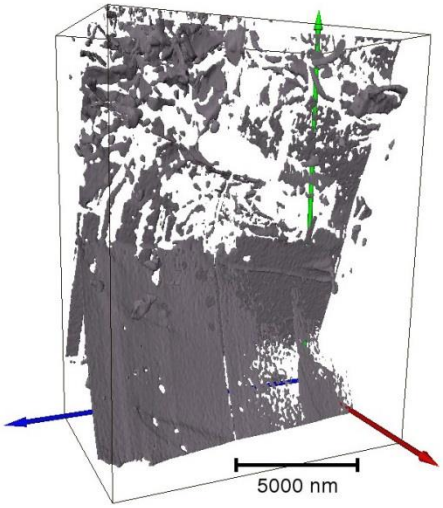

Figure 5: Pore network given by FIB/SEM (3D reconstruction with Amira software, FEI)

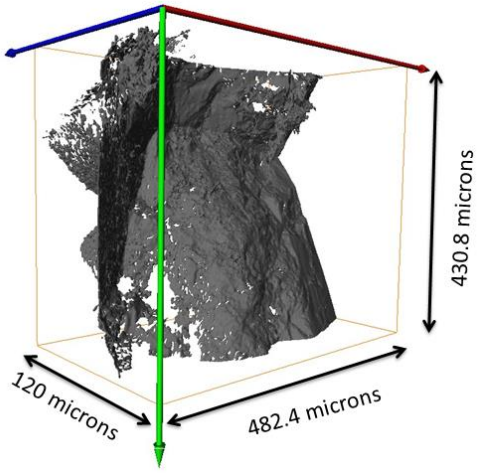

Figure 6: Pore network given by micro-CT on a 0.8mm rod (3D reconstruction with Amira software, FEI)

Direct Characterization of the Pore Structure: FIB/SEM. The focused ion beam (FIB) cuts a U-shaped hole in order to isolate a plane-parallel sandstone volume [7]. Following this, the FIB cuts regularly-spaced 50nm thick slices from the plane-parallel volume, perpendicularly to the sample polished surface. Between each FIB cutting, the sandstone matter perpendicular to the polished surface is observed with an electron detector of the in lens type. A stack of 300 images is computed. Sample T-2390-82 has a voxel size of 14.65x35.71x50.0 nm^3, and a total investigated volume of (9874x20069x15000) nm^3. The 3D pore network is obtained from the raw FIB/SEM image stack, by filtering and segmentation of each individual image using the ImageJ software. The 3D object is generated by using the Amira (FEI) software, by using the method described in [8] (Fig. 5). The 2D and 3D Continuous Pore Size Distributions (CPSD) are deduced form the binary images, as described by [9].

Direct Characterization of the Pore Structure: micro-CT. For comparison purposes, three image series of the same T-2390-82 sample are acquired with three voxel sizes of 13 microns (measured on the 20 mm diameter sample used for gas permeability), 4.4

microns (on a parallelepipedic sample of 5 mm width) and 0.6 microns (on a thin rod of 0.8mm width). Image filtering and segmentation by Image J and 3D visualization by Amira (Fig. 6) are performed as for FIB/SEM.

Comparison between the Various Pore Structure Assessment Methods. Indirect and direct methods for pore structure assessment are compared in Table 1. For a = 13 micron and 4.4 micron, pore volumes of micro-CT samples are not connected from one surface to another, despite porosities of 1.016% +/-0.36 and 1.88% +/-0.17. Compared to water porosity (2.8-3.2%), M.I.P. provides a greater value, possibly due to sample damage. On the opposite, micro-CT of the 0.8mm rod provides a connected pore volume (Fig. 6), corresponding to an individual fissure between two quartz grains, of porosity 1.34% +/-0.15 and average opening of 4 micron. Although significantly smaller, the FIB/SEM sample provides a porosity of 1.25%, which is similar to micro-CT, and a typical opening on the order of 60-100nm. At this stage, it is difficult to determine whether or not both 3D fissures (given by micro-CT and FIB/SEM) contribute to fluid transport.

Sample	Water imbibition	20mm diam. micro-CT	M.I.P.	5mm parallelepepipoid micro-CT	2D SEM medium density zone	2D SEM high density zone	0.8mm rod micro-CT	FIB/SEM
Volume (or Area)	53.8 cm^3	2.61 cm^3	1.43 cm^3	43.7mm ^{3}	6 mm^2	6 mm^2	0.216 microns ^{3}	26157 nm^3
d_peak (microns)	-	52.4	0.35 ; (60.3)	17.5	6	4	4	(0.06) ; 0.1
porosity (%)	2.8-3.2	1.016 +/-0.36	4.89	1.88 +/-0.17	5.3 +/-2.2	6.6 +/-1.6	1.34 +/-0.15	1.27 +/-0.02

Table 1: Main characteristics of the pore structure of the same T-2390-82 sandstone sample.

PERMEABILITY PREDICTION

Macroscopic permeability K is calculated in two steps. On the small scale, the fracture transmissivity is calculated by solving the Stokes equation on several portions of the measured connected fissures by micro-CT and FIB/SEM. A single phase Lattice Boltzmann code is used; according to the standard terminology, it is a D3Q19 code with two relaxation times; the classical bounce-back condition is used at the solid interface. Each sample is completed by its mirror image in order to avoid overall boundary effects. More details can be found in [10].

On the large scale, the density of fissures is estimated by three different means based on the number of intersections with scanlines, on the surface density of fissures and on the intersections between fissures per unit surface. These three means show that the network is relatively isotropic. They provide very close estimations of the density. Then, a general formula derived from systematic numerical computations [2] is used to derive the macroscopic dimensionless permeability which is proportional to the fracture transmissivity $K=\sigma\ \alpha\ \Delta\rho'^2/[R(1+\beta\ \Delta\rho')]$ where α =0.037, β=0.155, $\Delta\rho'=\rho'-2.3$. R is a

measure of the lateral fracture extension. ρ' is the average number of intersections per fracture. A closely related application is given in [11].

The combination of the two previous results yields the dimensional macroscopic permeability. For the combination of 2D SEM and FIB/SEM, permeability predictions K range between 3 10^{-21}- 6.2 10^{-20} m^2 (3 to 62 nanoDarcy). This is three to four orders of magnitude smaller than actual gas permeability measurements. For the combination of 2D SEM and micro-CT, permeability is predicted at values ranging between 6 10^{-18} - 7.4 10^{-16} m^2 (6 to 740 microDarcy). This is in better agreement with experimental gas permeability on centimetric samples.

CONCLUSION

For tight sandstone T-2390-82, the relevant pore structure for fluid transport is well described on two separate scales: (1) the fissure network is imaged and characterized by 2D SEM, (2) the individual fissure between quartz grains is characterized at a 350 nm size by M.I.P., which is the same order of magnitude as the 100nm opening given by FIB/SEM. This fissure scale contributes by three-four orders of magnitude less to transport than the micrometric fissure aperture obtained by micro-CT (of 4 microns wide). The latter provides macroscopic permeability prediction consistent with gas permeability identification on centimetric samples. This original approach needs to be validated on other tight sandstones to prove its generality.

ACKNOWLEDGEMENTS

Financial support by GDFSUEZ E&P International SA is gratefully acknowledged. The SEM national facility available at the Centre Commun de Microscopie de Lille (France) is supported by the Conseil Regional du Nord-Pas de Calais, and by the European Regional Development Fund (ERDF).

REFERENCES

1. Z. Duan, C. A. Davy, F. Agostini, L. Jeannin, D. Troadec, F. Skoczylas, *International Journal of Rock Mechanics and Mining Science*, Vol.65, pp.75-85, 2014.
2. P.M. Adler, J.-F. Thovert, V.V. Mourzenko: Fractured porous media, *Oxford University Press*, 2012.
3. X. T. Chen, Th. Rougelot, C.A. Davy, W. Chen, F. Agostini, F. Skoczylas and X. Bourbon, *Cement and Concrete Research*, Vol.39 (12), pp. 1139-1148, 2009.
4. W. Chen, J. Liu, F. Brue, F. Skoczylas, C. A. Davy, X. Bourbon, J. Talandier, *Cement and Concrete Research*, Vol.42, pp. 1001-1013, 2012.
5. Shafer J. and Neasham J. *Mercury Porosimetry International Symposium of the Society of Core Analysts*, 2000, SCA 2021.
6. Dewhurst D. N., Jones R. M. and Raven M. D. *Petroleum Geoscience*, 2002;8:371–383.
7. Holzer, L., Indutnyi, F., Gasser, P., Munch, B., and Wegmann, M. *Journal of Microscopy*, 216(1):84-95 (2004).

8. Y. Song, C. A. Davy, D. Troadec, A.-M. Blanchenet, F. Skoczylas, J. Talandier, J.-C. Robinet, *Marine and Petroleum Engineering*, 65 (2015) 63-82.
9. Munch, B. and Holzer, L. (2008). *Journal of the American Ceramic Society*, 91(12):4059–4067.
10. A. Pazdniakou, P.M. Adler, Dynamic permeability of porous media by the lattice Boltzmann method, *Advances in Water Resources*, 62, 292, 2013.
11. I. Malinouskaya, J.-F. Thovert, V.V. Mourzenko, P.M. Adler, R. Shekhar, S. Agar, E. Rosero, M. Tsenn, Fracture analysis in the Amellago outcrop and permeability predictions, *Petroleum Geoscience*, 20, 93, 2014.

NUMERICAL MODELING OF NMR SURFACE RELAXATION IN POROUS MEDIA WITH IMPROVED PORE SURFACE AREA EVALUATION AND DERIVATION OF INTERFACIAL ABSORPTION PROBABILITY

Danyong Li[1], Xuefeng Liu[2], Feng Huang[3], Tianpeng Zhao[1], Weifeng Lv[4], Sven Roth[1]
[1] iRock Technologies, Beijing, China; [2] China University of Petroleum, Tsingtao, Shandong, China; [3] Wuhan University of Technology, Wuhan, Hubei, China; [4] Research Institute of Petroleum Exploration and Development, Beijing, China

This paper was prepared for presentation at the International Symposium of the Society of Core Analysts held in St. John's Newfoundland and Labrador, Canada, 16-21 August, 2015

ABSTRACT

In digital rock physics, surface relaxation of NMR decay on a 3D porous media is often simulated with Random-Walker methods, where Brownian walkers representing the magnetized nuclei are absorbed by the solid surface under an interfacial absorption probability. Previous simulations usually neglected the blocky pixel appearance of 3D pore space images, which results in over estimation of the surface area, particularly for unconventional reservoir rocks with large fractions of micropores, such as tight sandstones or shale. This leads to arbitrary adjustments of the interfacial absorption probability by tuning the value of the surface relaxivity strength (SRS) in order to match simulation results with experimental measurements. However, this arbitrary adjustment violates the fact that SRS is a rock dependent physical property. In this study a new interfacial absorption probability for NMR simulations is presented that honours the physical principles. This new absorption probability computation depends on accurate evaluation of the surface area, which is assured by a new approach of 3D pore space surface area evaluation. The new algorithm is verified by performing NMR Random-Walker simulation tests on both standard geometries and realistic 3D heterogeneous porous media.

INTRODUCTION

In Random-Walk NMR simulation the decrease of random walkers, which simulates the

transverse decay of magnetization, is controlled by an absorption probability of the solid grain surface, usually called the killing probability, which is proportional to the surface relaxivity, the random walker step size, and is reversely proportional to the bulk diffusivity [1]. Traditionally, the expression of killing probability derived by Bergman and Dunn [1] was used as an input to the simulation program [2-4]. However, this expression of killing probability, based on the assumption of random walkers hitting a planar surface was neglecting the discretized voxel effect and thus, required unphysical adjustment of input parameters. This effect is increasingly evident in unconventional rock types, with high surface-to-volume ratio (S/V).

In this study two aspects are discussed to reduce the uncertainties from the previously used killing probability approaches. Firstly, an updated killing probability is derived based on the physical process of transverse magnetization decay. The new killing probability effectively includes the surface-to-volume ratio and the global hitting probability of the entire pore space geometry and is adaptable to any rock type. Secondly, an algorithm is proposed, which more accurately evaluates the surface area and reduces the voxel discretization effect. The new NMR simulation is verified by testing on both standard geometrical pore spaces and digital images of realistic rock samples of various rock types and shows that the previously shifted T2 distribution is successfully corrected.

THEORY AND METHODS

Nuclear magnetic resonance occurs when an ensemble of spinning hydrogen protons performing Larmor precession in a uniform magnetic field $\boldsymbol{B_0}$ are tilted by an oscillating magnetic field pulse $\boldsymbol{B_1}(t)$ with oscillation frequency the same as the Larmor precession frequency and perpendicular to $\boldsymbol{B_0}$. The net macroscopic magnetization $\boldsymbol{M_0}$ previously along the direction of $\boldsymbol{B_0}$ is tilted away from its longitudinal direction to the transverse plane. As the magnetic pulse is turned off, the tilted magnetization relaxes back to its longitudinal direction and the transverse component of macroscopic magnetization $\boldsymbol{M}_\perp$ follows an exponential decay [5],

$$\boldsymbol{M}_\perp(t) = \boldsymbol{M}_\perp(0)e^{-t/T_2} \tag{1}$$

where T_2 is determined by three effects, bulk relaxation, surface relaxation and bulk relaxation, which is defined as the combination of [6]

$$\frac{1}{T_2} = \frac{1}{T_{2bulk}} + \frac{1}{T_{2surface}} + \frac{1}{T_{2diffusion}} \tag{2}$$

It is well understood that in pore space, where the scale satisfies the fast diffusion limit,

the surface relaxation time $T_{2surface}$ is related to the mineralogy on the pore solid surface and the surface-to-volume ratio of the pore space [7],

$$\frac{1}{T_{2surface}} = \rho \frac{S}{V} \tag{3}$$

where ρ is the surface relaxivity, S the pore surface area and V the pore space volume.

In this study, the surface relaxation described by Eq. (1) is simulated by Random-Walk methods, in which an ensemble of random walkers representing the spinning hydrogen protons is seeded into porous space to imitate diffusive Brownian motion [1]. The random walkers travelling to the image pixels near to the solid-void boundary are absorbed by the solid interface, leading to the decrease of random walkers, analogous to the surface relaxation process in which the spinning nuclei is relaxed by interaction with the solid grain surface.

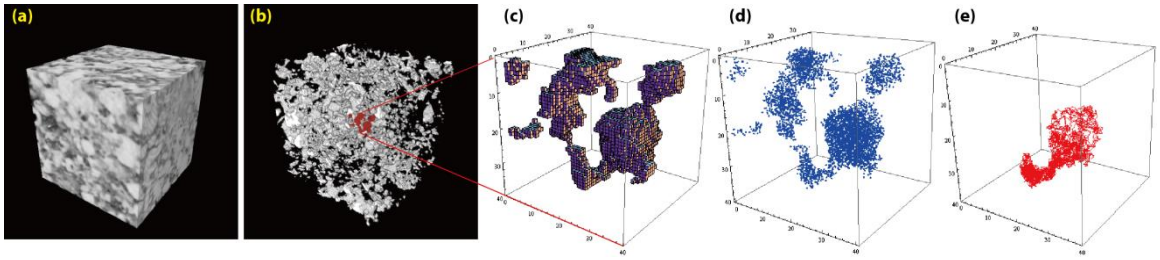

Figure 1. Scheme of Random-Walk NMR simulation on MCT image: (a) a typical MCT greyscale image with lighter area indicating the high density grains and darker area the pores. (b) segmented pore space extracted from the greyscale image. (c) zoom-in of a part of the pore space shows the pore space is compiled by cubic voxels. (d) random walkers (blue) seeded into the pore space. (e) the track of one random walker in one pore space.

Initially, a number of N random walkers are uniformly seeded into a 100% wetting phase saturated pore space. After an infinitesimal time Δt, the number of random walkers decreases by $Nh\gamma$, where h is the global probability of random walkers hitting the pore surface and γ the probability of random walkers being absorbed by the surface. Relating the decrease of random walkers with the decay of magnetization in Eq. (1), we obtain

$$h\gamma = \frac{\Delta t}{T_2} \tag{4}$$

In our simulation the time step Δt is determined by the law of Brownian motion of

spatial diffusive particles in a 3D space, $\epsilon^2 = 6D_0\Delta t$, where D_0 is the bulk fluid diffusivity and ϵ the diffusion distance of random walkers within a time step. Therefore Eq. (4) can be rewritten as the expression for killing probability,

$$\gamma = \frac{\rho\epsilon^2 S}{6D_0 hV} \tag{5}$$

Effective implementation of Eq. (5) into the whole process of NMR simulation requires both accurate evaluation on the surface area S and the global hitting probability h of the pore space. In this study, an optimized marching cubes algorithm [8] is employed to evaluate the pore space surface area by interpolating a virtual smoothed surface along the discretized solid-pore interfaces and random walkers hitting the surface are determined by judging whether the random walkers cross this virtual surface. The hitting probability h depends on the structural geometry of the pore space and is calculated as

$$h = \sum_{i=1}^{N}(1 - Z_i)(h_s \sum_{s=1}^{6} Z_i^s + h_c \sum_{c=1}^{8} Z_i^c + h_e \sum_{e=1}^{12} Z_i^e) \tag{6}$$

where Z_i is the pixel registration of the *i*th pixel of a 3D image with $Z_i = 0$ for void and $Z_i = 1$ for solid grain. Z_i^s (Z_i^c or Z_i^e) are the 6 (8 or 12) sided (corner or edge) neighboring pixels of Z_i, and h_s, h_c and h_e are the constant probabilities of random walkers in pixel Z_i jumping into sided, corner and edge pixels, respectively.

RESULTS

Standard Geometrical Benchmarks

The validity of the NMR simulation program with updated killing probability and smoothed surface area evaluation is first verified by performing tests on standard geometries and comparing the simulated results with the theoretical ones. The consistency between simulation and theoretical results ensures the reliability of performing the simulation on realistic pore spaces, where the porous structures are highly irregular and the pore sizes are multiple-scale.

The simulation results (Table 1) show significant improvement of pore space surface area evaluation and better consistency between the predicted and theoretical T2s than the previous version of NMR simulations. It is obvious that while the previous program works well on cubic pore space consisting of planar surfaces, it fails to correctly evaluate the surface area of spherical and irregular pores which are dominant in most rock samples.

Application on Digital Rock Images

The new simulation is further tested on realistic digital images of various rock types including sandstone, carbonate and tight sandstone (Table 2). The validity of NMR simulation on realistic rock samples can only be verified by matching with experimental measurements. However, the improvement of the simulation algorithm can be verified by comparing the simulation results with the previous ones. Figure 2 shows one testing result, including decaying magnetization and its corresponding T2 distribution. With more accurate killing probability realized by corrected evaluation of the pore space surface area and more physical based random walker diffusion scheme, the T2 distribution of all rock types shift rightwards, which indicates that the previous over estimated surface area is effectively corrected. The level of correction increases as the pore space becomes more tight and tortuous.

Table 1. Simulation results on standard geometrical pore space shows that the updated simulation algorithm significantly improves evaluation of surface area and T2 for spherical pores. The testing are perform on a 200^3 image with pixel size 1.0μm and surface relaxivity 3.0μm /s.

Cubic Pore						
Length(μm)	**S_{th}(μm^2)**	**$T2_{th}$(ms)**	**S_{old}(μm^2)**	**$T2_{old}$(ms)**	**S_{new}(μm^2)**	**$T2_{new}$(ms)**
10.0	600.0	555.6	600.0	543.3	564.1	605.5
20.0	2400.0	1111.1	2400.0	1117.7	2329.0	1174.6
50.0	15000.0	2777.8	15000.0	2802.9	14820.0	2923.1
100.0	60000.0	5555.6	60000.0	5672.9	59650.0	5906.9
Spherical Pore						
Radius(μm)	**S_{th}(μm^2)**	**$T2_{th}$(ms)**	**S_{old}(μm^2)**	**$T2_{old}$(ms)**	**S_{new}(μm^2)**	**$T2_{new}$(ms)**
5.0	314.2	555.6	486.0	424.0	341.0	516.5
10.0	1256.6	1111.1	1902.0	937.3	1372.0	1047.9
25.0	7854.0	2777.8	11770.0	2380.8	8539.0	2654.9
50.0	31415.9	5555.6	47070.0	4827.9	34140.0	5332.8

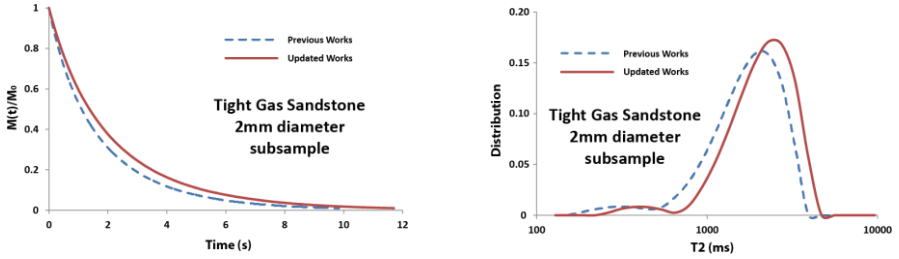

Figure 2. Comparisons of previous and updated works of NMR simulation on digital images of a 2mm diameter tight gas sandstone subsample.

Table 2. Simulation results of various rock types and scales. The surface relaxivity is taken as 4.0μm /s.

Sample	Image Size (voxel)	Voxel Size (μm)	Porosity (%)	S_{old} (μm^2)	S_{new} (μm^2)	$T2_{old}$ (ms)	$T2_{new}$ (ms)
Sandstone	300^3	8.68	14.13	1.73E-04	1.28E-04	4438.03	5722.38
Carbonate	800^3	4.93	7.82	7.19E-04	5.16E-04	869.82	1178.16
Tight gas 1	1000^3	14.30	1.99	4.42E-03	3.28E-03	3720.65	5323.14
Tight gas 2	1000^3	2.77	7.10	2.33E-04	1.67E-04	2306.66	2928.23
Tight gas 3	1000^3	1.15	6.59	2.32E-05	1.66E-05	1608.27	2111.32

More accurately simulated T2 distributions provide several important potential practical applications. The SRS is largely unknown but is needed to convert the experimental T2 distribution from time scale to length scale. Another example is to provide accurate porous surface area which is important for some surfactant experiments.

CONCLUSIONS

We propose two important updates to previous NMR simulations. One is a newly derived killing probability, based on the physical process of an ensemble of random walkers diffusing, hitting and being absorbed by a porous space solid surface, to replace the previous killing probability which fails to recognize the global irregularity of the pore shapes. The other is an optimized algorithm to increase the accuracy of porous space surface area evaluation, which was over estimated, previously. Both successfully reduce the uncertainties resulting from previous works. With the new killing probability and smoothed surface area evaluation, the NMR simulation can be reliably matched with experimental measurements and thus, provides a more accurate surface relaxivity strength and surface-to-volume ratio. Based on these improvements, NMR simulations can be extended to images with different saturation stages. Families of T2 distributions under various saturations can be simulated to calibrate NMR well logging data and to obtain more accurate estimates of irreducible water saturation.

REFERENCES

[1] Bergman, D.J., Dunn, K.J., Schwartz, L.M. and Mitra, P.P., “Self-diffusion in a periodic porous medium: A comparison of different approaches”, *Physical Review E* **51**, 3393 (1995).

[2] Talabi, O., Alsayari, S., Iglauer S. and Blunt, M.J., “Pore-scale simulation of NMR response”, *Journal of Petroleum Science and Engineering* **67**, 168-178 (2009).

[3] Toumelin, E., Torres-Verdin, C. and Chen, S., “Modeling of Multiple Echo-Time NMR Measurements for Complex Pore Geometries and Multiphase Saturations”, *SPE Reservoir Evaluation & Engineering*, 234 (2003).

[4] Toumelin, E., Torres-Verdin, C. Sun, B. and Dunn K.J., “Random-walk technique for simulating NMR measurements and 2D NMR maps of porous media with relaxing and permeable boundaries”, *Journal of Magnetic Resonance*, **188**, 83-96 (2007).
[5] Bloch, F., “Nuclear Induction”, *Physical Review* **70**, 460 (1946).
[6] Bloembergen, N., Purcell, E.M. and Pound, R.V., “Relaxation Effects in Nuclear Magnetic Resonance Absorption”, *Physical Review* **73**, 679 (1948).
[7] Brownstein, K.R. and Tarr, C.E., “Importance of classical diffusion in NMR studies of water in biological cells”, *Physical Review A* **19**, 2446 (1979).
[8] Lindblad, J. and Nystrom I., “Surface Area Estimation of 3D Digitized Objects Using Local Computations”.

SYSTEMATIC PARAMETER STUDY FOR FORMATION FACTOR MODELING AT THE PORE SCALE

Matthias Halisch [(1)], Sven Linden [(2)], Jens-Oliver Schwarz [(2)], Sarah Hupfer [(1)], Andreas Wiegmann [(2)]
[(1)] Leibniz Institute for Applied Geophysics (LIAG), Stilleweg 2, D-30655 Hannover, Germany
[(2)] Math2Market GmbH, Stiftsplatz 5, D-67655 Kaiserslautern, Germany

This paper was prepared for poster presentation at the International Symposium of the Society of Core Analysts held in St. John's Newfoundland and Labrador, Canada, 16-21 August, 2015

ABSTRACT

Digital Rock Physics (DRP), in combination with state of the art 3D imaging techniques, such as high resolution micro CT (µ-CT) or Synchrotron CT (Sr-CT), has progressed to a well established methodical instrument for petrophysical process modeling and simulations at the pore scale, respectively. Besides hydraulic and acoustic (elastic) rock properties, which probably form the largest field of interest for DRP, electric conductivity / resistivity is also of great interest since it is essentially used to determine (e.g.) water saturation, formation producibility, and at least the volume of oil- and/or gas in place of the formation. For this, formation resistivity factor (F) is measured by default during classic core analysis in the laboratory, in order to evaluate the parameters as mentioned above and to characterize the pore system of the rock in more detail. Nevertheless, to provide reliable statistics, experimental time increases significantly, same as the amount of cores that need to be investigated. This is where DRP and non-destructive 3D imaging become relevant. Though the experiment as well as the analytical calculation of F is straight forward, numerical modeling of this parameter by using CT obtained geometries is significantly affected by different boundary conditions, such as:

a) The 3D scan resolution (voxel resolution);
b) The image processing / phase segmentation;
c) The ratio of mineral to water resistivity;
d) The overall computational domain size;
e) The micro-scale sample (formation) heterogeneity.

The amount of pores that can be detected is directly linked to the resolution of the imaging, since F is mostly dominated by the porosity. False or inaccurate segmentation of phases can increase this effect in addition. The parametric setup of the model greatly increases computational power and time. Finally, the domain needs to be representative, which is especially challenging for heterogeneous (e.g. layered) samples. In this systematic parameter study, the authors showcase a selection of these effects by using data from three different rock samples (i. young sandstone; ii. reservoir sandstone; iii. porous carbonate). The results are compared to experimental, i.e. laboratory obtained data, and discussed critically in order to evaluate and develop better and optimized numerical tools and workflows for this specific modeling purpose.

INTRODUCTION

The classical and empirical relationship between rocks and the saturation fluids is essential for the interpretation of electrical borehole measurements since the early 1940's [1, 2]. The

fundamental proportionality between the resistivity of a water saturated rock (ρ_0) and the resistivity of the pore fluid (ρ_w) led to the infamous and so called Archie's law:

$$\rho_0 = F \bullet \rho_w \tag{E1}$$

The introduced parameter *F*, the formation resistivity factor, is a measure of the increase in resistivity of a pore fluid by presence of a non-conductive rock matrix. Formation factor is dependent on the geometrical (spatial) distribution of the electrolyte within the rock, related to the internal structure of the rock, of the pore space and of the wettability conditions therein [3]. Hence, F mostly – but not exclusively – is assigned to the (effective) porosity of the investigated rock. This finding led to the first Archie equation [2]:

$$F = \frac{1}{\Phi^m} \ , \tag{E2}$$

where *m* denotes the so called cementation exponent. Since porosity can be easily assessed by modern 3D digital imaging techniques and evaluation software tools, reliable modeling results are still challenging to derive, and strongly depend upon the boundary conditions as mentioned in the introducing abstract. The toolbox GeoDict (developed and distributed by Math2Market GmbH) is a generic approach for computer aided material engineering, and has been used for the formation factor modeling. It contains geometric models for virtual material synthesis and provides numerical tools for the prediction of material properties on the micro-scale. The basic concept is the simulation of physical processes on digital objects that are derived from either µ-CT images, or from synthesized images and models. This toolbox is able to predict a broad range of mechanic, electric and hydraulic rock properties, including parameters of routine and special core analysis [5, 6].

Explicit Jump Immersed Interface Method for Electrical Conduction

The Explicit-Jump immersed interface method is a very fast finite difference method to solve partial differential equations [7, 8]. Here it is applied to solve the stationary electrical conduction, heat conduction and diffusion equation in reservoir rocks:

$$\nabla \cdot (\sigma \nabla U) = f \, , \tag{E3}$$

where *U* denotes the electric potential and $\sigma > 0$ the piecewise constant electric conductivity. The equation is composed of Ohm's and Kirchhoff's law. The stationary electrical conduction equation is directly solved on segmented µ-CT images, where each individual phase is assigned an individual electrical conductivity value. Harmonic averaging is used to derive conductivities between material interfaces. The potential is discretized in a regular grid even in solid phases. Additional jump variables across material interfaces are introduced, where the continuity of the electrical flux yields the need for extra equations. A so called Schur complement formulation for these new variables is derived such, that fast Fourier transforms (FFT) and BiCGStab methods can be used to solve the linear system. If the values of the jump variables are known, the FFT solves the electrical conduction equation directly. This means that instead of solving a 3D problem in order to find the electrical potential, a 2D problem is solved derive the jump variables. Hence, computational time is reduced significantly. In addition, this method has a very good convergence rate even in geometries with high contrast in conductivity, such as it is mandatory

for natural rocks. The convergence rate solely depends on the number of jumps, i.e. the surface area of the material interfaces.

SAMPLE MATERIAL, µ-CT IMAGING & MODEL SETUP

For this study, three different rocks have been used (Fig.1, left to right): a highly porous carbonate, a young tertiary sandstone, and a cretaceous reservoir sandstone. The carbonate (denoted as EBK) is characterized by high porosity (up to 48 %) composed of inter- and intra-granular void space, and by a high degree of mineralogical pureness (> 99 % CaCO3). The tertiary sandstone (denoted as IG) features large and sharp edged quartz grains that are covered by cristobalite needles, an overall low clay mineral content (< 2 %) and few but large muscovite crystals. The porosity can reach 37 % and is dominated by intergranular voids only. The reservoir sandstone (denoted as BE) features a porosity of up to 25 %, which is composed of inter-granular voids of the quartz grain matrix as well as of micro-pores, which are related to the clay agglomerations (up to 9 vol.-%) within.

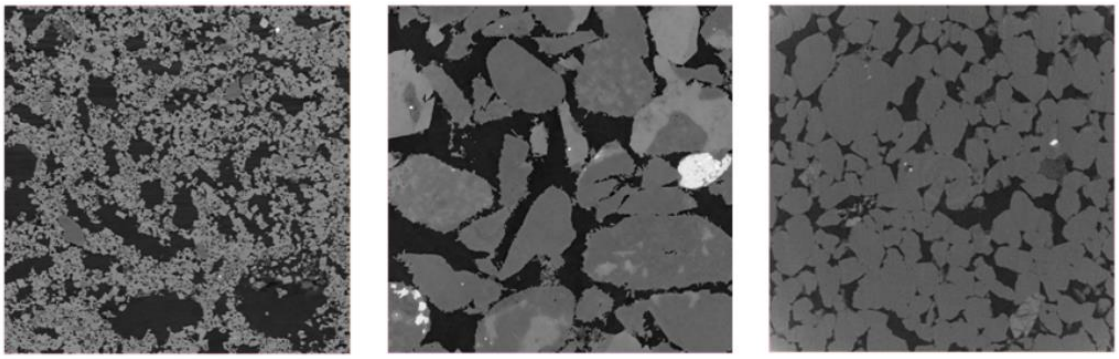

Figure 1: µ-CT cross sections of the three investigated samples at a scanning resolution of 2 microns each (from left to right hand side): carbonate, young (tertiary) sandstone, reservoir (cretaceous) sandstone.

From all materials, a small plug (4 mm diameter, 8 mm length) has been prepared for the µ-CT imaging. The samples have been entirely scanned with a GE phoenix nanotom S tomograph, with three different voxel resolutions: 2 µm, 5 µm and 10 µm. Within the 2 µm scan, a region of interest of 1000^3 has been cropped and registered to the 5 µm scan, which then has been cropped at the same relative domain size and registered to the 10 µm scan, which has been cropped in the same way. Hence, for all samples, the exact same region of interest, i.e. 2 mm edge length (= 1000^3 @ 2 µm, 400^3 @ 5 µm and 200^3 @ 10 µm) has been extracted for three different scan resolutions. The 3D data sets have been processed individually, which means that they have been filtered (non local mean) and registered with scanning electron data for a best fit segmentation solution by using Otsu [9] and watershed algorithms [10]. For the formation factor modeling, the following conductivities have been used [3, 11]: σ_w = 5 S/m, σ_{matrix_EBK} = 1e-10 S/m; σ_{matrix_IG} = 1e-12 S/m; σ_{matrix_BE} = 1e-12 S/m. Boundary conditions have been set to periodic, stopping criteria was a model (σ_0) accuracy equal or better than 0.001 S/m and a maximum of 10,000 iterations or 240 h maximum run time, respectively.

RESULTS

First of all, results of segmentation errors are showcased (Fig.2), since the segmentation threshold directly influences the amount of porosity of the 3D data set, and hence of the modeled F-value. The "best fit threshold" has been used as starting (center) point to vary the threshold stepwise for selected percentages to this value. It is clearly visible, that the segmentation threshold, as a function of scan resolution, has a tremendous influence upon the measurable porosity of the 3D data sets, even for very small segmentation misfits. The resolution effect is especially for the carbonate detectable, due to the clearly visible spreading of the error curves, caused by the loss of intra-granular voids with increasing voxel resolution. ± 2 % threshold error may cause already ± 2.5 % to 6 % of porosity change. For the IG sample, this effect is below ± 2.5 % change in porosity, due to the absence of micro porous structures.

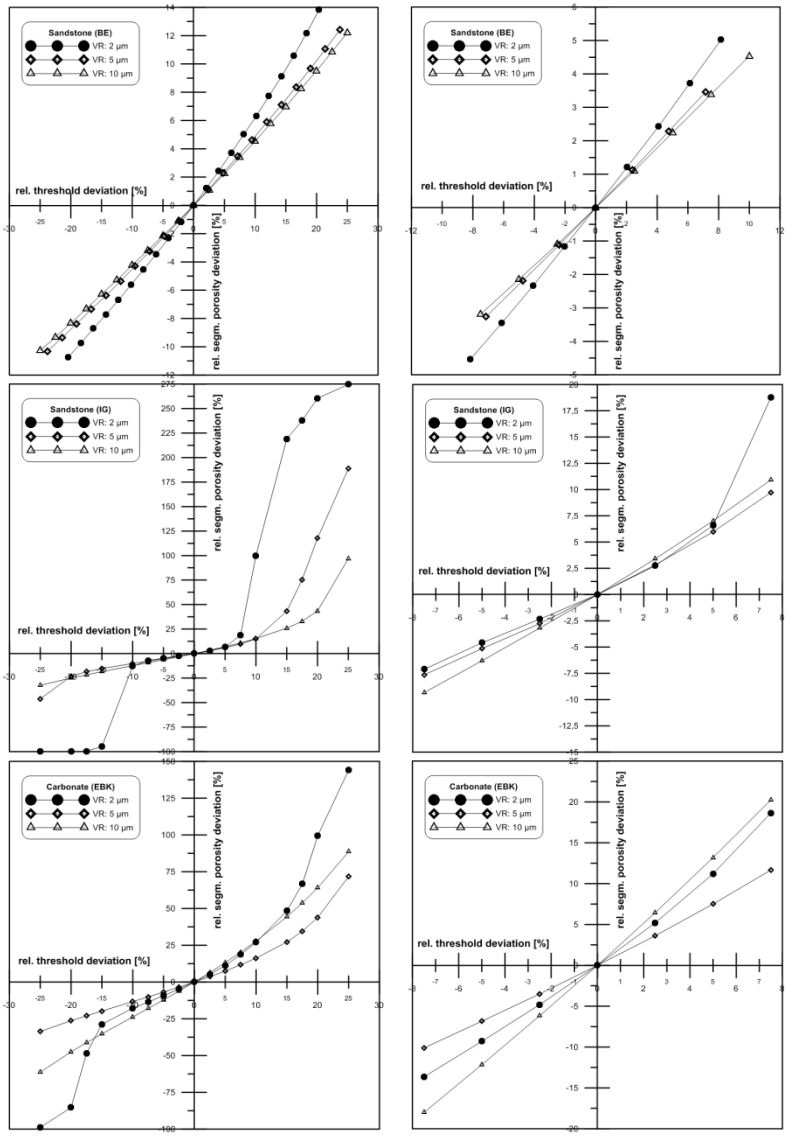

Figure 2: Results of the segmentation error (x-axis = rel. threshold deviation related to the best fit threshold) on the segmented data set porosity (y-axis: rel. porosity deviation related to the best fit threshold) for the carbonate (top), tertiary (middle) and cretaceous sandstone (bottom). The right column is zoomed in (± 7.5 % on x-axis) for a better view on deviations at small changes for each sample. Hence, the left hand column showcases the full investigated deviation range (± 25 % on x-axis).

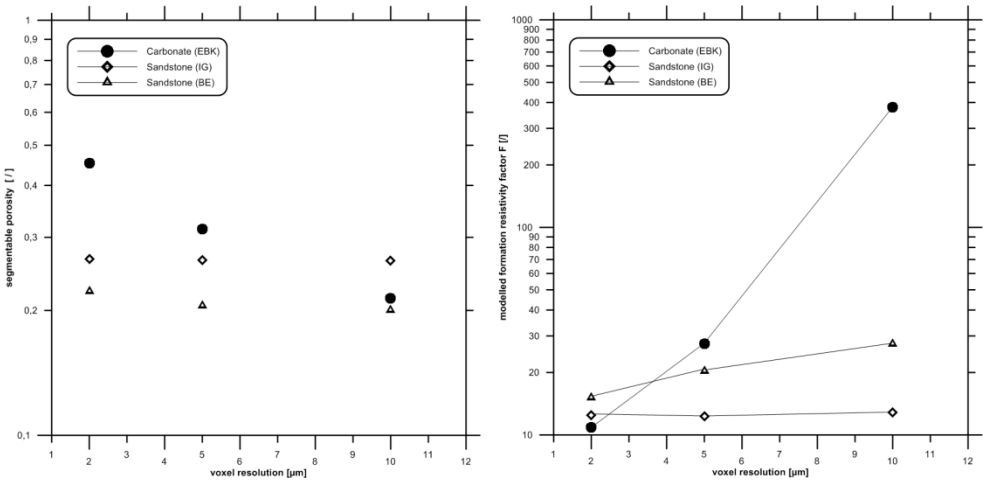

Figure 3: Relationship between scan resolution and segmented porosity (left hand side) and modeled F (right hand side), respectively, for each of the three samples.

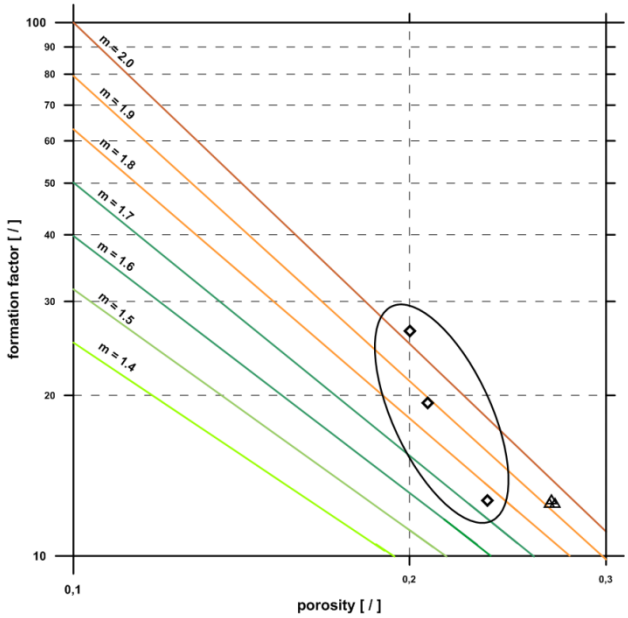

Figure 4: Scan dependent formation factor values versus porosity, including cementation exponent ranges related to (E2), for the two different investigated sandstones. Diamonds = BE; triangles = IG.

CONCLUSIONS & OUTLOOK

This study has shown that formation factor modeling is very case sensitive towards the 3D scan resolution, the segmentation threshold, and hence the segmented porosity. As a result, additional information of the sample material (e.g. scanning electron microscopy images for a highly reliable segmentation procedure; mineralogical information to estimate the amount and expected types of pore structures) in close combination with high 3D image resolution is highly recommended. Though modeling time may be drastically decreased (factor 50 for the EBK, 130 for the IG and for the BE) by using coarse image resolution, i.e. smaller model domains, results may lead to significantly different interpretation of the reservoir characteristics.

This data base is being constantly increased for a broader range of rocks in order to transfer this knowledge to get reliable interpretation results. For this, ongoing studies on representativeness of the 3D data sets, on impact of the pore fluid (conductivity) and on heterogeneous (anisotropic) rock types are performed and hopefully published in the near future.

REFERENCES

1. K. Sundberg: *Effect of impregnating waters on electrical resistivity of soils and rocks*. Trans. AIME. Geoph. Prosp. (1932), p. 367.
2. G.E. Archie: *The electrical resistivity log as an aid in determining some reservoir characteristics.* Trans. Americ. Inst. Mineral. Met. 146 (1942), p. 54 – 62.
3. J. Schön: *Petrophysik – Physikalische Eigenschaften von Gesteinen und Mineralen*. Ferdinand Enke Scientific Publishers, Stuttgart, 1983.
4. V.N. Dachnov: *Promyslovaja geofizika*. Izdat. Gostoptechizdat, Moscow, 1959.
5. H. Andrä, N. Combaret, J. Dvorkin, E. Glatt, J. Han, M. Kabel, Y. Keehm, F. Krzikalla, M. Lee, C. Madonna, M. Marsh, T. Mukerji, E. Saenger, R. Sain, N. Saxena, S. Ricker, A. Wiegmann, X. Zhan: *Digital Rock Physics benchmarks – Part 1: Imaging and Segmentation*. Computers & Geosciences 50 (2013), p. 25-32.
6. H. Andrä, N. Combaret, J. Dvorkin, E. Glatt, J. Han, M. Kabel, Y. Keehm, F. Krzikalla, M. Lee, C. Madonna, M. Marsh, T. Mukerji, E. Saenger, R. Sain, N. Saxena, S. Ricker, A. Wiegmann, X. Zhan: *Digital Rock Physics Benchmarks – Part 2: Computing effective properties*. Computers & Geosciences 50 (2013), p. 33-43.
7. A. Wiegmann and K. P. Bube: *The Explicit-Jump immersed interface method: Finite difference methods for PDE with piecewise smooth solutions*. SIAM Journal on Numerical Analysis, 1997 (37), p. 827-862.
8. A. Wiegmann and A. Zemitis: *EJ-Heat: A fast Explicit-Jump harmonic averaging solver for the effective heat conductivity of composite materials*. ITWM report Fraunhofer, 2006.
9. N. Otsu: A *Threshold Selection Method from Gray-Level Histograms*. IEEE Transactions on Systems, Man, and Cybernetics, Vol. SMC-9 (1979), 1: 62-66.
10. J. Ohser & K. Schladitz: *3D Images of Material Structures – Processing and Analys*is. Wiley-VCH Publishers, Weinheim, 2009.
11. D. Tiab, E. Donaldson: *Petrophysics – Theory and Practice of Measuring Reservoir Rock and Fluid Transport Properties*. Second edition, Elsevier, Amsterdam, 2003.

MICRO-CT IMAGING AND MICROFLUIDICS FOR UNDERSTANDING FLOW IN COAL SEAM RESERVOIRS

Peyman Mostaghimi[1], Ryan T. Armstrong[1], Alireza Gerami[1], Majid Ebrahimi Warkaini[2], Hamed Lamei Ramandi[1], and Val Pinczewski[1]
[1]School of Petroleum Engineering, University of New South Wales, NSW 2052, Sydney, Australia.
[2]School of Mechanical and Manufacturing Engineering, Australian Centre for Nanomedicine, University of New South Wales, NSW 2052, Sydney, Australia.

This paper was prepared for presentation at the International Symposium of the Society of Core Analysts held in Newfoundland, Canada, 16-21 August 2015

ABSTRACT

We investigate transport through fractured coal samples using microfluidic experiment. Firstly, micro-CT imaging at dry and wet conditions are performed to identify sub-resolution natural fractures in coal (cleats). Scanning Electron Microscopy (SEM) is also performed to image cleats at resolution of 100 nm. A novel image segmentation method is developed to segment the micro-CT image and measure the fracture apertures based on SEM data. We fabricate micro-models based on observed geometrical features on the segmented coal images. Microfluidic facility and high speed video microscopy are used to capture displacement of gas by brine on the fabricated model. This is a first step for understanding and analysis of high-viscosity ratio displacement in complex coal cleat systems and to optimize gas recovery from coal beds.

INTRODUCTION

Coal seam methane is a form of natural gas stored in coal beds and is one of the most important unconventional resources of energy. The flow and transport in coal beds occurs in a well-developed system of natural fractures that are also known as cleats. The cleat systems in coals have been the subject of intensive studies in recent years. The techniques used range from two-dimensional visual observations of coal outcrops and mine sites, high magnification and scanning electron microscopy (SEM) studies of rock fragments [3, 7, 8] to three-dimensional studies using X-ray micro-computed tomography (micro-CT) imaging with resolutions down to approximately a micron [2, 5, 9]. These studies show that the natural cleat system in coals spans all length scales from meters to hundreds of meters for exogenous fractures resulting from tectonic activity down to micro and nano-meters for endogenous micro and sub-micro fissures formed during coalification.

Although cleat orientation, density, aperture, height, length and connectivity are suggested to be important to the development of permeability none of the existing studies attempt to relate these features to flow properties of coal [1, 4]. This is a major

shortcoming in the current understanding of the production characteristics of coal seam gas and in the ability of the industry to assess the value of laboratory measured core data.

In this paper, we discuss a workflow where coal samples are imaged twice, i.e. without and with an X-ray attenuating fluid present in pore spaces. This will allow for visualisation of micro-cleats under the resolution of the micro-CT scanner. Following this, a novel image segmentation method is developed that employs data from SEM to find the cleat aperture on the micro-CT image. We fabricate micro-models based on observed geometrical features in the coal images and study transport phenomena at micrometer scales using microfluidic technology. This will assist in understating transport phenomena in coals and optimising recovery from coal seam gas reservoirs.

MATERIALS AND METHODS

Imaging

The coal sample is a volatile bituminous coal from Queensland, Australia. Micro-CT imaging was performed using a high-resolution, large-field, helical scanning instrument at Australian National University. The sample was saturated with 1.5 molar Sodium Iodide (NaI) brine to increase the X-ray attenuation of the coal fractures. The sample was a full size core plug, i.e. 25 mm diameter and 35 mm length, imaged at a resolution of 16.5 micrometers. The collected images were segmented using a watershed-based segmentation technique. After micro-CT imaging the sample was cut, parallel to butt cleats, and polished for the SEM imaging. SEM images were registered to the micro-CT data using the method developed by Latham et al. [6].

Flow Simulations

We calculate permeability and find the pressure and velocity profiles of coals on images obtained from micro-CT imaging. After image segmentation, the pore space is used as a computational domain to solve for Stokes flow. The governing equations for flow at the pore scale are:

$$\nabla \cdot \mathbf{v} = 0 \tag{1}$$

$$\mu \nabla^2 \mathbf{v} = \nabla P \tag{2}$$

where $\mathbf{v}$ is the velocity vector, P is pressure and μ is viscosity of the fluid flowing in the porous medium. The equations are discretized using the finite difference method. The main numerical challenge in solving the Stokes equation – Eq. (2) – is the weak coupling of the pressure and velocity fields. For decoupling pressure and velocities, the Semi Implicit Method for Pressure Linked Equations (SIMPLE) is used.

Experimental Setup

To perform the microfluidic experiment, a CAD (Computer-Aided Design) model based on the observed coal features is designed. A micro-model is fabricated using Polydimethylsiloxane (PDMS) based on the CAD design using softlithography technique. Then 1/16” PTFE tubes are connected to the flow inlet and outlets and a syringe pump

with the accuracy of 0.35% and step resolution of 0.046 microns is used for flow injection. The injection rate is 1 μl/min. To visualise the flow pattern inside the microfluidic channels, an inverted microscope with equipped high-speed and CCD camera (Oympus IX81 and DP80) with 1360×1024 pixels resolution is used.

RESULTS

Figure 1 shows the workflow used in this study for creating the micro-models and running the experiments. Figure 1(A) shows the grey scale image obtained from micro-CT imaging of the coal sample. The image has the resolution of 16 microns and imaging has been performed at wet and dry conditions. The grey scale image is obetained by subtracting the dry image from the wet image. This will enable us to visualise features smaller than the scanner resolution [5].

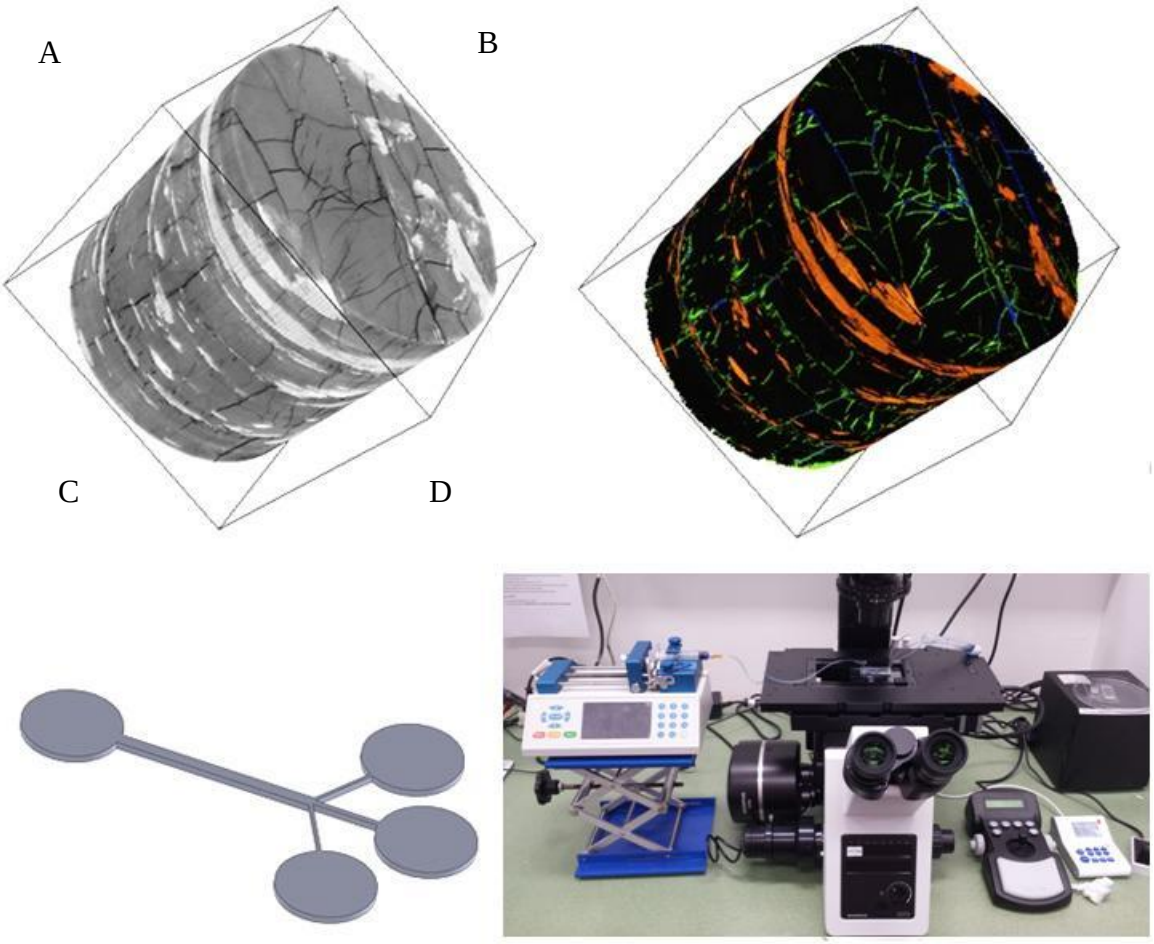

Figure 1: Workflow for the fabrication of micromodels based real cleat geometries. Micro-CT images of coal at wet and dry conditions are used to obtain a grey scale image (A). The image will be segmented (B) and the cleat system features will be visualised to be fabricated (C). The fabricated micro-model is used for microfluidic flow experiments using advanced microscopy tools (D).

The segmentation of coal images is of high importance due to existence of very narrow connectivities in coal samples. Figure 2 shows results of flow simulation over a region of interest (ROI) on the coal image. As can be seen from the velocity profile, there is a single voxel connecting the cleat system. Therefore, losing a single voxel in segmentation may lead to losing the connectivity.

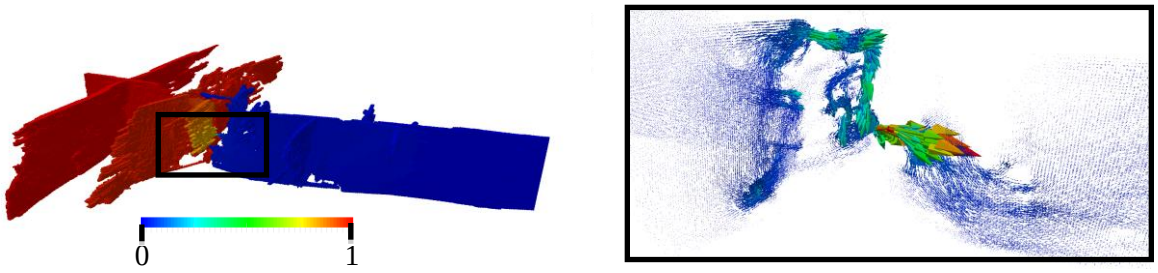

Figure 2: Single-phase flow simulation on extracted fracture geometry (Left: normalized pressure profile, Right: normalized velocity vectors in the black rectangle).

To segment the grey scale image, we use data from SEM imaging performed at a resolution of 100 nm and relate the grey scale micro-CT values to the measured aperture for the cleat system on the SEM image. Figure 3 shows a single cleat as observed in micro-CT and SEM imaging. The aperture of the cleat has been measured on SEM image and is related to the grey scale value. Repeating this process for different apertures will result in a curve that shows the corresponding aperture size for each grey scale value on the micro-CT image (Figure 3). The curve is used for image segmenation and the grey scale image is segmented into four different phases: (1) resolved fractures, (2) sub-resolution porous regions, (3) minerals, and (4) solid regions.

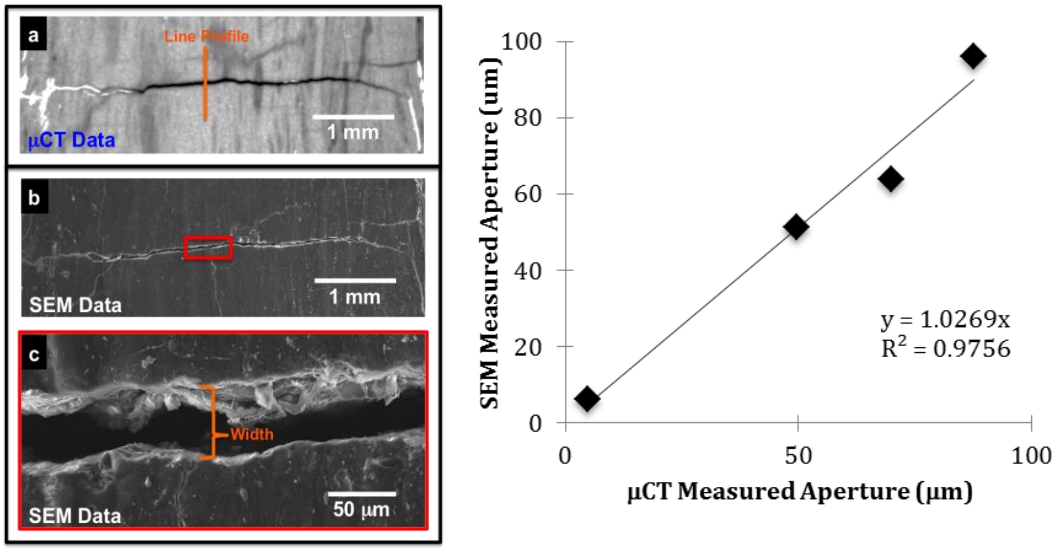

Figure 3: Registered micro-CT and SEM data for measurement of coal fracture apertures.

After segmentation, the resolved cleat system can be visualised and we generate CAD models based on the observed features in the cleat system. In this paper, we focus on a small region of interest where a junction of four fractures is observed (Figure 4). A micromodel is fabricated with similar topology and fracture aperture. Brine is injected from the widest fracture to the junction at the rate of 1 µl/min and the displacement of air is captured using the high speed camera. Figure 4 shows the movement of interface between fluids accurately with a contact angle of almost 90°. In our future works, we will use plasma treatment to change the wettability of surfaces and study the effect of wettability on gas recovery in coal seam reservoirs at micrometer scale. In addition, we will extract several unique features observed on segmeneted coal images and fabricate micro-models based on them. Then, displacement at each of these micromodels will be captured and investigated. This provides a comprehensive framework for investgating flow characteristics of coals and validation data for numerical computations.

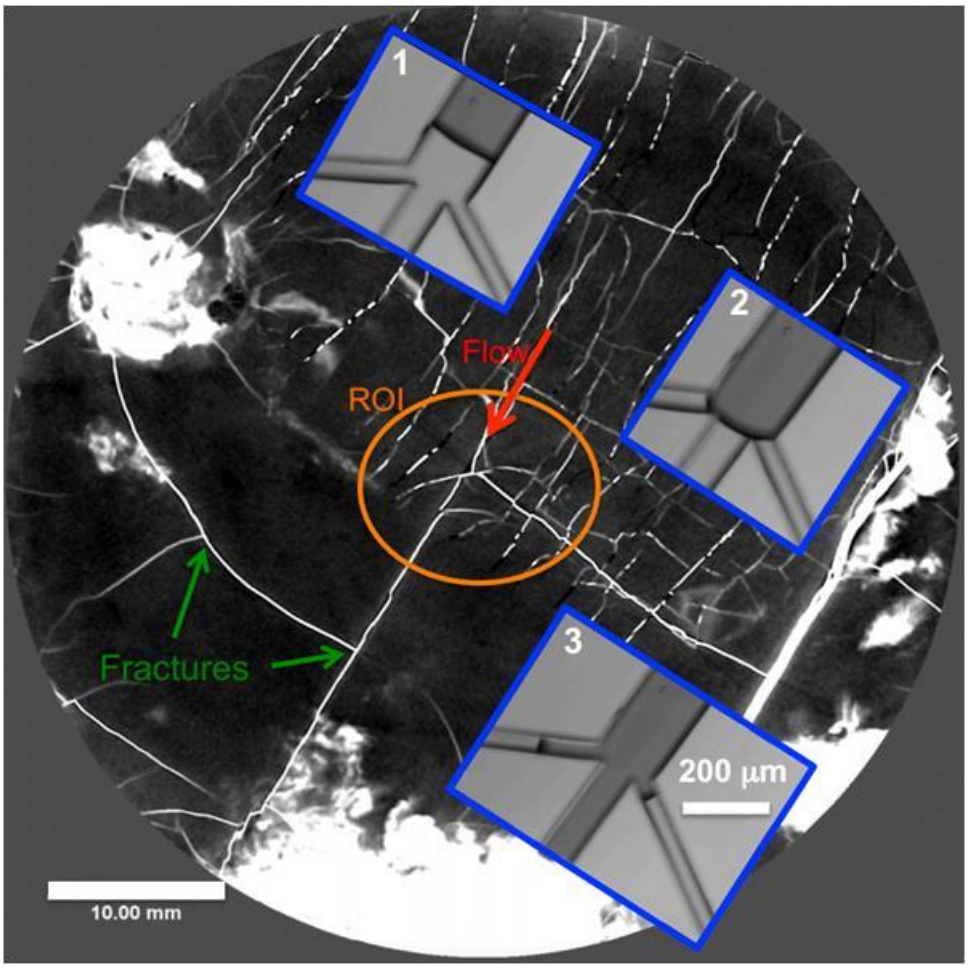

Figure 4: A 2D slice of the micro-CT image of coal where a region of interest (ROI) is chosen to be fabricated. The displacement of air by water at three stages is shown on the fabricated model representing a junction of coal cleat system. The dimension and the shape of the fabricated micromodel is chosen based on measurement of the fracture aperture size of the micro-CT image.

CONCLUSION AND FUTURE WORK

A novel workflow for investigating the effect of cleat topology and geometry on fluid flow in coals is discussed. Coal is imaged at dry and wet conditions. This allows for visualisation of sub-resolution cleats in the image. An original segmentation method is used to extract the cleat network from the micro-CT data. Numerical simulation of flow shows that the cleat systems have very narrow connection that needs to be honoured in the segmentation. A unique feature of the cleat system is fabricated for microfluidic flow experiments. Preliminary flow experiments are performed to capture the interface between brine and air and to understand transport at cleat junctions. In future, we will conduct several experiments on a range of observed topological features in coals. This data presented herein is the first stage of an ongoing research effort to better understand flow in coal seam gas reservoirs.

REFERENCES

1. Aminian, K., Rodvelt, G., Chapter 4 – Evaluation of Coalbed Methane Reservoirs, in Thakur P., Schatzel S. and Aminian K. (Eds) .*Coalbed Methane*, Elsevier, Oxford, (2014), 63-91.
2. Cai, Y., Liu, D., Mathews, J., Pan, Z., Elsworth, D., Yao, Y., Li, J. Guo, X., "Permeability evolution in fractured coal," *International Journal of Coal Geology*, (2014) **122**,91-104.
3. Dawson, G., Esterle, J., "Controls on coal cleat spacing", *International Journal of Coal Geology*, (2010) **82**, 213-218.
4. Flores, R., Chapter 5 – Coal composition and reservoir characterization, in Thakur P., Schatzel S. and Aminian K. (Eds). *Coalbed Methane*, Elsevier, Oxford, (2014), 93-100.
5. Golab, A., Ward, C., Permana, A., Lennox, P., and Botha, P., "High-resolution three-dimensional imaging of coal using microfocus X-ray computed tomography with special reference to modes of mineral occurrence," *International Journal of Coal Geology*, (2013) **113**, 97-108.
6. Latham, S., Varslot, T. and Sheppard, A., "Image registration: enhancing and calibrating X-ray micro-CT imaging," *International Symposium of the Society of Core Analysts*, (2008) Abu Dhabi, UAE.
7. Laubach, S., Marrett R., Olson, J., and Scott A., "Characteristics and origin of coal cleat: A review," *International Journal of Coal Geology*, (1998) **35**, 175-207.
8. Liu, S., Sang S., Liu H., and Zhu, Q., "Growth characteristics and genetic types of pores and fractures in a high rank coal reservoir of southern Qinshui basin," *Ore Geology Reviews*, (2015) **64**, 140-151.
9. Yao, Y., Liu, D., Che, Y., Tang, D., Tang, S., and Huang, W., "Non-destructive characterization of coal samples from China using microfocus X-ray computed tomography," *International Journal of Coal Geology*, (2009) **80**, 113-123.

DETERMINATION OF PHYSICAL PROPERTIES OF TIGHT POROUS MEDIA USING DIGITAL CORE PHYSICS/ANALYSIS

Shahin Ghomeshi, Saeed Taheri, Evgeny Skripkin, Sergey Kryuchkov,
Apostolos Kantzas
University of Calgary

This paper was prepared for presentation at the International Symposium of the Society of Core Analysts held in St. John's Newfoundland and Labrador, Canada, 16-21 August, 2015

ABSTRACT

In this study we use pore-scale SEM images of tight porous media, and generate threholded binary images which are then used to reconstruct three-dimensional (3-D) pore structures. Computational physics is then employed in order to calculate the physical properties of the porous media, such as the porosity, permeability, electrical resistivity and formation factor, and the NMR spectra. This involves generating an unstructured 3-D grid in the pore space in which we solve the corresponding governing equations. The original thresholded images have high resolution which allows a more precise masking of the pore spaces. However, there is a high computational cost associated with the high resolution images. Reducing the resolution will reduce the mask precision in the pore areas and this will lead to a different numerical solution. Therefore, we much optimize between the computational cost and accuracy when performing the numerical simulation. The threshold values for the samples at hand were selected by trying to match porosity and permeability of a neighboring plug. The choice of threshold value has a profound effect on the porous medium properties. For the fluid flow calculations, we solve the velocity and pressure in the pore space by solving the Navier-Stokes equations and using the results to obtain the absolute permeability. The electrical resistivity is obtained by solving for the current density through Ohm's law, and for the NMR study we solve for the equations of molecular diffusion. This approach can be described as a version of digital core analysis (DCA) or digital core physics (DCP).

INTRODUCTION

The main goal of this work is to characterize and determine the physical properties in tight porous media from actual pore samples of a tight formation. The method we employ is based on a computational physics approach where we discretize the 3-D structure into a computational mesh where the governing equations are then solved.

This study uses three scanning electron microscope (SEM) images of the tight sample as in Figure 1, and poses a method for numerically determining the physical properties of the reconstructed image, which includes the porosity, absolute permeability, electrical

resistivity and formation factor, and the NMR spectra. We then compare and validate the results to the experiment.
There are several challenges associated with this task. The main challenges include: the 3-D reconstruction of the sample with only three 2-D images, the effect of different threshold of the 2-D images on the calculation of the physical properties, and the computational cost involved in the solution to the 3-D heterogeneous (therefore noted as "upscaled") geometry.

The work here relies on 3-D reconstruction based on only three SEM images. Previous approaches of reconstruction include the work of Okabe and Blunt [1, 2] which reconstructed porous media based on only a single training image. A major assumption for them is that they assumed isotropy where the measured statistics on the XY plane is transformed to the XZ and YZ planes. We do not make such assumption in this work as several images were extracted directly from the given SEM images and used to recreate a 3-D digital porous media pattern.

The SEM images are 5120 × 3828 pixels (~ 637 × 476 microns) and are highly heterogeneous with large range of grain sizes. We provide a given tolerance for the different grain sizes into small, medium, and large. The smallest grains have bounding boxes ranging in size from 2×2 microns to 10×10 microns, the medium sized grains are from 10 × 10 microns to 50 × 50 microns, and the large grains have bounding boxes larger than 50 × 50 microns. The images are then decomposed into permeable domains and non-permeable domains, where the non-permeable domains include the large and medium sized grains. The permeable domains are at sub-pore scales where we extract from the original image to include the small grain sizes with tiny pores in between (Figure 2). We crop 33 of these images which are 256 × 256 pixels (or ~32 × 32 microns) from the three available SEM images. More images are required in order to reproduce a 3-D structure where we will perform pore-scale simulations. We do a spline interpolation between the greyscale of each 2-D image cropped images, in order to produce more 2-D images which we use to reconstruct the 3-D structure as show in Figure 3.a.

We perform pore-scale numerical simulations to calculate the permeability, resistivity and formation factor for the reconstructed geometry. The reconstruction, modeling and simulating process is an approach that is used in the areas of digital rock physics (see for example, [3, 4]) for understanding the macroscopic rock properties. Here we ignore the effects of adsorption, and assume that we are in the regime where the Navier-Stokes equations apply. For the permeability calculations we impose a simple pressure inlet condition and a 0 outlet condition, and solve the Stokes' equation to calculate average velocity of the flow within the pores as shown in Figure 3.b. Using the velocity and pressure profiles, we then back calculate the Darcy equation to obtain the permeability. We change the inlet and outlet, and calculate the permeability in different directions. Resistivity and formation factor calculations are obtained by solving for the current density using Ohm's law, see Figure 3.c. The calculated properties of the porous media

are tabulated in Table 1. We also solve the equations of molecular diffusion and evaluate the NMR spectrum which is shown in Figure 3.d.

Following the pore-scale computations, we use the obtained values as properties of the permeable domain, while the grain properties are set to zero. We then solve for the fluid properties of the complex upscaled geometry. The upscaled geometry is constructed by using imageJ and tracing out the large and medium sized grains from the three SEM images, as seen in Figure 4.a. In order to represent the 3-D structure of the grains, we apply a dilation / erosion algorithm in several slices for both the medium and large sized grains as seen in Figure 4.b. The final set of images is then assembled by merging the medium and large grains together as shown in Figure 4.c. We then used these composite images in order to re-construct the upscaled representative geometry of the original image (see Figure 5.a) based on the three SEM images. In between the medium and large grains we assume a permeability of 3 μD in the z-direction as seen from Table 1. The porosity φ will be given by

$$\varphi = \begin{cases} 0 & \text{On medium and large grains} \\ \varphi_0 & \text{Everywhere else} \end{cases} \quad (1)$$

where φ_0= 0.09 from Table 1. The porosity of the upscaled geometry will then be the averaged porosity φ_{av} over the entire volume V given by

$$\varphi_{av} = \frac{\int \varphi \, dV}{\int dV} = \frac{2.015 \times 10^{-12} \ m^3}{2.8663 \times 10^{-11} \ m^3} \cong 0.07 \quad (2)$$

We assume Darcy flow where the permeability is given by

$$\kappa = \begin{cases} 0 & \text{On medium and large grains} \\ \kappa_0 & \text{Everywhere else} \end{cases} \quad (3)$$

where k_0 is the permeability of the cropped region (Figure 3.a). This resulting pressure and velocity profiles is then used to calculate the average permeability of the medium (Figure 5). Using Darcy's law, assuming incompressible fluid, we have

$$\nabla . \rho \boldsymbol{u} = 0 \,, \quad \mathbf{u} = -\frac{\kappa_0}{\mu} \nabla \mathrm{p}, \quad (4)$$

where μ is the viscosity of the fluid, and ρ is the density. We inject a velocity of $1.0 \times 10^{-7} \ m/s$ at the inlet in the x-direction and a pressure of 0 Pa at the outlet. This will result in a $\Delta \mathrm{p} = 6818$ Pa (see Figure 5. b). The average permeability will then be given by

$$\kappa = \frac{u_p \, \mu \, \Delta L}{\Delta p}, \quad (5)$$

where $u_p = u \, \varphi_{av}$ is the Darcy velocity at inlet, which will lead to the result of 6.9 μD.

CONCLUSION

A new approach of imaging and computing is presented in this paper for determining the petro-physical properties in tight formations using SEM images. SEM-CT images give higher resolution than micro-CT images and can handle smaller sized pores specifically in tight pores. This approach allows us to reconstruct the 3-D image based on only three SEM images and to numerically simulate various physical properties in this digital object such as permeability, porosity, electrical conductivity, and NMR.

The new component of the work relies firstly on the fact that images were not statistically created and we do not make any isotropy assumptions. Images are extracted directly from three SEM images provided. The only assumption is that the correlation length in the z-direction is the same as in the x and y directions.

Secondly, the reconstructed cropped images which are $256 \times 256 \times 256$ pixels lead to relatively high number of pores, approximately 10,000 – 15,000. At this number of pores the properties of the sample is same as what will be observed at much bigger sample. Therefore we performed the pore-scale simulations at the lower scales and then attempted early upscaling where we started describing the flow as Darcy flow.

We note that these results were based on a given threshold, and for very tight media we must have a very high resolution in order to be able to capture very low porosities without losing connected pores. Moreover, based on our grey scale, we assume pore regions which instead could have been organic material with nano sized pores. This would complicate gas flow simulations that would be necessary to take into account the effects of adsorption. This would in turn lead to different set of governing equations.

ACKNOWLEDGEMENTS

We would like to acknowledge the financial support from NSERC AITP/i-CORE Industrial Research Chair in Modeling of Fundamentals of Unconventional Resources, and the sponsoring partners: Alberta Innovates, Athabasca Oil Corporation, Brion Energy, Canadia Natural, Devon Foundation CMP, Husky Energy, Laricina Energy LTD., NSERC, Schulich School of Engineering-University of Calgary.

REFERENCES

1. Okabe, H., Blunt, M. J., "Prediction of permeability for porous media reconstructed using multiple-point statistics," *Phys. Rev.*, (2004) E**70**, 6, 066135.
2. Okabe, H., Blunt, M. J., "Pore space reconstruction using multiple-point statistics," *J. Petroleum Science and Engineering*, (2005) **46**, 121-137.
3. Andrä, H. *et al.*, "Digital rock physics benchmarks-Part I: Imaging and segmentation," *Computers and Geosciences*, (2013) **50**, 25-32.
4. Andrä, H. *et al.*, "Digital rock physics benchmarks-Part II: Imaging and segmentation," *Computers and Geosciences*, (2013) **50**, 33-43.

Table 1: Tabulated results from the pore-scale simulations

Porosity	Resistivity, Ω.m	Permeability, μD		
		K_x	K_y	K_z
0.09	145	3.0	2.3	9.2

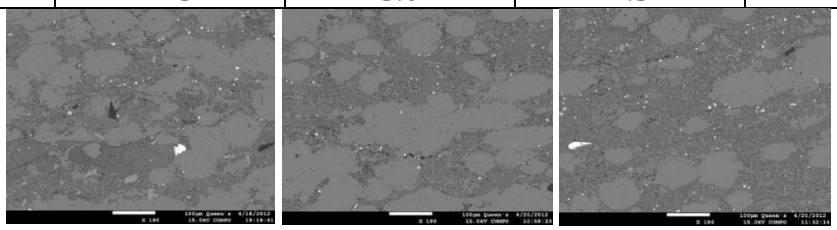

Figure 1: Three SEM images of a tight formation

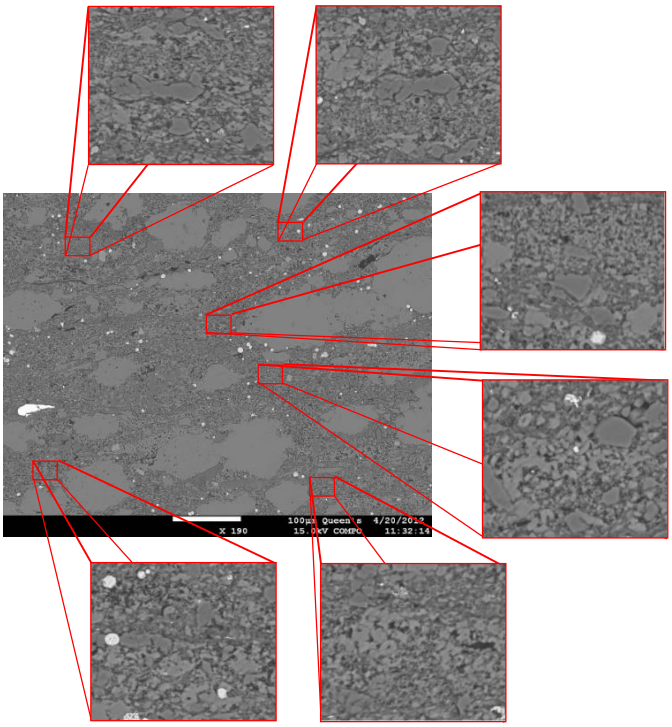

Figure 2: Several Cropped images from SEM images

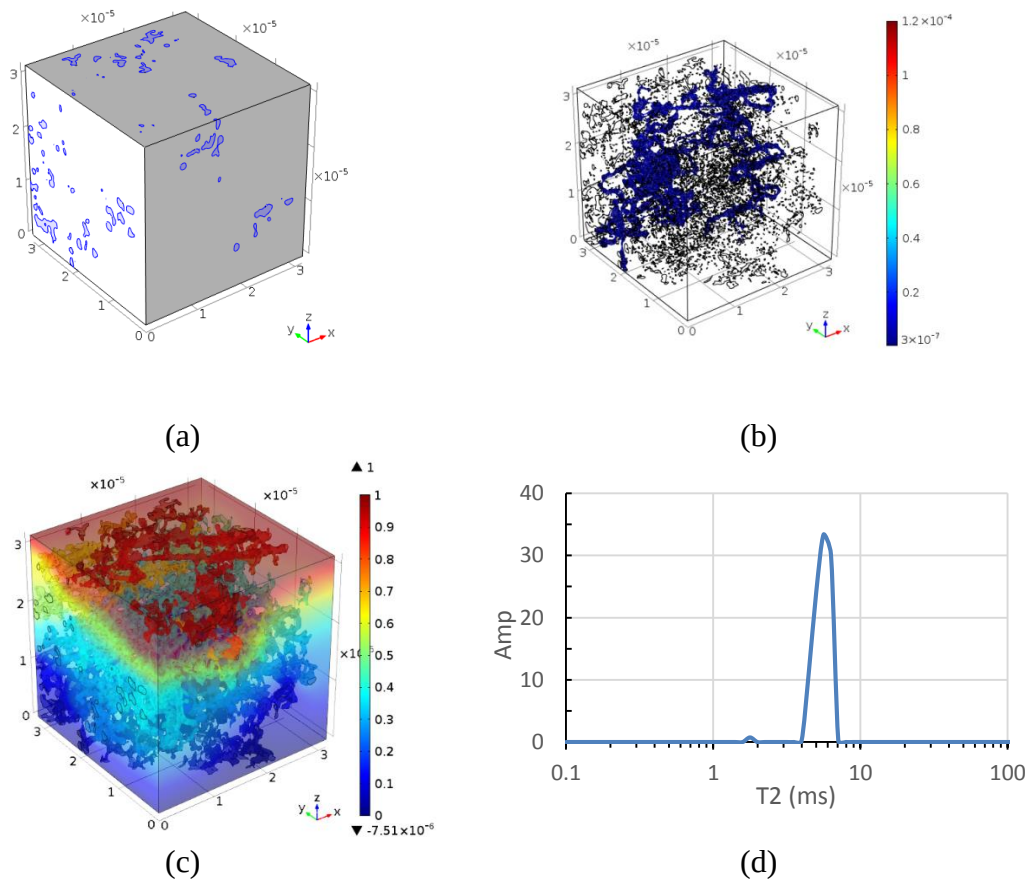

Figure 3: (a) computational domain (b) permeable regions, (c) current density (d) NMR spectra

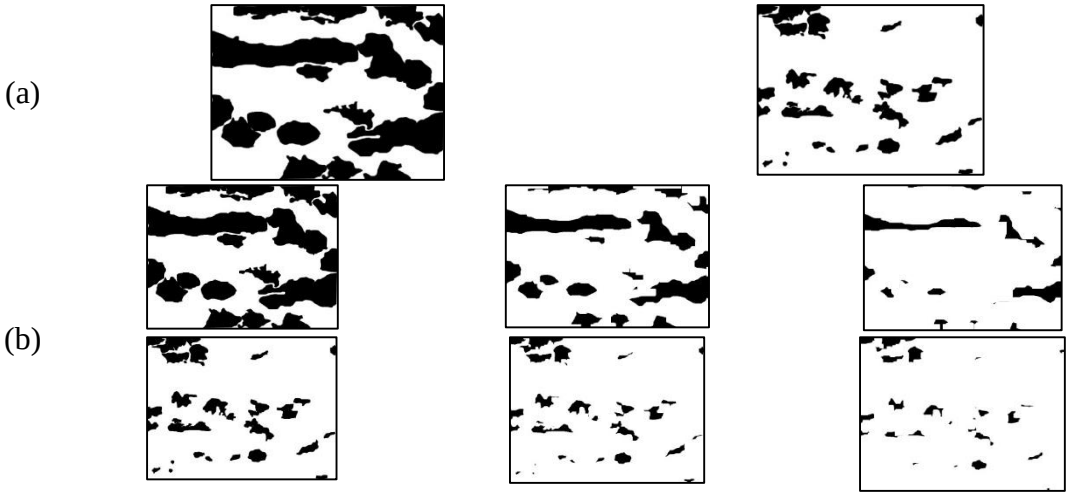

(c)

Figure 4: (a) large and medium sized grains, (b) dilation sequence (c) merging of the large and medium grains

(a)

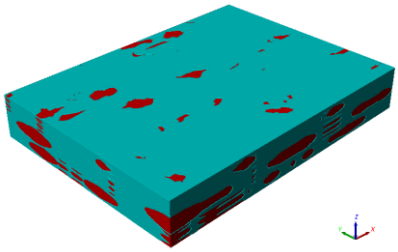

(b)

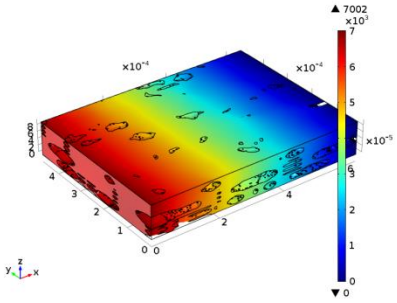

Figure 5: a. Upscaled geometry with dimensions 637 μm ×475 μm ×96 μm, b. Surface pressure profile for the upscaled geometry

PORE-SCALE OBSERVATION OF RESIDUAL OIL IN LOW SALINITY SURFACTANT FLOODING

Hamid Hosseinzade Khanamiri, Ole Torsæter, Norwegian University of Science and Technology; Jan Åge Stensen, Sintef Petroleum Research

This paper was prepared for presentation at the International Symposium of the Society of Core Analysts held in St. John's Newfoundland and Labrador, Canada, 16-21 August, 2015

ABSTRACT

Low salinity water injection provides favorable conditions for chemical enhanced oil recovery (EOR). Lower surfactant adsorption and lower chemical consumption is an advantage of combined low salinity water and surfactant injection. However at lower ionic strength the value of interfacial tension (IFT) is usually higher than the IFT at higher or optimal salinities. Recently it has been found that existence of small amount of calcium in low salinity surfactant can reduce the oil/water IFT. In this work, a coreflooding experiment is performed at the micro-CT scale. In tertiary injection the surfactant solution contained only NaCl, while the after-tertiary surfactant injection contained both NaCl and $CaCl_2$. After every step, the sample was scanned to observe the saturation and distribution of residual oil. It was observed that calcium-enhanced low salinity surfactant mobilized and recovered mainly the residual oil clusters which were affected but not recovered by tertiary surfactant. The oil which was not affected by tertiary surfactant mainly remained unaffected. It was also observed that oil recovery by low salinity surfactant in pore scale was higher than in normal core scale flooding experiment. In other words, microscopic sweep efficiency by low salinity surfactant was stronger than the macroscopic sweep efficiency.

INTRODUCTION

Both surfactant flooding and low salinity waterflooding may improve oil recovery. The goal of this work was to search for possible improvements in the performance of the combined low salinity water and surfactant by only modifying the ionic composition instead of adding extra chemicals. Observation of residual oil in pore scale by micro-CT was used to examine outcomes of the flooding experiment.

EXPERIMENTAL MATERIAL

Rock. The rock sample had a diameter of 4mm and a length of about 10mm. The sample was extracted from a Berea outcrop sandstone plug with permeability in the range of 200-300mD. Porosity of the scanned portion was 15.9%.

Oil. The oil phase is mixture of a crude oil (Table 1) and *1-Iododecane*. The volume fraction of *1-Iododecane* and crude oil is 6/4 in the mixture. *1-Iododecane* increases the x-ray attenuation coefficient of oleic phase.

Table 1. Composition in weight % and physical properties of the crude oil, [1]

Composition (%)		Physical properties	
Saturates	61.19	TAN [mg KOH/g]	1.08
Aromatics	32.42	TBN [mg KOH/g]	1.16±0.35
Resins	4.93	Density, 15°C [g/cm3]	0.8582
Asphaltenes	1.46	Density, 60°C [g/cm3]	0.8252
		API gravity [°API]	33.5
		Viscosity, 15°C [mPas]	19.90
		Viscosity, 60°C [mPas]	4.07

Brines and Surfactant. Details of the experimental brines are given in Table 2. 500 mg/l of *sodium dodecylbenzenesulfonate* (*SDBS*) is used in surfactant injection steps.

Table 2. Ionic composition of the brines and IFTs; IFT of doped crude was impossible to be measured by spinning drop as denser phase (oil) is not transparent and water/surfactant drop is invisible.

Brine	NaCl mg/l	$CaCl_2.2H_2O$ mg/l	SDBS mg/l	TDS mg/l	Ionic strength mmol/l	IFT, only crude mN/m	IFT, only 1-Iododecane mN/m
in-situ	32500	-	-	32500	556.1		84
LSW-Na	3250	-	-	3250	55.61		88.7
LSS-Na	3250	-	500	3250	57.05	1.6	15.6
LSS-Ca	3087.5	136.2	500	3690	57.05	0.33	-
HSW-Na	32500	-	-	32500	556.1	-	84

EXPERIMENTAL PROCEDURE

The rock sample was mounted in the micro-CT core holder, vacuumed and then saturated with *in-situ* brine (Table 2). Oil was then injected to drain mobile water. EOR injection was started with low salinity sodium chloride brine (*LSW-Na* in Table 2). Low salinity surfactant injection with sodium chloride (*LSS-Na*) was then performed. The next step was also low salinity surfactant injection. The difference was that small amount of sodium was replaced by calcium (*LSS-Ca*). Final injection was high salinity sodium chloride brine (*HSW-Na*). The experiment was performed at 27°C and atmospheric pressure. At the end of *LSW-Na*, *LSS-Na*, *LSS-Ca* and *HSW-Na* the injection was stopped and core holder was isolated for about 1hour to scan the sample. The sample was also scanned before saturation (dry scan) and afterward at initial state with connate water and initial oil. The details of injection experiment are given in Table 3. The scans were performed by micro-CT Skyscan 1172 with a resolution of 5.44µm/pixel.

Table 3. Details of EOR injection, the PVI (pore volume injected) is calculated roughly based on the pore volume of the whole sample (≈0.02cm3) with length of 10mm, while the scanned length is 6mm.

Injection	Flow rate (ml/min)	Equivalent pore velocity (ft/day)	Duration (min)	PVI	Scan name	Initial So	Final So	Rec. % OOIP
Oil injection	0.004-0.04	10-95	88	36.6	1-soi	0	0.864	-
	0.002	4.7	60	6	-	-	-	-
LSW-Na	0.004	9.4	30	6	-	-	-	-
	0.008	18.8	30	12	2-sorlsw	0.864	0.636	26.4
LSS-Na	0.008	18.8	93	37.2	3-sorlssna	0.636	0.529	12.4
LSS-Ca	0.008	18.8	93	37.2	4-sorlssca	0.529	0.426	11.9
HSW-Na	0.008	18.8	30	37.2	5-sorhsw	0.426	0.317	12.7
Total						**0.864**	**0.317**	**63.3**

RESULTS AND DISCUSSION

Image processing was performed using *CTAn*. The difference of gray scale index (GSI) between oleic and aqueous phases is about 100 units in the interval of 0-255. This large difference makes the fluids segmentation less subjective.

Although measurement of produced oil in micro-CT flooding experiments are almost impossible, oil recovery during all four steps of injection was observed. It was also observed that the recovered oil by *HSW-Na* in the last injection was in form of emulsion as opposed to larger oil clusters produced during low salinity water and surfactant flooding steps. The emulsions were formed at improved phase behavior of surfactant at higher salinity. The salinity of *HSW-Na* is close to the optimal salinity of surfactant solution with un-doped crude at elevated temperature of 60°C. Interfacial tension between crude and surfactant was about 0.005mN/m in that condition.

The saturation profiles are given in Figure 1. The average saturations and recoveries based on original oil in place are also given in Table 3. The recovery of low salinity waterflood was 26.5% which seemed to be lower than waterflooding recovery in normal cores. The reason might be the high density of oil phase which is 1.1g/cm^3 due to addition of *1-Iododecane*. High density difference may not cause strong segregation in micro scale but it may bring fingering of the injected water. Another reason would be the high IFT of dopant agent with brine which is about 80mN/m (Table 2). On the other hand the recovery of *LSS-Na* is 12.4% which is 9% higher than the recovery in normal core scale performed using the same rock type, though the oleic phase and experimental conditions were different. Specifications of normal core flooding experiment are summarized in Table 4. There is also 11.9% oil recovered in the *LSS-Ca* step. This high difference of recoveries by surfactant in pore scale and normal core implies that microscopic sweep efficiency of oil by surfactant is stronger than its macroscopic sweep efficiency.

Table 4. Specifications of the normal coreflooding experiment – both µCT sample and normal core were extracted from an identical Berea block

length	9.9cm	Crude	crude in Table 1
diameter	3.8cm	In-situ brine	*in-situ* in Table 2
k	309mD	1st flood (LSW-Na) recovery	51.5% OOIP
Ø	15.5%	2nd flood (LSS-Na) recovery	3% OOIP
Soi	76.7%	*Flooding at 60°C*	*Aging after drainage: 3 weeks at 80°C*

Further, the saturation profiles in Figure 1 show that although in many parts of the sample oil mobilization occurred; in the two intervals of 3200-3500µm and 5800-6100µm low salinity surfactant with sodium (*LSS-Na*) could not mobilize oil. However in the next step (*LSS-Ca*) oil mobilization occurred. This extra oil mobilization at 3200-3500µm was most probably produced. If it was trapped again, the oil saturation at some part of the sample ahead of this point would have increased resulting in higher residual oil saturation than the previous surfactant injection (*LSS-Na*).

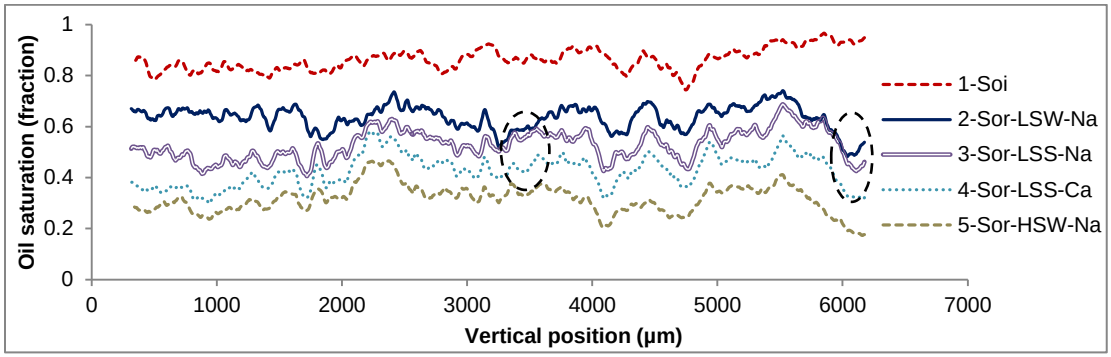

Figure 1. Oil saturation profile at initial condition (1-Soi) and after every injection (Sor's); the two dashed ovals represent two parts of the sample where LSS-Na was ineffective while LSS-Ca could mobilize and recover oil.

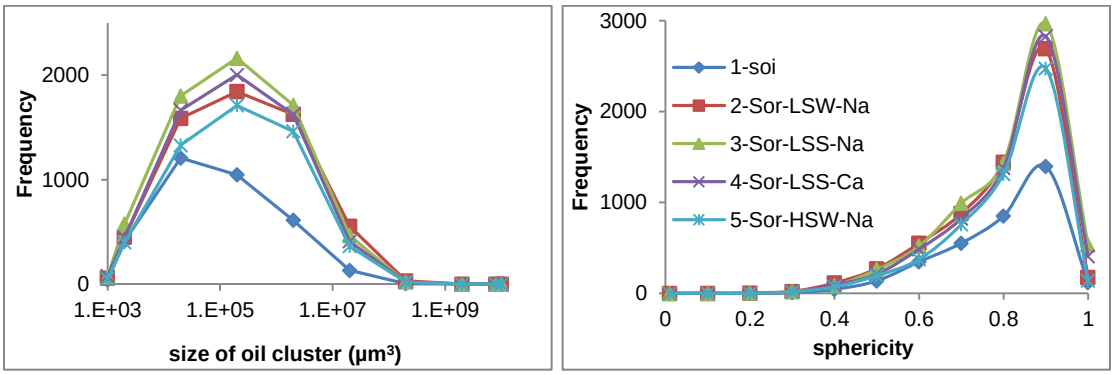

Figure 2. Oil cluster size (left) and sphericity (right) distribution at initial conditions and after every flooding

As shown in Figure 2 (left), number of oil clusters is minimum at initial conditions (*1-Soi*). The number has a sharp rise after low salinity waterflooding (*2-Sor-LSW-Na*). Afterwards, number of clusters increases slightly during low salinity surfactant with sodium (*3-Sor-LSS-Na*), while it decreases after the second surfactant injection with calcium (*4-Sor-LSS-Ca*). The sphericity of the oil clusters, Figure 2 (right), has similar trend in different steps of the experiment. Sphericity of a normal sphere is 1 and as the cluster becomes more irregular in shape, sphericity tends to 0. Normally sphericity of smaller clusters is more than that of larger ones.

1-Soi and 2-Sor-LSW-Na. Comparison of the low salinity water images with initial conditions shows that whenever oil is mobilized in a small pore the whole oil is often swept out the pore (Figure 3-A) while in medium pores some oil is left behind in form of trapped oil in the corner of pore (Figure 3-B). In larger pores the residual oil has more rounded profile and is mainly in the middle of the pore (Figure 3-C). This means that although the viscous force was high enough to invade the large pore it just peeled and displaced layers of oil instead of pushing the whole drop out of the pore. It was also observed that there was residual oil at some points where it was initially occupied by connate water (Figure 3-D). This type of residual oil was certainly mobilized initially but re-trapped later.

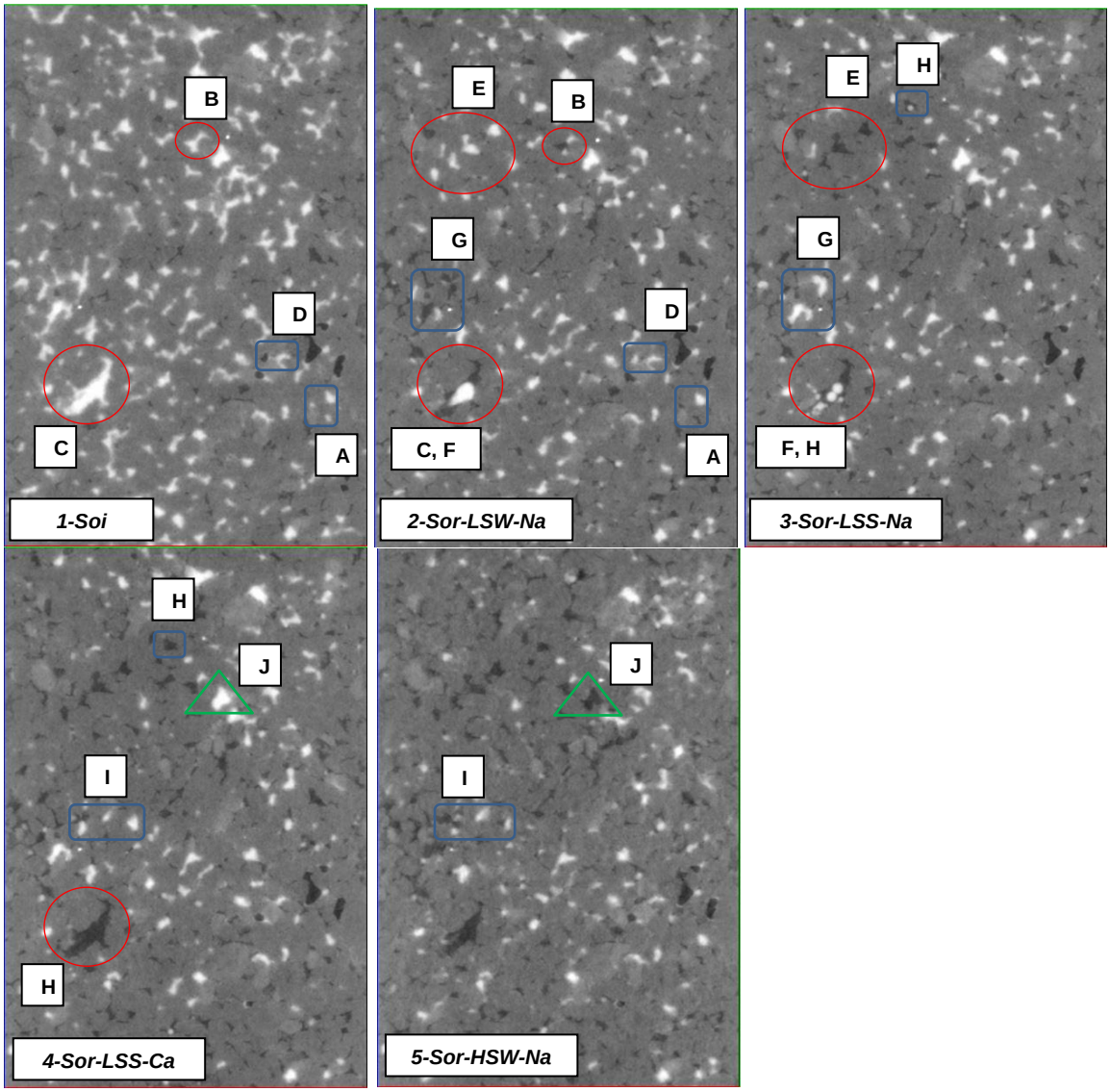

Figure 3. A vertical cross section of the cylindrical rock sample (D≈4000µm & L≈6000µm) after different steps; the injection was from top to bottom. Oil is the white phase and water is dark one.

2-Sor-LSW-Na and 3-Sor-LSS-Na. There are many small and medium pores where the whole residual oil after waterflooding or major part of it was displaced by first surfactant flooding, *Sor-LSS-Na* (Figure 3-E), while in larger pores oil was disintegrated into smaller (increase in number of oil clusters, Figure 2) and more rounded clusters (increase in sphericity, Figure 2) after layers of oil was peeled off (Figure 3-F). At some points, the mobilized oil was re-trapped again (Figure 3-G). The amount of this oil was 12.9%OOIP.

3-Sor-LSS-Na and 4-Sor-LSS-Ca. It seems that major part of the swept oil by calcium-assisted surfactant flooding (*LSS-Ca*) is the more spherical residual oil drops which changed their shape during previous surfactant injection (*LSS-Na*) (Figure 3-H). Reduction in sphericity and number of residual oil clusters after *LSS-Ca* was also

represented in Figure 2. Oil was rarely swept out of the pores which were not considerably affected by the first surfactant injection (*LSS-Na*). Moreover less oil was re-trapped after mobilization (only 4.8%OOIP compared to 12.9% in previous step). This is another advantage of *LSS-Ca* to *LSS-Na*. Although *LSS-Ca* could not effectively invade the relatively unaffected oil by *LSS-Na*, its oil recovery was 11.9% of OOIP which was a considerable amount of difficult residual oil after one step of surfactant injection (*LSS-Na*). This extra oil recovery was gained by only a minor change in ionic composition.

4-Sor-LSS-Ca and 5-Sor-HSW-Na. The mobilized oil by *HSW-Na* at some points is similar to the last surfactant injection where the more spherical oil clusters which were affected previously but not produced, were mobilized (Figure 3-I). However, oil mobilization was also observed in some pores where the two surfactant injections were ineffective (Figure 3-J). Coalescence of small and more rounded clusters occurred also (Figure 2). *HSW-Na* mixes with the surfactant from previous injection making a lower IFT surfactant solution. It seemed the mixing happened quickly as oil production was observed in form of emulsion just after some minutes of *HSW-Na* injection.

CONCLUSION

In the studied rock-fluid system with the mentioned experimental conditions it was observed that: calcium-enhanced low salinity surfactant recovered mainly part of the residual oil which was affected but not recovered by tertiary surfactant with only sodium. Oil re-trapping after mobilization by *LSS-Ca* is less than by *LSS-Na*. Comparison of recoveries in micro scale with those of normal core flooding implied that microscopic sweep efficiency of low salinity surfactant was higher than its macroscopic sweep efficiency. Therefore investigating the effect of mobility control during or after low salinity surfactant seems to be necessary as it may help producing the bypassed oil.

ACKNOWLEDGEMENT

We would like to thank Lundin Norway AS, Statoil ASA, Det Norske Oljeselskap, GDF Suez, Unger Fabrikker AS and the Research Council of Norway for their financial support.

REFERENCES

1. Tichelkamp, T., Vu, Y., Nourani, M., Øye, G. 2014. Interfacial tension between low salinity solutions of sulfonate surfactants and crude and model oils. Energy Fuels 28, 2408−2414.

A MULTI-SCALE DYNAMIC PREDICTIVE MODEL FOR DRAINAGE AND IMBIBITION CAPILLARY PRESSURE IN HETEROGENEOUS ROCKS

X. Nie, C. Baldwin, Y. Mu, A. Grader and J. Toelke
Ingrain Inc

This paper was prepared for presentation at the International Symposium of the Society of Core Analysts held in St. John's Newfoundland and Labrador, Canada, 16-21 August, 2015

ABSTRACT

A multi-scale model for multiphase flow in heterogeneous rocks has been developed to predict drainage and imbibition porous plate capillary pressures. The need for such a simulation model arises from the inability to image and simulate at high-resolution large enough volumes that are representative of multi-scale rocks. The overall distribution of the different resolutions is defined by multi-scale x-ray imaging. A representative volume from the micro-CT image is segmented into pores, solids and Darcy regions with unresolved pores. The properties of Darcy region are further determined by separate high-resolution imaging and multiphase flow simulations for a smaller volume. Two-phase flow in the pore space is directly simulated using a lattice-Boltzmann model. Pore size in the Darcy region is smaller than the resolution of the lattice-Boltzmann simulation. The flow entering or exiting a Darcy region is determined by the fluid phase and its pressure around the Darcy region and the intrinsic properties of the Darcy region like the porosity and the Pc-Sw relationship. The boundary condition of the lattice-Boltzmann simulation on the surface of a Darcy region depends on the solid wettability and the fluids present in the Darcy region. The fluid distributions in pores and Darcy regions, and therefore the boundary conditions for different regions dynamically change with the applied capillary pressure. The multi-scale model has been used to compute the displacement parallel and perpendicular to a layered system packed with solid spheres of different size and compared to a fully resolved simulation to validate the model.

INTRODUCTION

The capillary pressure (Pc) and relative permeability in drainage and imbibition processes are important inputs for reservoir simulations. The capillary pressures have been experimentally measured in a core or a plug [1-3] for many decades. Recently digital core analysis has become an important alternative method. In the digital analysis, the rock geometry is digitized into a 3D matrix data to represent solids and pores by computerized tomography (CT). To calculate the transport of multiphase flow, either pore network model or direct simulation can be used. The pore network model replaces real pore bodies and throat shapes with simple geometric shapes [4, 5]. The fluid transport and distribution are determined by coupling semi-analytical solutions for the individual

elements. The lattice-Boltzmann method (LBM) is a direct simulation method [6, 7]. The LBM solves a simplified kinetic equation and directly simulates the fundamental equations of multiphase flow in pores in a digitized rock sample.

This study develops a dynamic multi-scale model to calculate the capillary pressures in drainage and imbibition processes in heterogeneous rocks based on the LBM method. Different digital resolutions are assembled into a representative flow unit volume. The model is validated by digital porous plate experiments of a system packed with different sizes of solid spheres.

MATERIAL AND SIMULATION METHODS

In our multi-scale simulation, the distribution of different resolutions of the structure of a rock sample is determined by multi-scale x-ray imaging. A representative volume from the coarse micro-CT image is segmented into pores, solids and Darcy regions. Pore size in the Darcy region is smaller than the coarse micro-CT. Small volumes of Darcy regions are further imaged by a separate higher-resolution micro-CT or nano-CT acquisition and segmented into pores and solid. The Pc curves and the breakthrough pressures of Darcy regions are determined by the LBM simulation in the high-resolution volumes. These properties are assigned to the Darcy regions.

Now the two phase flow in the whole representative volume is simulated using the dynamic multi-scale LBM simulator. Two-phase flow in the resolved pore space is directly simulated using the LBM. The flow entering or exiting a Darcy region is determined by the fluid phases around the Darcy region, the Pc curves and the breakthrough pressures of the Darcy region. In the drainage process the Darcy region is first occupied by water. If a Darcy region contacts with oil phase, the oil enters the Darcy region gradually as the capillary pressure increases. The amount of oil entering the Darcy region at each time step of the LBM simulation is determined by the Pc curve of the Darcy region and the capillary pressure at that time step. When the capillary pressure becomes larger than the breakthrough pressure the oil is allowed to pass through the Darcy region. In the imbibition process, a Darcy region may be first completely or partially occupied by oil. If the Darcy region is connected to water through bulk water or a water film, the water enters the region gradually as the capillary pressure decreases. The amount of water entering the Darcy region is determined by the imbibition part of the Pc curve of the Darcy region.

We used the model in [8] to assign a contact angle at the interface between resolved pore space and Darcy region. The contact angle depends on the porosity, the intrinsic wettability and the fluid phases present in the Darcy region and is imposed through the interaction of LB nodes at the interface between Darcy region volume and resolved pore volume. The fluid distributions in pores and Darcy regions, and therefore the boundary conditions and the contact angle dynamically change with the applied capillary pressure.

In order to validate the multi-scale model, we simulated a digital porous-plate experiment [9] of a rock sample in a fine resolution that completely resolves all pores of the rock sample using a recently developed LBM solver [10]. Then we used the dynamic multi-scale model to simulate the porous-plate experiment of the same rock sample in a 10 times coarser resolution and compared the two results obtained from the two simulations. In the digital porous plate experiment [9], the one surface of the rock is attached to an oil reservoir and the opposite surface is attached to a water reservoir. The water pressure is kept constant throughout the simulation. In the drainage process the oil pressure increases step by step till the desired residual water saturation is reached. In the imbibition process the oil pressure decreases till it reaches the water pressure to simulate controlled spontaneous imbibition. In the recently developed LBM solver [10], we developed special boundary conditions at the solid wall to model thin water-film flows that allow transport of fluids through those thin films. These boundary conditions prevent e.g.: unrealistic high values of trapped water in the drainage and allow snap-off effects through the films in imbibition.

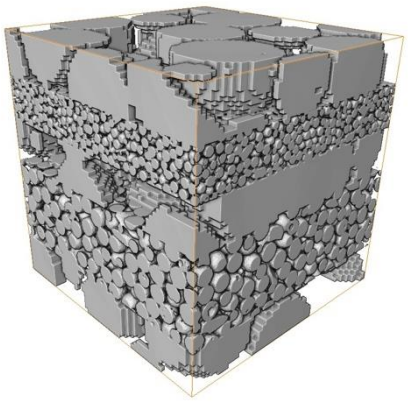

Fig. 1. The rock sample synthetized by packed solid spheres. The pixel size is 2 microns. The sample is a cube of 600^3 pixels. Three different pore sizes are present in the sample.

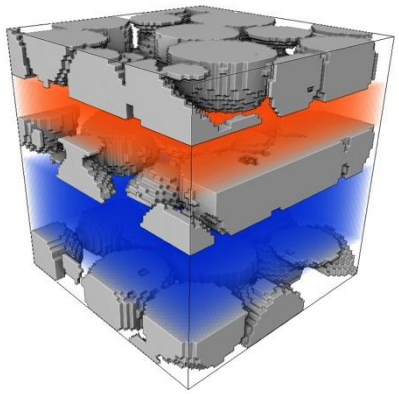

Fig. 2. The rock sample in figure 1 shown in a 10 times coarser resolution. The cube consists of 60^3 pixels. The pixel size is 20 microns. The pores in the Darcy regions colored by blue and red are unresolved.

As shown in Fig. 1, the rock sample was synthetized by packed solid spheres to simulate a multi-scale rock. The sample is a cube with side length of 600 pixels and is composed of 5 regions. The pixel size is 2 microns. In the resolution of 2 microns, all pores are resolved. Starting from the bottom, the thickness of the second region is 200 pixels and 100 pixels for each of the other four regions. The first, third and fifth regions have the largest pores. The second region has smaller pores and the fourth has the smallest. The average pore throat radii in the three different fabrics are 46, 9.2 and 4.6 microns respectively. The average pore radii in the three fabrics are 67, 13.4 and 6.7 microns respectively. The porosity of all regions is 0.4. Fig.2 shows the same rock sample in a 10 times coarser resolution. The sample is a cube with the side length of 60 pixels. The pixel size is 20 microns. The largest pores in the first, the third and the fifth region are still

resolved with the 20 micron resolution. The pores in the second and the fourth regions are unresolved. The capillary pressures as functions of water saturations and the breakthrough pressures of the two unresolved regions have been obtained by separate LBM simulations for the tighter rock fabrics at a resolution of 2 microns and were assigned to the corresponding Darcy regions in the multi-scale predictive LB model to simulate the whole sample.

RESULTS AND DISCUSSIONS

Two digital porous plate experiments of the rock sample shown in Fig. 1 and 2 were carried out (Case A and Case B) to validate the multi-scale model. In Case A, the bottom surface of the rock sample is attached to an oil reservoir and the top surface is attached to a water reservoir. In Case B, the left-front surface is attached to an oil reservoir and the right-back surface is attached to a water reservoir. The other side are walls with the properties of the rock. The multi-scale predictor was using the system with 60^3 grids points depicted in Fig.4 and the single-scale LBM solver was applied to the rock cube with 600^3 grids depicted in Fig.3. The interfacial tension was set to 0.03 Nm^{-1}. Strongly water wet conditions were assumed and a contact angle of 30 degree was used in the simulations. The sample is initially filled with water, then a drainage with oil as invading fluid follows and finally an imbibition with water as invading fluid is performed.

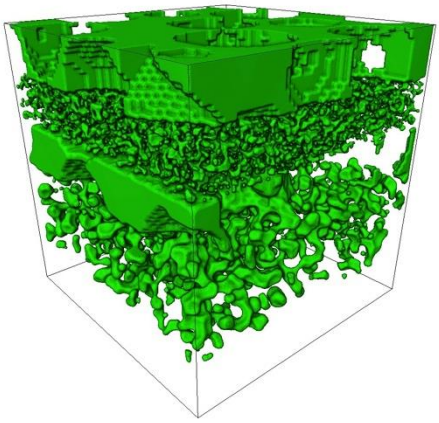

Fig. 3. Oil distribution after imbibition from the fully resolved LBM simulation for case A.

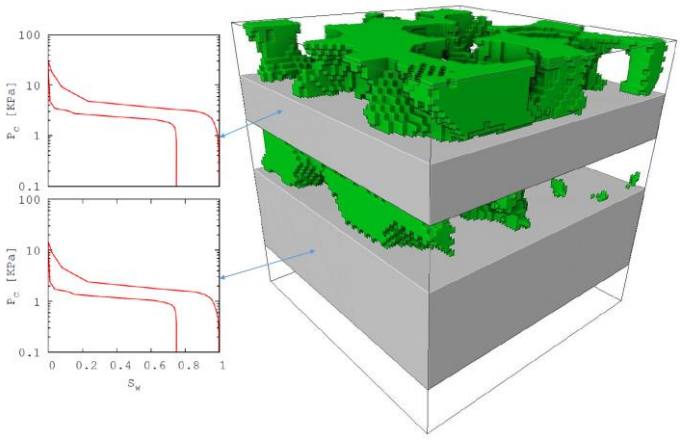

Fig.4 Oil distribution after imbibition from the multi-scale simulation for case A. Left Pc curves are from the separated high-resolution simulations in two Darcy regions.

Figs. 3 and 4 show the residual oil distributions after imbibition for Case A. The trapped oil distributions in regions 3 and 5 for the two simulations are very similar. The oil in pores of these two regions are almost completely trapped since the pore body to throat ratio is very large for this synthetic rock sample. As is shown in [10, 11] the residual oil saturation highly correlated with the pore body to throat ratio. The average pore body radius in the largest-scale pores is 67 microns and the pore throat radii in the two regions with small-scale pores are 4.6 and 9.2 microns respectively. The effective pore body to

throat ratio is 14.6 for the imbibition process in regions 4 and 5, and 7.3 for the imbibition process in regions 2 and 3. The trapped oil in the two small-scale pore regions is shown in Fig.3 for the fully resolved LBM simulation. In the multi-scale simulation the amount of residual oil in the two unresolved regions, colored in Darcy in Fig.4, are given by the residual oil saturation in the Pc functions shown in Fig.4 which were computed by separate fine scale simulations. Fig.5 shows the capillary pressures as functions of water saturations of the two simulations in Case A. Each region has a similar porosity of about 0.4, so that each region 1,3,4,5 contributes 17% and region 2 contributions 33% to the pore volume. After an incremental fill-up of region 1 (Sw=0.83..1), the breakthrough of oil in the second region is clearly visible. The third region has large throats and no incremental pressure is needed to enter that region. The second and third region (Sw=0.33..0.83) are filled after the breakthrough in the second region. The region 4 and 5 (Sw=0..0.33) are filled as the pressure further increases. The amounts of residual oil and the whole Pc curves of the two simulations agree very well. Fig.6 shows the capillary pressures as functions of water saturations of the two simulations in Case B. The two simulations produce fairly consistent capillary pressures. The first plateau of the pressure curve in the drainage part (Sw=0.5..1) indicates the breakthrough of oil in the largest pores in the first, the third and the fifth regions. Then a breakthrough in the second region (Sw=0.17..0.5) occurs and finally in region 4 with the smallest pore throats. The amounts of residual oil obtained from the two simulations agree very well. The amount of residual oil in Case B is smaller than in Case A since the flow direction in Case B is parallel to the layers and in Case A perpendicular. The imbibition process first happens in small-scale pore regions and then the large-scale pore regions. The effective pore body to throat ratio inside these regions is about 1.5. For Case A the effective ratio is much larger as discussed earlier.

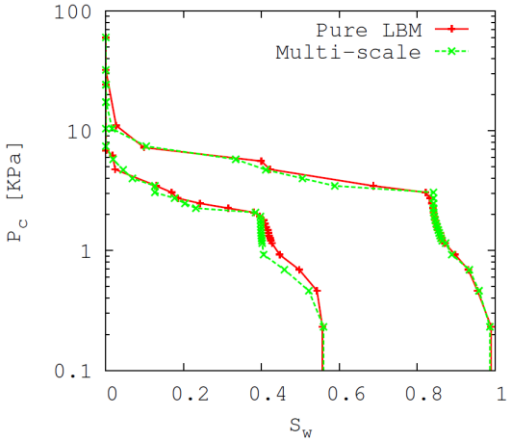

Fig. 5 Capillary pressures as functions of water saturations in Case A of the digital porous-plate experiments.

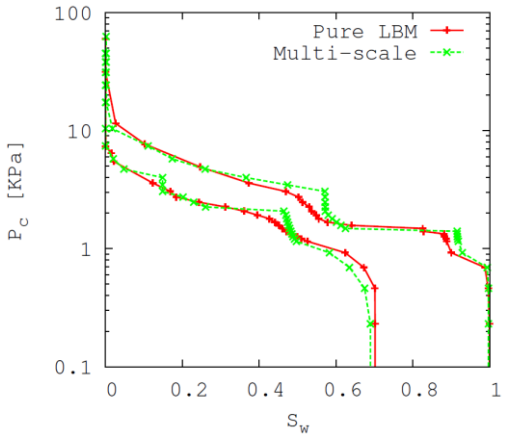

Fig. 6 Capillary pressures as functions of water saturations in Case B of the digital porous-plate experiments.

CONCLUSION

We have developed a dynamic multi-scale predictive model to determine two-phase flow distributions at certain capillary pressure for complex multi-scale rocks. The model was validated by two digital porous plate experiments of a synthetic multi-scale rock sample. The results of the multi-scale mode in a coarse grid agree well with these of a lattice-Boltzmann simulation in a 10 times finer grid that resolves all pores in the rock sample. The new multi-scale model differs from a common assembling approach that computes regions with different resolutions independently and then upscales in a post-processing operation to obtain the properties of the representative volume. The dynamic exchange of information about pressures and saturations between different regions in the multi-scale model improves the accuracy of the prediction.

REFERENCES

1. Jerauld G.R., "Gas-oil relative permeability of Prudhoe bay", SPE 35718 presented at the western regional meeting held in Anchorage, Alaska, (1996), pp 653-670. Text for References in Times New Roman 12 Point (margins justified),
2. Suzanne, K., Hamon, G., Billiote, J. and Trocme, V., "Distribution of Trapped Gas Saturation in Heterogeneous Sandstone Reservoir", Proceedings of the Annual Symposium of the Society of Core Analysts, SCA2001-14, Edinburgh, Scotland, UK.
3. Pentland, C., Tanino, Y., Iglauer, S., Blunt, M., Capillary Trapping in Water-Wet Sandstones: Coreflooding Experiments and Pore-Network Modeling. Paper SPE 133798 Proceedings of SPE Annual Technical Conference and Exhibition, Florence, Italy. 2010.
4. Spiteri, E.J., Hamon, Juanes, R., Blunt, M.J., and Orr, F.M. Jr. A New Model of Trapping and Relative Permeability Hysteresis for All Wettability Characteristics. SPE J. 13 (3) 277-288. SPE-96448-PA. doi: 10.2118/96448-PA.
5. Al-Futaisi1 A. and Patzek T. W., Impact of wettability alteration on two-phase flow characteristics of sandstones: A quasi-static description, Water Resources Research, V. 39, pp. 1042-1051, 2003.
6. Chen S, Doolen GD. Lattice Boltzmann method for fluid flows. Ann Rev Fluid Mech 1998; 30:329–64.
7. Nie, X., Martys, N.S., Breakdown of Chapman-Enskog expansion and the anisotropic effect for lattice-Boltzmann models of porous flow, Physics of Fluids, 19 (1), 011702-4, 2007.
8. A. B. D. Casseie and S. Baxter, Trans. Faraday Soc., 40, 546-551 (1944).
9. Mu, Y., Fang, Q., Baldwin, C., Toelke, J., Grader, A., Dernaika, M., and Kalam. Z., Drainage and imbibition capillary pressure curves of carbonate reservoir rocks by digital rock physics. Proceedings of the Annual Symposium of the Society of Core Analysts, SCA 2012-056, Aberdeen, Scotland, UK.
10. Nie X., Mu Y., Sungkorn R., Gundepalli V. and Toelke J., Numerical Investigation of the Dependence of Residual Oil Saturation on Geometry, Wettability, Initial Oil Saturation and Porosity, Proceedings of the International Symposium of the Society of Core Analysts, SCA2014-39, Avignon, France.

11. Aissaoui A., Etude théorique et expérimentale de l'hystérésis des pressions capillaires et des perméabilités relatives en vue du stockage souterrain de gaz, Thesis Ecole des Mines de Paris (1983), 223 p.

SAND CONTROL FOR UNCONSOLIDATED HEAVY OIL RESERVOIRS: A LABORATORY TEST PROTOCOL AND RECENT FIELD OBSERVATIONS

U.G. Romanova, M. Piwowar and T. Ma
Weatherford Laboratories Canada, Calgary, Canada

This paper was prepared for presentation at the International Symposium of the Society of Core Analysts held in St. John's Newfoundland and Labrador, Canada, 16-21 August, 2015

ABSTRACT

Sand production is one of the major challenges in oil and gas industry, in particular for unconsolidated heavy oil reservoirs. Achieving maximum well productivity without excessive sand production or plugging in such deposits requires new technical solutions and better understanding of reservoirs and sand control phenomena.

A laboratory protocol test has been developed for the sand control design for the heavy oil deposits located in unconsolidated reservoirs, both clastic and carbonate. The protocol allows evaluation of the different type of the sand control media (slotted liners, gravel packs, wire wrapped screens and premium screens). The protocol is used in sand control studies for thermal production operations and water disposal wells. Recent field data indicate that results of the laboratory tests are in a good agreement with field observations. The paper provides details of the laboratory test protocol and recent field data for Western Canada.

INTRODUCTION

Production of formation sand is one of the oldest problems in oil and gas industry [1]. Heavy, extra heavy oil and bitumen are often found in the unconsolidated, shallow, geologically young formations. Thermal technology based on steam injection such Cyclic Steam Stimulation (CSS) and Steam Assisted Gravity Drainage (SAGD) is effective for in situ production of heavy oil crude. As large volumes of water are utilized in such operations, disposal wells are often required. Sand control media which will allow maximum flow rates and minimal plugging or pressure build up is needed for both injection and production wells. Efficiency of sand control depends on a variety of factors such as geology, fluid type, fluid viscosity, production rates, thermal effects, etc.

Slotted liners (SL), gravel packs, wire wrapped (WWS) and premium screens are commonly used for sand control in unconsolidated heavy oil reservoirs. Straight cut (SC) and rolled top (RT) SL, standalone or with gravel packs, are commonly used in heavy oil and bitumen production operations. Pressure build up and lost production due to liner

plugging, corrosion and scale [2] are the main challenges for SL. WWS and premium screens, in particular as standalone screens, are becoming more popular due to a larger open flow area and resistance to corrosion.

Laboratory work to select sand control devices prior to well completion is required. Lost production and additional cost associated with acidizing, perforation, re-entry and side wells, etc. can be avoided with proper planning and laboratory testing.

LABORATORY TEST PROTOCOL

A laboratory protocol test has been developed for the sand control design for unconsolidated heavy oil reservoirs [3, 4]. The protocol was first used to evaluate SL for SAGD operations in unconsolidated sandstone. Later, the protocol proved to be successful in the evaluation of WWS and premium screens for both injection and production wells in thermal production operations other than SAGD, for both sandstone and carbonates, and for water disposal wells.

The protocol includes the following:

1. understanding geology of the reservoir and lithological facies, with the focus on particle size distribution;
2. obtaining typical reservoir core for each lithological facies;
3. core preparation for the study (cleaning, homogenization, etc.);
4. sand control coreflood tests; tests are conducted with a synthetic brine of the same composition as formation water, mineral oil of the same viscosity as viscosity of heavy oil/bitumen in situ under steam injection conditions in case of thermal production, laboratory test rates representing field rates;
5. analysis of produced fine solids and/or post test analysis of sand control coupons by epoxy impregnation and by means of scanning electron microscopy and X-ray energy dispersive spectrometry.

In a coreflood test, pressure differential across the sand pack, on top of the sand control media and the amount of produced fine solids versus production rates are measured. A schematic of the test apparatus is provided in Figure 1. Performance is evaluated by measuring weight of produced fines and increase in delta P. If more than 0.1 g of fines is produced or more than 5 psi delta P is developed, the sand control device is judged to be inadequate. These parameters are somewhat arbitrary and are used for the purpose to compare relative performance of different sand control devices.

Tests results provide data which allow the best possible sand control media for a particular reservoir and specific operational conditions to be determined. Such sand control media would minimize pressure build up and would provide the lowest amount of produced solids at the maximum production rates. The protocol also allows a better understanding of the sand control phenomena. The protocol has been used extensively for a variety of projects in Western Canada, California, Latin America and the Middle East.

Over 1000 tests have been conducted. In Western Canada, the protocol became an industry standard [5, 6].

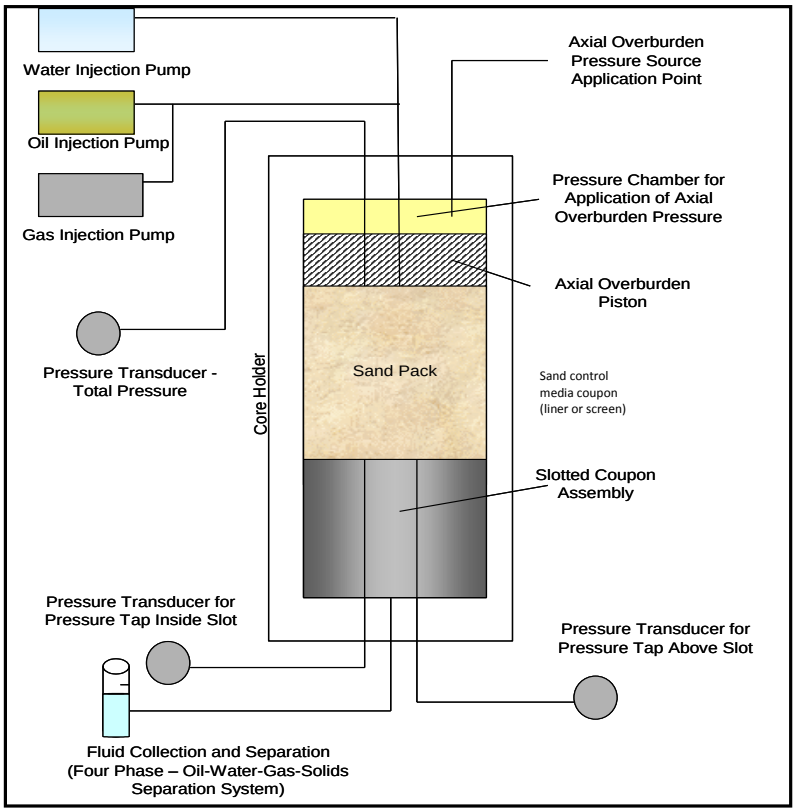

Figure 1. Schematic of sand control apparatus

TYPICAL TEST RESULTS

Formation of sand bridges on top of the sand control media and their stability under different flow conditions can be determined in the sand control experiments. Test results show that "the rules of thumb" commonly used for completion design for convention oil and gas do not apply to heavy oil. For example, instead of the rule of 2 x D10, where D10 is the grain-size diameter from the distribution scale where 10% by weight of the sand is of a larger size and 90% is of a smaller size, to determine the aperture of SC slot, one typically needs to use 1.8 x D10. This applies only to sand which has less than 5 wt% of fines, particles with less than 44 micron diameter. If sand has more than 5 wt% of fines, SL will likely fail and screens are a better option.

Typical results of sand control tests to simulate SAGD operations for unconsolidated sandstone (oil sands) from Western Canada are provided below. Delta P on top of sand control media versus different flow regime and production rates is shown in Figure 2. Amount of produced solids versus different flow regime and production rates is shown in

Figure 3. The test results presented in Figures 2 and 3 are reservoir specific and can be used as a reference only. However, the test results show a few typical trends.

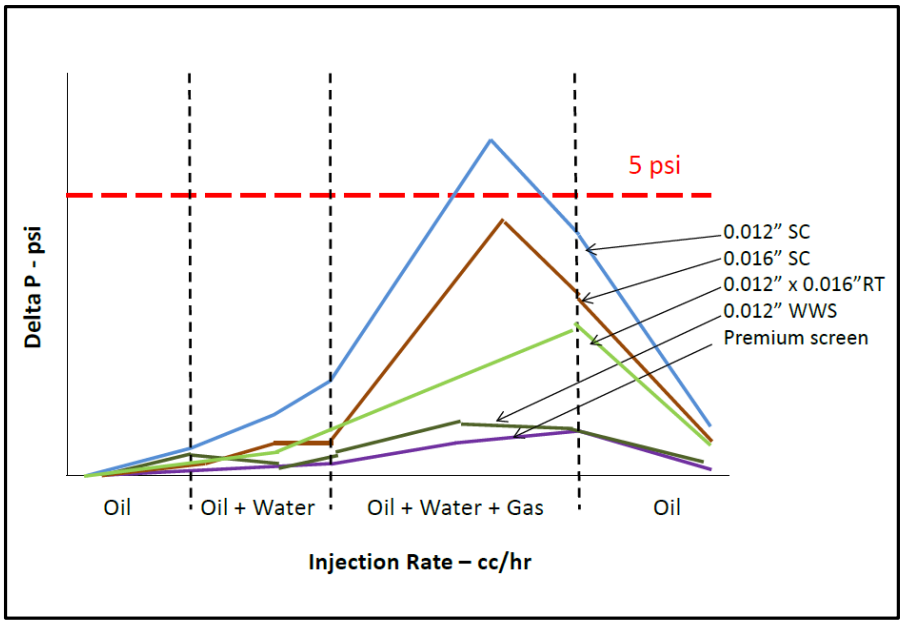

Figure 2. Delta P on top of sand control media versus different flow regime and production rates, SAGD operations, oil sands from Western Canada

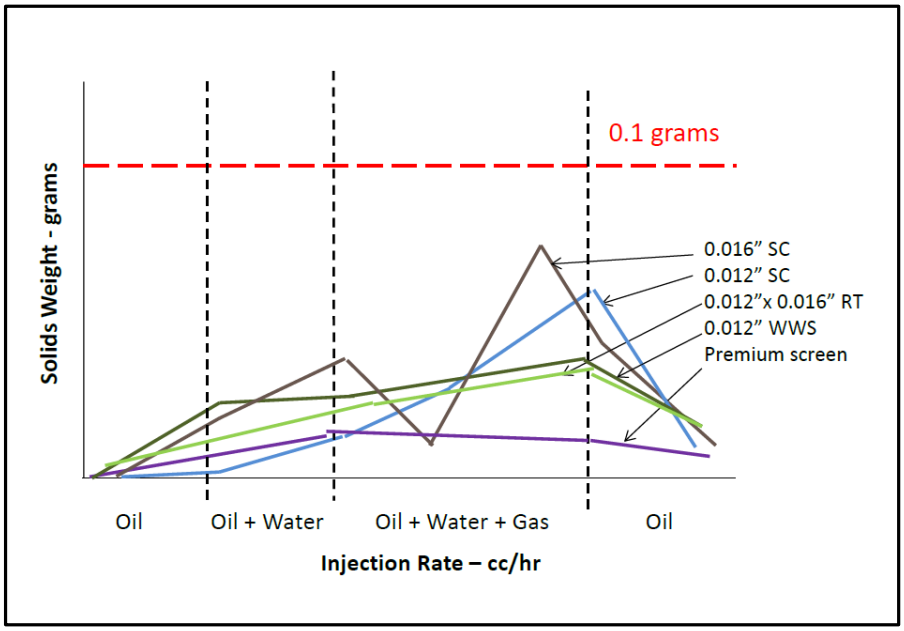

Figure 3. Produced solids versus different flow regime and production rates, SAGD operations, oil sands from Western Canada

Test results show that:

1. Type and aperture of sand control media is specific to the reservoir and operational conditions.
2. RT outperforms SC in terms of both delta P and amount of produced fine solids.
3. WWS outperforms SC and RT SL from a plugging perspective.
4. Solids production for WWS is marginally higher than for SL at the same aperture width but the aperture is chosen correctly, only colloidal size particles are produced.
5. WWS designs, even with smaller aperture width, have a lower pressure drop than SL and the smaller aperture width of the WWS results in an effective sand control design.
6. Premium screens have in general similar performance as WWS.

RECENT FIELD OBSERVATIONS

Recent field data from heavy oil projects in Canada confirm trends observed in the laboratory experiments. A good example is the Leismer SAGD Demonstration project of Statoil [5, 6]. Twenty three SAGD well pairs were completed with both liners (SC for injectors and RT for producers) and WWS. First production started in January 2011. The majority of SL producers show a gradual increasing drawdown with time which could be indicative of gradual plugging. Another example is the JACOS Hangingstone SAGD project [7]. Field data collected over the period of 15 years of production show low pressure drop for WWS and a premium screen. Nine years of production for SL show initially good sand control and good conformance but multiple liner failures and high pressure drops.

The laboratory test protocol allows determination of the type and aperture of the sand control media for a specific reservoir which would provide economical production rates without pressure build up or excessive sand production. Sand control is one of the factors which need to be taken into account for well design. Other factors such as operational practices and mechanical stresses also need to be taken into consideration. Work on the correlation of field data and lab data is ongoing.

CONCLUSIONS

1. A laboratory test protocol has been developed for sand control design for unconsolidated heavy oil deposits. The protocol allows evaluation of the different type of the sand control media with reservoir core material at test conditions simulating field conditions.
2. Test results provide recommendations for the sand control media which would be the most suitable for a particular reservoir and would provide maximum flow rates and minimal plugging or pressure build up.
3. Recent field data indicate that results of the laboratory tests are in a good agreement with field observations.

ACKNOWLEDGEMENTS

The authors would like to express their gratitude to the late Dr. Brant Bennion for the contribution to the study.

REFERENCES

1. Coberly, C.J., *Selection of Screen Openings for Unconsolidated Sands*, American Petroleum Institute, 1937, API-37-189.
2. Romanova, U.G. and Ma, T. *An Investigation of the Plugging Mechanisms in a Slotted Liner from the Steam Assisted Gravity Operations.* SPE paper 165111-MS, SPE European Formation Damage Conference and Exhibition, Noordwijk, The Netherlands, June 5-7, 2013.
3. Bennion, D.B., Ma, T., Thomas, F.B., and Romanova, U.G. *Laboratory Procedures for Optimizing the Recovery from High Temperature Thermal Heavy Oil and Bitumen Recovery Operations.* Paper 2007-206, Canadian International Petroleum Conference, Calgary, Canada, June 12 – 14, 2007.
4. Bennion, D.B., Gupta, S., Gittins, S., and Hollies, D. *Protocols for Slotted Liner Design for Optimum SAGD Operations.* Paper 2008-186, Canadian International Petroleum Conference, Calgary, Canada, June 17 – 19, 2008.
5. Romanova, U.G., Gillespie, G., Sladic, J., Ma, T., Solvoll, T.A., and Andrews, J.S. *A Comparative Study of Wire Wrapped Screens vs. Slotted Liners for Steam Assisted Gravity Drainage Operations.* Paper WHOC14-113, World Heavy Oil Congress 2014, New Orleans, USA, March 5-7, 2014.
6. Romanova, U.G., Gillespie, G., Sladic, J., Solvoll, T.A., Andrews, J, and Thomson, S., *A Comparative Study of Wire Wrapped Screens vs. Slotted Liners, Leismer Demonstration Project,* SPE Thermal Well Design and Integrity Workshop, Banff, Canada, November 18 – 20, 2014.
7. Park, B., *Back to the Future: JACOS Hangingstone SAGD Well Completion Design*, SPE Thermal Well Design and Integrity Workshop, Banff, Canada, November 18 – 20, 2014.

HETEROGENEITY ANALYSIS OF OIL SANDS CORES

A. Kantzas[1], S. Kryuchkov[1], J. Vanegas Prada[2], M. Parliament[2]
[1]PERM Inc., [2]Athabasca Oil Corporation

This paper was prepared for presentation at the International Symposium of the Society of Core Analysts held in St. John's Newfoundland and Labrador, Canada, 16-21 August, 2015

ABSTRACT

Thermal recovery of bitumen in oil sands requires the ability to propagate steam within the formation, and to have drainage of heated fluids to production wells. As such, reservoir heterogeneities can play a very significant role in these processes. Many of these heterogeneities are not easy to define at the scale of logging tools. The objective of this study is to develop a work flow and set of output parameters that can provide a much higher resolution characterization of heterogeneities present in an oil sand, based on non-destructive testing of core. Oil sands cores with variable quality of sand and shale were acquired and tested using an ensemble of techniques including CT scanning at 1mm intervals, continuous NMR and EM sweeps. The continuous NMR is done by moving the core in 1 cm intervals and then de-convoluting the signal from subsequent echo trains to extract information in high resolution. The EM sweeps are done using two different designs of probes (one induction and one plate design). Density and porosity are extracted from CT. Oil and water contents are extracted from NMR and CT porosity. Resistance is extracted from the induction probe and frequency dependent capacitance is extracted from the plate probe. All the information is then reprocessed together to extract a number of data in a high resolution log of the core. Although the initial interest is in the quantitative distribution of the V-shale parameter, the results can be used to characterize heterogeneity in both porosity and fluid distributions within the core.

INTRODUCTION

When conducting experiments in oil sand cores we often experience very poor injectivity and very low permeability to water at initial core conditions. When core selection is done based on logs, the core intervals appear homogeneous but at the core scale, local heterogeneities are observed. As oil and gas development moves towards less homogeneous sands, the log resolution for heterogeneity detection is inadequate. An alternative process is demonstrated in this paper. Several core pieces from an oil sand well were collected to demonstrate the work flow intended in high resolution heterogeneity detection. The core pieces represent various oil sand layers containing inclined heterolithic stratifications (IHS) some with more sand and some with more mud, as well as breccia and cap rock. The core pieces were slabbed and kept frozen, but the core was found to be desiccated at the start of the tests. Thus the core had to be hydrated. All pieces were soaked with predefined amounts of fresh water, which was dripped onto the surface of the core. Following that, the pieces were weighted and wrapped to maintain moisture. All core pieces underwent CT scanning, continuous NMR scanning

and two novel EM sweep procedures. Each of these modalities was analyzed independently and the results were combined to provide an integrated characterization. The difference in resolution of the different modalities does not allow for simultaneous treatment of all the results. Thus, for the purposes of this work the modalities are interpreted sequentially.

SCANNING METHODS

X-ray Tomography

The core was scanned in 1mm intervals at two energies (120 and 100kV) [1, 2]. However, dual energy contrast was not sufficient for atomic number characterization. Thus only the high energy scans (proportional to density) were used in the interpretations of this study.

CT image analysis creates density maps for each slice. The density numbers for each pixel of a given slice are plotted and a density distribution is generated for each slice. In a uniform sand (40% porosity) this distribution is a Gaussian with a mean at around 2,000kg/m^3 and a fairly narrow standard deviation (approximately 20kg/m^3). Lower densities denote more porous sands and at some point lower densities denote sand parting (or coring induced dilation) and presence of fractures. When higher densities are present in the distributions, depending on the shape and size of the density areas, one can get boundaries for shale (clay laminations), pebbles, and inclusions such as siderite or pyrite.

The precise cut-off points depend on the machine used and the size of the core sample. Thus it is very difficult to provide unilateral numbers. The most precise method for identification of each density domain (sand, clay, pebble and siderite) would be through statistical deconvolution, coupled with pairing against other data (e.g. particle size analysis). This method is currently under development. For the current report the simplification of cut-off points (used commonly in NMR for phase determination) is used. After the cut-offs are determined, the density images are reprocessed and the four domains are created. Currently, the sand is split in two domains sand and the rest as shale. V-shale is determined as:

$$V_{shale} = \frac{Volume\ of\ clay\ domain}{Total\ slice\ volume} \quad (1)$$

V_{shale} is then plotted as a function of depth.

Low Field Magnetic Resonance

An NMR scanning system for full diameter core was created for testing native cores and also for core used in full diameter core floods. The system does not have gradients for NMR imaging. Instead spectra and T_2 relaxation time distributions are measured. The system used in this study scans core at 30cm intervals (NMR sensitivity area – sweet spot). In order to generate higher resolution measurements, the core was scanned, moved in 1cm intervals and scanned again. Thus in two successive NMR scans, 29cm of the core within the sweet spot would be the same and 1cm would be different.

A proprietary algorithm was created that takes these successive scans and de-convolutes them to provide spectra of approximately 3cm intervals. These spectra are then further decomposed to provide amplitudes of oil, clay bound and capillary bound water. When this is done, the NMR estimate of V_{shale} is calculated by normalizing the clay bound water amplitude to the total amplitude as follows:

$$V_{shale} = \frac{A_{clay}}{A_{clay}+A_{cap\ water}+(A_{oil}/RHI)} \quad (2)$$

Given the appropriate cut-off points the only unknown is the value of the relative hydrogen index (*RHI*) which denotes the relative signal strength of oil as compared to the same volume of water. If the reservoir oil is homogeneous with depth then an oil sample can be tested and the *RHI* number can be extracted. However, if the oil is not homogeneous then Equation (2) is not sufficient to provide an accurate V_{shale}. As an alternative, a clay indicator (*CI*) can easily be created through Equation (3).

$$CI = \frac{A_{clay}}{A_{clay}+A_{cap\ water}} \quad (3)$$

Small values of *CI* ($CI \rightarrow 0$) indicate sandy environment, while large values ($CI \rightarrow 1$) indicate shale.

Electromagnetic Sweep Measurements

With the increasing popularity (at least in the research world) of electromagnetic heating technologies for oil sands heating and bitumen recovery [3], there has been an increased effort in understanding the dielectric properties of reservoir rocks and in particular oil sands. When a rock sample is exposed to electrodes and then a variable frequency sweep is applied on to it, measurements of capacitance and resistance can be made. Given appropriate calibrations, these measurements can be translated into resistivity and dielectric constant measurements as functions of frequency. If the electrodes cannot touch the core, then the resistivity measurement becomes more problematic, but there are still ways to calculate dielectric constant [4].

When a partially water saturated sand is exposed to an EM sweep, the resulting conductivity and dielectric constant dispersions with frequency are recorded. The conductivity (real component of complex impedance) dispersion is relatively flat and is greatly affected by the amount and salinity of the water present in the core. The dielectric constant (extractable from the imaginary component of complex impedance) is also affected by the same parameters but the dispersion is much stronger. This is the principle of the new dielectric logs [5] but the frequencies used for the EM sweeps in this work are a very small fraction of the log sweeps. When it comes to clay, conductivity dispersions should be different than sand's and the dielectric constant dispersions should be distinctly different than those of sand.

In order to extract conductivity and dielectric constant from resistance and capacitance, details of what is the equivalent circuit of the core and the environment must be constructed [6, 7]. This aspect for a complete core with vertical heterogeneity is still under investigation. Thus in this paper data of capacitance and resistance are presented. In order to capture resistance data, an induction coil probe was designed and implemented. In order to capture capacitance data, a parallel plate probe was designed and implemented. All the core pieces were scanned at the maximum spatial resolution possible of approximately 1cm per measurement. The frequency range used was between 0.08MHz and 20MHz. The useful data were between 0.1MHz and 10MHz.

The Core Log Suite

When combining all the recovered data, and allowing for adaptations that will give comparable resolutions, the following information can be obtained.

CT Scanning: **Density profile**, separation in different domains, with knowledge of grain density per domain **Porosity profile**. From density profile and domain identification **V-Shale profile**.

NMR Scanning: Water amplitude profile and subsequently (through combination with porosity) **Water Saturation profile**. Oil amplitude profile. If *RHI* is known then Oil Saturation and V-Shale can be calculated but at this point *RHI* is considered unknown. The Geometric mean relaxation times from water and oil phases are calculated.

Combination of CT and NMR: From the water saturation profile and the porosity profile the **Oil Saturation profile** is extracted. From oil amplitude profile and using the oil saturation profile and V-shale profile the ***RHI* profile** is extracted. From the Oil Amplitude geometric mean relaxation time and *RHI* profile the **Oil Viscosity profile** [8] is extracted.

EM Sweep: **Resistance** and **Capacitance** profiles. There is correlation between capacitance profile and clay content.

RESULTS

Figure 1 shows the photos and CT reconstructions of several pieces of core. It is evident that the photography, no matter how high quality, does not capture all the heterogeneities of the samples. This is especially evident in oil-bearing regions of the core, which show up as simple black uniform-looking zones in the photographs. Figure 2 shows the detailed NMR spectrum of a sample of bitumen and water representative of the area. The fastest relaxing peak represents oil, the slowest relaxing peak represents water in bulk and the smaller peaks in between represent various water in oil emulsion droplets.

Figures 5 and 6 show the calculated shale information from CT (Equation 1) and NMR (Equation 3) for the four core pieces. The bulk heterogeneity levels are captured. The porosity variability was captured as expected and in not shown here for brevity. The fact

that the core is not perfectly preserved does not allow for reservoir predictions but demonstrates clearly the capability of the technique. Equation 3 rather than equation 2 is used here for many reasons. In the clay zones in this core, the NMR clay water content increases and the capillary water drops. When comparing CT and NMR we get qualitative agreement but quantitative agreement was not always achieved. Trend wise CT and NMR calculations are aligned. In the case of cap rock (piece 9) and IHS, both CT and NMR are successful. CT with its finer resolution provides better description of the IHS. NMR does not have the spatial resolution. However, NMR shows high Clay Index in areas (particularly in piece 16A), where CT shows nothing. Utilization of equation 2 would be much better but the inter echo time values used in full diameter coils is not sufficient to extract enough points for a clear description of the oil peak of the equivalents of Figures 2-4. Alternative approaches are sought. The NMR signal of high clay content shown in piece 16A is believed to be correct. But since the scanner does not pick up distinct laminations we believe that the clay is more dispersed rather than layered.

Figures 5 and 6 show two samples of capacitance measurements from the EM sweeps. It can be seen that sand and shale have distinctively different capacitance signatures. The observed scatter of the experimental data below 80 kHz is due to experimental limitations and the data at those frequencies are not used. By looking at the capacitance profiles we can detect two distinct regions which can be fit in simple power functions. From the presented examples we can see that the slopes of these functions are different for IHS and oil sand. However, since the salinity is not independently measured it is difficult to quantify the results into a predictive tool. Figure 7 shows a few such distinct profiles from different parts of the core samples. The signatures are distinct and can be collected in 1cm intervals. However, at this point there is not much more that can be said. Moreover, it is noted that the core areas that are expected to have dispersed clay have a capacitance signature that is a mixture of the two distinct shale vs. oil sand signatures shown in Figure 7. Work in this area continues.

The major drawback of this work was that the core was dehydrated to begin with and that did not allow for more quantitative water/salinity based measurements. It will be very productive to repeat such measurements in fresh core. Currently direct contact with the core provides much more accurate measurements but this is difficult to achieve and guarantee that oil sand core integrity will be maintained. The smaller the core diameter the easier the smaller the coil that can be used. Subsequently the inter echo time can be faster and the method will be able to capture more of the bitumen signature (relaxing faster than 1ms and even below 0.1ms) for a better description of the fluid distribution. The capacitance measurements show great promise even though they are at much lower frequencies than those of the dielectric logs.

CONCLUSIONS

- Single energy CT scanning with density profile deconvolution provides detailed V-sand vs. V-Shale discrimination.
- Discrimination of clay bound water vs. capillary bound water provides a second V-sand vs. V-Shale discrimination.
- The EM sweeps indicate that shale and sand have distinctly different capacitance responses with varying frequency.

ACKNOWLEDGEMENTS

The contributions of Jim Wang, Jon Bryan, Abdi Yussuf, Jennifer Amaechi and Jessica Butron of PERM Inc. are gratefully appreciated. Funding for this project from Athabasca Oil Corporation is also gratefully appreciated.

REFERENCES

1. Kantzas, A. "Investigation of Physical Properties of Porous Rocks and Fluid Flow Phenomena in Porous Media Using Computer Assisted Tomography", (1990), *In Situ*, **14**(1), 77-132.
2. Kantzas, A., Marentette, D.F. and Jha, K.N., "Computer Assisted Tomography: From Qualitative Visualization to Quantitative Core Analysis", (1992), *J. Can. Pet. Tech.*, **31**(9), 48-56.
3. McPherson, R.G., Chute, F.S. and Vermeulen, F.E., "Recovery of Athabasca Bitumen with the Electromagnetic Flood (EMF) Process", (1985), *J. Can. Pet. Tech.*, **24**,
4. Taherian, M.R., Kenyon, W.E. and Safinya, K.A., (1990), "Measurement of Dielectric Response of Water-Saturated Rocks", *Geophysics*, **55**(12), 1530-1541
5. Hizen, M., Budan, H., Deville, B., Faivre, O., Mosse, L., Simon, M., "Dielectric dispersion; a new wireline petrophysical measurement", (2008), SPE116130 SPE ATCE Colorado, USA
6. Mazzagatti, R.P., Dowling, D.J., Sims, J.C., Bussian, A.E. and Simpson, R.S., "Laboratory Measurement of Dielectric Constant near 20 MHz", (1983), SPE 12097, presented at the 58th Annual Technical Conference and Exhibition held in San Francisco, CA
7. Josh, M., Esteban, L., Delle Diane, C., Sarout, J., Dewhurst, D.N., Clenell, M.B., "Laboratory characterization of shale properties", (2012) *J. Pet. Sci. Eng.*, **88-89**, p.107-124.
8. Bryan, J., Moon, D. and Kantzas, A., "In-situ Viscosity of Oil Sands Using Low Field NMR", CIM 2003-107, (2005), *J. Can. Pet. Tech.*, **44**(9), 23-30

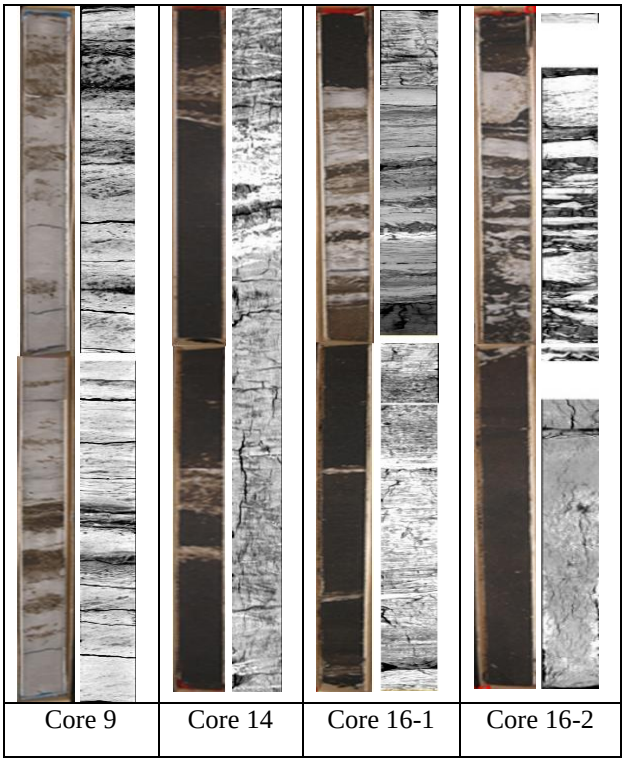

Figure 1: Core photos and corresponding CT image sequences

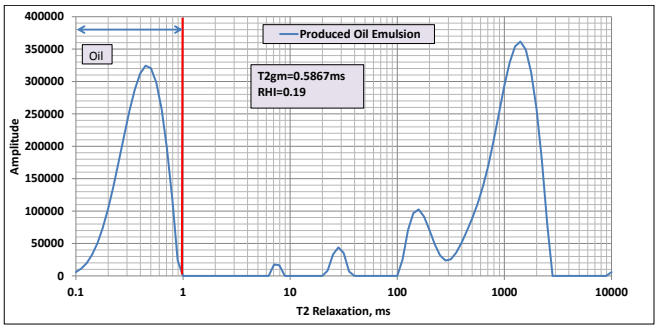

Figure 2: T_2 relaxation distribution of produced bitumen emulsion

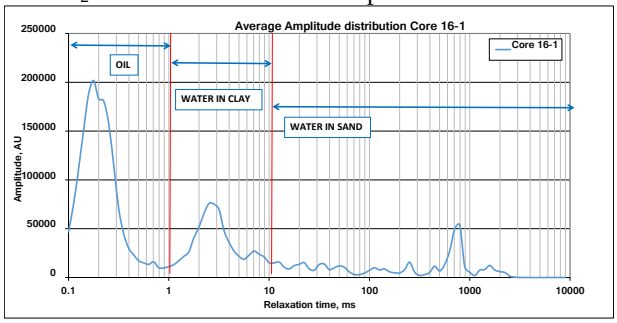

Figure 3: T_2 relaxation distribution of oil rich core

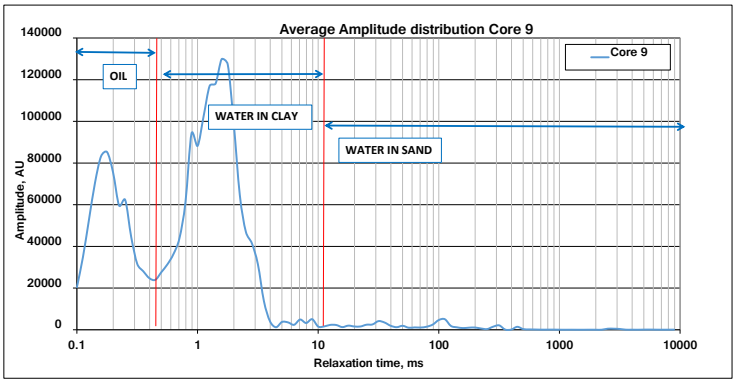

Figure 4: T_2 relaxation distribution of clay rich core

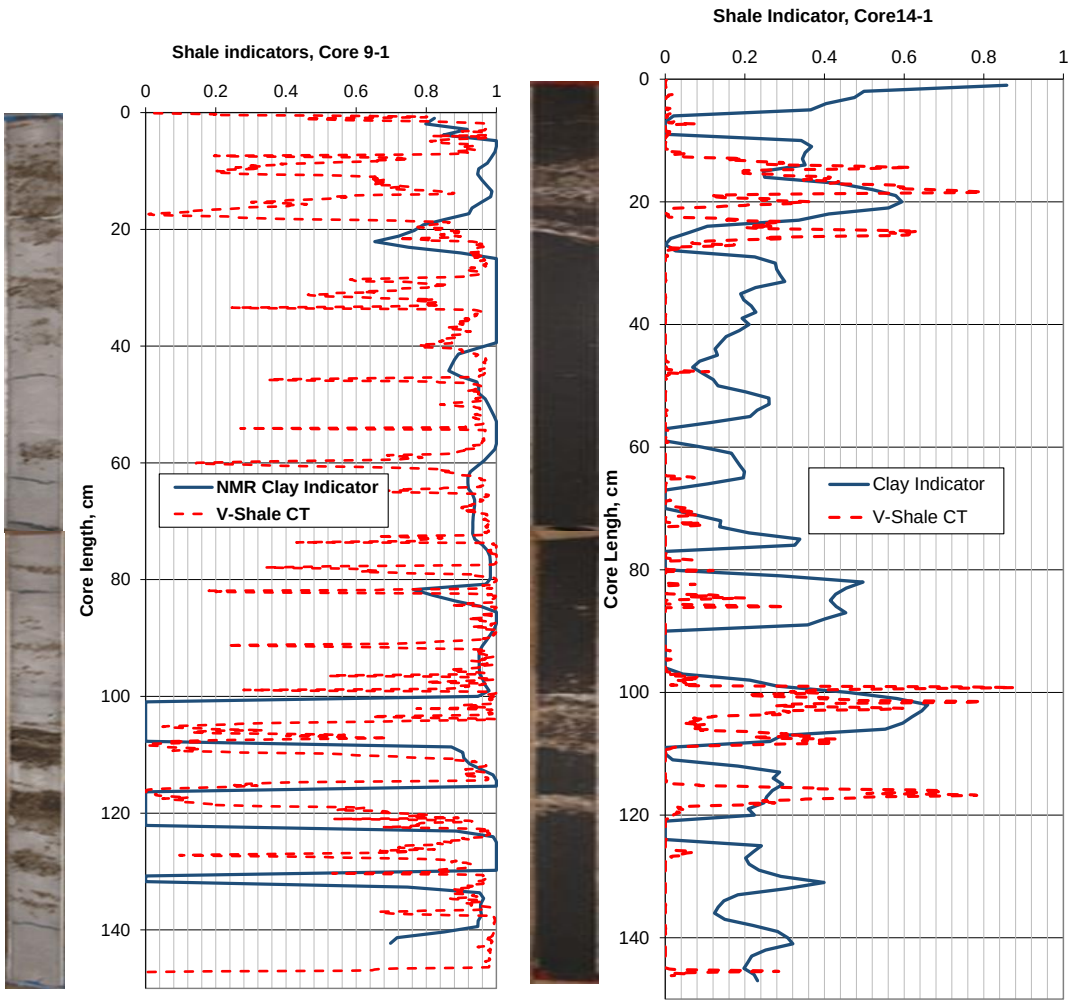

Figure 5: CT V-Shale and NMR Clay Indicator Comparison Cores 9 and 14

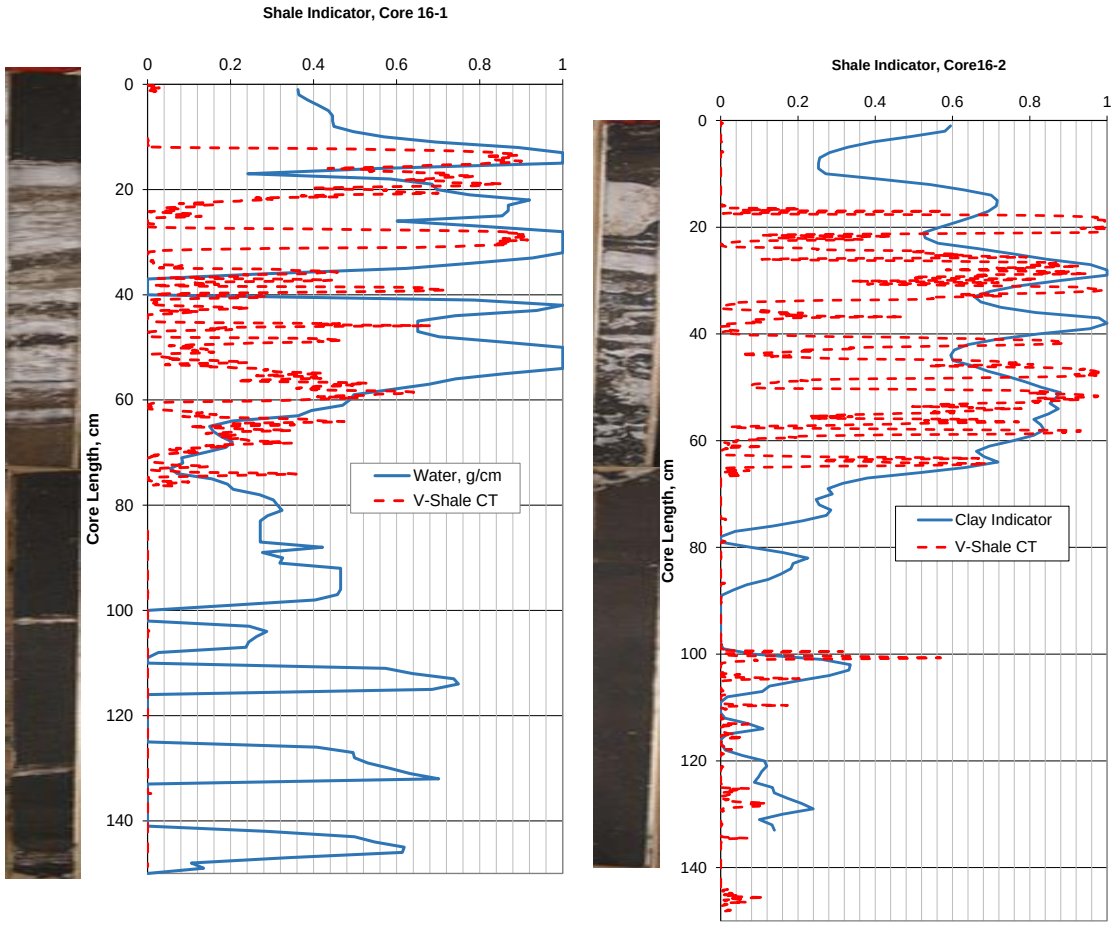

Figure 6: CT V-Shale and NMR Clay Indicator Comparison Cores 16A and 16B

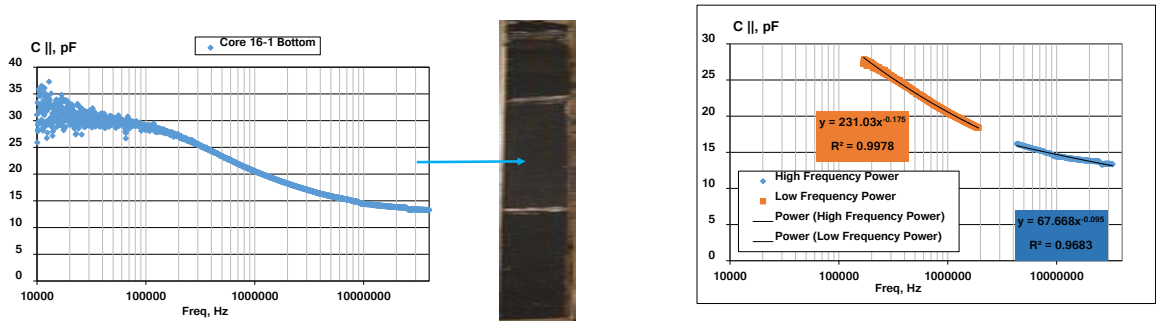

Figure 7: EM sweep and power fit from an oil sand sample

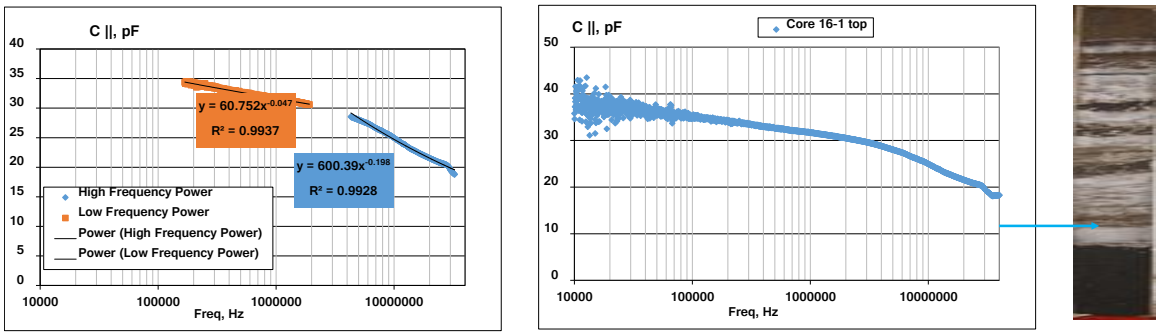

Figure 8: EM sweep and power fit from an inter-bedded shale sample

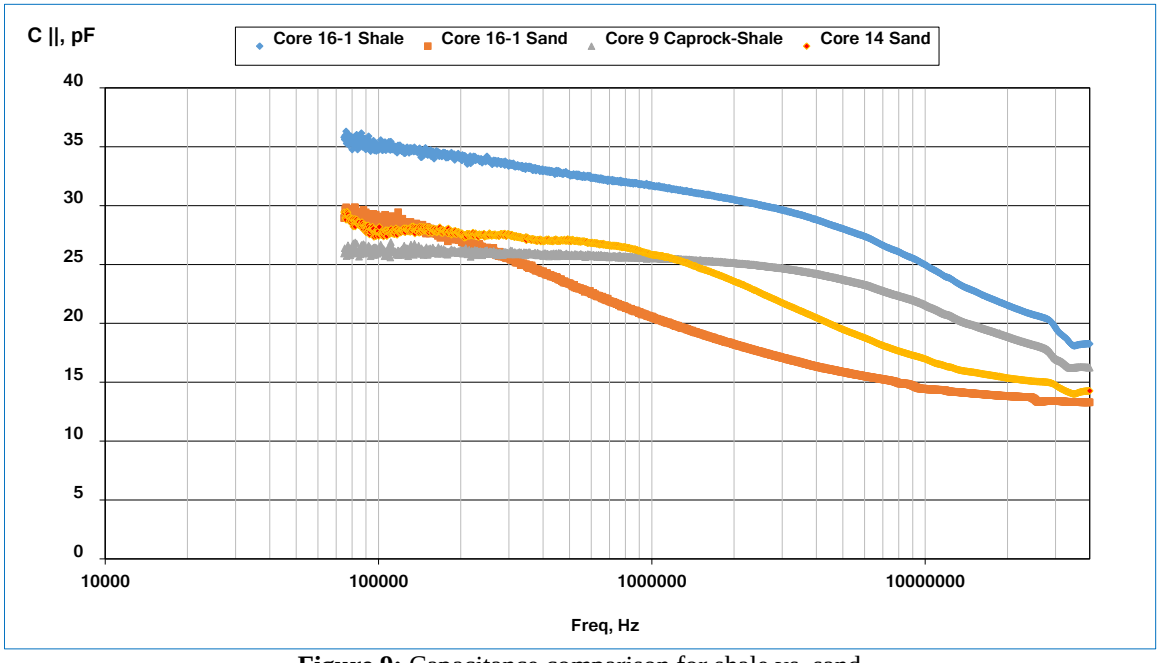

Figure 9: Capacitance comparison for shale vs. sand

CORRELATION OF COMPOSITIONAL PHASES AND WETTABILITY-BASED FLUID-TRACERS IN FINE-GRAINED RESERVOIRS

Qinhong Hu[1]; Jamil J. Clarke[2]; Rod Baird[2]; Chad Ostrander[2]; Zhiye Gao[3]; Yuxiang Zhang[1]; Kibria Golam[1]
[1]The University of Texas at Arlington, Arlington, TX 76019, USA.
[2]Hitachi High Technologies America, Inc., Clarksburg, MD 20871, USA.
[3]State Key Laboratory of Petroleum Resources and Prospecting, China University of Petroleum, Beijing 102249, China.

This paper was prepared for presentation at the International Symposium of the Society of Core Analysts held in St. John's, Newfoundland and Labrador, Canada, 16-21 August, 2015

ABSTRACT

Fine-grained reservoirs can contain distinct compositional phases, with oil-wetting organic matter/carbonate and other water-wetting mineral phases. Despite their importance in hydrocarbon storage and production, the intertwined wettability, nanopore distribution, and pore connectivity of these phases are not well understood. The approach presented here involves tracers in two fluids (API brine and *n*-decane) that are used to specifically interrogate the spatial wettability of organic-matter and mineral phases, through an integrated approach of phase imaging by Scanning Electron Microscopy (SEM) and tracer mapping with laser ablation-inductively coupled plasma-mass spectrometry (LA-ICP-MS). A core sample from Eagle Ford was used for a testing area of 2.1mm×1.8mm that was argon-ion milled and imaged with a Hitachi SU3500 SEM with image montage (Zig-Zag) capabilities for compositional distribution. The same sample area was then treated with tracers in brine and *n*-decane fluids, followed with LA-ICP-MS mapping for tracer distribution at different spatial resolutions (8μm, 12μm, and 75μm). A negative correlation between brine-tracers (ReO_4^- and Eu^{3+}) and *n*-decane-tracer of 1-iododecane was observed.

INTRODUCTION

Since 2000, the technological advances of horizontal drilling and hydraulic fracturing in North America have led to a dramatic increase in hydrocarbon (gas and oil) production from shale formations, changing the energy landscape in the U.S.A. and worldwide. However, the sustainable shale resource development is implicated by the steep hydrocarbon production decline and overall low recovery. For example, the top five US resource plays typically produced 80–95% less gas after 3 years, and the productivity of new wells in two leading tight-oil plays (Bakken and Eagle Ford) dropped by about 60% within the first year [1]. Total gas recovery from the Barnett, the most developed shale play, was reported to be only 8–15% of gas-in-place in 2002, and 12–30% in 2012 [2]. The recovery rate for tight oil is even lower at 5–10% [3].

Hydrocarbon storage and production in hydraulically-stimulated shale are affected by the intertwined correlation of compositional phases, wettability, nanopore distribution, and pore connectivity of shales. As shales contain distinct oil-wetting organic-matter (e.g., kerogen) and water-wetting mineral phases, the novel method of unique tracers in two fluids to interrogate the wettability and connectivity of organic-matter and mineral pore spaces is realized in this work. The organic fluid (*n*-decane) is expected to be preferentially attracted to the hydrophobic component (e.g. organic particle) of the shale matrix, with reported sizes ranging from less than 1μm to tens of μm [4]. Organic grains are found to be dispersed through the matrix of shales such as Barnett [2], but their connection through surrounding mineral phases is unknown, despite its implication in steep initial decline and low overall recovery.

This paper presents our collaborative studies of correlating compositional phases from SEM imaging (performed at Hitachi High Technologies America of Clarksburg, MD) with wettability-tracers and laser ablation-ICP-MS (LA-ICP-MS) elemental mapping at the University of Texas at Arlington.

PROCEDURES

In this work, we used a proprietary core sample from Eagle Ford to develop the technical approaches and showcase the findings. The sample was cut into a rectangular bar with a width and length of ~2.2 mm and height of ~10 mm. The sample surface was first milled with a Hitachi Ar-ion milling system (Model IM4000, Hitachi High Technologies America, Inc.). At a maximum milling rate of 300 μm/h for silicon, this broad ion milling system was used to prepare a high-quality cross-section. An area of 4.867mm^2 was processed by two 4-hr mill sessions at a voltage acceleration energy of 6 kV with a stage swing of ±40° (Fig. 1A). The area of 2,147μm×1,799μm (the shaded region of Fig. 1B) was then used for producing an image montage by Zig-Zag function of a Hitachi SU3500 SEM. The SU3500 SEM has a variable-pressure design that eliminates the need for coating non-conductive materials for image acquisition. An acceleration energy of 5kV was applied to the SEM for acquiring images at a magnification of 1,000 times. Each image was captured at a resolution of 2,560×1,920, with 8-bit grayscale, 512×512 dpi, and 121.3 μm horizontal field width (Fig. 1C). The image montage was composed of 460 images that were stitched together, and the total time to acquire the entire image tile array was ~7 hrs with the integrated Zig-Zag function which automates the entire process. The image tiles were acquired along with a 20% margin of overlap, and this margin is needed for the stitching software to align each image tile on all four sides. In addition, this margin also includes some mechanical stage movement backlash which is why the margin percent is needed to compensate for this deficit. Therefore, each image tile is not a true side by side acquisition but a series of semi-overlapping images.

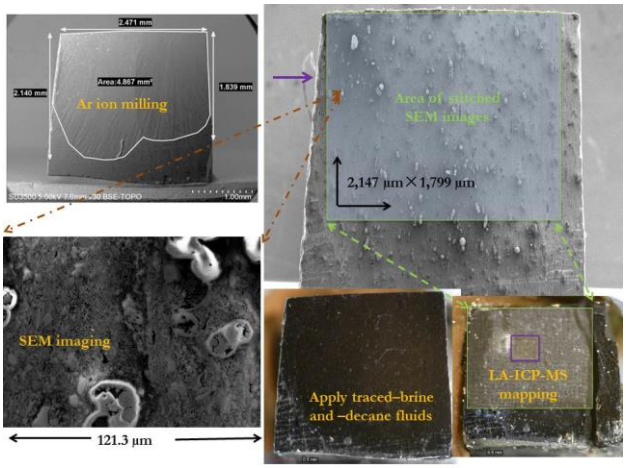

Figure 1. Work flow of Ar ion milling, SEM imaging, and elemental mapping of applied wettability-tracers (scale bars are shown for each graph).

We used 0.1 mM each of $NaReO_4$ and $EuBr_3 \cdot 6H_2O$ (Sigma-Aldrich Co., St. Louis, MO) dissolved in API brine (8% NaCl and 2% $CaCl_2$ by weight, with perrhenate anion (ReO_4^-) and europium cation (Eu^{3+}) as non-sorbing and sorbing tracers, respectively. For organic-phase *n*-decane tracer, organic-I (1-iododecane) [$CH_3(CH_2)_9I$, molecular weight of 268.18 g/mol] (>99% pure, Sigma-Aldrich Co.] was directly added to *n*-decane fluid at a volume ratio of 1%. The elements rhenium (Re), europium (Eu), and iodine (I) of these tracer chemicals are readily detected by LA–ICP–MS.

To investigate the association of wettability to compositional phases, we applied one drop (0.16 mL) of brine tracer solution in the middle of an imaged area, and waited for an hour for the beaded-up fluid to slowly evaporate and spread on and within the sample. Next, an additional drop of brine tracer (Fig. 2A-B) was applied. After another hour, some localized zones of salt precipitates were observed and removed with a razor blade (Fig. 2C-D). Two drops of *n*-decane tracers were then applied, in a similar fashion as brine at two settings; *n*-decane was found to quickly spread on the sample surface (Figure not shown), which was much different from API brine. After seven hours that the 1st application of brine tracer was dropped, LA–ICP–MS mapping analyses were performed on the sample (Fig. 1D).

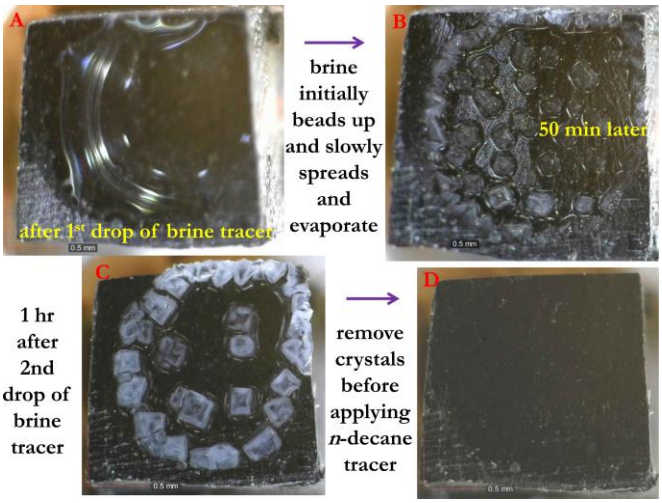

Figure 2. Spreading behavior of traced-API brine on an Eagle Ford sample (a scale bar is shown on each picture).

The laser ablation system (UP-213, New Wave; Freemont, CA) used a 213 nm laser to vaporize a hole in the rock sample at sub-micron depth for each laser pulse; elements entrained in the vapor were analyzed with ICP-MS (PerkinElmer/SCIEX ELAN DRC II; Sheldon, CT). For different research purposes, this LA-ICP-MS approach can generate 2-D and 3-D maps of chemical distributions in rock at a spatial resolution of microns, and a concentration limit of low-mg/kg [5]. For this work, two mapping-area approaches were used. The first, and a wider, mapping area (2,175μm×1,800μm; called Grid A) nearly matched the SEM-imaged area (2,147μm×1,799μm), and we used 75μm as the laser spot size and spacing between spots; the laser was fired for 60 pulses at each spot (Fig. 1D). This produced a total of 750 data spots, a duration of 10 hours for completion. The 2nd, and a finer, grid (Grid B) was located near the middle of the mapped SEM region, and was selected at 500μm below, and to the right of, the starting point of Grid A (Fig. 1D). This finer grid covered an area of 612μm×240μm, and used smaller spot sizes and larger laser pulses (8μm and 400 pulses; 12μm and 200 pulses) in order to collect more sample mass for ICP-MS detection; a total of 26 hrs was taken to complete the mapping of Grid B. During the data processing, the differences in spot size and laser pulse were corrected.

RESULTS

LA-ICP-MS elemental mapping results for Grids A and B are shown as Figs. 3-4. For these figures, the scale bars indicate the measured elemental background level of the analyte in the sample (as the lowest value, and cold color, in scale bar) and detected high concentrations of tracer element (as the highest value, and warm color, in scale bar). Therefore, any color difference in these figures indicates the presence of tracers.

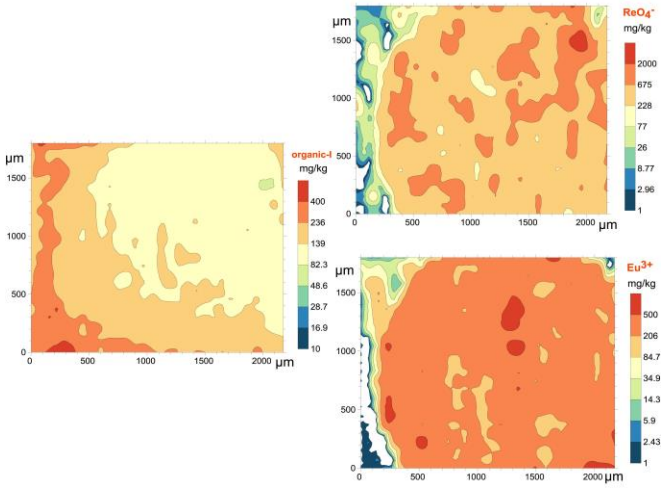

Figure 3. Tracer distribution in Grid A.

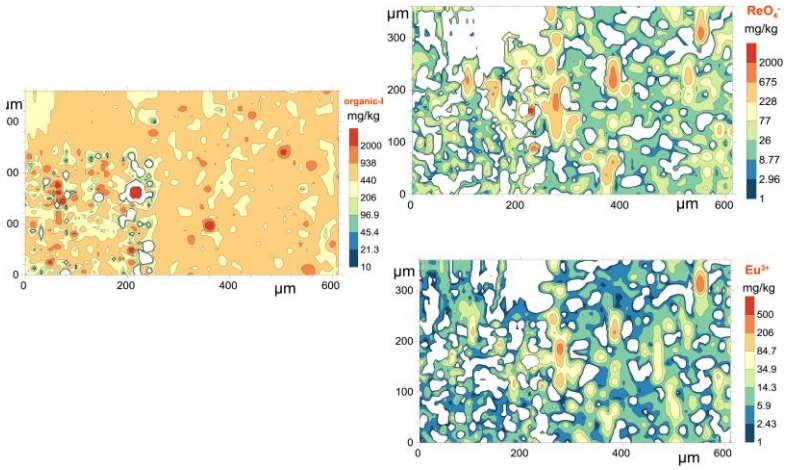

Figure 4. Tracer distribution in Grid B with higher mapping resolutions; the 1st 240 µm (from the left) and 2nd 360 µm zones were mapped at 8 µm and 12 µm spatial resolutions, respectively.

DISCUSSION

The Eagle Ford sample has a high carbonate content [6], which was confirmed from the SEM images showing an abundant presence of coccospheres (Fig. 1C). Carbonate rock tends to exhibit an oil-wetting characteristics[7], consistent with our observed spreading behavior of API brine and *n*-decane. The application of wettability-based tracers and resultant LA-ICP-MS mapping further illustrate the spatial variability of wettability regions, on the scale of microns. Fig. 3 was mapped at the scale of 75 µm and shows relatively less spotty behavior of high-concentration tracer regions than Fig. 4 at finer (8 and 12 µm mapping resolutions). Furthermore, for both Figs. 3-4, brine tracers of ReO_4^- and Eu^{3+} follow the similar pattern, while *n*-decane tracer of organic 1-iododecane shows higher concentrations at different regions from brine tracers. The overall results illustrate the presence of spatially variable water-wetting mineral phases and oil-wetting phase (carbonate for this Eagle Ford sample), which is consistent with other tests (imbibition,

diffusion, and vacuum-saturation for edge-accessible pore spaces) of the sample (results not shown).

CONCLUSIONS

Using an integrated approach of SEM phase imaging and wettability-based tracer mapping of LA-ICP-MS, we illustrate the seemingly negative correlation of API brine-based tracers with *n*-decane tracer to indicate the spatial variability, at microns scale, of water- and oil-wetting compositional phases of an Eagle Ford sample. Using these developed approaches, additional tests will be conducted for shale samples with a range of total organic content to interrogate the wettability patterns, and associated pore sizes, of compositional phases of shale. The integrated studies on intertwined correlation of compositional phases, wettability, nanopore distribution, and connectivity of fine-grained reservoirs will help understand the hydrocarbon storage and production in stimulated reservoirs.

ACKNOWLEDGEMENTS

Funding for this project was partially provided by the Foundation of State Key Laboratory of Petroleum Resources and Prospecting, China University of Petroleum, Beijing.

REFERENCES

1. Hughes, J.D. 2013. *Drill, Baby, Drill: Can Unconventional Fuels Usher in a New Era of Energy Abundance?* Post Carbon Institute, 2013, 178 pp.
2. Hu, Q.H., and R.P. Ewing. *Integrated Experimental and Modeling Approaches to Studying the Fracture-Matrix Interaction in Gas Recovery from Barnett Shale*. Final Report, Research Partnership to Secure Energy for America (RPSEA), National Energy Technology Laboratory, Department of Energy, 2014, 80 pp.
3. Hoffman, T. *Comparison of various gases for enhanced oil recovery from shale oil reservoirs*. This paper was presented for presentation at the Eighteenth SPE Improved Oil Recovery Symposium held in Tulsa, OK, USA, 14-18 April 2012, SPE 154329.
4. Loucks, R.G., R.M. Reed, S.C. Ruppel and D.M. Jarvie. 2009. Morphology, genesis, and distribution of nanometer-scale pores in siliceous mudstones of the Mississippian Barnett Shale. *J. Sed. Res.*, 2009, 79(11-12), 848-861.
5. Hu, Q.H., T.J. Kneafsey, J.S.Y. Wang, L. Tomutsa, and J.J. Roberts. 2004. Characterizing unsaturated diffusion in porous tuff gravels. *Vadose Zone J.*, 2004, 3(4), 1425-1438.
6. Slatt, R.M., N.R. O'Brien, A. Miceli Romero, H.H. Rodriguez. *Eagle Ford condensed section and its oil and gas storage and flow potential*. AAPG Annual Convention and Exhibition, Long Beach, California, April 22-25, 2012. Search and Discovery Article #80245, 2012.
7. Roychaudhuri, B., T.T. Tsotsis, and K. Jessen. An experimental investigation of spontaneous imbibition in gas shales. *J. Petro. Sci. and Eng.*, 2013, 111, 87-97.

THRESHOLD PRESSURE IN TIGHT GAS RESERVOIRS OF CENTRAL EUROPEAN FORMATIONS

Budak P., Cicha-Szot R., Leśniak G., Majkrzak M., Such P.
Instytut Nafty i Gazu - Państwowy Instytut Badawczy, Krakow, Poland

This paper was prepared for presentation at the International Symposium of the Society of Core Analysts held in St. John's Newfoundland and Labrador, Canada, 16-21 August, 2015

ABSTRACT

Increasing development activities for tight gas reservoirs during recent years have stimulated basic research on the flow characteristics of this kind of reservoirs. Investigated tight gas reservoirs are characterized by low porosity, low permeability and occasionally high water saturation which impact flow characteristics of gas reservoirs. In this kind of reservoirs so called nonlinear flow or non-Darcy flow occurs. Despite recent progress, the flow characteristics of tight gas reservoirs have not been thoroughly investigated. One of the important parameter to characterize reservoir in the context of production and basin modeling is threshold capillary pressure [1].

Threshold pressure is defined as the ability of a porous medium saturated with a wetting phase to block the flow of a non-wetting phase. Its value corresponds to the size of the largest pore throat in the porous medium. Therefore, the pressure difference between the non-wetting and the wetting phase must exceed the threshold pressure before the non-wetting phase can start draining the porous medium and flow.

There are several methods for evaluating threshold pressure which has their own advantages and disadvantages [2]. In this study, we present the comparison of estimated threshold pressure from corrected high pressure MICP (Mercury Injection Capillary Pressure) and measured directly by displacement methods. The application of the detailed integrated petrophysical and petrographic data obtained by CAMI (Computerized Analysis of Microscopic Images) show the main factors which affect the values of obtained threshold pressures.

INTRODUCTION

The main target for tight gas exploration in Central Europe is the Rotliegend eolian and fluvial sandstones. The possibility of this type of gas deposits are mainly associated with eolian sandstone complexes with originally fair porosity values. Simulations of reservoir parameters of the Rotliegend sandstone indicate porosity up to 12 % on the burial depth up to 4500-5500 m [3]. It can be associated with the development of secondary porosity formed as a result of the dissolution and/or transformation of cement and detrital grains (feldspars), often leading to inversion of reservoir properties [4]. Although, this formation has been studied for a long time determination of correlation between time of gas

saturation and time of partial loss of porosity and permeability mainly due to burial is still key issue [5]. Accumulations of tight gas might exist also in the Cambrian sandstones of the East European Craton. Although, numbers of diagenesis alterations, mainly quartz cementation, affect vertical and lateral heterogeneity of reservoir properties, prospects are promising for this structure mainly due to: 1) the spread over a wide area, 2) a simple tectonic structure (Baltic Basin), 3) an increase in thickness in the area of gas window.

The Rotliegend and Cambrian sandstones are characterized by low porosity, low or ultra-low permeability and high water saturation which lead to flow characteristics significantly different from that the ones in conventional gas reservoirs.

Threshold Pressure is defined as the overpressure needed for the non wetting phase to start flowing against the capillary forces. If the fluid flow is a linear, the pressure is converted into a pressure per unit length and is called *Threshold Pressure Gradient* (TPG). As one of the most important parameter to characterize flow, TPG has been studied extensively for a long time and several approaches for TPG estimation (like mercury intrusion, continuous injection, step-by-step, residual capillary pressure, dynamic threshold) were introduced that give results with good medium or poor accuracy.

In this study we compare two tight reservoir rocks in order to show which parameters should be taken into consideration before choosing proper approach for TPG estimation.

EXPERIMENTAL

There are several laboratory methods used for evaluation threshold pressure gradient or threshold pressure each having its advantages and disadvantages. In this study, mercury intrusion, continuous flow and step-by-step approaches were applied to estimate threshold pressure which give results with good or medium accuracy. As Egermann (2006) reported mercury intrusion approach ignores the influence of the overburden pressure and dry sample is used which may affect pore space properties. Appropriate synthetic brines for each kind of rock samples, i.e. for each reservoir type, were used. For MICP based method raw data were corrected according to the gas/brine interface and temperature by using in calculations values of IFT measured for the specific system brine/rock taking into account reservoir conditions [6].

In order to see the impact of sample conditions on threshold pressure continuous flow and step-by-step approach was used. All above mentioned methods were extensively described elsewhere [2,7,8]. Accuracy of the measurement was 0.07 kPa for flow methods and 0.01% for MICP.

Experiments were carried out using plugs and cuttings from Cambrian and Rotliegend sandstone reservoirs which are typical tight gas reservoirs located in Central Europe. Selected properties of cores used in this study are shown in Table 1.

RESULTS AND DISCUSSION

The most significant difference between analysed reservoir rocks is porosity which affect other petrophysical properties.

Generally, Cambrian sandstones (quartz arenites) are composed of quartz grains in 95 % and are strongly cemented by quartz (quartz overgrowths and quartz basic cement), resulting in almost total destruction of porosity (Fig.1). Some of Cambrian sandstones (samples 10-15 Table 1) show fracture permeability. The fractures are either empty or filled with clays/mudstone, quartz or bitumens. The content of pores >1 μm is between 8 - 94% and practically there is no microporosity in that rocks.

Pore space of the Rotliegend sandstone (lithic, sublithic, subarcose arenites) is much more complicated and consists mainly of intergranular pores and variable number of micropores (Fig. 1). These sandstones are composed mainly of quartz, feldspars and fragments of rocks. Cement is represented by ferruginous-clay overgrowths, quartz, calcite and anhydrite (basic cement). There is a great diversity in the mineral compositions which affects the rocks and cement as well as diagenesis processes (dissolution, crystallization) and the creation of different amounts of micropores in the analyzed rocks (the content of pores <1 μm is between 44 - 89%).

Table 1 Specification of cores

Core #	Formation	Sample depth [m]	Plug length [cm]	Porosity [%]	Avarage capillary [μm]	Specific area [m^2/g]	Treshold diameter [μm]	Permeability [mD]
1	Cambrian	2324.60	5.43	3.86	2.53	0.02	12.0	0.63
2		2327.20	5.50	4.39	0.47	0.15	1.2	0.08
3		2327.80	5.32	6.25	0.40	0.25	1.0	0.03
4		2328.70	5.28	3.74	0.68	0.08	4.5	0.11
5		2330.40	5.53	5.31	0.89	0.09	4.5	0.32
6		2331.20	5.53	3.11	0.37	0.11	0.9	0.02
7		2333.20	5.55	3.54	0.90	0.06	4.5	0.24
8		2339.70	5.20	2.29	0.15	0.24	1.2	0.06
9		2340.90	5.17	2.17	0.17	0.20	0.9	0.02
10		2282.40	5.23	4.03	0.13	0.45	0.9	0.01
11		2289.50	5.37	5.50	1.13	0.08	3.8	0.24
12		2293.00	5.16	3.45	0.42	0.12	2.0	0.16
13		2290.10	5.23	3.77	0.17	0.14	0.9	0.07
14		2292.20	5.04	4.33	0.11	0.47	0.4	0.40
15		2299.00	4.95	6.02	0.64	0.10	6.0	0.01
16	Rotliegend Sandstone	4245.15	4.59	3.89	0.09	0.69	1.0	0.49
17		4351.25	5.04	5.52	0.09	0.99	2.0	0.38
18		4359.50	5.19	6.18	0.12	0.84	3.0	0.29
19		4460.60	4.92	13.75	0.23	1.04	5.0	0.85
20		4551.00	5.03	7.09	0.11	1.03	4.0	0.13
21		4558.25	4.44	3.23	0.05	0.98	0.4	0.13
22		4642.20	5.52	12.02	0.16	1.28	4.0	4.33
23		4650.25	4.67	14.04	0.19	1.30	3.0	1.18
24		4656.40	5.05	9.83	0.12	1.37	3.0	0.76

In Cambrian sandstones, the results of TPG obtained by mercury intrusion and step-by-step approach were quite similar for samples with average values of porosity for this formation. The highest discrepancy was in the case of samples with relatively high

microporosity (surface area ca. 0.5 m^2/g) where mercury intrusion overestimates values of TPG. Underestimation of TPG applying MCIP approach occurs when samples are mesoporous (average capillary over 0.6 μm). These general observations were confirmed by direct correlation of TPG and surface area and inverse correlation with average capillary radius (Table 2).

In the case of samples 10 – 15, the highest discrepancy between analysed methods was observed. It may be caused by distinct potential pathways for hydrocarbon migration in this samples which are presumably fractures together with microstylolites.

In the case of Rotliegend sandstone, an inverse correlation of TPG with depth was found what suggest that, except compaction, diagenesis processes and consequently secondary porosity affect flow through such reservoir (Table 4). Effect of reservoir conditions during TPG estimation increases with decreasing porosity and specific area. In such cases flow methods are more relevant. Underestimation of threshold pressure using mercury injection approach may occur also in the case of very heterogeneous parts of the reservoir especially when very thin beds of various petrophysical properties exist (sample 19).

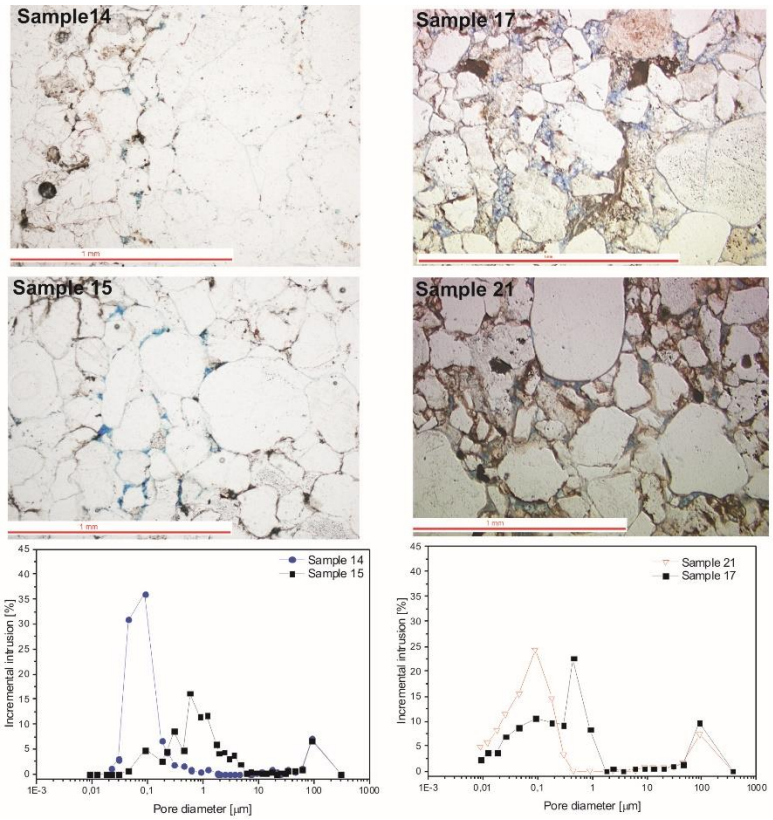

Figure 1. Selected thin sections (sample impregnated with blue resin) and pore size distribution for samples of Cambrian sandstone (sample 14, 15) and Rotliegend sandstone (sample 21 and 17). In the case of Cambrian rocks intergranular pores are observed. The Rotliegend sandstone shows diverse porosity with quite complex microporosity which steers the values of threshold pressure.

Table 2. Correlation coefficients of petrophysical parameters with threshold pressure for Cambrian sandstones

	Depth	*Effective porosity*	*Average capillary*	*Specific surface*	*% of pores >1 μm*	*Treshold diameter*	*Absolute permeability*	*Pth MICP*	*Pth flow*	*Pth step-by-step*	*TPG flow*
Pth MICP	-0.23	-0.27	**-0.62**	**0.82**	**-0.68**	**-0.70**	-0.11	**1.00**			
Pth flow	**0.72**	0.07	-0.25	0.06	-0.31	-0.30	-0.41	0.14	**1.00**		
Pth step-by-step	**0.53**	**-0.48**	**-0.81**	**0.70**	**-0.84**	-0.30	0.12	**0.64**	0.18	**1.00**	
TPG flow	**0.71**	0.06	-0.26	0.07	-0.32	-0.31	-0.41	0.14	**1.00**	0.35	**1.00**
TPG step-by-step	**0.58**	**-0.99**	**-0.94**	**0.69**	**-0.91**	-0.34	0.09	**0.62**	0.30	**1.00**	**0.68**

Table 3. Correlation coefficients of petrophysical parameters with threshold pressure for Cambrian sandstones (with no fractures – Samples 1-9)

	Depth	*Effective porosity*	*Average capillary*	*Specific surface*	*% of pores >1 μm*	*Treshold diameter*	*Absolute permeability*	*Pth MICP*
Pth MICP	0.44	-0.18	**-0.72**	**0.76**	**-0.77**	**-0.83**	**-0.80**	**1.00**
Pth flow	0.35	0.01	**-0.65**	**0.92**	**-0.91**	**-0.88**	**-0.72**	**0.84**
TPG flow	0.38	-0.01	**-0.65**	**0.93**	**-0.91**	**-0.88**	**-0.72**	**0.83**

Table 4. Correlation coefficients of petrophysical parameters with threshold pressure for Rotliegend sandstones

	Depth	*Effective porosity*	*Average capillary*	*Specific surface*	*% of pores >1 μm*	*Treshold diameter*	*Absolute permeability*	*Pth MICP*	*Pth flow*	*Pth step-by-step*	*TPG flow*
Pth MICP	**-0.69**	**-0.67**	**-0.57**	**-0.64**	**-0.63**	**-0.89**	-0.26	**1.00**			
Pth flow	-0.17	-0.34	-0.40	-0.06	-0.28	-0.19	0.15	0.33	**1.00**		
Pth step-by-step	**-0.92**	**-0.85**	**-0.57**	**-0.93**	**-0.61**	**-0.80**	**-0.74**	**0.95**	**0.46**	**1.00**	
TPG flow	**-0.64**	**-0.76**	**-0.66**	**-0.56**	**-0.52**	-0.43	-0.20	**0.52**	**0.72**	**0.80**	**1.00**
TPG step-by-step	**-0.91**	**-0.84**	**-0.56**	**-0.92**	**-0.60**	**-0.79**	**-0.71**	**0.96**	0.44	**1.00**	**0.80**

**In the Tables 1 – 3 above: direct correlation – blue, indirect correlation – red, no correlation – black. If the correlation coefficient is close to 1, it would indicate that the variables are positively linearly related (both variables are increasing or decreasing) and the scatter plot falls almost along a straight line with positive slope. For -1, it indicates that the variables are negatively linearly related (one variable is increasing, second decreasing and vice versa) and the scatter plot almost falls along a straight line with negative slope. Correlation coefficient equal 0 indicates no linear relationship between the variables.*

On Figures 2 and 3 the results of TPG calculations obtained on the basis of using MICP and flow methods are presented. Figure 2 shows the cross plot for Cambrian sandstones (with no fractures) and Figure 3 the cross plot for Rotliegend sandstones. Squares of correlation coefficients for both data sets show good correlation of results.

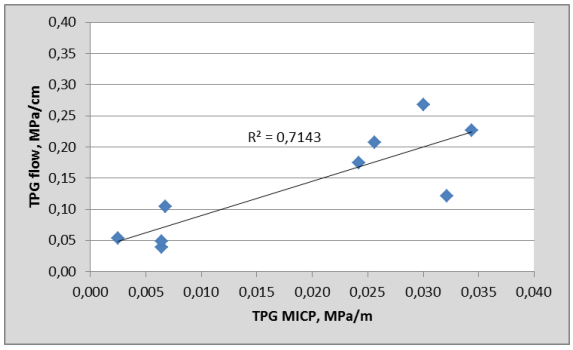

Figure 2. TPG flow vs. TPG MICP for Cambrian sandstones

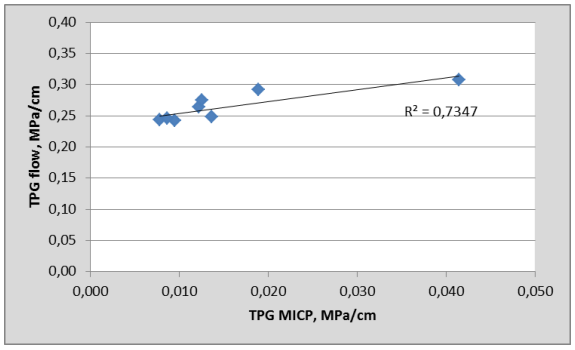

Figure 3. TPG flow vs. TPG MICP for Rotliegend sandstones

CONCLUSION

The analyses conducted in tight sandstones show completely different structure of the pore space due to mineral composition and diagenesis processes which has a strong impact on threshold pressure and consequently on its gradient.

Observed weaker correlations with continuous flow method may be caused by limitation of laboratory equipment (too high minimum flow rate), which generally implies higher values of threshold pressure.

In Cambrian sandstones direct correlation between depth, specific surface and threshold pressure obtained by flow and step-by step method was observed. Estimated correlation between specific surface and threshold pressure for Cambrian rocks without fractures (samples 1 – 9, Table 3) is not typical. Probably, this direct correlation is caused by very low value of specific surface (below 0.2 m^2/g) and suggests slight shift of pore size distribution to lower pore diameters of mesopores.

Moreover, indirect correlations of average capillary, percent of pores > 1 μm and Pth (MICP) and Pth as well as TPG (step-by step) were found.

In the Rotliegend sandstones, indirect correlations between depth, pore space parameters and threshold pressures and their gradients (measured using MICP and step by step method) were observed. Correlation between depth and other analysed parameters shows that evolution of pore space is dependent not only on compaction but also on diagenesis processes (development of secondary porosity).

Obtained results and correlation showed that in the case of Cambrian sandstones without microfactures, mercury intrusion gives very reliable results and might be used as a standard method. For this type of sample, low value of specific surface is a good indicator for choosing MICP approach. In the case of Rotliegend sandstone with more complex pore space distribution, the mercury intrusion approach underestimates the threshold pressure values and another method with higher accuracy should be used to achieve more reliable results.

ACKNOWLEDGEMENTS

The research leading to these results was partially founded from the Polish-Norwegian Research Programme operated by the National Centre for Research and Development under the Norwegian Financial Mechanism 2009 - 2014 in the frame of Project Contract No *Pol-Nor*//196923/49/2013.

REFERENCES

1. Djaouti K., Egermann P., Hennebelle P. "An intergrated approach to estimate threshold capillary pressure from core and log data", *paper prepared for presentation at the International Symposium of the Society of Core Analysts held in Napa Valley, California, USA, 16 - 19 September 2013*
2. Egermann P., Lombard J.M., Bretonnier P. "A fast and accurate method to measure threshold capillary pressure of caprocks under representative conditions", *paper prepared for presentation at the International Symposium of the Society of Core Analysts held in Trondheim, Norway 12-16 September, 2006*
3. Leśniak G., Such P., Sota-Valim M. "Quantitative porosity and permeability characterization of potential Rotliegend tight gas reservoirs", Polish Geological Review, (2010) **58**, 4, 345–351.
4. Poprawa P., Kiersnowski H., "Potential for shale gas and tight gas exploration in Poland", *Biuletyn PIG-NRI*, (2008), 429, 145-152.
5. Schwarzer D., Littke R., "Petroleum generation and migration in the "Tight gas" area of the German Rotliegend natural gas play: a basin modelling study", *Petroleum Geoscience*, (2007) **13**, 1, 37-62.
6. Cicha-Szot R., Steinbach A., Marsh M., Gelb J., Linden S., Wiegmann A., Glatt E., Leśniak G., "Survey of recent advances in digital rock physics – benefits of DRP and their application to reservoir characterization", *paper prepared for presentation at the Geopetrol Conference held in Zakopane-Kościelisko, Poland 15 -18 September 2014*
7. Hildenbrand A., Ghanizadeh A., Krooss B.M. "Transport properties ofunconventional gas systems", *Marine and Petroleum Geology*, (2012) **31**, 1, 90 - 99.
8. Hildenbrand A., Schlömer S., Kroos M. "Gas breakthrough experiments on fine grained sedimentary rocks", *Geofluids*, (2002) **2**, 1, 3-23.

ROCK SURFACE CHARACTERIZATION BY IMMERSION CALORIMETRY: WETTABILITY AND SPECIFIC SURFACE AREA

E. Dyshlyuk[1], D. Korobkov[2], V. Pletneva[2]
Schlumberger, [1-]Dahran Carbonate Research and [2-]Moscow Research Center

This paper was prepared for presentation at the International Symposium of the Society of Core Analysts held in St. John's Newfoundland and Labrador, Canada, 16-21 August, 2015

ABSTRACT

Petrophysical properties such as wettability and surface area control hydrocarbon storage and transport properties. In the work being reported in this paper, we present the theoretical aspects as well as experimental technique and results of testing and validating a proposed calorimetry technique for specific surface area and wettability characterization. Identical immersion calorimetry experiments with slightly different initial conditions of the sample are analyzed to obtain these two properties of a core sample. Validation of the experimental technique is an important step, which is performed in this work by comparing the surface areas of the samples obtained by the proposed technique with the surface area obtained by the well-known Brunauer-Emmett-Taylor (BET) gas-adsorption technique. Surface area measurements are performed on a set of core plugs and reference samples, including hydrophilic and hydrophobic powders of pure substances, minerals, and clays.

INTRODUCTION

This paper is a continuation and enhancement of our previous studies on rock characterization by calorimetry [1, 2]. The differential scanning calorimetry (DSC) technique, which is used in the current study, allows one to measure transient differential heat flows between the two cells of a differential scanning calorimeter. Implementation of the DSC technique to laboratory core analysis can provide a significant amount of valuable information with unprecedented accuracy. In particular, the DSC technique can help to determine wettability heterogeneity of a core sample from adsorption calorimetry [2] pore size distribution from the thermoporometry method, as well as the surface area and average wettability state of a rock from immersion calorimetry [1].

In the immersion calorimetry experiments, a core sample is immersed in liquid and the associated small heat effect (immersion enthalpy) is measured with a calorimeter. The heat effect is related to the alteration of the surface energy of the rock surface during the immersion process. Immersion experiments are commonly conducted with the use of a sealed glass ampule containing the sample, which is broken inside the calorimeter cell filled with liquid. After the ampule is broken, liquid fills the surface of the sample; thus, changing the surface energy of the sample. Depending on the choice of initial conditions

of the rock surface, the associated heat effect is related either to the wettability state of the surface or to the surface area of the sample. As a result, two important petrophysical parameters can be measured by an accurate thermodynamic technique with calorimetry.

The total heat that evolves, ΔH, during an immersion experiment or the enthalpy of immersion is related to the variation of the Gibbs free energy (ΔG) of the system by the following expression: $\Delta H = S\left(\Delta G - T\partial\Delta G/\partial T\right)$, where S is the sample surface area and T is temperature. The variation of the Gibbs energy of the system is in fact equal to the variation of the surface energy of the system. If a solid is immersed from vacuum conditions, then $\Delta G = \gamma^{S} - \gamma^{SL}$, where γ^{S} is the solid-vacuum interface surface tension and γ^{SL} is the solid-liquid interface surface tension (Figure 1a). At the same time, if a liquid film is on the surface of the sample prior to immersion, the variation of the Gibbs energy is given by $\Delta G = \left(\gamma^{SL} + \gamma^{LV}\right) - \gamma^{SL} = \gamma^{LV}$ (Figure 1b), where γ^{LV} is the liquid-vapor interfacial surface energy/surface tension.

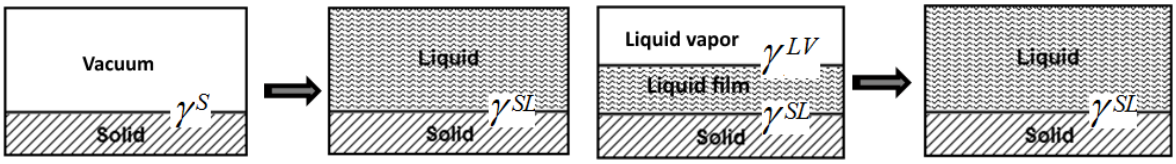

$\Delta G = \gamma^{S} - \gamma^{SL}$

(a) Wettability characterization: $\cos\Theta$

$\Delta G = \left(\gamma^{SL} + \gamma^{LV}\right) - \gamma^{SL} = \gamma^{LV}$

(b) Surface area characterization: S

Figure 1. Illustration of the two immersion experiments—(a) immersion from vacuum for wettability characterization;(b) immersion after precoverage of the sample with a liquid film for surface area characterization.

The first experiment (solid is immersed from vacuum conditions) can be used to characterize the wettability of a sample [1, 3, 4]. Since the surface tension of a liquid, γ^{LV}, (e.g., water surface tension ~ 72 mN/m at 25°C) and its variation with temperature, $\partial\gamma^{LV}/\partial T$, can be measured or are known from the literature, the second experiment (also known as the modified Harkins-Jura procedure [5], which was developed after the original work [6]) can be used for sample surface area measurements as follows :

$$S = \Delta H \Big/ \left(\gamma^{LV} - T\partial\gamma^{LV}/\partial T\right). \quad (1)$$

Although the assessment of wettability of a core sample is the primary target of these experiments, it is quite difficult to perform any other quantitative experiments on wettability measurements to compare the results. Thus, standard core analysis methods such as USBM, Amott, or their modifications do not provide information on the contact angle, while the contact angle method is difficult to implement on porous media. Because the surface area measurement is much easier to quantify by other methods, we decided to validate this technique first by quantitative comparison of surface areas of different

samples measured by the proposed method and the well-known BET gas adsorption technique [7]. The next step of our procedure would be to compare wettability obtained by this method with other known methods.

EXPERIMENT DESCRIPTION AND RESULTS

Immersion experiments are commonly conducted with the use of a sealed glass ampoule containing the sample, which is broken inside the cell that contains the immersion liquid. Another variant of the cell is a membrane cell [8], which consists of two compartments divided by thin metal foil; the upper compartment contains liquid and the lower compartment contains the sample. During the experiment, the membrane is broken by a rod and the liquid wets the sample. For each of these configurations, it is necessary to take into account additional thermal effects appearing in the experiment due to breaking of the ampoule or rupture of the membrane. The disadvantage of using these cells for our future applications in the determination of wettability is that they are not capable of working in high-pressure environments, which is required for wettability experiments at reservoir conditions. To overcome this problem, a special calorimetry cell was developed [9].

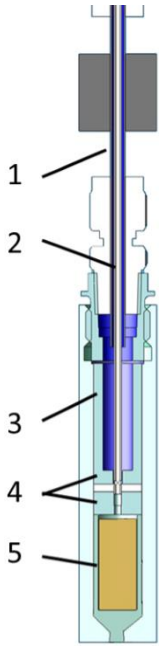

Figure 2. Experimental cell design: 1 external tube; 2 internal moveable tube; 3 wetting liquid compartment; 4 friction-less valve; 5 sample compartment.

The special calorimetry cell provides: 1) a means for connecting the sample to the vacuum/ vapor system for pretreatment the sample; i.e., vacuum the sample and/or adsorb the liquid film on the surface; 2) both the immersion liquid and the sample had to be in the same calorimetric cell during the experiment in order to exclude mass-heat transfer during immersion of the sample; 3) for the heat effect due to combining both volumes of

the sample and the liquid so as to not influence the results and be reproducible and for being systematically accounted.

The designed cell (Figure 2) is equipped with two coaxially arranged tubes (1 and 2 in Figure 2) (1/16-in. tube into a 1/8-in. tube, respectively), independently connected to external volumes. The internal tube is used for evacuation of the sample and vapor adsorption, while the external tube is used for filing of the cell with the wetting liquid. The inner tube can move in the vertical direction; i.e., when it is in the bottom position, the sample is in a contact with a line for evacuation and vapor adsorption, but when it is lifted up vertically (with a special pneumatic device), the cell compartments are connected and the liquid fills the sample volume through the valve. The sample compartment is a 9-mm diameter, 20-mm tall cylinder.

Prior to the experiment, a sample in the lower compartment should be dried in a vacuum under a specific temperature (typically 85°C) to remove any loosely adsorbed vapors from the surface. An experiment is initiated under a "zero" pressure condition. The preliminary evacuated cell containing the sample to be studied is filled with the wetting liquid vapor to create continuous film on the sample surface. The heat effect due to vapor adsorption can be used for surface wettability heterogeneity evaluation [2] (not described here). The immersion step is now completed, resulting in the second heat effect peak (Figure 3), which is used for surface area assessment in accordance with Eq. (1).

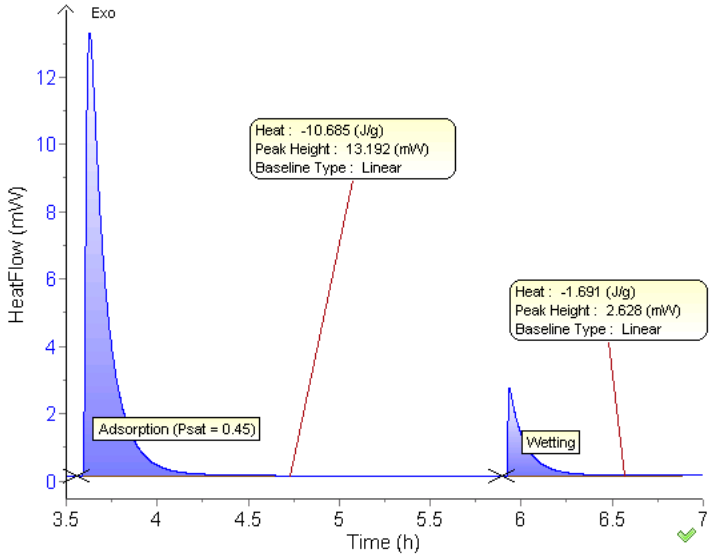

Figure 3. Adsorption-immersion heat flow curve

It is important with the proposed method that the absorbed liquid layer be sufficiently thick so that the liquid layer screens the surface from the other molecules. In this case, the variation of the Gibbs energy during the immersion step is equal to γ^{LV} and the interpretation of the results of experiments with Eq. (1) is valid. This condition is fulfilled

when the thickness of the adsorbed layer is equal to approximately 1.5 monolayers of adsorbed species [5]. When using water as a liquid, this condition is most often fulfilled for hydrophilic samples if the liquid layer is adsorbed with humidity of ~ 45 % [5]. At the same time, this condition might not hold with the hydrophobic samples or when the adsorption isotherm of a hydrophilic sample is starting very slowly during the first half of the adsorption isotherm, as for example probably the case with the carbonate samples [2]. All of the experiments performed in this work were with distilled water, and the liquid film is adsorbed from the 45% humidity atmosphere, which is created by an external water-filled and temperature-controlled tank.

Surface area measurements with calorimetry were performed on artificial and natural powders and carbonate rocks (Table 1). The measurement time at each step of ordinary adsorption-immersion experiment was approximately 2 hours. In the case of clays, we had to increase the experimental time (three to six times until the baseline stabilized) for both the adsorption and immersion step to measure complete adsorption and immersion heat effects accurately. The specific surface area of the porous samples was also measured by the BET method (some by two independent laboratories to evaluate the measurement precision).

As shown in Table 1, the correspondence between the measured specific surface areas is very good for a majority of the samples (including some mesoporous controlled pore glass CPG powders) except for those samples marked in gray. Poor correspondence in the surface areas is indicated with the bentonite powder, most likely due to the swelling of bentonite in water. Thus, the BET method is able to measure only the external surface of the bentonite, while the calorimetry method can also measure internal surface of the clay. From the opposite point of view, we see a good correspondence between the montmorillonite sample measurements. Montmorillonite is also a swelling clay (actually, the main constituent of bentonite) and one would expect (at least we did) it to behave similar to the bentonite behavior. Our present conclusion is that the montmorillonite powder sample could have gone through an irreversible change in its structure due to eventual water vapor adsorption/condensation. Now, the full surface, including internal one, is exposed to both of the methods.

As was explained previously, proposed method cannot be successfully implemented with hydrophobic samples (carbon) or with samples having a low adsorption of vapor during the first part of the adsorption isotherm (carbonate samples). It is difficult to reach some exact conclusions from the data of these carbonate core sample experiments because the specific surface areas of these samples are very small and consequently, the accuracy of both the BET and calorimetry experiments is not overly high. For now, we can observe that both techniques give the same order of magnitude values and show the same systematic variation; i.e., an increase in the surface area after extraction of the cores. The difference between the measurements with cores can be also explained by the presence of clays (about 5%) and halite (about 5%).

CONCLUSION

Immersion calorimetry experiments allow measuring the surface area of a core sample and its wettability state by two identical experiments with slightly different initial conditions. A special calorimetry cell was developed to allow for determining core sample wettability at reservoir conditions in this experimental work and for future tests. Although understanding wettability is a primary goal of the ongoing study, in the present phase of this work, validation of the measurement technique was required. It is difficult to validate wettability measurements by independent tests; therefore, the current work focused on the validation of the technique by comparing the surface areas of different artificial and natural samples as well as actual core samples. The values for comparison were obtained by a well-known BET gas adsorption technique. Respectable correspondence between the measured surface areas was obtained for most hydrophilic samples, which proves the accuracy of the procedure. Hydrophobic samples and carbonate samples show a more complex behavior, which is anticipated from the theory of the method. Special care should be taken in the future tests during the measurements of samples that contain a considerable amount of swelling clays. Future tests will include analogous experiments with nonpolar hydrocarbons, which will hopefully allow us to overcome the mentioned hindrances when implementing the method for surface area measurements, followed by experiments on core sample wettability measurements.

REFERENCES

1. E. Dyshlyuk, "Application of Differential Scanning Calorimetry to Core Analysis," in *Society of Core Analysts*, SCA2013-055, Napa Valley, California, USA, 2013.
2. E. Dyshlyuk, N. Bogdanovich, D. Korobkov and V. Pletneva, "The measurements of core sample surface wettability heterogeneity by adsorption calorimetry," in *Society of Core Analysts*, SCA2014-088, Avignon, France, 2014.
3. E. Dyshlyuk, "Method for Determining Wettability of a Surface". Russia Patent Claim # 2014109083, February 2015.
4. E. Dyshlyuk, "Method for Reservoir Wettability Properties Determination". Russia Patent 2497098, 2013.
5. S. Partyka, F. Rouquerol and J. Rouquerol, "Calorimetric determination of surface areas Possibilities of modified Harkins and Jura procedure," *Journal of Colloid and Interface Science*, vol. 68, pp. 21-32, January 1979.
6. W. Harkins and G. Jura, "An Absolute Method for the Determination of the Area of a Finaly Divided Crystalline Solid," *Am. Chem. Soc.*, vol. 66, pp. 1362-1366, 1944.
7. S. Brunauer, P. Emmett and E. Teller, "Adsorption of Gases in Multimolecular Layers," J. *Am. Chem. Soc*., vol. 60, p. 309, 1938.
8. P. Aukett, "A New Membrane Cell for the Determination of Heats of Immersion Using the Setaram C-80 Microcalorimeter," J. *Thermal Analysis*, vol.33, p.323, 1988.
9. E. Dyshlyuk and V. Baldygin, "Device for Measurement of Heats of Adsorption and Wetting". Russia Patent 2524414, 2014.

Table 1. Specific surface area of powders and core plugs obtained by different methods.

Powder and core samples name, material	Surface area, from manufacture, m^2/g	Surface area by immersion calorimetry, m^2/g	Surface area by BET, m^2/g
Reference samples (artificial and natural powders)			
CPG 3000C (pore Ø: 300 nm), borosilicate glass	8.4	9.3	9.5
CPG 1000C (pore Ø: 100 nm), borosilicate glass	26.6	23	27
CPG 500C (pore Ø: 50 nm), borosilicate glass	49.5	43	54
Corundum, Al_20_3	155	197	153
Corundum, Al_20_3		11.3	12.4 - 14.5*
Corundum, Al_20_3		11.5	12.2 - 14.0*
Quartz, SiO_2		6.0	6.9 - 8.3*
Kaolinite		10.3	10
Montmorillonite		265	232
Bentonite		250	15.6
Calcium carbonate, $CaCO_3$		1.2	3.8
Carbon, C		1.0	1.75
Core plugs, carbonate rock, before/after extraction (described in [2])			
Sample 1		0.20 / 0.54	0.04 / 0.27
Sample 2		0.07 / 0.40	0.00 / 0.30
Sample 3		0.57 / 0.62	0.18 / 0.33
Sample 4		0.63 / NA	0.20 / 0.28
Sample 5		NA / 0,63	0.12 / 0.24

* BET measurements by two independent laboratories